UNIVERSITÀ
DELLA CALABRIA

Self-Assembling Supramolecular, Nanometric and Mesoscaled Materials: Synthesis, Optical and Morphological Characterization

Giuseppe Di Maio

Supervisor: Massimo La Deda

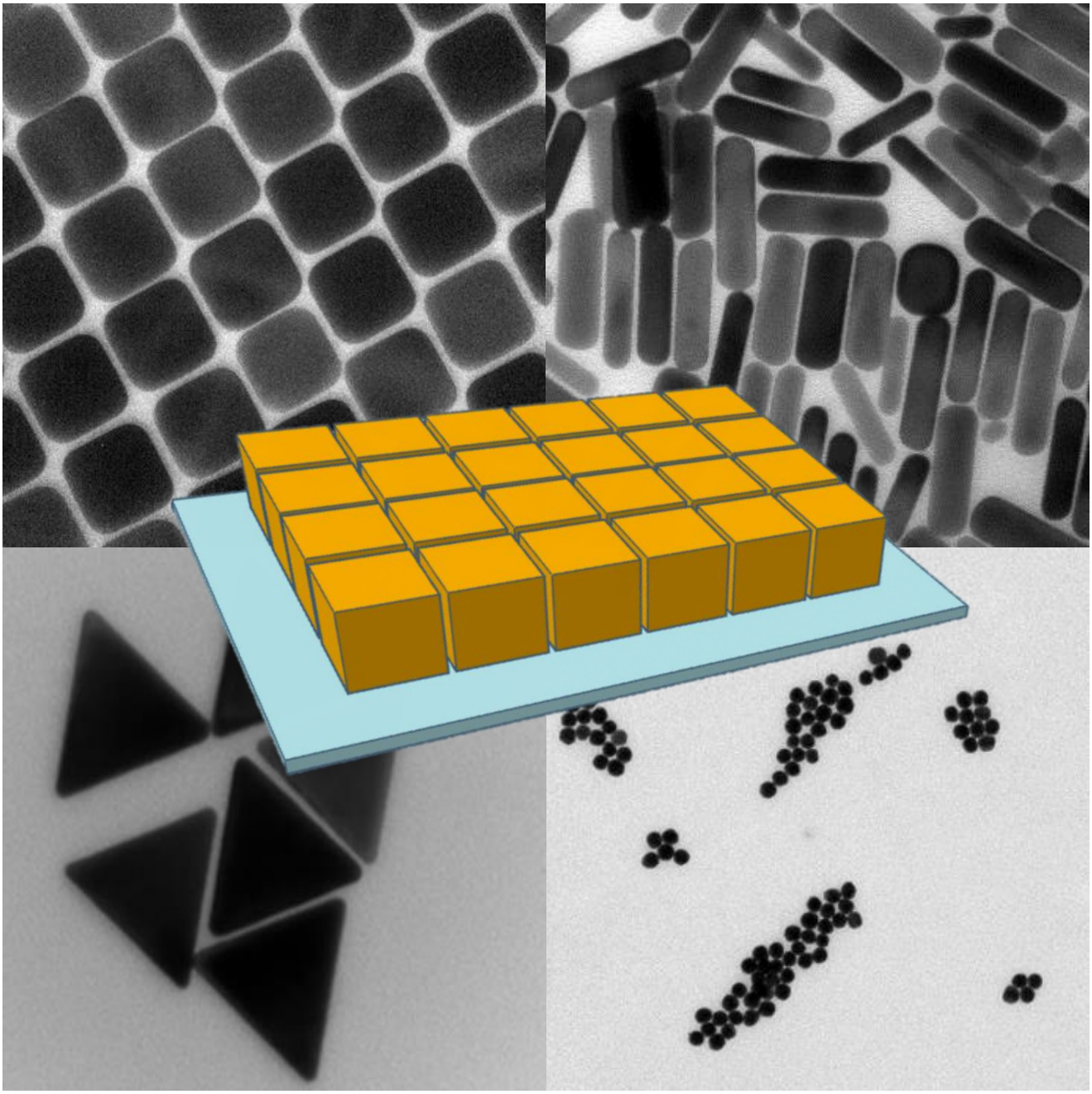

Department of Chemistry and Chemical Technologies

UNIVERSITA' DELLA CALABRIA

Dipartimento di Chimica e Tecnologie Chimiche

Dottorato di Ricerca in

Scienze e Tecnologie Chimiche, Fisiche e dei Materiali

Con il contributo di

Regione Calabria

XXXV CICLO

SELF-ASSEMBLING SUPRAMOLECULAR, NANOMETRIC AND MESOSCALED MATERIALS: SYNTHESIS, OPTICAL AND MORPHOLOGICAL CHARACTERIZATION

Settore Scientifico Disciplinare CHIM/03

Coordinatore: Ch.mo Prof. Gabriella Cipparrone

Firma Firma oscurata in base alle linee guida del Garante della privacy

Supervisore/Tutor: Ch.mo Prof. Massimo La Deda

Firma Firma oscurata in base alle linee guida del Garante della privacy

Dottorando: Dott. Giuseppe Di Maio

Firma oscurata in base alle linee guida del Garante della privacy

"La borsa di dottorato è stata cofinanziata con risorse del Programma Operativo Regionale Calabria FSE/FESR 2014 – 2020 (CCI 2014IT16M2OP006)"

UNIVERSITY OF CALABRIA

Department of Chemistry and Chemical Technologies

Doctorate School of Physical, Chemical and Materials Science and Technologies

PhD Thesis

Self-Assembling Supramolecular, Nanometric and Mesoscaled Materials: Synthesis, Optical and Morphological Characterization

SUPERVISOR

Prof. Massimo LA DEDA

PhD CANDIDATE

Giuseppe DI MAIO

XXXV Cycle

“Good material often stands idles for want of an artist.”
Lucius Annæus Seneca

Acknowledgements

First, I would like to express my sincere and infinite gratitude to my supervisor, **Professor Massimo La Deda**, for the knowledge shared with me and for their continuous support during these three years. He gave me complete freedom to express and test my ideas in the laboratory, giving me the best opportunity to grow as a person and as a scientist.

I am deeply grateful to **Dr. Elisabeta Ildyko Szerb**, who supervised my collaboration with the Institute of Chemistry "Coriolan Dragulescu" – Timisoara, Romania. Unfortunately, the pandemic situation does not allow me to reach Timisoara to carry out my training period abroad in person. Anyway, this collaboration has been very inspiring and productive for me.

A special mention goes to Dr. Angela Candreva, for everything she taught me about the synthesis and characterization of gold nanoparticles.

Furthermore, I thank all the other people who have been part of the MAT_IN Lab group (Department of Chemistry and Chemical Technologies of the University of Calabria) in these three years: Prof. Iolinda Aiello, Prof. Alessandra Crispini, Prof. Nicolas Godbert, Prof. Nadia Marino, Dr. Debora Policastro, Dr. Eugenia Giorno, Dr. Francesco Parisi, Dr. Andreea Ionescu, Dr. Rossella Caligiuri, Dr. Francesca Scarpelli, and Dr. Loredana Ricciardi of the CNR NANOTEC of Rende. They helped me in everything I needed, contributing to make these 3 years of PhD wonderful and inspiring.

I am very grateful to Dr. Roberto Termine, of the CNR NANOTEC of Rende, for both theoretical and practical support in the preparation of the samples and in the measurement of the electrical conductivity of the AuNC monolayers.

I would like to express my appreciation to Dr. Daniela Perrotta, and to Dr. Mariano Davoli (Laboratory of Electron Microscopy - Department of Biology, Ecology and Earth Sciences of the University of Calabria), who respectively performed the TEM and SEM images of all my samples, working patiently to fulfill all my requests.

Last but not least, I want to thank my family and all my friends for their continued help and support during this long and challenging journey.

A glance at the Thesis: scope and limitations

Investigating the difference between matter and material may appear obvious or superfluous; instead, the question can generate an interesting discussion, especially if we involve the properties, structure and processing of the material. The main difference between matter and material is that material it is designed by man to perform a certain function, which depends on the properties of the material itself, which in turn depend on its structure (see Fig. 1).

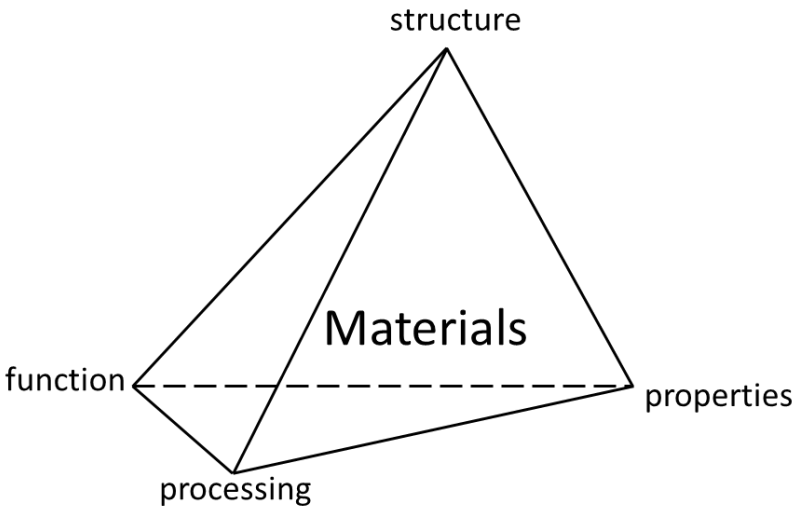

Figure 1 - Material science is the investigation of the relationship among structure, properties, processing, and function of materials.

Referring to the categories shown in the figure, a material can be classified according to function, properties, structure and processing. In this way we have materials to support or to build, such as concrete or steel pillars, wooden beams, bricks and so on; or materials to coat or protect or decorate (such as paints, refractory bricks, sheaths, textile fibers, etc.). From this point of view, a drug is a material intended to cure; there are materials to transduce or store energy that make up the devices: think of a solar panel or an OLED lamp or a battery. In each case these are applications of materials designed for a function based on their properties.

As far as their properties are concerned, a material has different ones depending on the external agents with which it interacts. For example, a material that interacts with a field of mechanical forces will show tensile or pressure resistance properties, while if it interacts with other substances it will show its chemical properties; if it interacts with heat, we will classify it according to its thermal properties. If it interacts with an electric field, it is classified according

to its conducting properties. Finally, if it interacts with the electromagnetic field, it will open the vast field of light-matter interaction.

The interaction of a material with an external agent, however, not only defines its properties, but is itself a means to determine these properties: once again, electromagnetic radiation is a formidable means of investigation to determine the structure of a material.

The properties of a material depend on the structure of its "building block", which can be of molecular, supramolecular or nanometric dimensions. Up to having a macroscopic dimension: for example, in a laminated wood beam, its main property, that of supporting, derives from the thickness and length of the beam (Fig.2).

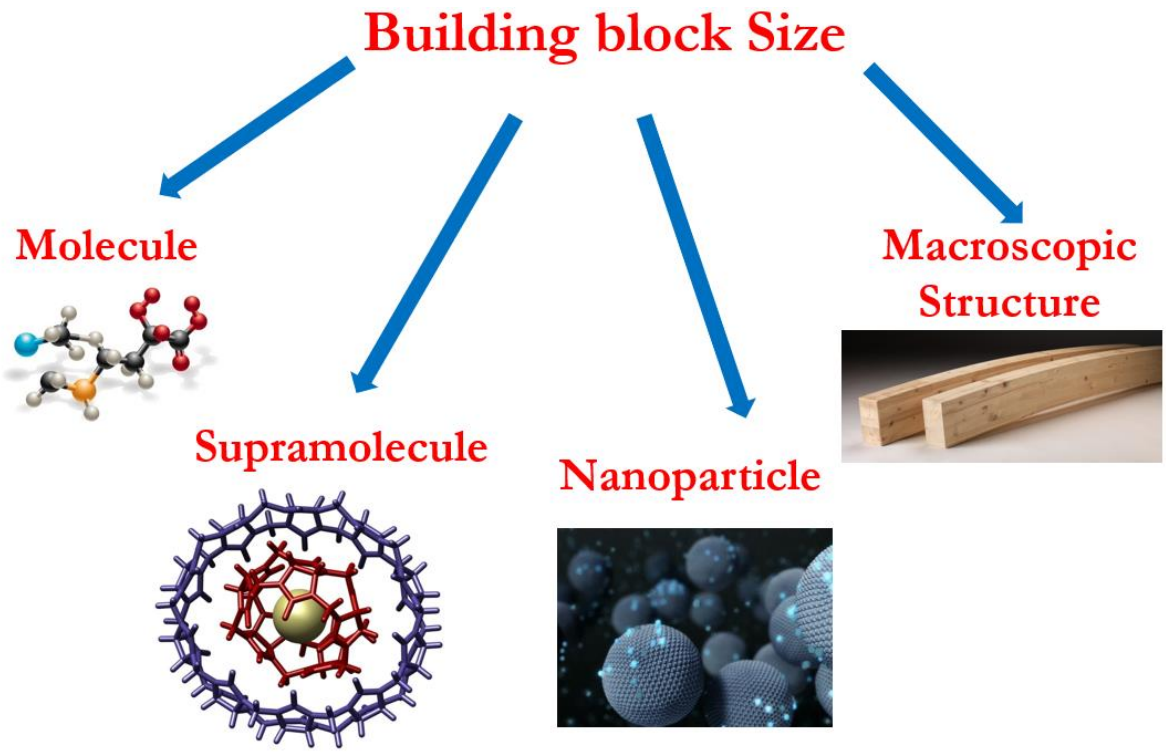

Figure 2 - Materials classified according to their building block size.

The building blocks in turn are held together by various types of bonds: for example, covalent bonds in molecules, van der Waals interactions or other types of weak interactions, in supramolecular systems, or metallic bonding in metal nanoparticles, just to name a few.

The aim of this PhD Thesis, which collects the results achieved in the three-years PhD course at the Department of Chemistry and Chemical Technologies of UniCal, is to correlate

morphological and optical properties of some type of materials ranging from supramolecular to nanoscale, showing, in the latter case, the peculiarities of the synthesis of nanomaterials with respect to the classical chemical synthesis of molecular materials.

The research work was performed at the Inorganic Materials Laboratory (MAT_IN Lab) of the University of Calabria under the supervision of Prof. Massimo La Deda, with the collaboration of Dr. E. Szerb research group of “Coriolan Dragulescu” Institute of Chemistry, based in Timisoara (Romania), which performed the synthesis and thermal characterization of liquid crystals studied during this course.

A series of metallomesogens will be illustrated as an example of supramolecular material, while gold nanoparticles of different shapes and sizes will be presented as a study of nanomaterials. In both cases their optical properties have been studied, and the different origin of these properties has been highlighted, closely linked to the different structure of these two types of materials: while in liquid crystals the photophysical properties are described in the context of theory of molecular electronic states, in the case of nanoparticles the optical properties derive from the cloud of electrons that surrounds a metallic nanoparticle, giving rise to the confinement of the electromagnetic radiation described by the localized surface plasmon resonance.

Concerning gold nanoparticles, their optical properties will be discussed in relation to their shape and size, the coupling effects of the plasmon field of self-assembled nanoparticles will be investigated, and finally we will look at the fascinating possibility of "talking” between the plasmon field of a gold nanoparticle and the electronic energy of molecular chromophores interacting with the nanoparticle.

All these aspects are strongly related to the preparation of these nanosized samples, their morphology and surface chemistry. Therefore, a large part of the Thesis will illustrate the methods of synthesis of nanoparticle systems, focusing on the specificity of this synthesis.

Nanoparticles synthesis is based on premises quite different from classical molecular synthesis. In fact, chemical synthesis methods are based on processes close to equilibrium and therefore generally reversible; from this it follows that the syntheses are repeatable, the control of the initial conditions is rather simple as they are well defined and depend on a few parameters, and above all the final product (a molecule) is well defined and individual.

The synthesis of metal nanoparticles, on the other hand, is a far from equilibrium process, in which small fluctuations of the initial conditions sometimes lead to very different results. This

implies that the syntheses are difficult to repeat, as the final product is not well defined: nanoparticles are obtained whose shapes are not identical to each other and whose dimensions cover a more or less wide range. In general, every synthesis, precisely due to the excessive importance that the initial conditions have on the final outcome (and therefore the impossibility of having rigorous control over them) leads to a statistical distribution of shapes and sizes centered on an ideal shape and size towards which the synthetic protocol is conceived.

However, having made these necessary premises, the conditions for directing the synthesis of gold nanoparticles towards the shapes and sizes necessary to obtain the desired plasmonic responses will be illustrated in the following pages. This is the result of an accurate study of the gold nanocrystal growth processes and of the environmental conditions (concentration, temperature, reaction volumes, coating agents, operating sequences) which allow them to be controlled. On the basis of the same premises, it is possible, through an accurate study of the surface chemistry of gold nanoparticles, to direct their self-assembly towards the formation of nanoparticle films that give rise to mesoscale organized systems, showing new and exciting plasmon couplings.

The final result illustrates how the principles of nanochemistry can be usefully used to obtain new materials for which the shape-property correlation takes on a new and deeper meaning and heralds interesting developments.

The Thesis in a nutshell

Chapter 1 – Introduction to light-matter interaction phenomena. A brief review of the essential theoretical concepts necessary to introduce the reader to main light-matter interaction phenomena has been made. In particular, the focus of this Thesis is on the interaction of light with molecules (*i.e.* absorption and emission of light) and gold nanoparticles (*i.e.* localized surface plasmon resonance).

Chapter 2 – Photophysical characterization of luminescent metallomesogens. In this chapter, we present the photophysical characterization of luminescent metallomesogens of Zn, and Pt. The photophysical properties of these materials are studied both in solution an in solid state and correlated with the structural properties of each sample.

Chapter 3 – The "seed-mediated growth": a versatile pathway for the synthesis of gold nanoparticles. Herein the synthesis and characterization of gold nanoparticles of various shape (cubes, spheres, triangles, and rods) were carried out through seed mediated growth approaches, followed by a thorough discussion about the main chemical-physical principles that conduct to the formation of different shapes and to their peculiar optical properties.

Chapter 4 – Self-assembling of AuNP at water/hexane interface: towards gold nanoparticles two-dimensional monolayers. Then, the synthesized AuNP are organized in large ordered arrays through the self-assembly at a water/hexane interface technique. The optical properties of AuNP arrays were studied trough UV-Vis spectroscopy and correlated with morphological properties arising from SEM and XRD characterization. Then, the electrical conductivity of these intriguing nanomaterials was measured.

Chapter 5 – Metal enhanced fluorescence from gold nanoparticles self-assembled monolayers. In the last part of the Thesis preliminary studies about the effectiveness of AuNP monolayers prepared during this PhD research work as plasmonic substrates for Metal Enhanced fluorescence were presented, depositing a fluorophore on AuNP film and measuring the variation of its emissive properties.

Appendix – Finally, in the appendix, all the experimental methods adopted during these studies were deeply described, and all supporting information are provided. Furthermore, in the section A5 all the scientific publications carried out by the author during its PhD course were reported. Two of these works, *i.e.* GD_1 and GD3, are part of this thesis and deeply discussed in chapter 2. The remaining works have not been included in this thesis, as they deviated from the main topics treated.

Summary

Chapter 1 – Introduction to light-matter interaction phenomena 1

1.1 - Light-molecules interactions: absorption of light 3

1.2 - Light-molecules interactions: excited state deactivation paths 5

1.3 - Interaction of light with noble metal nanoparticles: localized surface plasmon resonance 9

1.4 - Collective properties of gold nanoparticles: plasmon coupling 11

1.5 - Interaction of gold nanoparticles with fluorophores: metal enhanced fluorescence 13

References 15

Chapter 2 – Photophysical characterization of luminescent metallomesogens 19

2.1 – Structural properties of Pt(II) and Zn(II) terpyridine complexes 21

2.2 - Photophysical characterization of Pt (II) – terpyridine complexes 26

2.3 - Photophysical characterization of Zn (II) – terpyridine complexes 30

2.4 – Conclusions 34

References 35

Chapter 3 – The "seed-mediated growth": a versatile pathway for the synthesis of gold nanoparticles 37

3.1 – Seed-mediated growth synthesis of AuNC@CTAB 43

3.2 - Synthesis and characterization of AuNS@$Na_3C_6H_5O_7$ 57

3.3 - Synthesis and characterization of AuNT@CTAC 59

3.4 - Synthesis and characterization of AuNR@CTAB 63

3.5 - Conclusions 67

References 70

Chapter 4 - Self-assembling of AuNP at water/hexane interface: towards gold nanoparticles two-dimensional monolayers 74

4.1 - Experimental procedure for the self–assembly of AuNP at water/hexane interface 76

4.2 - Principles that control the self-assembly of AuNP at water/hexane interface 78

4.3- Improving the quality of AuNP 2D arrays 80

4.4 - Morphological analysis 86

4.5 - PXRD characterization of AuNP monolayers *91*

4.6 – UV-Visible characterization: effect of the film morphology on the plasmon response of AuNP monolayers *96*

4.7 - UV-Visible characterization: effect of nanoparticles shape on the plasmonic response of AuNP monolayers *100*

4.8 - Substitution of 1-dodecanethiol with p-terphenyl-4,4'-dithiol *101*

4.9 - Electrical response of AuNP monolayers *106*

4.10 – Conclusions *110*

References and notes *112*

Chapter 5 - Metal enhanced fluorescence from gold nanoparticles self-assembled monolayers *116*

5.1 - Preliminary studies of AuNP monolayers as MEF substrates *117*

5.2 – Conclusions *123*

References *124*

Final Remarks *126*

References *132*

APPENDIX *134*

A.1 - Experimental section *134*

References *140*

A.2 - Tables *141*

A.3 – Figures *146*

A.4 – AuNP samples collection *154*

A.5 –Scientific Publications *164*

Chapter 1 – Introduction to light-matter interaction phenomena

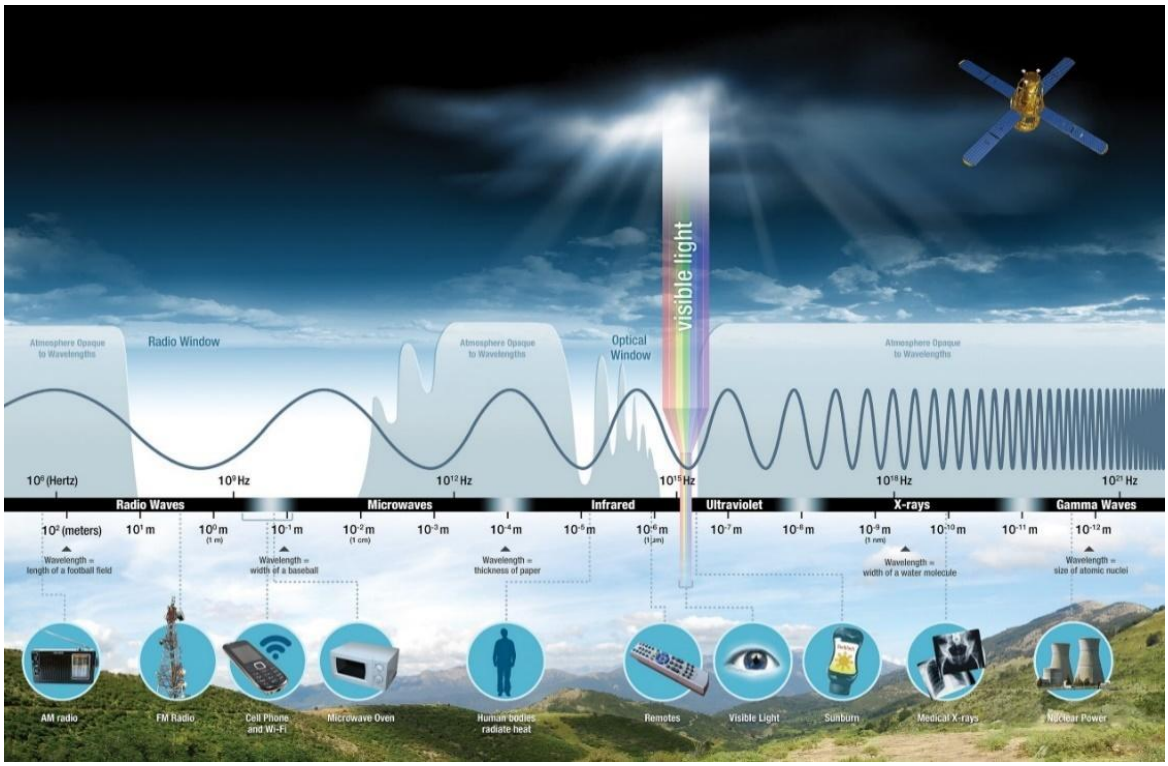

Figure 1.1 – The electromagnetic spectrum collects all the possible frequencies of electromagnetic radiation. [1]

With the term "light" is commonly indicated the portion of electromagnetic spectrum perceptible by the human eye, characterized by wavelength that range between 400 and 700 nm (see Figure 1.1). This type of energy, united with UV and IR electromagnetic radiation, is produced by nuclear fusion reactions in the Sun, and constitutes the most important form of energy in our solar system. Our presence on Earth was possible thanks to solar energy, which triggered several photochemical reactions essential for the development and proliferation of life forms. At the start, UV sunlight transformed the hydrocarbons and cyanocarbons present on the atmosphere of primordial Earth, bringing to the formation of more complex molecules like proteins and nucleic acids, which are the building blocks of living organisms. Then, through the photosynthesis, bacteria, algae, and plants start to absorb sunlight and convert H_2O and CO_2 in energy rich compounds, producing as "waste product" the oxygen necessary for life of all others living organisms. [2] Millions years later, the uncontrolled development of human civilization is leading to the depletion of the planet's energy resources. Once again, the exploitation of solar energy in substitution of fossil fuels could be the key for a sustainable subsistence of humankind on Earth.

For all these reasons, the study and understanding of interaction between light and matter constitutes a crucial as well as fascinating research field. When a UV-Visible photon interacts with matter, various phenomena can take place, depending on what we mean with the term "matter". For example, if we consider a single atom or a molecule, the photon can be absorbed depending on its wavelength, and the energy acquired can be returned as light (through a phenomenon called *luminescence*) or converted in other energy forms like heat or chemical energy. An extraordinary example of spontaneous emission of visible electromagnetic radiation from atoms and molecules is represented by bioluminescence generated by various molecules or enzymes in some living organisms like firefly, algae, and jellyfishes (Figure 1.2).

Figure 1.2 - Bioluminescence of some aquatic living organism like algae and jellyfishes generates beautiful optical effect by night. [3]

If the material is bigger in size than a molecule, e.g. fine solid dust or colloidal liquid dispersions, the interacting photons will be scattered randomly in any direction. Both these phenomena, i.e. absorption and scattering of electromagnetic radiation at optical frequencies, generates incredible optical properties when the materials considered are noble metal nanoparticles (*i.e.* gold, silver, copper, platinum and so on). The exotic properties of gold and silver nanoparticles were exploited, but not understood, already from the IV century. The Lycurgus cup, a human artefact from the Roman era exposed at British Museum in London, is an extraordinary example of noble metal nanoparticles properties, that emerges from the

interaction with visible electromagnetic radiation: it appears green if radiated from the front, while appears red if back-illuminated (Figure 1.3). This extraordinary *dichroic effect* is due to the presence of gold, silver and copper nanoparticles with size up to 100 nm inside the glass used for its realization. The red colour observed is the result of absorption of light by gold particles. The purple colour results due to the absorption by the larger particles while the green colour is attributed to the light scattering by colloidal dispersions of silver particles with size bigger than 40 nm. [4]

Figure 1.3 - Images of Lycurgus cup exposed at the British Museum in London. [5]

The phenomenon on the basis of this behaviour of noble metals at the nanoscale is called, as we see, *surface plasmon resonance* and obviously did not generates only such beautiful optical effects but is also responsible of many interesting functional properties of noble metal nanoparticles that can be found applications in various fields like electro-optical devices, energy conversion, and medicine only to name a few. [6-14]

1.1 - Light-molecules interactions: absorption of light

The interaction of light with molecules is studied by photophysics. When a photon of frequency in the UV-visible range interacts with a molecule it can "excite" their electrons in the HOMO, *i.e.* the energy of the photon is absorbed by the electron and an electronic transition from the *ground state* to an *excited state* takes place. This happens if the energy of the incident photon corresponds exactly to the difference in energy between the electronic states involved in the transition. The intensity of an absorption event depends on selection rules, which establish if a particular electronic transition is allowed or not. In the case of the absorption of a photon, two

selection rules must be taken into account: the symmetry selection rule attests that an electronic transition can take place between different orbitals, *i.e.* $\Delta l \pm 1$; the spin selection rule attests that electronic transitions are allowed if the multiplicity of electronic spins is conserved, *i.e.* $\Delta S \neq 0$. However, some electronic transitions theoretically forbidden by selection rules can be observed under particular conditions, but their intensity is lower compared to those allowed. [15] The *absorption spectrum* of a sample, *i.e.* the ensemble of all the electronic transitions allowed for that chemical specie, is obtained by comparing the radiation intensity transmitted by the sample (I) with that transmitted by a reference (I_0) according to Lambert-Beer law:

$$A = \ln(T) = \ln(I/I_0) = cd\varepsilon(\lambda) \qquad \text{Eq. 1.1}$$

Where: A is the absorbance of the sample, *i.e.* the natural logarithm of the transmittance (T), c is the molar concentration of the sample, d is the optical path of the light within the sample and $\varepsilon(\lambda)$, called *molar absorptivity*, is a parameter typical of the sample, representing the probability that an electronic transition takes place at a specific wavelength. The structure of the absorption spectrum of a molecule is very different from that of a single atom (see Figure 1.4). In an atom, only the pure electronic transitions was observed, which results in a line structure. In a molecule, there are also rotational and vibrational degrees of freedom, so each electronic transition is accompanied by transitions between roto-vibrational energy states. For this reason, the spectrum of molecules shows a more complex band structure.

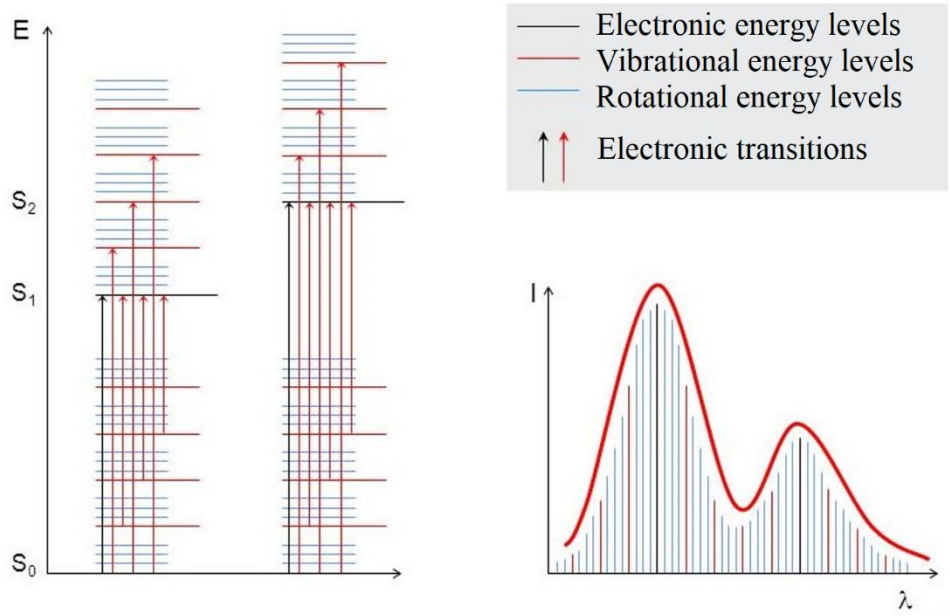

Figure 1.4 - The bands that compound the absorption spectra of a molecule are generated by the sum of electronic transitions each accompanied by transitions between roto-vibrational energy states.

Because electronic transitions that are active in a molecule depend on the presence of particular functional groups, called *chromophores* because they are responsible for the substance colour, the shape and the position of the absorption bands can give extensive information about the molecular structure and their excited state energies. Furthermore, knowing ε(λ) of a sample makes it possible to extrapolate its concentration, enabling various applications in analytical chemistry due to the high sensitivity of this technique.

1.2 - Light-molecules interactions: excited state deactivation paths

Molecules remain in the excited state for a certain time. After that, they spontaneously return the energy acquired. The deactivation of the excited states can follow both chemical and physical pathways. In the case in which the energy of the interacting photon is of the same magnitude of the bound energies a chemical deactivation can take place, *i.e.* the energy acquired is enough to start a *dissociation*, *isomerization*, or a *chemical reaction* that bring to the formation of a new chemical specie. In the case of physical pathways, the energy acquired is returned by the molecule itself radiatively or converted in other forms like heat or mechanical energy. Otherwise, it can be transferred to another molecule through mechanisms like vibrational relaxation, energy or electron transfer, though deactivation processes usually referred to as *quenching* (see Figure 1.5).

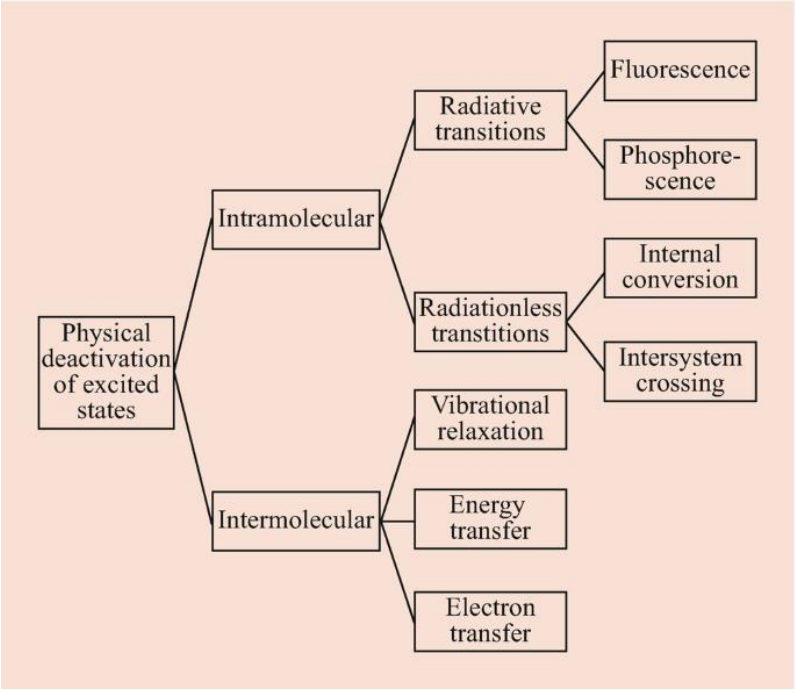

Figure 1.5. Main excited state physical deactivation pathways. [15]

Furthermore, other possible intermolecular pathways involve the interaction of the excited molecule with other molecules to form dimeric structures. If the dimer is formed with a molecule of the same type in the ground state are call *excimer* (excited dimer), while if the interaction takes place with a different chemical species in the ground state we called it *exciplex* (excited complex). The physical processes that can occur in a molecule after an absorption event can be accurately described through energy diagrams known as Jablonski diagrams (see Figure 1.6).

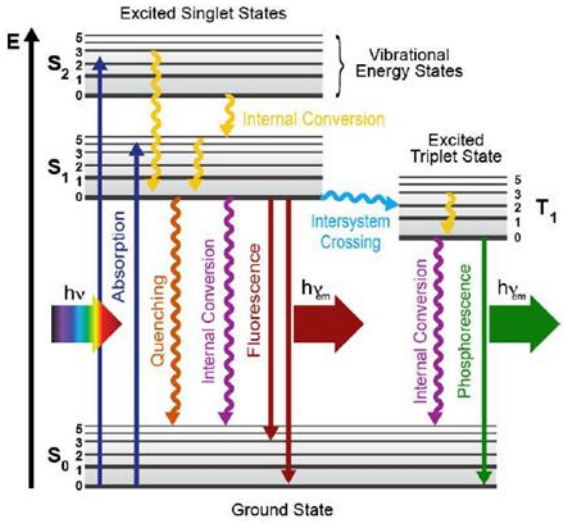

Figure 1.6. Jablonski diagram describes accurately what could happen in a molecule after the absorption of a photon. [16]

Generally, the electronic ground state of a molecule is a singlet (indicated with S_0), while S_1 and S_2 indicate the first two excited states of singlet, and T_1 the first excited state of triplet. Incident electromagnetic radiation can induce the population of different excited states based on its wavelength, this process is known as *excitation* or *absorption* (see paragraph 1.1). Now suppose that a photon with wavelength λ_1 excites the fourth vibrational energy states of the excited state S1, while a photon with wavelength $\lambda_2 > \lambda_1$ excites the third vibrational energy state of the excited state S_2 (blue arrows in figure 1.6). In both cases, the first process that takes place is the partial dissipation of the energy acquired through roto-vibrational energy levels that bring the electron in the lowest energy level of S_1, with a process called *internal conversion (IC)* that generally happens in 10^{-12} s. [17]

From this electronic state, the different processes described in Figure 1.6 can take place:

- The non-radiative decay to the ground state S_0 through the almost cited *internal conversion* or *quenching* with other molecules;
- The radiative emission of the residual energy from the excited state S_1 to the ground state S_0, with a process known as *fluorescence*, typically occurs in 10^{-8} - 10^{-9} s. Because the kinetic of fluorescence is slower than IC processes, the latter happens always before the first, so fluorescence is observed only from the first excited state of the molecule, *i.e.* S_1, this principle is known as *Kasha's rule* and makes the emission spectra of a pure substance independent from excitation wavelength. Furthermore, due to the rapid roto-vibrational relaxation due to IC, the emission wavelength is always lower than the excitation wavelength. The difference in wavelength between the emission maximum and the absorption maximum of the level S_1 is called *Stokes shift* and provides valuable information about the stiffness of the molecular structure.
- The population of the first triplet state T_1, through a process named *intersystem crossing (ISC)*, with consequently non-radiative decay from T_1 to S_0 through IC or a radiative emission process called *phosphorescence*. Because the transition between two electronic states with different spin multiplicity is forbidden by selection rules, the rate constant of phosphorescence is greater than fluorescence (from 10^{-6} to seconds) and their intensity and energy are usually lower. Phosphorescence is usually observed in molecules with heavy atoms like metals and halogens.

The deactivation processes described above can occur simultaneously, *e.g.* for the same molecule some electrons can return to the ground state emitting light while others trough IC.
From an applicative point of view, the most interesting deactivation paths are the radiative ones, *i.e.* fluorescence and phosphorescence. The wavelengths and the intensity at which a molecule emits light after an absorption event can be characterized through the registration of an *emission spectrum*, that is obtained exciting the sample to a fixed wavelength and measuring the intensity of the emission over a given wavelength range (Figure 1.7, blue line). If the Kasha rule applies, and there are systems with only one chemical species present, the position and shape of the emission spectrum will be independent of the excitation wavelength. Usually, coupled to the emission spectra an *excitation spectrum* is reported (Figure 1.7, cyano line), obtained by monitoring the changes in fluorescence intensity as a function of the wavelength of the excitation light. If the Kasha rule is valid, the excitation spectrum results very similar to the absorption spectrum of the sample, confirming the origin of the emission and providing information on how the electronic states communicate.

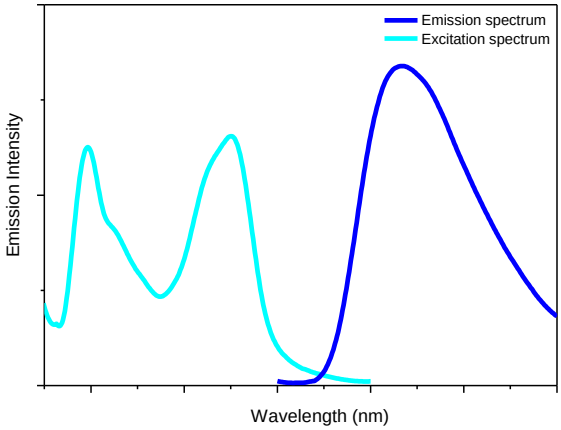

Figure 1.7. Emission (blue line) and excitation (cyano line) spectra of a common dye extensively used as standard in photophysical characterization, i.e. $[Ru(Bipy)_3]Cl_2$.

Until now absorption, emission and excitation spectra have been defined, which allow to understand how a molecule or more generally a chemical species interacts with UV-Visible electromagnetic radiation varying the wavelength. To describe completely the photophysical properties of a sample two other quantities must be defined, i.e. the *emission quantum yield* and the *emission lifetime*. [17] *Emission quantum yield (φ)* quantifies in which proportion a molecule emits (in this case it is called *fluorophore*) the energy previously absorbed, so it is defined as the ratio between photon emitted and photon absorbed. The following Eq. 1.2 can express this ratio in a meaningful way:

$$\Phi = \frac{\Gamma}{\Gamma + k_{nr}} \qquad \text{Eq. 1.2}$$

where: Γ is the rate of fluorescence or phosphorescence, and k_{nr} is the rate of the non-radiative processes.

The *lifetime of the excited state* is defined as the average time that a molecule spends in the excited state prior returning to the ground state, and can be expressed by the following Eq. 1.3:

$$\tau = \frac{1}{\Gamma + k_{nr}} \qquad \text{Eq. 1.3}$$

Generally, fluorescence lifetimes range from hundred nanoseconds to a few picoseconds, while for phosphorescence longer lifetime, even in the order of seconds, can be obtained. Because luminescence is a random process, it will follow a first order kinetic, with an exponential decay.

Therefore, the number of photons emitted will be directly proportional to the concentration of the species in the excited state. What is measured experimentally is a mean emission lifetime, defined as the time at which the concentration of excited states is reduced by a factor of 1/e after the sample was excited many times with a pulsed light source.

The knowledge of how a molecule interacts with UV-Visible light and how return the energy acquired is very important nowadays, because molecules with precise fluorescence properties are required in various technological applications. For example, high luminescent molecules in blue, green, and red regions of visible electromagnetic spectrum are employed in OLED and LCD display technologies (in this case the excitation energy do not come from electromagnetic radiation but from an electrical current), while molecules that emits NIR radiation can be used in biomedical imaging, due to transparency of human tissues at these frequencies. [18, 19]

1.3 - Interaction of light with noble metal nanoparticles: localized surface plasmon resonance

As already said in the introduction of this chapter, when UV-Visible photons interact with noble metal nanoparticles, *localized surface plasmon resonance (LSPR)* can take place. The origin of this phenomenon lies both in the particular size of these materials and in the peculiar characteristic of the metal bond. In a metal, the external electron shell of each metal atom (i.e. the conduction band) overlaps with a large number of neighbouring atoms. Consequently, these electrons continually move from one atom to another and are not associated with any specific pair of atoms. In short, the valence electrons in metals, unlike those in covalently bonded substances, are non-localized, capable of moving relatively freely throughout the entire crystal lattice, forming a *plasma*. Furthermore, at the nanoscale the number of atoms at the surface of the crystals are higher than the atoms in the core, so their properties will determine the properties of the entire nanocrystal. When an incident electromagnetic radiation with wavelength much larger than the nanoparticles size interact with it, a resonance condition was reached, so the electrons in the conduction band start to oscillates, generating an intense electric field, named *plasmon field*, propagating along the surface of the nanoparticle. This results in an intense band, *i.e.* the *plasmon band*, in the extinction spectra of the material (Figure 1.8 A). In the case of nanoparticles, we talk about extinction spectra rather than absorption spectra because two different light-matter interaction phenomena are involved at the same time, i.e. absorption and scattering of the incident electromagnetic radiation both induced by LSPR. Generally, for

nanoparticles with size smaller than 50 nm the absorption prevails on scattering, while for nanoparticles bigger than 50 nm is exactly the opposite.

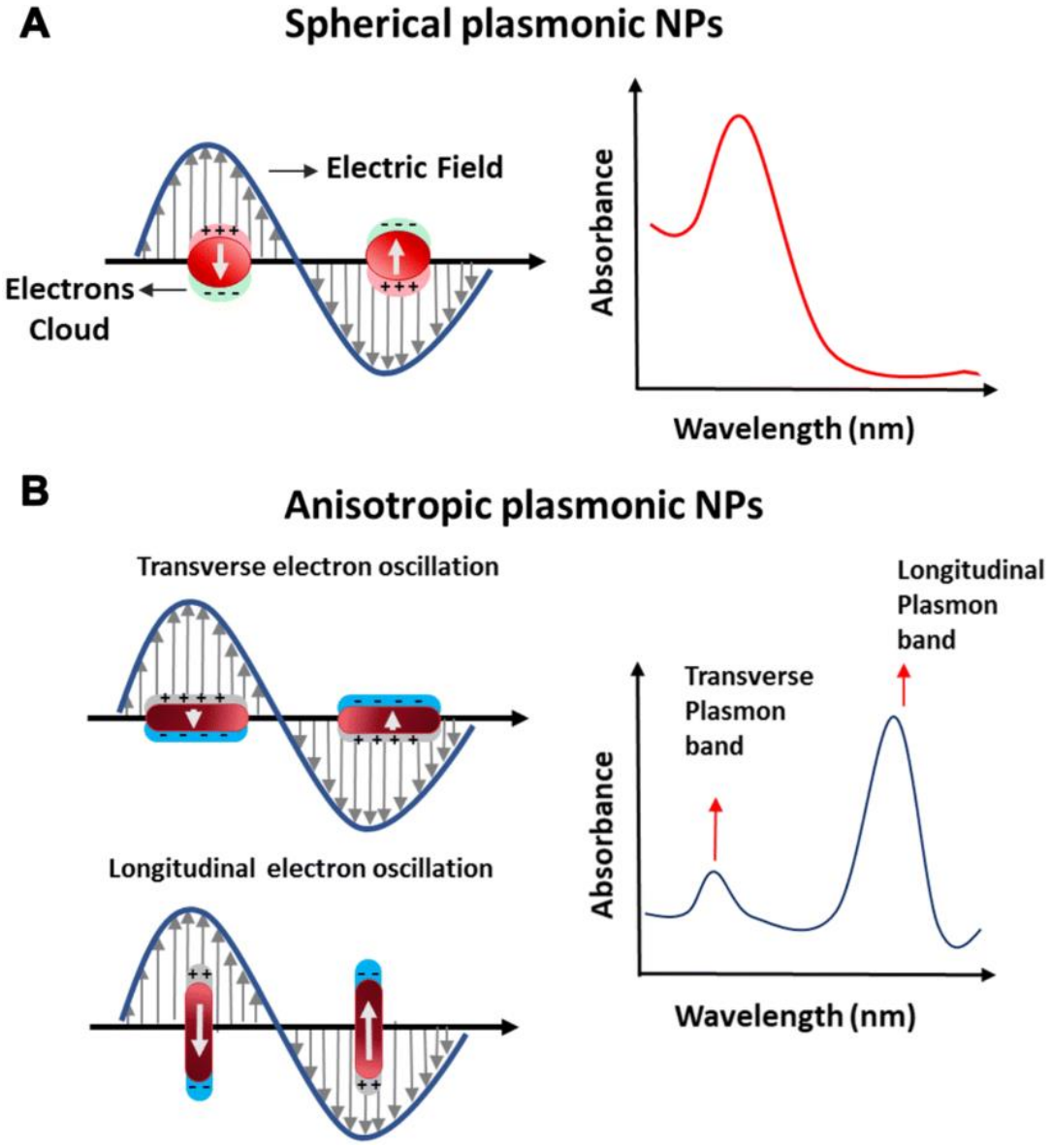

Figure 1.8 – Surface plasmon is the collective oscillation of electron clouds in metal nanoparticles, due to the interaction with an incident electromagnetic field. For spherical particles, it results in an intense band in the extinction spectra of the nanoparticles, called plasmon band (A). In the case of anisotropic particles, more than one plasmon mode are active (B). [20]

An interesting property of noble metal nanoparticles that arise from the fact that surface plasmons propagates along the surface of the particles, at the metal/dielectric interface, is that the resonance frequency depends not only from the intrinsic properties of the metal, but also strongly from the shape and size of nanoparticles, and from the refractive index of their

chemical environment. This means that optical properties of nanoparticles can be finely tuned by changing their shape and/or size in the synthetic phase or by changing their coating agent or the solvent in which they are dispersed. [21, 22] As example, the extinction spectra of Au nanoparticles colloidal dispersion with different shapes, i.e. spheres and rods, were reported in figure 1.8. The shape of the plasmonic band is deeply different, because varying the shape of the nanoparticles also varies the possible oscillation modes of electronic clouds. In the case of a nanosphere, a sharp band centred around 550 nm were observed because the oscillation of electronic clouds is isotropic in any direction of the nanocrystal (Figure 1.8 A). In the case of Au nanorods two oscillation modes are possible: one along the vertical axis, that correspond to the weak plasmon band centred at 515 nm, and the second along the longitudinal axis, which produce an intense plasmon band at longer wavelength (Figure 1.8 B). The position of the longitudinal plasmon band of gold nanorods depends strongly from the aspect ratio of the nanoparticle, i.e. the ratio between the length of the long and the short axis. In particular, the longitudinal plasmonic band red-shifts as the aspect ratio of the nanoparticle increases.

These differences in optical properties of noble metal nanoparticles make them suitable for different technological applications. For example, the plasmon resonance of gold nanospheres at optical frequencies were employed for improve the performance of organic photovoltaic devices or OLEDs, while the strong absorption in the NIR of gold nanorods were used for photothermal therapy and cancer cells imaging. [23-25] Between the various noble metals available, Au is the most promising for use at optical and NIR frequencies because its plasmon resonance can be shaped to coincides with these specific wavelength range of electromagnetic spectra, furthermore it shows enhanced chemical stability than other noble metals. As will see in chapter 3, in the last decades many different synthetic routes were developed to obtain gold nanoparticles, based mainly on the *"seed mediated growth"* approach. These methods bring to the synthesis of gold nanoparticles with size ranging from 2 to 200 nm and with very different shapes (spheres, cube, triangles, rods, stars and so on). [26, 27]

1.4 - Collective properties of gold nanoparticles: plasmon coupling

Another interesting property of noble metal nanoparticles arise from the combination of the plasmonic fields of single nanoparticles when these are in close proximity. When two nanoparticles approach each other, each one will experience not only the incident electromagnetic field (E_0) but also the near-field of the neighbouring particles (E_{np}). Therefore,

each nanoparticle will feel an electric field E that it is exactly the sum between the incident field and the neighbours nanoparticles plasmon fields: [28]

$$E = E_0 + \sum_i E_{np} \qquad \text{Eq. 1.4}$$

This interaction modulates the plasmon response of the system. In fact, the plasmon oscillation when nanoparticles are coupled is favoured, and this results in a red-shift of the plasmon band. The intensity of the red-shift is strongly dependent on the distance between nanoparticles (see Figure 1.9). In detail, lower is the distance between particles stronger is the red-shift of the plasmonic band. When the number of coupled nanoparticles increases, the effect is stronger; furthermore, if the distance between nanoparticles is not constant the plasmonic band experiences an enlargement, because the environment of nanoparticles and therefore the electric field felt is not the same for any particle.

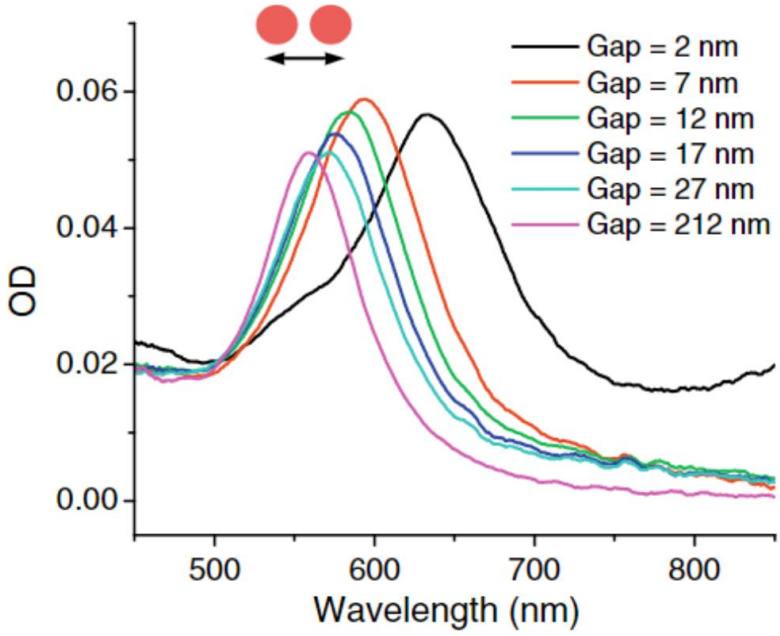

Figure 1.9 – When two nanoparticles are in close proximity the plasmonic band red shift decreasing the distance among particles, due to the optical coupling between their plasmonic fields. [28]

The practical exploitation of plasmon coupling goes through the realization of ordered clusters and arrays of nanoparticles both in solution and in solid state. The creation of a coupled system in solution was performed, for example, through the functionalization of AuNP with dithiols or other molecular linkers that can create clusters of gold nanoparticles bound together. [29, 30] But the greatest efforts have been produced in the last decades for the realization and the study

of coupled nanoparticle systems in solid state. The most used techniques for the creation of AuNPs coupled systems was drop casting, spin coating, dip coating, electrochemical approaches, and interfacial assembling. [31-34] This extensive work produced AuNPs arrays that were used as mechanical sensors [35], plasmon rulers [36] and in metal enhanced spectroscopies in particular to enhance the Raman (Surface Enhanced Raman Scattering, *i.e.* SERS) or the fluorescence signal (Metal Enhanced Fluorescence, *i.e.* MEF) of a chemical species in close proximity. [37, 38]

1.5 - Interaction of gold nanoparticles with fluorophores: metal enhanced fluorescence

How is it possible to enhance the emissive signal of fluorophores using gold, or more generally, noble metal nanoparticles? As known when a fluorophore is located very close to a metal nanoparticle, an energy transfer from fluorophore to nanoparticle occurs, with a nanoparticle that converts the energy acquired in heat, resulting in the quenching of the emission signal. [39] However, when the distance AuNP-fluorophore was higher, *i.e.* from few nanometers up to tens nanometres, a strong increase in the emission signal (until hundreds of times) were detected, accompanied sometimes with a decrease of the lifetime of the excited state and therefore an increase of the photostability of the emitter. [40, 41]

The unified theory of MEF, proposed by Geddes and Lakowicz who first discovered this phenomenon in 2002, attributes the increase of the emission signal to two different effects, called *enhanced absorption* and *enhanced emission* and both these phenomena can contribute to MEF at the same time. *Enhanced absorption* is the simplest one, consisting essentially in the increase of the absorption cross-section of a fluorophore due to the interaction with the plasmonic field of nanoparticles. Because it increases only the rate of absorption events no modifications of the emissive properties of the fluorophores were observed, and take place when there is a superposition of the absorption spectra of the fluorophore with the plasmon band of the metal nanostructure. [42] *Enhanced emission* consist in the coupling of a fluorophore with the plasmon field of the nanostructure, which will act like an antenna and will radiate the coupled quanta. The radiation of the quanta absorbed by fluorophore from surface plasmon is difficult to distinguish from the free space emission of the fluorophore and require a particular experimental configuration. [43] In this case, the coupled quanta radiated by surface plasmon reduce the emission lifetime and increase the quantum yield of the fluorophores. This happens because the metallic nanoparticle constitutes an additional radiative deactivation path

for the energy acquired by the fluorophore. Considering the Eq. 1.2 and 1.3, that defines the quantum yield and the emission lifetime of a fluorophore in the free-space, therefore an additional term, Γ_m, which represent this new deactivation path due to the nanoparticles proximity must be added to take into account the *enhanced emission effect:*

$$\Phi = \frac{\Gamma + \Gamma_m}{\Gamma + k_{nr} + \Gamma_m} \qquad \tau = \frac{1}{\Gamma + k_{nr} + \Gamma_m} \qquad \text{Eq. 1.5}$$

From Eq. 1.5 is clear that greater is Γ_m, greater will be the increase of the quantum yield, while the emission lifetime will be reduced. From these equations it is also clear that the MEF effect will be more effective for fluorophores with low quantum yields. Furthermore, Zhang et al. demonstrate that the maximum effect is achieved when the emission spectra of the fluorophore and the scattering portion of the plasmon band of the nanostructure overlaps. [44]

This strong dependence of MEF from the distance between the fluorophore and the nanostructure, and from their spectral characteristic, make challenging to engineer systems suitable for this purpose, but the enhancement of fluorescence is strongly pursued by researchers because emissive molecules are employed nowadays in various applicative fields like OLEDs, bio-imaging, and in single-molecule detection systems.

References

[1] Website: https://www.media.inaf.it/2021/06/04/viaggio-nello-spettro-elettromagnetico;

[2] B. N. Nunes, C. L. De Barros, D. W. Bahnemann, and A. O. T. Patrocinio, Historical Development of Inorganic Photochemistry, 2022, Springer, 3–25;

[3] Website:https://www.tempostretto.it/news/lo-spettacolare-fenomeno-della-bioluminescenza-marina-ecco-dove-si-puo-ancora-osservare.html;

[4] M. Loos, Nanoscience and Nanotechnology Carbon Nanotube Reinforced Composites, 2015, Elsevier, pp 1–36;

[5] Website: https://en.wikipedia.org/wiki/Lycurgus_Cup;

[6] R. R. Arvizo, S. Bhattacharyya, R. A. Kudgus, K. Giri, R. Bhattacharya, and P. Mukherjee, Intrinsic therapeutic applications of noble metal nanoparticles: past, present and future, 2012, Chem. Soc. Rev., 41, 2943;

[7] C. Dhand, N. Dwivedi, X. Loh, A. Jie Ying, N. Verma, R. Beuerman, R. Lakshminarayanan, S. Ramakrishna, Methods and strategies for the synthesis of diverse nanoparticles and their applications: a comprehensive overview, RSC Advances, 2015, , 5(127), 105003-105037;

[8] X. Huang, S. Neretina, and M. El-Sayed, Gold Nanorods: From Synthesis and Properties to Biological and Biomedical Applications, 2009, Advanced Materials, 21(48), 4880-4910;

[9] C. Yao, L. Zhang, J. Wang, Y. He, J. Xin, S. Wang, H. Xu, Z. Zhang, Gold Nanoparticle Mediated Phototherapy for Cancer, 2016, Journal of Nanomaterials, vol. 2016, 1-29;

[10] S. Fang, C. Li, J. Lin, H. Zhu, D. Cui, Y. Xu, Z. Li, Gold Nanorods-Based Theranostics for Simultaneous Fluorescence/Two-Photon Luminescence Imaging and Synergistic Phototherapies, 2016, Journal of Nanomaterials, vol. 2016, 1-10;

[11] J. L. Wu, F. C. Chen, Y. S. Hsiao, F. C. Chien, P. Chen, C. H. Kuo, M. H. Huang, and C. S. Hsu, Surface plasmonic effects of metallic nanoparticles on the performance of polymer bulk heterojunction solar cells, 2011, ACS Nano, 5, 959–67;

[12] L. Qiao, D. Wang, L. Zuo, Y. Ye, J. Qian, H. Chen, S. He, Localized surface plasmon resonance enhanced organic solar cell with gold nanospheres, 2011, Applied Energy, 88(3), 848-852;

[13] M. Notarianni, K. Vernon, A. Chou, M. Aljada, J. Liu, N. Motta, Plasmonic effect of gold nanoparticles in organic solar cells, 2014, Solar Energy, 106, 23-37;

[14] V. Pareek, A. Bhargava, R. Gupta, N. Jain, and J. Panwar, Synthesis and Applications of Noble Metal Nanoparticles: A Review, 2017, Adv. Sci. Eng. Med., 9, 527–44;

[15] A. Sarto Polo, and K. Passalacqua Morelli Frin, Fundamentals of Photochemistry: Excited State Formation/Deactivation and Energy Transfer Processes, 2022, Springer, 27–48;

[16] Website: https://www.simtrum.com/WebShop/SolutionInfo.aspx?id=1669;

[17] J. R. Lakowicz, Principles of fluorescence spectroscopy, 2006, Springer;

[18] G. Hong, X. Gan, C. Leonhardt, Z. Zhang, J. Seibert, J. M. Busch and S. Bräse, A Brief History of OLEDs—Emitter Development and Industry Milestones, 2021, Adv. Mater., 33, 2005630;

[19] G. Hong, A. L. Antaris, and H. Dai, Near-infrared fluorophores for biomedical imaging, 2017, Nat Biomed Eng, 1, 0010;

[20] D. Alba-Molina, J. J. Giner-Casares, and M. Cano, Bioconjugated Plasmonic Nanoparticles for Enhanced Skin Penetration, 2020, Top. Curr. Chem., 8, 378;

[21] F. Vallée, Optical Properties of Metallic Nanoparticles Nanomaterials and Nanochemistry, 2007, Springer, 197–227;

[22] V. Amendola, R. Pilot, M. Frasconi, O. M. Maragò and M. A. Iatì, Surface plasmon resonance in gold nanoparticles: A review, 2017, Journal of Physics Condensed Matter, 29, 203002;

[23] Y. Harada, K. Imura, H. Okamoto, Y. Nishijima, K. Ueno, and H. Misawa, Plasmon-induced local photocurrent changes in GaAs photovoltaic cells modified with gold nanospheres: A near-field imaging study, 2011, J. Appl. Phys., 110, 104306;

[24] Y. Zhuang, L. Liu, X. Wu, Y. Tian, X. Zhou, S. Xu, Z. Xie, and Y. Ma, Size and Shape Effect of Gold Nanoparticles in “Far-Field” Surface Plasmon Resonance, 2019, Particle & Particle Systems Characterization, 36, 1800077;

[25] X. Huang, I. H. El-Sayed, W. Qian and M. A. El-Sayed, Cancer Cell Imaging and Photothermal Therapy in the Near-Infrared Region by Using Gold Nanorods, 2006, J. Am. Chem. Soc., 128, 2115–20;

[26] P. Zhao, N. Li, and D. Astruc, State of the art in gold nanoparticle synthesis, Coord. Chem. Rev., 2013, 257, 638–65;

[27] Y. Xia, K. D. Gilroy, H. C. Peng, and X. Xia, Seed-Mediated Growth of Colloidal Metal Nanocrystals, 2017, Angewandte Chemie - International Edition, 56, 60–95;

[28] P. K. Jain, and M. A. El-Sayed, Plasmonic coupling in noble metal nanostructures, 2010, Chem. Phys. Lett., 487, 153–64;

[29] M. Quintiliani, M. Bassetti, C. Pasquini, C. Battocchio, M. Rossi, F. Mura, R. Matassa, L. Fontana, M. V. Russo and I. Fratoddi, Network assembly of gold nanoparticles linked through fluorenyl dithiol bridges, 2014, J. Mater. Chem. C, 2, 2517–27;

[30] S. K. Ghosh and T. Pal, Interparticle Coupling Effect on the Surface Plasmon Resonance of Gold Nanoparticles: From Theory to Applications, 2007, Chem. Rev., 107, 4797–862;

[31] Song L., Huang Y., Nie Z., and Chen T. Macroscopic two-dimensional monolayer films of gold nanoparticles: Fabrication strategies, surface engineering and functional applications, 2020, Nanoscale, 12, 7433–60;

[32] J. Magura, A. Zeleňáková, V. Zeleňák, and M. Kaňuchová, Thiol-modified gold nanoparticles deposited on silica support using dip coating, 2014, Appl. Surf. Sci., 315, 392–9;

[33] H. Schlicke, J. H. Schröder, M. Trebbin, A. Petrov, M. Ijeh, H. Weller, and T. Vossmeyer, Freestanding films of crosslinked gold nanoparticles prepared via layer-by-layer spin-coating, 2011, Nanotechnology, 22, 305303;

[34] M. Retsch, Z. Zhou, S. Rivera, M. Kappl, X. S. Zhao, U. Jonas, and L. Qin, Fabrication of large-area, transferable colloidal monolayers utilizing self-assembly at the air/water interface, 2009, Macromol. Chem. Phys., 210, 230–41;

[35] L. Minati, A. Chiappini, F. Benetti, G. Speranza, D. Zonta, A. Piotrowska, M. Marciniak, A. Vaccari, and M. Ferrari, Fabrication and optical properties of assembled gold nanoparticles film on elastomeric substrate, 2015, Colloids Surf. A Physicochem, Eng. Asp., 482, 431–7;

[36] R. T. Hill, J. J. Mock, A. Hucknall, S. D. Wolter, N. M. Jokerst, D. R. Smith, and A. Chilkoti, Plasmon Ruler with Angstrom Length Resolution, 2012, ACS Nano, 6, 9237–46;

[37] Y. Wang, H. Chen, and E. Wang, Facile fabrication of gold nanoparticle arrays for efficient surface-enhanced Raman scattering, 2008, Nanotechnology, 19, 105604;

[38] C. Joyce, S. M. Fothergill, and F. Xie, Recent advances in gold-based metal enhanced fluorescence platforms for diagnosis and imaging in the near-infrared, 2020, Mater. Today Adv., 7, 100073;

[39] A. Synak, B. Grobelna, Raut S, P. Bojarski, I. Gryczyński, J. Karczewski, and T. Shtoyko, Metal enhanced fluorescence of flavin mononucleotide using new plasmonic platform, 2016, Opt. Mater., 59, 136–40;

[40] A. I. Dragan, E. S. Bishop, J. R. Casas-Finet, R. J. Strouse, J. McGivney, M. A. Schenerman, and C. D. Geddes, Distance Dependence of Metal-Enhanced Fluorescence, 2012, Plasmonics, 7, 739–44;

[41] K. Ray, R. Badugu, and J. R. Lakowicz, Distance-Dependent Metal-Enhanced Fluorescence from Langmuir−Blodgett Monolayers of Alkyl-NBD Derivatives on Silver Island Films, 2006, Langmuir, 22, 8374–8;

[42] R. Knoblauch, and Geddes C. D., Review of Advances in Metal-Enhanced Fluorescence, 2019, Springer, 253–83;

[43] H. Mishra, A. Dragan, and C. D. Geddes, UV to NIR Surface Plasmon Coupled and Metal-Enhanced Fluorescence Using Indium Thin Films: Application to Intrinsic (Label-less) Protein Fluorescence Detection, 2011, The Journal of Physical Chemistry C, 115, 17227–36;

[44] Y. Zhang, A. Dragan and C. D. Geddes, Wavelength dependence of metal-enhanced fluorescence, 2009, Journal of Physical Chemistry C, 113, 12095–100;

Chapter 2 – Photophysical characterization of luminescent metallomesogens

Liquid crystals well illustrate a step of the molecule-nanostructure process, as they represent not only an intermediate phase between the liquid phase and the solid one (a mesophase) but also an intermediate dimension, the supramolecular dimension, whose properties depend significantly on both the shape of the molecule and their supramolecular organization.

For example, it is very clear how the shape of a molecule determines its organization in the mesophase, and how the latter determines its thermal, electrical, and optical properties.

An ensemble of molecules shows a certain grade of order (both rotational and/or translational) that is typical of crystalline solids, maintaining the flows properties of liquid systems (no positional order). Liquid crystals can be differentiated in *thermotropic* and *lyotropic*: the former shows mesophases varying the temperature, and are of interest for applications in electro-optic displays, temperature, and pressure sensors; the latter shows mesophases varying the concentrations and/or the solvent and are of great interest biologically playing an important role in living systems. [1] Thermotropic liquid crystals can be classified based on the structural properties of its molecules, which determines the type of ordered system obtained. The main mesophases observed for thermotropic liquid crystals are depicted in figure 2.1.

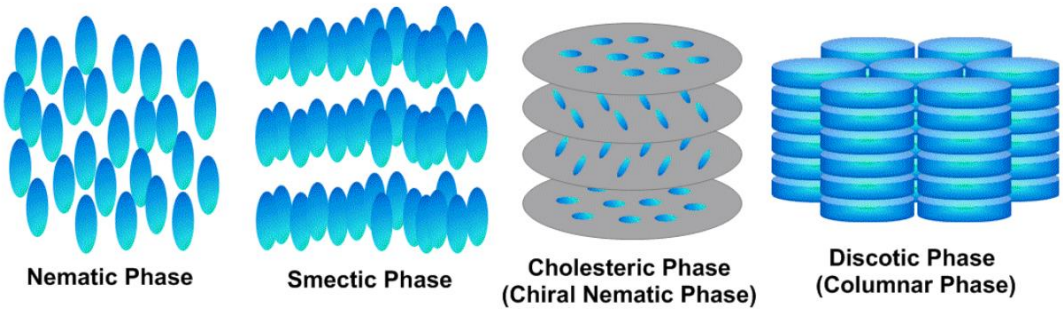

Figure 2.1 – Main mesophase that can be observed in thermotropic liquid crystalline systems from ref. [2].

The nematic, cholesteric, and smectic phases are typical of molecules with elongated shape. The nematic phases are the less ordered (and thus more fluid); there is long-range orientational order, i.e., the molecules tend to align parallel to each other, but no-long range correlation of the molecular centre of mass positions. [1] A particular case are the cholesteric phases, typical of chiral molecules, which show the same characteristics of nematic phases but with a periodicity in the alignment of molecules that tend to form a long-range helicoidal periodic

structure. On the other hand, the smectic phases, are the most ordered, since in addition to the rotational order, the molecules also possess a degree of translational order which induces the formation of long-range layered structures (this make these phases more viscous and thus more similar to a solid phase). Finally, the discotic, or columnar, phases are typical of aromatic system (with a disk-like shape), which can form a one-dimensional columnar structure due to the possibility of stacking intermolecular interactions.

Photophysical characterization in dilute solution is a valid instrument for studying the optical properties of single molecules, because the large distance between them prevent intermolecular interactions. For this reason, the comparison between the photophysical properties in solution and in mesophase can be a valid aid to investigate the effect of the supramolecular structure on these properties. Furthermore, the solid phase characterization will help to understand the differences between the solid and the mesophase, emphasizing the different intensities of the intermolecular forces governing the formation of supramolecular structures.

In order to understand how supramolecular organization can influence the optical properties of single molecules the photophysical characterization of various Pt(II) and Zn(II) metal complexes were carried out both in dilute solution and in solid state and correlated with thermal and structural studies. These studies are parts of research works already published, thanks to the collaboration with Dr. E. Szerb research group of "Coriolan Dragulescu" Institute of Chemistry, in Timisoara and Professor B. Donnio group in Strasbourg. [3, 4] The former dealt with the synthesis and thermal characterization (POM, DSC, TGA) of the samples, the latter with structural characterization trough X-ray diffraction techniques (S/WAXS, GIWAXS).

2.1 – Structural properties of Pt(II) and Zn(II) terpyridine complexes

The structural formulas of the metal complexes studied in this chapter, synthesized by Dr. E. Szerb research group of "Coriolan Dragulescu" Institute of Chemistry, in Timisoara (Romania), were depicted in Figure 2.2 and 2.3.

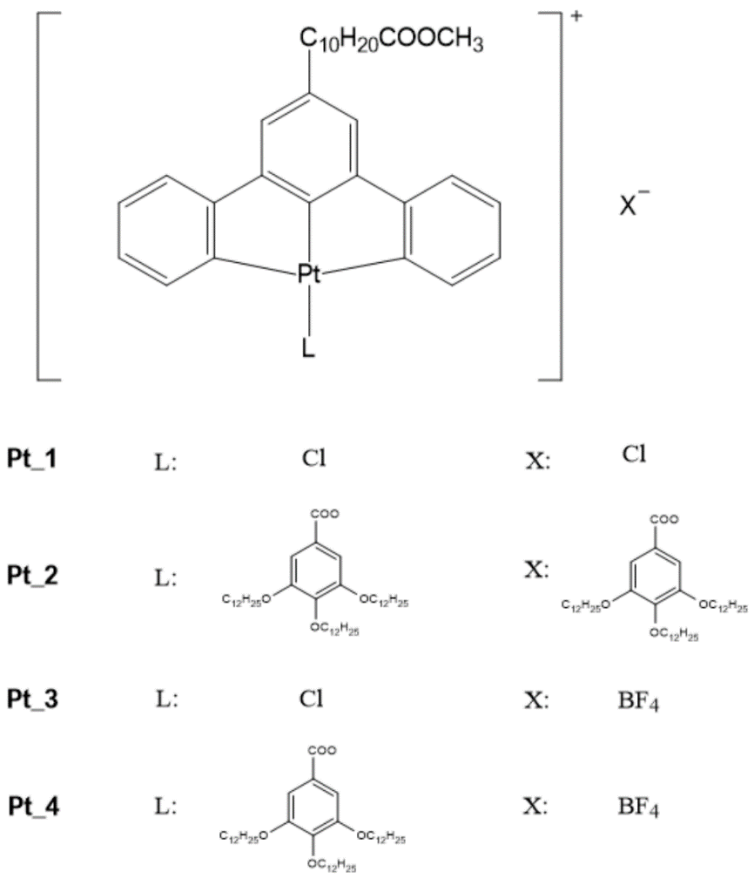

Figure 2.2 - Structural formulas of Pt(II) terpyridine complexes.

The Pt(II) complexes (**Pt_1-4,** Figure 2.1) are all constituted of a terpyridine (tpy) ancillary ligand functionalized with methyl 11-hydroxyundecanoate (R) and due to the electronic configuration of the metal centre, the complexes results positively charge. They differ in the secondary ligand (L) and in the counterion (X). In particular, **Pt_1** and **Pt_3** have a chloride as a secondary ligand and Cl^- and BF_4^- as counterion respectively, while **Pt_2** and **Pt_4** have as secondary ligand a 3,4,5-tridodecyloxy benzoic acid, with the 3,4,5-tris(dodecyloxy)benzoate as counterion the first, and a BF_4^- the latter.

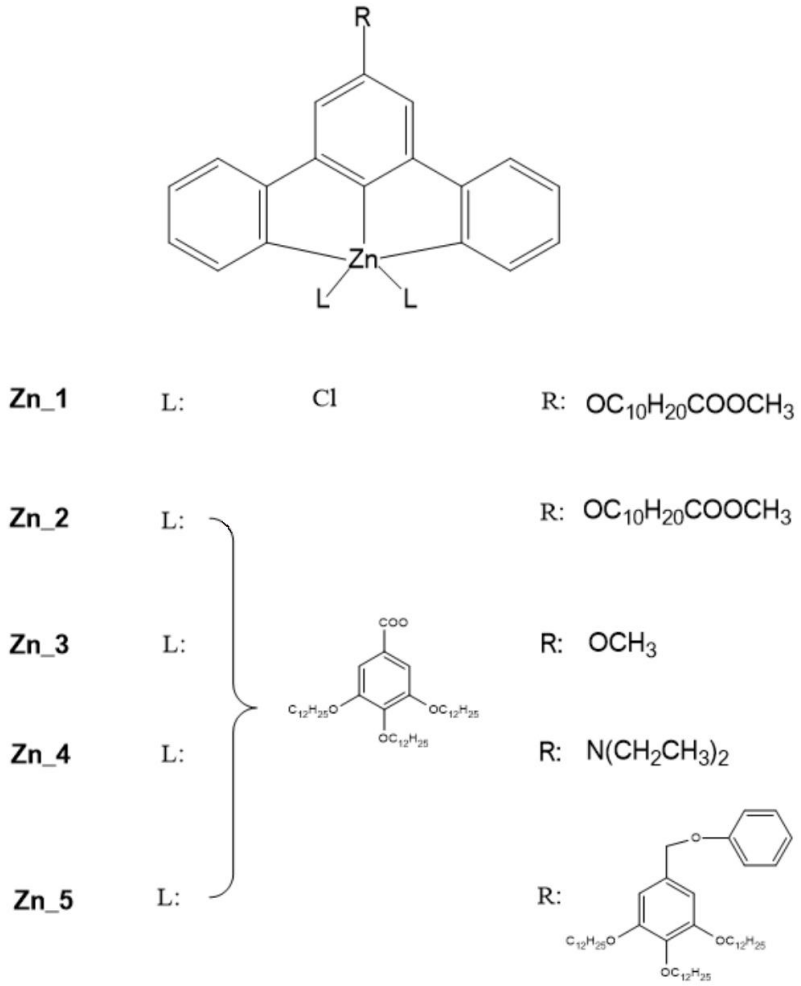

Figure 2.3 - Structural formulas of Zn(II) terpyridine complexes.

By substituting Pt with Zn, neutral complexes were obtained instead (Figure 2.3). **Zn_1** and **Zn_2** are the structural analogous of **Pt_1** and **Pt_2** presenting as secondary ligands two chloride and two 3,4,5-tris(dodecyloxy)benzoate units respectively. Finally, in samples **Zn_3-5** what varies respect to **Zn_2** is the tpy substituent, with the 11-hydroxyundecanoate replaced by methoxybenzene, N,N-diethylaniline, and 3,4,5-tris(dodecyloxy)benzylphenylether unit for **Zn_3**, **Zn_4**, and **Zn_5** respectively.

The result of the thermal and morphological characterizations of these samples (see references [3], and [4] for details) evidenced a different thermal behaviour, due to different types of supramolecular organizations, which are generated by the different molecular structures. The main results of these analyses were reported in table 2.1 and discussed below.

Table 2.1 - Thermal behaviour of Pt(II) and Zn(II) terpyridine complexes.

Complex	$T_{dec\ 5\%}$ *(°C)* [a]	*Thermal behaviour: …starting phase [transition temperature*[b]*(in °C)] final phase…*
Pt_1	**155**	**Dec**
Pt_2	**303**	**Cr [37.1] M + Col_{hex} [~100-155] Iso [140.0] Iso + Col_{hex} [84.9] M + Col_{hex} [18.5] Cr [39.2] M + Col_{hex} [89.3] Iso + Col_{hex} [155] Iso**
Pt_3	**280**	**Cr [170] Iso**
Pt_4	**285**	**Lam_{Colr} [65-135] Lam_{Col} [255] Iso**
Zn_1	**246**	**Cr [243] Iso**
Zn_2	**309**	**Col_{hex} [101] Iso [108] Col_{hex}**
Zn_3	**297**	**M_{hex} [229] Iso [228] M_{hex}**
Zn_4	**301**	**M_{hex} [188] Iso [187] M_{hex}**
Zn_5	**314**	**Col_{hex} [164] Iso [167] Col_{hex}**

[a] Decomposition temperature at 5% weight-loss (from TGA). [b] Determined on first cooling and second heating for mesomorphous compounds, and only first heating for the others.
Legend: Cr, crystalline phase; M, melting; Col_{hex}, hexagonal columnar mesophase; Iso, isotropic liquid; Lam_{Col}, lamellar columnar mesophase; Lam_{Colr}, lamellar columnar mesophase with rectangular symmetry; M_{hex}: three-dimensional mesophase with a two-dimensional hexagonal lattice symmetry (see text), Col_{hex}: two-dimensional columnar hexagonal mesophase.

The complexes with chloride as ligand (L), *i.e.* **Pt_1**, **Pt_3,** and **Zn_1**, were obtained as amorphous or crystalline solids, and their thermal behaviour is simple. Increasing the temperature **Pt_3**, and **Zn_1** will pass directly from the solid (Cr) to the liquid phase (Iso), while, in the case of **Pt_1** before this transition take place the thermal decomposition (Dec) of the sample occurs. The presence of lipophilic benzoate units as ligands (**Pt_4** and **Zn_2-5** in Scheme 1) or as both ligand and counter anion (**Pt_2** in Scheme 1) results in the induction of mesomorphic properties varying temperature (see table 2.1).

The thermal behaviour of **Pt_2** is rather peculiar and complicated. Various mesophases, in some cases coexisting, have been observed during the heating/cooling cycles and was attributed to the partial dissociation of one benzoate group during the first thermal treatment. Unfortunately, this lack of thermal stability precludes any conclusive remarks on its supramolecular behaviour.

Pt_4, and **Zn_2-5** complexes are all room temperature liquid crystals. In details, the platinum complex with only one gallate group, **Pt_4**, shows lamello-columnar phases until 255 °C. These

phases are constituted by **Pt_4** molecules π-stacked into columns that self-assemble with counter-ions into layers alternating with aliphatic chains (see Figure 2.4). At low temperature, rings are nearly orthogonal to layers, and chains stretched onto the layer normal; the superimposition of layers defines a rectangular lattice of one lamella and two columns periodicity (Lam_{colr}). At higher temperature, fluctuations of ring orientations out of the lamellar plane are enhanced, which causes elongation of columns and lateral expansion of lamellae, which in turn affects the regularity of π-stacking. The columnar superstructure finally vanishes in the following lamello-columnar mesophase (Lam_{Col}) that preserves the long-range correlated lamellar structure and a local-range ribbon periodicity from average lateral distances between piled complexes.

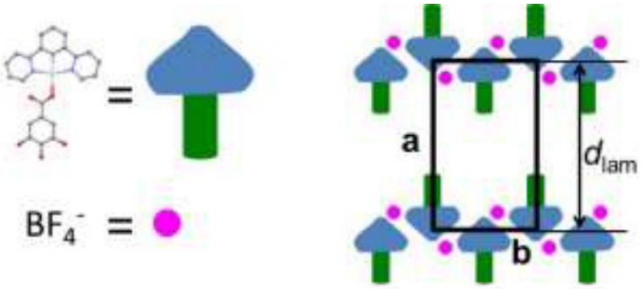

Figure 2.4 - Left: model of Pt_4 complex moieties and benzoate units, as reconstructed from single crystal structures; Right: schematic representation of the likely molecular organization in the LamColr mesophase. Columns of stacked complexes and BF_4^- counter-ions arrange in staggered rows; gallate units and molten alkyl chains (not represented) fill the gap between successive staggered rows. The *a*-axis coincides with a lamellar periodicity *d*lam, maintained after heating in the LamCol mesophase, while the rectangular long-range lattice is suppressed by thermal fluctuations allowing successive column rows to move laterally one to another. [3]

Zn_2 and **Zn_5** self-assemble into two-dimensional columnar hexagonal mesophases (Col_{hex}) until 108 °C the former, and 164 °C the latter. Columns are constituted by π-stacking interactions between the aromatic cores, and are surrounded by a crown of irregularly closed-packed alkyl chains formed by substituents of the tpy and benzoate rings (see figure 2.5, right side).

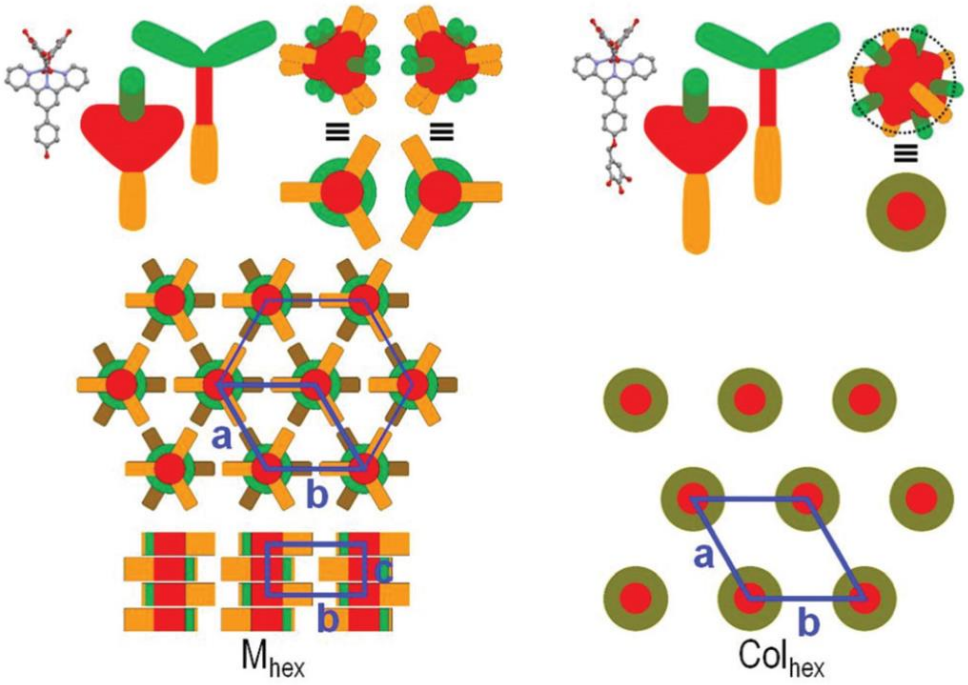

Figure 2.5 - Left, top: view of the aromatic moiety of Zn_1, representations of the molecular architecture and of groups of p-stacked molecules; left, centre: supramolecular self-assembly of Zn_1 and Zn_2 in the M_{hex} phase: hexagonal arrangement of groups of π-stacked molecules (chains not represented, dark green: groups from the layer below the top layer); left, bottom: superposition of groups of π-stacked molecules into a row of segmented columns. Right, top: view of the aromatic moiety of Zn_3, representations of the molecular architecture and of columns of π-stacked complexes surrounded by a shell mixing benzoate and benzyloxyphenyl segments; right, bottom: arrangement of columns and chains (not represented) in the Col_{hex} phase. [4]

Finally, **Zn_3** and **Zn_4** give rise to complexes 3D superstructures with a 2D hexagonal symmetry (M_{hex}). These compounds self-organize through π-stacking of tpy rings into columnar structures (Fig. 2.5, left). The crowding of the long chains connected only on one side of the cores forces the complexes to stack on top of each other with rotation angles in the order to distribute equally chains and R-benzyloxyphenyl groups around the columnar cores. Consequently, the protruding benzyloxyphenyl moieties confer the shape of a cross with three branches to the cross-section of columns. The columns, disposed at the nodes of the hexagonal lattice, adopt the most compact in-plane arrangement for this shape that consists in directing ‘‘crossed branches’’ toward ‘‘cross centres’’ of neighbouring columns. This arrangement by nature follows the hexagonal symmetry but combines the segmentation of columns into smaller subunits. Only three over six neighbouring columns are indeed pointed by crossed branches (due to the chains’ deficit on one side of the complex) and optimal space-filling presumably requires that pointed and non-pointed columns regularly swap along columnar axes, resulting in segmentation in groups of stacked molecules with inverted orientations.

2.2 - Photophysical characterization of Pt (II) – terpyridine complexes

Photophysical characterization in solution. The photophysical properties of the complexes in solution have been investigated in DMSO for **Pt_1**, **Pt_3**, **Pt_4**, and in CH_2Cl_2 solution for **Pt_2**. The results are summarized in Table A.2.1 in appendix. All Pt (II) complexes present a pale yellow colour in diluted solutions and absorb in the UV region with weak bands in the visible region of the electromagnetic spectra (Figure 2.6). The spectra show a well-resolved structure with numerous peaks that can be collected in three main regions: lowest intensity bands in the 450-500 nm range; medium-intensity peaks in the 370-400 nm region; high-intensity bands below 350 nm. While the spectral shape is almost unvaried by changing the counterion or the ancillary ligand, the ε-values are different.

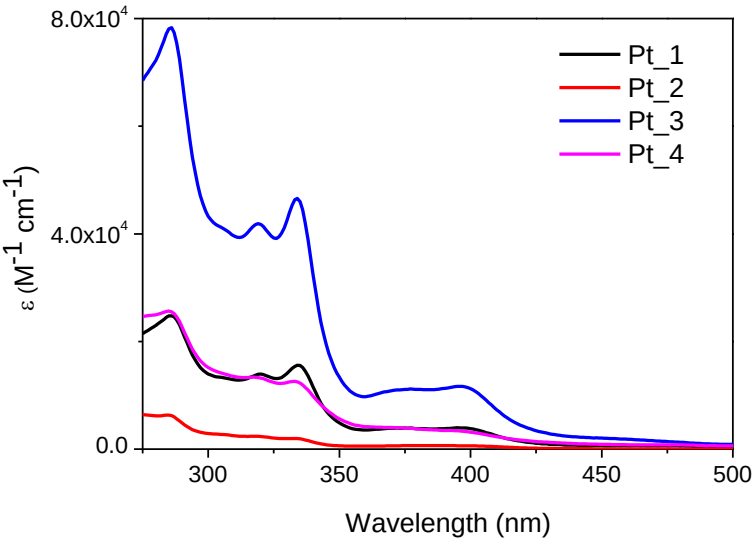

Figure 2.6 - Absorption spectra of Pt (II) complexes in dilute DMSO (Pt_1; Pt_3; Pt_4) or CH_2Cl_2 (Pt_2) solutions.

All solutions are weakly fluorescent at room temperature (Figure 2.7), with broad and structureless emission bands in the green-red region (peaks located from 600 to 650 nm) of the visible spectrum. The emission quantum yields measured in air-equilibrated solution at room temperature are low and range from 0.2 to 1.7 %. The emission intensity decay has been fitted with a mono-exponential function giving lifetime values between 251 and 397 ns (Table A.2.1 in Appendix).

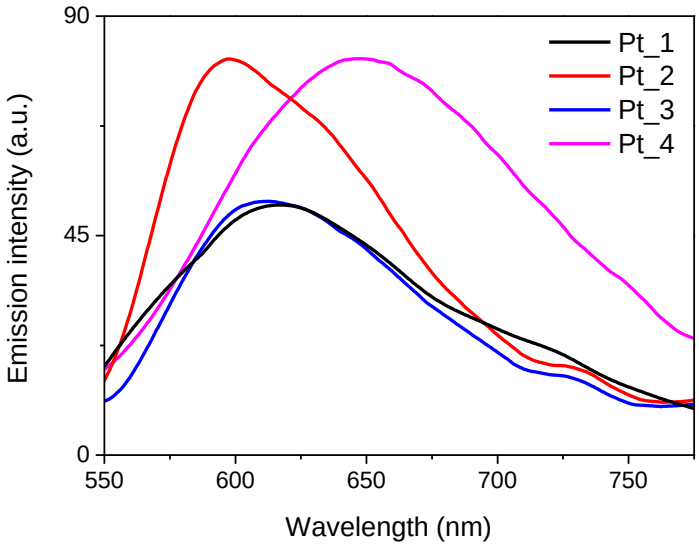

Figure 2.7 - Emission spectra of Pt (II) complexes in dilute DMSO (Pt_1; Pt_3; Pt_4) or CH_2Cl_2 (Pt_2) solutions at room temperature.

Platinum tpy complexes are well known to form aggregates through metal-metal/π-π interactions [5-7] which give rise to various excited states. The combined effect of the counterion nature, the solution concentration and the solvent polarity modulates the photophysical properties of these complexes. On these bases, the 459 nm (**Pt_1**) and 455 nm (**Pt_3**) absorption bands in the first spectral region above identified, are attributed to a metal-metal-to-ligand charge transfer (MMLCT) excited state, indicative of Pt-Pt dimerization in **Pt_1** and **Pt_3**, both bearing the chlorine ancillary ligand. When this ligand is replaced by a benzoate, as in the case of **Pt_2** and **Pt_4**, the bands at 459 and 469 nm, respectively, are attributed to a π–π* transition on tpy-tpy bound dimer, the Pt-Pt interaction being hampered by the steric hindrance of the benzoate ligand. The absorption bands in the second spectral region (superimposable in the DMSO-dissolved complexes, and slight red-shifted in the CH_2Cl_2-dissolved compounds) are due to metal-to-ligand charge transfer (d-π* MLCT) transition from Pt(II) to tpy ligand. Finally, the bands in the third region are attributed to ligand-centered (π-π*) transition on tpy ligand. **Pt_1** and **Pt_3** show an emission band at 620 and 615 nm, respectively, due to the MMLCT deactivation. The **Pt_2** and **Pt_4** broad, unstructured emission band (peaked at 600 and 650 nm, respectively) is ascribed to an excimeric emission that accounts for the large Stokes shift observed for **Pt_4** respect to **Pt_1** and **Pt_3**. The blue shift observed for **Pt_2** emission is ascribed to the different solvent in which the compound has been dissolved. This different aspect of the emission spectra of the complexes bearing a chlorine as an ancillary ligand (**Pt_1** and **Pt_3**) compared to those that bind benzoate (**Pt_2** and **Pt_4**),

confirms the different attribution of the lowest excited state, *i.e.* an MMLCT in the case of the first pair, and an excimer (formed by means of π–π interactions between the aromatic rings of tpy) in the case of the second pair. In Appendix (Figure A.3.1) the absorption spectra of Pt complexes at different concentrations are reported. It can be seen that as the concentration increases, the ratio between the bands attributed to the intermolecular interactions and those attributed to transitions on the single molecule, tends to grow, evidence for aggregation in solution.

Photophysical characterization in the solid state. Emission spectra recorded from powder samples at room temperature (Figure 2.8) have the same structure of those collected in solution under the same conditions. All show a red-shift respect to the solutions, but more accentuated for the complexes that bind chlorine (**Pt_1** and **Pt_3**, that emit with a maximum at 676 and 690 nm, respectively) than those that bind benzoate (**Pt_2** and **Pt_4**, that emit with a maximum at 650 and 660 nm, respectively). Emission quantum yields and lifetimes in condensed phase undergo a significant variation with respect to the values recorded in solution for **Pt_2** and **Pt_4**, but this variation is much more consistent for **Pt_1** and **Pt_3** (see Table A.2.1 and A.2.2 in Appendix). In fact, the complexes bearing chlorine in solid sample show a red-shifted emission maximum and an enhancement of the luminescence intensity respect to the solution, while for the complexes with benzoate ligand these differences are smaller. This behaviour reflects the different origin of the emitting state for the two classes of compounds: for **Pt_1** and **Pt_3** the small steric hindrance of chlorine reinforces the Pt-Pt interaction in solid, giving rise to an MMLCT excite-state. On the contrary, the bulky benzoate group in **Pt_2** and **Pt_4** does not allow a Pt-Pt interaction, while weak π–π interactions on the tpy ligands give rise to the formation of excimers, similarly to the solution.

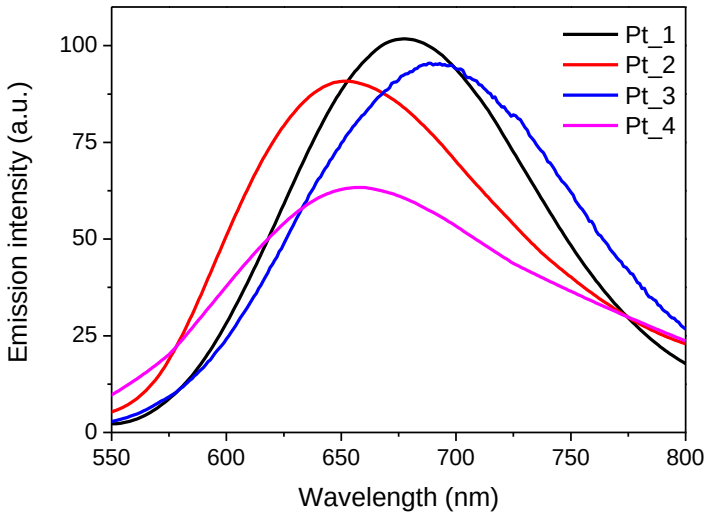

Figure 2.8 - Emission spectra of Pt (II) complexes in solid at room temperature.

The photophysical behavior of **Pt_2** and **Pt_4** was explored by changing temperature. Both samples continue to emit during the heating and cooling cycles between 30 and 160°C, retaining their emission maxima exhibited in solid sample, *i.e.* 650 nm and 660 nm for **Pt_2** and **Pt_4**, respectively. The emission quantum yields have been measured at various temperatures (Tables A.2.3 and A.2.4 in Appendix). For **Pt_2**, two heating/cooling cycles have been recorded, interspersed with cooling in the freezer (at -20°C) for 30 minutes. For **Pt_4**, three cycles have been performed; between the end of second cycle and the start of third cycle, the sample was cooled in the fridge (at 4 °C) for 2 hours. Generally, the quantum yield decreases as the temperature increases, due to thermal agitation, which promote non-radiative deactivation pathway. For **Pt_4**, the experimental data follow this trend, after an initial steeper decrease on first heating, related to the development of the Lam_{Colr} structure with the softening of the sample. [3] Values on cooling and second heating stabilize around 0.5 % in this phase and decrease to 0.2 % in the less- ordered Lam_{Col} phase, prior dropping to below 0.1% in the isotropic liquid state. This rational dependence upon structure contrasts with findings for **Pt_2** sample, which shows an increase in the quantum yield during the I^{st} cycle, while from the beginning of the second cycle, the emission quantum yield is higher than the value measured in solid. This peculiar behavior can be rationalized considering that by heating **Pt_2** during the first cycle eliminates one benzoate unit and the metal centers are getting closer, explaining the increase of luminescence by Pt-Pt interactions.

2.3 - Photophysical characterization of Zn (II) – terpyridine complexes

Photophysical characterization in solution. The absorption spectra of **Zn_1-5** were reported in Figure 2.9, while the main photophysical data are resumed in table A.2.5 in Appendix. All the sample are colourless in dilute solution, except for **Zn_4**, that show a pale green coloration.

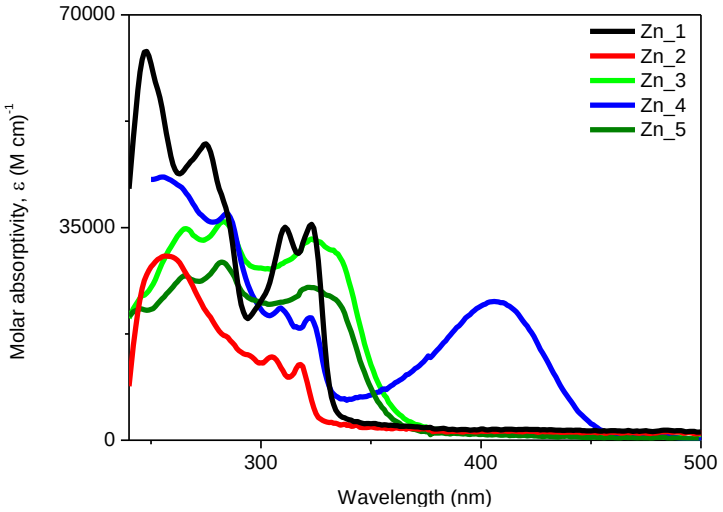

Figure 2.9 - Absorption spectra of Zn_1-5 in dilute CH_2Cl_2 solutions.

The absorption band below 280 nm is present in all the complexes and it is due to ligand-centred (LC) transitions on the benzoate ligands (see for example in Figure A.3.2 in Appendix a comparison between the **Zn_4** and its dichloride precursor **Zn_P4** absorption spectra). The group of bands between 280 and 325 nm are attributed to charge-transfer (CT) transitions from the benzoate to the tpy ligands.[8] The electronic transition on **Zn_1 and Zn_2** are located at higher energy than other samples due to the lower conjugation for the presence of non-aromatic substituents in terpyridine ligands. In particular, for **Zn_2**, these transitions overlap with those localized on benzoate ligand, giving rise to a broad band below 300 nm.

The band centred at 406 nm, present only in the **Zn_4** spectrum and responsible for the pale-green colour of this sample, is due to a strong intraligand charge-transfer (ILCT) from the diethylaniline fragment to the aromatic rings of the tpy. [9]

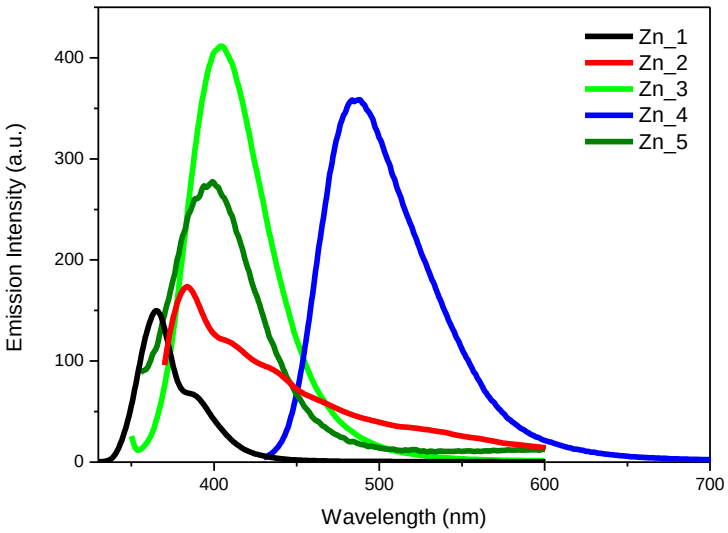

Figure 2.10 – Emission spectra of Zn_1-5 in dilute CH_2Cl_2 solutions.

Fluorescence emission was registered for all samples (see Figure 2.10). The emission from the CT excited state, observed for **Zn_1-3** and **Zn_4** at 365, 379, 405, and 400 nm respectively, are relatively weak, providing an emission quantum yield (ϕ) value of 6.4 %, 24,5 %, 6.5 % , and 0.5%, respectively. Interestingly, the fluorescence originated from the ILCT excited state in **Zn_2** (centred at 488 nm) reaches the outstanding ϕ-value of 95%. The decay from the excited state follows a first order kinetic for all samples, with lifetime values between 2.0 and 4.2 ns (see Table A.2.5 in Appendix).

Photophysical characterization in the mesophase. The photophysical properties in the mesophase were carried out for complexes with liquid crystalline properties, i.e. **Zn_2-5**, in order to evaluate the effect of temperature on emission spectra and emission quantum yields of each sample and correlate them to the result of the structural analysis. The emission spectra of the sample at room temperature are reported in figure 2.11, while data acquired varying the temperature were collected in Tables A.2.6 –10 in the Appendix.

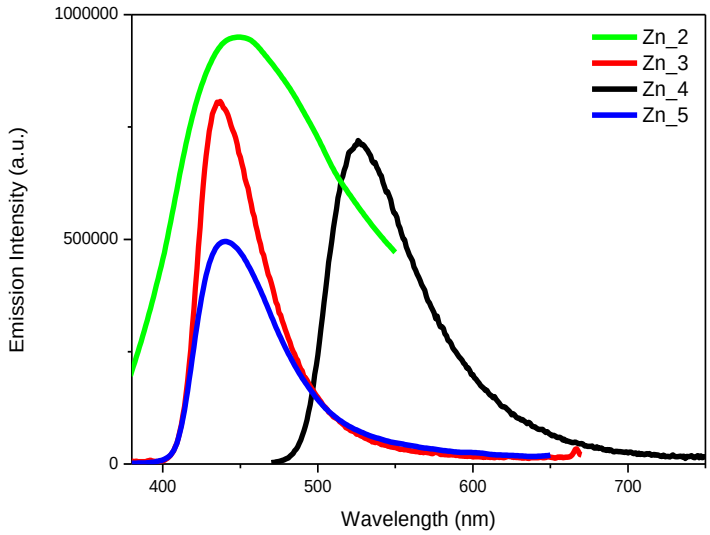

Figure 2.11 - Emission spectra of the samples in the mesophase at room temperature.

Starting from **Zn_2**, whose behaviour is different from that of the other complexes, we first notice a consistent red-shift of the emission in the mesophase (450 nm, Table A.2.6 and figure 2.10) respect to the solution (379 nm, Table A.2.5 and Figure 2.9) with a drastic reduction of the emission quantum yield, passing from 24.5 % to 7.1 %.

The temperature increase (during both the first and the second heating / cooling cycle) involves a red-shift of the emission band and a decrease of quantum yield. As found for **Pt_4** (see paragraph 2.2), trends are reversible by decreasing temperature, but the initial higher values are never restored in relation with structural changes on first heating. The columnar structure of **Zn_2** is indeed initially disordered, with only average distances between irregularly arranged columns, and the regular hexagonal arrangement only develops with the softening of the sample on first heating.[4] Such a transformation obviously creates interactions between the compounds, which stabilize the excited state, as indicated by the red-shift of the emission band. The quantum yield decreases is due to the non-radiative deactivations raise triggered by the high temperature.

Considering the other complexes their emission spectra recorded from mesophase samples at room temperature (Fig. 2.11 and Table A.2.6) show the same structure as those collected in solution. All suffer a red-shift with respect to the solutions, showing peaks at 435 nm for **Zn_3** (+30 nm) and **Zn_5** (+35 nm), and at 542 nm for **Zn_4** (+54 nm). Compared to that measured in solution, the ϕ-value of **Zn_5** increases in the room-temperature mesophase (from 0.5 to 1.5%), while for **Zn_3** it decreases from 6.5 to 4.0%; for **Zn_4** it undergoes a drastic reduction

from 95.0 to 20.2%. Generally, ongoing from solution to a condensed phase, the molecular packing reduces the vibrational motions and the consequent decrease of the non-radiative rate constant (k_{nr}) causes an increase in the luminescence intensity. While this statement is true for **Zn_5**, it is not for **Zn_3** and **Zn_4**. Mesophase type of **Zn_5** (Colhex) and of **Zn_3** and **Zn_4** (Mhex) exerts an effect on the quantum yield which adds to the reduction of vibrational motions. In fact, the columnar core of **Zn_3** and **Zn_4** consist of a three-molecule strand of p-stacked tpy rings, and this aggregation partially quenches luminescence; this is not effectively compensated by the reduction of k_{nr} and ultimately causes a reduction in the emission quantum yield for these compounds in the mesophase compared to the solution. In the columnar core of **Zn_2**, the poor π–π stacking does not effectively counterbalance the decrease in k_{nr}, and the quantum yield increases in the mesophase with respect to the solution. The behaviour of **Zn_4** (which, as already highlighted, undergoes a drastic reduction of the ϕ-value) deserves a particular explanation, also considering that the mesophase is the same as **Zn_3**. This depends on the nature of the emissive state of this complex, which (unlike **Zn_3** and **Zn_5**) is an ILCT from the diethylaniline fragment to the aromatic rings of the tpy. This transition became partially symmetry-forbidden in the mesophase, where the packing distorts the orientation between the diethylaniline fragment and the tpy core, causing a noticeable reduction of the emission quantum yield. Nevertheless, the quantum yield value of **Zn_4** remains considerable high even in the mesophase. To correlate the orientational order of the liquid crystal with its optical anisotropy properties, it is necessary to consider the orientation of the molecular emission transition dipole moment (TM) with respect to the columnar director. Theoretical calculations demonstrate that in the **Zn_4** molecule the TM vector lies on the plane of the aromatic rings of the tpy, oriented by the amino group towards the centre of gravity of the molecule.[10-12]

2.4 – Conclusions

Photophysical characterization of Pt(II) and Zn(II) terpyridine both in diluted solution and in solid state varying temperature was carried out to study the correlation between the molecular structure and the resulting optical properties of the samples.

The characterization of Pt(II) complexes evidence the role of metal-metal interactions in the formation of excited states involving the metal centre, and the steric hindrance of the ancillary ligands in directing such interactions. For **Pt_1** and **Pt_3** the small steric hindrance of chlorine allows a Pt-Pt interaction (already present in solution and more strongly reinforced in solid), giving rise to an MMLCT excite-state in the mesophase. On the contrary, the bulky benzoate group of **Pt_2** and **Pt_4** does not allow a Pt-Pt interaction, while weak π–π interactions on the tpy ligands give rise to the formation of excimers, similarly to the solution. Therefore, the use of benzoate units for inducing room temperature mesomorphism is detrimental for the luminescence of the Pt (II) complexes.

By substituting the Pt (II) with Zn(II), a good emitter in solution was obtained (**Zn_2**) but their columnar mesomorphic organization quench its fluorescence in the mesophase. However, varying the substituent on the terpyridine ligand the emissive properties can be finely tuned and improved. While **Zn_3** and **Zn_5** emit modestly, the fluorescence originated from the ILCT excited state in **Zn_4** from the electron-donating –NEt2 group to the electron-withdrawing aromatic rings of the tpy ligand reach a record luminescence quantum yield in solution (95%). Although the efficiency is reduced in the mesophase due to distortion of the diethylaniline with respect to the aromatic rings of tpy, it still remains as high as 20%.

References

[1] E. B. Priestley, P.J. Wojtowicz, P. Sheng, Introduction to Liquid Crystals, 1975, *Plenum Press*;

[2] Website: https://www.tcichemicals.com/US/en/c/12775;

[3] M. La Deda, G. Di Maio, A. Candreva, B. Heinrich, A. A. Andelescu, E. Popa, E. Voirin, V. Badea, M. Amati, O. Costişor, B. Donnio, and E. I. Szerb, Very intense polarized emission in self-assembled room temperature metallomesogens based on Zn(ii) coordination complexes: an experimental and computational study, 2022, *J. Mater. Chem. C Mater.*, 10, 115–25;

[4] A. A. Andelescu, B. Heinrich, M. A. Spirache, E. Voirin, M. La Deda, G. Di Maio, E. I. Szerb, B. Donnio, and O. Costisor, Playing with PtII and ZnII Coordination to Obtain Luminescent Metallomesogens, 2020, *Chemistry - A European Journal*, 26, 4850–60;

[5] J, A, Bailey, M. G. Hill, R. E. Marsh, V. M. Miskowski, W. P. Schaefer, and H. B. Gray, Electronic Spectroscopy of Chloro(terpyridine)platinum(II), 1995, *Inorg. Chem.*, 34, 4591–9;

[6] S. C. F. Kui, Y-C Law, G. S. M. Tong, W. Lu, M-Y Yuen, and C-M Che, Spectacular luminescent behaviour of tandem terpyridyl platinum acetylide complexes attributed to solvent effect on ordering of excited states, "ion-pair" formation and molecular conformations, 2011, *Chem. Sci.*, 2, 221–8;

[7] G. Arena, G. Calogero, S. Campagna, L. Monsù Scolaro, V. Ricevuto, and R. Romeo, Synthesis, Characterization, Absorption Spectra, and Luminescence Properties of Organometallic Platinum(II) Terpyridine Complexes, 1998, Inorg. Chem., 37, 2763–9;

[8] D. Myśliwiec, B. Donnio, P. J. Chmielewski, B. Heinrich, and M. Stępień, Peripherally Fused Porphyrins via the Scholl Reaction: Synthesis, Self-Assembly, and Mesomorphism, 2012, *J. Am. Chem. Soc.*, 134, 4822–33;

[9] X. Bi, and Y. Pang, Optical Response of Terpyridine Ligands to Zinc Binding: A Close Look at the Substitution Effect by Spectroscopic Studies at Low Temperature, 2016, *J. Phys. Chem. B,* 120, 3311–7;

[10] F. Schlütter, A. Wild, A. Winter, M. D. Hager, A. Baumgaertel, C. Friebe, and U. S. Schubert, Synthesis and Characterization of New Self-Assembled Metallo-Polymers Containing Electron-Withdrawing and Electron-Donating Bis(terpyridine) Zinc(II) Moieties, 2010, *Macromolecules*, 43, 2759–7;

[11] I. Eryazici, C. N. Moorefield, and G. R. Newkome, Square-Planar Pd(II), Pt(II), and Au(III) Terpyridine Complexes: Their Syntheses, Physical Properties, Supramolecular Constructs, and Biomedical Activities, 2008, *Chem. Rev.*, 108, 1834–95;

[12] M. Humbert-Droz, C. Piguet, and T. A. Wesolowski, Fluorescence quantum yield rationalized by the magnitude of the charge transfer in π-conjugated terpyridine derivatives, 2016 , *Physical Chemistry Chemical Physics*, 18, 29387–94;

Chapter 3 – The "seed-mediated growth": a versatile pathway for the synthesis of gold nanoparticles

The amazing optical properties of AuNP due to LSPR and the possibility to finely tune them modulating their shape and size, pushes researchers to the development of several synthetic strategies that would allow them a fully exploitation of the high applicative potential of these intriguing materials.

At the current state, several strategies for the preparation of AuNP are available following both the top-down and bottom-up approaches. [1-4] In the bottom-up approaches bulk gold substrates are subdivided into smaller and smaller fragments until the nanoscale using techniques like laser ablation or nanolithography. Contrarily, in the bottom-up approaches wet-chemical methods based on the chemical reduction of a gold salt are employed to produce Au atoms that coalesce together to form clusters of growing size, stopping the growth process when the desired size is reached (see Figure 3.1).

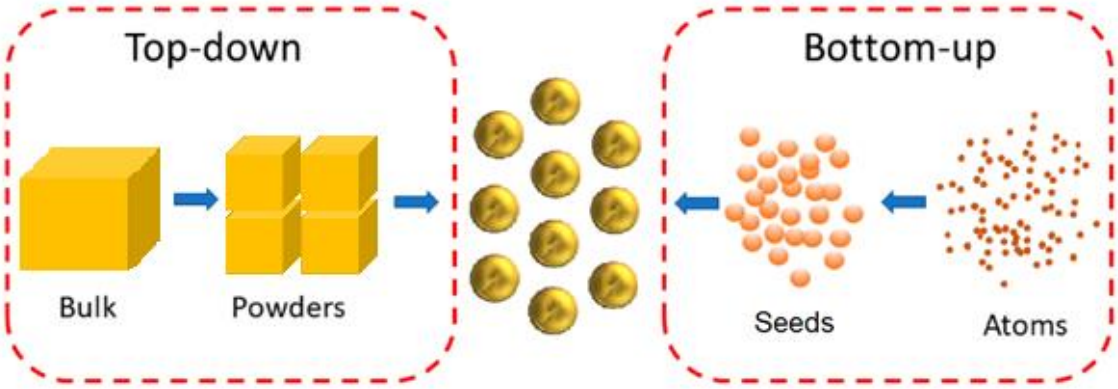

Figure 3.1. Scheme of top-down and bottom-up synthesis of AuNPs adapted from reference [4].

Bottom-up methodologies are suitable at industrial level but require expensive instrumentation and do not guarantee control on shape and size of produced nanoparticles. [5] On the other hand, chemical routes offer the possibility to separate temporally and spatially the *nucleation* and the *growth* phases in the nanoparticle growth process. This approach, named *seed-mediated growth* guarantees an incomparable control over both shape and size of the nanoparticles, and therefore over its optical properties. [5-7]

Scheme 3.1 reports the essential steps, i.e. the (a) nucleation and the (b) growth, of a typical seed-mediated growth synthetic pathway. In some cases, as we will see, the growth step may be more than one.

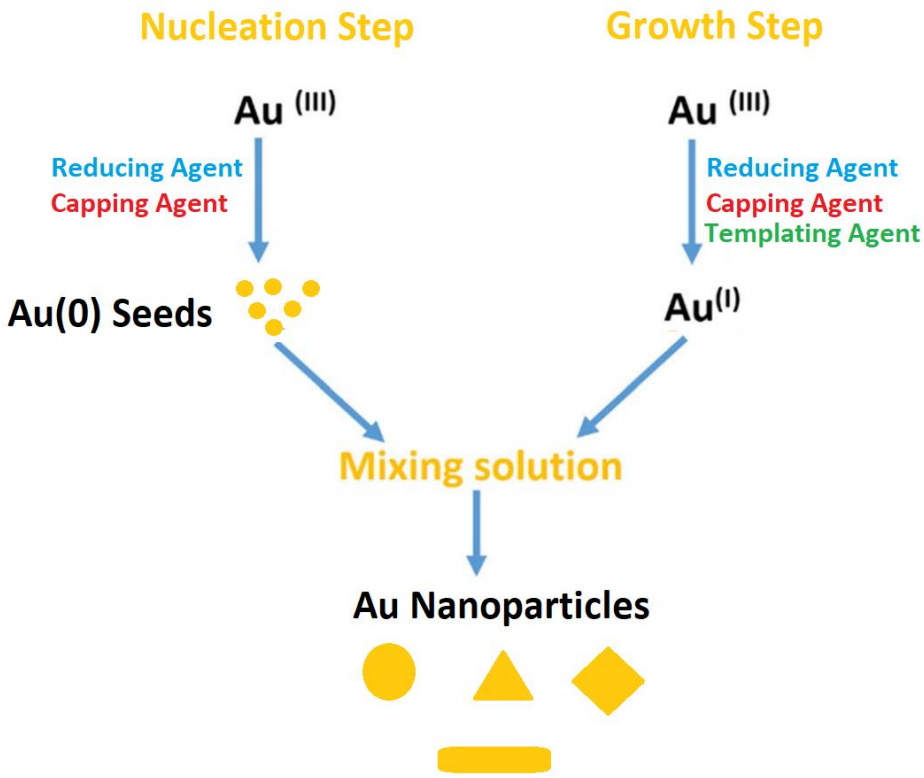

Scheme 3.1 General pathway for the seed-mediated growth synthesis of Au NPs adapted from [8].

To better understand the discussion that follows on nucleation and growth of Au nanoparticles, it can be useful to consider that gold crystallizes in an fcc (face centered cubic) lattice. Gold nanoparticles are crystals obtained under particular thermodynamic and kinetic conditions in which the crystalline lattice growth, once terminated due to depletion of the Au(0) precursor (typically an Au(III) salt), results in a crystal with some crystallographic planes exposed, that are surfaces with some missing bonds respect to that required for an fcc lattice. In this case, the crystallographic planes that can be exposed (referred also as facets) are the {111}, {100}, and {110}. These planes have a different number of missing bonds (3, 4, and 5 respectively, see Figure 3.2), and therefore shows a different surface free energy (more bonds are missing, greater is the surface free energy) and this determines their probability of formation and their reactivity. [7, 9] The ensemble of facets exposed by a nanocrystal is its *crystalline habit*, i.e. the characteristic external shape of the particle.

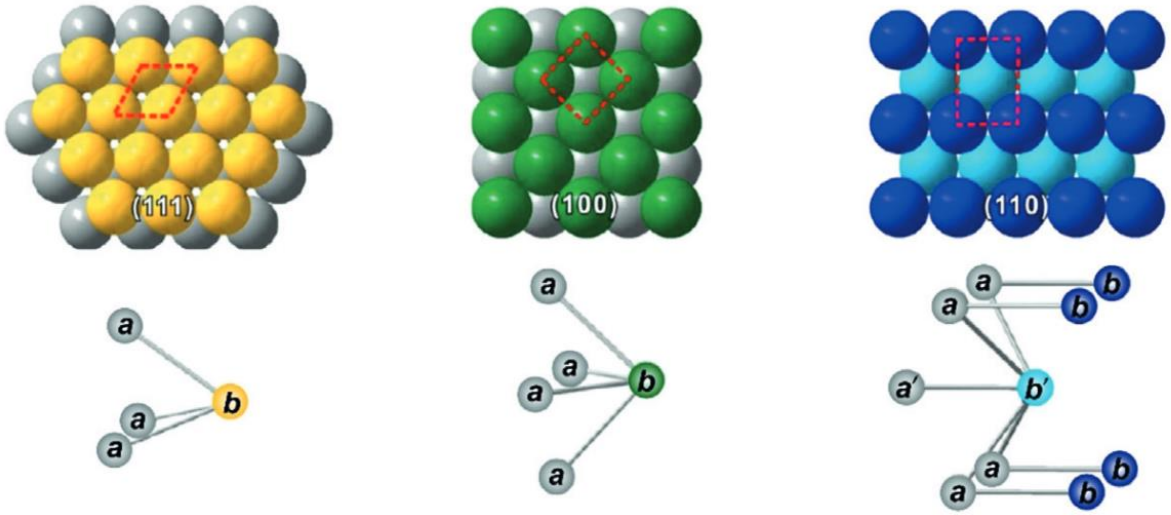

Figure 3.2 - Graphical representations of {111}, {100}, and {110} facets in a fcc metal and corresponding number of missing bonds (corresponding missing atoms are evidenced in grey) adapted from ref. [9].

a) Nucleation step: the birth of a seed

The *nucleation step* is the first one in the formation of metal nanocrystals and it is the result from the coalescence of single metal atoms until they form clusters with a stable and well-defined crystalline habit, namely *seeds*. In seed-mediated growth synthesis these clusters are formed starting from a *gold precursor* (typically a gold salt, like $HAuCl_4$) in presence of a strong *reducing agent* (e.g. $NaBH_4$) that aims the reduction of Au(III) ions to Au(0) atoms, and a *capping agent* that prevents the coalescence of the formed clusters (e.g. polymers, surfactants, long chain alkanes). Typical sizes of Au seeds obtained in this way are in the 2-10 nm range, and can show different crystalline habit as described in Figure 3.3, that reports the possible pathways for the seed-mediated growth synthesis of fcc metal nanoparticles. The mechanism that bring to the formation of seeds is not fully understood because of the lack of experimental tools that allow the observation of phenomena on atomic scale, but their crystalline habit heavily depends on kinetic and thermodynamic conditions under which they are formed. So, acting on some reaction parameters (e.g. temperature, rate of Au(0) atoms generation) a specific crystalline habit can be promoted over others.

As depicted in Figure 3.3 seeds resulting from the reduction of Au salt can be subdivided in four main types: *single crystals, single- and multi-twinned, plate with stocking faults.* Single crystals seeds are truncated cuboctahedron bounded by the lowest energy facets, *i.e.* {111}, and {100}, and this is the most thermodynamically stable crystalline habit, because, according the Wulff's theorem for fcc lattice, the total surface free energy is minimized.

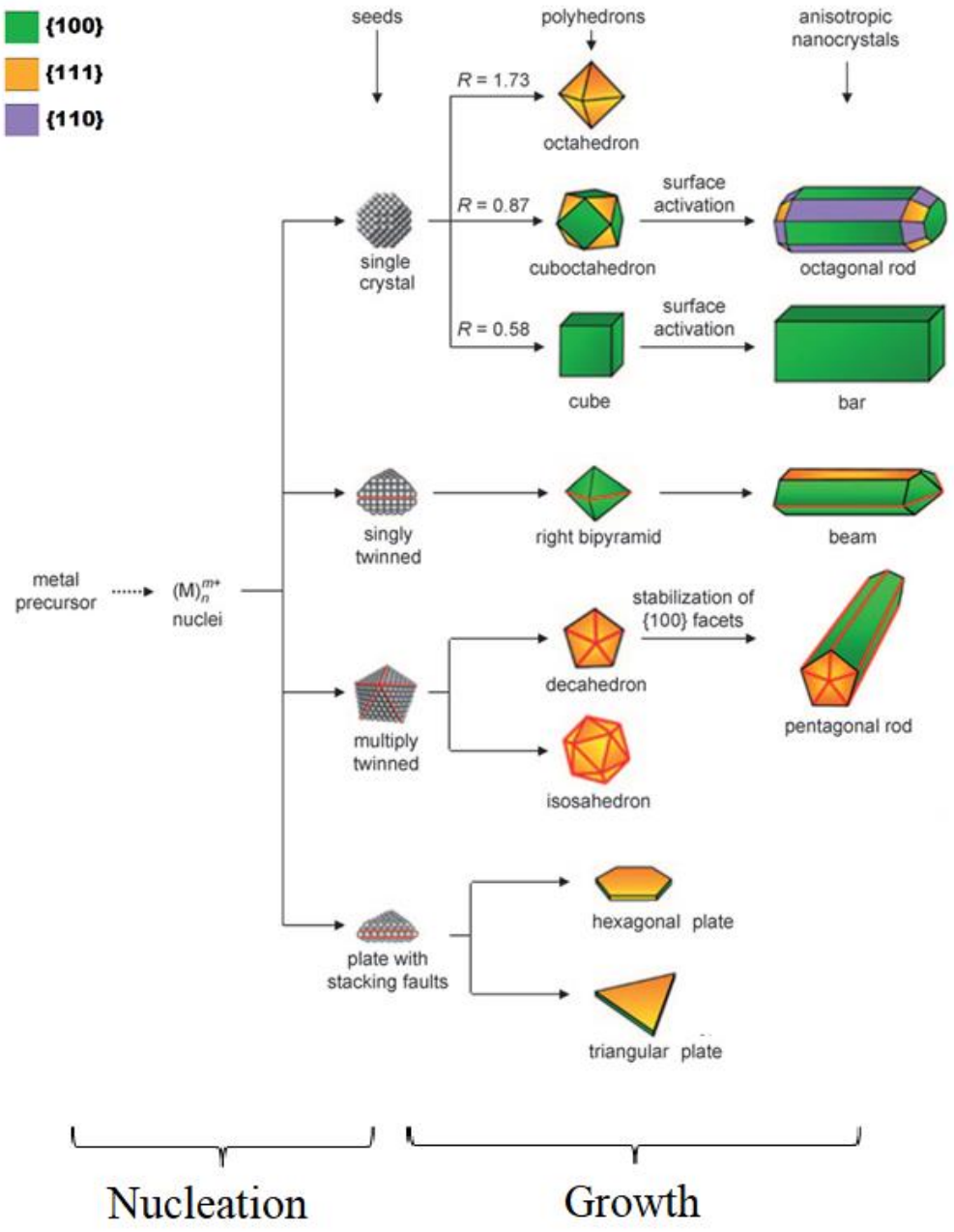

Figure 3.3 - General pathways for the seed-mediated growth synthesis of fcc metal nanoparticles of different shapes (adapted from reference [7]). The parameter R is defined as the ratio between the growth rate along the {100} facets versus the growth rate along the {111} ones.

In addition to single crystal, also single- and multi-twinned seeds can be obtained, that are also bounded by the lower energy facets, but incorporates in their structure one or more twin defects. Finally, in some particularly kinetic conditions, plate-like seeds can be obtained, that are seeds bounded by two parallel {111} facets, separated by a stacking fault. In principle, from a reduction reaction, a mixture of all these seeds can be obtained, but acting on the rate of the reduction reaction (by changing some reaction parameters such as temperature, reactants

concentrations and their ratio, stirring speed) the formation of a specific crystalline habit can be promoted over others. For example, by maximizing the reduction rate of the Au ions, the reaction will evolve towards the most thermodynamically stable product, so the number of *single crystal seeds* will be maximized. Contrarily, reducing it abruptly the Au(0) atoms will coalesce assembling themselves into in a random hexagonal close packing (*rhcp*) that bring to the formation of *plate with stocking faults* seeds. [7]

Successively, by controlling the growth process, a specific reaction path can be selected, making accessible a great variety of different shapes (i.e. cuboctahedron, rods, cubes, bipyramids, triangles and so on).

b) <u>Growth step: where chemistry meets art</u>

Once a seed is formed, in the successive reaction conditions, it is very stable (except for a particular process known as oxidative etching, based on the re-oxidation of Au(0) under low pH conditions [10]), and, due to the presence of a protective coating agent, does not suffer any coalescence processes, so the number of seeds remains unchanged, while their size could increase due to a further addition of Au(0) atoms. On these premises is based the second step of the seed-mediated growth mechanism, the growth step. In a classical seed-mediated growth reaction, the seeds dispersion was then mixed with a solution containing a gold precursor and a weak reducing agent able to reduce Au(III) to Au(I). The further step of the reduction process, *i.e.* Au(I) to Au(0), takes place on the catalytic surface of the seeds and the adsorption of the newly formed Au atoms on to the seed surface brings to the growth in size of the nanoparticle. Now suppose that a nucleation reaction that brings to the formation of *single crystal seeds* was successfully completed. At this point, as attested by Figure 3.3, there are three different possible pathways, that could bring to the formation of nanoparticles with octahedral, cuboctahedral, or cubical shape. The final shape of the nanoparticle is determined by the growth rate of the various crystallographic facets (in Figure 3.3 it is indicated by R, i.e. the ratio between the growth rate along the {100} facets versus the growth rate along the {111} ones). It can be done exploiting the different affinity of molecules (called templating agents) towards the different facets, essentially due to the different surface free energy of the facets discussed above; this make these molecules able to preferentially absorb on a specific facet, hindering the adsorption of Au atoms on the forming nanoparticle surface and slowing down its growth along this specific crystallographic direction.[10-13] Therefore, considering the path in fig. 3.3 that has as starting point *single crystal seeds*, if a templating agent that binds strongly to the {111} facets (R=1.73) was used, the growth of the nanoparticles will be faster along the {100} ones, which at a certain

point of the process disappear, having as a result a polyhedron bounded with only {111} facets, i.e. an octahedron. Contrarily, if the templating agent shows a better affinity for the {100} facets the resulting shape will be the cube. The high variety of capping agents available (e.g. polymers, surfactants, long chains amine ad thiols, and so on) give the possibility to finely tune the growth rate along the crystallographic directions [10-13], make access to a wide range of possible shape and thus functional properties of gold nanoparticles, the only limit in this field is the scientists fantasy!

In this chapter, a seed-mediated growth protocol was developed for the synthesis of gold nanocubes (AuNC), one of the main challenges of this PhD work, focusing on the parameters that control the cubic shape formation. Furthermore, nanoparticles with different shape, i.e. sphere (AuNS), triangles (AuNT), and rods (AuNR) are also synthesized to demonstrate the high versatility of this synthetic approach to produce both isotropic and anisotropic gold nanoparticles. The experimental results of each synthesis and of the relative optical and morphological characterization were reported, followed by a thorough discussion about the main chemical-physical principles that conduct to the formation of different shapes.

3.1 – Seed-mediated growth synthesis of AuNC@CTAB

The synthetic protocol used for the synthesis of Au nanocubes was first proposed by Dovgolevsky *et al.*[14] In the following we will illustrate the synthesis of gold nanocubes coated with cetyltrimethylammonium bromide (CTAB), a surfactant used to perform a dual function, i.e. prevent coalescence of nanoparticles and as a templating agent; the synthesis was carried out in an aqueous environment maintaining the constant temperature of 25°C using a thermostatic water bath, to guarantee the reproducibility of the process and to avoid the precipitation of CTAB during the synthesis. The product obtained, AuNC@CTAB, was characterized from an optical and morphological point of view.

Nucleation: production of Au seed capped with CTAB (AuSeeds@CTAB). In the first step of the synthesis 250 µL of 10 mM $HAuCl_4$ were added to 7.5 mL of 100 mM CTAB. Then 600 µL of ice-cold 10 mM $NaBH_4$ were injected "one-shot" and under vigorous stirring in the reaction flask. The speed of addition of the reducing agent is the key step of the nucleation processes: the formation of the gold nuclei must occur simultaneously throughout the solution and the agitation must ensure a homogeneous distribution of all the nuclei throughout the volume of the solution. [15] For these reasons the "vigorous stirring" method was preferred respect to inversion mixing used in literature; [14] furthermore the possibility to fix the stirring speed guarantees a better reproducibility. After the addition, the colour of the solution turns immediately from yellow to brown, indicating the instantaneous reduction of the Au(III) ions dissolved in solution to Au(0) performed by $NaBH_4$ (see figure 3.4). The seed dispersion was then left undisturbed for at least 1 hour to exhaust all the excess reductant before use.

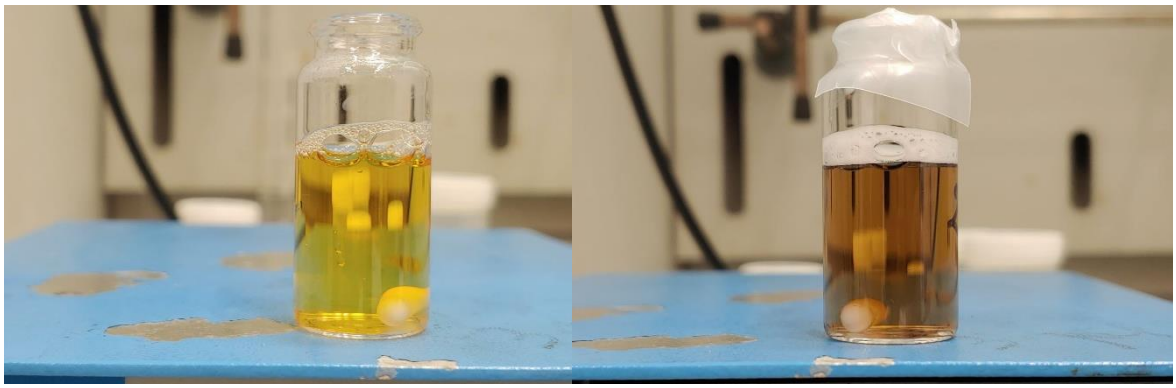

Figure 3.4 - Au seeds solution before (left) and after (right) the addition of $NaBH_4$. The brownish colour attests the formation of seeds by reduction of Au(III) ions to Au(0) atoms.

***Growth: preparation of the growth solution and mixing with Au seeds*.** In the synthesis of AuNC@CTAB, to 32 mL of Milli-Q water were added, in sequence and under magnetic stirring, 6.4 mL of CTAB solution 100 mM, and 800 µL of 10 mM $HAuCl_4$. After the complete dissolution of the gold precursor, 3.8 mL of ascorbic acid 100 mM, a weak reducing agent, were added. At this point, the growth solution, initially yellow, became colourless attesting the reduction of Au(III) ions to Au(I) (see Figure 3.5). Then, 20 µL of the Au seeds dispersion, AuSeeds@CTAB, diluted 1 to 10, were added to the growth solution and mixed under magnetic stirring for 10 second at 350 RPM. At this point, the growth solution starts to colouring, becoming red/fuchsia after 1 h (Figure 3.5). The dispersion was left undisturbed for 24 h, and then was centrifuged twice at 4000 RPM for 30 minutes to quench the growth process and purify the dispersion by all excess reactants. The precipitate was then dispersed in Milli-Q water and characterized by UV-visible spectroscopy and TEM.

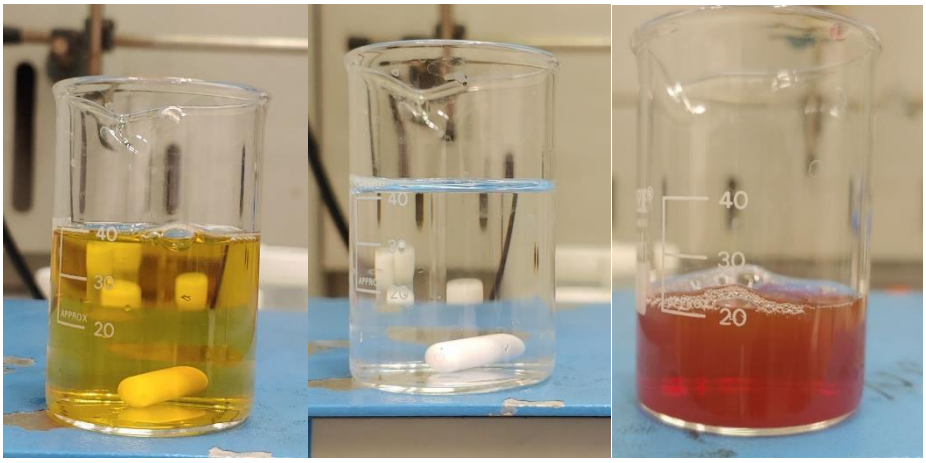

Figure 3.5 - Picture of the growth solution before the addition of ascorbic acid (left), when the reduction process is complete (centre), and after the addition of Au seeds, when the growth process of Au nanocubes is complete (right).

Optical and morphological characterization of AuNC@CTAB. Extinction spectrum and TEM image of an AuNC@CTAB aqueous dispersion synthesized using the procedure described above (AuNC#1) were reported in figure 3.6.

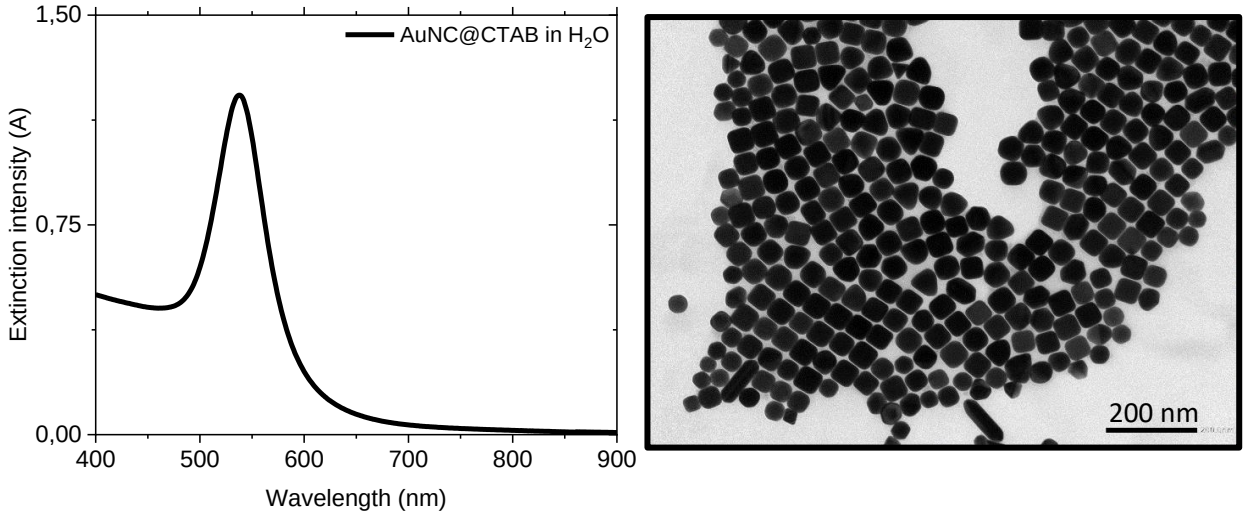

Figure 3.6 - Extinction spectra (left) and representative TEM image (right) of sample AuNC#1.

The spectrum shows a narrow plasmonic band with a maximum centred at 540 nm and a FWHM (full width at half maximum) of 80 nm. The cubic shape belongs to 45% of the total number of synthesized nanoparticles (evaluated against 500 particles directly on TEM images); obtained cubes show round corners (*i.e.* the {111} facets are not completely extinct during the growth) and an edge length of 49 ± 3 nm (obtained as *mean value* ± *standard deviation* of 50 AuNC edge lengths measured directly on TEM images using the software ImageJ). As we see from TEM image in figure 3.6, cubes are not the only shape produced, but also spheroids (40%), triangles (10%) and rods (5%) of various size can be observed. The plasmonic feature registered is attributed to the sum of dipolar plasmonic modes of cubes and spheroids. Despite theoretical calculations have shown that spheres have a blue-shifted plasmonic band respect to AuNC of the same size, the superposition of their extinction spectra experimentally observed is probably due to two concomitants factors not considered in theoretical analysis. [16] The first factor is that the synthesized cubes have round corners that reduce their effective size and therefore shift their plasmonic modes to lower wavelengths;[16] the second one is the widening of plasmonic bands due to the polydispersity of synthesized nanoparticles. Regarding the others shapes, *i.e.* triangles and rods, their plasmonic bands, which are strongly red-shifted respect to cubes and spheres, were not observed, probably for their small concentrations (15% in total). The

demonstration of this statement comes from a sample where both rods and triangles were obtained in higher number than usual (about 50% of the total nanoparticles) when the CTAB concentration is reduced respect to the usual protocol (see sample AuNC#5 in section A.4 of the Appendix). In this case, the extinction spectrum of the sample (reported in the figure 3.7 with their representative TEM image) changes dramatically, showing besides the narrow plasmon band at 540 nm due to the AuNC and AuNS, both an intense shoulder at 565 nm attributed to AuNT, and a band centred at 870 nm due to the presence of high-aspect ratio AuNR.

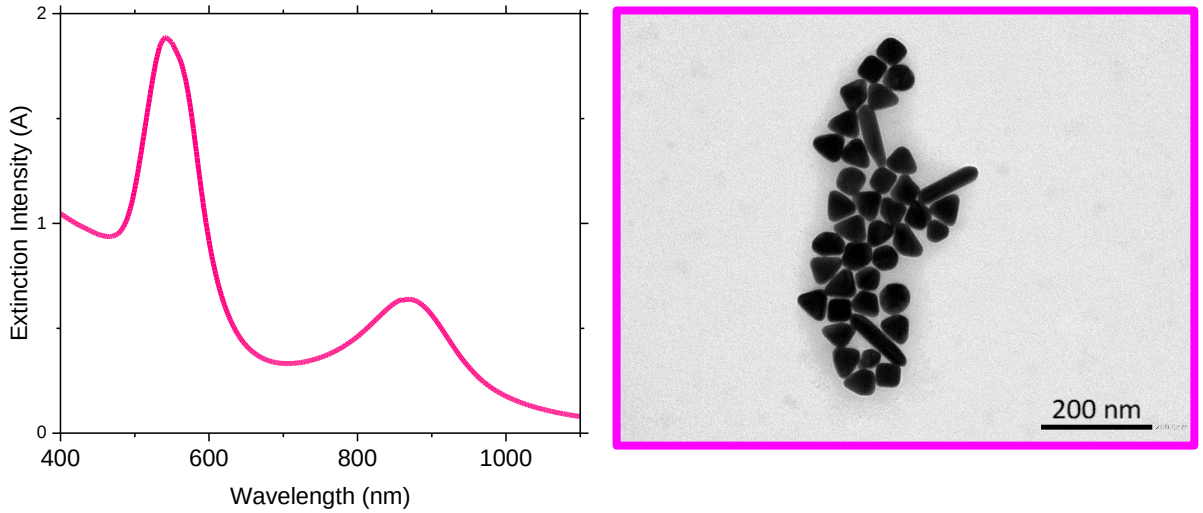

Figure 3.7 - Extinction spectrum and representative TEM image of AuNC#5 where a high quantity of rods and triangles are present as by-products.

As reported above, the quantity of cubic-shaped nanoparticles obtained from this reaction is attested at around 46 ± 5 % (see the results of synthesis AuNC#1-4 in section A.4 of the Appendix), while in the same experimental conditions, literature reports a yield of 95%. [9] The strong dependence on factors that are difficult to control and reproduce in each laboratory such as temperature variations, water and reagents purity are a known issue in the nanoparticles wet-chemical synthesis. [17] In this context, cube is a "very sensitive shape" (taking into account thermodynamic concerns) and consequently the low yield of AuNC synthesis is a largely discussed problem, and constitutes an important limitation for their practical use. [18] Keeping in mind the growth mechanism of AuNC, briefly illustrated in the next section, modifications of the synthetic protocol were performed in the nucleation and in the growth steps, with the aim of improve the reaction yield. Furthermore, a purification method based on the selective depletion-induced flocculation, was adapted to separate the obtained cubes from by-products.

Growth mechanism of AuNC. Based on the known concepts about seed-mediated growth synthesis discussed in the introductive part of this chapter and schematized in figure 3.3, the growth mechanism of gold nanocubes can be easily understood. The first step of the reaction, *i.e.* the *nucleation*, takes place rapidly to give *single crystals seed*. For an fcc lattice, which is the case for gold, single crystal seeds have a truncated cubooctahedrical shape, *i.e.* are bounded by six {100} and eight {111} facets. This shape is the thermodynamically stable product, as attested by Wulff's theorem, because minimizes the total free surface energy. Therefore, the *single crystals seed* concentration increases as the rate of atomic generation increases. [7] For this reason their synthesis was conducted under vigorous stirring and with a fast addition of the reductant: with these experimental tricks is possible to maximize the number of *single crystal seeds* produced. When these seeds were added to the growth solution, their catalytic surface reduces the Au(I) ions in solution to Au(0) carrying to the growth of the nanoparticles. As we reported in Fig. 3.3, it is necessary to reduce R to obtain the cubic shape (R is the ratio between the growth rate of {100} on the growth ratio of {111} facets). This is obtained by using CTAB as capping agent, which binds strongly to {100} facets than {111} ones. [10, 11] So, because CTAB "protects" {100} facets, Au(I) ions, electrostatically interacting with the electron-clouded single crystals, will adsorb mainly on {111} facets, suffering a catalytic reduction to Au(0), therefore the gold lattice growths faster along {111} directions than along the {100} ones; consequently, the area of the{111} facets is drastically reduced in favour of the six {100} facets, which define the cubic crystal habit.

Improve AuNC yield controlling the seeds formation. By TEM analysis of the samples, we see that the main shapes of the observed by-products can be collected in three main categories: spheroids, rods, and triangles (see figure 3.8). Furthermore, a great polydispersity in size of the by-products emerges.

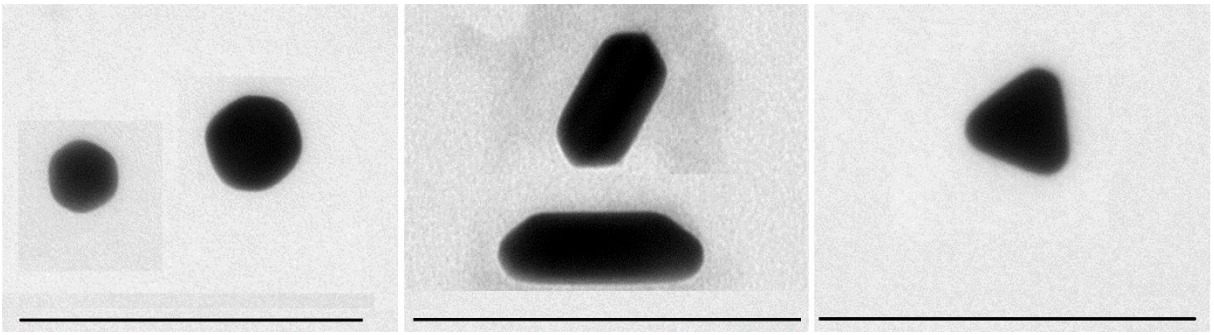

Figure 3.8 - Representative TEM images of the main by-products generated during AuNCs synthesis, from left to right: spheroids, rods, triangles (scale bars are 200 nm).

From figure 3.3, we infer that triangles are generated from *plate with stacking faults seeds*, while rods can be obtained from various paths. From TEM images (Figure 3.6, 3.7, and 3.8), we see that rods produced in this synthesis have sharp ticks and a strong red-shifted plasmon band. These features are typical of pentatwinned rods generated from the *multiply twinned* seeds, while spheroids (that have a cubooctahedric crystal habit) comes from the same type of seeds that generated cubes, i.e. *single crystal.* [7, 15] Therefore, the first effort was trying to increase the number of thermodynamically stable seeds (*single crystals seed*) acting on the nucleation stage of the synthesis. In particular, we tried to increase the rate of Au(0) generation to produce more truncated cuboctahedron clusters. Unfortunately, the size and crystal habit of the seeds cannot be directly evaluated with the instruments available (a HR-TEM is needed to observe such small particles). Therefore, the effects of protocol modifications were indirectly evaluated by observing the optical and morphological characteristics of the nanoparticles synthesized by mixing the seed solution, obtained by modifying the protocol, with a growth solution prepared according to the standard protocol. The first attempt was to increase the quantity of the reducing agent, keeping all the other parameters unvaried. Unfortunately, this change did not have any improvement effect, probably because the reductant is already in strong excess, so a further addition did not increase the rate of the reduction. In the second experiment, we increased the speed of addition of the $NaBH_4$ in the reaction mixture, without varying the stoichiometric ratios between the reactants. In details, we prepared three $NaBH_4$ solutions at different concentrations (0.01 M, 0.1 M, and 1 M) and added them to the $HAuCl_4$/CTAB solution in three different volumes (*i.e.* 600 µL, 60 µL, and 6 µL respectively), so that the $NaBH_4$ moles number results identical to that used in the standard protocol for seeds preparation. Figure 3.9a reports the extinction spectra of the three seed solutions, while fig. 3.9b and fig. 3.10 report respectively the extinction spectra and the TEM images of the final AuNC samples. Table 3.1 reports the main experimental data of the AuNC@CTAB aqueous dispersion, obtained by changing the volume of the seed solution in the nucleation step, namely AuNC#1, AuNC#6 and AuNC#7 corresponding to the addition of 600 µL, 60 µL, and 6 µL volume of $NaBH_4$ solution.

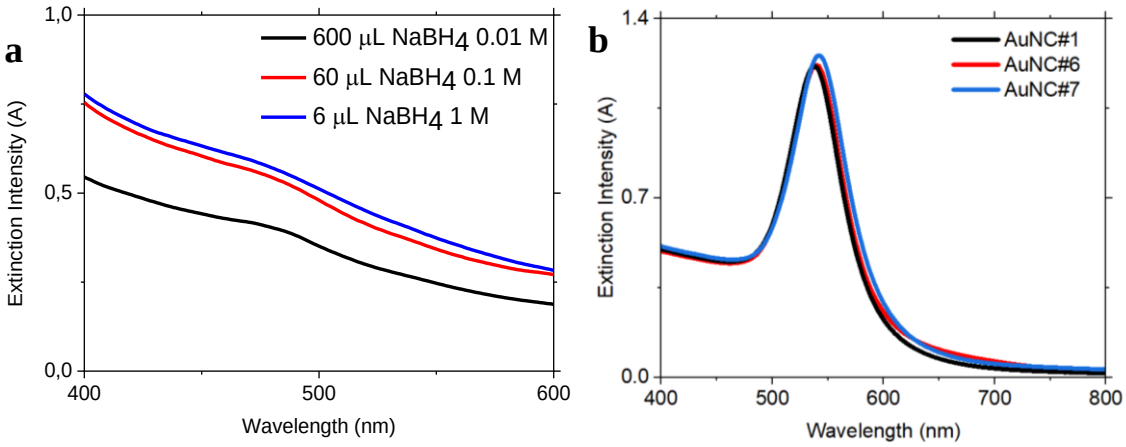

Figure 3.9 – *a*: extinction spectra of AuSeed@CTAB obtained varying the volume of $NaBH_4$ added in the nucleation step and *b*: corresponding extinction spectra of AuNC@CTAB in H_2O after the synthesis was completed.

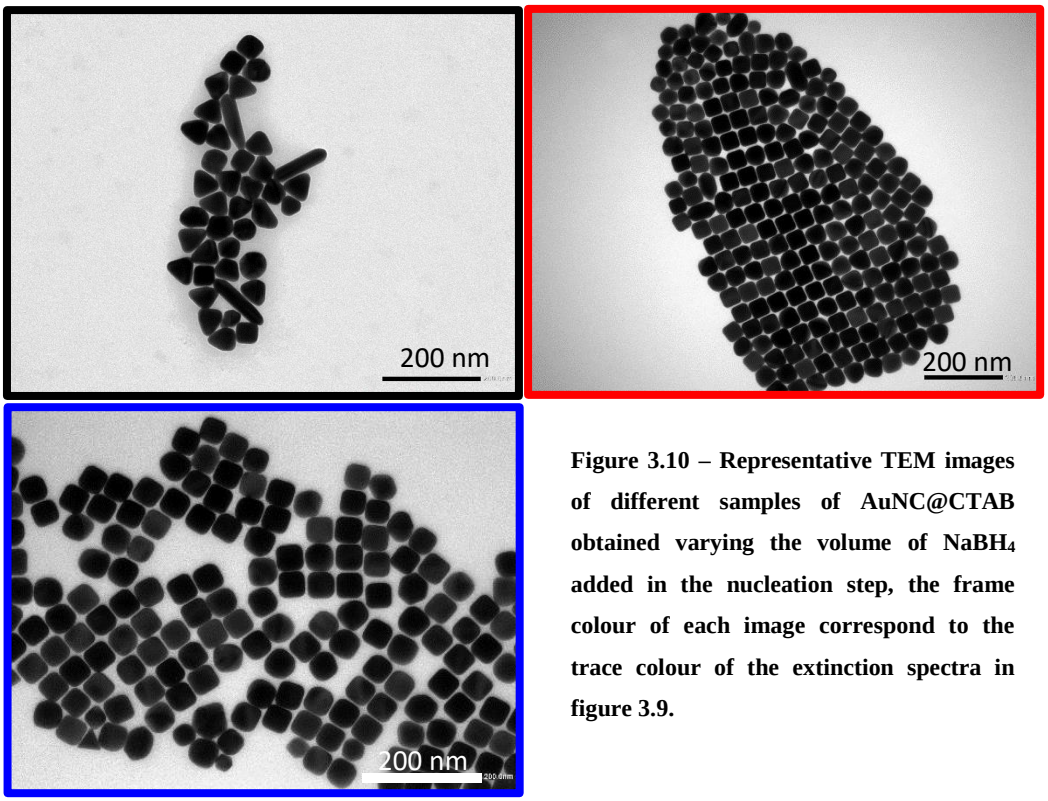

Figure 3.10 – Representative TEM images of different samples of AuNC@CTAB obtained varying the volume of $NaBH_4$ added in the nucleation step, the frame colour of each image correspond to the trace colour of the extinction spectra in figure 3.9.

The first interesting result come from the comparison of the extinction spectra of the three Au seeds dispersions prepared as described above (Fig. 3.9 a). In these spectra, a very weak plasmonic feature appears centred at around 470 nm: when the volume of the added reductant is reduced, an increase of the extinction signal was detected (Figure 3.9a, blue and red traces). Because the moles of $NaBH_4$ was not varied, and therefore the number of Au(0) atoms produced by the reduction reaction are the same for each sample, the increase of band intensity is attributed to the increase of the seed size, which in turn depends on the reduced volume in which the Au(0) atoms coalescence takes place (the variation of the intensity of the band could in principle be attributed to the variation of the volume, but in this case its trend should appear linear, while the observed trend shows an inverse quadratic dependence on the concentration; this is the result of a reduced mean-free path of each Au(0) atom before impinging inelastically the forming seed, the cross-section of which increases in a quadratic manner with respect to the mean number of impinges in the unit of time). As attested by literature, when seeds growth in size the *single crystal* shape it is favoured over the others. [7]

Table 3.1. Main data of AuNC@CTAB synthesized varying the rate addition of reductant.

Sample	λ_{max} (nm)	FWHM (nm)	Shape (yield %)	Nanocubes Mean Size (nm)
AuNC#1 (standard protocol)	**538**	**69**	***Cubes (45), spheres (40), triangles (10), rods (5)***	***49 ± 3 nm***
AuNC#6	**540**	**69**	***Cubes (65), spheres (31), rods (3), triangles (1)***	***47 ± 3 nm***
AuNC#7	**542**	**70**	***Cubes (60), spheres (34), rods (4), triangles (2)***	***48 ± 3 nm***

The extinction spectra of the resulting AuNC@CTAB, red and blue traces reported in Figure 3.9b, appear red-shifted decreasing the volume of $NaBH_4$ than the standard protocol (black trace), while no significant variation in the FWHM values and mean size of nanocubes were observed (Table 3.1). As already said above the spectra is the sum of the plasmonic resonance of AuNC and AuNS, with the firsts that have a plasmon resonance red-shifted than the latter. [16] Thus, the shift to higher wavelengths of the plasmon band suggests an increase of the cubic-shaped nanoparticles in these samples. The confirm of that comes out from the analysis of TEM images of the samples (Figure 3.10), where an increased yield of AuNC from 40 to 65 % was observed when the volume of $NaBH_4$ was reduced 10 times in the seed solution respect

to the standard protocol. A quite similar result (60%) was obtained reducing by 100 times the volume of reductant, indicating that a further reduction of the volume does not increase the yield of the reaction. In table 3.1 the main experimental parameters extrapolated by extinction spectra (λ_{max} and FWHM maximum of the plasmon band) and from TEM image analysis (percentage yield in terms of shape of nanoparticles produced and AuNC mean size) were resumed. Interestingly, the increased yield of AuNC of 20% is due for 10% to the expected decrease of the triangular and rod-like shapes, while for a 10% to an unexpected reduction of the quantity of spheroidal shapes. We think that this result comes from the difficult to distinguish between shape like cuboctahedron, decahedron or icosahedron in a TEM image, and therefore is coherent with an increase of single crystal seeds.

Improve the AuNC yield controlling the growth. In the last paragraph we see how, acting on the nucleation step, the yield of AuNC was increased from 40 to 65 %, but a large prevalence of spherical shape as by-product was still observed. Now, starting by the previous results, the next step is to promote the cubic shape over spherical one. We have already discussed that the formation of a cube over a sphere takes place when the facets {100} were opportunely capped, so that their growth rate is lower than the growth rate of the {111} ones (Figure 3.3). Clearly, there is no way to quantify precisely the growth rate of the facets during the growth of a nanoparticle. Therefore, starting from the gold seeds described in the previous paragraph we increase the concentration of the capping agent in the growth solution, i.e. CTAB, from 0.1 M to 0.125 M and examine the resulting dispersion of AuNC. The TEM images and extinction spectrum of this sample are reported in figure 3.11. The obtained AuNC#8 show a plasmonic band centred at 542 nm. The mean edge length of cubes was 45 ± 2 nm and the resulting yield increases until 85 %. Further increases in CTAB concentration over 0.125 M bring to lower reaction yields. This is because CTAB not only control the speed of growth of the nanoparticles facets but also the reduction rate of the $HAuCl_4$. [19]

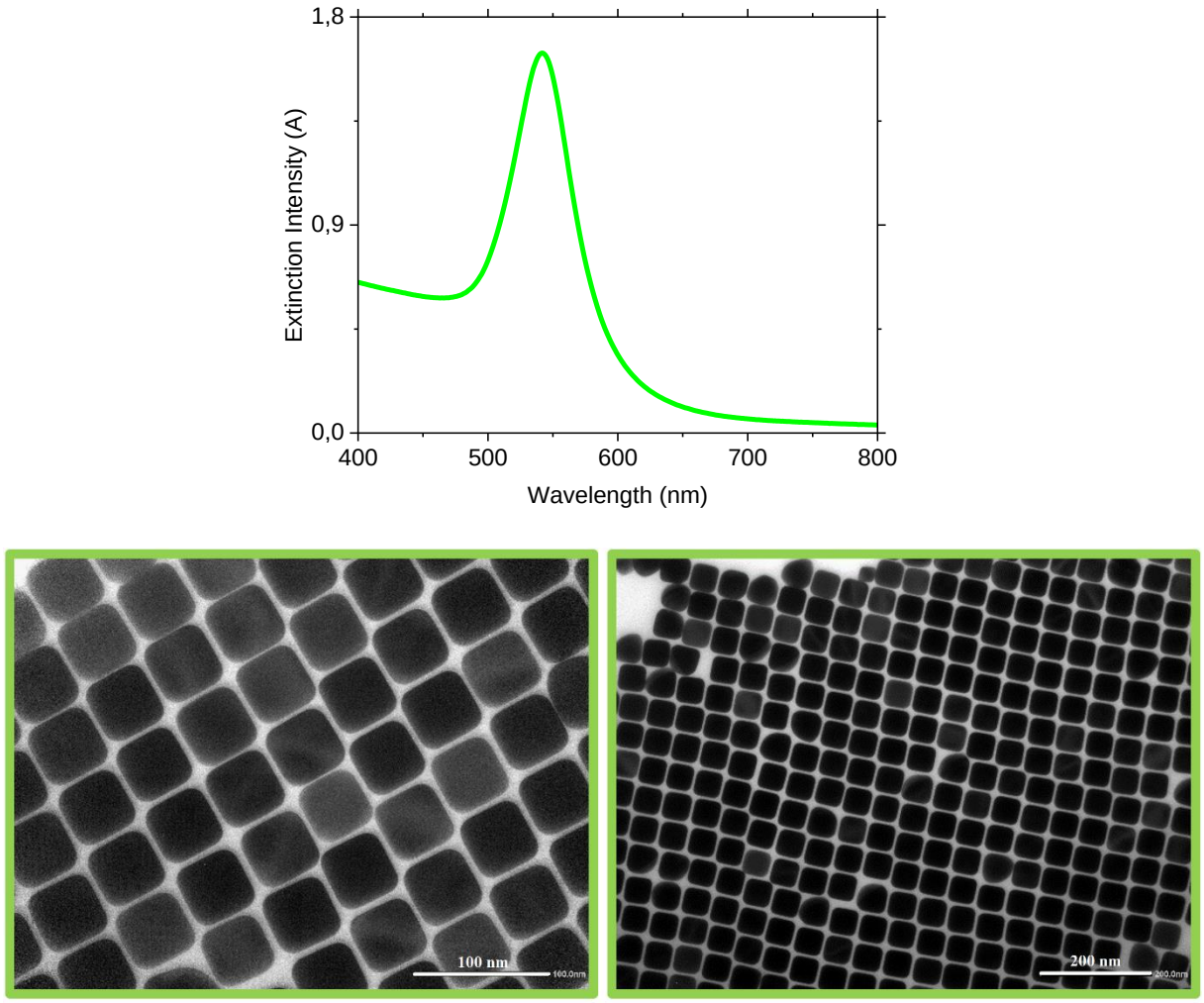

Figure 3.11 - Extinction spectrum (top) and TEM images (bottom) of AuNC#8, obtained increasing the concentration of CTAB in the growth solution.

Summarizing, with two simple changes both in the nucleation and in the growth step, based on understanding the processes that conduct to the cubic shape formation, it was possible to obtain a strong increase of AuNC yield up to 85 %.

Improve the AuNC yield through depletion-induced flocculation. In the previous section, a way to increase the yield of AuNC in the new synthetic batches was explored. To increase the yield in terms of cubic-shaped AuNP starting from the synthesis carried out following the original protocol, a technique that effectively separates them from by-products is needed. One of the most common technique for the purification of AuNP samples is centrifugation, based on the use of centrifugal forces to separate particles with different shape and size in solution: bigger particles will deposit on the bottom of the vials as *precipitate* while the smaller will remain dispersed in the *supernatant*. When differences between particles are small as in the

case of cubes and spheroidal by-products, centrifugation is not so effective because does not well discriminate between the two shapes. In this case is possible to obtain the selective separation of nanoparticles exploiting particular properties of colloidal dispersions, the so-called depletion forces. [20-23] This type of interaction occurs when in a colloidal dispersion there are objects (*e.g.* polymers or surfactant micelles) with dimensions between those of the objects present in the dispersion and those of the solvent molecules (see Figure 3.12). When two nanoparticles approach each other, the volume between the two NP is very small, resulting inaccessible also to little objects; in this so-called depletion zone (yellow area in figure 3.12) the absence of small objects creates a concentration gradient in the colloidal dispersion. This gradient generates an osmotic pressure that induces an attractive interaction between nanoparticles and therefore their flocculation.

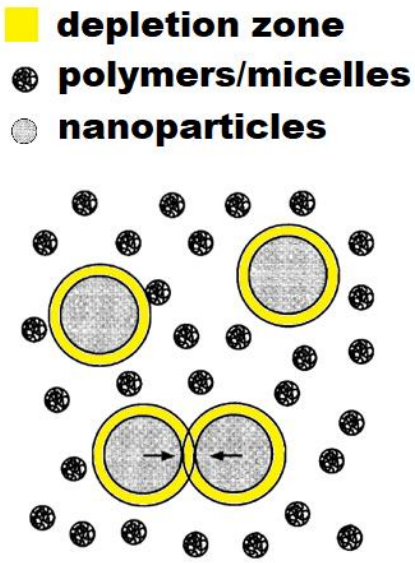

Figure 3.12 - Graphical representation of depletion forces in gold nanoparticles dispersion, modified from ref. 22.

For a colloidal dispersion of nanoparticles mixed with surfactant micelles (*e.g.* CTAB, CTAC and so on), the following Eq. 3.1 expresses the conditions for the depletion-induced flocculation:

$$|U(c_s)| = (2\,a_m)\,A\,\frac{(c_s - c_m)}{n}\,N_0\,K_B\,T \cong 4 - 5\,K_B\,T \qquad \text{(Eq. 3.1)}$$

where: a_m is the radius of the micelles, A is the nanoparticle cross section, c_s is the molar concentration of the surfactant, c_m is the critical micellar concentration, n is the number of surfactant molecules per micelle, N_0 is the Avogadro Number, K_B is the Boltzmann constant, and T is the temperature. As attested by Eq. 3.1 the flocculation potential is proportional both to the cross section of the nanoparticles and to concentration of micelles (*i.e.* A and c_s). Because the cross section of nanoparticles is strongly related to their shape and size, finely tuning the surfactant concentration it is possible to induce flocculation of nanoparticle with a specific shape and/or size. This powerful purification method was already employed for purification of AuNC samples. [23] Given the strong dependence of the flocculation potential from the size and shape of nanoparticles, a careful analysis of TEM images of the sample is needed to extrapolate the shape parameters to be included in Eq. 3.1. The experiment was conducted on the sample AuNC#3, that displays a cubic-shape yield of 48 % (see section A.4 of the Appendix for further details); by analysing various TEM images of this sample (which a representative picture is reported in Fig. 3.13a) a mean edge length of 54 ± 4 nm has been evaluated.

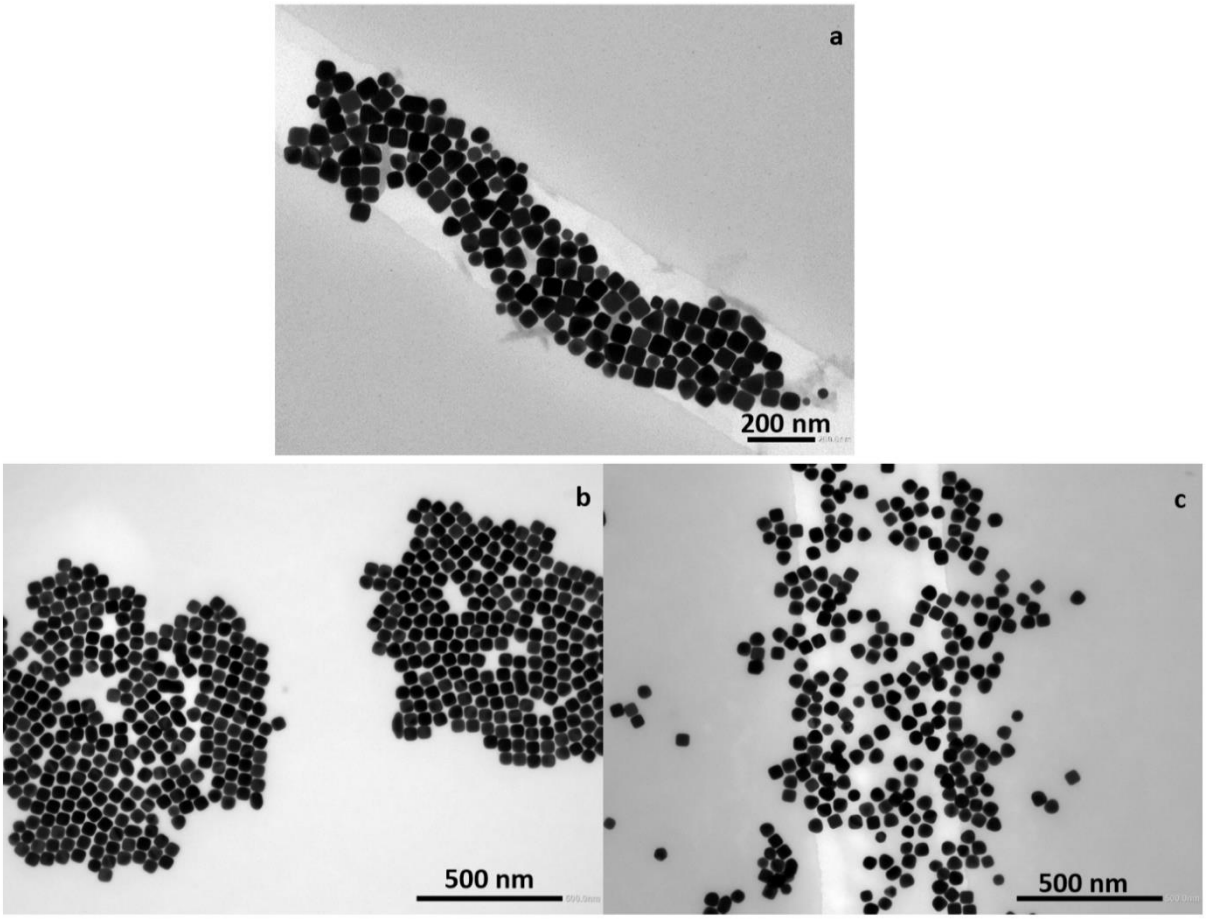

Figure 3.13 – Representative TEM image of AuNC#3 before flocculation (a). TEM images of AuNC#3 precipitate (p) and supernatant (c) after depletion induced flocculation with CTAC 134 mM.

To promote the flocculation of cubes with respect to the other shapes present in the dispersion, it is necessary to determine the appropriate surfactant concentration value on the basis of the cross section of NP. The cross section of a cube, *i.e.* the surface area of its face, was estimated assuming a perfect cubic shape with pointed vertices, and considering an edge length of 50 nm (which corresponds to the lower end of the confidence interval of the measured AuNC size). By-products, *i.e.* spheroidal, triangular, and rod-like nanoparticles have a much lower cross section so they should flocculate under higher potential values than the cubes. Hexadecyltrimethylammonium chloride (CTAC) was used as surfactant for their higher solubility in water respect to similar molecules (*e.g.* Benzyldimethylhexadecylammonium chloride, CTAB) that ensures no precipitation issue during the process. The parameters of the surfactant in the Eq. 3.1 (*i.e.* c_m = 0.001 M, n = 120, and a_m = 3nm) are selected according to literature [24, 25].

To find the proper CTAC solution concentration, under which flocculation of cubic-shaped particles in the colloidal dispersion takes place, 2 mL of AuNC#3 in H_2O were vigorously hand-shacked with 2 mL of five different CTAC aqueous solutions (Table 3.2). In details, the concentration of CTAC was changed between 70 – 200 mM, which, based on eq. 3.1, corresponds to flocculation potential between 5 and 15 K_BT. The dispersion was then left undisturbed overnight waiting flocculation to occur. Subsequently, the supernatant was removed and the precipitate was dispersed in 2 mL of H_2O. Both precipitate and supernatant were purified via centrifugation (4000 RPM per 30 minutes) to remove CTAC, dispersed again in 2 mL of H_2O, and characterized by TEM. The results of this experiment were summarized in Table 3.2. When CTAC solutions of 70 and 100 mM concentration, were added to AuNC dispersion no flocculation was observed, despite the theoretical predictions.

For a surfactant concentration of 134 mM, a value twice higher than the expected theoretical value, the best result was obtained; indeed, the TEM analysis shows that 81% of the cubes were found in the precipitate (fig. 3.13b), while the supernatant retains by-products with a residual percentage of 35% of cubic form (fig. 3.13c).

The difference between the value of the CTAC concentration used to obtain the best result and the theoretical value can be ascribed to the choice to approximate the nanoparticles shape to that of a cube with pointed vertices, instead of consider the corner's curvature, which entails an overestimation of the nanoparticles cross section and therefore an underestimation of the corresponding potential.

For increasing CTAC concentration (167 and 200 mM; see Table 3.2), the percentage of nanocubes in the precipitate is reduced, due to the contemporary flocculation of by-products as

well as smaller sized cubes, as confirmed by the contemporary reduction of the mean size of nanocubes.

Table 3.2 - Main experimental data carried out from characterization of flocculated AuNC@CTAB samples.

$U(c_s)$	c_s (mM)	% AuNC Precipitate/Supernatant	l_{cubes} Precipitate/Supernatant (nm)
5 K_BT	**70**	**n.a.**	
7.5 K_BT	**100**	**n.a.**	
10 K_BT	**134**	***81 % / 35 %***	***56 ± 4 / 51 ± 6***
12.5 K_BT	**167**	***71 % / n.a.***	***52 ± 4 / n.a.***
15 K_BT	**200**	***54 %/40 %***	***53 ± 3 / 46 ± 6***

3.2 - Synthesis and characterization of AuNS@$Na_3C_6H_5O_7$

The synthesis of Au nanospheres coated with trisodium citrate (AuNS@$Na_3C_6H_5O_7$) was carried out using a seeded growth strategy protocol based on the Turkevich/Frens reaction system. [26] The reaction was conducted in aqueous environment, controlling its kinetic by temperature. $Na_3C_6H_5O_7$ acts both as reducing and capping agent. The temperature of the reaction determines which reductive process occurs in the $HAuCl_4$ aqueous solution: in the first step, at 100 °C, reduction of Au(III) to Au(0), with nucleation and production of the AuSeed@$Na_3C_6H_5O_7$ (~ 10 nm), takes place. Decreasing temperature to 90 °C the reduction kinetic changes, so the Au(III) ions is reduced to Au(I), and start the growth process of nanoparticles on the catalytic surface of the AuSeed@$Na_3C_6H_5O_7$ seeds (Figure 3.14).. The presence of $Na_3C_6H_5O_7$, that binds more strongly to {111} facets than {100} ones [10], promotes the growth of the first crystalline facets than the latter, bringing to the growth of nanoparticles with a cubooctahedric shape, that can be approximated with a sphere.

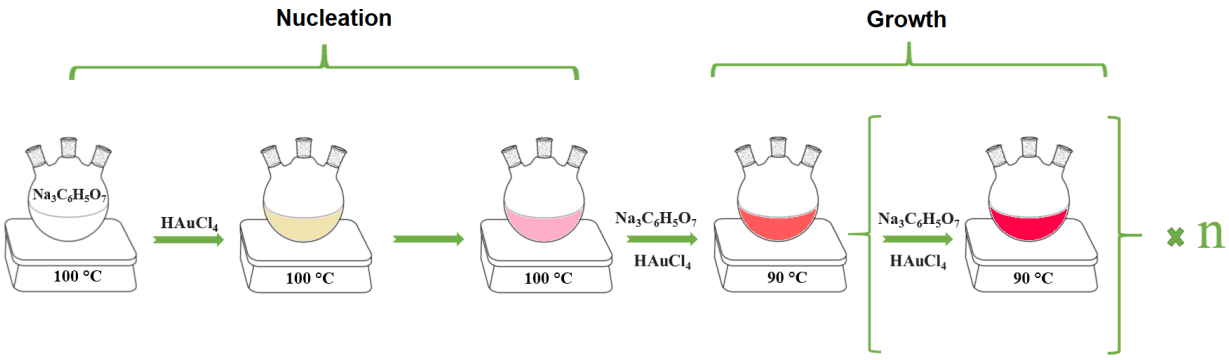

Figure 3.14 - Summary scheme of AuNS@$Na_3C_6H_5O_7$ seed mediated growth synthesis.

Experimental procedure. Briefly, 1 mL of $HAuCl_4$ water solution 25 mM was added to a boiling water solution of $Na_3C_6H_5O_7$ (150 mL, 2.2 mM) at reflux and under vigorous stirring. After 15 minutes, the solution, initially colourless, became pink. This colour changes certifying the reduction of Au(III) to Au(0) with formation of AuSeed@$Na_3C_6H_5O_7$ with a medium size of 10 nm (*nucleation step*). After the seed formation the temperature of the reaction was decreased to 90 °C, then 1 mL of $Na_3C_6H_5O_7$ 60 mM was added, followed by 1 mL of $HAuCl_4$ 25 mM after 2 minutes (*growth step*). The colour of the reaction solution starts to change from pink to pale red, attesting the growth in size of the starting spherical seeds. Iterating n-times the growth step of the process a gradual growth in size of the spheres until 30 nm takes place. Alternatively, an *accelerated growth* until the size of 180 nm can be obtained iterating the

following process: 55 mL of the nanoparticles dispersion were extracted and replaced with 53 mL of distilled H_2O and 2 mL of $Na_3C_6H_5O_7$ 60 mM. Then 6 mL of $HAuCl_4$ 25 mM were added in three aliquots of 2 mL, waiting 30 minutes between one addition and the next for the completion of the reduction process. After that, the sample was purified by centrifugation (4000 RPM per 20 minutes) to remove all the reactants in excess, and then it was characterized by UV-Vis spectroscopy and TEM.

Optical and morphological characterization of AuNS@$Na_3C_6H_5O_7$. In this case four *growth steps* and an *accelerated* one were performed, and AuNS#1 (see Appendix A.4) was obtained. The results of UV-Vis and TEM characterization were reported in Figure 3.15. The sample shows a plasmonic band centred at 523 nm, attributed to the dipolar plasmon mode. The medium size of the nanoparticles, calculated by TEM image analysis, was 38 ± 3 nm with a yield in terms of spheroidal shape of 98 %.

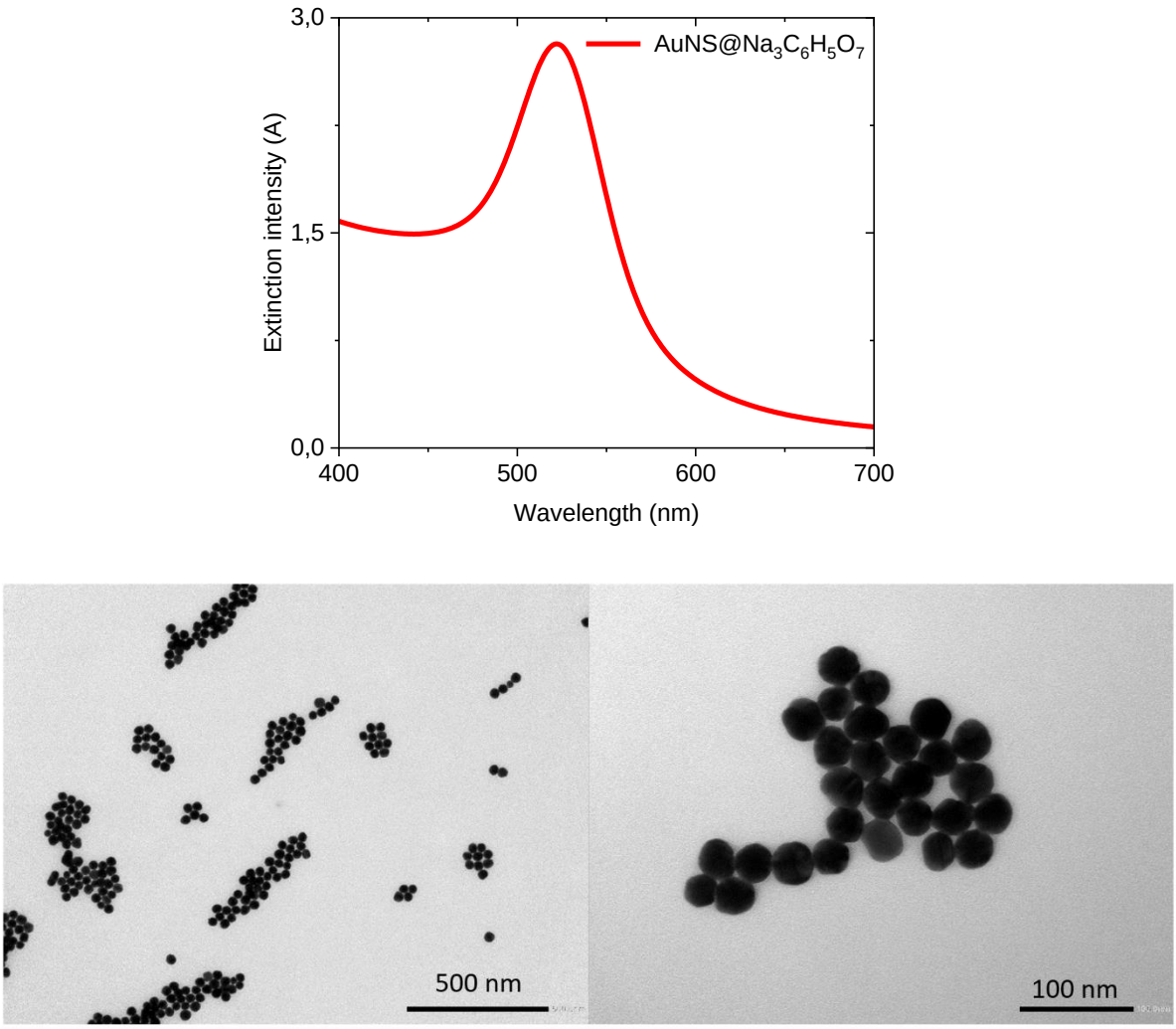

Figure 3.15 - Extinction spectrum and corresponding TEM images of AuNS#1 .

3.3 - Synthesis and characterization of AuNT@CTAC

The synthesis of Au nanotriangles coated with CTAC (AuNT@CTAC) was performed in aqueous environment following the work of Scarabelli *et al.* [27] This synthetic procedure consists in a nucleation step followed by two growth steps that allow high shape-yield and homogeneity of the final products (see Figure 3.16). In the nucleation step, Au seeds are formed in a similar way than AuNC seeds, *i.e.* using $NaBH_4$ as strong reducing agent. The use of CTAC as capping agent instead of CTAB generates bigger single crystal seeds, with medium size of 7 nm, because Cl^- anions bind more weakly to Au(0) than Br^-. [28]

The seed solution is added consecutively to two growth solutions, where the reduction from Au(III) to Au(I) takes place by means of a mild reducing agent (*e.g.* ascorbic acid) and where, thanks to the presence of directing agents (*e.g.* NaI) nanoparticles assume a triangular shape. From figure 3.3, we see that a particular type of seed, *i.e.* a plate with stacking faults, generates triangular plates. A stacking fault is a particular kind of defect that consists in an alteration of the usual alternation of the crystallographic planes in a crystal. Because seeds with crystallographic defects are thermodynamically unfavourable, they must be generated under kinetically controlled conditions, which are reached reducing the speed of ions reduction. [7, 29] This condition was obtained spatiotemporally splitting the growth process by using sequentially two growth solutions, and adding NaI to both solutions; actually, it is known that add iodide ions to a solution of Au(III) and Cl^- ions decreases the reducing power of ascorbic acid. [28] When the rate of atomic generation is low, the seeds cannot grow into large polyhedral structure, but the newly generated Au atoms tend to bind to the sides of the clusters, creating plate-like structures. [7] Furthermore, I^- ions bind preferentially on {111} facets, promoting the formation of nanocrystals bounded by low index facets, such as AuNT. [27, 28]

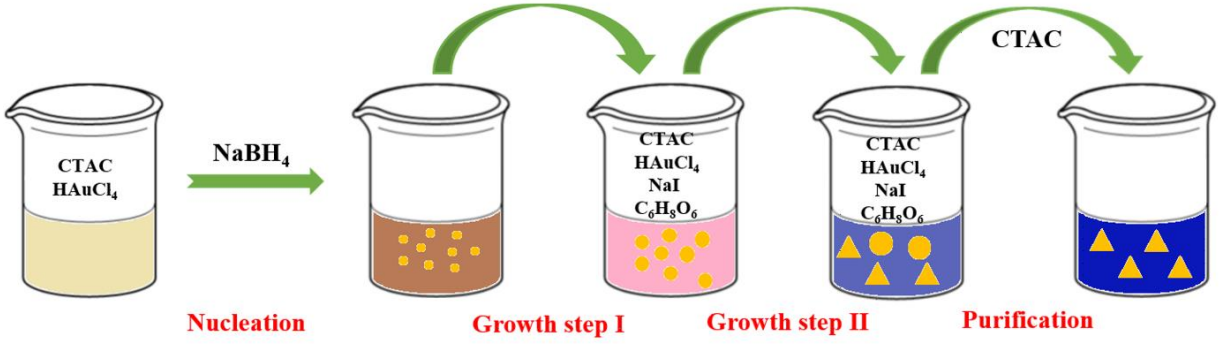

Figure 3.16. Summary scheme of AuNT@CTAC seed mediated growth synthesis.

Experimental procedure.

Preparation of AuSeeds@CTAC: 25 µL of 50 mM $HAuCl_4$ were added to 4.7 mL of a 100 mM CTAC solution. Then, 300 µL of ice-cold 10 mM $NaBH_4$ were injected "one-shot" and under vigorous stirring in the reaction flask. The change of the solution colour from yellow to brown attests the reduction of Au(III) to Au(0) and the formation of AuSeeds@CTAC. The as formed seeds were left undisturbed for 1 hour before use to exhaust all the $NaBH_4$ in excess.

Preparation of growth solution A: At 16 mL of milli-Q H_2O were added in sequence 3.2 mL of CTAC 100 mM, 80 µL of $HAuCl_4$ 0.05 M, and 30 µL of 10 mM NaI.

Preparation of growth solution B: The second growth solution was prepared by adding in sequence 156.5 mL of 50 mM CTAC, 1.955 mL of 50 mM $HAuCl_4$, and 1.175 mL of 10 mM NaI.

Mixing of the solutions: Before starting, the seeds solution was diluted ten times with H_2O. Then, 80 µL and 1.565 mL of 100 mM ascorbic acid, a weak reducing agent, were added to growth solutions A and B, respectively, followed by a quick manual stirring. This causes the reduction of the Au(III) to Au(I) attested by the complete discoloration of the two solutions (initially yellow) as already observed during the AuNC synthesis. Finally, 200 µL of the diluted seed solution were added to the growth solution A. The solution was manually hand-shacked for few seconds until it starts to turns pale-pink, and then was rapidly added entirely to growth solution B. After a rapid handshake, growth solution B was left undisturbed for 2 hours, during which it starts to assume violet colouration. The as-obtained AuNP dispersion was then characterized with UV-Vis spectroscopy and TEM.

Purification and characterization of AuNT@CTAC. The optical and morphological characterization of the resulting sample, AuNT#1, were reported in Figure 3.17. TEM characterization (red frame image) shows that equilateral AuNT with a medium side length of 49 ± 4 nm and a yield of 45 % has been generated. At the same time, spheroidal by-products are also present. This explains the presence of two plasmonic features in the extinction spectrum (see the spectrum in Figure 3.17, red line): the maximum centred on 640 nm is typical of Au nanotriangles while the large and intense shoulder around 538 nm is due to spheroidal particles. The purification of AuNT was performed using CTAC to induce osmotically driven depletion induced flocculation, as already done in section 3.1 for AuNC@CTAB. In this case, the surface area of an equilateral triangle was used as nanoparticle cross section ($A = \frac{\sqrt{3} \times l^2}{4}$) in the Eq.

3.1, considering a side length (l) of 45 nm. The theoretical concentration of CTAC needed for induce flocculation of triangular shapes was 0.188 M, but, as in the case of AuNC#3, also for AuNT#1 the quantity of surfactant needed for their flocculation was double the predicted theoretical value (0.376). A similar discrepancy was already reported in the reference work, and attributed to the fact that the sides of the NT are not perpendicular to the most extended crystallographic facets; so, using the TEM images as a reference, their interaction cross-section is significantly overestimated. [27] The successful purification was confirmed by TEM image of flocculated (Figure 3.17, black frame images) where the quantity of triangular particles reaches the 82 % of the total particles. The extinction spectra of AuNT after the purification (Figure 3.17, black line) show a dramatic intensity reduction of the shoulder at 538 nm (due to by-products) and a slight red-shift of 4 nm of their main plasmonic band.

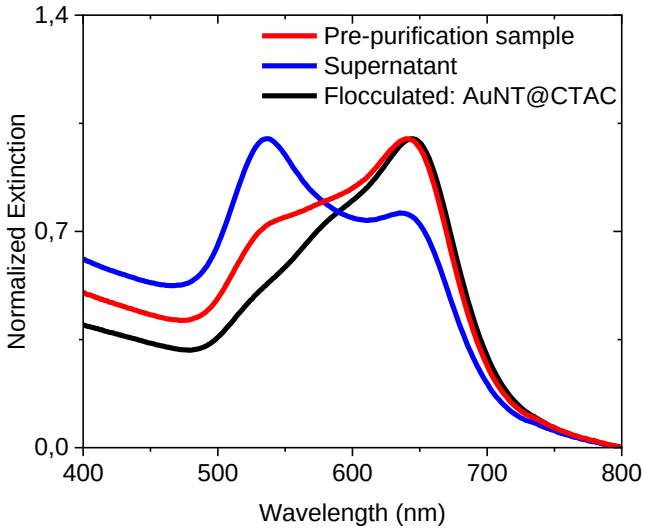

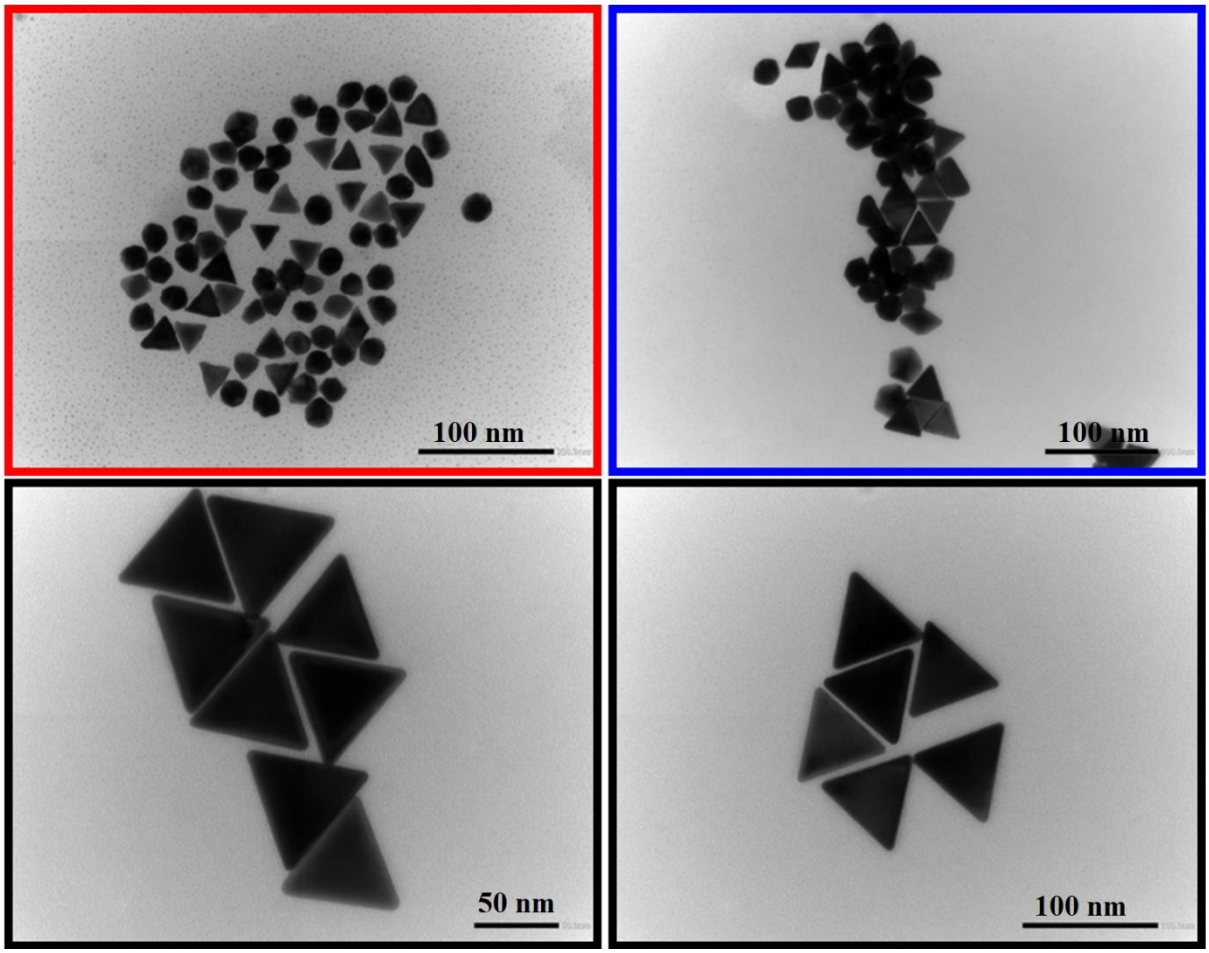

Figure 3.17. Normalized extinction spectra of AuNT#1 before (red line) and after (black and blue lines for precipitate and supernatant respectively) depletion induced flocculation. Representative TEM images of AuNT@CTAC in H_2O immediately after the synthesis (red frame), and of flocculated (black frame) and supernatant (blue frame) obtained from depletion induced flocculation process: the frame colour correspond to the traces of extinction spectra.

3.4 - Synthesis and characterization of AuNR@CTAB

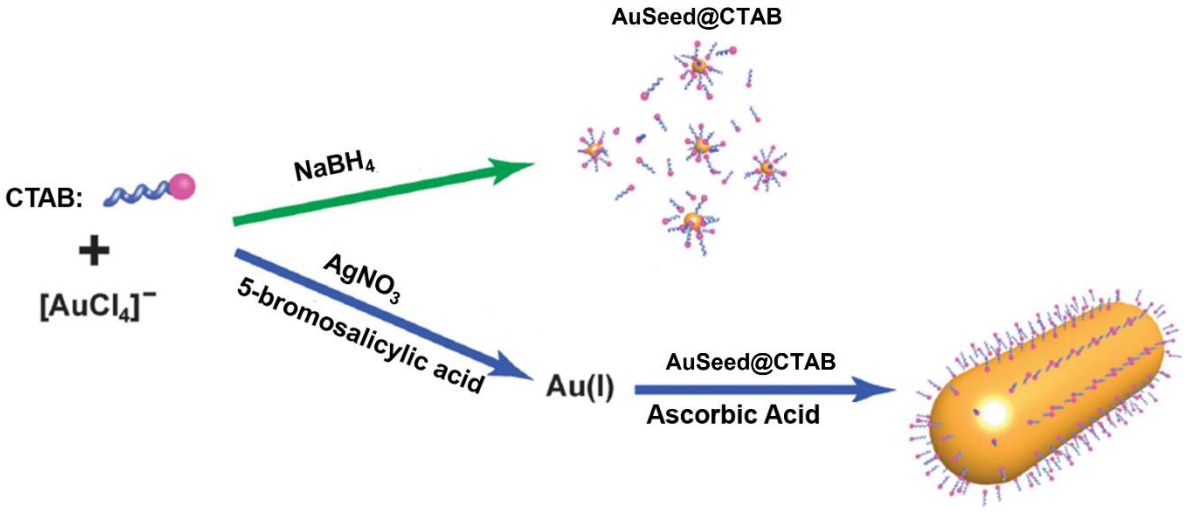

Figure 3.18 - Summary scheme of AuNR@CTAB seed-mediated growth synthesis. [30]

The seed-mediated growth strategy employed in this case was proposed by Liz-Marzan *et al.* providing Au nanorods coated with CTAB (AuNR@CTAB) in H_2O. [15, 30] It can be divided into 3 main steps: *nucleation of AuSeed@CTAB, preparation of the growth solution, mixing of the solutions* (see Figure 3.18). As reported in figure 3.3, AuNR (namely octagonal rods) can be produced through the anisotropic growth of single crystal seeds; it means that seeds formation is conducted under thermodynamic control while nanoparticle growth is conducted under kinetic control. Therefore, the separation between nucleation and growth offered by seed-mediated growth strategy is ideal for this purpose. The nucleation step is similar to that reported in AuNC@CTAB synthesis section (paragraph 3.1), and produces *single crystal* seeds with a diameter of 3-5 nm. The anisotropic growth was induced using two different capping agents, *i.e.* CTAB and $AgNO_3$. CTAB, over its c.m.c. (critical micellar concentration), will form elongated micelles in the growth solution, which act as templates for the growth of elongated particles. The role of $AgNO_3$ is still under debate, but it is believed that after its reduction to Ag(0), it binds to the lateral facets of nanoparticles, promoting their anisotropic growth along the direction {100} (tips will grow faster than lateral facets) in order to give the characteristic elongated shape. [30]

Experimental procedure.

Preparation of AuSeed@CTAB: 25 µL of 50 mM $HAuCl_4$ were dissolved in 4.7 mL of an aqueous 100 mM CTAB solution. Then, 300 µl of 10 mM was rapidly injected in the solution under vigorous stirring. The change in colour of the dispersion from yellow/orange to brown attest the reduction of Au(III) ions and the production of Au(0) seeds, similarly to what has been observed in the synthesis of AuNC@CTAB (see Figure 3.4). Also in this case, the as-produced seeds were left undisturbed for 1 hour to exhaust reductant excess.

Preparation of the growth solution: 45 mg of 5-bromosalicylic acid ($C_7H_5BrO_3$) were solubilized in 50 mL of an aqueous solution of 50 mM CTAB. Then were added in sequence 480 µL of 10 mM $AgNO_3$ and 500 µL of 50 mM $HAuCl_4$ after 15 minutes. At this point the pre-reduction of Au(III) to Au(I) takes place due to the action of 5-bromosalicylic acid. The reduction is evidenced by the gradual discoloration of the solution, initially orange (see Figure 3.19).

Mixing of AuSeed@CTAB with growth solution: First, 130 µL of 100 mM ascorbic acid were added to the growth solution. After 30 seconds 80 µL of AuSeed@CTAB were added under vigorous stirring. The addition of the seeds starts the anisotropic growth process of nanoparticles mentioned above. This process is described by the following disproportion reaction:

$$3\ Au^{+} \longrightarrow 2\ Au\ (0) + Au^{3+}$$

The Au(III) produced by the latter reaction is reduced again to Au(I) by the action of the specially added ascorbic acid, and then let the growth goes on until all the Au (I) was exhausted. At this point, the reaction mixture will have assumed the typical wine-red colour of gold nanorods colloidal dispersion (Figure 3.19).

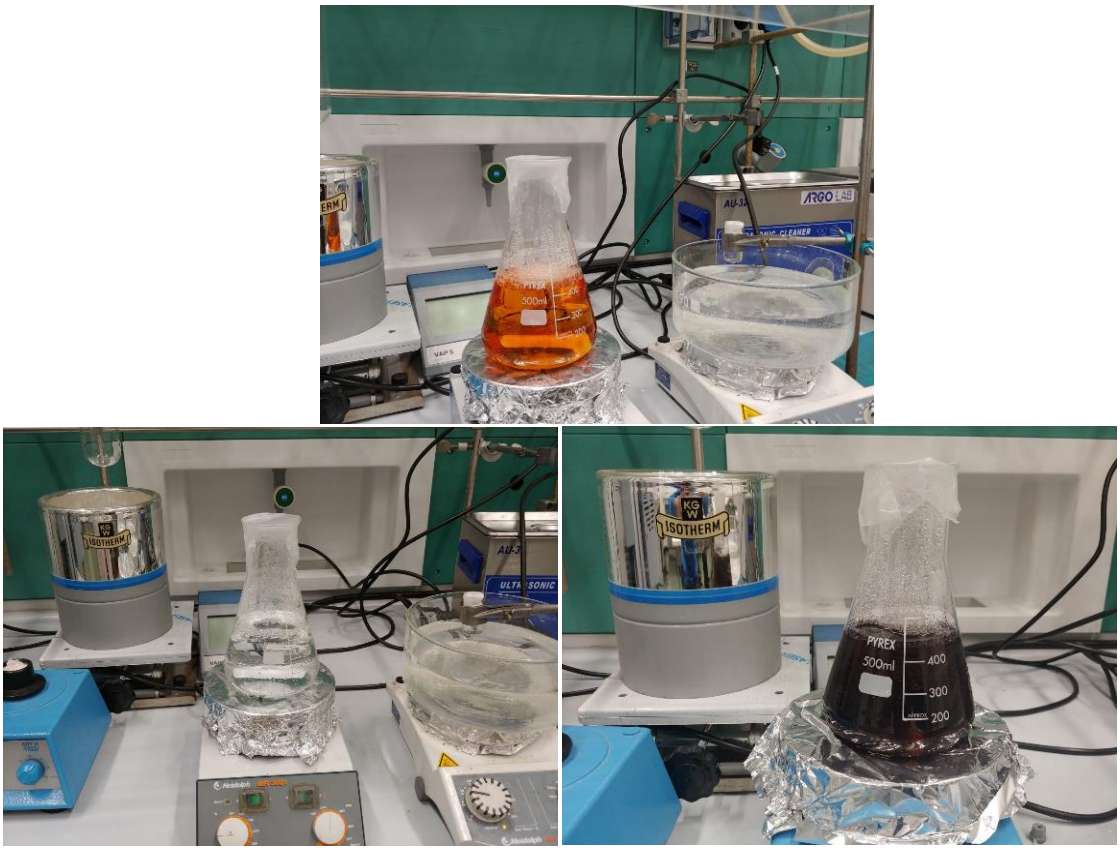

Figure 3.19 - Evolution of the growth process: freshly prepared growth solution (top), as the reduction process goes on (bottom, left), and after the addition of seeds when the formation of nanorods is complete (bottom, right).

The aspect ratio (i.e. the ratio between the length of long axis vs the length of the short one, A.R.) of the nanorods is determined by the ratio between the amount of Au(I) present in the growth solution (at the time of seed addition) and the amount of Au(0), i.e. the amount of seeds added. [15, 30] In the followed protocol the use of 5-bromosalicylic acid slows down the pre-reduction process of Au(III) (respect to other protocols where only ascorbic acid were used), allowing to monitor Au(III)/Au(I) ratio spectrophotometrically, through the measure of 396 nm Au(III) ions absorption band intensity in the growth solution. The intensity of this band decreases over time due to 5-bromosalicylic acid (see Figure 3.20). Correlating this data with the results of optical and morphological characterization of samples where seeds were added at different times (seeds addition stops the reduction process and starts the nanorods growth) a calibration curve can be build, which allow to predict the A.R. of the obtained AuNR@CTAB, as depicted in Figure 3.20. Briefly, by increasing time, and therefore the amount of Au(I) in the growth solution, increases at the expense of Au(III), and the AuNR aspect ratio decreases.

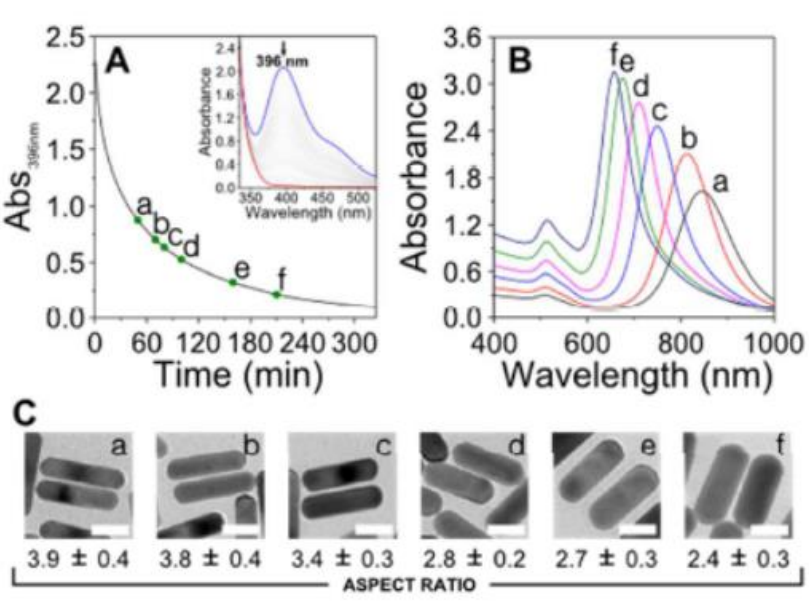

Figure 3.20 - Reduction over time of the intensity of the band centered at 396 nm in the spectrum of the growth solution (A). Absorption spectrum of the resulting nanorods (B) and related TEM images (C). [15]

Purification and characterization of AuNR@CTAB. After 12 h the sample was centrifuged to eliminate all excess reactants and at the same time separate the rod nanoparticles from the by-products (mainly spherical and cubic nanoparticles) through 2 centrifugation cycles of 20 minutes each at 9000 RPM. The pellet was re-dispersed in H_2O and characterized by UV-Vis spectroscopy and TEM. The results of optical and morphological characterization are reported in Figure 3.21.

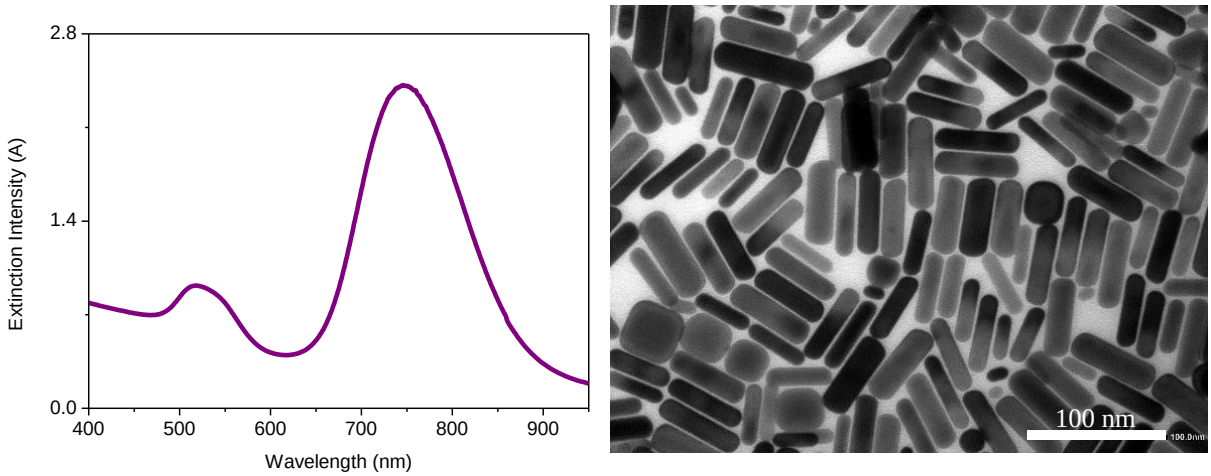

Figure 3.21 - Extinction spectrum of an AuNR#1 synthesized during this thesis work (left) and representative TEM image of the sample (right).

TEM image analysis shows AuNR with a medium size of 56 ± 6 nm x 16 ± 3 nm, with a calculated A.R. of 3.8. The calculated yield, in terms of AuNR produced than by-products, was 84 %. The extinction spectrum of AuNR#1 shows two plasmonic bands due to the anisotropy of electronic clouds that induces two different oscillation modes: the *transversal mode* plasmonic band is centred at 514 nm, while the *longitudinal mode* band has is maximum at 746 nm. The position of the transversal plasmon band is fixed for any sample, around 515 nm, while that of the longitudinal plasmon band varies according to the A.R. (see Figure 3.20). In particular, the longitudinal plasmon band red-shift as the A.R. increasing as a consequence of the greater amplitude of the oscillatory motion of the electrons. Another important aspect, able to give valuable information on the sample quality, concerns the shape of the two plasmonic bands. In fact, in an optimal situation, only two bands relating to the electron oscillation motions will appear in the sample spectrum, both with a perfectly symmetrical shape. However, the presence of by-products (*e.g.* spheres and cubes) or inhomogeneity in the size of AuNR can deform the aspect of the spectrum. In the case of the presence of inhomogeneous AuNR the longitudinal plasmon band will be asymmetrical. To quantify the homogeneity of a sample of nanorods, the full widths at half maximum (FWHM) of the longitudinal plasmon band is measured. A homogeneous sample generally has a FWHM between 100 and 150 nm, obviously more homogeneous AuNRs are, lower this value will be. In the case of the presence of by-products like spheres and cubes, a shoulder on the transverse plasmon band will be visible in the spectrum (around 540 nm), whose intensity will be directly proportional to the concentration of these impurities.

3.5 - Conclusions

In this chapter, synthesis of gold nanoparticles of various shapes (cubes, spheres, triangles and rods) and size were successfully carried out exploiting the high versatility of seed-mediated growth strategies, that trough the spatial and temporal separation of the two main phases of nanoparticles formation, i.e. *nucleation* and *growth*, allow a fine-tuning of the final nanoparticles shape. Clearly, like in any other chemical reaction, the most important parameter to evaluate the effectiveness of a synthetic strategy is the reaction yield. In the case of AuNP the reaction yield can be defined as the number of nanocrystals of the desired shape respect to the total number of nanoparticles in the obtained colloidal dispersion. Unfortunately, due to the great number of parameters hard to control involved in the growth of nanocrystals (*e.g.* temperature fluctuations, reactant purity and so on) it is very difficult to obtain the same results

in each world laboratories, and the gold nanoparticles synthesis usually suffer of reproducibility issues. In this context, understanding the mechanisms that control the nanoparticles growth according to a specific crystalline habit, it is possible to adapt any protocol to the specific conditions, improving the yield of the reaction and bringing to higher concentrations of the desired products. This was evident during AuNC@CTAB synthesis, where very low yields in term of cubic shaped AuNP were obtained at first. However, with opportune changes in both seed formation and growth (*i.e.* increasing speed of addition of the $NaBH_4$ in the reaction mixture and increasing the concentration of CTAB in the growth step, respectively) an improvement of the yield from 45 to 85 % was reached. Another important tool that helps to obtain monodispersed nanocrystals in both shape and size, is the purification step that can be performed trough centrifugation or depletion induced flocculation, depending on how the by-products differs in shape and size from the desired nanocrystals. Given the strong dependence of nanoparticles optical properties from their shape and size, sample purity is an essential feature if nanoparticles are meant to be used in any technological application.

The extinction spectra collected from AuNP of various shapes synthesized during the PhD research work were reported in figure 3.22.

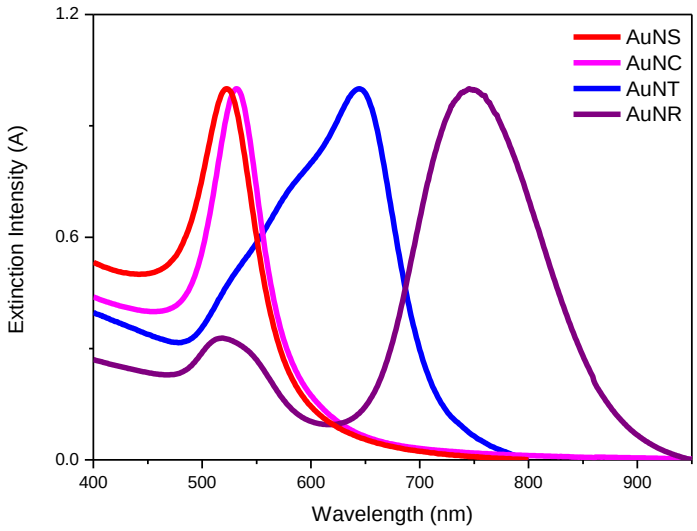

Figure 3.22 – Normalized extinction spectra of AuNPs synthesized during the PhD period.

The comparison between the four samples shows how different can be the optical response of AuNP varying their crystalline habit, due to the different oscillation modes possible for the electronic clouds of each nanoparticles, and thus their different resonance frequencies. In theory, opportunely engineering shape and size of AuNP system resonant at any wavelength of visible and NIR regions of electromagnetic spectra can be obtained, making them suitable for a very wide range of different applications. For example, AuNR@CTAB reported in figure 3.22

(purple line), show a longitudinal plasmon resonance band centred at 793, which is in the middle of the phototherapeutic window, so they can find application as phototherapeutic agents for the diagnosis and treatment of cancer.[37- 41] The LSPR of AuNT@CTAC (blue line), AuNC@CTAB (magenta line), and AuNS@CTAB (red line) centred respectively at 645, 533, and 522 nm, were exploited for improving the performance of organic solar cells, because the strong scattering and absorption of these nanoparticles in the region where the solar emission is maximum, can improve the optical performances of the active layer (responsible for the absorption of solar radiation and its conversion into electricity). In this context, play also a pivotal role the shape and size of nanoparticles employed, in fact due to the low thickness of organic solar cells layers, small sized AuNP or AuNT with their reduced thickness are the better choose because do not perturb the structure of the cell, preserving the charge transport trough the device.[37-41] Another example of the impact of the shape on the application of AuNP is constituted by AuNS and AuNC, which, as we see from figure 3.22, show a similar LSPR (the LSPR position of AuNC and AuNS of equal size differs of few nm). [16] However, the presence of sharp corners and tips in AuNC enhances strongly the plasmonic field generated by nanoparticles increasing their performances in sensing and field enhancement based applications. [42] Furthermore, because they expose facets with greater surface free energy than a sphere of equal size, shows a better catalytic activity.[43]

References

[1] P. Zhao, N. Li, and D. Astruc, State of the art in gold nanoparticle synthesis, *Coord. Chem. Rev.*, 2013, 257, 638–65;

[2] P. Jamkhande, N. Ghule, A. Bamer , M. Kalaskar, Metal nanoparticles synthesis: An overview on methods of preparation, *Journal of Drug Delivery Science and Technology*, 2019, 53, 101174;

[3] C. Dhand, N. Dwivedi, X. Loh, A. Jie Ying, N. Verma, R. Beuerman, R. Lakshminarayanan, S. Ramakrishna, Methods and strategies for the synthesis of diverse nanoparticles and their applications: a comprehensive overview, *RSC Advances*, 2015, , 5(127), 105003-105037;

[4] H. Lu, S. Y. Tang, G. Yun, H. Li, Y. Zhang, R. Qiao, and W. Li, Modular and Integrated Systems for Nanoparticle and Microparticle Synthesis—A Review, 2020, *Biosensors*, 10, 165;

[5] D. T. Nguyen, D. J. Kim, and K. S. Kim, Controlled synthesis and biomolecular probe application of gold nanoparticles, 2011, *Micron*, 42, 207–27;

[6] Y. Xia, K. D. Gilroy, H. Peng, and X. Xia, Seed-Mediated Growth of Colloidal Metal Nanocrystals, 2016, *Angew. Chem. Int.*, 2016, 55, 2 – 38;

[7] Y. Xia, Y. Xiong, B. Lim, and S. Skrabalak, Shape-controlled synthesis of metal nanocrystals: Simple chemistry meets complex physics? 2009, *Angewandte Chemie - International Edition*, 48, 60–103;

[8] A. Candreva, F. Parisi, G. Di Maio, F. Scarpelli, I. Aiello, N. Godbert, and M. La Deda, Post-synthesis heating, a key step to tune the LPR band of gold nanorods covered with CTAB or embedded in a silica shell, 2022, *Gold Bulletin*, 55, 195–205;

[9] Y. Zheng, J. Zeng, A. Ruditskiy, M. Liu, and Y. Xia, Oxidative etching and its role in manipulating the nucleation and growth of noble-metal nanocrystals, 2014, *Chemistry of Materials*, 26, 22–33;

[10] T. H. Yang, Y. Shi, A. Janssen, and Y. Xia, Surface Capping Agents and Their Roles in Shape-Controlled Synthesis of Colloidal Metal Nanocrystals, *Angewandte Chemie - International Edition*, 2020, 59, 15378–401;

[11] S. B. Gómez-Graña, Goris, T. Altantzis, C. Fernández-López, E. Carbó-Argibay, A. Guerrero-Martínez, N. Almora-Barrios, N. López, I. Pastoriza-Santos, J. Pérez-Juste, S. Bals,

G. Van Tendeloo, L. Liz-Marzán, Au@Ag Nanoparticles: Halides Stabilize {100} Facets, 2013, *The Journal of Physical Chemistry Letters*, 4(13), 2209-2216;

[12] M. Bakshi, S. Sachar, G. Kaur, P. Bhandari, G. Kaur, M. Biesinger, F. Possmayer, N. Petersen, Dependence of Crystal Growth of Gold Nanoparticles on the Capping Behaviour of Surfactant at Ambient Conditions, 2008, *Crystal Growth & Design*, Vol. 8 (5), 1713-19;

[13] S. Lohse, N. Burrows, L. Scarabelli, L. Liz-Marzán, C. Murphy, Anisotropic Noble Metal Nanocrystal Growth: The Role of Halides, 2014, *Chem. Mater.*, 26, 34−43;

[14] E. Dovgolevsky, and H. Haick, Direct observation of the transition point between Quasi-spherical and cubic nanoparticles in a two-step seed-mediated growth method, 2008, *Small*, 4, 2059–66;

[15] L. Scarabelli, A. Sánchez-Iglesias, J. Pérez-Juste, and L. M. Liz-Marzán, A "Tips and Tricks" Practical Guide to the Synthesis of Gold Nanorods, 2015, *Journal of Physical Chemistry Letters*, 6, 4270–9;

[16] M. Alsawafta, M. Wahbeh, and V. Truong, Simulated optical properties of gold nanocubes and nanobars by discrete dipole approximation, 2012, *Journal of Nanomaterials*, vol. 2012;

[17] L. M. Liz-Marzán, C. R. Kagan, and J. E. Millstone, Reproducibility in Nanocrystal Synthesis? Watch out for Impurities! 2020, *ACS Nano*, 14, 6359–61;

[18] M. Thiele, J. Z. E. Soh, A. Knauer, D. Malsch, O. Stranik, R. Müller, A. Csáki, T. Henkel, J. M. Köhler and W. Fritzsche, Gold nanocubes - Direct comparison of synthesis approaches reveals the need for a microfluidic synthesis setup for a high reproducibility, 2016, *Chemical Engineering Journal*, 288, 432–40;

[19] J. Rodríguez-Fernández, J. Pérez-Juste, P. Mulvaney, and L. M. Liz-Marzán, Spatially-directed oxidation of gold nanoparticles by Au(III)-CTAB complexes, 2005, *Journal of Physical Chemistry B*, 109, 14257–61;

[20] T. G. Mason, Osmotically driven shape-dependent colloidal separations, 2002, *Phys. Rev. E*, 66, 060402(R);

[21] K. Park, H. Koerner, and R. A. Vaia, Depletion-induced shape and size selection of gold nanoparticles, 2010, *Nano Lett.*, 10, 1433–9;

[22] R. A. L. Jones, Soft condensed Matter, *OUP Oxford*, 2002;

[23] J. E. Park, Y. Lee, and J. M. Nam, Precisely Shaped, Uniformly Formed Gold Nanocubes with Ultrahigh Reproducibility in Single-Particle Scattering and Surface-Enhanced Raman Scattering, 2018, *Nano Lett.*, 18, 6475–82;

[24] A. Malliaris , W. Binana-Limbele , and R. Zana, Fluorescence Probing Studies of Surfactant Aggregation in Aqueous Solutions of Mixed Ionic Micelles, 1986, *Journal of Colloid and Interface Science*, 110 (1), 114-120;

[25] V. K. Aswal, and P. S. Goyal, Counterions in the growth of ionic micelles in aqueous electrolyte solutions: A small-angle neutron scattering study, 2000, *Phys. Rev. E*, 61, 2947;

[26] N. G. Bastús, J. Comenge and V. Puntes, Kinetically controlled seeded growth synthesis of citrate-stabilized gold nanoparticles of up to 200 nm: Size focusing versus Ostwald ripening, 2011, *Langmuir*, 27, 11098–105;

[27] L. Scarabelli, M. Coronado-Puchau, J. J. Giner-Casares, J. Langer, and L. M. Liz-Marzán, Monodisperse gold nanotriangles: Size control, large-scale self-assembly, and performance in surface-enhanced RAMAN scattering, 2014, *ACS Nano*, 8, 5833–42;

[28] M. R. Langille, M. L. Personick, J. Zhang, and C. A. Mirkin, Defining rules for the shape evolution of gold nanoparticles, 2012, *J Am. Chem. Soc.*, 134, 14542–54;

[29] M. A. Mahmoud, Simultaneous Reduction of Metal Ions by Multiple Reducing Agents Initiates the Asymmetric Growth of Metallic Nanocrystals, 2015, *Crystal Growth Design*, 15, 4279–86;

[30] L. Scarabelli, M. Grzelczak, and L. M. Liz-Marzán, Tuning gold nanorod synthesis through pre-reduction with salicylic acid, , 2013, *Chemistry of Materials*, 25, 4232–8;

[31] X. Huang, S. Neretina, and M. El-Sayed, Gold Nanorods: From Synthesis and Properties to Biological and Biomedical Applications, 2009, *Advanced Materials*, 21(48), 4880-4910;

[32] C. Yao, L. Zhang, J. Wang, Y. He, J. Xin, S. Wang, H. Xu, Z. Zhang, Gold Nanoparticle Mediated Phototherapy for Cancer, 2016, *Journal of Nanomaterials*, vol. 2016, 1-29;

[33] S. Fang, C. Li, J. Lin, H. Zhu, D. Cui, Y. Xu, Z. Li, Gold Nanorods-Based Theranostics for Simultaneous Fluorescence/Two-Photon Luminescence Imaging and Synergistic Phototherapies, 2016, *Journal of Nanomaterials*, vol. 2016, 1-10;

[34] L. Arellano, E. Villar-Alvarez, B. Velasco, V. Domínguez-Arca, G. Prieto, A. Cambón, S. Barbosa, P. Taboada, Light excitation of gold Nanorod-Based hybrid nanoplatforms for simultaneous bimodal phototherapy, 2023, *Journal of Molecular Liquids*, 377, 121511;

[35] J. Liu, C. Detrembleur, M. De Pauw-Gillet, S. Mornet, C. Jérôme, E. Duguet, Gold Nanorods Coated with Mesoporous Silica Shell as Drug Delivery System for Remote Near Infrared Light-Activated Release and Potential Phototherapy, 2015, *Small*, 11(19), 2323-2332;

[36] X. Huang, I. El-Sayed, W. Qian, M El-Sayed, Cancer Cell Imaging and Photothermal Therapy in the Near-Infrared Region by Using Gold Nanorods, 2006, *Journal of the American Chemical Society*, 128(6), 2115-2120;

[37] C. E. Petoukhoff, Z. Shen, M. Jain, A. Chang and D. M. O'Carroll, Plasmonic electrodes for bulk-heterojunction organic photovoltaics: a review, 2015, *Journal of Photonics for Energy*, 5(1), 057002;

[38] J. L. Wu, F. C. Chen, Y. S. Hsiao, F. C. Chien, P. Chen, C. H. Kuo, M. H. Huang, and C. S. Hsu, Surface plasmonic effects of metallic nanoparticles on the performance of polymer bulk heterojunction solar cells, 2011, *ACS Nano*, 5, 959–67;

[39] L. Qiao, D. Wang, L. Zuo, Y. Ye, J. Qian, H. Chen, S. He, Localized surface plasmon resonance enhanced organic solar cell with gold nanospheres, 2011, *Applied Energy*, 88(3), 848-852;

[40] C. Wang, W. Choy, C. Duan, D. Fung, W. Sha, F. Xie, F. Huang, Y. Cao, Optical and electrical effects of gold nanoparticles in the active layer of polymer solar cells, 2012, *J. Mater. Chem.*, 22(3), 1206-1211;

[41] M. Notarianni, K. Vernon, A. Chou, M. Aljada, J. Liu, N. Motta, Plasmonic effect of gold nanoparticles in organic solar cells, 2014, *Solar Energy*, 106, 23-37;

[42] C. Deeb, X. Zhou, Miller R, S. K. Gray, S. Marguet, J. Plain, G. P. Wiederrecht, and R. Bachelot, Mapping the Electromagnetic Near-Field Enhancements of Gold Nanocubes, 2012, *J. Phys. Chem. C*, 116(46), 24734–24740;

[43] C. S. Bhatt, B. Nagaraj, and A. K. Suresh, Nanoparticles-shape influenced high-efficient degradation of dyes: Comparative evaluation of nano-cubes vs nano-rods vs nano-spheres, 2017, *J. Mol. Liq.*, 242, 958–65.

Chapter 4 - Self-assembling of AuNP at water/hexane interface: towards gold nanoparticles two-dimensional monolayers

As already discussed in Chapter 1 (see paragraph 1.4) when AuNP are in close proximity each other the mutual interaction between their plasmonic fields enhance the optical and electrical properties respect to stand-alone nanoparticles. The practical exploitation of plasmon coupling between nanoparticles goes through the realization of ordered two-dimensional arrays, which would guarantee an isotropic in plane optical and electrical response in a reduced thickness, corresponding to the height of a single nanoparticle. A similar combination of optical, electrical and morphological properties make AuNP 2D arrays very promising materials for applications in various technological fields, such as energy conversion, electronic, biomedicine, and sensing. [1-5] Among the myriad of AuNP available shapes, the cubic one with their six planar facets and a strong plasmonic field localized on their sharp edges, are ideal candidates as building blocks for the realization of ordered arrays. [6,7] However, the realization of these arrays is not a trivial problem. This is due to the large number of parameters and interactions forces that are usually involved in the realization processes of thin films, regarding both the interaction between building blocks and interaction of building block with solvents and solid substrates (interfaces). In the case of AuNP, these interfacial interactions became even more important, due to the enormous surface area involved. [8]

In Chapter 1 various methodologies have been described to obtain 2D arrays, the most interesting one is the interfacial self-assembly. This methodology is very promising because allows the formation of large-scale arrays of AuNP maintaining a high control during the film preparation, which results in an accurate control on the optical and morphological properties of the resulting film. Furthermore, these techniques result quick and low-cost because do not require any particular experimental setup. In this context, the self-assembly of AuNP at water/hexane interface firstly reported by Reincke *et al.* in 2004, constitutes a landmark in this field. [9,10] Adding a certain amount of EtOH to an aqueous dispersion of citrate-coated AuNS, in presence of a hexane layer above, the discoloration of gold colloid and the spontaneous formation of nanoparticles layer both to the interface and on the walls of the container was observed. The morphological characterization of the layer reveals the formation of an extended array of AuNS. After this pioneering work, the research in this field grew up exponentially,

with the aim of obtain multifunctional materials that exploit the incredible properties of coupled nanoparticles.

In this chapter, an experimental strategy already proposed in literature, based on self-assembly at a water/hexane interface, was adapted to obtain large two-dimensional arrays of AuNP of various shape (i.e. cubes, spheres, rods and triangles). The optical properties of these AuNP arrays were studied trough UV-Vis spectroscopy and correlated with morphological properties arising from SEM and XRD characterization. Then, the electrical conductivity of these intriguing nanomaterials was measured, to attest the suitability of these substrates as bases to build-up innovative electro-optical devices.

4.1 - Experimental procedure for the self–assembly of AuNP at water/hexane interface

The experimental procedure chosen for the deposition of AuNP at water/hexane interface was depicted in Figure 4.1, and is based on the works published by Park *et al.* [11,12] This technique improves the results obtained by Reincke *et al.* in terms of order and density of NP at the interface, through the *in-situ* functionalization of AuNP surface with 1-dodecanethiol. Furthermore, finely tuning the experimental parameters two-dimensional monolayers of various shaped AuNP could be obtained. In the above cited reference works, spheres and nanorods were successfully deposited; in this PhD work, the procedure was extended also to nanocubes and nanotriangles.

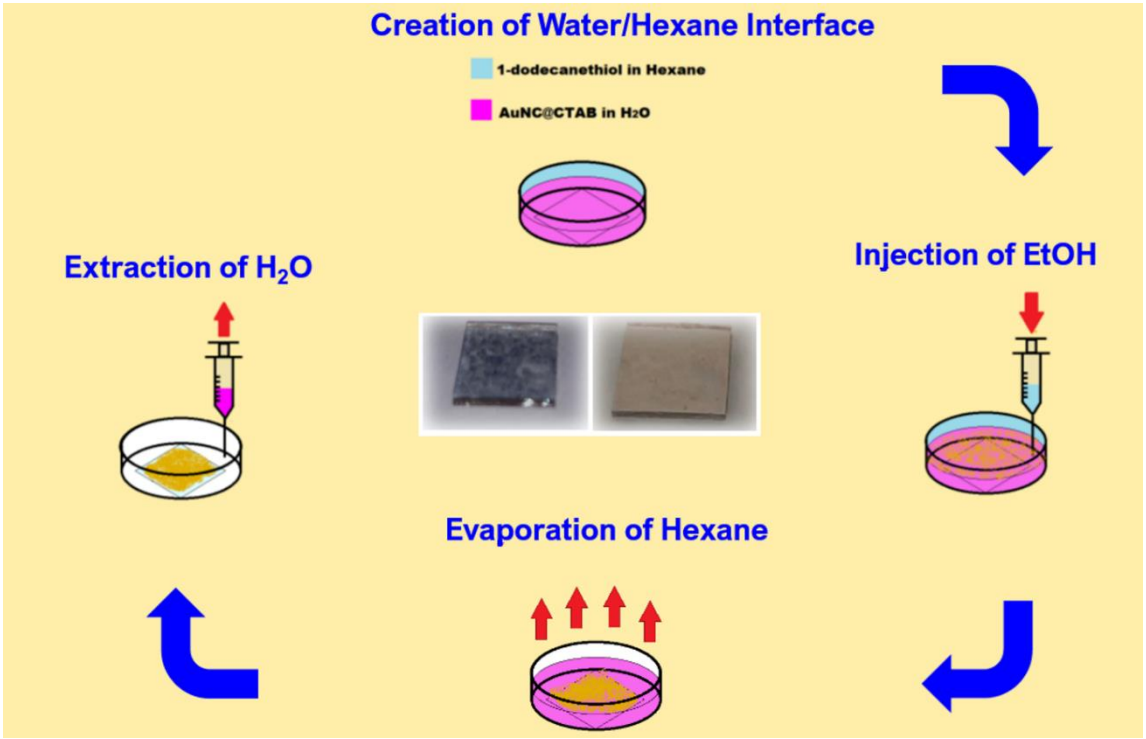

Figure 4.1 - Schematic illustration of the experimental procedure through which AuNP 2D monolayer were obtained. In the centre, photos of a typical AuNC monolayer after the deposition on an ITO glass taken from two different angles, showing the characteristical double coloration of these films.

For this purpose, hand-cut ITO or glass slides were opportunely treated using an appropriate procedure. Glass slides were immersed for 15 minutes into a piranha solution (3:1 mixture H_2SO_4 and H_2O_2), while ITO glasses were rinsed in a ternary mixture $H_2O/NH_3/H_2O_2$ 17:3:1 for 2 hours. [13,14] These cleaning procedures are crucial not only because remove most of the

organic contaminants from the substrate surface, but also because will promote the adhesion of the NP film to the substrate, making it hydrophilic. The cleaned substrate was then repeatedly washed with milli-Q H_2O, dried at air and finally placed on the bottom of a Petri dish with diameter of 28 mm. Then were added in sequence 2 mL of an aqueous dispersion of suitably coated AuNP, at the concentration of 3.25×10^{-4} M (estimated by the measurements of the absorption band centred at 400 nm [15], and 2 mL of 1-dodecanethiol in hexane at a given concentration depending on nanoparticles shape, to create a water/oil interface. The optimal concentration of 1-dodecanethiol in hexane solution is reported in Table 4.1, and was derived from a series of tests described below (see paragraph 4.4).

Table 4.1 -Concentration of 1-dodecanethiol used for the preparation of films of AuNP with various shapes.

AuNP	Size range (nm)	[1-dodecanethiol] (mol/L)
AuNS@$Na_3C_6H_5O_7$	**35 ÷ 40**	**2.0×10^{-6}**
AuNC@CTAB	**45 ÷ 50**	**4.0×10^{-5}**
AuNR@CTAB	**50 ÷ 55 x 15 ÷ 20**	**1.33×10^{-5}**
AuNT@CTAC	**50 ÷ 55**	**4.0×10^{-5}**

After water/oil interface formation, using a syringe, 1.2 mL of EtOH were slowly injected in the aqueous phase at the centre of the Petri dish in order to destabilize AuNP aqueous dispersion. As the volume fraction of EtOH in the aqueous phase increases an increasingly large golden layer of AuNP starts to form at the interface, accompanied by the simultaneous discolouration of the aqueous phase, that attests the successful migration of AuNP to the interface. The as-formed floating layers were left undisturbed until the complete evaporation of hexane, which combined with the functionalization of AuNP surface with 1-dodecanethiol molecules compact the layer. After that, the aqueous phase was carefully extracted using a syringe.

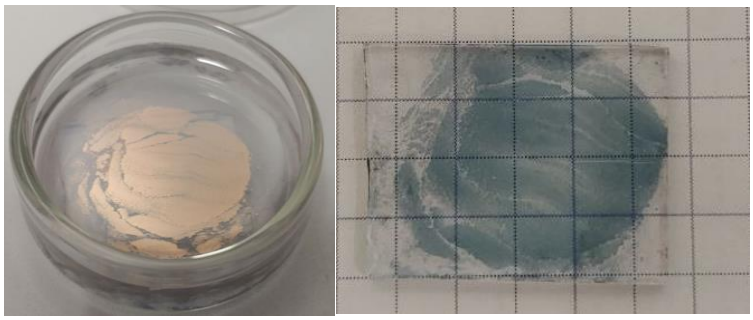

Figure 4.2 - Photos of typical AuNRs self-assembled monolayers at the water/air interface after the evaporation of hexane (left) and deposited on to a glass slide by draining the aqueous phase: the structure formed at the interface was preserved perfectly after the deposition on the solid substrate.

After hexane evaporation, the layer remains located at water/air interface and it behaves like a single-body; as the aqueous phase is extracted, the film slowly falls down on the bottom of the Petri, where will stick on the substrate surface (ITO or glass), keeping its structure intact as attested by the photos in Figure 4.2. After drying at air, the film was carefully washed twice with H_2O milli-Q, dried and then characterized by UV-visible spectroscopy, SEM, and XRD. The photos in Figure 4.1 and 4.2 shows how a typical AuNP film appears after the deposition on ITO glass (analogous results were obtained after deposition on glass slides). It shows a dark-blue coloration if observed in transmittance mode (obtained with the objective parallel to the film surface and with flashlight on), and a gold-shining colour if observed in reflectance mode (obtained with objective inclined respect the surface of the glass and under ambient lights). This was already observed for others nanoparticles extended arrays [16, 17]. The blue colour is typical of AuNP systems that experience strong plasmonic coupling due to the red-shift of the plasmonic band, while the gold coloration is very interesting, since attests intermediate properties between that of a single nanoparticle and bulk gold. [16, 17]

4.2 - Principles that control the self-assembly of AuNP at water/hexane interface

The choose to perform the assembly of AuNPs at the interface between two immiscible solvents is due to the fact that an interface can be considered as a planar and defect-free surface, therefore it will not influence the final morphology of the AuNP layer, differently from usual solid substrates. Among the wide range of available organic solvents, hexane was preferred to form the interface with H_2O for its strong volatility, non-polarity, low density, and stability. [3] Let

now consider what happens during the deposition process step-by-step, as depicted in figure 4.1. At the start of the process, when the interface is formed, the contact angle of AuNP colloid with the aqueous phase (θ_w) is lower than 90°. This means that they are perfectly dispersed in H_2O and the positive surface charge density on its surface, due to the presence of CTAB/CTAC electric double-layer (or negative in the case of AuNS, which are coated with $Na_3C_6H_5O_7$), prevents any coalescence phenomenon. When EtOH is added to the aqueous phase a double effect is produced: there is a reduction of the dielectric constant of the medium in which the AuNPs are dispersed and at the same time EtOH reduces the surface charge density of the AuNPs weakening the coating agent. Overall, the contact angle of the AuNPs increases approaching to 90°, they are destabilized in the hydroalcoholic solvent and start to migrate to the interface [9,10]. Because they maintain a residual amount of surface charge their hydrophobicity results enough to leave the aqueous phase but not enough to coalesce or disperse in the upper oil phase. So AuNP will stay to the interface, equally wetted by the two solvents, and form a floating gold-shining layer. At the interface, 1-dodecanethiol, dissolved in the hexane phase, will functionalize the exposed AuNP surface, creating Van der Waals attractive forces between the alkyl chains of the thiols molecules that compact the layer (see Figure 4.3). At this point, the film has two sides; one coated with CTAB in contact with the polar interface and the second, coated with alkyl chains in contact with the non-polar interface. After the slow evaporation of hexane, the layer, now at the water/air interface, behaves like a rigid body, which can be transferred onto solid substrates by gently drain the aqueous phase below by a syringe.

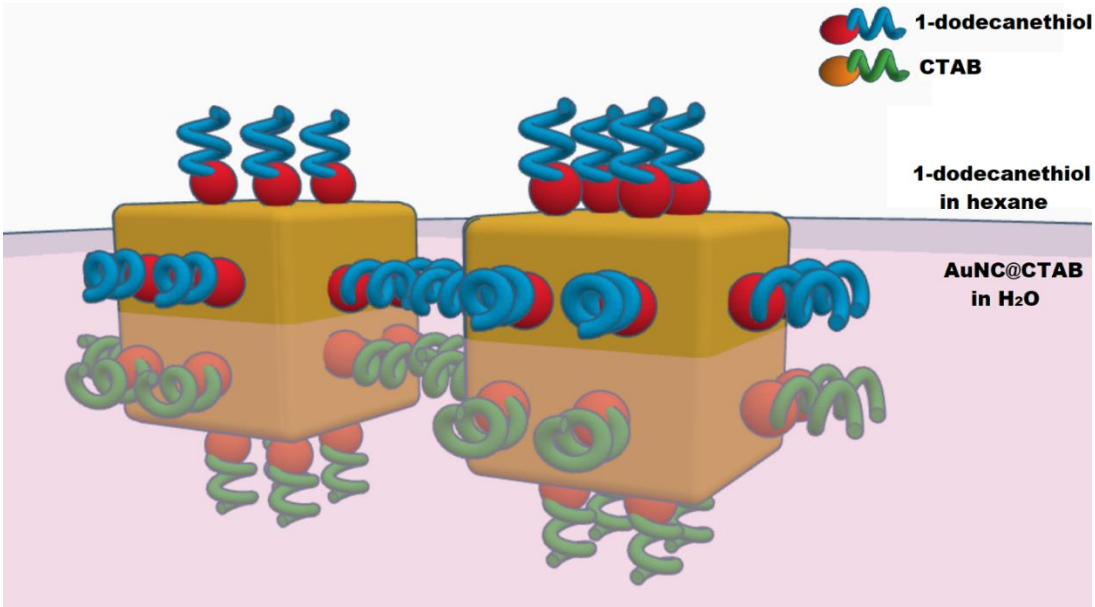

Figure 4.3 - Graphical illustration of AuNC at water/hexane interface, gold nanoparticles surface will be partially coated with 1-dodecanethiol molecules and assembles densely.

From the discussion above it results clear that the coating agent of AuNP plays a pivotal role in the formation of AuNP arrays at water/hexane interface. The destabilization of the aqueous colloidal dispersion of AuNP trough EtOH addition lies on the reduction of surface charge on AuNP. So, this tecnique can be applied only to AuNP sample coated with chemical species that interact electrostatically with nanoparticles. Furthermore, the coating agent must ensure a perfect stability of AuNP in water and contemporarly must not make them soluble in ethanol and hexane, in order not to have a simple AuNP phase migration. The three coating agents with which our different samples are coated (CTAB for AuNC and AuNR, CTAC for AuNT and $Na_3C_6H_5O_7$ for AuNS) possess all the characteristics described above, so AuNP synthesized Chapter 3 were suitable for self-assembly at water/hexane interface without any modification of its coating.

4.3- Improving the quality of AuNP 2D arrays

As described in the last paragraph the formation process of 2D self-assembled AuNP arrays at water/hexane interface involves various factors that can affect the quality of the resulting materials. In the following paragraph, the impact of each parameter on the formation of AuNP films was discussed separately.

Ethanol volume fraction. As we have seen, the addition of an opportune quantity of EtOH reduces the surface charge density on AuNP. Figure 4.4 shows clearly that increasing the ethanol quantity added to a colloidal dispersion of Au nanospheres coated with $Na_3C_6H_5O_7$ their surface charge density decreases. [9] Consequently the number of nanoparticles that leaves the aqueous phase and populate the interface increases. The relation between these two parameters is not linear, so at a certain point a plateau is reached, *i.e.* adding more ethanol, surface charge density does not decrease anymore, and this means that a residual charge always remains on AuNP surface that avoid particles coalescence.

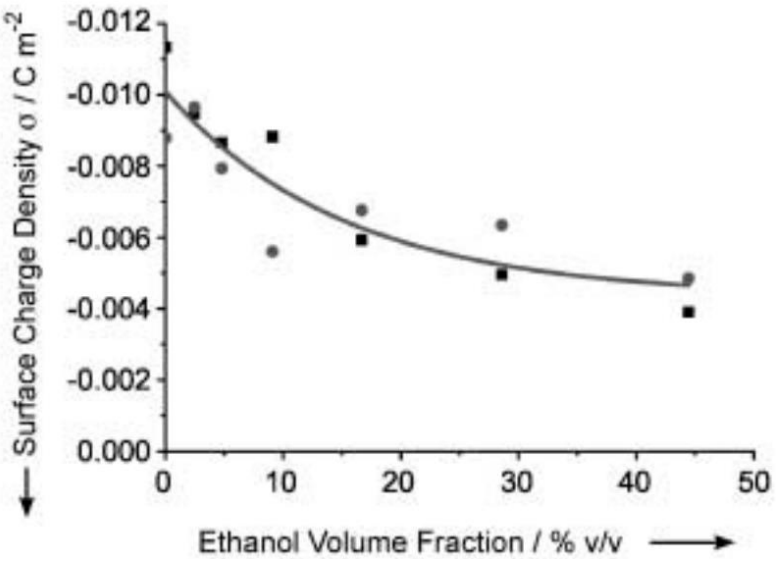

Figure 4.4 – Reduction of the surface charge density of Au nanospheres coated with $Na_3C_6H_5O_7$ colloidal dispersion increasing the ethanol volume fraction, reported from ref [9].

However, we have found that in our experiments there is an upper limit to the amount of ethanol that can be added without observing coagulation of the nanoparticles. In fact, we found that if the quantity of EtOH exceed the 60% volume fraction of the AuNP colloidal dispersion the colour of the latter starts to became grey, and after a while a dark precipitate, *i.e.* aggregated nanoparticles, will deposit on the bottom of the Petri. For this reason, the quantity of EtOH added was fixed to 1.2 mL for 2 mL of AuNP, in order to maximize the number of AuNP that left the dispersion and migrate to the interface avoiding any coalescence phenomena.

Amount of the coating agent. Another critical parameter of the deposition process is the amount of the coating agent in the starting AuNP colloidal dispersion. To verify the effect produced on film formation, two AuNR arrays were prepared starting from the sample AuNR#1 synthesized in chapter 3 (see section A.4 in Appendix for details). The sample was divided into two aliquots: the first was used as it was, while the second was centrifuged at 4000 RPM for 30 minutes, in order to reduce the amount of CTAB contained in it. After that two AuNR arrays was deposited on glass slides, **NR_1** and **NR_2** respectively, using the procedure described in section 4.1.

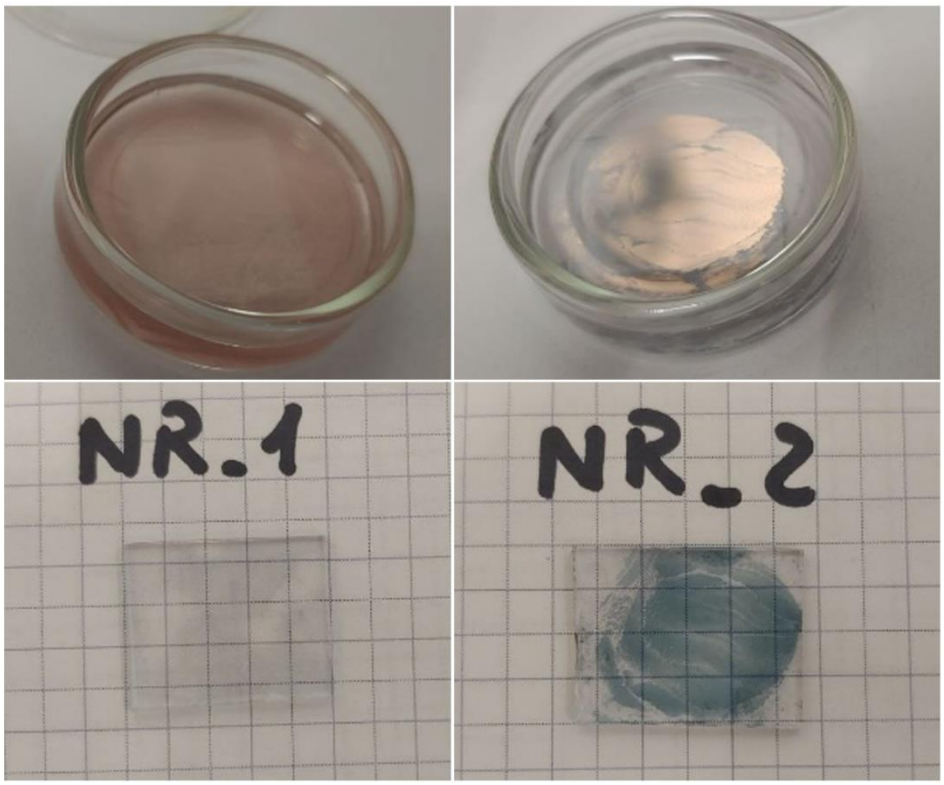

Figure 4.5 - Photos of NR_1 and NR_2 at water/air interface after the hexane evaporation (top) and after their deposition on to the glass slide (bottom).

The as-prepared samples show clear differences: sample **NR_2**, with less CTAB, appears more compact and denser with a brghter gold/deeper blue coloration than **NR_1,** which results hardly visible to naked eye instead, both at the interface and onto the slide (see figure 4.5). Moreover, the residual aqueous dispersion of **NR_2** resulted colourless, while **NR_1** maintains the typical coloration of AuNR aqueous dispersions after adding the same volume of EtOH (1.2 mL). The reason of the observed difference lies in the principle of the technique used for the deposition, which is based on the reduction of the surface charge density of gold nanoparticles by addition of EtOH. In **NR_1** where the concentration of CTAB in solution is higher than **NR_2**, due to the fewer number of purification steps, the surface charge density on nanoparticles is higher too. In these conditions, the quantity of EtOH added induces the migration of a lower amount of nanoparticles at the interface and consequently the deposition obtained is poorer than **NR_2**. For this reason an additional centrifugation step at 4000 RPM for 30 minutes were performed to all AuNP samples prior to the self-assembling procedure.

Effect of hexane evaporation. The evaporation of hexane is one of the most important step in the film formation because the forces generated during this process contribute to compact the obtained layer of AuNP. However, the evaporation of a solvent is strongly influenced by environmental conditions, so, if not controlled, generates reproducibility issues of the film structure at macroscopic scale. The impact of the hexane evaporation speed on the resulting films aspect was studied trough the preparation of three different samples of AuNC arrays, varying the speed of hexane evaporation (sample AuNC#8 were used for these depositions, see section A.4 in Appendix for details). In the first case the evaporation was conducted in environmental condition (*i.e.* 20 °C, and it requires almost 40 minutes); in the second case was speed-up using the hood (the evaporation time reduces to 15 minutes); finally, in the third case a hexane-saturated environment was created to heavily slow-down evaporation that in these conditions requires almost 4 hours.

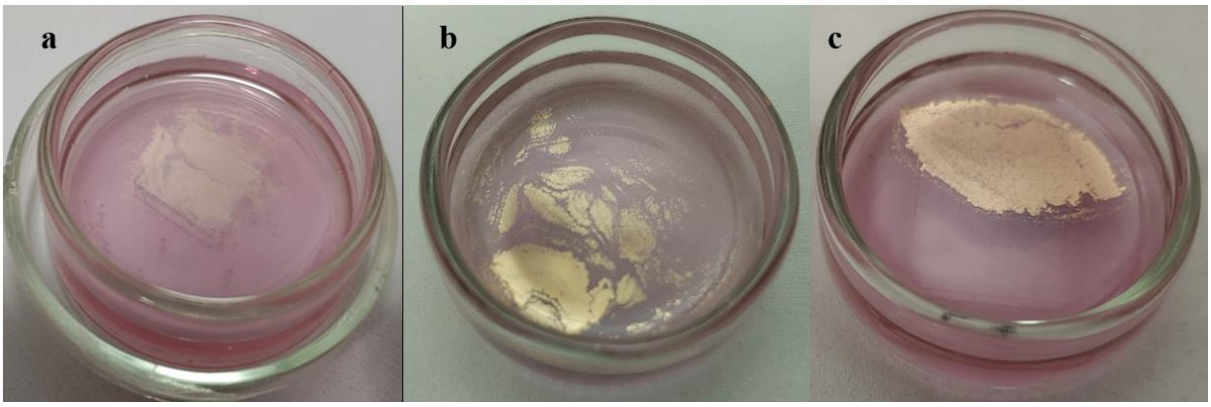

Figure 4.6 - AuNC arrays at water/hexane interface after the evaporation of hexane at (a) room temperature, (b) speeding up the evaporation using the hood, and (c) slowing it in a saturated chamber.

The results of these experiments were reported in figure 4.6, where photos of the AuNC arrays at water/air interface, after the fully evaporation of hexane, were reported. The three sample were named a, b, and c, respectively. As we see from figure 4.6b, when the hexane evaporation occurs quickly the structure of the film appears more fragmented and dispersed on the interfacial surface than the sample used as reference (figure 4.6a). Slowing-down the evaporation process (figure 4.6c) all the macroislands of AuNC assembles togheter producing a film with a more compact structure. This is of a great importance because the plasmonic response, as we will see in paragraph 3.5, is strongly influenced by the morphology of the nanoparticles assembly. In Figure 4.7 exctinction spectra of samples a and c after their deposition on the glass slides were reported. The spectra are registered placing the glass slide in two different positions on the sample holder, therefore two different areas of the films were

irradiated, indicated in Fig. 4.7 by black and red line. As we see, in the case of sample c, the extinction spectra is pratically indentical in the two cases, while there are clear differences in extinction maximum considering the sample a. As expected, the improved density and compactness of the film obtained after the slow evaporation of the hexane makes the plasmon response of the resulting films constant over the entire slide surface.

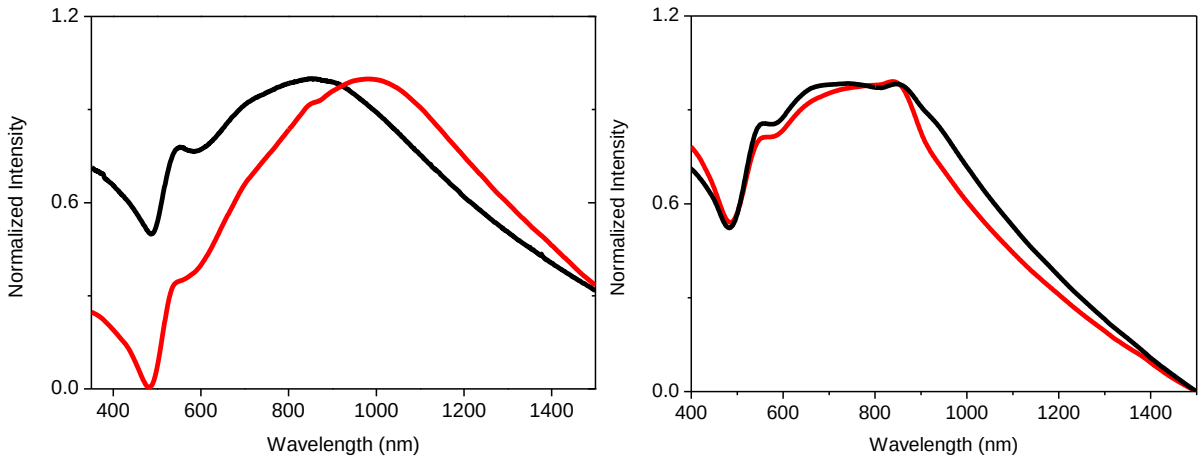

Figure 4.7 – Extinction spectra of samples a, and c irradiated in two different area of the glass slide.

Janus nature of AuNP arrays and deposition on solid substrates. Regarding the deposition technique used to collect the AuNP array on substrates (*i.e.* ITO, glass), two different techniques were tested in this PhD work. In particular, AuNP film was tried to transfer from water/air interface (after the hexane evaporation) onto a substrate with two different approaches, *i.e. drain-to-deposit* and *horizontal lifting (or Langmuir–Schaeffer deposition).* [16,18] In the first case, the AuNP array will stick on a substrate, placed on the bottom of the Petri dishes, by slowly draining the residual aqueous dispersion by a syringe. Because the interaction takes place between the substrate and the polar face of the film (coated with residual CTAB molecules, see Fig. 4.3), a previous hydrophilic treatment of the substrate is required for a successful deposition. Attempting to deposition using an untreated substrate leads to film cleavage, which tends to follow the aqueous phase flowing off the substrate surface rather than adhering to its surface. If the substrate is sufficiently hydrophilic, a water layer will remain on its surface after the draining, allowing the adhesion of the film on it (see Fig. 4.8).

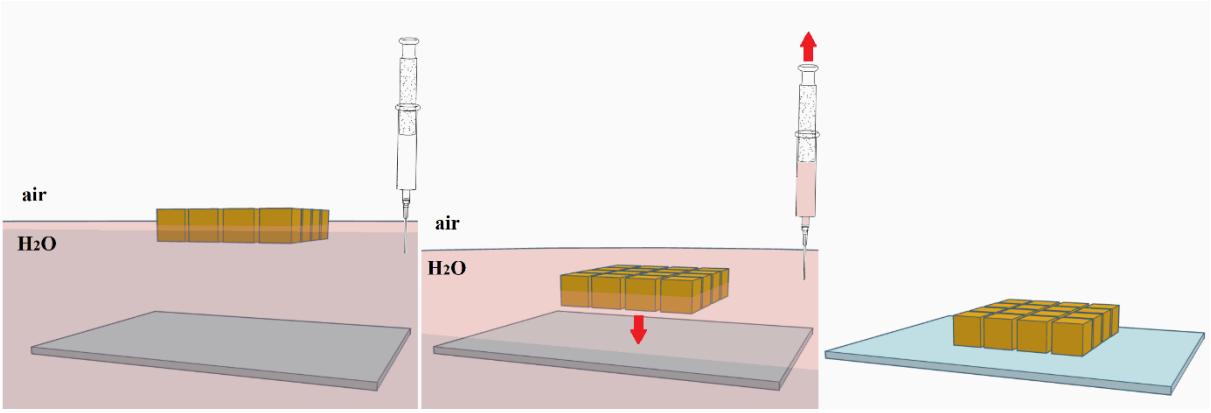

Figure 4.8 – Graphical representation of drain-to-deposit technique for the collection of AuNP arrays on solid substrates.

The horizontal lifting approach is to bring the substrate surface parallel and slowly into contact with the air/water interface where the AuNP array is located, with consequent sticking of it onto the substrate surface. In this case, the interaction is between the apolar face of the film, which exposed the hydrophobic 1-dodecanethiol alkyl chains (see Fig. 4.3), and the substrate surface (see Fig. 4.9).

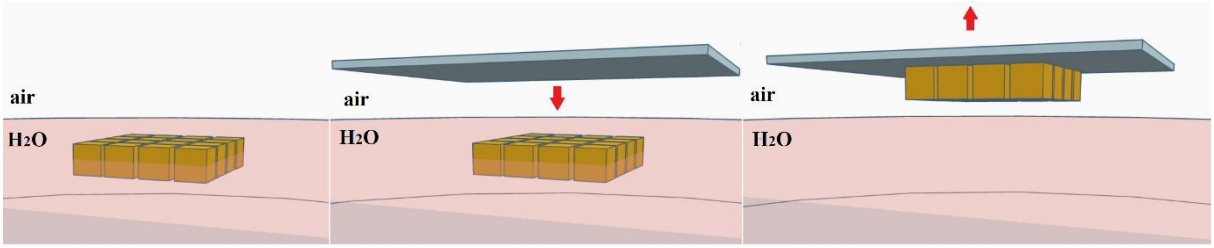

Figure 4.9 – Graphical representation of horizontal lifting technique for the collection of AuNP arrays on solid substrates.

In conclusion, if the *drain-to-deposit* approach is used, the film transfer will be successful if a hydrophilic substrate is used. Conversely, if the *horizontal lifting* approach is chosen, the transfer will be achieved using a hydrophobic substrate.

Regarding the effectiveness of the tested deposition techniques, the *drain-to-deposit* is the most reliable; in fact, it is more reproducible because less dependent from operator. In the case of *horizontal lifting*, sometimes the process fails also in the case of substrate slide opportunely treated, for difficulties in scaling opportunely the approach speed to the interface. Therefore, because the surface wettability of AuNP arrays is not relevant for this PhD thesis purpose, the *drain-to-deposit* method was chosen as standard technique to collect AuNP arrays from the water/air interface.

These experimental trails demonstrate indirectly the Janus nature of the AuNP monolayers: the upper and bottom surfaces have different wettability, and chemical properties, due to the different coating agents, *i.e.* 1-dodecanethiol and CTAB/CTAC/$Na_3C_6H_5O_7$. This characteristic was confirmed by literature trough contact angle measurements. [12] This is a very important aspect, which must be considered from the applicative point of view, *e.g.* in future device engineering.

4.4 - Morphological analysis

From what has been described so far it is clear that the morphology of the AuNP array is strongly dependent, among other things, on the concentration of 1-dodecanthiol. [11, 12] For this purpose, an accurate morphological study of the AuNP films in relation to the thiol concentration was performed by using a scanning electron microscope (SEM). In Figure 4.10, representative SEM images in two different magnification (*i.e.* 5000 X and 87500 X) of three **AuNC** arrays deposited on ITO glasses were reported, obtained without using 1-dodecanethiol (**NC_0**), and with thiol concentration of 4.0×10^{-5} M and 1.2×10^{-4} M (named **NC_1** and **NC_2** respectively). These arrays were obtained using AuNC#9 as starting colloidal dispersion of AuNC (see section A.4 in the Appendix). At low magnification (5000 X in Figure 4.10, left), the structure of the film is discontinuous, constituted by many islands of self-assembled gold nanoparticles. The islands have various shape and sizes that range between 5-20 μm. The percentage area covered by the depositions were calculated with ImageJ software, through the threshold method. At this magnification, the covered area appears almost regardless of the amount of 1-dodecanthiol, the estimated values are around 50 % of the total area, and follow the order **NC_2** > **NC_1** > **NC_0** (see table 4.2).

Table 4.2 - Morphological and spectroscopic data of AuNC films on ITO glass.

Sample	NC_0	NC_1	NC_2
Covering percentage: 5000X / 87500X	**47 % / 66 %**	**52 % / 80 %**	**54 % / 88 %**

Observing the high magnification images (87500X in Figure 4.10, right), that correspond to observe the arrangement of AuNC into each island, we see a very different organization of the nanoparticles. **For NC_0** the layer of AuNC is very disordered, with numerous voids and a covering percentage of 66 %. Despite some superposition were observed (visible on the SEM image as brightest white particles), the structure formed is clearly a monolayer. This is true for every island observed. By considering the sample **NC_1** where 1-dodecanethiol 4.0×10^{-5} M was used, a consistent increasing of the covering percentage was obtained, from 66 to 80 % of the total area. The film is still a monolayer and appears most ordered with less voids and overlaps than **NC_0**. A further increase of the 1-dodecanethiol concentration (sample **NC_2**) brings to an even better covering (88 %), but at the same time there are numerous areas where a multi-layered distribution (visible as the white stripe in the corresponding SEM image in Figure 4.10) were observed. This experimental evidence is totally in accord with the literature: a too high concentration of 1-dodecanethiol in the hexane phase promotes the formation of 3D structures. [11, 12] The morphologic differences observed for AuNP can be explained considering the forces that act among AuNC, responsible of the film formation.

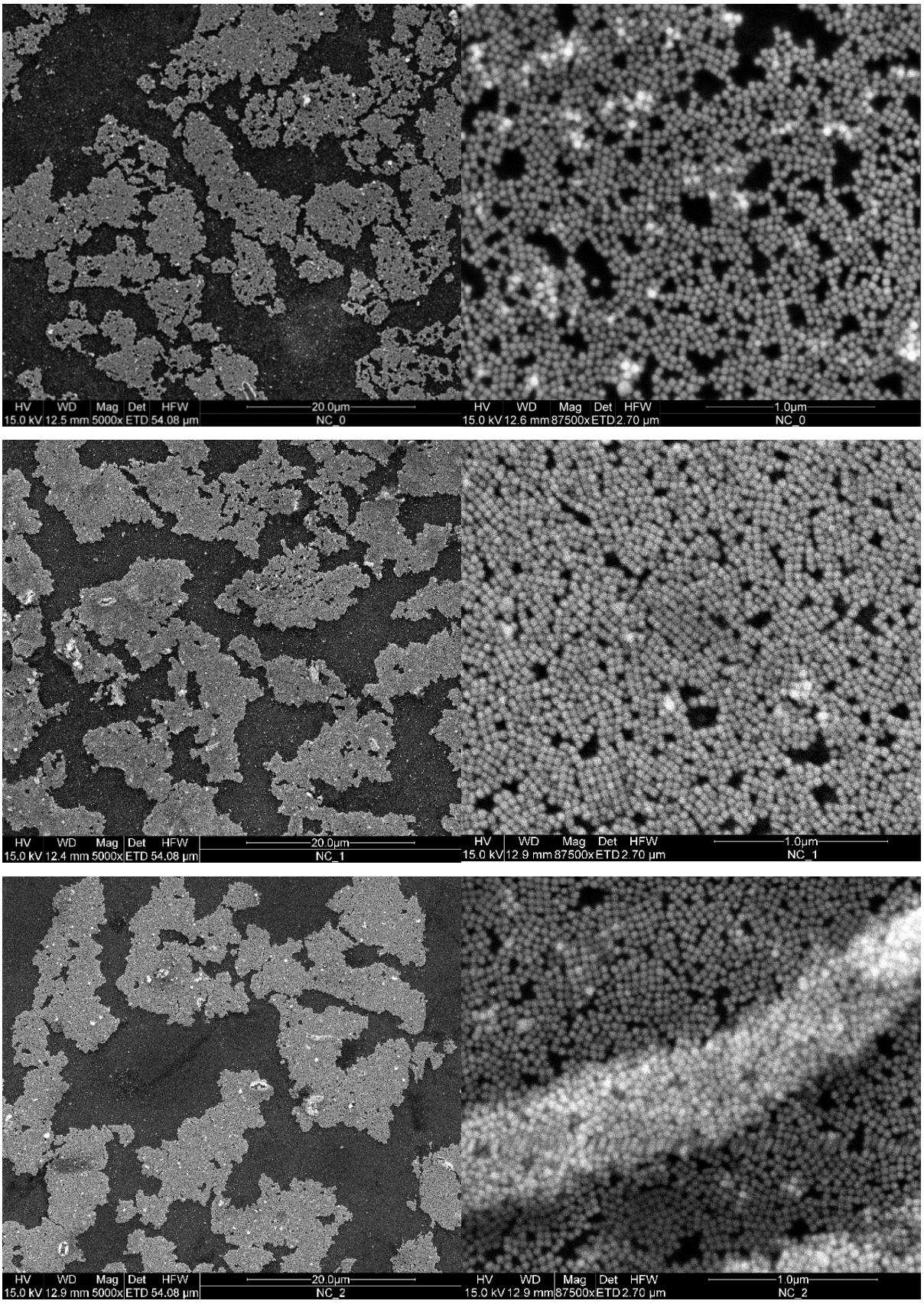

Figure 4.10. SEM images in two different magnification, 5000X (left) and 87500X (right), of three AuNC films (NC_0, NC_1, NC_2) on ITO glass with different concentration of 1-dodecanethiol in the hexane phase: 0 (top), 4.0 10^{-5} (centre), and 1.2 10^{-4} M (bottom).

When 1-dodecanethiol is absent (**NC_0**), AuNC are coated only with the residual molecules of CTAB, positively charged. In this context, the electrostatic repulsion between AuNP is maximum; therefore, the coverage percentage is the lowest. When 1-dodecanethiol is added (**NC_1**), the attractive forces generated by Van der Waals interaction among the alkyl chains of the thiol molecules counteract the repulsion due to CTAB. Because Van der Waals forces are weak and short-range physical interactions, the coverage percentage increases abruptly at short distances. However, at long distances, where the electrostatic repulsive interaction prevails, only a slight increase in the coverage percentage was registered. If the concentration of 1-dodecanethiol is further increased (**NC_2**), the short-range interactions forces among NP became so strong to promote the formation of 3D structures at the interface, that bring to the formation of multi-layered arrays. This is true not only for AuNC but also, for AuNS and AuNR (see below). Finely tuning the 1-dodecanethiol concentration for each AuNP shape, monolayers as dense as possible were obtained (see Table 4.1 and Fig. 4.11), named **NS_1** and **NR_3** respectively (these sample was obtained using sample AuNS#1 and AuNR#1 samples, see section A.4 in Appendix for details). The size of nanoparticles used and the 1-dodecanethiol concentration needed to obtain a monolayer were reported in table 4.1, while representative SEM images that attest the successful formation of dense monolayer for AuNS and AuNR were reported in figure 4.11. AuNT constitutes an exception. SEM images of the samples **NT_0-2** reported in Figure 4.11 and Figure A.3.3 in Appendix show a dense and disordered multilayer compared with other samples, regardless of 1-dodecanethiol concentration (that was varied between 0 and 8.0×10^{-5} M following the protocol reported in section 4.1, using as starting AuNP dispersion the sample AuNT#1).

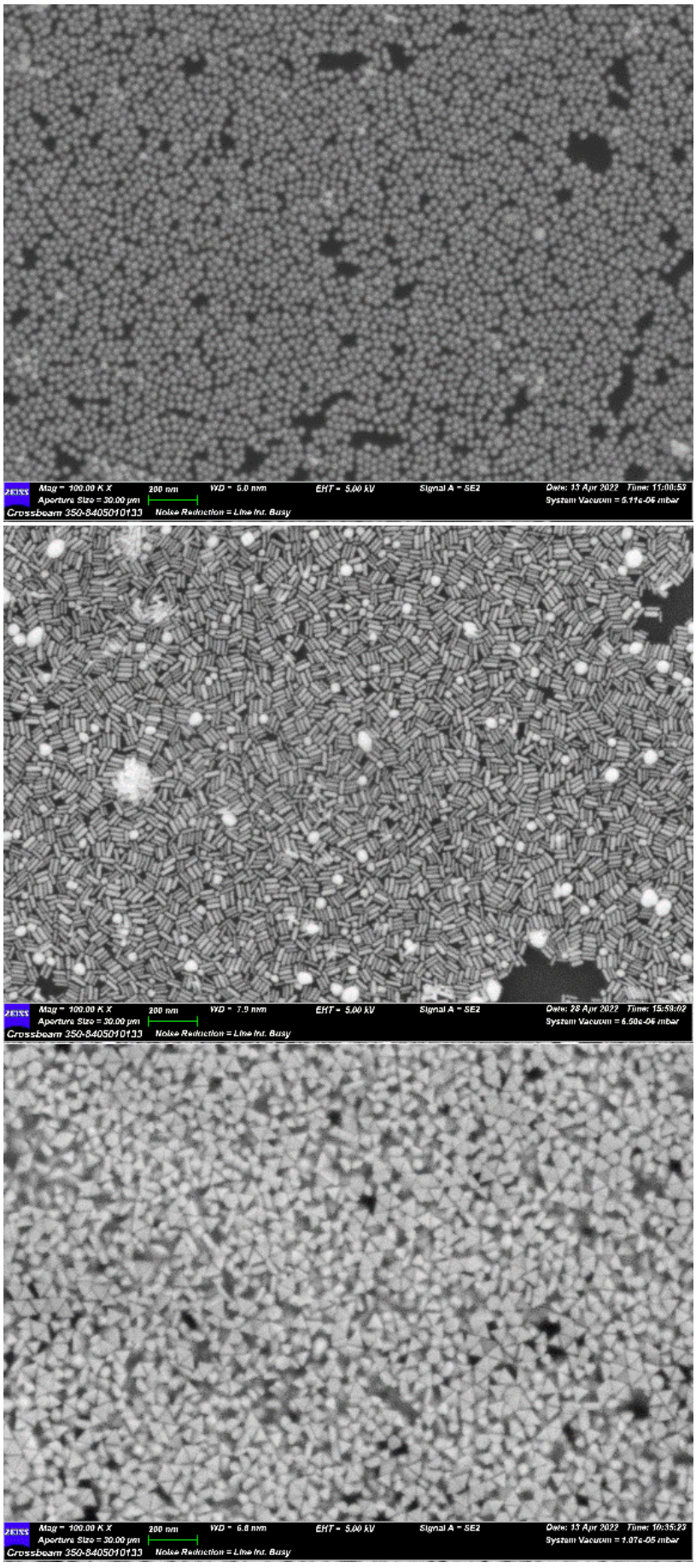

Figure 4.11 - Representative SEM images of NS_1, NR_3, and NT_1 (bottom). Scale bar is 200 nm).

Both the disorder and the multilayer formation depend on the particular crystalline habit of AuNT, which are constituted by two {111} planar facets more extended than the {100} lateral ones. [19] AuNP tend to organize at the interface with their extended facets parallel to the interface, due to the thermodynamic tendency to reduce the interfacial area. The disordered structure is due to the fact that the surface of lateral facets of AuNT is less extended respect to the other nanoparticles shapes, therefore attractive forces among AuNT are weaker and do not allow an ordered distribution. The multi-layered nature of AuNT arrays lies in the fact that both the EtOH addition and the 1-dodecanethiol surface functionalization increases AuNT hydrophobicity, the first trough the reduction of surface charge density of nanoparticles, the second trough the chemical functionalization with hydrophobic groups. In this context, when the contact angle is sufficiently high, *i.e.* the contact angle increases beyond 90°, particles at the interface will be wetted mainly by the hexane, leaving space at the interface for the formation of more than one layer of particles. [11, 12] The conditions under which this happens are more easily accessible for the AuNT, due to their reduced lateral thickness, and this leads to the formation of multilayer systems even in the absence of 1-dodecanethiol. Obviously, increasing the concentration of 1-dodecanethiol both the overlap of nanoparticles and the density of the obtained layer increases (see fig. A.3.3 in Appendix).

4.5 - PXRD characterization of AuNP monolayers

Powder X-Ray Diffraction (PXRD) is a powerful and non-destructive technique for the characterization of crystalline solid materials and thus AuNP. The technique lies on the interaction between an incident X-ray radiation with known frequency and a solid specimen. When X-Ray radiation interacts with a solid sample can be reflexes-back or enter in the crystalline material; thus, if the atoms of the sample are arranged symmetrically with a separation distance d, they will be diffracted by a certain angle, 2θ (atomic spacing in a crystalline lattice behaves like a diffraction grating). The diffracted waves will interfere constructively only where the path-length difference $2d \sin\theta$ is equal to an integer multiple of the wavelength, producing a diffraction signal according to Bragg's law. The ensemble of all diffraction signals collected by the detector varying the angle with respect the sample, 2θ, constitutes the PXRD diffraction pattern of the material and is typical of a particular atomic arrangement. The analysis of the obtained pattern gives information about the crystalline habit and the preferential orientation of AuNP samples on the substrate. [20 -22] PXRD patterns of

AuNP monolayers deposited on glass slides, *i.e.* **NS_1**, **NR_3**, **NT_1**, and **NC_3**, and of bulk gold used as reference (COD 9013035) were reported in figure 4.12, while in table 4.3 the normalized intensity of collected reflection signals were reported. The preparation of the samples NS_1, NR_3 and NT_1 was already described in the previous section, while NC_3 was prepared from sample NC#8 (see section A.4 of Appendix for details) using the procedure reported in section 4.1 for AuNC.

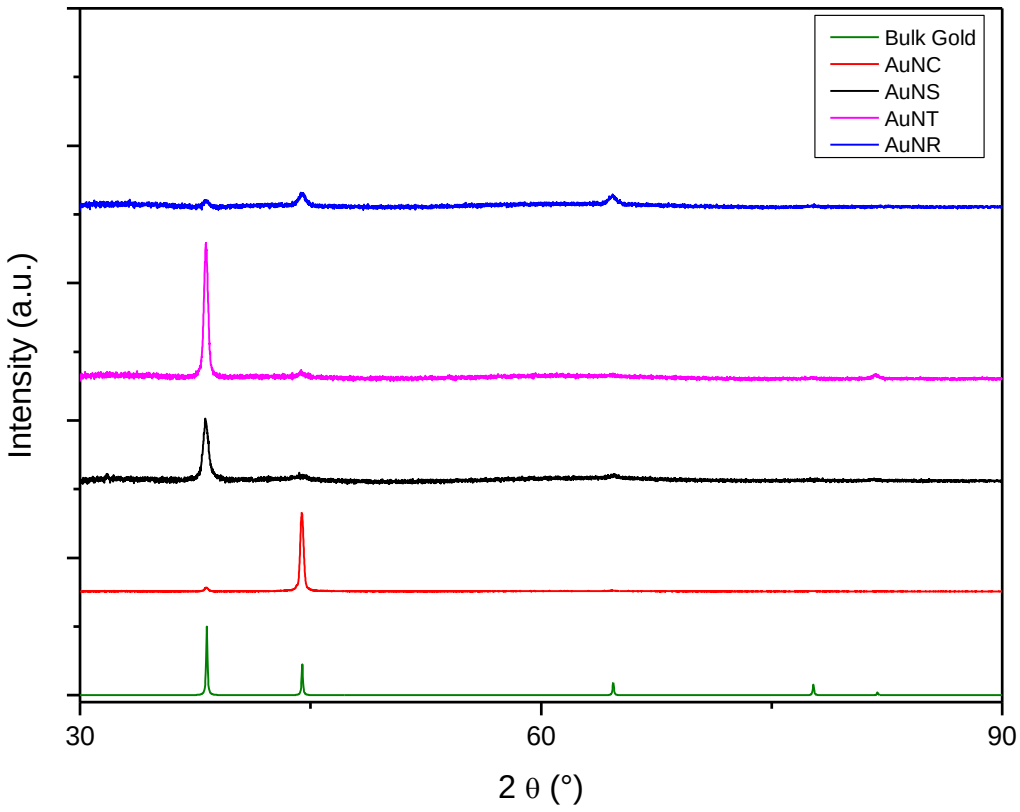

Figure 4.12 – PXRD pattern of bulk gold (green) and self-assembled monolayers of AuNC (red), AuNS (black), AuNR (blue), and AuNT (magenta) on glass slides.

The XRD patterns of **NC_3**, **NR_3**, and **NS_1** shows the same three main Bragg reflections peaks respect to bulk gold, which are centred at 38.3 °, 44,5 °, and 64.7 °; they can be indexed as the {111}, {200}, {220} reflection planes respectively and confirm the presence of *fcc* Au in all the samples. For **NT_1**, {220} reflection signal is too weak to be detected. [23]

The reflection peaks visible in the bulk gold pattern at high 2θ values, centred at 77.7 ° and 81.9 °, due to the reflections by {311}, and {222} planes respectively, are barely visible in AuNP sample for instrumental limits and will not be considered in the discussion that follows.

Table 4.3 – Relative intensities of PXRD patterns of bulk gold and AuNPs samples. The values were normalized in order that the higher peak correspond to 100% of relative intensity for each sample.

	Rel. Intensity {111}	Rel. Intensity {200}	Rel. Intensity {220}
Bulk Gold (COD 9013035)	**100 %**	**47.9 %**	**28.4 %**
NS_1	**100 %**	**4.4 %**	**6.7 %**
NR_3	**42 %**	**100 %**	**34.7 %**
NT_1	**100 %**	**3.5 %**	**-**
NC_3	**5 %**	**100 %**	**0.7 %**

In Table 4.3, the normalized relative intensities of each reflex, including bulk gold as reference, were reported for all the samples. The relative intensities of AuNP monolayers are very different from that of bulk gold, and are very different varying the shape of the nanoparticles.

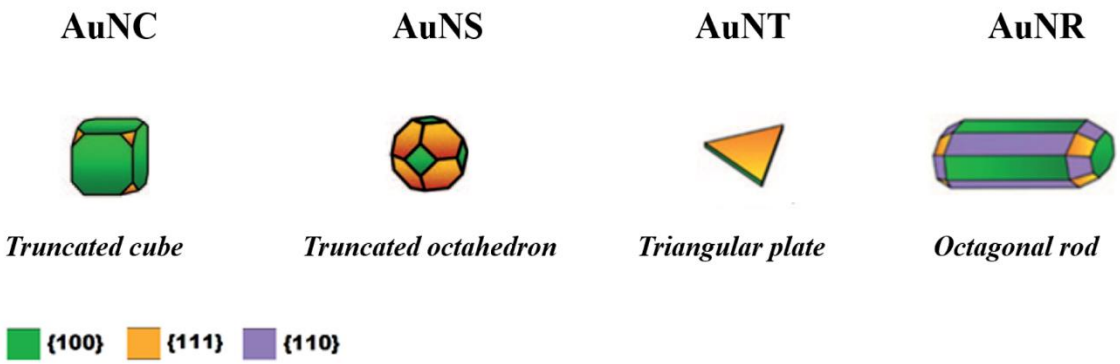

Figure 4.13 – Crystalline habits of AuNP samples synthetized during this PhD research work.

The orientation of AuNP on the glass slide depends on the deposition technique and can be confirmed by SEM characterization. In detail, the self-assembly at water/hexane interface lies on the destabilization of AuNP aqueous dispersion trough addition of EtOH, that causes the migration of colloids to the interface. The assembly of AuNP at the interface is driven by the thermodynamic tendency to reduce the interfacial area, in order to minimize the contact area between the two phases; therefore, the preferred orientation of the AuNP will be the one in which the most extended facet is parallel to the interface. At the interface, the in-situ functionalization of AuNP surfaces with 1-dodecanethiol increases the reciprocal Van der Waals attractive forces, compacting densely the monolayers and fixing the orientation, which

is maintained after the deposition onto the solid substrate. This assumption is confirmed by SEM images of AuNP monolayers (SEM images for **NT_1**, **NR_3**, and **NS_1** were already reported in Figure 4.11, while a representative SEM image of **NC_3** was reported in figure A.3.4 in appendix). Based on this evidence a graphical model that shows how AuNP monolayer is oriented was carried out (see Figure 4.14), considering the facets that each AuNP sample should expose. Thus, it is possible to correlate the relative intensities of diffractions peak with the expected crystalline habit of each AuNP sample, as reported in Fig. 4.13.

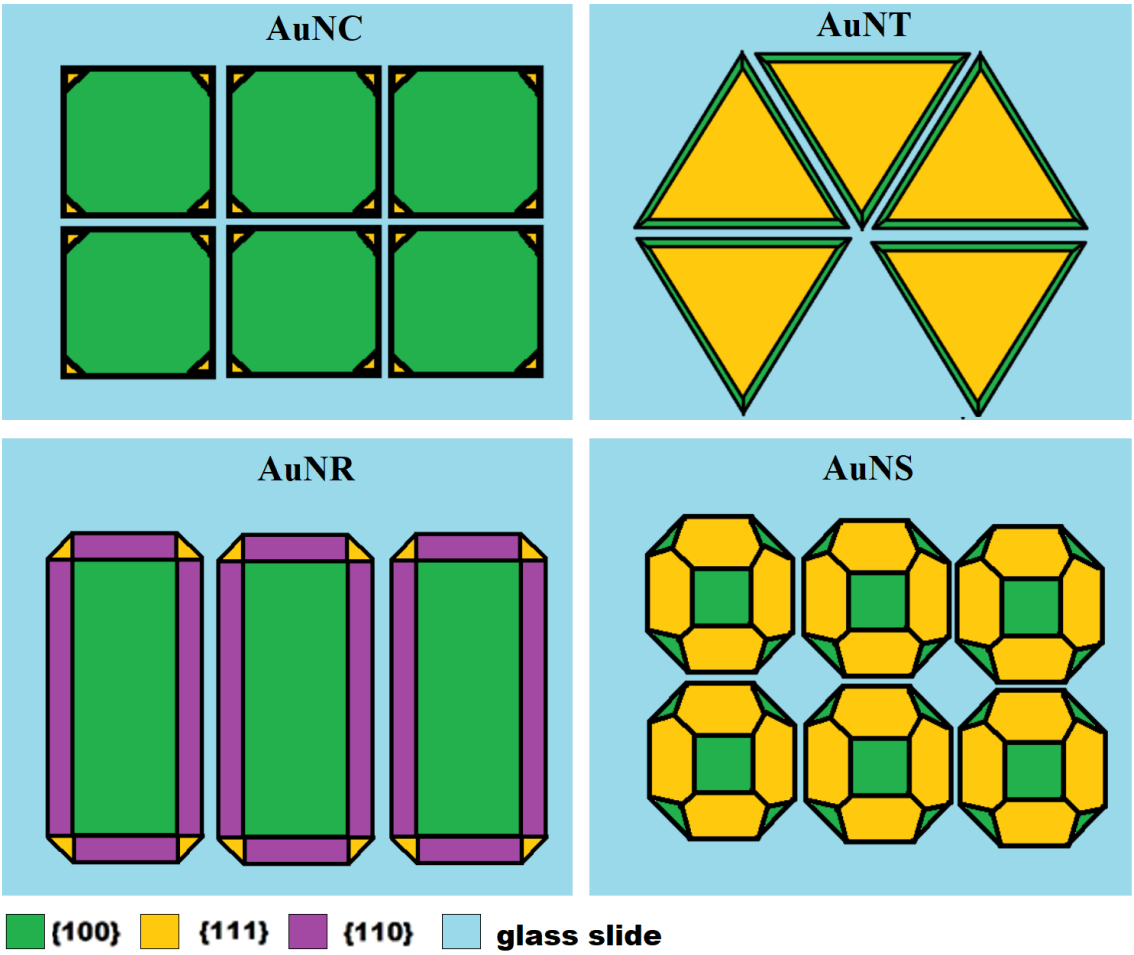

Figure 4.14 – Graphical representation of facets orientation of AuNP when form monolayers on glass slides based on XRD analysis (the plane of the sheet corresponds to the plane of the glass).

From TEM characterization we already see that AuNC@CTAB have rounded corners (see Figure 3.11), therefore their crystalline habit is a truncated cube (figure 4.13) with {100} facets more extended than {111} ones. They adhere onto the glass substrate with one of the six {100} facets, showing the opposite facet toward the incident beam (see figure A.3.4 in appendix). The corresponding XRD pattern (figure 4.12, red trace), which shows the maximum reflection along

the {200} peak and the {111} peak with an intensity equal to 5% of the intense one, is consistent with the crystalline habit attributed to the AuNC. The weak signal coming from the {220} facet (0.7 %), which should not exist in an ideal cube, can be due to some shapes that deviate from it.

AuNT crystalline habit show two extended triangular {111} facets and three thin lateral {100} facets each crossed by the stacking fault plane. Corresponding SEM image (figure 4.11) shows that they predominantly expose the {111} facet, but evidence also some nanoparticles that expose the {100} lateral facets, for the disorder generated by the multi-layered structure. The XRD pattern, with the signal arising from {111} facets dramatically greater than the {200} ones, is consistent with the crystalline habit of AuNT, with the {220} peak that does not generate any signal as expected from the assumed shape.

The case of AuNR is more interesting, because nanorods were modelled as an octagonal rods, so they are bounded by alternating the {100} and {110} facets along its side, and the tips that are bounded by all gold crystallite orientations. In the arrangement observed in the SEM images (*i.e.* the horizontal one, that minimized the interfacial area during its interfacial assembling), they could expose both {100} and {110} lateral facets. XRD diffractogram helps to clarify which is the facets exposed, attesting the {200} direction as the prevalent signal. The reason of this preference is attributed to the fact that the glass slide surface is hydrophilic, and the bottom side of AuNR monolayer is coated with a hydrophilic molecule as CTAB (see paragraph 4.3). CTAB affinity for {100} facets is greater respect to the {110} ones [24, 25], so the adhesion on glass from this side is favoured.

Finally, considering the AuNS, they can be modelled as truncated octahedron bounded by {100} and {111} facets. The XRD pattern shows also a strong signal form {220} facets, which in theory should not belong to this polyhedron. So, the synthesis generated spheroidal nanoparticles with a crystalline habit different from that theoretically assumed and further analysis are required to establish its real crystalline habit before doing any consideration about its orientation on to the glass slide.

4.6 – UV-Visible characterization: effect of the film morphology on the plasmon response of AuNP monolayers

The effect of the film morphology on the plasmon response of AuNP 2D monolayers was investigated comparing the extinction spectra of the three different AuNC arrays prepared as described in the previous paragraph (*i.e.* **NC_0**, **NC_1**, and **NC_2**), and the extinction spectrum of the starting AuNC@CTAB aqueous dispersion, all reported in Figure 4.15. We first discuss the main differences between plasmonic bands of AuNC in solution and deposited on solid substrates, and then we try to correlate differences among the three depositions to morphological aspect observed in the SEM characterizations.

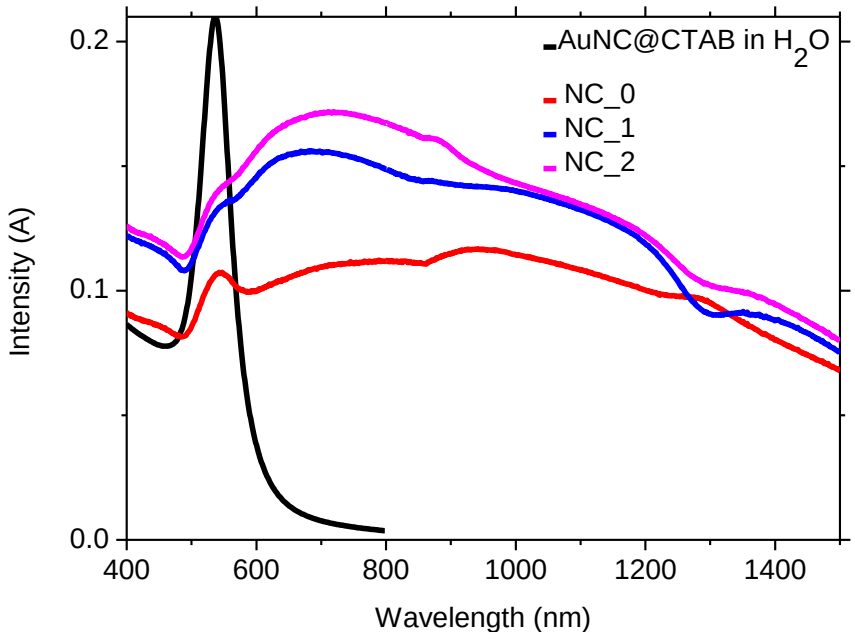

Figure 4.15 - Extinction spectra of NC_0, NC_1, and NC_2 on ITO glass slide and AuNC@CTAB in H_2O.

The extinction spectrum of the starting AuNC@CTAB in H_2O shows a plasmon band centred at 537 nm with a FWHM (full width at half maximum) of 67 nm attributed to the dipolar plasmon modes. In AuNC self-assembled films, there is a splitting and a dramatic red-shift and enlargement of the plasmonic response (the spectra from samples **NC_0**, **NC_1**, and **NC_2** present maxima centered at 941, 686, and 711 nm respectively). Their extinction spectrum can be described as formed by two different bands: a thick and a high-energy band centred around 550 nm, and a large red-shifted one centred between 700-800 nm with a tail in the NIR region. Plasmon response of coupled systems of gold nanocubes on ITO surface was studied thorough by Chen *et al.* [7]. They analyzed with SEM the 2D assemblies of small ordered arrays ranging

from 1 to 9 nanocubes, and correlate the morphology of each cluster to both theoretical and experimental plasmon spectra. Their detailed work on small size assemblies helps to understand the origin of such complex plasmonic response. We first consider the peak centred at around 550 nm, which is very narrow and in the same position for all the samples, thus independent from arrangement of nanoparticles on to the substrate. Because some isolated AuNC were observed during the SEM characterization, the first possible explanation about the origin of this plasmon band was the presence of non-coupled AuNC. However, this hypothesis is invalidated by a simple consideration about the position of this plasmonic band. *This band results 10 nm red-shifted than the plasmonic band of the starting AuNC@CTAB dispersion* (see Figure 4.15). The red-shift of a plasmonic band is usually due to an increase of the refractive index of the media where AuNPs are dispersed; conversely, if the refractive index is reduced the plasmonic band experiences a blue-shift. [26] The refractive index of the environment for the starting AuNC@CTAB dispersion can be assumed equal to that of water, *i.e.* n_w = 1.333 (RefractiveIndex.INFO website, λ = 600 nm). When deposited on ITO glass slide an isolated nanocube had 5 facets exposed to the air and one facet that lies on the ITO surface. The averaged refractive index for this particular case is 1.15 (obtained through the weighted average on the six facets of a cube of the refractive indexes of air and ITO, *i.e.* 1.0003 and 1.3884, respectively at 600 nm). Therefore, if this band was generated only from isolated AuNC it should have been at shorter wavelengths than the plasmonic band of AuNC@CTAB in H_2O. An experimental confirm of this was obtained through the dipping of both ITO and glass slide in 2 mL of the same AuNC@CTAB dispersion used for the realization of self-assembled monolayers. Using this method, AuNC result sparse on the substrate, and do not generate any array as attested by SEM image and photo in Figure 4.16.

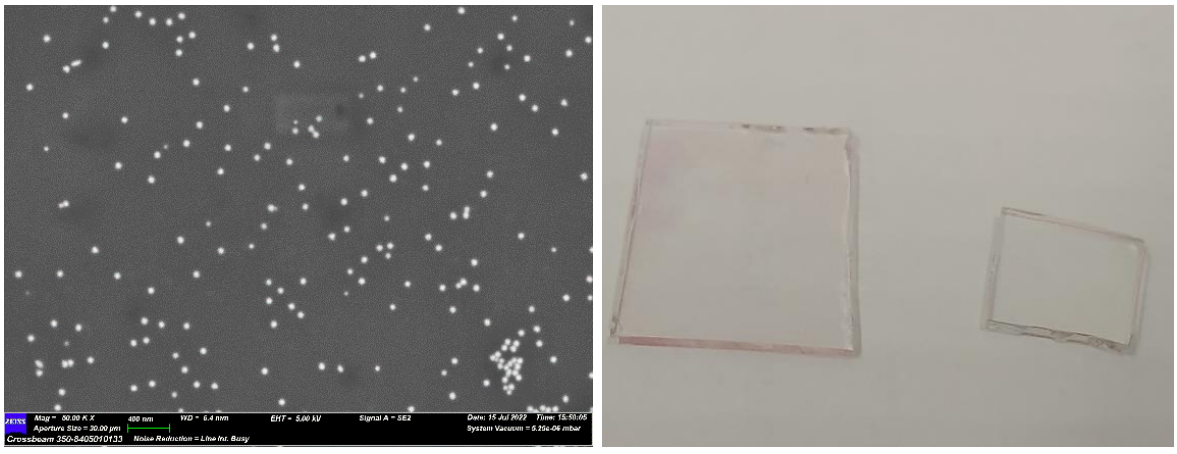

Figure 4.16 – SEM image of AuNCs@CTAB deposited on glass, and picture of the same sample depositedon glass (left) and ITO (right) slides trough dip coating.

This distribution of AuNC@CTAB on these substrates generates a sharp plasmonic band with maximum centred at 525 and 530 nm for ITO and glass slide, respectively (see Figure 4.17). As expected, their spectra result clearly blue-shifted than AuNC@CTAB in H_2O.

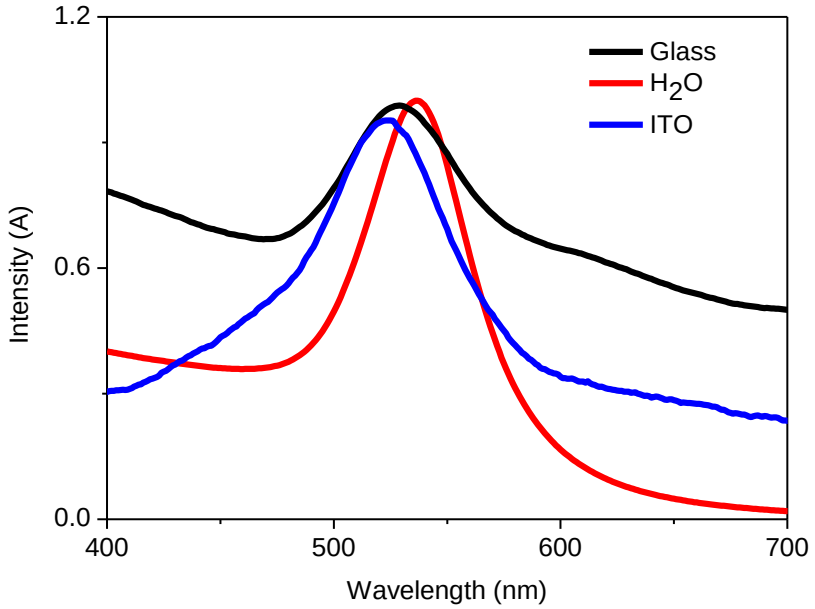

Figure 4.17 – Normalized extinction spectra AuNCs@CTAB in H_2O (red line) and deposited by dip coating on ITO (blue line) and glass (black line) slides.

Because in our case the band results red-shifted, this behaviour cannot be attributed to the refractive index variation suffered by isolated AuNC; an explanation about the origin of this band proposed in literature is the activation of higher order plasmon modes (*i.e.* quadrupolar, and octupolar). Higher order plasmon modes are usually observed for colloidal dispersion of AuNP bigger than 100 nm. In the case of system with strong optical coupling like AuNP self-assembled monolayers, these oscillations are also observed for mid-nanosized particles. [17] Considering the second feature of the spectra, *i.e.* the low-energy spectral features with the long tail in the NIR region, they are attributed to dipolar plasmon modes of gold nanocubes, that in solution appears at 537 nm. The reason of such dramatic changes respect to the sample in water is due to dense arrays of nanocubes obtained after the self-assembly process. In particular, the red-shift observed is due to the strong optical coupling experienced by nanocubes arising from the dense packing obtained into nanoparticles islands and from the short distance between nanocubes (see Figure 4.10). In fact, the distance among the NC, due to the interdigitation between the 1-dodecanethiol alkyl chains that cover the cubes surfaces, range between 1 and 2 nm, originating a strong coupling interaction. The enlargement of the plasmonic response is

strictly connected with the film structure at the nanoscale and could be attributed to two factors. The first factor is that an extended monolayer of AuNC is made by a large number of "sub-clusters" with different shapes and sizes (made by coupled nanocubes dimers, trimers, tetramers and so on), each resonant at a specific frequency. [7] The second factor is the unavoidable presence of voids and overlaps in the film structure, which causes nanocubes composing the arrays do not experience the same chemical environment, introducing irreproducibility in the film structure and thus in the plasmonic response. Therefore, the overall plasmonic response of AuNC monolayer will result very complex and difficult to predict. Generally, larger and denser the 2D AuNC clusters are, more red-shifted the dipolar mode bands appear.

Focusing on the differences in the extinction spectra of film samples attributable to the change in concentration of 1-dodecanethiol (*i.e.* **NC_0**, **NC_1**, and **NC_2**), the extinction intensities follow, as expected, the covering percentage trend, *i.e.* **NC_2** > **NC_1** > **NC_0**. This is coherent with the lower number of voids and defects in the film structure increasing the concentration of 1-dodecanethiol, as confirmed by SEM characterization (see Figure 4.10). Contrarily, the extinction maximum does not follow the same trend, because λ_{max} **NC_0** > λ_{max} **NC_2** > λ_{max} **NC_1.** This is highly surprisingly, because **NC_0** was prepared without adding 1-dodecanethiol, so the medium size of the clusters should be theoretically lower and the band should result blue-shifted than that of **NC_1** and **NC_2**. As we said above the overall plasmonic response of AuNP monolayers is the sum of various contributes and results very difficult to interpret. Probably the absence of thiols molecules makes the film formation process less controllable and disordered: this creates sub-clusters with different size, and the prevalence of one size over another is a random process; in fact, the spectral response of AuNC monolayers without thiol is poorly reproducible. The introduction of 1-dodecanethiol as linker between nanoparticles increases the AuNP order and the reproducibility of the plasmonic spectra, fixing the distance among nanocubes and reducing the number of voids and defects.

4.7 - UV-Visible characterization: effect of nanoparticles shape on the plasmonic response of AuNP monolayers

To study the effect of the building blocks shape on the plasmonic properties of the film, the extinction spectra of four different nanoparticles monolayers deposited on glass slides, *i.e.* **NC_3**, **NS_1**, **NR_3**, and **NT_1**, whose preparation was already described in the previous sections, were compared in Figure 4.18.

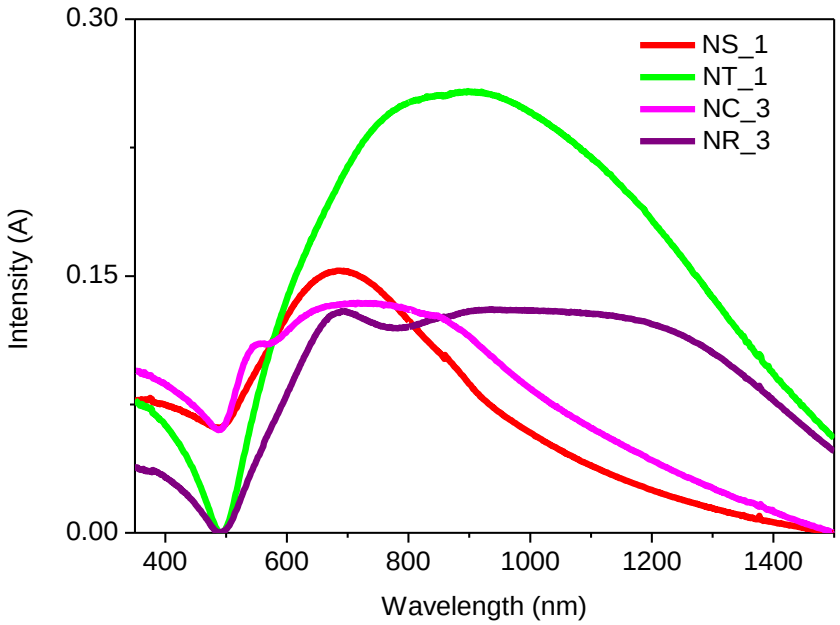

Figure 4.18 - Extinction spectra of self-assembled monolayer of AuNS (red), AuNC (magenta), AuNT (green), and AuNR (violet).

As we see from the reported spectra, the extinction intensity is similar for **NS_1**, **NC_3**, and **NR_3** around 1.5, while it is almost double for **NT_1**. This difference is coherent with the different morphologies obtained, which is monolayer in the first cases, and multi-layered in the second one, and is attributed to the greater optical density in the case of **NT_1**.

Indeed, the intensity of the extinction spectra of a monolayered film of plasmon nanoparticles is the result of two contributions: the number of NP per unit area, and the intrinsic intensity of the NP plasmon due to the size of the individual building blocks. For this reason it is evident that as one increases, the other decreases; in fact, increasing the average size of the NP increases the intensity of plasmon scattering, but decreases the number of irradiated NPs, as the number of NPs per unit area decreases.

Regarding the shape of the plasmonic band, two considerations must be done. The first regards the band due to multipolar plasmon modes. It is clearly visible for **NC_3** and **NR_3**, while is absent for **NS_1** and **NT_1**. Furthermore, in the case of **NR_3**, it is strongly red-shifted than

NC_3, probably because the active modes are along the long axis of the rods. The absence of this band for **NS_1** can be due to the smaller size of spheres (around 40 nm) than other nanoparticles (medium size around 50 nm); in fact, it is known that the presence of higher order plasmonic modes depends on the size of the nanoparticle, and it starts to appear for nanoparticles films with NP size upper than 50 nm. [17] For **NT_1** the medium size is similar to **NC_3**, so this band probably exists but is incorporated in a unique, large plasmon feature, considering that the possible plasmon modes are greater in number for **NT_1** respect to the other samples for the possibility, in a multi-layered films, to have coupling interactions in the direction perpendicular to the glass substrate. The second interesting aspect that must be underlined is the width of the plasmon band, which is higher for **NR_3** and **NT_1** than **NC_3**, and **NS_1**. This is due to the greater anisotropy in shapes of the first couple than the second, which enables an increase possible orientation of nanoparticles, enlarging the plasmonic response. The largest plasmon band is presented by AuNT film respect to the AuNR one, because the presence of multilayer further increases the number of possible interaction between nanoparticles.

4.8 - Substitution of 1-dodecanethiol with p-terphenyl-4,4'-dithiol

In order to improve the optical and morphological properties of AuNC self-assembled monolayers the substitution of 1-dodecanethiol with other molecules was considered. In literature AuNP monolayer were formed using also alkyl amine of various length, and PEGylated thiols. These alternative linkers act in the same way of 1-dodecanethiols, promoting AuNP assembly trough Van der Waals interaction established between the alkyl chains. The use of one molecule rather than another made it possible to modulate the optical and electrical properties of the AuNP monolayers by varying the distance between them proportionally to the length of the alkyl chain used. [27,28]

During this PhD work AuNP 2D monolayers were also formed by substituting 1-dodecanethiol with p-terphenyl-4,4'-dithiol (TPDT), a molecule that consist of two thiols groups separated by three phenyl rings (see Figure 4.19).

Figure 4.19 - Structural formula of p-terphenyl-4, 4'-dithiol.

The attempt to use the TPDT for interfacial functionalization of nanoparticles is due to the peculiar structural characteristics of this molecule. The two thiol groups at opposite sides of the aromatic chain could offer the possibility to bind two different nanoparticles, with the aim to create a dense and extended 2D lattice of AuNP, linked through covalent bonds. [28] Because covalent bonds are stronger than Van der Waals interactions, this in theory could contribute to increase both homogeneity of the layer and their mechanical properties. Furthermore, similar molecular systems are fluorescent and their strong conjugation can enable molecular wire type electrical conduction, and could improve both the optical and the electrical properties of AuNC monolayers.

The sample was prepared starting from a dispersion of AuNC@CTAB (AuNC#9, see section A.4 in the Appendix), following the standard procedure (see Paragraph 4.1), using 2 mL of TPDT 2×10^{-5} M instead of 1-dodecanethiol 4×10^{-5} M. The concentration of TPDT used is half of that used in the case of 1-dodecanethiol since, while with the latter two molecules are needed to bind two AUNPs, in the case of TDPT it is sufficient to use one. After the deposition onto glass slide, the sample was repeatedly washed with hexane to remove any eventual excess of TPDT untied from AuNC.

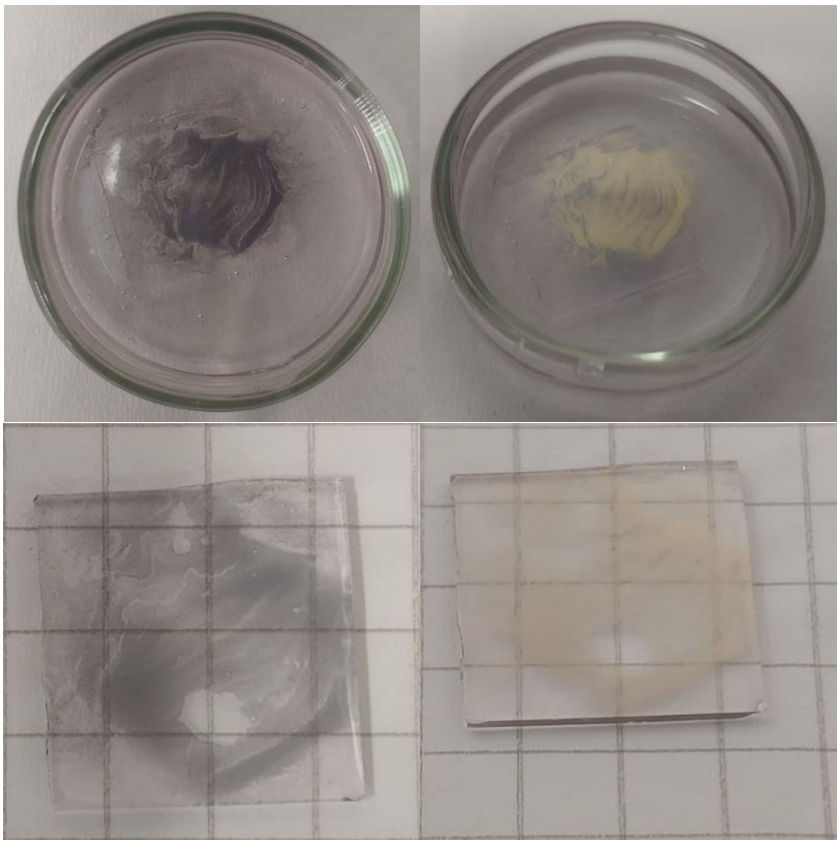

Figure 4.20 - Photos of AuNC self-assembled monolayers obtained using TPDT at the water/air interface after the evaporation of hexane (top) and deposited on glass slide by draining the aqueous phase (bottom). You can see the different colour as the lighting angle changes.

In Figure 4.20, four photos of the obtained layer at water/air interface and after the deposition on to glass substrate were reported. The aspect of the film is very similar to that obtained using 1-dodecanethiol, presenting the same double coloration if irradiated from different angles (Figure 4.2). A layer with a very dense and continuous structure interrupted by some macroscopic defect can be observed. These defects can be divided in two types, *i.e.* "hole-shaped" and "stripe-shaped" ones. The first kind of defects can be easily prevented. They were generated after the deposition process, in fact was not observed when the film was at water/air interface, and are due to a non-perfect adhesion of the film on the glass substrate. The second type of defects (already observable at the water/air interface) are previously observed in 1-dodecanethiol films (see section 4.3) and was attributed to a fast hexane evaporation.

Morphological characterization. Two representative SEM images of the sample were reported in Figure 4.21. Unfortunately, the introduction of TPDT as linker did not produce the desired results. If compared with the sample with 1-dodecanethiol, this deposition produced a monolayer with smaller AuNC self-assembled islands (Figure 4.21, left). Into the islands, the AuNP density is poor, with the tendency of AuNC to form chains rather large and dense assemblies. The reason of that can be related to the fact that the crosslinking of AuNC with TPDT require the formation of 2 chemical bonds (S-Au bonds) between a TPDT molecule and two different AuNC. The formation of a chemical bond require more strictly thermodynamic conditions than that necessary for the creation of Van der Waals interaction, and this probably hinder the formation of more ordered monolayers.

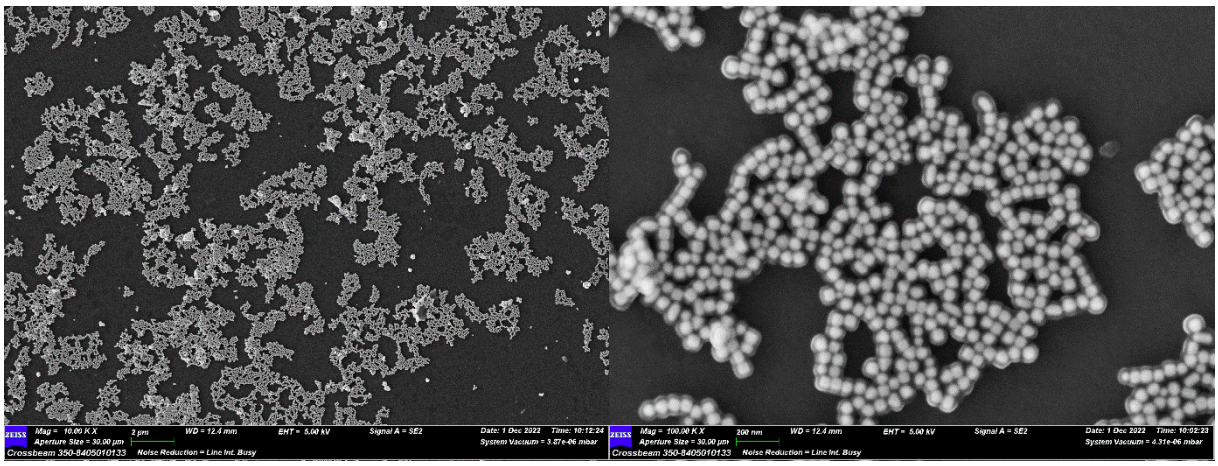

Figure 4.21 – SEM images in two different magnification, 10000x (left) and 100000x (right), of AuNCs film with TPDT deposited on glass slide (scale bars are 200 nm).

Optical characterization. The extinction spectrum of AuNC TPDT monolayer was reported in Figure 4.22. The spectrum shows a narrow and red-shifted plasmon band compared with that of AuNC functionalized with 1-dodecanethiol (see blue line in Figure 4.15), with an extinction maximum centred at 865 nm. The red-shift could be attributed to a low medium distances between nanocubes, since the chain length of TPDT was estimated around 1.5 nm. The smaller thickness of the band is due to the poor density that reduces the number of possible interactions between nanocubes, and consequently a lower number of coupled plasmon modes are active., The use of glass as substrate for the deposition of AuNC monolayers does not allow the registration of TPDT absorption band; in fact, glass starts to absorb strongly below 350 nm, while the absorption band of TPDT was expected around 290 nm, considering their absorption spectrum in solution (see Figure A.3.5 in Appendix).

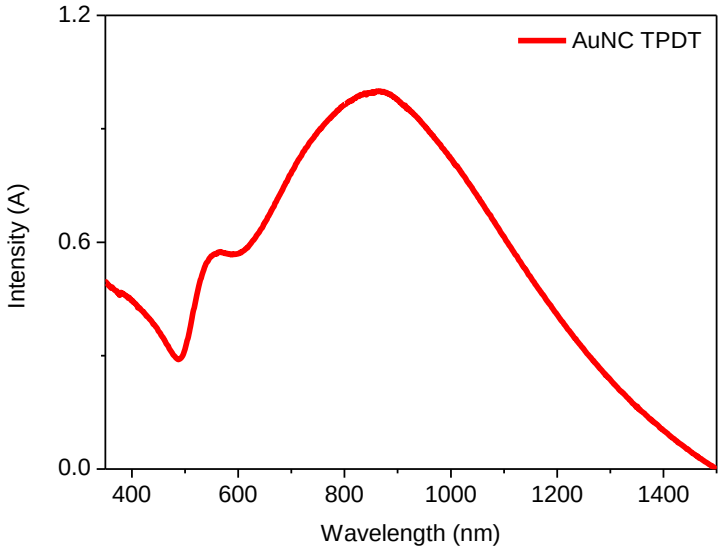

Figure 4.22 - Absorption spectra of starting AuNC@CTAB aqueous dispersion (red line) and AuNC-TPDT monolayer deposited on glass slide.

This does not constitute a problem because TPDT is a fluorescent molecule, so their presence on AuNC can be ascertained through the registration of the emission spectrum of the sample. Two different emission band, centred at 370 and 445 nm, were detected for AuNC monolayer formed with TPDT, and the excitation spectra collected on both emissions confirm that the signal arises from only one chemical species that absorb at 315 nm (see Figure 4.23). The emission lifetimes collected on these peaks are 1.74 ns and 30.3 ns respectively (see Table A.2.11 in Appendix).

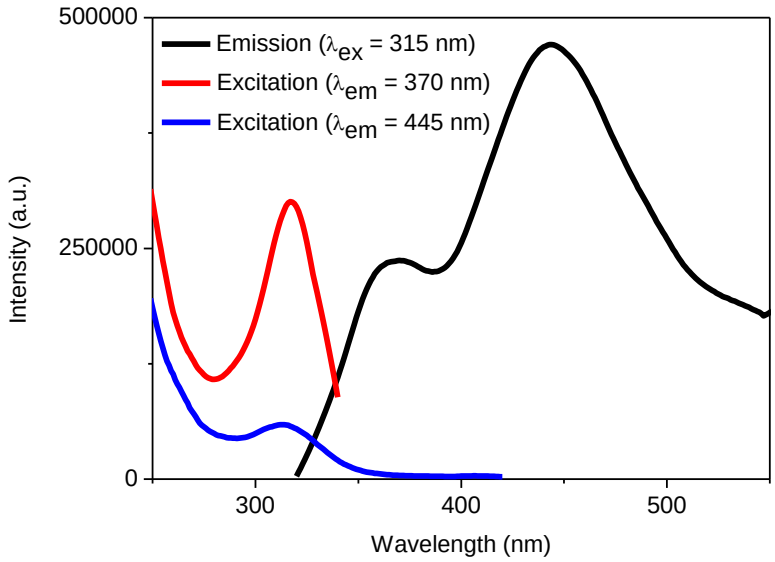

Figure 4.23 - Emission and excitation spectra of AuNC-TPDT monolayer deposited on glass slide.

For the attribution of these emission signals, the photophysical properties of TPDT in hexane solution and of the powders were recorded (see Figure A.3.5 and Figure A.3.6 in Appendix). On this basis, the UV emission band, centred at 370 nm, are attributed to the emission of the single molecule for analogy with the emission of TPDT in hexane solution. An elongation of the emission lifetime (+ 1 ns), respect to the value measured in solution, were detected, and attributed to the immobilization of TPDT on the AuNC surface (see table A.2.11 in Appendix). The blue band with a maximum at 450 nm is attributed to aggregation phenomena due to π-π* interaction between aromatic rings of two TPDT molecules, as observed in the emission spectra of TPDT powders (see Figure A.3.6 in Appendix). Also, in this case the interaction AuNC-fluorophore increases the emission lifetime of the latter in powder (+ 15 nm; see table A.2.5 in Appendix). Interestingly, a TPDT film on glass slide (obtained from drop casting of the same hexane solution used for the deposition of the AuNC monolayer) shows the same emissive properties of AuNC-TPDT monolayer, but with different lifetimes of the excited states (see table A.2.11 in Appendix). This data confirms the fact that in AuNC sample TPDT molecules are bounded on the nanoparticles surfaces.

4.9 - Electrical response of AuNP monolayers

Various studies on AuNP self-assembled monolayers have shown that these superstructures exhibit electrical conductivity and photoconductivity due to the low distance (few nanometers) that separates their building blocks, which enables transport of electrical charges through mechanisms of tunnelling and hopping. Yang *et al*. demonstrate electrical conductivity into self-assembled gold nanospheres monolayers linked through alkyl amine of various chain length, registering an ohmic behaviour of the I-V curves and an exponential dependence from interparticle distance. [29] Furthermore, Mangold *et al*. measured a photoconductive gain effect in similar films after irradiation with a laser at SPR frequency. [30] The electrical responses of AuNP monolayers were usually measured by depositing them on interdigitated electrodes (IDEs), measuring the current that passes through the system at a fixed voltage, in order to extrapolate the electrical conductivity of the material measuring the electrical resistance and knowing the geometry of the circuit. In fact, the electrical conductivity is related to the resistance of a material by the equation that follows:

$$\sigma = \frac{l}{S\,R} \qquad \text{Eq. 4.1}$$

Where: l is the length of the conductor; S is its section; R the electrical resistance of the material. For the measurements of the electrical properties of AuNC monolayers prepared during this PhD, Test Patterns (TPs) purchased from FBK were used. The factory specifications of these substrates and the cleaning protocol to be performed before their use were accurately described in experimental section in the Appendix. AuNC monolayers (see Figure 4.24) were deposited on TPs following the protocol described in paragraph 4.1. The SEM images show clearly how the discontinuous structure of the AuNC films alternate areas where AuNC islands form bridges between the gold stripes of TPs, which close the circuit and allow current to pass, and large void areas where current cannot pass (the AuNC coverage percentage was estimated around 50 % of the total area). To measure the electrical conductivity the sample was connected to a picoamperometer (Keithkey 6571a electrometer) through two micro pins, and the temporal behaviour of the electrical current for an applied constant voltage was registered. This measure was repeated for many voltage values in the range 0.2-20 V. The area under electrical voltage, in which current was measured, is circled in red in figure 4.24.

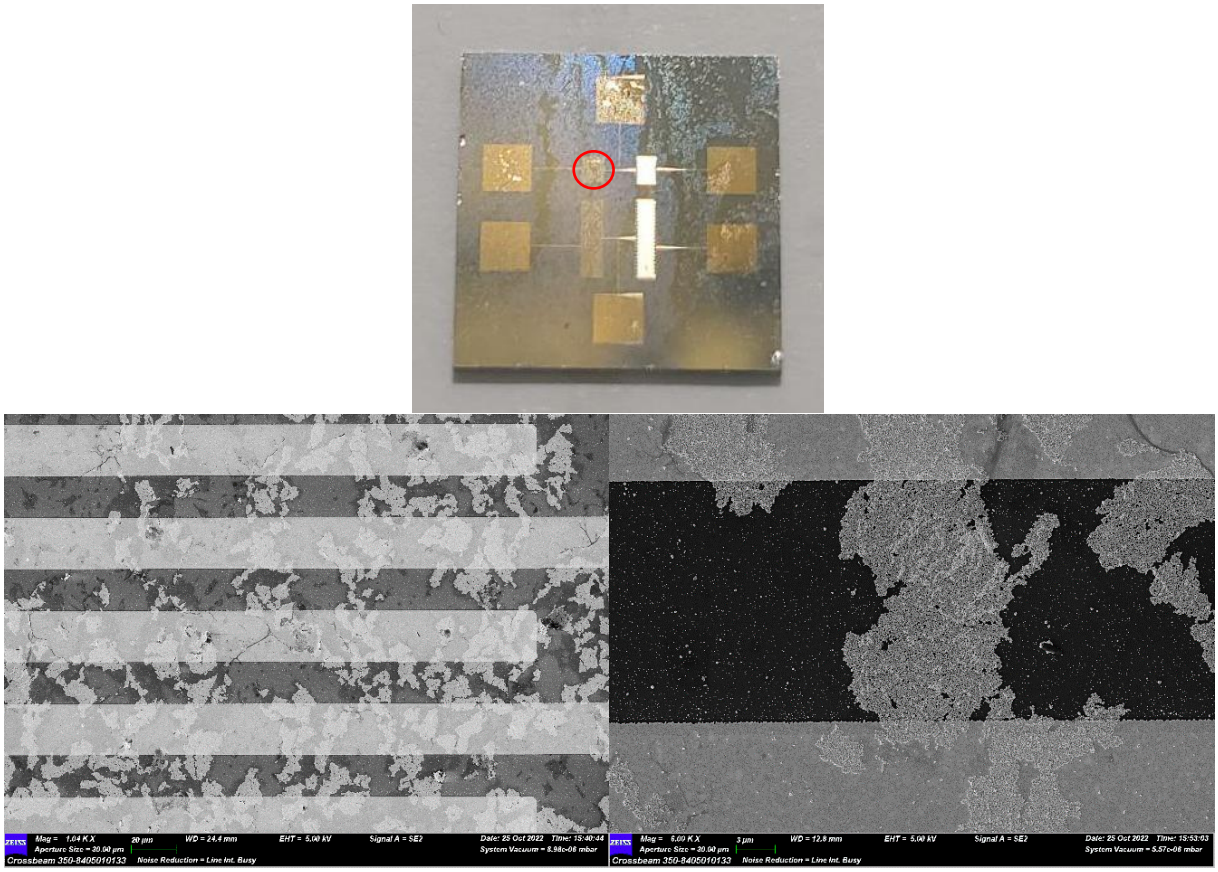

Figure 4.24 – Photo of AuNC monolayer deposited on TPs (top). Representative SEM images in two different magnifications of AuNC deposited between interdigitated electrodes of TPs (below). The zone observed and characterized was circled in red in the photo.

The system response in terms of current measured was reported in Figure 4.25, which is representative of the general behaviour recorded at all applied voltages. When the voltage is applied, the current reaches immediately a maximum, then decreases rapidly until reaches a stationary value. When the voltage is removed, the sign of the current that flows in the system is inverted but the behaviour is specular: immediately a high negative value is measured, followed by a rapid increase until zero. The reason of the observed behaviour is probably due to polarization phenomena induced by the particular morphology of the sample. The material is made by numerous metal-dielectric junctions, which are responsible of the electrical conductivity. The electron transport along gold nanocubes is much more effective than that along the 1-dodecanethiol chains. This probably creates a negative charge accumulation at the interface between the two materials, which results in an electric field opposite to the applied one. This polarization phenomenon results in the rapid decreasing of electrical current in the initial phase of the measurements, until a positive stationary value was reached, and in the opposite, specular trend when the voltage is removed.

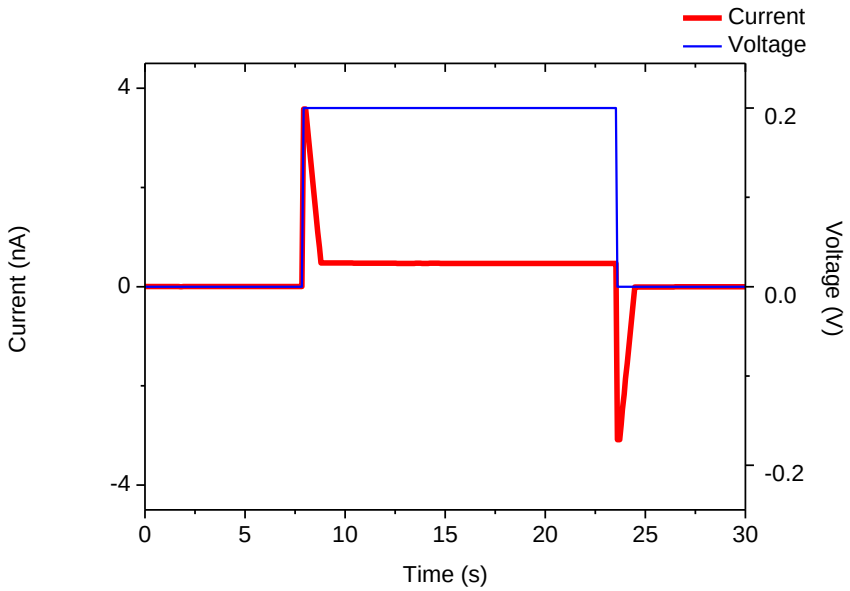

Figure 4.25 – Voltage applied to AuNC monolayer (blue line) and system response in terms of electrical current that flows in the circuit (red line). This trend was recorded by applying a voltage V = 0.2 V.

Changing the voltage between 0.2 and 20 V the behaviour does not change, but the electrical current (measured in the stationary range of the curve) increases linearly with the applied voltage according to the Ohm's law (see Figure 4.26).

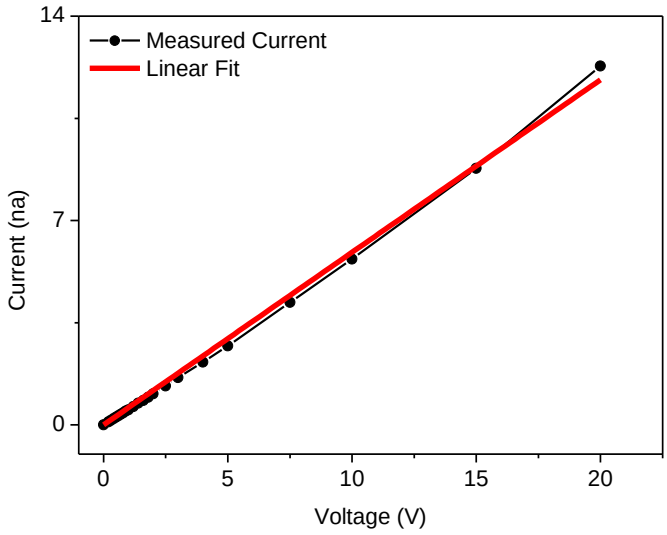

Figure 4.26 – Linear fit of the V-I curve obtained measuring the current intensity in the stationary zone varying the voltage applied.

The electrical resistance (R) obtained by the linear fit of the I-V curve (*i.e.* the inverse of the slope), is equal to 1.7 GΩ. To extrapolate the electrical conductivity of the AuNC film (σ) we assume that the film is a monolayer with a coverage percentage of 50 % of the total area, as attested by SEM characterization. Therefore, introducing R in Eq. 4.1, with the length of the conductor (l) equal to 20 µm (see experimental section Appendix A.1), and its section (S) equal to the AuNC mean edge length (49 nm) multiplied for the channel width of IDE used (11200 µm, see experimental section Appendix A.1), it was obtained an electrical conductivity of 1×10^{-7} S/cm. This value is 12 order of magnitude lower to the electrical conductivity of bulk gold (*i.e.* 4.5×10^{5} S/cm) and results lower than others gold arrays reported in literature. In particular, for Au nanospheres monolayers (d = 13 nm) formed using a 1-hexaneamine as linker, a value of 10^{-3} S/cm were reported. [29] The use of smaller size AuNP and a linker with a shorter alkyl chains ensures better value of electrical conductivity but this cannot explain the 4 order of magnitude of difference among our values and that obtained by authors. The reason of such different electrical conductivity can be ascribed to the different morphology of the sample: in fact, in our case, the presence of islands separated by large gap reduces drastically the current flow through the sample.

4.10 – Conclusions

In this chapter AuNP of various shape (cubes, spheres, triangles and rods) were self-assembled at water/hexane interface generating a centimetre scale array that can be collected on both glass and ITO solid substrates using a drain-to-deposit approach. The technique lies on the destabilization of the AuNP colloidal dispersion through the addition of ethanol, which causes the migration of nanoparticles at the interface, where the self-assembly occurs, driven by the thermodynamic tendency to reduce interfacial area. The density and thickness of the obtained layer can be controlled by the *in-situ* functionalization of AuNP surface by 1-dodecanethiol, which induces Van der Waals attractive interactions among nanoparticles. Depending on the chosen deposition technique on to the solid substrate and by controlling experimental parameters such as volume fraction of ethanol, evaporation rate of hexane, concentration of coating agent in AuNP colloidal dispersion, it was possible to improve the density and homogeneity of the obtained depositions.

The morphological properties of these arrays were studied through scanning electron microscopy and X-ray powders diffraction, and correlated with the optical properties of the arrays studied by UV-Visible spectroscopy. SEM images showed that AuNP forms extended monolayer arrays constituted by islands of nanoparticles tens of microns large and separated by large gap. Inside islands, AuNP are densely packed (the minimum distance observed between two nanoparticles ranged between 1-2 nm), showing very few voids and overlaps, which depends on the amount of 1-dodecanethiol dissolved in the hexane phase. This morphology is attributed to the balance of forces acting among nanoparticles; at short-range the Van der Waals attractive forces prevail, generating a dense and ordered structure, while at long-range the electrostatic repulsion due to the residual surface charge density on AuNP surface dominates, introducing a degree of disorder into the system.

Shape of nanoparticles is also important in the formation of ordered monolayer. We found that opportunely tuning the 1-dodecanethiol concentration a dense monolayer was obtained for AuNC, AuNS, and AuNR; conversely, for AuNT a disordered and multi-layered structure was obtained, attributed to the reduced thickness of these nanoparticles that promotes the formation of more than one layer of particles at the interface, independently by 1-dodecanethiol quantity.

Moreover, through XRD techniques, it was possible to correlate the obtained signal to the crystalline habit of each nanoparticle sample by comparing it with the theoretically expected one. The data obtained are consistent with the theoretical ones for AuNC, AuNR and AuNT,

while the presence of the {110} facet in the AuNS pattern remains to be clarified. Knowing the crystalline habit of nanoparticles is very important not only from a synthetic point of view, as it allows to obtain indirect information about the nanoparticles shape, but also from an applicative point of view as the catalytic activity of these systems with respect to some reactions depends on the exposed facets. [31-33] Thus, the XRD pattern of self-assembled AuNP monolayers could be used for a qualitative evaluation of the suitability of specific nanoparticle sample towards the catalysis of a precise reaction.

The optical properties of the obtained monolayer were studied trough UV-visible spectroscopy. All the samples investigated, *i.e.* AuNS, AuNC, AuNT, and AuNR, experienced a dramatic enlargement and red shift of the plasmon band respect to the starting colloidal dispersion, due to the close proximity of AuNP in the islands, which induces strong optical coupling phenomena. The differences observed between various shapes are carefully analysed and correlated to the shape of the nanoparticle and to the morphology of the obtained film. The wide frequency range covered by plasmon resonance of these systems make them suitable in sensing, in particular in Surface Enhanced Raman Scattering (SERS) and Metal Enhanced Fluorescence (MEF).

Finally, an AuNC monolayer was deposited onto interdigitated electrodes and its electrical conductivity was measured. AuNC monolayer shows an electrical conductivity equal to 1×10^{-7} S/cm. The electrical conductivity of AuNP arrays, attributed by literature to hopping and tunnelling phenomena is promoted by the close-proximity of AuNC and to the presence of thiolate alkyl chains on their surface. [29, 30] The obtained value is 12 order of magnitude lower to the electrical conductivity of bulk gold (*i.e.* 4.5×10^5 S/cm). Furthermore, it results lower than others gold arrays reported in literature and this difference was mainly attributed to the discontinuous morphology of our samples, than reduced the number of AuNC islands large enough to bridging two gold stripes of the IDE. Further studies will be carried out to investigate the effect of the AuNP shape on the electrical conductivity of these systems.

References and notes

[1] N. J. Halas, S. Lal, W. S. Chang, S. Link, and P. Nordlander, Plasmons in strongly coupled metallic nanostructures, 2011, *Chem. Rev.*, 111, 3913–61;

[2] J. B. Edel, A. A. Kornyshev, and M. Urbakh, Self-assembly of nanoparticle arrays for use as mirrors, sensors, and antennas, 2013, *ACS Nano*, 7, 9526–32;

[3] L. Song, Y. Huang, Z. Nie, and T. Chen, Macroscopic two-dimensional monolayer films of gold nanoparticles: Fabrication strategies, surface engineering and functional applications, 2020, *Nanoscale*, 12, 7433–60;

[4] D. Lyvers, J. Moon, A. Kildishev, V. Shalaev, A. Wei, Gold Nanorod Arrays as Plasmonic Cavity Resonators, 2008, *ACS Nano*, 2(12), 2569-2576;

[5] F. Le, D. Brandl, Y. Urzhumov, H. Wang, J. Kundu, N. Halas, J. Aizpurua, P. Nordlander, Mtallic Nanoparticle Arrays: A Common Substrate for Both Surface-Enhanced Raman Scattering and Surface-Enhanced Infrared Absorption, 2008, *ACS Nano*, 2(4), 707-718;

[6] B. Sturman, E. Podivilov, and M. Gorkunov, Metal nanoparticles with sharp corners: Universal properties of plasmon resonances, 2013, *EPL*, 101, 57009;

[7] H. Chen, Z. Sun, W. Ni, K. C. Woo, H. Q. Lin., L. Sun, C. Yan, and J. Wang, Plasmon coupling in clusters composed of two-dimensionally ordered gold nanocubes, 2009, *Small*, 5, 2111–9;

[8] B. L. V. Prasad, C. M. Sorensen and K. J. Klabunde, Gold nanoparticle superlattices, 2008, *Chem. Soc. Rev.*, 37, 1871–83;

[9] F. Reincke, S. G. Hickey, W. K. Kegel, and D. Vanmaekelbergh, Spontaneous Assembly of a Monolayer of Charged Gold Nanocrystals at the Water/Oil Interface, 2004, *Angewandte Chemie - International Edition*, 43, 458–62;

[10] F. Reincke, W. K. Kegel, H. Zhang, M. Nolte, D. Wang, D. Vanmaekelbergh, and H. Möhwald, Understanding the self-assembly of charged nanoparticles at the water/oil interface, 2006, *Physical Chemistry Chemical Physics*, 8, 3828–35;

[11] Y. K. Park, S. H. Yoo, and S. Park, Assembly of highly ordered nanoparticle monolayers at a water/ hexane interface, 2007, *Langmuir*, 23, 10505–10;

[12] Y. K. Park, and S. Park, Directing close-packing of midnanosized gold nanoparticles at a water/hexane interface, 2008, *Chemistry of Materials*, 20, 2388–93;

[13] D. Wright, B. Flavel, J. Quinton, Streaming Zeta Potential Measurements Of Surface-Bound Organosilane Molecular Species, 2006, *International Conference on Nanoscience and Nanotechnology*, vol. 2006;

[14] B. Juárez, C. López, C. Alonso, Formation of Zinc Inverted Opals on Indium Tin Oxide and Silicon Substrates by Electrochemical Deposition, 2004, *The Journal of Physical Chemistry B*, 108(43), 16708-16712;

[15] L. Scarabelli, A. Sánchez-Iglesias, J. Pérez-Juste, and L. M. Liz-Marzán, A "Tips and Tricks" Practical Guide to the Synthesis of Gold Nanorods, 2015, *Journal of Physical Chemistry Letters*, 6, 4270–9;

[16] G. Yang, and D. T. Hallinan, Self-assembly of large-scale crack-free gold nanoparticle films using a 'drain-to-deposit' strategy, 2016, *Nanotechnology*, 27, 225604;

[17] L. Minati, A. Chiappini, F. Benetti , G. Speranza, D. Zonta, A. Piotrowska, M. Marciniak, A. Vaccari, and M. Ferrari, Fabrication and optical properties of assembled gold nanoparticles film on elastomeric substrate, 2015, *Colloids and Surfaces A: Physicochemical and Engineering Aspects*, 482, 431-437;

[18] D. R. Talham, T. Yamamoto, and M. W. Meisel, Langmuir–Blodgett films of molecular organic materials, 2008, J. Phys.: Condens. Matter, 20, 184006;

[19] Y. Xia, Y. Xiong, B. Lim, and S. Skrabalak, Shape-controlled synthesis of metal nanocrystals: Simple chemistry meets complex physics?, 2009, *Angewandte Chemie - International Edition*, 48, 60–103;

[20] D. Shajari, A. Bahari, P. Gill, and M. Mohseni, Synthesis and tuning of gold nanorods with surface plasmon resonance, 2017, *Optical Materials*, 64, 376–83;

[21] S. Kundu, S. Panigrahi, S. Praharaj, S. Basu, S. K. Ghosh, A. Pal and T. Pal, Anisotropic growth of gold clusters to gold nanocubes under UV irradiation, 2007, *Nanotechnology*, 18, 075712;

[22] N. N. Long, L. Van Vu, C. D. Kiem, S. C. Doanh, C. T. Nguyet, P. T. Hang, N. D. Thien, and L. M. Quynh, Synthesis and optical properties of colloidal gold nanoparticles, 2009, *J. Phys.: Conf. Ser.*, 187, 012026;

[23] The signals relative to the low index {100} and {110} planes are not observed in diffraction patterns of *fcc* Au, because of the systematic absences due to the *fcc* lattice type (*hkl* all add or all even). On the other hand, the higher index planes {200} and {220}, which indicates the same crystallographic direction, are observed instead. Thus, they were used instead of {100} and {110} facets in the discussion that follows.

[24] T. H. Yang, Y. Shi, A. Janssen, and Y. Xia, Surface Capping Agents and Their Roles in Shape-Controlled Synthesis of Colloidal Metal Nanocrystals, *Angewandte Chemie - International Edition*, 2020, 59, 15378–401;

[25] S. B. Gómez-Graña, Goris, T. Altantzis, C. Fernández-López, E. Carbó-Argibay, A. Guerrero-Martínez, N. Almora-Barrios, N. López, I. Pastoriza-Santos, J. Pérez-Juste, S. Bals, G. Van Tendeloo, L. Liz-Marzán, Au@Ag Nanoparticles: Halides Stabilize {100} Facets, 2013, *The Journal of Physical Chemistry Letters*, 4 (13), 2209-2216;

[26] H. Chen, X. Kou, Z. Yang, W. Ni, and J. Wang, Shape- and size-dependent refractive index sensitivity of gold nanoparticles, 2008, *Langmuir*, 24, 5233–7;

[27] Y. Ding, Y. You, Y. Sang, Y. Wang, M. Zhao, C. Liang, C. Lu, D. Liu, J. Zhou, Z. Tang, and J. Shi, Broadband Surface-Enhanced Photoluminescence Based on Gold Nanocubic Self-Assembly, 2017, *Adv. Optical Mater.*, 5, 1700551;

[28] J. Im, J. Singh, J. W. Soares, D. M. Steeves, and J. E. Whitten, Synthesis and optical properties of dithiol-linked ZnO/gold nanoparticle composites, 2011, *Journal of Physical Chemistry C*, 115, 10518–23;

[29] G. Yang, L. Hu, T. D. Keiper, P. Xiong, and D. T. Hallinan, Gold Nanoparticle Monolayers with Tunable Optical and Electrical Properties, 2016, *Langmuir*, 32, 4022–33;

[30] M. A. Mangold, C. Weiss, M. Calame, and A. W. Holleitner, Surface plasmon enhanced photoconductance of gold nanoparticle arrays with incorporated alkane linkers, 2009, *Appl. Phys. Lett.*, 94, 161104;

[31] P. Priecel, H. A. Salami, R. H. Padilla, Z. Zhong, J. A. Lopez-Sanchez, 2016, *Chinese Journal of Catalysis*, 37, 1619–1650;

[32] C. Chun-Ya, C. Pei-Ju, L. Ka-Un, L. Ching-Wen, Facet-Dependent Catalytic Activity of Gold Nanocubes, Octahedra, and Rhombic Dodecahedra toward 4-Nitroaniline Reduction, 2012, The Journal of Physical Chemistry C, 116 (44), 23757–23763;

[33] J. Rongchao, The impacts of nanotechnology on catalysis by precious metal nanoparticles, 2012, *Nanotechnol. Rev.*, 1, 31–56;

Chapter 5 - Metal enhanced fluorescence from gold nanoparticles self-assembled monolayers

As already discussed in Chapter 1, when a gold nanostructure showing plasmonic properties is in close proximity of a fluorophore, the luminescence of the latter can be enhanced by a mutual interaction phenomenon called metal enhanced fluorescence (MEF). The plasmonic field produced by nanoparticles can in fact enhances the fluorescence intensity, by increasing the absorption cross section of the fluorophore (a phenomenon known as *enhanced absorption*). Furthermore, the irradiated nanoparticle can act as an antenna, this phenomenon, known as *enhanced emission*, causes the fluorophore to transfer part of the absorbed energy to the nanostructure, which re-emits it much more rapidly. Consequently the number of photons emitted in the unit of time, and therefore its quantum yield, increase. [1,2]
The strong dependence of MEF on the distance between nanostructure and fluorophore, and on the spectral characteristic of the emissive specie, is a strong limitation for the practical exploitation of this phenomenon, so a fine engineering is required to build up reliable plasmonic platforms for this purpose.

In this context, nanoparticle arrays were intensively studied for their strong plasmonic field and their optical response due to the plasmon coupling between nanoparticles. Gold and silver nanoparticles arrays are particularly studied because their plasmonic resonance is in the UV-Visible-NIR range of the electromagnetic spectrum. The MEF effect induced by NP arrays is studied both in the case of dyes in solution and in the solid state. Geddes *et al*. using silver islands films (SIFs) as plasmonic substrate, performed a thorough study of MEF in solution. Experimentally, a given volume of the dye solution was incorporated between two glass slides and on one or both the slides were deposited the SIF film. The emission signal of the dye was collected in front face geometry and compared with a reference sample.[3] MEF in solid state was demonstrated both for SIF and AuNP arrays, for example by depositing Langmuir-Blodgett monolayers of fluorophores on SIFs, by depositing polymeric layers that, contemporarily, incorporates the dye and act as a spacer, using templates to produce ordered nanostructures. [4-6]

Using these techniques MEF was demonstrated for various commercial dyes (*e.g.* Fluorescein, Blue Nile, Rhodamine B, Red Nile), obtaining enhancement factors that ranged 10-100 fold with a decrement of the emission lifetime generally of one order of magnitude compared with the emission of the dye alone.

In this chapter preliminary studies of the effectiveness of AuNP monolayers prepared during this PhD research work as plasmonic substrates for MEF were presented. In details, the effect of the presence AuNC monolayer on the emission properties of a thin film of a porphyrin derivative in its close proximity was investigated.

5.1 - Preliminary studies of AuNP monolayers as MEF substrates

To demonstrating MEF from AuNP monolayer, a solid-state substrate was prepared, using as dye a free-base porphyrin, named NH_2TPPH_2, synthesized by E. Gallo's organic chemistry research group at Statale University of Milan, which structure is reported in Figure 5.1.

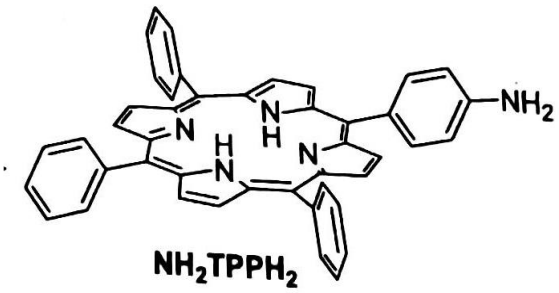

Figure 5.1 - Structural formula of porphyrin used for MEF characterization at the solid state.

NH_2TPPH_2 was chosen as dye for demonstrating MEF because its photophysical properties; in fact, porphyrins are characterized by an emission in the range between 640 and 750 nm, so perfectly overlapping with the plasmon band of AuNC monolayers, and by five absorption bands, which allow to excite them at different wavelengths, consenting to investigate the wavelength dependence of MEF. Furthermore, porphyrins are easily filmable due to the capacity to form various typology of aggregates in solid state. [7-9]

Sample preparation. The deposition of the fluorophore directly on the AuNP monolayer did not provide appreciable results, because the wettability of the AuNP monolayer varies along the glass slide for their discontinuous structure, and this hinder the formation of a homogeneous layer both with drop casting and spin coating techniques. Therefore, a NH_2TPPH_2 thin film on glass slides was obtained by spin coating a 2 mg/mL $CHCl_3$ solution of the dye at 4000 RPM for 60 seconds. The photophysical properties (absorption, emission, excitation spectra, and emission lifetimes in Table 5.2) of the obtained NH_2TPPH_2 film were collected to be used as reference and then, an AuNC monolayer was self-assembled at water/hexane interface using the procedure described in chapter 4, and deposited onto the NH_2TPPH_2 film using the horizontal lifting technique (see Figure 5.2).

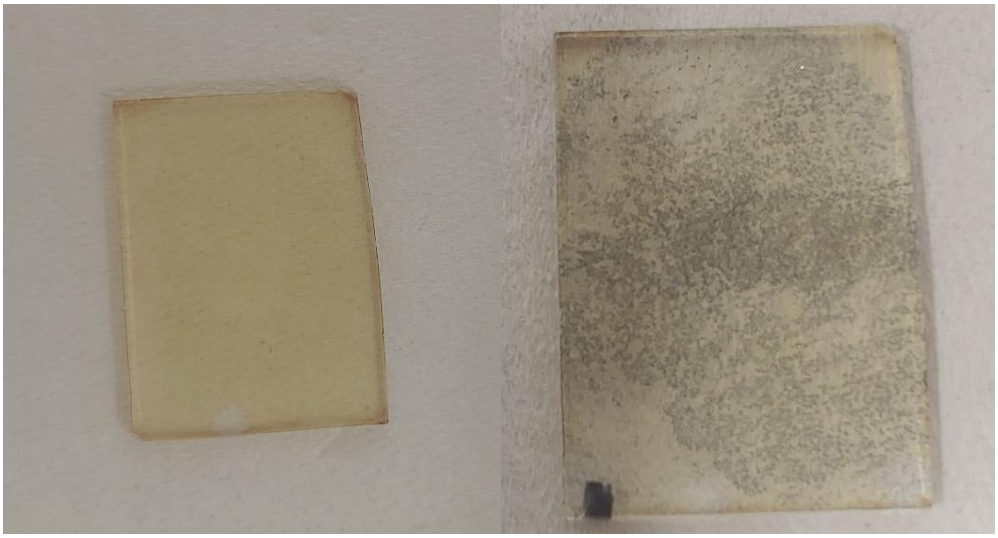

Figure 5.2 - NH_2TPPH_2 film on glass slide before (left) and after (right) the deposition of AuNC monolayer.

The photophysical characterization of both films were performed in a right angle geometry (45°) with a 610 nm cut-off filter (655 nm for lifetimes measurements) in emission to cut all reflections signals generated from excitation source. The irradiation of the films was performed from the glass side, in order to excite first the dye than the superimposed plasmonic nanostructure. This choice is due to the higher reflectivity of the AuNC monolayer respect to the glass slides, attested by the reflectance spectra reported in figure A.3.7 in Appendix (The reflectivity of AuNP monolayer would have reduced the excitation light that reach the NH_2TPPH_2 film, increasing the signal/noise ratio and would have made it difficult to observe the dye emission).

Results and discussion. The absorption spectrum of NH_2TPPH_2 film deposited on glass slide shows the typical structure already observed for porphyrins in solution. [8,10] It shows five absorption bands, an intense one centred at 438 nm and four weaker bands with maxima at 523, 560, 595, and 645 nm (see Figure 5.3). The first one was called "Soret" or B band, while the others are known as Q bands and are all due to π-π* type electronic transitions; in particular the B band corresponds to the excitation towards the second excited state, and the Q bands toward the first excited state. The particular structure of the absorption spectra of porphyrins comes out from a process called configurational interaction: the two highest occupied π orbitals have almost the same energy, but rather than generate a unique, large absorption band the interference phenomenon produces the intense B band (constructive interference) and the four weak Q bands (destructive interference). [10]

When AuNC were deposited onto the dye layer, the sum of NH_2TPPH_2 film absorption spectrum and AuNC monolayer extinction spectrum was obtained. A large plasmon band with a maximum around 700 nm is observed, with the five bands system typical of porphyrin clearly visible. A slight shift of some NH_2TPPH_2 absorption bands were observed after the deposition, which now are centred at 433, 523, 561, 601, and 651 nm.

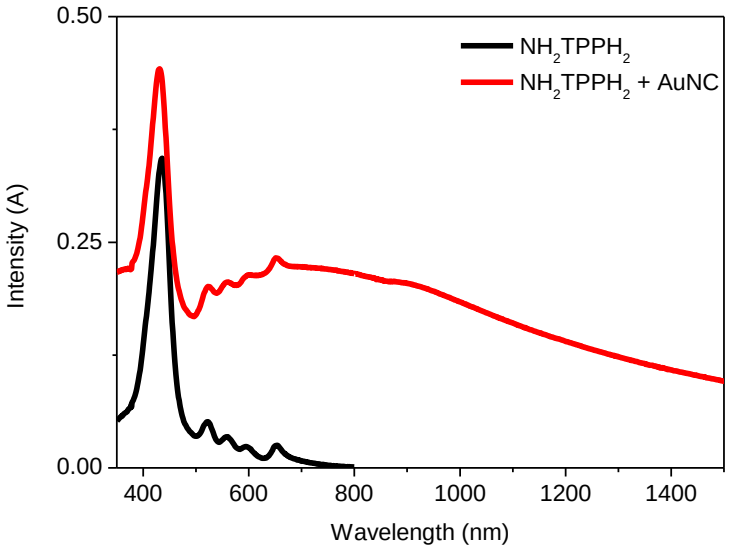

Figure 5.3 – Absorption spectra of NH_2TPPH_2 on glass slide before (black line) and after (red line) the deposition of AuNC monolayer.

Fluorescence from NH_2TPPH_2 film (without AuNC monolayer), due to the deactivation from the first excited state, was collected on all B and Q bands (except for the band at 560 nm for the lack of an opportune cut-off filter). Emission spectra (reported in fig. 5.4) show two principal bands centred at 665 nm and 730 nm by exciting on the Q bands, while by exciting on the Soret

band (*i.e.* at 438 nm) we observe an enlargement of the peaks and a red-shift of the high-energy band and a blue-shift of the low-energy one.

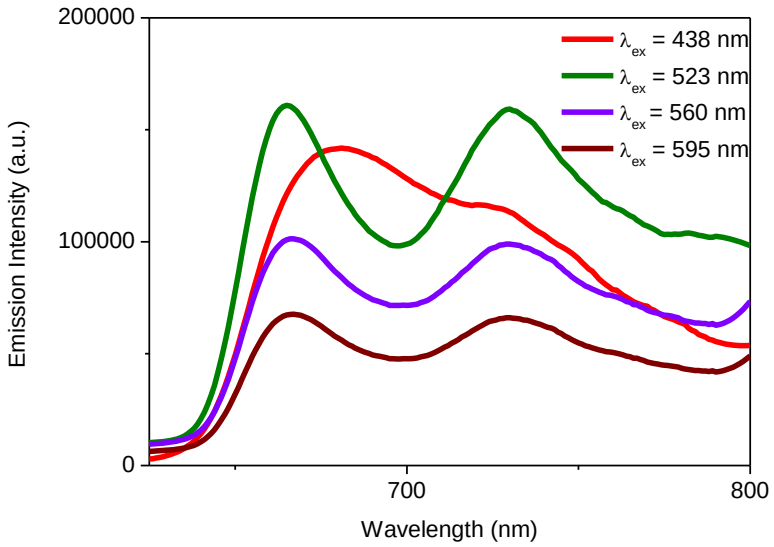

Figure 5.4 - Emission spectra of NH_2TPPH_2 film on glass slide varying the excitation wavelength.

After the deposition of AuNC on the NH_2TPPH_2 film (see figure A.3.8 - A.3.11 in Appendix), an increase of the fluorescence intensity was detected when the film was excited at 523, 560, and 595 nm. For the emission obtained exciting at 438 nm a slight decrease of emission intensity was observed instead, and the blue-shifted band of the spectra is now centred at 665 nm, similarly to others excitation wavelengths. The fluorescence enhancement was expressed in terms of an enhancement factor (E.F.), defined as the ratio between the intensity measured on each emission maximum of the sample (NH_2TPPH_2 film + AuNC) and the intensity of the respective emission maximum of the reference (NH_2TPPH_2 film), for each excitation wavelength investigated. The results are reported in table 5.1 and shows that the E.F. increases when the excitation wavelength increases. In fact, the maximum enhancement of the emission signal (five times and six times the reference value) was obtained when the sample was excited at 595 nm. This was attributed to the fact that increasing the excitation wavelength the incident light activates the AuNC plasmon more and more consistently (which has a broad band centred at about 700 nm), and thus a greater plasmonic field was generated by AuNC monolayer (see Figure 5.3). The influence of the plasmonic band was also confirmed from data arising from excitation at λ = 438, where the AuNC plasmon resonance was not active. In this case no MEF effect was detected, contrarily a slightly decrease of the emission signal was detected, that could

be attributed to the quenching of the dye molecules that are in close proximity of AuNC monolayer.

Table 5.1 – E.F. varying the excitation wavelength calculated from emission spectra in figures A.3.9 - A.3.12 in Appendix.

	λ_{em} (nm)	E.F. (λ_{ex} = 438 m)	E.F. (λ_{ex} = 523 nm)	E.F. (λ_{ex} = 560 nm)	E.F. (λ_{ex} = 595 nm)
NH_2TPPH_2 film + AuNC	**665**	**0.8**	**2.6**	**3.9**	**5.0**
	730	**0.9**	**3.3**	**4.8**	**6.1**

A further confirm of the MEF effect from AuNC monolayer comes from the time-resolved measurement. The emission lifetimes measured on both the emission bands (at 670 and 730 nm) of NH_2TPPH_2 was collected both for the reference (NH_2TPPH_2 film) and for the sample (NH_2TPPH_2 film + AuNC), using two excitation sources at different wavelengths, *i.e.* 485 and 635 nm, and the collected exponential decays were reported in figure A.3.12 and A.3.13 (see section A.3 of the Appendix) respectively. From reported figures, we see clearly that in both cases a reduction of the emission lifetime occurs, but when the sample was excited with the 635 nm light source, *i.e.* in the case in which the plasmon resonance of AuNC monolayer is activated, this reduction results more prominent. The fitting of these decays was performed using a three-exponential function, and the results were reported in table 5.2. The three lifetimes obtained for each decay curve reflect the complexity of the NH_2TPPH_2 systems in condensed phase, due to the strong interaction among molecules that bring to the formation of various typology of aggregates. We try to understand what happens to the dye emission signals after the deposition of AuNC monolayer by the analysis of the obtained lifetime and of their percentage contribution of each lifetimes to the total decay (that are reported in square brackets in table 5.2). From table 5.2 we see that the lifetime obtained from the 670 nm emission wavelength and that obtained from the 730 nm are almost similar in any conditions, thus for greater clarity we focused only on the data collected at 670 nm. By firstly considering the data collected from NH_2TPPH_2 film (*i.e.* the reference sample) exciting the sample at 485 nm three different lifetime of 0.06, 0.3 and 3.6 ns was detected, whit the larger contribute due to the longest lifetime. Because at this excitation wavelength plasmon resonance was not excited, an evaluation of the effect of the physical presence of AuNC monolayer can be extrapolated.

Table 5.2 – Results of the fitting of exponential decays of NH_2TPPH_2 film and NH_2TPPH_2 + AuNC collected on both emission bands of the samples (670 and 730 nm) exciting it with two laser sources at 485 and 635 nm.

Sample	λ_{ex} (nm)	τ (ns) (λ_{em} = 670 nm)			τ (ns) (λ_{em} = 730 nm)		
NH_2TPPH_2 film	**485**	**0.06 [33%]**	**0.3 [21 %]**	**3.6 [46 %]**	**0.06 [25 %]**	**0.3 [30 %]**	**3.0 [45 %]**
	635	**0.03 [13 %]**	**0.8 [17 %]**	**4.4 [70%]**	**0.04 [23%]**	**0.6 [14 %]**	**3.9 [63 %]**
NH_2TPPH_2 + AuNC	**485**	**0.05 [63 %]**	**0.3 [23 %]**	**2.7 [14 %]**	**0.05 [53 %]**	**0.3 [34 %]**	**1.9 [13 %]**
	635	**0.005 [49 %]**	**0.2 [31 %]**	**2.9 [20 %]**	**0.003 [67 %]**	**0.3 [25 %]**	**2.1 [8 %]**

After the deposition of the AuNC monolayer a reduction of the longer lifetime of about 1 ns was detected accompanied by a strong reduction of their weight on the total signal (from 46 to 14 %). The other lifetimes remains unchanged in the limit of experimental error. This reduction was attributed to the quenching of dye molecules that are localized nearby the metal monolayers, confirmed by the reduction of emission intensity obtained exciting the sample at 438 nm. [11-13] When also the plasmon resonance of AuNC monolayer was excited, for λ_{ex} = 635 nm, the reduction of the longer lifetime is even greater (-1.5 ns), and in addition the other lifetimes result reduced (from 0.8 to 0.2 ns and from 0.03 to 0.005 ns). This effect is attributed to MEF.

5.2 – Conclusions

In this chapter, we have compared the photophysical properties of a NH_2TPPH_2 thin film with those of the same film covered by an AuNC monolayer: an increase of its fluorescence and the temporary decreasing of its emission lifetimes were observed. Furthermore, the phenomenon was observed only when the sample was excited at SPR frequencies of the AuNC nanostructure, and these data strongly confirm the MEF. The maximum enhancement factor, measured exciting the sample at 595 nm for the emission band centred at 730 nm was equal to 6.1. The obtained data are clearly qualitative, because for instrumental limits they were not carried out at the maximum of the plasmon resonance of AuNC monolayer, where the effect should be stronger. Furthermore, it would be necessary to have information regarding the thickness of the dye layer, because it is well known that MEF depends also on the distance between the fluorophore and the plasmon nanostructure.

Considering all these aspects, we can conclude that AuNP monolayers are very good candidates as substrate for MEF, not only for their performance in increase the emission signal but also for their spectral amplitude of the plasmon response that make them suitable with a wide range of dyes. Further studies will be carried out to improve the performance of these systems trying to reduce the voids in the AuNP film structure, and to extend the experiment to the other AuNP monolayers prepared during this PhD course.

References

[1] A. Synak, B. Grobelna, S. Raut, P. Bojarski, I. Gryczyński, J. Karczewski, and T. Shtoyko, Metal enhanced fluorescence of flavin mononucleotide using new plasmonic platform, 2016, *Optical Materials*, 59, 136–40;

[2] R. Knoblauch, and C. D. Geddes, Review of Advances in Metal-Enhanced Fluorescence, *Reviews in Plasmonics 2017*, Springer, 253–283;

[3] R. Pribik, A. I. Dragan, Y. Zhang, C. Gaydos, and C. D. Geddes, Metal-Enhanced Fluorescence (MEF): Physical characterization of Silver-island films and exploring sample geometries, 2009, *Chem. Phys. Lett.*, 478, 70–4;

[4] K. Ray, R. Badugu, and J. R. Lakowicz, Distance-Dependent Metal-Enhanced Fluorescence from Langmuir−Blodgett Monolayers of Alkyl-NBD Derivatives on Silver Island Films, 2006, *Langmuir*, 22 8374–8;

[5] C. Joyce, S. M. Fothergill and F. Xie, Recent advances in gold-based metal enhanced fluorescence platforms for diagnosis and imaging in the near infrared, 2020, *Mater. Today Adv.*, 7, 100073;

[6] A. Synak, P. Bojarski, B. Grobelna, I. Gryczyński, R. Fudala, and M. Mońka, Enhanced emission of Nile Red on plasmonic platforms, 2018, *Optical Materials*, 78, 82–7;

[7] R. F. Khairutdinov, and N. Serpone, Photoluminescence and transient spectroscopy of free base porphyrin aggregates, 1999, *Journal of Physical Chemistry B*, 103, 761–9;

[8] F. Scandola, C. Chiorboli, A. Prodi, E. Iengo, and E. Alessio, Photophysical properties of metal-mediated assemblies of porphyrins, 2006, *Coord. Chem. Rev.*, 250, 1471–96;

[9] D. Myśliwiec, B. Donnio, P. J. Chmielewski, B. Heinrich, and M. Stępień, Peripherally Fused Porphyrins via the Scholl Reaction: Synthesis, Self-Assembly, and Mesomorphism, 2012, *J. Am. Chem. Soc.*, 134, 4822–33;

[10] H. L. Anderson, Building molecular wires from the colours of life: conjugated porphyrin oligomers, 1999, *Chem. Commun.*, 2323-2330.

[11] V. N. Pustovit, and T. V. Shahbazyan, Fluorescence quenching near small metal nanoparticles, 2012, *J. Chem. Phys.*, 136, 20470;

[12] J. R. Lakowicz, Radiative Decay Engineering: Biophysical and Biomedical Applications, 2001, *Analytical Biochemistry*, 298, 1–24;

[13] A. Campion, A. R. Gallo, C. B. Harris, H. J. Robota, and P. M. Whitmore, Electronic energy transfer to metal surfaces: a test of classical image dipole theory at short distances, 1980, *Chemical Physics Letters*, 73 (3), 447-450.

Final Remarks

The experimental work described in this PhD Thesis is focused on the study of two different materials at different dimensional scales able to interact with the UV-Visible electromagnetic radiation, *i.e.* luminescent metallomesogens and gold nanoparticles.

Luminescent metallomesogens of Pt(II), and Zn(II), whose photophysical characterization is described in detail in **Chapter 2**, were suitably designed to control the phase type, transition temperatures and thermal stability, as well as to improve their luminescence in the mesophase.

The characterization of Pt(II) complexes evidenced the role of metal-metal interactions in the formation of excited states involving the metal centre, and the steric hindrance of the ancillary ligands in directing such interactions. For **Pt_1** and **Pt_3** (see Fig. 2.1) the small steric hindrance of chlorine allows a Pt-Pt interaction (already present in solution and more strongly reinforced in solid), giving rise to an MMLCT excite-state in the mesophase. On the contrary, the bulky benzoate group of **Pt_2** and **Pt_4** (see Fig. 2.1) does not allow a Pt-Pt interaction, while weak ππ interactions on the tpy ligands give rise to the formation of excimers, similarly to the solution. Therefore, the use of gallate units for inducing room temperature mesomorphism, was detrimental for the luminescence of the Pt(II) complexes.

By substituting Pt(II) with Zn(II), a good emitter in solution was obtained (**Zn_2** in Fig. 2.1) but its columnar mesomorphic organization quenches fluorescence in the mesophase. However, varying the substituent on the terpyridine ligand the emissive properties can be finely tuned and improved. While **Zn_3** and **Zn_5** emit modestly, the fluorescence originated from the ILCT excited state in **Zn_4** (see Fig. 2.1) from the electron-donating $–NEt_2$ group to the electron-withdrawing aromatic rings of the tpy ligand reaches a record luminescence quantum yield in solution (95%). Although the emission efficiency is reduced in the mesophase due to distortion of the diethylaniline with respect to the aromatic rings of tpy, it remains as high as 20%.

Furthermore, these photophysical studies confirm how it is possible, through an accurate engineering of the molecular structures of metallomesogens to improve their functional properties. In this context, the high sensitivity of the metal centre with respect to its molecular environment evidenced in Pt(II) and Zn(II) terpyridine-based metallomesogens is a potentially good property for application in sensing, while the high emission quantum yield evidenced by **Zn_4** is promising for possible applications in display technologies.

In **Chapter 3**, the synthesis of gold nanoparticles of various shapes (cubes, spheres, triangles and rods) exploiting seed-mediated growth procedures were described. Clearly, like in any other chemical reaction, the most important parameter to evaluate the effectiveness of a synthetic strategy is the reaction yield. In the case of AuNP the reaction yield can be defined as the number of nanocrystals of the desired shape respect to the total number of nanoparticles in the obtained colloidal dispersion. Unfortunately, due to the great number of parameters hard to control involved in the growth of nanocrystals (*e.g.* temperature fluctuations, reactant purity and so on) it is very difficult to obtain repeatable results, so the gold nanoparticles synthesis usually suffers of reproducibility issues. In this context, understanding the mechanisms that control the nanoparticles growth according to a specific crystalline habit, it is possible to adapt any protocol to the specific conditions, improving the yield of the reaction and bringing to higher concentrations of the desired products. This was evident during AuNC@CTAB synthesis, where very low yields in term of cubic shaped AuNP were obtained at first. However, with opportune changes in both seed formation and growth (*i.e.* increasing speed of addition of the $NaBH_4$ in the reaction mixture and increasing the concentration of CTAB in the growth step, respectively) an improvement of the yield from 45 to 85 % was reached. Another important tool that helps to obtain monodispersed nanocrystals in both shape and size, is the purification step that can be performed trough centrifugation or depletion induced flocculation, depending on how the by-products differ in shape and size from the desired nanocrystals. Given the strong dependence of nanoparticles optical properties from their shape and size, sample purity is an essential feature if nanoparticles are meant to be used in any technological application.

The extinction spectra collected from AuNP of various shapes synthesized during the PhD research work were reported in figure 3.22.

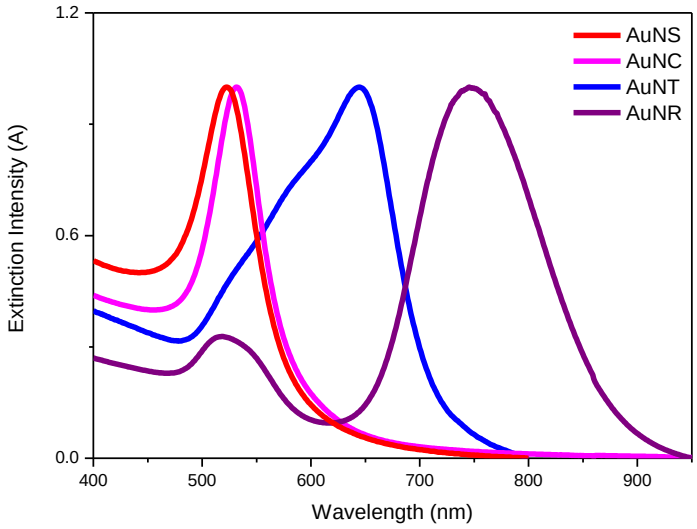

Figure 3.22 – Normalized extinction spectra of AuNP synthesized during the PhD period.

The comparison between the four samples shows how different can be the optical response of AuNP varying their crystalline habit, due to the different oscillation modes possible for the electronic clouds of each nanoparticles, and thus their different resonance frequencies. In theory, opportunely engineering shape and size of AuNP system resonant at any wavelength of visible and NIR regions of electromagnetic spectra can be obtained, making them suitable for a very wide range of different applications. For example, spectrum of AuNR@CTAB reported in figure 3.22 (purple line) shows a longitudinal plasmon resonance band centred at 793, which is in the middle of the phototherapeutic window, so they can find application as phototherapeutic agents for the diagnosis and treatment of cancer. [1- 5] The LSPR of AuNT@CTAC (blue line), AuNC@CTAB (magenta line), and AuNS@CTAB (red line) centred respectively at 645, 533, and 522 nm, are suitable to be exploited for improving the performance of organic solar cells, because the strong scattering and absorption of these nanoparticles in the region where the solar emission is maximum can improve the optical performances of the active layer (responsible for the absorption of solar radiation and its conversion into electricity). In this context, play also a pivotal role the shape and size of employed nanoparticles: in fact due to the low thickness of organic solar cells layers, small sized AuNP or AuNT with their reduced thickness are the better choose because do not perturb the structure of the cell, preserving the charge transport through the device.[1-5] Another example of the impact of the shape on the application of AuNP is constituted by AuNS and AuNC, which, as we see from figure 3.22, show a similar LSPR (the LSPR position of AuNC and AuNS of equal size differs of few nm). [6] However, the presence of sharp corners and tips in AuNC enhances strongly the plasmonic field generated by nanoparticles increasing their

performances in sensing and field enhancement based applications. [7] Furthermore, because they expose facets with greater surface free energy than a sphere of equal size, shows a better catalytic activity. [8]

The synthesized AuNP of various shape (cubes, spheres, triangles and rods) were self-assembled at water/hexane interface generating a centimetre scale array that can be collected on both glass and ITO solid substrates using a drain-to-deposit approach (**Chapter 4**). The technique lies on the destabilization of the colloidal dispersion AuNP through the addition of ethanol, which causes the entrapment of nanoparticles at the interface, where starts to self-assembly driven by the thermodynamic tendency to reduce the interfacial area. The density and thickness of the obtained layer can be controlled by the *in-situ* functionalization of AuNP surface by 1-dodecanethiol, which induce Van der Waals attractive interaction between nanoparticles. By controlling experimental parameters like ethanol volume fraction, hexane evaporation speed, concentration of coating agent in AuNP colloidal dispersion, deposition technique on to the solid substrate it was possible to improve the obtained result in terms of density and homogeneity of the obtained depositions.

The morphological properties of these arrays were studied trough scanning electron microscopy and X-ray powders diffraction, and correlated with the optical properties of the obtained arrays studied by UV-Visible spectroscopy. SEM images showed that AuNP form monolayer extended arrays constituted by islands of nanoparticles tens of microns large, within which AuNP are densely packed (the minimum distance observed between two nanoparticles ranged between 1-2 nm), showing very few voids and overlaps, which depend from the amount of 1-dodecanethiol dissolved in the hexane phase. The formation of this fractal structures is attributed to the balance of forces acting between nanoparticles. At short range the Van der Waals attractive forces prevail, generating a dense and ordered structure, while at long-range the electrostatic repulsion due to the residual surface charge density on AuNP surface dominate, interrupting the order in the system.

Shape of nanoparticles is also important in the formation of ordered monolayer. We found that opportunely tuning the 1-dodecanethiol concentration a dense monolayer could be obtained for AuNC, AuNS, and AuNR, but for AuNT a disordered and multi-layered structure was obtained, attributed to the reduced thickness of these nanoparticles that promote the formation of more than one layer of particles at the interface, regardless of the 1-dodecanethiol quantity. Moreover, through the XRD characterization, by knowing the organization of the particles on to the solid

support induced by the deposition technique, it was possible to correlate the obtained signal to the crystalline habit of each nanoparticle sample, comparing it with the theoretically expected one. The data obtained are consistent with the theoretical ones for AuNC, AuNR and AuNT, while the presence of the {110} facet in the AuNS pattern remains to be clarified.

Knowing the crystalline habit of nanoparticles is very important not only from a synthetic point of view, as it allows to obtain indirect information about the nanoparticles shape, but also from an applicative point of view as the catalytic activity of these systems with respect to some reactions depends on the exposed facets. [9-11] Thus, the XRD pattern of self-assembled AuNP monolayers could be used for a qualitative evaluation of the suitability of specific nanoparticle sample towards the catalysis of a precise reaction.

The resulting optical properties of the obtained monolayer were studied trough UV-visible spectroscopy. All the samples investigated, *i.e.* AuNS, AuNC, AuNT, and AuNR, experienced a dramatic enlargement and red shift of the plasmon band respect to the starting colloidal dispersion, due to the close proximity of AuNP in the observed islands, which induces strong optical coupling phenomena. The differences observed among various shapes are carefully analysed and correlated to the shape of the nanoparticle and to the morphology of the obtained film. The wide frequency range covered by plasmon resonance of these systems make them suitable in sensing, in particular in Surface Enhanced Raman Scattering (SERS) and Metal Enhanced Fluorescence (MEF).

Finally, an AuNC monolayer was deposited on interdigitated electrodes and their electrical conductivity were measured. AuNC monolayers show an electrical conductivity of 2×10^{-7} S/cm. The electrical conductivity on AuNP arrays attributed by literature to hopping and tunnelling phenomena is promoted by the close-proximity of AuNC and to the presence of thiolate alkyl chains on its surface. [12, 13] The obtained value is 12 order of magnitude lower to the electrical conductivity of bulk gold (*i.e.* 4.5×10^{5} S/cm). Furthermore, it results lower than others gold arrays reported in literature and this difference was attributed to the discontinuous morphology of our samples, than reduced the number of electrons carriers, *i.e.* AuNC islands large enough to bridging two gold stripes of the IDE. Further studies will be carried out to investigate the effect of the AuNP shape on the electrical conductivity of these systems.

The AuNC monolayers were the ideal substrate to study "talking" effect between plasmonic nanomaterials and electronic excited states of molecular materials (**Chapter 5**). By depositing an AuNC monolayer on a NH_2TPPH_2 (see Fig. 5.1) thin film an increase of its fluorescence and the temporary decreasing of its emission lifetimes were observed. Furthermore, the phenomenon was observed only when the sample was excited at SPR frequencies of the AuNC nanostructure, and this data strongly confirm the effectiveness of MEF. The maximum enhancement factor, measured exciting the sample at 595 nm for the emission band centred at 730 nm attributed to NH_2TPPH_2 aggregation, was 6.1. The obtained data are clearly qualitative, because for instrumental limits were not carried out at the maximum of the plasmon resonance of AuNC monolayer, where the effect should be stronger. Furthermore, for the discontinuities observed in the AuNC monolayer (see section 4.4), we can speculate that not all the irradiated dye molecules were at the right distance from gold nanoparticles to experience this effect. Considering all these aspects, we can conclude that AuNP monolayers are very good candidates as substrate for MEF, not only for their performance in increase the emission signal but also for their large plasmon response that make them suitable with a wide range of dyes. Further studies will be carried out to improve the performance of these systems trying to reduce the voids in the AuNP film structure, and to extend the experiment to the other AuNP monolayers prepared during this PhD course.

In this journey we have explored the profound correlation between size, shape and properties, especially those due to light-matter interaction. We clearly observed that as the scale of the building block increases, the properties depend less and less on atomicity and more and more on organization. In this observation we must realize that this principle is always present in Nature, which shapes matter to obtain surprising functions starting from poor bricks, atoms like H, C, N, O and a few others, but organizing surprising architectures at every possible scale.

Unlike our technologies, which require building blocks having atoms with high chemical potential, but little organization, Nature uses atoms with low chemical potential, widely present on Earth, but organized with marvellous mastery in nano- and meso-scale structures. And this organization seems increasingly evident to derive from processes far from equilibrium, in which dissipative structures have played a preponderant role [14].

After all, Nature is the most skilled craftswoman of materials, that is, of matter organized to perform a function.

References

[1] C. E. Petoukhoff, Z. Shen, M. Jain, A. Chang and D. M. O'Carroll, Plasmonic electrodes for bulk-heterojunction organic photovoltaics: a review, 2015, *Journal of Photonics for Energy*, 5(1), 057002;

[2] J. L. Wu, F. C. Chen, Y. S. Hsiao, F. C. Chien, P. Chen, C. H. Kuo, M. H. Huang, and C. S. Hsu, Surface plasmonic effects of metallic nanoparticles on the performance of polymer bulk heterojunction solar cells, 2011, *ACS Nano*, 5, 959–67;

[3] L. Qiao, D. Wang, L. Zuo, Y. Ye, J. Qian, H. Chen, S. He, Localized surface plasmon resonance enhanced organic solar cell with gold nanospheres, 2011, *Applied Energy*, 88(3), 848-852;

[4] C. Wang, W. Choy, C. Duan, D. Fung, W. Sha, F. Xie, F. Huang, Y. Cao, Optical and electrical effects of gold nanoparticles in the active layer of polymer solar cells, 2012, *J. Mater. Chem.*, 22(3), 1206-1211;

[5] M. Notarianni, K. Vernon, A. Chou, M. Aljada, J. Liu, N. Motta, Plasmonic effect of gold nanoparticles in organic solar cells, 2014, *Solar Energy*, 106, 23-37;

[6] M. Alsawafta, M. Wahbeh, and V. Truong, Simulated optical properties of gold nanocubes and nanobars by discrete dipole approximation, 2012, *Journal of Nanomaterials*, vol. 2012;

[7] C. Deeb, X. Zhou, Miller R, S. K. Gray, S. Marguet, J. Plain, G. P. Wiederrecht, and R. Bachelot, Mapping the Electromagnetic Near-Field Enhancements of Gold Nanocubes, 2012, *J. Phys. Chem. C*, 116(46), 24734–24740;

[8] C. S. Bhatt, B. Nagaraj, and A. K. Suresh, Nanoparticles-shape influenced high-efficient degradation of dyes: Comparative evaluation of nano-cubes vs nano-rods vs nano-spheres, 2017, *J. Mol. Liq.*, 242, 958–65;

[9] P. Priecel, H. A. Salami, R. H. Padilla, Z. Zhong, J. A. Lopez-Sanchez, 2016, *Chinese Journal of Catalysis*, 37, 1619–1650;

[10] C. Chun-Ya, C. Pei-Ju, L. Ka-Un, L. Ching-Wen, Facet-Dependent Catalytic Activity of Gold Nanocubes, Octahedra, and Rhombic Dodecahedra toward 4-Nitroaniline Reduction, 2012, The Journal of Physical Chemistry C, 116 (44), 23757–23763;

[11] J. Rongchao, The impacts of nanotechnology on catalysis by precious metal nanoparticles, 2012, *Nanotechnol. Rev.*, 1, 31–56;

[12] G. Yang, L. Hu, T. D. Keiper, P. Xiong, and D. T. Hallinan, Gold Nanoparticle Monolayers with Tunable Optical and Electrical Properties, 2016, *Langmuir*, 32, 4022–33;

[13] M. A. Mangold, C. Weiss, M. Calame, and A. W. Holleitner, Surface plasmon enhanced photoconductance of gold nanoparticle arrays with incorporated alkane linkers, 2009, *Appl. Phys. Lett.*, 94, 161104;

[14] I. Prigogine, I. Stengers, La nuova alleanza, 1999, *Piccola Biblioteca Einaudi Ns.*

APPENDIX

A.1 - Experimental section

Chemicals. Spectrofluorometric grade solvents were used for the photophysical investigations in solution without further purification. Hexadecyltrimethylammonium bromide (CTAB, ≥ 96%), Cetyltrimethylammonium chloride solution (25 % in H_2O), 5-bromosalicylic acid (technical grade, 90%), hydrogen tetrachloroaurate trihydrate ($HAuCl_4 \cdot 3H2O$, ≥ 99.9%), silver nitrate ($AgNO_3$, ≥99.0%), L-ascorbic acid ($C_6H_8O_6$, ≥ 99%), sodium iodide (NaI 99.99%), trisodium citrate ($Na_3C_6H_5O_7$, 99%), sodium borohydride ($NaBH_4$, 99%), 1-dodecanethiol, p-Terphenyl-4,4'-Dithiol were purchased from Aldrich. All the chemicals were used as received. Milli-Q water (resistivity 18.2 MΩ·cm at 25 °C) was used in all experiments.

Glassware cleaning procedure. All glassware was accurately washed with aqua regia (HCl/HNO_3 3:1 mixture), rinsed with water, washed with Milli-Q water, and dried before use. Cuvettes, quartz slides and all the glassware used during the photophysical characterization were accurately washed with a reducing solution (obtained by dissolving a small amount of $KMnO_4$ in H_2SO_4) and repeatedly rinsed with H_2O. Then, were washed with an oxidant mixture (H_2O, H_2O_2, HCl 1:1:0.1), rinsed again with abundant H_2O, and dried in an oven at 70 ºC for 24 hours.

Test patterns for electrical measurements. For the measurement of its electrical properties the AuNCs self-assembled monolayer was collected on a test pattern manufactured by FBK (Fondazione Bruno Kessler, Trento, Italy). The Test Patterns (TP) as shown in Figure 1 were fabricated on a heavily doped Silicon wafer, 500 μm thick, with a resistivity of 0.01– 0.03 Ω*cm. 200 nm thick SiO_2 was thermally grown to make a dielectric layer. The capacitance of the dielectric is 17.25 nF/cm^2. Interdigitated Au electrodes (125 ± 25 nm thick) were photolithographically patterned onto the SiO_2 by using Chromium adhesive layer (3–5 nm). On each test pattern, there are four interdigitated electrodes (IDEs) consisting of different channel length (L), i.e. the distance between a gold stripe and the next one), and different channel width (W), defined as the total length of all the gold stripes. In details the IDEs labelled as A_1 and B_1

(see Figure 1) have L = 20 μm, and W = 11200 μm, while the IDEs named A_2 and B_2 have L = 40 μm, and W = 22400 μm. The W/L ratio for all the four IDEs is 560.

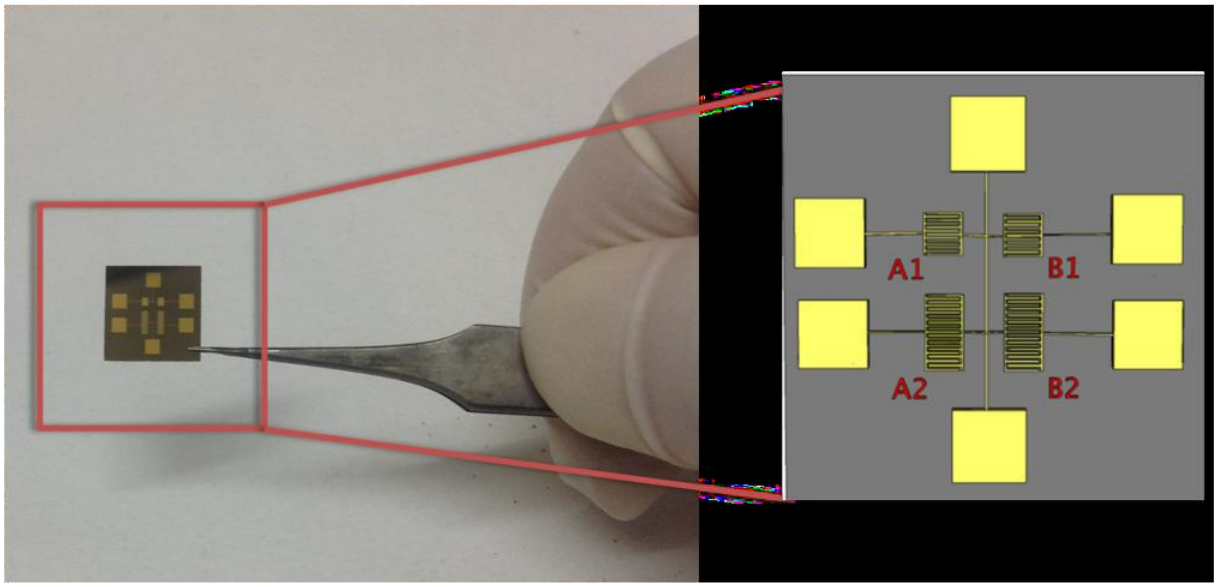

Figure 1 - The photo on the left shows the Au electrodes used for this experiment and (right) shows a schematic drawing. A1, B1, A2 and B2 are the names given to the four independent electrodes according to their geometry and position.

Prior to the deposition of AuNCs monolayer, the TPs were heavily cleaned by following a standard protocol. The protocol consists the following procedure:

i) We first rinse the TPs with acetone in order to remove the photoresistive layer, followed by blowing it with dry nitrogen.

ii) Then we dip the TPs in hot piranha (H_2SO_4:H_2O_2, 1:1) for 15 minutes in order to remove organic contaminants. After that, the TPs are then rinsed de-ionised water and blowing with dry nitrogen.

UV-Vis characterization: absorption and extinction spectra. A Perkin Elmer Lambda 900 spectrophotometer was employed to register the absorption spectra of fluorophores and the extinction spectra of AuNPs samples; quartz cuvettes of a 1 cm path length were used.

UV-Vis characterization: emission, excitation spectra and time resolved measurements.

Emission and excitation spectra in solution were carried out through a Perkin-Elmer LS 50B spectrofluorometer; quartz cuvettes of a 1 cm path length were used.

Steady-state emission spectra of solid samples in Chapter 2 were recorded on a HORIBA Jobin-Yvon Fluorolog-3 FL3-211 spectrometer (Fig. A.1) equipped with a 450 W xenon arc lamp (L), double-grating excitation (Mex) and single-grating emission (Mem) monochromators (2.1 nm/mm dispersion; 1200 grooves/mm), a Hamamatsu R928 photomultiplier tube (PM) or a TBX-04-D single-photon-counting detector (DTCSPC) or a InGaAs liquid nitrogen-cooled solid-state detector (DInGaAs), and excitation and emission automated Glen-Thompson polarizers. Emission and excitation spectra were corrected for source intensity (lamp and grating) and emission spectral response (detector and grating) by standard correction curves. With regard to the solid-state measurements, samples were prepared by placing a given amount of powder between two quartz slides and standardizing the layer. Measurements varying temperature were performed through a heating sample holder connected to a heating plate (CaLCTec Instruments). For time resolved measurements NanoLEDs pulse centred at 379 nm and 265 nm (FWHM 750 ps with 1 MHz repetition rate) were used as the excitation source and fixed directly on the sample chamber at 90° to a single-grating emission monochromator (2.1 nm mm−1 dispersion; 1200 grooves per mm). Data analysis was performed using the commercially available DAS6 software (Horiba Jobin Yvon IBH). The quality of the fit was assessed by minimizing the reduced χ^2 function and visual inspection of the weighted residuals.

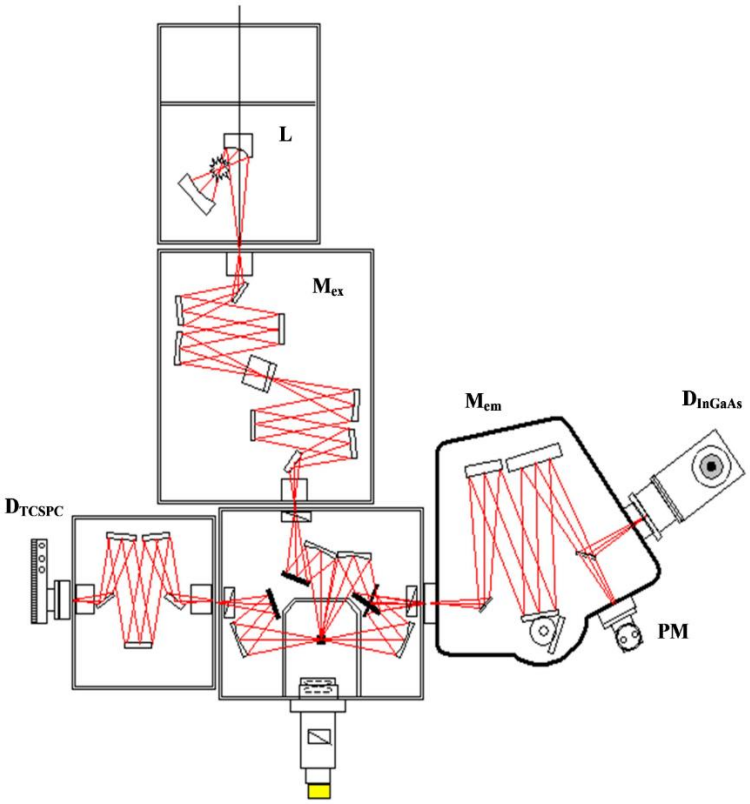

Figure A.1 – Optical configuration of HORIBA Jobin-Yvon Fluorolog-3 FL3-211 spectrometer.

Steady-state emission spectra of solid samples in Chapter 5 were recorded on an Edinburgh FLS100-SS-tt spectrometer (Fig. A.2) equipped with a 450 W Xenon lamp (Xe_2), single excitation and single emission 325 mm focal length monochromators in Czerny Turner configuration (1.7 nm/mm dispersion; 1800 grooves/mm), a MCP-900 PMT or a R298P photon counting detector both in fan assisted TE cooled housing and excitation and emission automated Glen-Thompson polarizers. Emission and excitation spectra were corrected for source intensity (lamp and grating) and emission spectral response (detector and grating) by standard correction curves. For time resolved measurements EPL picosecond pulsed diode lasers centred at 485 ± 5 nm (typical pulse width 100 ps@10 MHz and RR 20 kHz – 20 MHz) and 635 ± 5 nm (typical pulse width 75 ps@10 MHz and RR 20 kHz – 20 MHz) were used as the excitation sources. Data analysis were performed using the Fluoracle spectrometer software. The quality of the fit was assessed by minimizing the reduced χ^2 function and visual inspection of the weighted residuals.

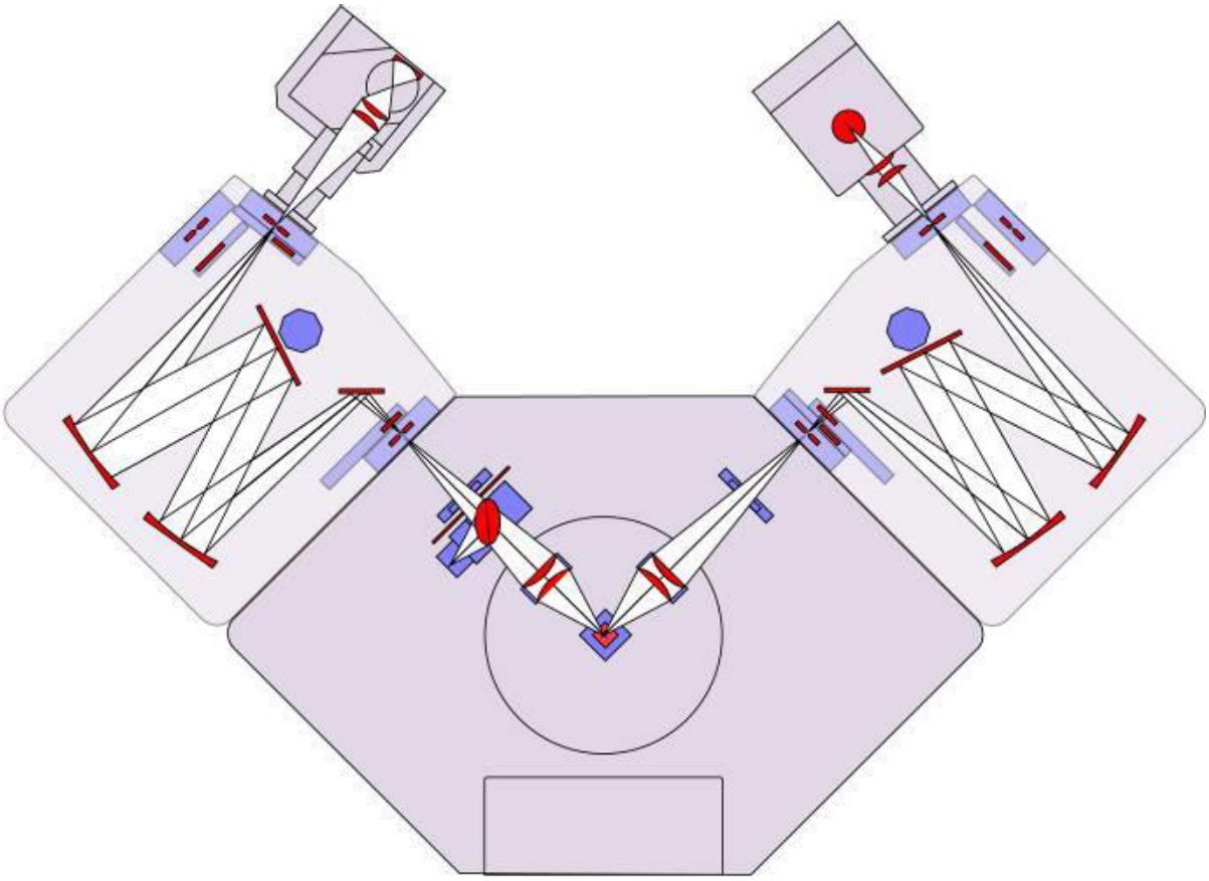

Figure A.2 – Optical configuration of Edinburgh FLS100-SS-tt spectrometer.

UV-Vis characterization: relative and absolute quantum yields. The relative emission quantum yields of samples in solution were determined using the optical dilution method [1] using $Ru(bpy)_3Cl_2$ in air-equilibrated water solution, 2-amminopyridine in ethanol solution, and 9,10-diphenylanthracene in cyclohexane solution as a reference standards ($\Phi = 0.040$ [2], $\Phi = 0.37$ [3], and $\Phi = 0.78$ [4] respectively). The absolute emission quantum yields for solid-state samples were obtained by means of a 102 mm diameter integrating sphere coated with Spectralon® and mounted in the optical path of the spectrofluorometer using, as the excitation source, a 450 W xenon lamp coupled with a double-grating monochromator for selecting wavelengths. The procedure for the measure of quantum yields with integrating sphere was based on De Mello method [5].

Transmission electron microscopy (TEM). The size and morphology of the gold nanoparticles colloidal dispersion were measured using a transmission electron Microscope (Jeol JEM-1400 Plus 120 kV). The samples for transmission electron microscopy (TEM) were prepared by depositing a drop of the colloidal dispersion on 300 mesh copper grids. After evaporation of the solvent in air at room temperature, the particles were observed at an operating voltage of 80 kV.

Scanning electron microscopy (SEM). The morphology of AuNPs arrays were measured using two different instruments: a Field Emission Scanning Electron Microscope (FESEM, FEI Quanta 200) and an Ultra High Resolution SEM (UHR-SEM, ZEISS CrossBeam 350). In the case of deposition on glass slide, the sample is made conductive through the sputtering of an ultra-pure graphite layer (Carbon Coater QUORUM Q150T-ES) with an approximately thickness of 5 nanometers (pulse current: 70 A, pulse time: 2.5 sec).

PXRD patterns. The PXRD patterns were acquired on a Bruker D2-Phaser equipped with a Cu Kα radiation (λ=1.5418 Å) and a Lynxeye detector, at 30 kV and 10 mA, with step size of 0.01° and step time of 2 s, over an angular range of 30–90° 2θ. The patterns were acquired by rotating the samples at a 10°/min rate (φ rotation). The obtained diffractograms were analysed with DIFFRAC.EVA diffraction software.

References

[1] G. A. Crosby, and J. N. Demas, Measurement of photoluminescence quantum yields, 1971, *Review J. Phys. Chem.*, 75, 991–1024;

[2] K. Suzuki, A. Kobayashi, S. Kaneko, K. Takehira, T. Yoshihara, H. Ishida, Y. Shiina, S. Oishi, and S. Tobita, Reevaluation of absolute luminescence quantum yields of standard solutions using a spectrometer with an integrating sphere and a back-thinned CCD detector, 2009, *Physical Chemistry Chemical Physics*, 11**,** 9850;

[3] R. Rusakowicz, and A. C. Testa, 2-Aminopyridine as a standard for low-wavelength spectrofluorimetry, 1951, *The Journal of Physical Chemistry*, 41, 2680-81;

[4] G. Heinrich, S. Schoof, and H. Gusten, 9,10-diphenylanthracene as a fluorescence quantum yield standard, 1974, *Journal of Photochemistry*, 3, 315–20;

[5] J. C. de Mello, H. F. Wittmann, and R. H. Friend, An improved experimental determination of external photoluminescence quantum efficiency, 1997, *Advanced Materials*, 9, 230–2.

A.2 - Tables

Table A.2.1 - Photophysical properties of Pt (II) complexes in solution

Sample	*Absorption, λ_{max} (nm)* (ε/M^{-1} cm^{-1})	*Emission, λ_{max} (nm)*	*Quantum yield, ϕ (%)*	*Lifetime, τ (ns) [%]*
Pt_1[a]	**286 (24780), 305 (13330), 320 (13940), 334 (15580), 372 (3930), 395 (3960), 459 (650)**	**620 nm**	**0.8**	**380**
Pt_2[b]	**285 (6310), 306 (2700), 317 (2370), 332 (1990), 381 (660), 393 (630), 459 (60)**	**600 nm**	**1.7**	**397**
Pt_3[c]	**286 (78320), 305(41990), 320 (41770), 334 (46580), 368 (10690), 396 (11670), 455 (1950)**	**615 nm**	**0.5**	**338**
Pt_4[d]	**285 (25630), 302(14650), 317(13370), 333 (12570), 367 (4030), 395 (3400), 469 (800)**	**650 nm**	**0.2**	**251**

[a] 1.08 10^{-5}; [b] 2.63 10^{-4} M; [c] 9.16 10^{-5} M; [d] 2.3 10^{-5} M;

Table A.2.2 - Photophysical properties of Pt (II) complexes in solid state at 298 K

Sample	*Emission, λ_{max} (nm)*	*Quantum yield, ϕ (%)*	*Lifetime, τ (ns) [%]*
Pt_1	**676**	**19.9**	**412**
Pt_2	**650**	**1.1**	**475**
Pt_3	**690**	**14.0**	**272**
Pt_4	**660**	**1.8**	**300**

Table A.2.3 - Quantum yields for Pt_2 by varying the temperature

Ist cycle				IInd cycle			
Heating		Cooling		Heating		Cooling	
T/°C	*Φ/%*	*T/°C*	*Φ/%*	*T/°C*	*Φ/%*	*T/°C*	*Φ/%*
30	**1.10**	**120**	**0.05**	**30**	**1.42**	**120**	**0.12**
50	**2.00**	**90**	**0.09**	**50**	**1.02**	**90**	**0.16**
90	**1.24**	**50**	**0.33**	**90**	**0.18**	**50**	**0.59**
120	**0.21**	**30**	**0.75**	**120**	**0.12**	**30**	**1.05**
160	**0.03**			**160**	**0.01**		

Table A.2.4 - Quantum yields for Pt_4 by varying the temperature

Ist cycle				IInd cycle			
Heating		Cooling		Heating		Cooling	
T/°C	Φ/%	T/°C	Φ/%	T/°C	Φ/%	T/°C	Φ/%
30	**1.80**	**150**	**0.07**	**30**	**0.56**	**150**	**0.11**
50	**1.29**	**100**	**0.17**	**50**	**0.45**	**100**	**0.19**
100	**0.50**	**50**	**0.41**	**100**	**0.22**	**50**	**0.41**
150	**0.08**	**30**	**0.56**	**150**	**0.11**	**30**	**0.57**
160	**0.06**			**160**	**0.08**		

Table A.2.5 - Photophysical properties of Zn (II) complexes in CH_2Cl_2 solution

Sample	Abs, λ_{max}/nm (ε/M^{-1} cm^{-1})	*Emission, λ_{max} (nm)*	*Quantum yields, ϕ (%)*	*Lifetime, τ (ns)*
Zn_1[a]	**248, 275, 311, 323**	**365**	**6.4**	**1.2**
Zn_2[b] *(ex Zn_3)*	**258 (28030), 285 (15150), 306 (11620), 319 (10100)**	**379**	**24.5**	**2.7**
Zn_3[c] *(ex Zn_1)*	**266 (34820), 284 (35910), 323 (33160), 333 (31300)**	**405**	**6.5**	**2.0**
Zn_4[d] *(ex Zn_2)*	**255 (43320), 284 (37310), 309 (21770), 322 (20180), 406 (22830)**	**488**	**95.0**	**4.2**
Zn_5[e] *(ex Zn_4)*	**265 (27100), 282 (29320), 322 (25250), 333 (23410)**	**400**	**0.5**	**3.0**
[a] Partially soluble, ε data not available;[b] 3.96x10^{-6} M; [c] 4.3 × 10^{-6} M; [d] 3.6×10^{-6} M; [e] 3.6 × 10^{-6} M;				

Table A.2.6 - Photophysical properties in the mesophase at room temperature

Sample	*Emission, λ_{max} (nm)*	*Quantum yields, ϕ (%)*
Zn_1	**n.d.**	**n.d.**
Zn_2	**450**	**7.1**
Zn_3	**435**	**4.0**
Zn_4	**542**	**20.2**
Zn_5	**435**	**1.5**

Table A.2.7 - Emission maximum and quantum yields for Zn_2 by varying the temperature (λ_{ex}= 345 nm)

Ist cycle						IInd cycle					
Heating			Cooling			Heating			Cooling		
T/°C	λ_{em}/nm	*Φ/%*	*T/°C*	λ_{em}/nm	*Φ/%*	*T/°C*	λ_{em}/nm	*Φ/%*	*T/°C*	λ_{em}/nm	*Φ/%*
30	450	**7.1**	**80**	497	**1.92**	**30**	478	**2.98**	**80**	493	**1.63**
80	478	**4.97**	**30**	478	**2.98**	**80**	500	**1.35**	**30**	482	**3.27**
140	507	**0.71**				**140**	509	**0.50**			

Table A.2.8 - Emission maximum and quantum yields for Zn_3 by varying the temperature (λ_{ex}= 340 nm)

Ist cycle		
Heating		
T/°C	*Φ/%*	λ_{em}/nm
30	**435**	**4**
80	**435**	**2.9**
150	**435**	**1.7**
180	**435**	**1.35**

Table A.2.9 - Emission maximum and quantum yields for Zn_4 by varying the temperature (λ_{ex}= 430 nm)

Ist cycle					
Heating			Cooling		
T/°C	λ_{em}/nm	*Φ/%*	*T/°C*	λ_{em}/nm	*Φ/%*
30	**542**	**20.2**	100	**544**	**14.4**
100	**544**	**14.7**	30	**542**	**20.2**
150	**546**	**11.3**			

Table A.2.10 - Emission maximum and quantum yields for Zn_5 by varying the temperature (λ_{ex}= 350 nm)

Ist cycle					
Heating			Cooling		
T/°C	*λ_{em}/nm*	*Φ/%*	*T/°C*	*λ_{em}/nm*	*Φ/%*
30	**435**	**2.3**	150	**435**	**0.4**
80	**435**	**1.2**	80	**436**	**1.1**
150	**435**	**0.3**	30	**434**	**1.5**
180	**435**	**0.07**			

Table A.2.11 – Photophysical properties of TPDT in hexane solution, powder, and in AuNC self-assembled monolayer

Sample	λ_{em} (nm)	Lifetime, τ (ns)	
TPDT in hexane	**370**	**0.75 ± 0.01**	
TPDT powder	**445**	**4.24 ± 0.03**	
TPDT on AuNC monolayer	**370, 450**	**1.74 ± 0.06**	**26.95 ± 0.05**
TPDT on glass slides (drop casting)	**375, 450**	**0.72 ± 0.004**	**16 .8 ± 0.4**

A.3 – Figures

Figure A.3.1 - Absorption spectra of Pt complexes in CH_2Cl_2 solution varying concentration.

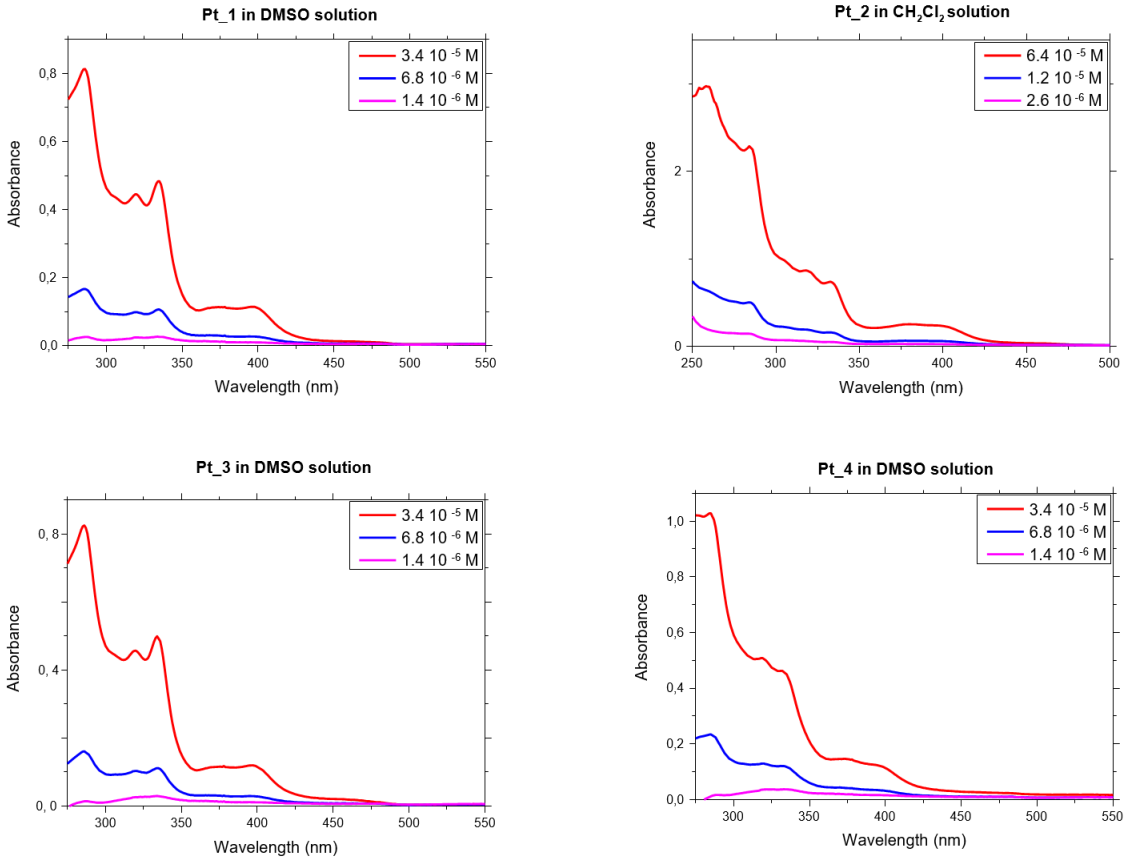

Figure A.3.2 - Absorption spectra of Zn_4 (black line) and its chlorinated precursor Zn_P4 (cyan line) in CH_2Cl_2 solution

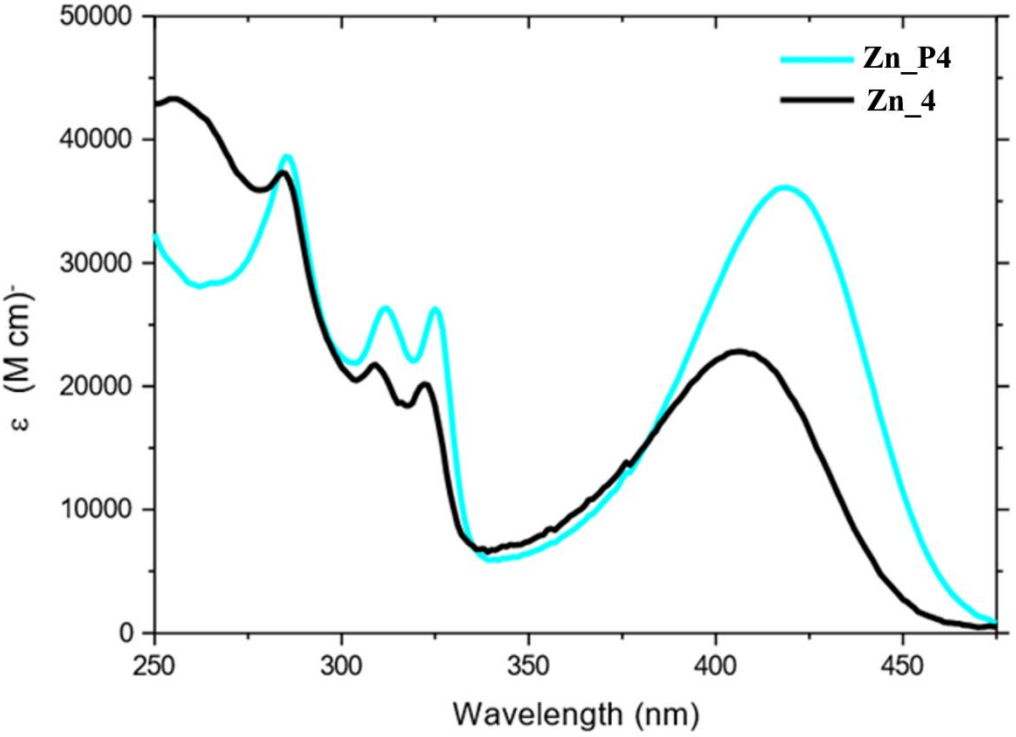

Figure A.3.3 – SEM images in two different magnifications (1000x on the left, 100000x on the right) of AuNT films varying the concentration of 1-dodecanethiol used

NT_0 ([1-dodecanethiol] = 0)

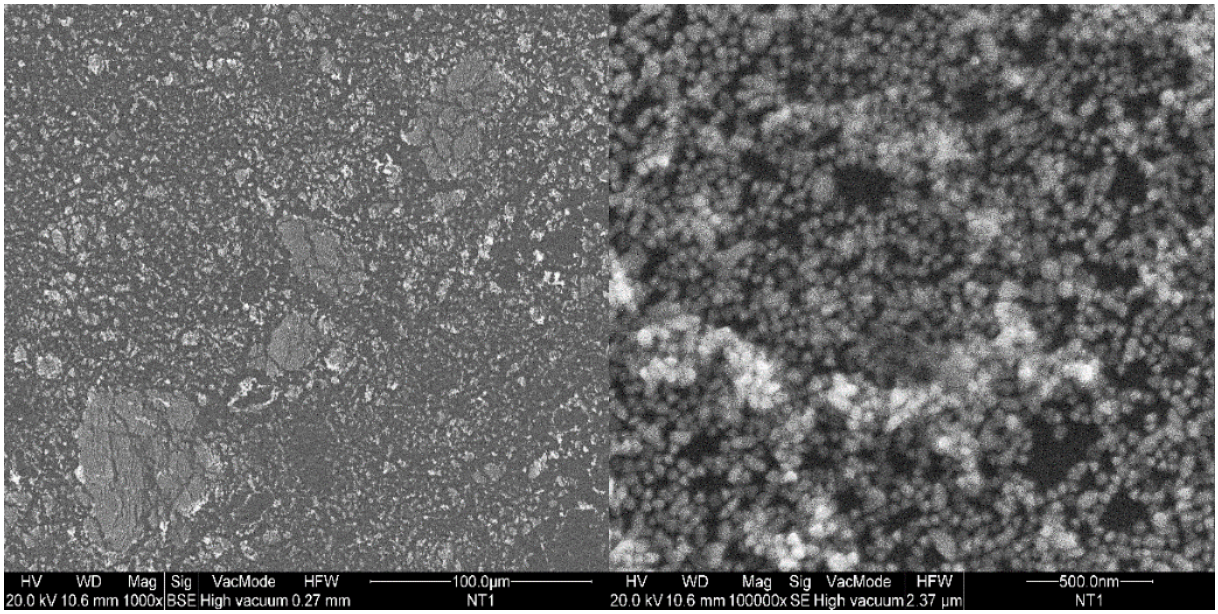

NT_1 ([1-dodecanethiol] = 1 10^{-5} M)

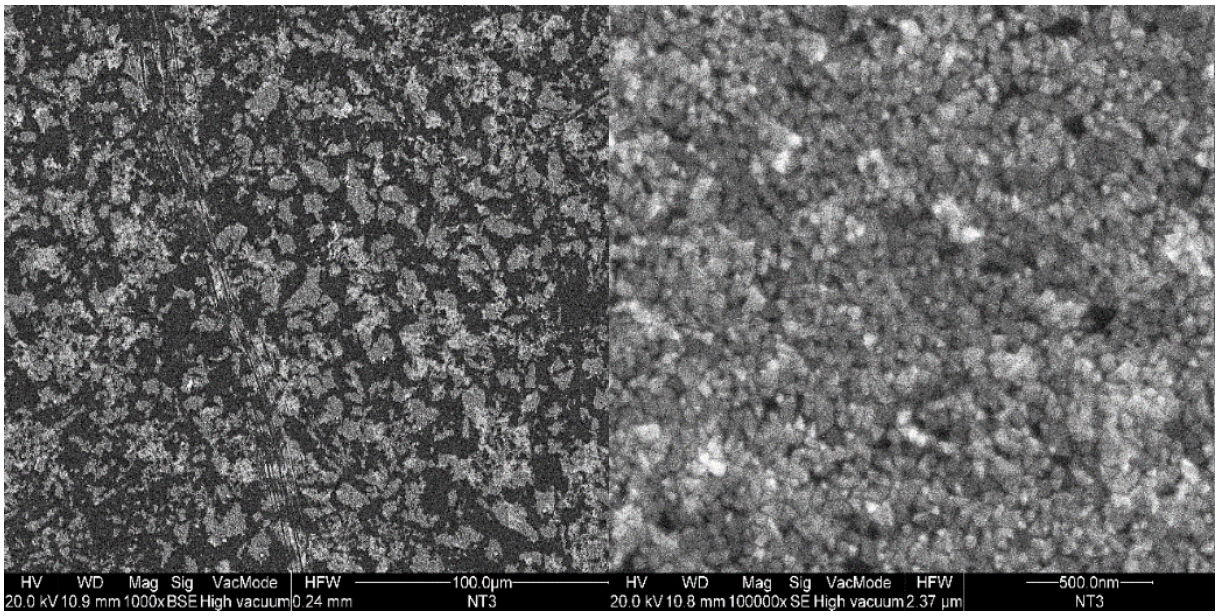

NT_2 ([1-dodecanethiol] = 8 10^{-5} M)

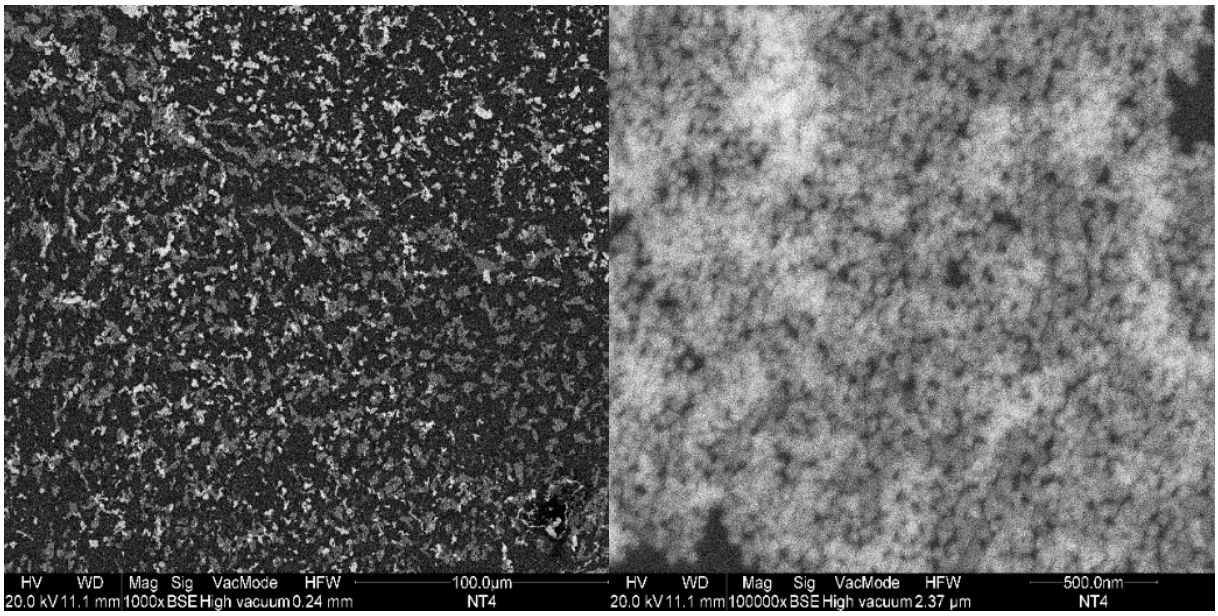

Figure A.3.4 – Representative SEM image of NC_3

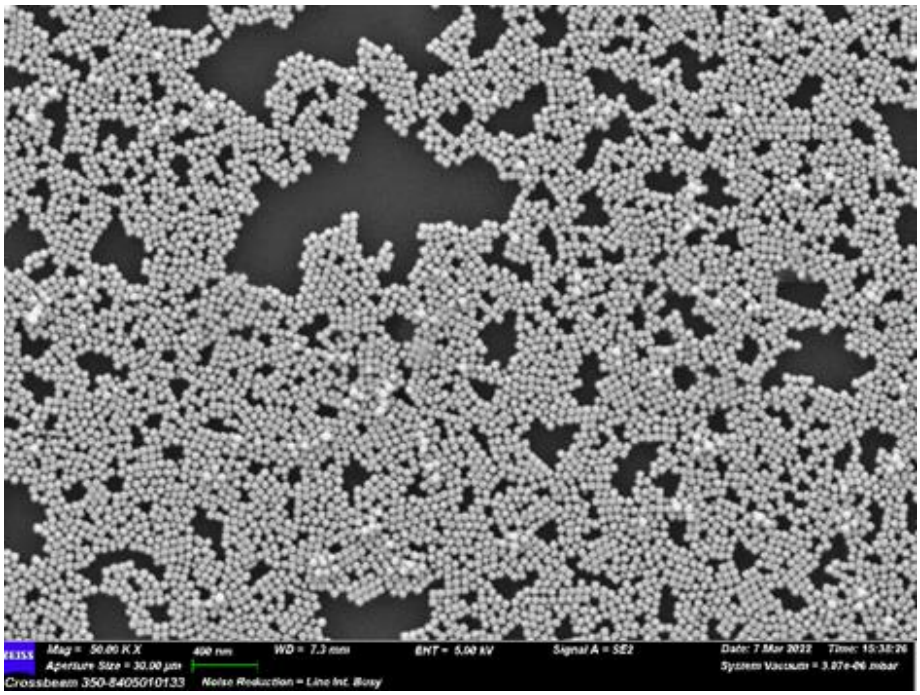

Figure A.3.5 – Absorption, emission, and excitation spectra of TPDT in hexane dilute solution

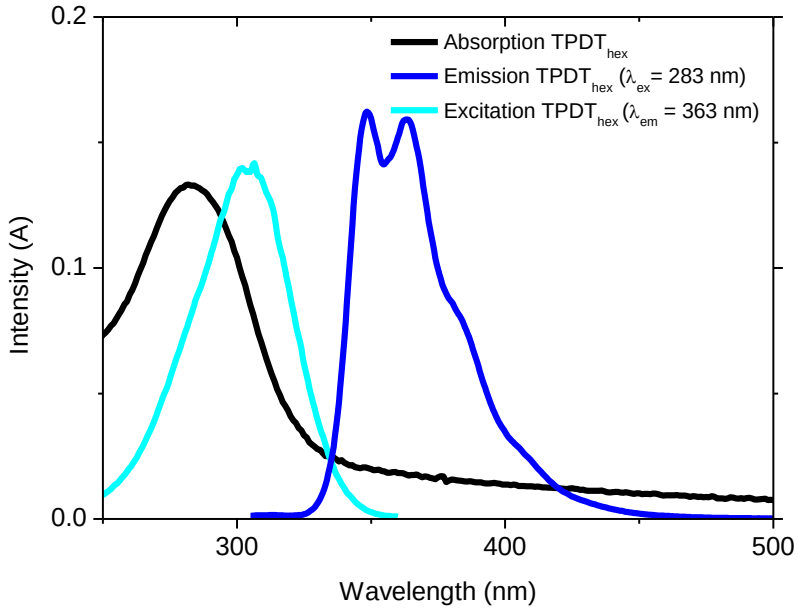

Figure A.3.6 – Emission and excitation spectra of TPDT powder

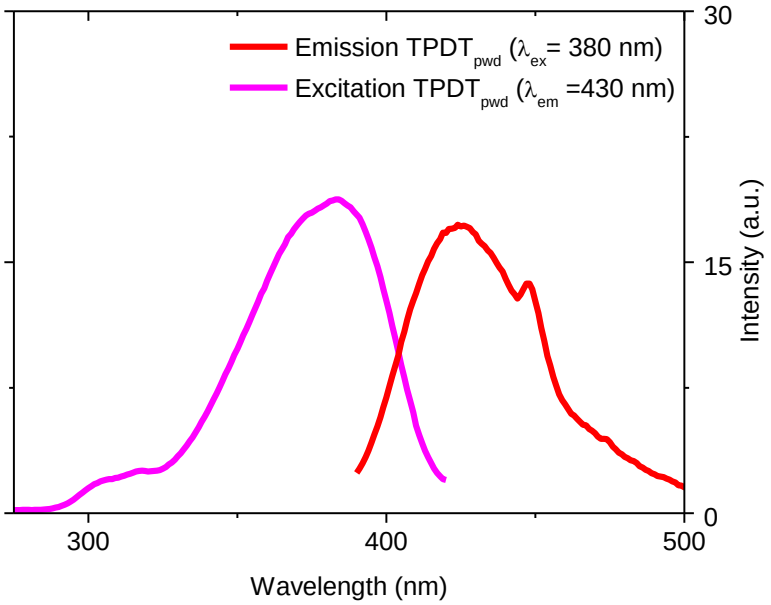

Figure A.3.7 – Reflectance spectra of AuNP monolayers on glass slide compared with bare glass slide.

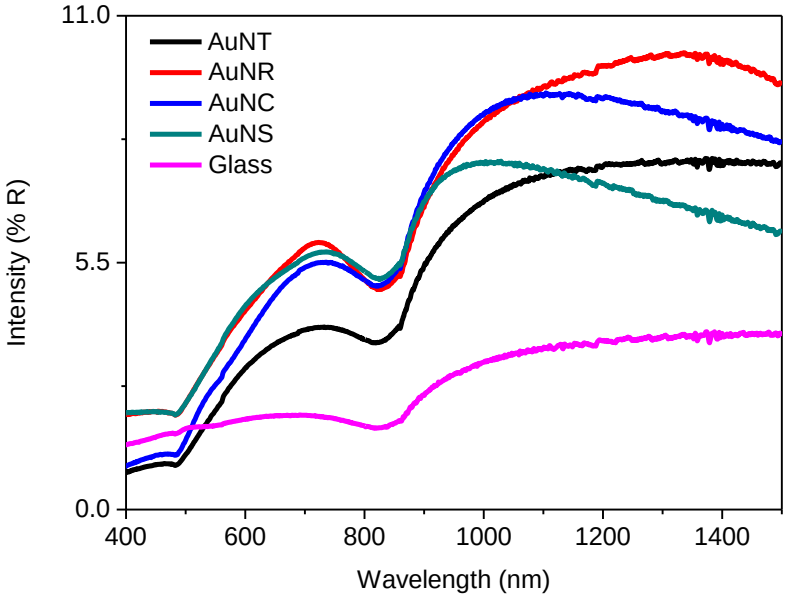

Figure A.3.8 – Emission spectrum of NH_2TPPH_2 on glass slide before and after deposition of AuNC monolayer (λ_{ex} = 438 nm)

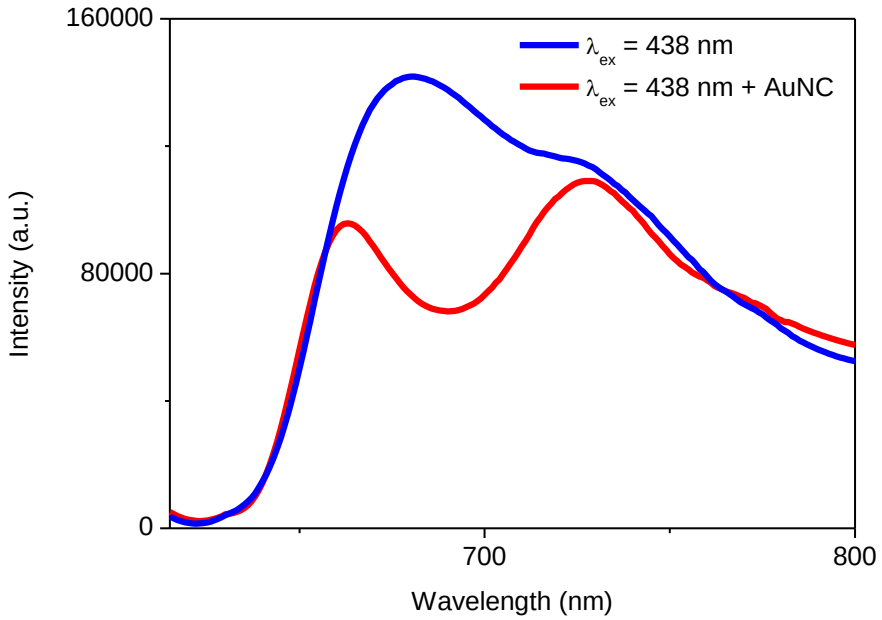

Figure A.3.9 – Emission spectrum of NH_2TPPH_2 on glass slide before and after deposition of AuNC monolayer (λ_{ex} = 523 nm)

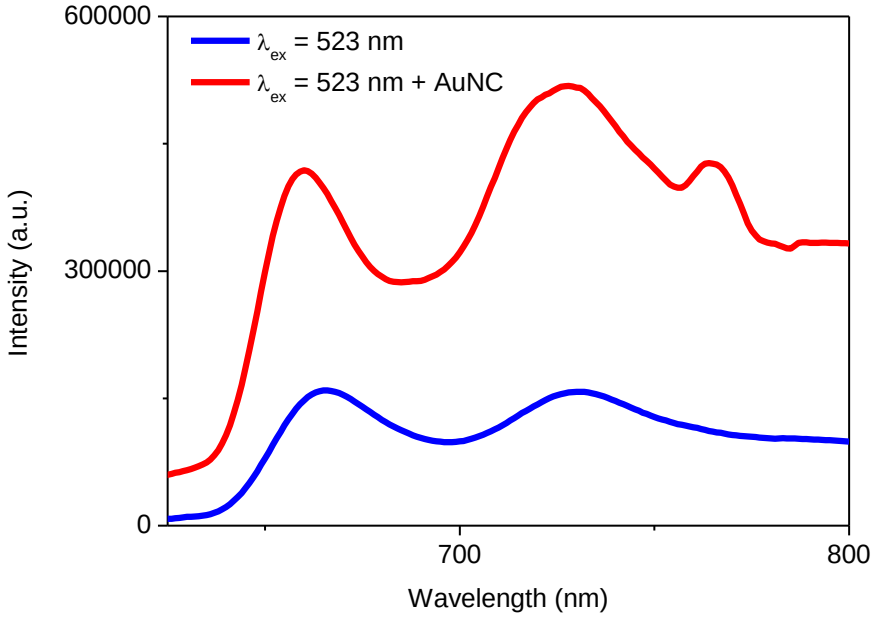

Figure A.3.10 – Emission spectrum of NH_2TPPH_2 on glass slide before and after deposition of AuNC monolayer (λ_{ex} = 560 nm)

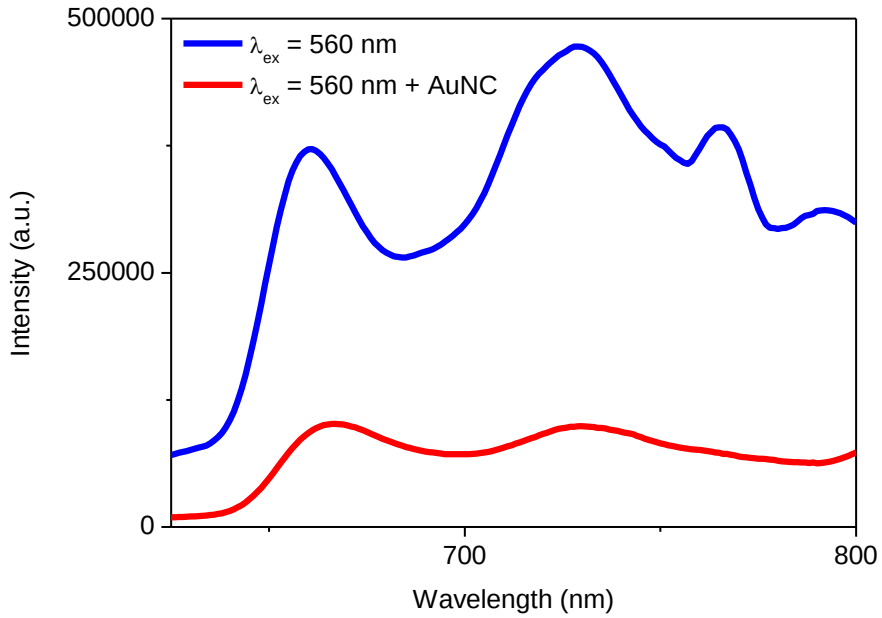

Figure A.3.11 – Emission spectrum of NH_2TPPH_2 on glass slide before and after deposition of AuNC monolayer (λ_{ex} = 595 nm)

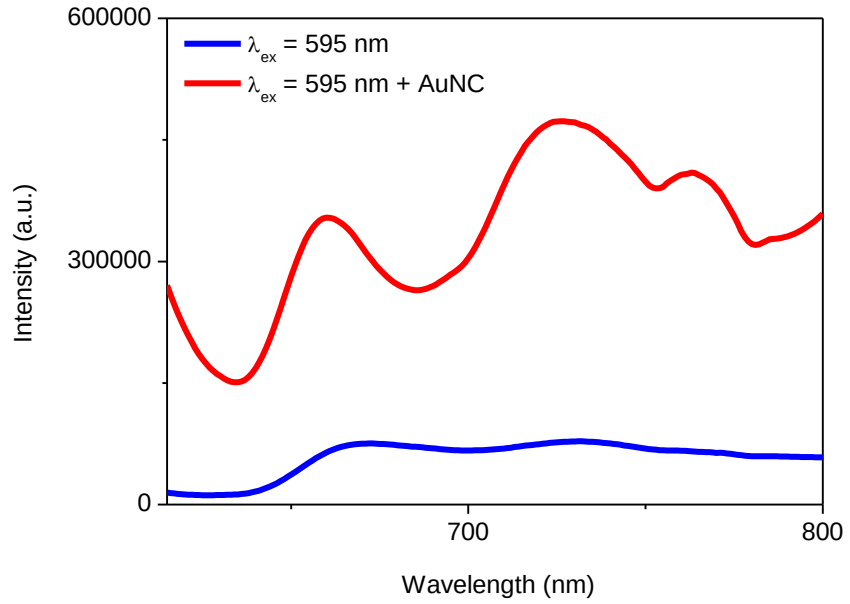

Figure A.3.12 – Exponential decays of excited state of NH_2TPPH_2 and NH_2TPPH_2 + AuNC on glass slide (λ_{ex} = 485 nm)

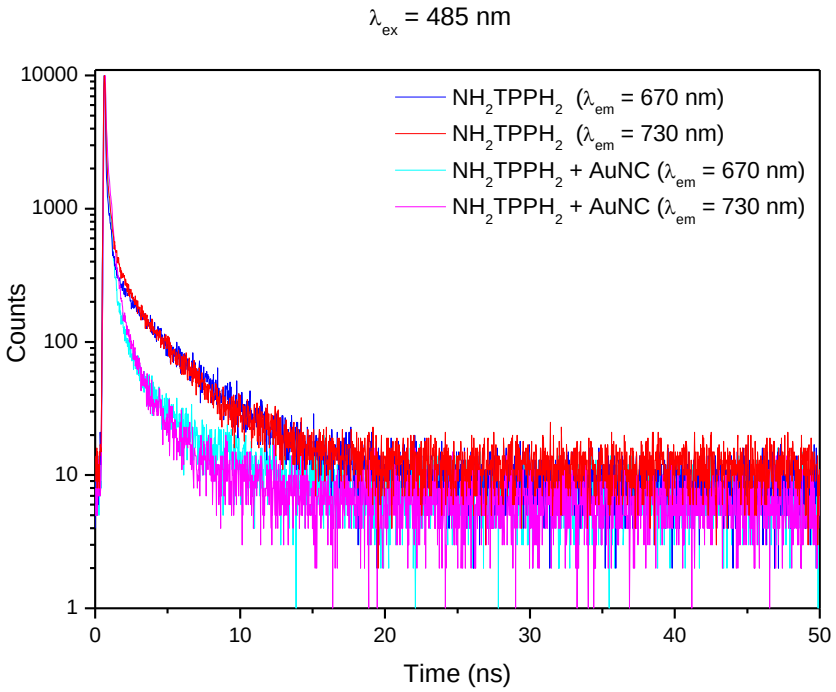

Figure A.3.13 – Exponential decays from excited states of NH_2TPPH_2 and NH_2TPPH_2 + AuNC on glass slide (λ_{ex} = 635 nm)

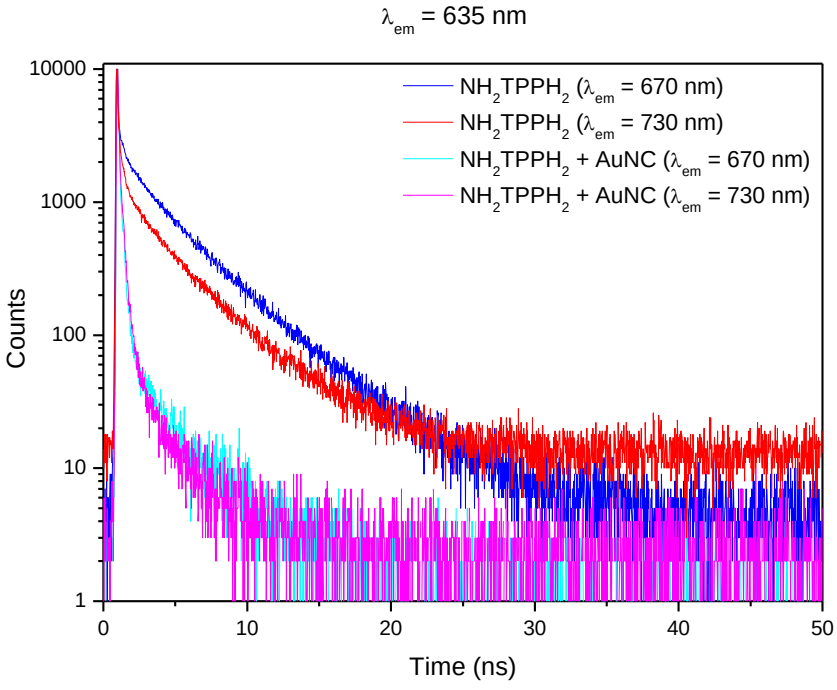

A.4 – AuNP samples collection

In this section all the colloidal dispersion of AuNP synthesized during this PhD research work were collected. The detailed synthetic protocols used for their synthesis was firstly reported, followed by the extinction spectra and representative TEM image of each sample. The main results arising from optical and morphological characterization were resumed in table A.4.1.

Synthesis of AuNC#1-4. 250 µL of 10 mM $HAuCl_4$ were added to 7.5 mL of 100 mM CTAB. Then 600 µL of ice-cold 10 mM $NaBH_4$ were injected "one-shot" and under vigorous stirring in the reaction flask. After the addition, the colour of the solution turns immediately from yellow to brown, indicating the reduction of the Au(III) ions dissolved in solution to Au(0) performed by $NaBH_4$. The seed dispersion was then left undisturbed for at least 1 hour. Then, a growth solution was prepared in a 50 mL beker adding in sequence and under magnetic stirring: 32 mL of Milli-Q water, 6.4 mL of CTAB solution 100 mM, and 800 µL of 10 mM $HAuCl_4$. After the complete dissolution of the gold precursor, 3.8 mL of ascorbic acid 100 mM were added. At this point, the growth solution, initially yellow, became colourless attesting the reduction of Au(III) ions to Au(I). Then, 20 µL of the Au seeds dispersion, diluted 1 to 10, were added to the growth solution and mixed under magnetic stirring for 10 second at 350 RPM. At this point, the growth solution starts to colouring, becoming red/fuchsia after 1 hour. The dispersion was left undisturbed for 24 h, and then was centrifuged at 4000 RPM for 30 minutes to quench the growth process and purify the dispersion by all excess reactants. The precipitate was then dispersed in Milli-Q water and characterized by UV-visible spectroscopy and TEM.

Synthesis of AuNC#5. 250 µL of 10 mM $HAuCl_4$ were added to 7.5 mL of 100 mM CTAB. Then 600 µL of ice-cold 10 mM $NaBH_4$ were injected "one-shot" and under vigorous stirring in the reaction flask. After the addition, the colour of the solution turns immediately from yellow to brown, indicating the reduction of the Au(III) ions dissolved in solution to Au(0) performed by $NaBH_4$. The seed dispersion was then left undisturbed for at least 1 hour. Then, a growth solution was prepared in a 50 mL beker adding in sequence and under magnetic stirring: 32 mL of Milli-Q water, 6.4 mL of CTAB solution 50 mM, and 800 µL of 10 mM $HAuCl_4$. After the complete dissolution of the gold precursor, 3.8 mL of ascorbic acid 100 mM were added. At this point, the growth solution, initially yellow, became colourless attesting the

reduction of Au(III) ions to Au(I). Then, 20 µL of the Au seeds dispersion, diluted 1 to 10, were added to the growth solution and mixed under magnetic stirring for 10 second at 350 RPM. At this point, the growth solution starts to colouring, becoming red/fuchsia after 1 h. The dispersion was left undisturbed for 24 h, and then was centrifuged at 4000 RPM for 30 minutes to quench the growth process and purify the dispersion by all excess reactants. The precipitate was then dispersed in Milli-Q water and characterized by UV-visible spectroscopy and TEM.

Synthesis of AuNC#6. 250 µL of 10 mM $HAuCl_4$ were added to 7.5 mL of 100 mM CTAB. Then 60 µL of ice-cold 100 mM $NaBH_4$ were injected "one-shot" and under vigorous stirring in the reaction flask. After the addition, the colour of the solution turns immediately from yellow to brown, indicating the reduction of the Au(III) ions dissolved in solution to Au(0) performed by $NaBH_4$. The seed dispersion was then left undisturbed for at least 1 hour. Then, a growth solution was prepared in a 50 mL beker adding in sequence and under magnetic stirring: 32 mL of Milli-Q water, 6.4 mL of CTAB solution 100 mM, and 800 µL of 10 mM $HAuCl_4$. After the complete dissolution of the gold precursor, 3.8 mL of ascorbic acid 100 mM were added. At this point, the growth solution, initially yellow, became colourless attesting the reduction of Au(III) ions to Au(I). Then, 20 µL of the Au seeds dispersion, diluted 1 to 10, were added to the growth solution and mixed under magnetic stirring for 10 second at 350 RPM. At this point, the growth solution starts to colouring, becoming red/fuchsia after 1 h. The dispersion was left undisturbed for 24 h, and then was centrifuged at 4000 RPM for 30 minutes to quench the growth process and purify the dispersion by all excess reactants. The precipitate was then dispersed in Milli-Q water and characterized by UV-visible spectroscopy and TEM.

Synthesis of AuNC#7. 250 µL of 10 mM $HAuCl_4$ were added to 7.5 mL of 100 mM CTAB. Then 6 µL of ice-cold 1 M $NaBH_4$ were injected "one-shot" and under vigorous stirring in the reaction flask. After the addition, the colour of the solution turns immediately from yellow to brown, indicating the reduction of the Au(III) ions dissolved in solution to Au(0) performed by $NaBH_4$. The seed dispersion was then left undisturbed for at least 1 hour. Then, a growth solution was prepared in a 50 mL beker adding in sequence and under magnetic stirring: 32 mL of Milli-Q water, 6.4 mL of CTAB solution 100 mM, and 800 µL of 10 mM $HAuCl_4$. After the complete dissolution of the gold precursor, 3.8 mL of ascorbic acid 100 mM were added. At this point, the growth solution, initially yellow, became colourless attesting the reduction of Au(III) ions to Au(I). Then, 20 µL of the Au seeds dispersion, diluted 1 to 10, were added to the growth solution and mixed under magnetic stirring for 10 second at 350 RPM. At this point,

the growth solution starts to colouring, becoming red/fuchsia after 1 h. The dispersion was left undisturbed for 24 h, and then was centrifuged at 4000 RPM for 30 minutes to quench the growth process and purify the dispersion by all excess reactants. The precipitate was then dispersed in Milli-Q water and characterized by UV-visible spectroscopy and TEM.

Synthesis of AuNC#8-9. 250 µL of 10 mM $HAuCl_4$ were added to 7.5 mL of 100 mM CTAB. Then 6 µL of ice-cold 1 M $NaBH_4$ were injected "one-shot" and under vigorous stirring in the reaction flask. After the addition, the colour of the solution turns immediately from yellow to brown, indicating the reduction of the Au(III) ions dissolved in solution to Au(0) performed by $NaBH_4$. The seed dispersion was then left undisturbed for at least 1 hour. Then, a growth solution was prepared in a 50 mL beker adding in sequence and under magnetic stirring: 32 mL of Milli-Q water, 6.4 mL of CTAB solution 100 mM, and 800 µL of 10 mM $HAuCl_4$. After the complete dissolution of the gold precursor, 3.8 mL of ascorbic acid 100 mM were added. At this point, the growth solution, initially yellow, became colourless attesting the reduction of Au(III) ions to Au(I). Then, 20 µL of the Au seeds dispersion, diluted 1 to 10, were added to the growth solution and mixed under magnetic stirring for 10 second at 350 RPM. At this point, the growth solution starts to colouring, becoming red/fuchsia after 1 h. The dispersion was left undisturbed for 24 h, and then was centrifuged at 4000 RPM for 30 minutes to quench the growth process and purify the dispersion by all excess reactants. The precipitate was then dispersed in Milli-Q water and characterized by UV-visible spectroscopy and TEM.

Synthesis of AuNS#1 1 mL of 25 mM $HAuCl_4$ aqueous solution were added to a boiling water solution of $Na_3C_6H_5O_7$ (150 mL, 2.2 mM) at reflux and under vigorous stirring. After 15 minutes, the solution, initially colourless, became pink. This colour change certifies the reduction of Au (III) to Au (0) with formation of AuSeed@$Na_3C_6H_5O_7$ with a medium size of 10 nm (*nucleation step*). After the seed formation the temperature of the reaction was decreased to 90 °C, then 1 mL of $Na_3C_6H_5O_7$ 60 mM was added, followed by 1 mL of $HauCl_4$ 25 mM after 2 minutes. The colour of the reaction solution starts to change from pink to pale red, attesting the growth in size of the starting spherical seeds. This process was repeated 4 times, and then 55 mL of the AuNS dispersion was extracted and replaced with 53 mL of distilled H_2O and 2 mL of $Na_3C_6H_5O_7$ 60 mM. Then 6 mL of $HAuCl_4$ 25 mM were added in three aliquots of 2 mL, waiting 30 minutes between one addition and the next for the completion of the reduction process. After that, the sample was purified by centrifugation (4000 RPM per 20

minutes) to remove all the reactants in excess, and then was characterized by Uv-Vis spectroscopy and TEM.

Synthesis of AuNT#1

Preparation of AuSeeds@CTAC: 25 µL of 50 mM $HAuCl_4$ were added to 4.7 mL of a 100 mM CTAC. Then, 300 µL of ice-cold 10 mM $NaBH_4$ were injected "one-shot" and under vigorous stirring in the reacti/on flask. The change of the solution colour from yellow to brown attest the reduction of Au (III) to Au (0) and the formation of AuSeeds@CTAC. The as formed seed were left undisturbed for 1 hour before use to exhaust all the $NaBH_4$ in excess.

Preparation of growth solution I: At 16 mL of milli-Q H_2O were added in sequence 3.2 mL of CTAC 100 mM, 80 µL of $HAuCl_4$ 0.05 M, and 30 µL of 10 mM NaI.

Preparation of growth solution II: The second growth solution was prepared adding in sequence 156.5 mL of 50 mM CTAC, 1.955 mL of 50 mM $HAuCl_4$, and 1.175 mL of 10 mM NaI.

Mixing of the solutions: Before starting, the seeds solution was diluted ten times with H_2O. Then, 80 µL and 1.565 mL of 100 mM ascorbic acid, a weak reducing agent, were added to growth solutions I and II respectively, followed by a quick manual stirring. This causes the reduction of the Au (III) to Au (I) attested by the complete discoloration of the two solutions (initially yellow). Finally, 200 µL of the diluted seed solution were added to the growth solution 1. The solution was manually hand-shacked for few seconds while start to turns pale-pink, and then was rapidly added entirely to growth solution 2. After a rapid handshake, growth solution 2 was left undisturbed for 2 hours, during which it start to assume violet colouration. The as-obtained AuNPs dispersion was then characterized with UV-Vis spectroscopy and TEM.

Purification: For AuNT purification the depletion induced flocculation technique were used. The AuNT colloidal dispersion were transferred in a cylinder, then a 25 % wt aqueous solution of CTAC were added to AuNT in order to reach a final concentration of CTAC equal to 0.376 M. The dispersion was vigorously hand-shacked and then left undisturbed overnight, after that supernatant was carefully removed and the precipitate were dispersed in H_2O milli-Q.

Synthesis of AuNR#1

Preparation of Auseed@CTAB: 25 µL of 50 mM $HAuCl_4$ were dissolved in 4.7 mL of an aqueous 100 mM CTAB solution. Then, 300 µl of 10 mM was rapidly injected in the solution under vigorous stirring. The change in colour of the dispersion from yellow/orange to brown attest the reduction of Au (III) ions and the production of Au seeds. The as-produced Auseed@CTAB were left undisturbed for 1 hour to exhaust all the excess of reductant.

Preparation of the growth solution: 45 mg of 5-bromosalicylic acid ($C_7H_5BrO_3$) were solubilized in 50 mL of an aqueous solution of 50 mM CTAB. Then were added in sequence 480 µL of 10 mM $AgNO_3$, and after 15 minutes 500 µL of 50 mM $HAuCl_4$. At this point take place the pre-reduction of Au (III) to Au (I) due to the action of 5-bromosalicylic acid that induce the gradual discoloration of the solution, initially orange.

Mixing of AuSeed@CTAB with growth solution: First, 130 µL of 100 mM ascorbic acid were added to the growth solution. After 30 seconds 80 µL of AuSeed@CTAB were added under vigorous stirring. At this point the growth solution starts to colouring, assuming the red-wine coloration typical of AuNR@CTAB aqueous dispersion.

Purification: After 12 hours the sample were centrifuged to eliminate all excess reactants and at the same time separate the rod-shaped nanoparticles from by-products through 2 centrifugation cycles of 20 minutes each at 9000 RPM. The pellet was then dispersed in H_2O and characterized by UV-Vis spectroscopy and TEM.

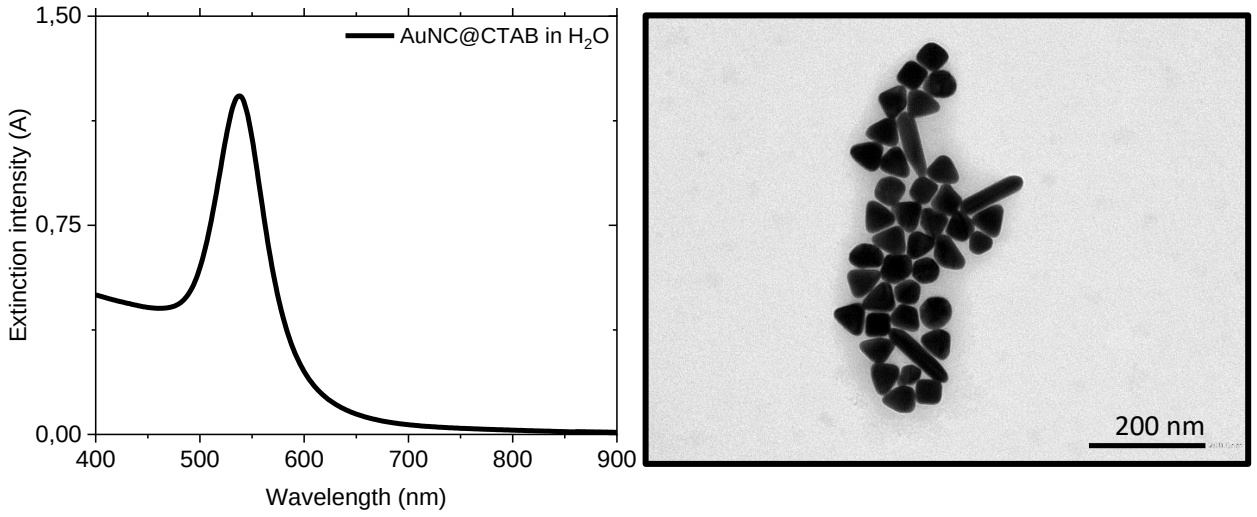

Figure A.4.1 - Extinction spectra (left) and representative TEM image (right) of AuNC#1.

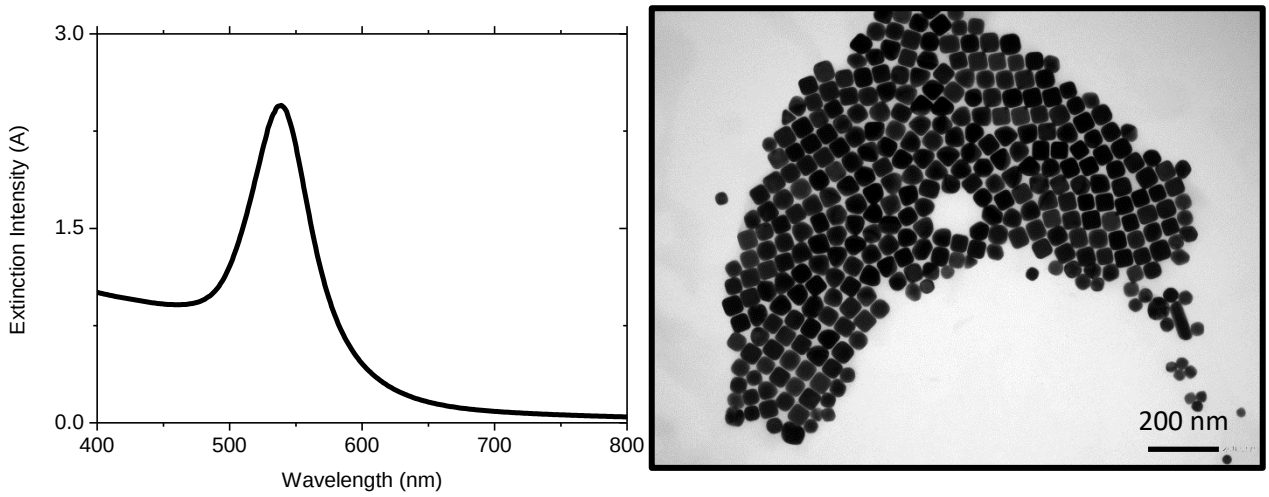

Figure A.4.2 - Extinction spectra (left) and representative TEM image (right) of AuNC#2.

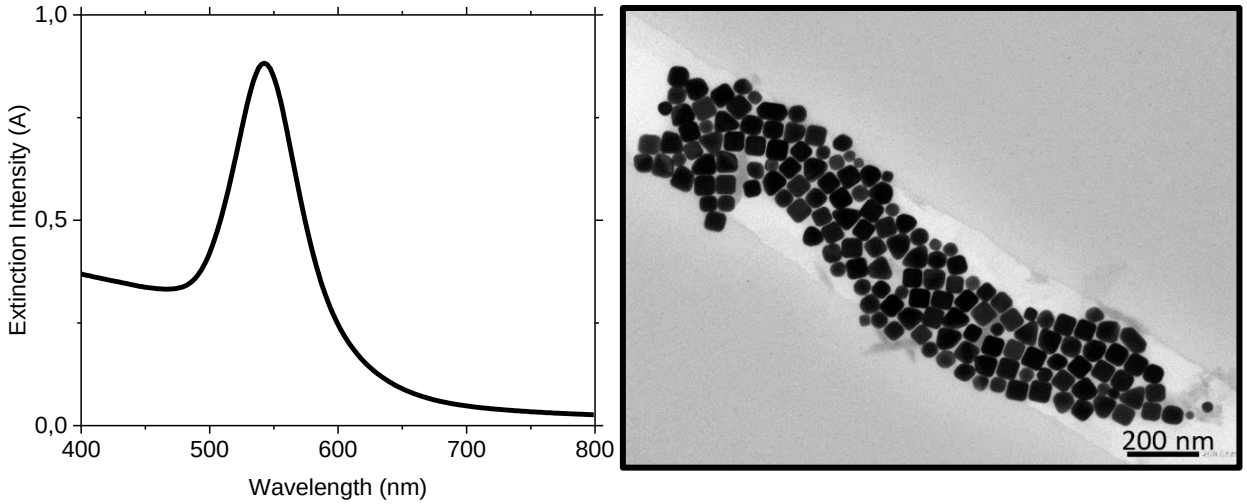

Figure A.4.3 - Extinction spectra (left) and representative TEM image (right) of AuNC#3.

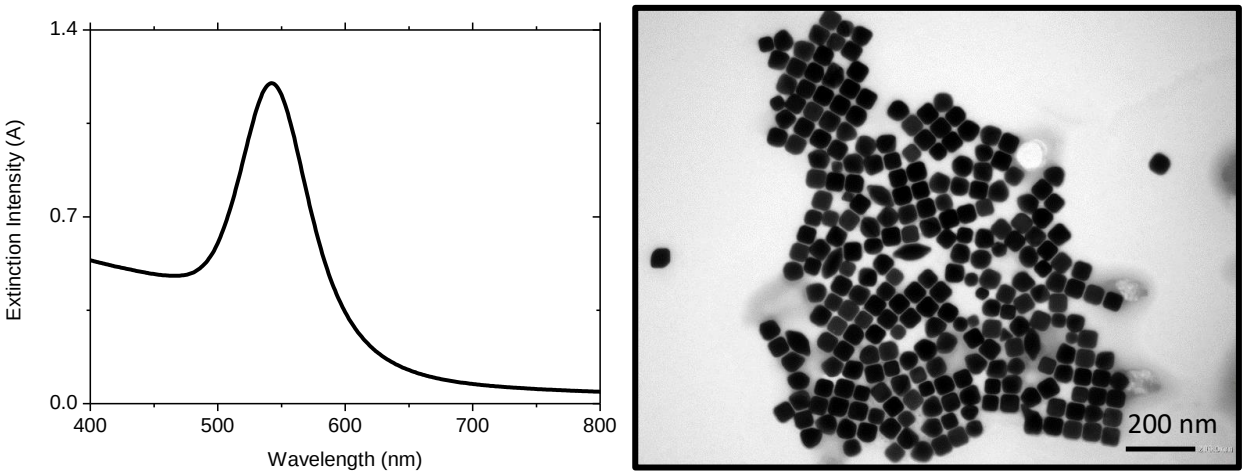

Figure A.4.4 - Extinction spectra (left) and representative TEM image (right) of AuNC#4.

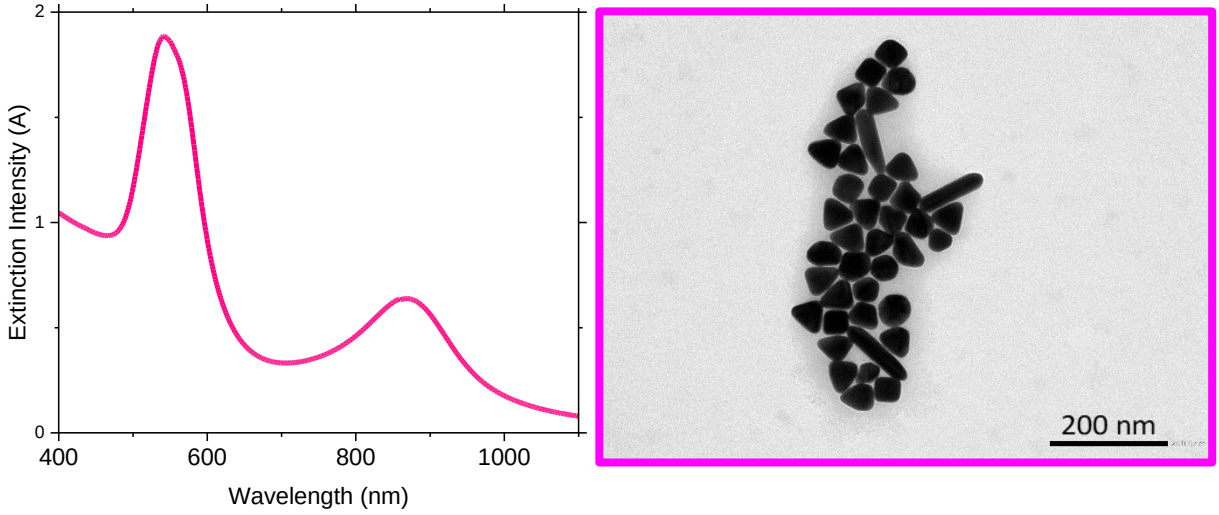

Figure A.4.5 - Extinction spectra (left) and representative TEM image (right) of AuNC#5.

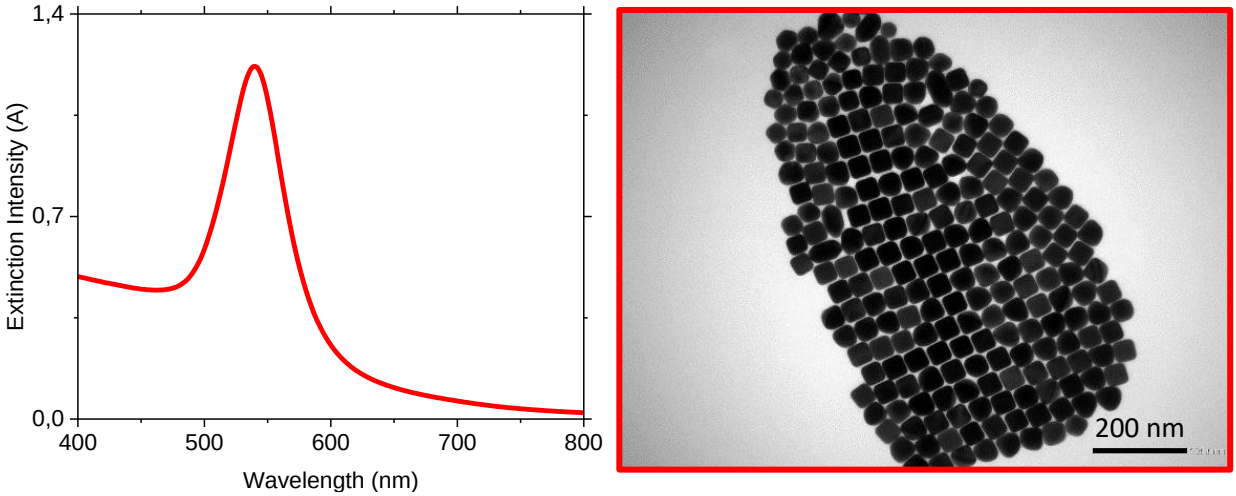

Figure A.4.6 - Extinction spectra (left) and representative TEM image (right) of AuNC#6.

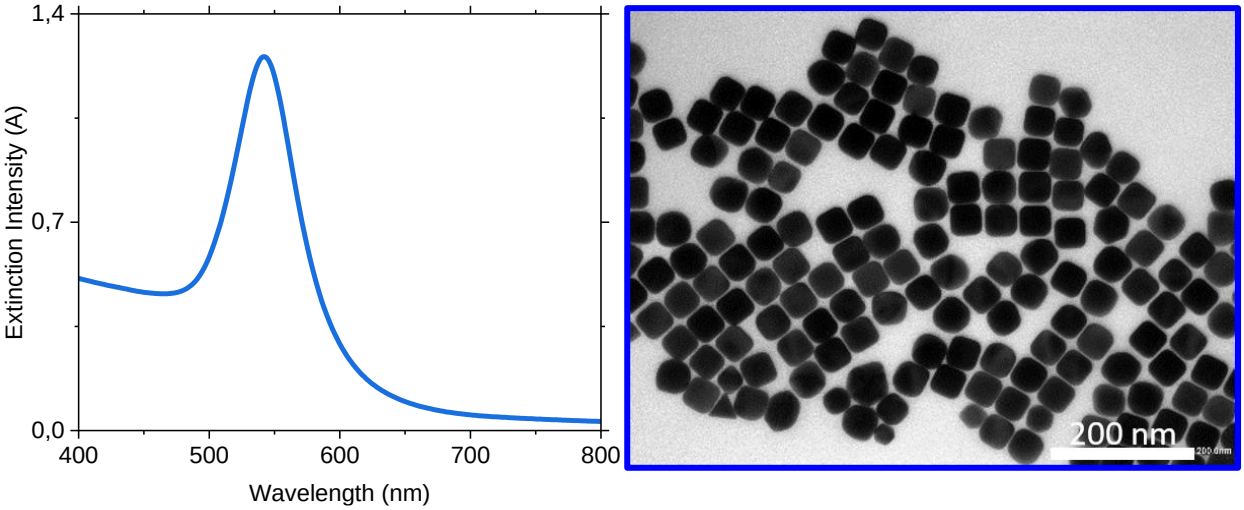

Figure A.4.7 - Extinction spectra (left) and representative TEM image (right) of AuNC#7.

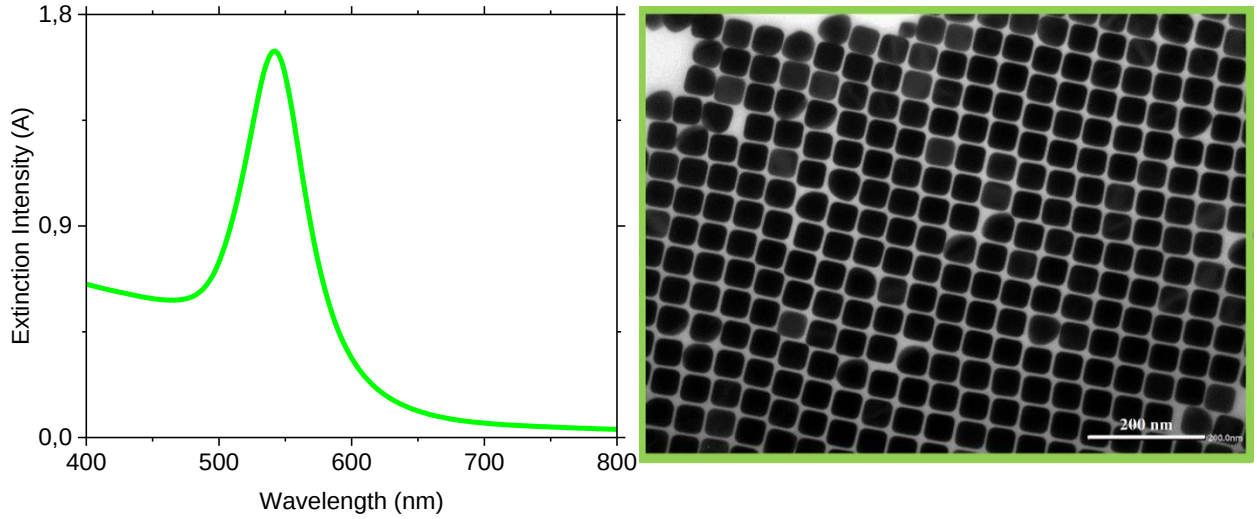

Figure A.4.8 - Extinction spectra (left) and representative TEM image (right) of AuNC#8.

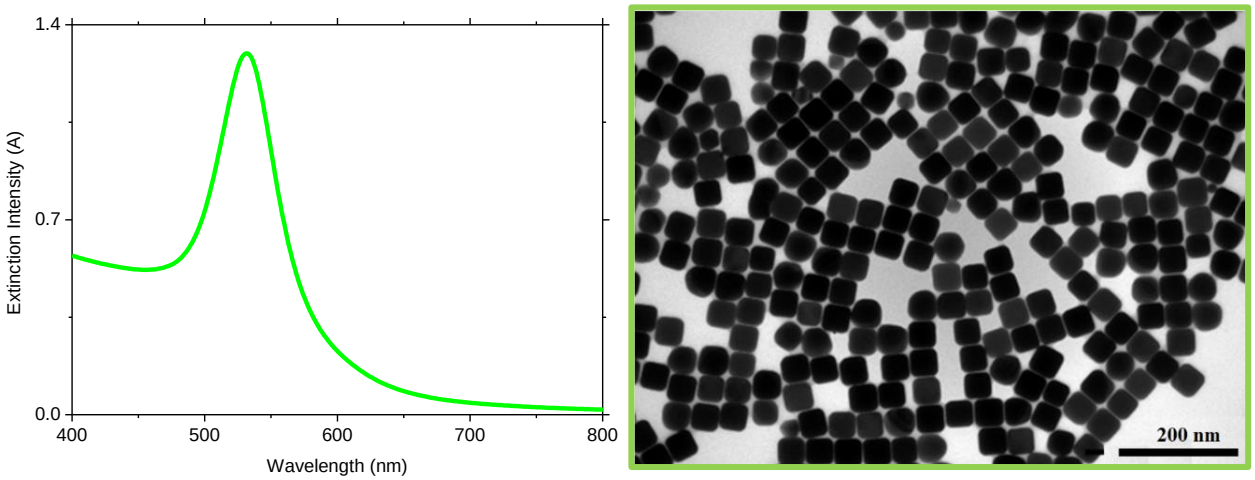

Figure A.4.9 - Extinction spectra (left) and representative TEM image (right) of AuNC#9.

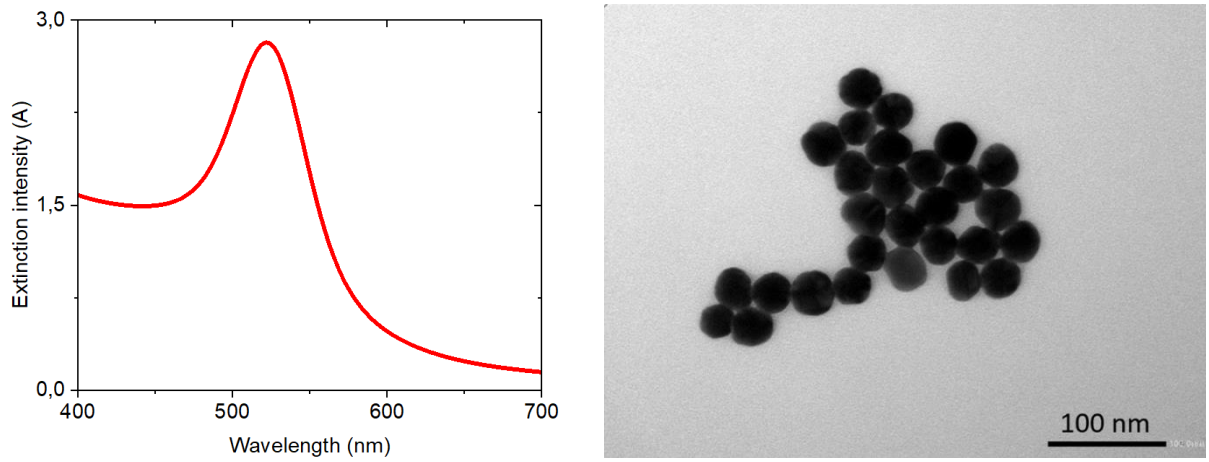

Figure A.4.10 - Extinction spectra (left) and representative TEM image (right) of AuNS#1.

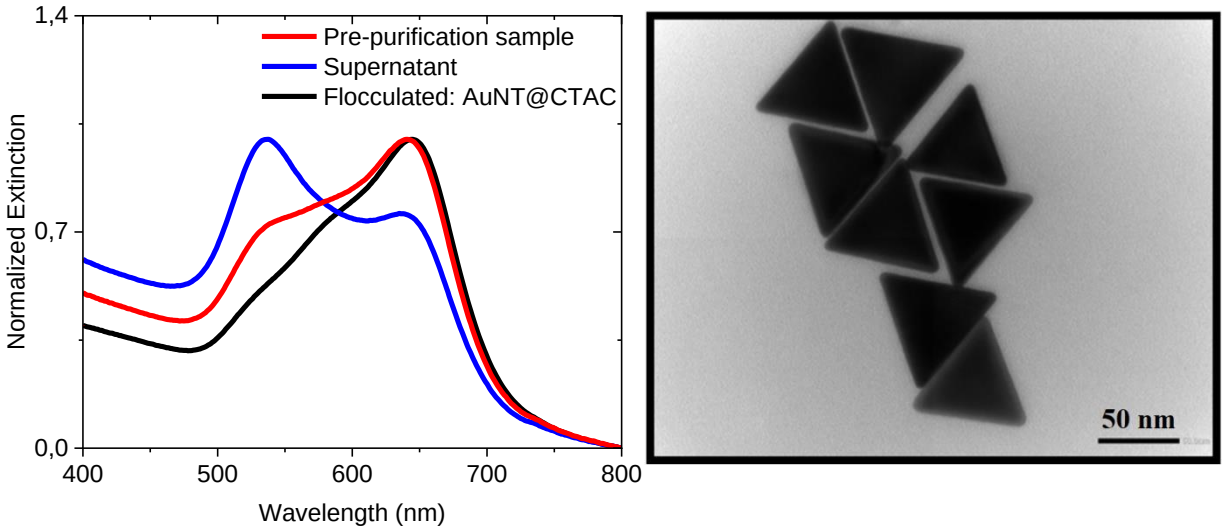

Figure A.4.11 - Extinction spectra (left) and representative TEM image (right) of AuNT#1.

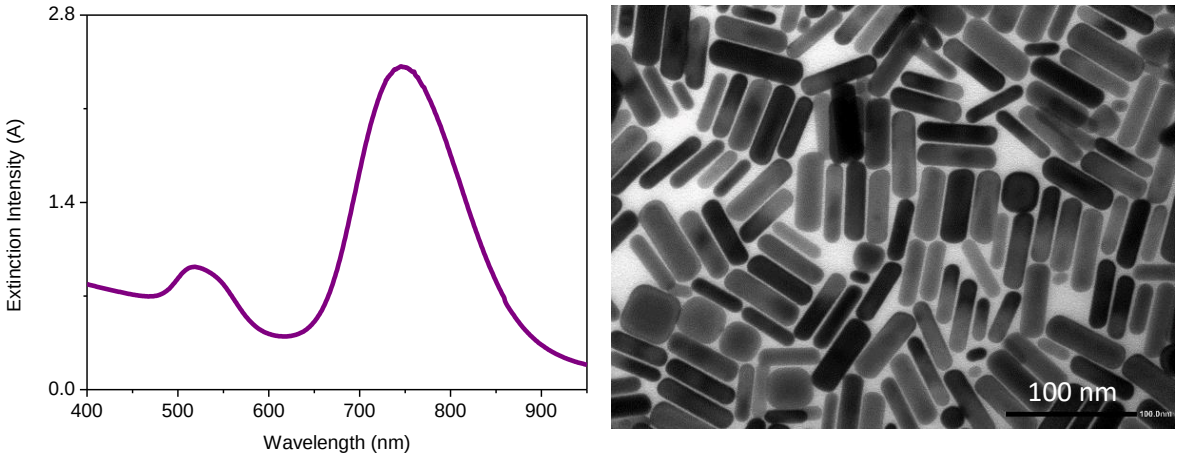

Figure A.4.12 - Extinction spectra (left) and representative TEM image (right) of AuNR#1.

Table A.4.1 – Main spectroscopic and morphological parameters of AuNP samples synthesized during this PhD research work.

Sample	λ_{max} (nm)	FWHM (nm)	Shape yield (%)	Mean Size (nm)
AuNC#1	**538**	**79**	**45**	**49 ± 3 nm**
AuNC#2	**539**	**74**	**51**	**44 ± 2 nm**
AuNC#3	**544**	**76**	**48**	**54 ± 4 nm**
AuNC#4	**542**	**81**	**41**	**49 ± 4 nm**
AuNC#5	**540, 560 , 870**	**122**	**25**	**45 ± 3 nm**
AuNC#6	**540**	**69**	**65**	**47 ± 3 nm**
AuNC#7	**542**	**70**	**60**	**48 ± 3 nm**
AuNC#8	**542**	**68**	**85**	**45 ± 2 nm**
AuNC#9	**537**	**67**	**82**	**44 ± 3 nm**
AuNS#1	**523**	**n.a.**	**98**	**38 ± 3 nm**
AuNT#1	**650**	**150**	**82**	**49 ± 4 nm**
AuNR#1	**746, 515**	**141**	**84**	**56 ± 6 nm x 16 ± 3 nm**

A.5 –Scientific Publications

In this section all the scientific publications carried out during this PhD course are reported in the following order:

GD_1 - *Playing with Pt(II) and Zn(II) Coordination to Obtain Luminescent Metallomesogens*

GD_2 - *A Quick One-Step Synthesis of Luminescent Gold Nanospheres*

GD_3 - *Very Intense Polarized Emission in Self-Assembled Room Temperature Metallomesogens Based on Zn(II) Coordination Complexes: An Experimental and Computational Study*

GD_4 - *Luminescent Self-Assembled Monolayer on Gold Nanoparticles: Tuning of Emission According to the Surface Curvature*

GD_5 - *Post-Synthesis Heating, a Key Step to Tune the LPR Band of Gold Nanorods Covered with CTAB or Embedded in a Silica Shell*

GD_6 - *Synthesis and Characterization of Hyper-Branched Nanoparticles with Magnetic and Plasmonic Properties*

GD_7 - *Structural Investigation of Anionic Cyclometalated Pt(II)-Tetrabromocatecholate Complexes: Quasi-Halogen Bonding and Elusive Polymorphism at Play*

GD_8 - *Curcumin-Based Ionic Pt(II) Complexes: Antioxidant and Antimicrobial Activity*

GD_9 - *The Rainbow Arching over the Fluorescent Thienoviologen Mesophases,* 2022, *Nanomaterials*

GD_10 - *Solvent-Dispersible Nanostructured MIMI: An Experimental and Computational Study*

GD_11 - *Conjugation of a Silver-Based Coordination Polymer with Curcumin: A New Case of an Inorganic Polymeric Co-crystal*

Full Paper
doi.org/10.1002/chem.202000124
Check for updates
Chemistry Europe
European Chemical Societies Publishing

Metallomesogens

Playing with Pt^{II} and Zn^{II} Coordination to Obtain Luminescent Metallomesogens

Adelina-Antonia Andelescu,[a] Benoît Heinrich,[b] Maria Angela Spirache,[a] Emilie Voirin,[b] Massimo La Deda,[c] Giuseppe Di Maio,[c] Elisabeta I. Szerb,*[a] Bertrand Donnio,*[b] and Otilia Costisor[a]

Abstract: Blue–green luminescent terpyridine-containing Pt^{II} and Zn^{II} complexes are reported. Equipped with lipophilic gallate units, which act as monodentate ancillary coordinating ligands and/or as anions, they display low-temperature mesomorphic properties (lamello-columnar and hexagonal mesophases for Pt^{II} and Zn^{II} complexes, respectively). The mesomorphic properties were investigated by polarised optical microscopy, differential scanning calorimetry, thermogravimetric analysis and X-ray scattering of bulk materials and oriented thin films. The model of self-assembly into the lamello-columnar phase of the Pt^{II} complex has been described in detail. The optical properties of the complexes were investigated in the liquid and condensed liquid crystalline states, highlighting the delicate balance between the role of the metal in determining the type of excited state responsible for the emission, and the role of the ancillary ligand in driving intermolecular interactions for proper mesophase formation.

Introduction

Luminescent d-block metallomesogens are promising functional materials for practical applications. They have mainly been investigated in terms of obtaining polarised emission to be used as backlighting in displays,[1–4] but also some studies concerning their use as stimuli responsive materials for sensing[5,6] or security inks,[7] or high-hole mobility materials for electroluminescent devices[8] have been reported. Despite recent progress with square-planar Pt^{II} and octahedral Ir^{III} complexes, which are considered among the best emitters, there is still considerable work to be done to control the phase type and transition temperatures or to improve the luminescence in the mesophase.[9] In fact, only a few studies on the mesophases of luminescent liquid-crystalline transition metal complexes have been carried out, with, just to cite non-exhaustively, the contributions of Bruce et al. on Ir^{III},[8,10–12] Espinet et al.[13] and Tsutsumi et al.[14,15] on Au^{I}, Gimenénez et al. on Ag^{I}[16] and Zn^{II},[17] Cârcu et al. on Pd^{II},[18–20] Cano et al. on Ag^{I}[21–22] and Pucci, Crispini and Ghedini et al. on Ru^{II},[23] Ag^{I},[24–26] Ir^{III}[27] and Zn^{II}[28,29] complexes. For practical applications, technological and economic issues have to be taken into account, such as thermal and optical stabilities, availability and cost of the precursors and straightforward syntheses. Lately, some ionic Pt^{II} complexes with terpyridine (tpy) or functionalised terpyridine ligands were showed to be good candidates for obtaining luminescent supramolecular assemblies both in liquid crystalline phases and gels,[30–33] owing to the extended aromatic region that favours π–π stacking and short Pt···Pt distances.[34] However, no study has demonstrated the retention of luminescence properties in the mesomorphic ranges of the bulk Pt^{II} terpyridine-based complexes yet.

In this context, our interest in luminescent d-block metallomesogens[24,27,35–37] prompted us to synthesise some luminescent Pt^{II} coordination complexes. They were prepared by a versatile and straightforward synthesis, which permits facile molecular engineering by using anions of different coordination strengths and dimensions, including non-coordinating medium sized BF_4, weakly coordinating bulky lipophilic benzoate and small and strongly coordinating Cl (Scheme 1). This strategy represents an easy way to induce liquid crystallinity in Pt^{II} complexes by avoiding the several steps necessary to precisely functionalise the ligands. To explore the role of the metal cation, the same strategy was extended to Zn^{II} complexes, but owing to the different electronic configuration only neutral penta-coordinated species were obtained.

In this study, we designed and synthesised tpy-containing Pt^{II} and Zn^{II} complexes by using this simple concept. Initially, the straight, non-functionalised 2,2′:6′,2″-terpyridine ligand was used, but the low solubility of the Pt^{II} chloro chloride (ana-

[a] A.-A. Andelescu, M. A. Spirache, Dr. E. I. Szerb, Dr. O. Costisor
"Coriolan Dragulescu" Institute of Chemistry
Romanian Academy, 24 Mihai Viteazu Bvd., 300223 Timisoara (Romania)
E-mail: szella73@gmail.com

[b] Dr. B. Heinrich, E. Voirin, Dr. B. Donnio
Institut de Physique et Chimie des Matériaux de Strasbourg (IPCMS)
UMR7504, CNRS-Université de Strasbourg, 67034 Strasbourg (France)
E-mail: bdonnio@ipcms.unistra.fr

[c] Prof. M. La Deda, G. Di Maio
Dipartimento di Chimica e Tecnologie Chimiche
Università della Calabria, via P. Bucci, Cubo 14/C
87036 Arcavacata di Rende (CS) (Italy)

Supporting information and the ORCID identification number(s) for the author(s) of this article can be found under:
https://doi.org/10.1002/chem.202000124.

© 2020 Wiley-VCH Verlag GmbH & Co. KGaA, Weinheim

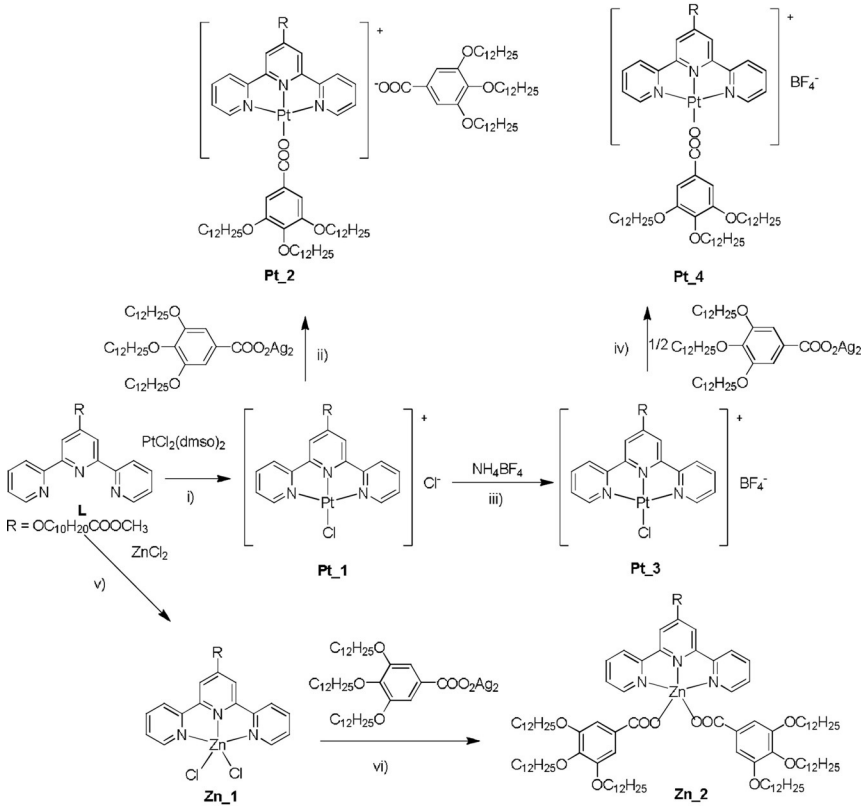

Scheme 1. Synthesis of Pt^{II} and Zn^{II} complexes: i) MeOH, ΔT, 1.5 h; ii) $CHCl_3$/MeOH 1:1, r.t., 2 h; iii) $CHCl_3$/MeOH 1:1, r.t., 1 h; iv) $CHCl_3$/acetone 1:5, r.t., 2 h; v) MeOH/$CHCl_3$, r.t., 1.5 h; vi) $CHCl_3$, r.t., 2 h.

logues of **Pt_1** in Scheme 1) and Zn^{II} dichloro (analogues of **Zn_1**) derivatives prevented the acceptable progress of the successive steps. Therefore, the ligand was functionalised with a long alkyl chain through an ether linkage (ligand L). The methyl ester group at the end of the chain is important for future applications of the complexes, as it allows derivatisation potentially to link the complexes onto functionalised metallic and/or oxide nanoparticles or mesoporous silica structures for theranostic purposes, in particular.

Of the three lipophilic complexes (i.e., **Pt_2**, **Pt_4**, **Zn_2** in Scheme 1), two were found to be mesomorphous, displaying room-temperature lamello-columnar (**Pt_4**, $LamCol_r$ and Lam_{Col}) and hexagonal columnar (**Zn_2**, Col_{hex}) phases, whereas **Pt_2** was found to be thermally unstable and to dissociate rapidly (see below). The thermal behaviour and liquid-crystalline self-assemblies were fully characterised by polarised optical microscopy (POM), differential scanning calorimetry (DSC), thermogravimetric analysis (TGA) and small- and wide-angle X-ray scattering (S/WAXS) of bulk materials, combined with grazing incidence wide-angle X-ray scattering (GIWAXS) on oriented thin films. Accurate structural and photophysical investigations in different solvents and condensed states were carried out, in an attempt to determine structure–property relationships. In particular, of capital interest was the investigation of the influence of the mesophase organization on the emitting states.

Results and Discussion

Synthesis and spectroscopic characterisation

Ligand **L** (tpy) was obtained from 2,6-bis-(2′-pyridyl)-4-pyridone[38] by etherification with methyl 11-bromoundecanoate[39] (see the Supporting Information). Complex **Pt_1**, synthesised by a slight modification of a method described in the literature for similar derivatives,[40] was used as precursor for both **Pt_2** and **Pt_3** ionic complexes: **Pt_2** was obtained by reacting **Pt_1** with 2 moles of the silver(I) salt of 3,4,5-tridodecyloxybenzoate,[41] whereas **Pt_3** was obtained by metathesis reaction by using an excess of NH_4BF_4. The intermediate coordination strength of the benzoate unit gives the possibility for this anion to act as both counter anion and as coordinating ligand on Pt^{II}, when no other competitor is present (complex **Pt_2**), or exclusively as a ligand in the presence of a non-coordinating anion like BF_4 (complex **Pt_4**).

The reaction of the tpy ligand **L** with $ZnCl_2$ afforded the neutral complex **Zn_1**, with the metal centre penta-coordinated by the tridentate terpyridine and two monodentate chlorine ligands. Although Zn^{II} can be forced to accommodate a square-planar geometry with salicyldimine Schiff base[42,43] or porphyrin[44] ligands, without steric constraints, it prefers tetrahedral or higher number coordination geometries. We tried to obtain analogue ionic Zn^{II} complexes but all attempts failed and only the neutral **Zn_2** complex was obtained with two benzoate ligands saturating the coordination sphere of the Zn^{II} metal

© 2020 Wiley-VCH Verlag GmbH & Co. KGaA, Weinheim

15213765, 2020, 21, Downloaded from https://chemistry-europe.onlinelibrary.wiley.com/doi/10.1002/chem.202000124 by Universita Della Calabria Sist. Wiley Online Library on [26/04/2023]. See the Terms and Conditions (https://onlinelibrary.wiley.com/terms-and-conditions) on Wiley Online Library for rules of use; OA articles are governed by the applicable Creative Commons License

centre. The proposed chemical structures of the ligand and its Pt^{II} and Zn^{II} complexes are supported by IR and accurate 1D and 2D NMR spectroscopy. The ionic character of the Pt^{II} complexes was evidenced in solution by conductivity measurements.[45] The complexes were obtained as yellow (Pt^{II} species) or white (Zn^{II} species) powder or waxy solids and were dried for several days under high-pressure vacuum and then equilibrated under air. All Pt^{II} complexes were hygroscopic; the presence of water molecules being evidenced both by IR spectroscopy (strong broad band centred at 3400 cm^{-1}) and by TGA experiments (Figures SI-1 to SI-7 in the Supporting Information) and elemental analysis.

The first indication of the dual coordination mode of the benzoate group in the case of the **Pt_2** complex was evidenced by the COO^- stretching frequencies, different from the frequencies of the alkyl chain methanoate ($\nu_{as} = 1740\ cm^{-1}$). Indeed, for the benzoate the asymmetrical stretching (ν_{as}) is around 1635 cm^{-1}, and the symmetrical stretching (ν_s) for the ionic band appears at 1555 cm^{-1} (**Pt_2**) and at 1340 cm^{-1} for a coordinated bond (**Pt_2** and **Pt_4**), giving a separation (Δ) of 80 and 295 cm^{-1}, respectively (Figure 1).[46] Moreover, for **Pt_4**, the characteristic band of the BF_4^- counter ion appears centred at 1062 cm^{-1} (Figure 1). The IR spectra of the Zn^{II} derivative **Zn_2** (Figure SI_1, in the Supporting Information) contain only the stretching COO^- vibrations corresponding to the coordinated specie ($\Delta \approx 250\ cm^{-1}$).

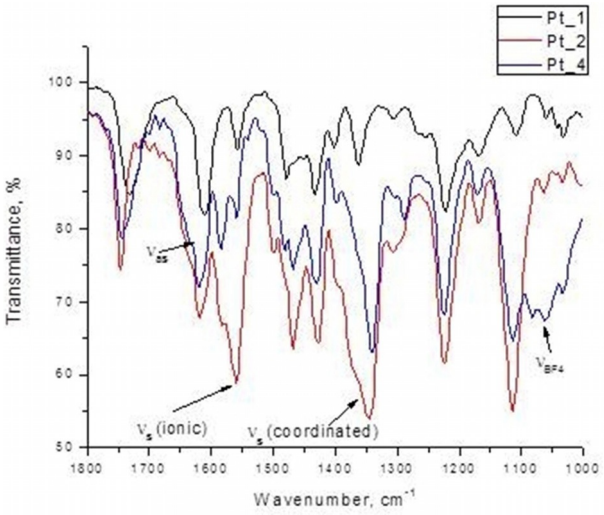

Figure 1. IR spectra of Pt^{II} complexes **Pt_1**, **Pt_2** and **Pt_4**, showing the two types of carboxylate coordination modes.

The chemical shifts of the aromatic protons were assigned on the basis of accurate 1D and 2D NMR investigations (Tables SI-1 to SI-6 in the Supporting Information). In the cases of **Pt_2** and **Pt_4**, the aromatic protons belonging to the benzoate groups have different chemical shifts when coordinated to the metal centre as a monodentate ligand or ensure the neutrality of the complex as a negatively charged ion (Figure 2). In particular, for the coordinated benzoate, the aromatic protons are less shielded, shifting to higher frequencies.

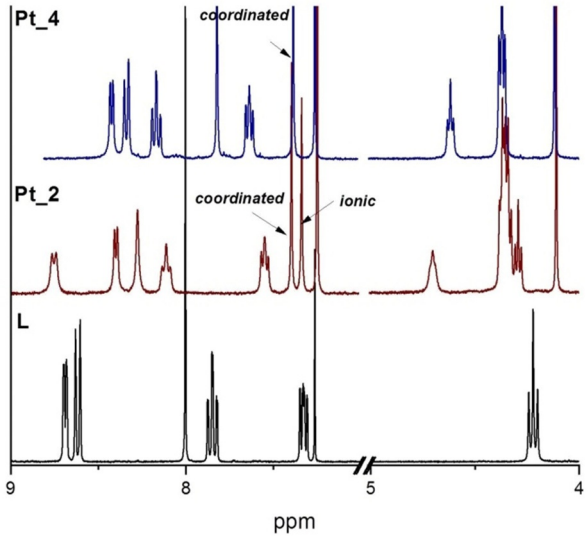

Figure 2. ^1H NMR spectra of ligand **L**, **Pt_2** and **Pt_4**, showing the different chemical shifts of the aromatic proton belonging to the benzoate when they are coordinated or ionic.

Thermal and mesomorphic behaviour (POM, TGA, DSC)

The thermal behaviour was first investigated by POM, TGA and DSC. The complexes without the benzoate group (**Pt_1**, **Pt_3** and **Zn_1** in Scheme 1) were obtained as amorphous or crystalline solids with high melting points, and, as expected, deprived of liquid crystalline properties owing to the absence of aliphatic chains. The introduction of lipophilic gallate units as monodentate ligands (**Pt_4** and **Zn_2** in Scheme 1) or as both ligand and counter anion (**Pt_2** in Scheme 1) resulted in the drastic lowering of the melting points for all and in the induction of mesomorphism for the former ones (Table 1).

The thermal behaviour of the platinum complex with two gallate groups, **Pt_2**, is rather peculiar and complicated, and requires some precision. During the first heating, a first broad, endothermic event is detected at around 37 °C by DSC, and a texture characteristic of a hexagonal (Col_{hex}) phase is easily recognised by POM (Figure 3 and Figure SI-9 in the Supporting Information). On further heating, above 90 °C, phase co-existence is observed (between Col_{hex} phase and isotropic liquid), and the birefringence persists until the sample fully clears at 155 °C, at which temperature no more birefringence is seen. This very broad transition, spreading over several tens of degrees Celsius, was not detected by DSC. On cooling, the isotropic liquid and the Col_{hex} phase were found to co-exist again until a transition was detected at around 85 °C by DSC, where two phases eventually co-exist. It is important to note that this transition was not seen by POM and that no textural change was evidenced either. On further cooling, the compound partly crystallises. This singular phenomenon is reversible on successive thermal cycles, and suggests the partial dissociation of one gallate group during the first thermal treatment, as later confirmed by S/WAXS. ^1H NMR and IR spectroscopy measurements performed on **Pt_2** after one cycle of heating and cooling indeed confirmed the dissociation of the ionic gallate (see

© 2020 Wiley-VCH Verlag GmbH & Co. KGaA, Weinheim

15213765, 2020, 21, Downloaded from https://chemistry-europe.onlinelibrary.wiley.com/doi/10.1002/chem.202000124 by Universita Della Calabria Sist. Wiley Online Library on [26/04/2023]. See the Terms and Conditions (https://onlinelibrary.wiley.com/terms-and-conditions) on Wiley Online Library for rules of use; OA articles are governed by the applicable Creative Commons License

Table 1. Thermal behaviour of Pt^{II} and Zn^{II} complexes.

Complex	$T_{dec\,5\%}$ [°C][a]	Thermal properties: mesophases,[b] transition temperatures[c] [°C] and enthalpies (ΔH [kJ mol^{-1}])
Pt_1	155	Dec[d]
Pt_2	303	Cr 37.1 (–)[e,f] M + Col_{hex} ~ 100–155 (–) Iso
		Iso 140.0 (–)[e,f] Iso + Col_{hex} 84.9 (−8.5) M + Col_{hex} 18.5 (−70.6) Cr
		Cr 39.2 (74.7) M + Col_{hex} 89.3 (8.3)[f] Iso + Col_{hex} 155 (–) Iso
Pt_3	280	Cr 170 (–)[e] Iso
Pt_4	285	$LamCol_r$ 65-135 (11.6)[f] Lam_{Col} 255 (–)[e] Iso
Zn_1	246	Cr 243 (–)[e] Iso
Zn_2	309	Col_{hex} 101 (2.2) Iso
		Iso 108 (−2.0) Col_{hex}

[a] Significant weight loss (5%) from degradation from the TGA trace. [b] Determined on first cooling and second heating (for mesomorphous compounds), and only first heating for the other: Cr, crystalline phase; Col_{hex}, hexagonal columnar mesophase; Lam_{Col}, lamellar columnar mesophase; $LamCol_r$, lamellar columnar mesophase with rectangular symmetry; Iso, isotropic liquid. [c] Onset peaks. [d] Decomposition before melting. [e] POM observations. [f] Broad transition.

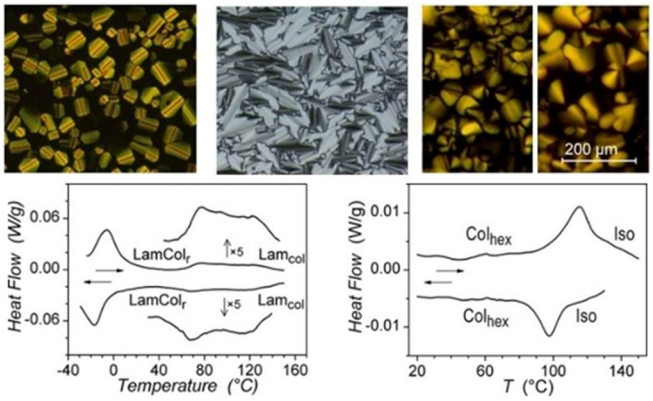

Figure 3. POM textures (top) of the **Pt_2** sample at 35 °C on first cooling, of **Pt_4** at 175 °C on second cooling, and of **Zn_2** at 80 and 20 °C, respectively, on cooling. DSC traces (bottom) of **Pt_4** and **Zn_2**.

Figures SI-18 and SI-19 in the Supporting Information). This lack of thermal stability therefore precludes any conclusive remarks on its supramolecular behaviour.

The platinum complex with only one gallate group (**Pt_4**) is clearly mesomorphous from room temperature up to 255 °C, with a reversible phase transformation spreading over 70 °C, from approximately 65 °C to 135 °C between two mesomorphic states. Another broad transition to a likely crystalline state was detected below 0 °C. **Pt_4** exhibits a fan-shaped texture reminiscent of a lamellar arrangement (Figure 3 and Figure SI-10 in the Supporting Information). The Zn complex (**Zn_2**) is mesomorphous at room temperature up to a reversible but broad clearing transition at 101 °C. POM textures at 80 °C in the mesophase and at room temperature, obtained on cooling from the isotropic state, display pseudo-focal-conic defects and homeotropic zones, which indicate the formation of an untilted Col_{hex} mesophase (Figure 3 and Figure SI-11 in the Supporting Information). In all cases, textures were preserved at room temperature.

Characterisation of the mesophases by small- and wide-angle X-ray scattering (S/WAXS)

Combined with S/WAXS investigation, lamello-columnar phases were eventually confirmed for **Pt_4** from room temperature up to 255 °C, whereas a hexagonal mesophase was confirmed for **Zn_2**. The S/WAXS patterns, recorded for both samples at various temperatures, revealed several sharp and intense reflections in the small-angle range characteristic of the various two-dimensional arrangements of mesogenic columns separated in space by a molten aliphatic continuum (Figure 4). For **Zn_2**, up to four reflections in the ratio $1:\sqrt{3}:2:\sqrt{7}$ were observed, unambiguously characterising a hexagonal *p6mm* lattice. The numerous sharp reflections of **Pt_4** could be indexed according to a *p2mg* rectangular lattice, with the arrangement of columns into a rectangular symmetry. In the large-angle region, a broad and diffuse scattering signal, emerging from undifferentiated lateral distances between the aliphatic chains and the gallate groups, respectively, $h_{ch} + h_{gal}$, was systematically present and confirmed the fluid and liquid crystalline nature of all mesophases: these average lateral distances give rise to scattering maxima h_{gal} and h_{ch}, which are not resolved from the large scattering contribution h_{ch} from the molten chains in the periphery of the columns. An additional signal is observed for **Pt_4**, h_π, arising from the stacking distances between successive tpy-platinum complexes into columns: this signal is rather sharp, suggesting a regular stacking of the complex along the columns. This signal is not present for the zinc complex, indicating that the stacking is completely undifferentiated from the broad scattering, $h_{ch} + h_{gal}$. For this latter complex, another scattering maximum with a two-core periodicity $(h_{ch} + h_{gal} + h_\pi)/2$ was distinguished, in relation to the change of in-plane orientation between successive cores. The S/WAXS patterns recorded at various temperatures for complex **Pt_2** unfortunately confirmed the erratic behaviour owing to the dissociation of the ionic gallate and the co-existence of two or more species, making the phase identification impossible (Figure SI-13 in the Supporting Information).

The columns of the Col_{hex} phase of **Zn_2** are constituted by a core of piled complexes and a crown of irregularly closed-

© 2020 Wiley-VCH Verlag GmbH & Co. KGaA, Weinheim

15213765, 2020, 21, Downloaded from https://chemistry-europe.onlinelibrary.wiley.com/doi/10.1002/chem.202000124 by Universita Della Calabria Sist. Wiley Online Library on [26/04/2023]. See the Terms and Conditions (https://onlinelibrary.wiley.com/terms-and-conditions) on Wiley Online Library for rules of use; OA articles are governed by the applicable Creative Commons License

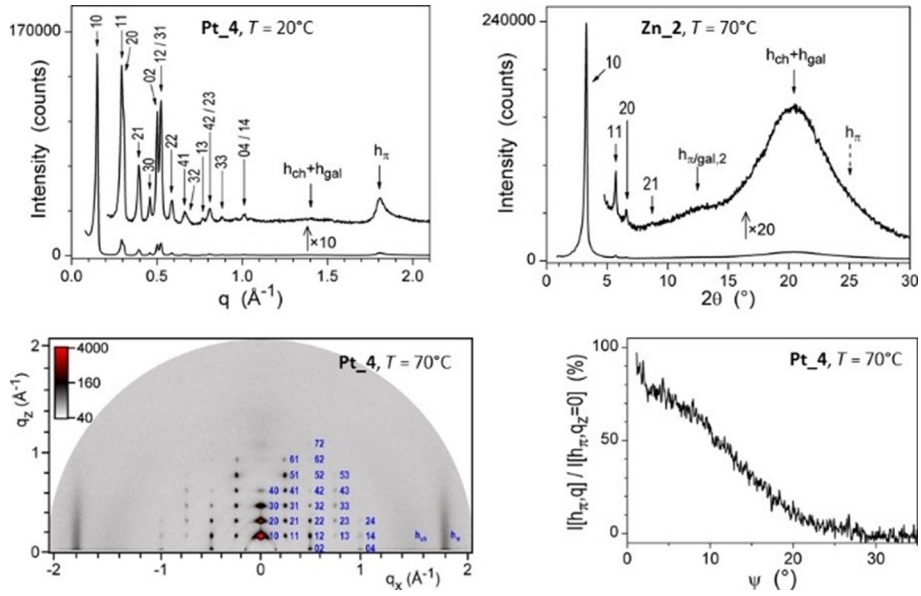

Figure 4. Representative S/WAXS (top) and GIWAXS (bottom) patterns of **Pt_4** (in the low-temperature LamCol$_r$ phase) and **Zn_2** (in the Col$_{hex}$). In the thin-film pattern, the *b*-axis and h_π scattering lie in the equatorial plane and lamellae are thus parallel to the substrate (see text). The profile analysis of the strip-like h_π scattering further reveals that complexes fluctuate out of the lamellar plane by roughly 10°.

packed gallate units, the average lateral distances of which give rise to scattering maximums h_{gal} and h_{ch}, which are not resolved from the scattering contribution h_{ch} from the molten chains in the periphery of columns. The distribution of gallate units and chains around piled complexes results in the appearance of a scattering maximum from a two-cores periodicity $h_{\pi/gal,2}$, in relation to the change of in-plane orientation of successive cores. For this compound, it turns out that the number of chains and the size of the cores are well adapted, so that molecules self-assemble in an untilted Col$_{hex}$ phase, with h_{mol} close to the natural stacking distance of tpy-zinc(II) (Figure SI-16 in the Supporting Information) and with a chain packing ratio,[47] q_{ch}, slightly above unity (Table 2). The stacking distance of the tpy rings is indeed 3.2945 Å at 25 °C in the single-crystal structure CSD-TPYZNC[48] of the dichloro-terpyridyl-zinc(II) complex, thus is nearly the same as in the frozen Col$_{hex}$ state of **Zn_2**. The q_{ch} value around 1.1 corresponds to almost stretched chains, favouring the formation of sharp nanosegregation interfaces with piled cores and thus columnar mesomorphism.

For the LamCol$_r$, the glide line coincides with the *b*-axis, along which column rows and counter ions compactly self-assemble into layers (Figure 5). The sequence of column layers and of intermediate molten chain layers along the *a*-axis generates a lamellar periodicity, d_{lam}, giving a very strong first-order reflection (1 0) and reflections series (*h* l) that extend to high *h*. In the thin-film pattern, the *b*-axis and h_π scattering lie in the equatorial plane and lamellae are thus parallel to the substrate. The profile analysis of the strip-like h_π scattering fur-

Table 2. Mesophase parameters of complex **Zn_2**.

Phase T[a]	V_{mol} ρ[b]	a A[Z][c]	h_{mol}[d]	χ_{Vch} A_{core}[e]	D_{cyl}[f]	$S_{ch,cyl}$[g]	$q_{ch,cyl}$[h]
Col$_{hex}$ 70	3025 1.04	31.32 850[1]	3.56	0.778 189	15.5	24.8	1.12
Col$_{hex}$ 30	2946 1.07	32.08 891[1]	3.31	0.775 200	16.0	23.7	1.11

[a] T, temperature of the measurement (°C). [b] V_{mol}, calculated molecular volume (Å^3); ρ, density (g cm^{-3}). [c] a, lattice parameter (Å); $A = a^2\sqrt{3}/2$, lattice area (Å^2); Z, number of columns per lattice. [d] $h_{mol} = V_{mol}/A$, molecular slice thickness (Å). [e] χ_{Vch}, calculated aliphatic volume fraction; $A_{core} = (1-\chi_{Vch}) \times (A/Z)$, cross-sectional area of columnar cores (Å^2). [f] $D_{cyl} = \sqrt{(4/\pi A_{core})}$, diameter (Å) of equivalent cylinder of cross-sectional area A_{core}. [g] $S_{ch,cyl} = \pi D_{cyl} \times h_{mol}/n_{ch}$: cylinder area per chain (Å^2), $n_{ch} = 7$, the number of chains per molecule. [h] $q_{ch} = S_{ch,cyl}/\sigma_{ch}$, chain packing ratio, $\sigma_{ch} = 21.2$ (Å^2), the cross-sectional area of a molten chain at 20 °C.

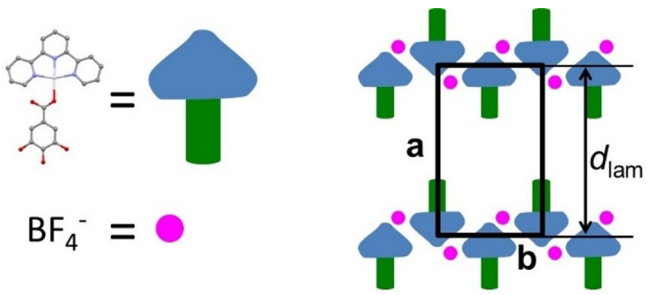

Figure 5. Left: model of terpyridyl-platinum complex moieties and gallate units, as reconstructed from single-crystal structures CSD-RAXFIH[49] and CSD-IJUMEG.[50] Right: schematic representation of the likely molecular organization in the LamCol$_r$ mesophase of *p2mg* symmetry. Columns of stacked complexes and BF_4^- counter ions arrange in staggered rows; gallate units and molten alkyl chains (not represented) fill the gaps between successive staggered rows. The *a*-axis coincides with a lamellar periodicity d_{lam}, maintained after heating in the Lam$_{Col}$ mesophase, whereas the rectangular long-range lattice is suppressed by thermal fluctuations allowing successive column rows to move laterally one to another.

© 2020 Wiley-VCH Verlag GmbH & Co. KGaA, Weinheim

15213765, 2020, 21, Downloaded from https://chemistry-europe.onlinelibrary.wiley.com/doi/10.1002/chem.202000124 by Universita Della Calabria Sist. Wiley Online Library on [26/04/2023]. See the Terms and Conditions (https://onlinelibrary.wiley.com/terms-and-conditions) on Wiley Online Library for rules of use; OA articles are governed by the applicable Creative Commons License

ther reveals that complexes fluctuate out of the lamellar plane by roughly 10° (Figure 4, bottom right).

Terpyridyl-platinum complexes stack into columns that self-assemble with counter ions into layers alternating with aliphatic chains. At low temperature, the rings are nearly orthogonal to layers ($h_{mol} \approx h_\pi$), and the chains stretch onto the layer normal ($q_{ch} \approx 1$); the superimposition of layers defines a rectangular lattice of one-lamella and two-column periodicity (Table 3). At higher temperature, fluctuations of ring orientations out of the lamellar plane are enhanced ($\langle\psi\rangle \gg 0$), which causes elongation of columns ($h_{mol} > h_\pi$) and lateral expansion of lamellae (higher A_{mol} and q_{ch}), which in turn affects the regularity of π-stacking (lower ξ). The columnar superstructure finally vanishes in the following lamello-columnar mesophase (Lam_{Col}), which preserves the long-range correlated lamellar structure and a local-range ribbon periodicity from average lateral distances between piled complexes (D).

Table 3. Mesophase parameters of complex **Pt_4**.

Phase T[a]	V_{mol} ρ[b]	a b $A[Z]$ $d_{lam}[N_L]$[c] $D[\xi]$[d]	A_{mol} S_{ch}[e]	q_{ch}[f]	D_{col} S_{col}[g]	h_{mol} h_π [ξ][h]	ψ[i]
$LamCol_r$ 20	1820 1.28	41.20 25.11 1035[2] 41.20[1] –	44.2 22.1	1.04	12.55 517	3.52 3.48 [90]	9
$LamCol_r$ 70	1880 1.24	40.60 25.16 1022[2] 41.60[1] –	46.3 23.1	1.05	12.58 511	3.68 3.51 [70]	17
Lam_{Col} 140	1960 1.19	– 36.90[1] 12.5[60]	53.2 26.6	1.15	12.5 462	4.24 3.54 [40]	33
Lam_{Col} 180	2010 1.16	– 35.17[1] 12.2[60]	57.1 28.6	1.20	12.2 429	4.68 3.56 [25]	40

[a] Temperature of the measurement (°C). [b] V_{mol}, calculated molecular volume (Å^3); ρ, density (g cm^{-3}). [c] a, b, $A = a \times b$, Z: lattice parameters (Å), lattice area (Å^2) and number of columns per lattice; d_{lam}, N_L: lamellar periodicity (Å) and number of molecular layers per lamella ($LamCol_r$: $d_{lam} = a$) (for $LamCol_r$ only). [d] D, ξ: average distance between columns from scattering maximum (Å) and associated correlation length (Å, Scherrer equation with $K = 0.9$) (for Lam_{Col} only). [e] $A_{mol} = V_{mol}/(d_{lam}/N_L)$ molecular area (Å^2); $S_{ch} = A_{mol}/2$: area per chain in the lamellar plane (Å^2). [f] $q_{ch} = S_{ch}/\sigma_{ch}$, chain packing ratio, $\sigma_{ch} = 21.2$ Å^2 at $T = 20$ °C, being the cross-sectional area of a molten chain. [g] D_{col}: distance between columns in the lamellar plane (Å) ($LamCol_r$: $D_{col} = b/2$; Lam_{col}: $D_{col} = D$); $S_{col} = D_{col} \times (d_{lam}/N_L)$: cross-sectional area of a column (Å^2). [h] $h_{mol} = V_{mol}/S_{col}$: molecular slice thickness (Å); h_π, ξ: distance between stacked complexes from scattering maximum (Å) and associated correlation length (Å, Scherrer equation with $K = 0.9$). [i] $\psi = a\cos(h_\pi/h_{mol})$: mean out of plane tilt angle of stacked complexes (°).

Photophysical characterisation

The photophysical properties of the complexes have been investigated in DMSO solution for **Pt_1**, **Pt_3**, **Pt_4**, in CH_2Cl_2 solution for **Pt_2**, **Zn_1**, **Zn_2** and in the solid state for all samples. The results are summarised in Table 4 and Table 5.

All Pt^{II} complexes present a pale-yellow colour in diluted solutions and absorb in the UV region with weak bands in the visible region of the electromagnetic spectra (Figure 6a). The spectra show a well-resolved structure with numerous peaks, which can be grouped in three main regions: lowest intensity bands in the 450–500 nm range; medium-intensity peaks in the 370–400 nm region; high-intensity bands below 350 nm. Although the spectral shape is almost unvaried on changing the counter ion or the ancillary ligand, the ε values are different.

All solutions are weakly fluorescent at room temperature (Figure 6b), with broad and structureless emission bands in the green–red region (peaks located from 600 to 650 nm) of the visible spectrum. The emission quantum yields measured in air-equilibrated solution at room temperature are low and range from 0.2 to 1.7%. The emission intensity decay has been fitted with a mono-exponential function giving lifetime values between 251 and 397 ns (Table 4).

Platinum tpy complexes are well known to form aggregates through metal···metal/π···π interactions,[51–54] which give rise to various excited states. The combined effect of the counter ion nature, the solution concentration and the solvent polarity modulates the photophysical properties of these complexes. On this basis, the 459 nm (**Pt_1**) and 455 nm (**Pt_3**) absorption bands in the first spectral region above identified, are attributed to a metal-metal-to-ligand charge transfer (MMLCT) excited state, indicative of Pt–Pt dimerization in **Pt_1** and **Pt_3**, both

Table 4. Photophysical properties of the complexes in solution at room temperature.

Sample	Absorption, λ_{max} [nm] (ε [M^{-1} cm^{-1}])	Emission, λ_{max} [nm]	Quantum yield, Φ [%]	Lifetime, τ [ns]
Pt_1[a]	286 (24780), 305 (13330), 320 (13940), 334 (15580), 372 (3930), 395 (3960), 459 (650)	620	0.8	380
Pt_2[b]	285 (6310), 306 (2700), 317 (2370), 332 (1990), 381 (660), 393 (630), 459 (60)	600	1.7	397
Pt_3[c]	286 (78320), 305 (41990), 320 (41770), 334 (46580), 368 (10690), 396 (11670), 455 (1950)	615	0.5	338
Pt_4[d]	285 (25630), 302 (14650), 317 (13370), 333 (12570), 367 (4030), 395 (3400), 469 (800)	650	0.2	251
Zn_1[e]	248, 275, 311, 323	365	6.4	1.2
Zn_2[f]	258 (28030), 285 (15150), 306 (11620), 319 (10100)	379	24.5	2.7

Concentration: [a] 1.08×10^{-5} M; [b] 2.63×10^{-4} M; [c] 9.16×10^{-5} M; [d] 2.3×10^{-5} M. [e] Partially soluble, ε data not available. [f] 3.96×10^{-6} M.

© 2020 Wiley-VCH Verlag GmbH & Co. KGaA, Weinheim

15213765, 2020, 21, Downloaded from https://chemistry-europe.onlinelibrary.wiley.com/doi/10.1002/chem.202000124 by Universita Della Calabria Sist, Wiley Online Library on [26/04/2023]. See the Terms and Conditions (https://onlinelibrary.wiley.com/terms-and-conditions) on Wiley Online Library for rules of use; OA articles are governed by the applicable Creative Commons License

Table 5. Photophysical properties of the complexes in the condensed state at room temperature.

Sample	Emission, λ_{max} [nm]	Quantum yield, Φ [%]	Lifetime, τ [ns] [α_i (%)]
Pt_1	676	19.9	412
Pt_2	650	1.1	475
Pt_3	690	14.0	272
Pt_4	660	1.8	300
Zn_1	360	15.8	78.5
Zn_2	450	7.1	0.4[23], 3[69], 11[8]

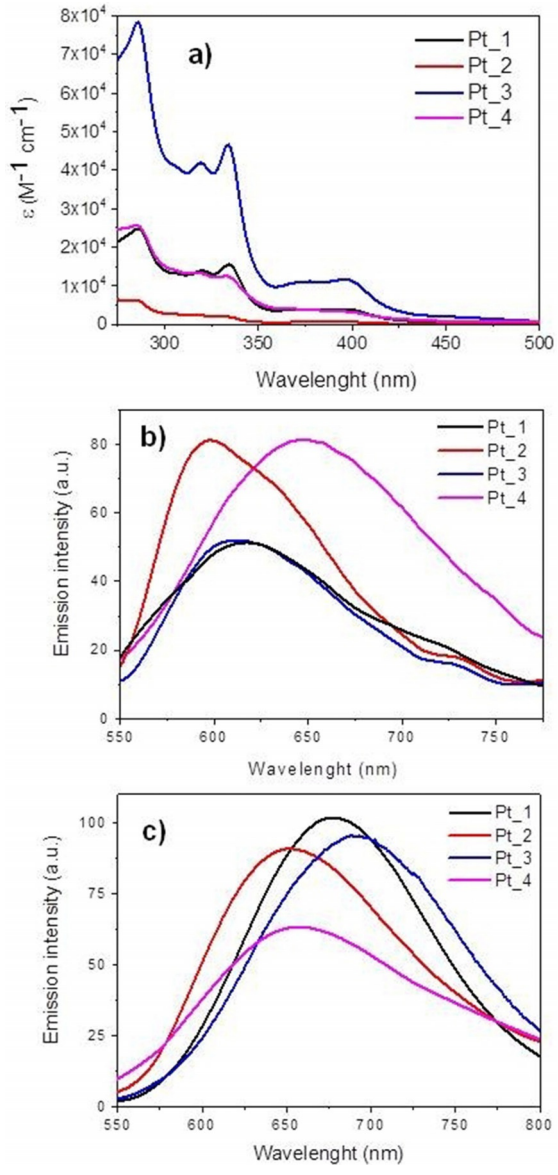

Figure 6. (a) Absorption spectra of Pt^{II} complexes in DMSO (**Pt_1**, **Pt_3**, **Pt_4**) or CH_2Cl_2 (**Pt_2**) solutions. (b) Emission spectra of Pt^{II} complexes in DMSO (**Pt_1**, **Pt_3**, **Pt_4**) or CH_2Cl_2 (**Pt_2**) solutions at room temperature. Concentrations are reported in Table 4. (c) Emission spectra of Pt^{II} complexes in condensed phase at room temperature.

bearing the chlorine ancillary ligand. When this ligand is replaced by a benzoate, as in the case of **Pt_2** and **Pt_4**, the bands at 459 and 469 nm, respectively, are attributed to a π–π* transition of the tpy–tpy bound dimer, the Pt–Pt interaction being hampered by the steric hindrance of the gallate ligand. The absorption bands in the second spectral region (superimposable in the DMSO-dissolved complexes, and slightly redshifted in the CH_2Cl_2-dissolved compounds) are due to a metal-to-ligand charge transfer (d–π* MLCT) transition from Pt^{II} to the tpy ligand. Finally, the bands in the third region are attributed to a ligand-centred (π–π*LC) transition on the tpy ligand. **Pt_1** and **Pt_3** show an emission band at 620 and 615 nm, respectively, owing to the ^{3}MMLCT deactivation. The **Pt_2** and **Pt_4** broad, unstructured emission band (peaked at 600 and 650 nm, respectively) is ascribed to an excimeric emission, which accounts for the large Stokes shift observed for **Pt_4** compared with **Pt_1** and **Pt_3**; the blueshift observed for **Pt_2** emission is ascribed to the different solvent in which the compound has been dissolved. This different aspect of the emission spectra of the complexes bearing a chlorine as an ancillary ligand (**Pt_1** and **Pt_3**) compared with those that bind a gallate (**Pt_2** and **Pt_4**), confirms the different attribution of the lowest excited state, that is, an MMLCT in the case of the first pair, and an excimer (formed by means of π–π interactions between the aromatic rings of tpy) in the case of the second pair.

In the Supporting Information (Figure SI-21), the absorption spectra of platinum complexes at different concentrations are reported. It can be seen that as the concentration increases, the ratio between the bands attributed to the intermolecular interactions and those attributed to transitions on the single molecule, tends to grow, which is evidence for aggregation in solution.

Emission spectra recorded from solid samples at room temperature (Figure 6c) have the same structure as those collected in solution under the same conditions. All show a redshift with respect to the solutions, but more accentuated for the complexes that bind chlorine (**Pt_1** and **Pt_3**, which emit with a maximum at 676 and 690 nm, respectively) than for those that bind benzoate (**Pt_2** and **Pt_4**, which emit with a maximum at 650 and 660 nm, respectively). Emission quantum yields and lifetimes in the condensed phase undergo a significant variation with respect to the values recorded in solution for **Pt_2** and **Pt_4**, but this variation is much more consistent for **Pt_1** and **Pt_3** (see Table 4 and Table 5). In fact, the complexes bearing chlorine in solid samples show a redshifted emission maximum and an enhancement of the luminescence intensity with respect to the solution, whereas for the complexes with benzoate ligand these differences are smaller. This behaviour reflects the different origin of the emitting state for the two classes of compounds: for **Pt_1** and **Pt_3**, the small steric hindrance of chlorine reinforces the Pt–Pt interaction in the solid, giving rise to an MMLCT excited state. On the contrary, the bulky benzoate group in **Pt_2** and **Pt_4** does not allow a Pt–Pt interaction, whereas weak π–π interactions on the tpy ligands give rise to the formation of excimers, similarly to the solution.

© 2020 Wiley-VCH Verlag GmbH & Co. KGaA, Weinheim

15213765, 2020, 21, Downloaded from https://chemistry-europe.onlinelibrary.wiley.com/doi/10.1002/chem.202000124 by Universita Della Calabria Sist. Wiley Online Library on [26/04/2023]. See the Terms and Conditions (https://onlinelibrary.wiley.com/terms-and-conditions) on Wiley Online Library for rules of use; OA articles are governed by the applicable Creative Commons License

Table 6. Quantum yields for **Pt_2** by varying the temperature; emission maximum $\lambda_{max}=650$ nm.

First cycle				Second cycle			
Heating		Cooling		Heating		Cooling	
T [°C]	Φ [%]	T [°C]	Φ [%]	T [°C]	Φ [%]	T [°C]	Φ [%]
30	1.10	120	0.05	30	1.42	120	0.12
50	2.00	90	0.09	50	1.02	90	0.16
90	1.24	50	0.33	90	0.18	50	0.59
120	0.21	30	0.75	120	0.12	30	1.05
160	0.03			160	0.01		

Table 7. Quantum yields for **Pt_4** by varying the temperature; emission maximum $\lambda_{max}=660$ nm.

First cycle				Second cycle			
Heating		Cooling		Heating		Cooling	
T [°C]	Φ [%]	T [°C]	Φ [%]	T [°C]	Φ [%]	T [°C]	Φ [%]
30	1.80	150	0.07	30	0.56	150	0.11
50	1.29	100	0.17	50	0.45	100	0.19
100	0.50	50	0.41	100	0.22	50	0.41
150	0.08	30	0.56	150	0.11	30	0.57
160	0.06			160	0.08		

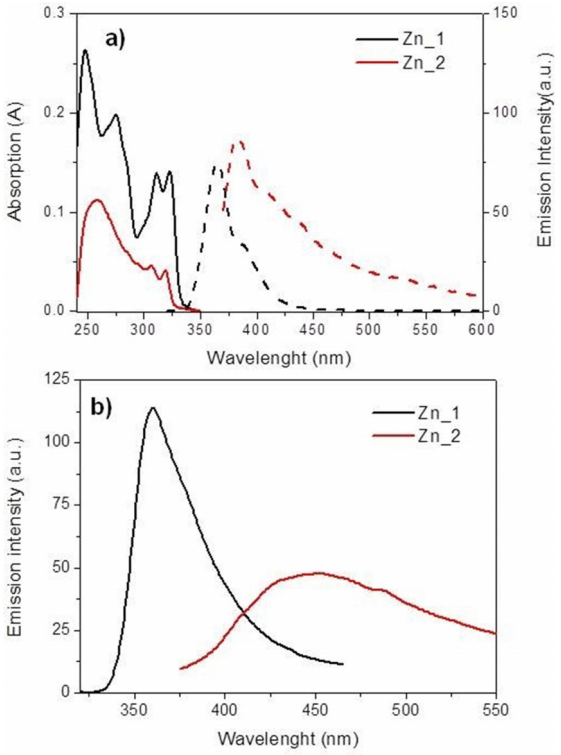

Figure 7. (a) Absorption (continuous line) and emission (dashed line) spectra of Zn^{II} complexes in CH_2Cl_2 solutions at room temperature. (b) Emission spectra of Zn^{II} in the pristine condensed states at room temperature.

The photophysical behaviour of **Pt_2** and **Pt_4** was explored by changing the temperature. Both samples continue to emit during the heating and cooling cycles between 30 and 160 °C, retaining their emission maxima exhibited in the solid sample, that is, 650 nm and 660 nm for **Pt_2** and **Pt_4**, respectively. The emission quantum yields have been measured at various temperatures (Table 6 and Table 7). For **Pt_2**, two heating/cooling cycles have been recorded, interspersed with cooling in the freezer (at −20 °C) for 30 min. For **Pt_4**, three cycles have been performed; between the end of the second cycle and the start of third cycle, the sample was cooled in the fridge (at 4 °C) for 2 h.

Generally, the quantum yield decreases as the temperature increases, owing to thermal agitation, which favours the non-radiative deactivation pathway. For **Pt_4**, the experimental data follow this trend, after an initial steeper decrease on first heating, related to the development of the LamCol, structure with the softening of the sample. Values on cooling and second heating stabilise around 0.5% in this phase and decrease to 0.2% in the less-ordered Lam_{Col} phase, prior to dropping to below 0.1% in the isotropic liquid state. This rational dependence upon structure contrasts with findings for the **Pt_2** sample, which shows an increase in the quantum yield during the first cycle, whereas from the beginning of the second cycle, the emission quantum yield is higher than the value measured in the solid. This peculiar behaviour can be rationalised by considering that on heating **Pt_2** during the first cycle eliminates one gallate unit and the metal centres are getting closer, which explains the increase of luminescence by Pt–Pt interactions.

The absorption spectra of **Zn_1** and **Zn_2** complexes recorded in CH_2Cl_2 solution (Figure 7a) show a series of bands (Table 4) in the UV portion of the electromagnetic spectrum, all originating from tpy LC transitions.[55,56]

In particular, for **Zn_2**, these transitions overlap with those localised on the benzoate ligand, giving rise to a broad band below 300 nm. Interestingly, by comparing the absorption spectra of the zinc complexes with that of the tpy ligand (see Figure SI-20 in the Supporting Information), it can be noted that in this last one the bands above 300 nm are very low in intensity, whereas in the absorption spectra of the complexes, these bands have an intensity comparable with those of the other bands. This different spectral behaviour is due to the different symmetry of the free and zinc-bonded terpyridine; the free tpy shows the nitrogen atoms of the lateral pyridines both facing the opposite side with respect to the nitrogen atom of the central pyridine,[56] whereas when the tpy binds a zinc ion all the nitrogen atoms are facing the same side. Both complexes are fluorescent, showing an asymmetric emission band at 365 nm (with a vibronic shoulder at 386 nm) for **Zn_1**, and at 379 nm (and a long tail extending towards the green spectral range) for **Zn_2** (Figure 7a). The luminescence intensity is quite high, with an emission quantum yield of 6.4% for **Zn_1** and 24.5% for **Zn_2**; time-resolved measurements give a mono-exponential decay of the excited states, with lifetimes of, respectively, 1.2 and 2.7 ns (Table 4). By comparing the photophysical properties of the two zinc complexes, it is evident that the substitution of the two chlorine atoms with two electron-donor benzoate groups involves a lowering of the energy of the emitting state, an increase of the Stokes shift and,

© 2020 Wiley-VCH Verlag GmbH & Co. KGaA, Weinheim

15213765, 2020, 21, Downloaded from https://chemistry-europe.onlinelibrary.wiley.com/doi/10.1002/chem.202000124 by Universita Della Calabria Sist. Wiley Online Library on [26/04/2023]. See the Terms and Conditions (https://onlinelibrary.wiley.com/terms-and-conditions) on Wiley Online Library for rules of use; OA articles are governed by the applicable Creative Commons License

above all, a considerable increase in the emission quantum yield.

In the pristine condensed states (Figure 7b), both samples are fluorescent. Comparing the luminescence properties of **Zn_1** in solution (Table 4) with those measured in the condensed state (Table 5), the emission maximum remains almost unchanged (365 vs. 360 nm, respectively), whereas the quantum yield doubles from 6.4% to 15.8%, and the lifetime increases from 1.2 ns to 78.5 ns. This behaviour is attributable to the reduction of non-radiative de-excitation pathways that occurs in the solid phase, where the vibronic modes of the single molecule are somewhat reduced. If we compare the behaviour of **Zn_2** in solution (Table 4) with the pristine condensed phase (Table 5), we first notice a consistent redshift of the emission band (379 nm in solution vs. 450 nm in condensed phase), a drastic reduction of the quantum yield from 24.5% to 7.1% and different kinetics of the excited-state decay: mono-exponential in solution (with a lifetime of 2.7 ns) and multi-exponential in the pristine condensed phase, with a relevant percentage of short lifetimes (Table 5). The effect of temperature variation on the photophysical properties of **Zn_2** is reported in Table 8. The temperature increase (both during the first and the second heating/ cooling cycle) involves a redshift of the emission band and a decrease of quantum yield. As found for **Pt_4**, trends are reversible by decreasing the temperature, but the initial higher values are never restored in relation to the structural changes on first heating. The columnar structure of the Zn complex is indeed initially disordered, with only average distances between irregularly arranged columns (Figure SI-16 in the Supporting Information), and the regular hexagonal arrangement only develops with the softening of the sample on first heating. Such a transformation clearly creates interactions between the compounds, which stabilise the excited state, as indicated by the redshift of the emission band, whereas the quantum yield decreases owing to the non-radiative deactivation increase triggered by the high temperature.

Table 8. Emission maximum and quantum yields for **Zn_2** by varying the temperature. Emission maximum varies with temperature.

First cycle					
	Heating			Cooling	
T [°C]	λ_{max} [nm]	Φ	T [°C]	λ_{max} [nm]	Φ
30	450	7.1	80	497	1.92
80	478	4.97	30	478	2.98
140 (isotropic)	507	0.71			
Second cycle					
	Heating			Cooling	
T [°C]	λ_{max} [nm]	Φ	T [°C]	λ_{max} [nm]	Φ
30	478	2.98	80	493	1.63
80	500	1.35	30	482	3.27
140 (isotropic)	509	0.50			

Conclusion

Luminescent metallomesogens are promising functional materials for various display applications. Although considered as an emerging and growing field of research, there are still relatively few reported examples of square-planar Pt^{II} and octahedral Ir^{III} complexes being considered as outstanding emitters. This leaves space for the design of new metal–ligand systems to control the phase type, transition temperatures and thermal stability as well as to improve their luminescence in the mesophases.

The use of lipophilic gallate units is shown to be a good strategy in inducing low-temperature liquid crystalline properties in terpyridine-based Pt^{II} and Zn^{II} coordination complexes by an elegant and straightforward synthetic approach. The tpy ligand also was functionalised with a long alkyl chain, which ends with a methyl ester group, allowing further functionality derivatisation.

Only one Zn complex (**Zn_2**) and one thermally stable Pt complex (**Pt_4**) exhibited mesomorphic properties, the latter forming an original $LamCol_r$ mesophase of *p2mg* symmetry, for which self-assembly and a structural model were proposed and discussed.

The photophysical properties of the complexes were investigated in solution and in the condensed state. In this work, we have highlighted the role of the metal in determining the type of excited state responsible for the emission, and the role of the ancillary ligand in driving intermolecular interactions. In the case of a d-block open-shell metal, such as platinum, we have studied the role of metal–metal interactions in the formation of excited states involving the metal centre, and the steric hindrance of the ancillary ligands in directing such interactions. For **Pt_1** and **Pt_3** the small steric hindrance of chlorine allows a Pt–Pt interaction (already present in solution and more strongly reinforced in the solid), giving rise to an MMLCT excited state in the mesophase. On the contrary, the bulky benzoate group of **Pt_2** and **Pt_4** does not allow a Pt–Pt interaction, whereas weak π–π interactions on the tpy ligands give rise to the formation of excimers, similarly to the solution.

Instead, in the case of a closed-shell metal such as zinc, the excited states are typically located on the ligand, so any variation of the intermolecular interactions (different in solutions rather than in the various condensed phases), which modifies the distances between the ligands of neighbouring complexes, entails a variation of the emission wavelength.

Finally, the presence of a metal centre, providing the optical properties tuning, requires great attention during molecular design, as the excited electronic states responsible for the luminescence can be modified by the supramolecular interactions that occur in the mesophase. The gallate unit, although beneficial for inducing room-temperature mesomorphism for both metal centres, is detrimental for the luminescence of the Pt^{II} complexes, whereas it is more favourable for the synthesis of luminescent Zn^{II} complexes. However, whereas in solution the **Zn_2** complex is a good emitter, in columnar mesomorphic organisation its luminescence decreases. The great sensitivity of the metal centre with respect to its molecular environment

© 2020 Wiley-VCH Verlag GmbH & Co. KGaA, Weinheim

15213765, 2020, 21, Downloaded from https://chemistry-europe.onlinelibrary.wiley.com/doi/10.1002/chem.202000124 by Universita Della Calabria Sist. Wiley Online Library on [26/04/2023]. See the Terms and Conditions (https://onlinelibrary.wiley.com/terms-and-conditions) on Wiley Online Library for rules of use; OA articles are governed by the applicable Creative Commons License

15213765, 2020, 21, Downloaded from https://chemistry-europe.onlinelibrary.wiley.com/doi/10.1002/chem.202000124 by Universita Della Calabria Sist. Wiley Online Library on [26/04/2023]. See the Terms and Conditions (https://onlinelibrary.wiley.com/terms-and-conditions) on Wiley Online Library for rules of use; OA articles are governed by the applicable Creative Commons License

is a potentially good property, which will be further exploited in sensing applications.

Acknowledgements

This research was partially supported by Regione Calabria (POR Calabria FESR 2014/2020-Azione 1.2.2) through the MERAVIGLIE project. M.L.D. and G.D.M. are grateful to Dr. Angela Candreva for her collaboration in spectral acquisition. We thank the Pohang Accelerator Laboratory (PAL) for giving us the opportunity to perform the GIWAXS measurements, MEST and POSTECH for supporting these experiments, Dr. Hyungju Ahn for adjustments and help, and other colleagues from the 9A USAXS beamline for assistance. E.V., B.D. and B.H. thank the CNRS and University of Strasbourg for support. A.A.A., M.A.S., E.I.Sz. and O.C. acknowledge the Romanian Academy, Program 4. A.A.A. is grateful for an "Ion Heliade Radulescu" mobility scholarship.

Conflict of interest

The authors declare no conflict of interest.

Keywords: columnar mesophases · luminescent metallomesogens · photophysics · Pt^{II} and Zn^{II} coordination complexes · X-ray scattering

[1] D. Pucci, B. Donnio, *Handbook of Liquid Crystals: Metal-Containing Liquid Crystals, Vol. 5: Non-Conventional, Supramolecular, Chromonic and Amphiphilic Liquid Crystals* (Eds.: J. W. Goodby, P. J. Collings, T. Kato, C. Tschierske, H. Gleeson, P. Raynes), Wiley-VCH, Weinheim, **2014**, ISBN: 9783527671403.
[2] Y. Wang, J. Shi, J. Chen, W. Zhu, E. Baranoff, *J. Mater. Chem. C* **2015**, *3*, 7993 – 8005.
[3] X. Yang, X. Wu, D. Zhou, J. Yu, G. Xie, D. W. Bruce, Y. Wang, *Dalton Trans.* **2018**, *47*, 13368 – 13377.
[4] X. Wu, G. Xie, C. P. Cabry, X. Xu, S. J. Cowling, D. W. Bruce, W. Zhu, E. Baranoff, Y. Wang, *J. Mater. Chem. C* **2018**, *6*, 3298 – 3309.
[5] C. Cuerva, J. A. Campo, M. Cano, C. Lodeiro, *Chem. Eur. J.* **2016**, *22*, 10168 – 10178.
[6] C. Cuerva, J. A. Campo, M. Cano, M. Caño-García, J. M. Otón, C. Lodeiro, *Dyes Pigm.* **2020**, *175*, 108098.
[7] A. Kishimura, T. Yamashita, K. Yamaguchi, T. Aida, *Nat. Mater.* **2005**, *4*, 546 – 549.
[8] Y. Wang, C. P. Cabry, M. Xiao, L. Male, S. J. Cowling, D. W. Bruce, J. Shi, W. Zhu, E. Baranoff, *Chem. Eur. J.* **2016**, *22*, 1618 – 1621.
[9] X. Wu, M. Zhu, D. W. Bruce, W. Zhu, Y. Wang, *J. Mater. Chem. C* **2018**, *6*, 9848 – 9860.
[10] A. M. Prokhorov, A. Santoro, J. A. G. Williams, D. W. Bruce, *Angew. Chem. Int. Ed.* **2012**, *51*, 95 – 98; *Angew. Chem.* **2012**, *124*, 99 – 102.
[11] A. Santoro, A. M. Prokhorov, V. N. Kozhevnikov, A. C. Whitwood, B. Donnio, J. A. Williams, D. W. Bruce, *J. Am. Chem. Soc.* **2011**, *133*, 5248 – 5251.
[12] N. S. S. Kumar, M. Z. Shafikov, A. C. Whitwood, B. Donnio, P. B. Karadakov, V. N. Kozhevnikov, D. W. Bruce, *Chem. Eur. J.* **2016**, *22*, 8215 – 8233.
[13] R. Bayón, S. Coco, P. Espinet, *Chem. Eur. J.* **2005**, *11*, 1079 – 1085.
[14] K. Fujisawa, N. Kawakami, Y. Onishi, Y. Izumi, S. Tamai, N. Sugimoto, O. Tsutsumi, *J. Mater. Chem. C* **2013**, *1*, 5359 – 5366.
[15] K. Fujisawa, Y. Okuda, Y. Izumi, A. Nagamatsu, Y. Rokusha, Y. Sadaike, O. Tsutsumi, *J. Mater. Chem. C* **2014**, *2*, 3549 – 3555.
[16] J. Barberá, I. Lantero, S. Moyano, J. L. Serrano, A. Elduque, R. Giménez, *Chem. Eur. J.* **2010**, *16*, 14545 – 14553.
[17] E. Cavero, S. Uriel, P. Romero, J. L. Serrano, R. Giménez, *J. Am. Chem. Soc.* **2007**, *129*, 11608 – 11618.
[18] M. Iliş, M. Micutz, V. Cîrcu, *J. Organomet. Chem.* **2017**, *836 – 837*, 81 – 89.
[19] M. Iliş, D. Batalu, I. Pasuk, V. Cîrcu, *J. Mol. Liq.* **2017**, *233*, 45 – 51.
[20] M. Micutz, M. Iliş, T. Staicu, F. Dumitraşcu, I. Pasuk, Y. Molard, T. Roisnel, V. Cîrcu, *Dalton Trans.* **2014**, *43*, 1151 – 1161.
[21] M. J. Mayoral, P. Ovejero, J. A. Campo, J. V. Heras, E. Pinilla, M. R. Torres, C. Lodeiro, M. Cano, *Dalton Trans.* **2008**, 6912 – 6924.
[22] M. J. Mayoral, P. Ovejero, J. A. Campo, J. V. Heras, M. R. Torres, C. Lodeiro, M. Cano, *New J. Chem.* **2010**, *34*, 2766 – 2776.
[23] D. Pucci, A. Bellusci, A. Crispini, M. Ghedini, N. Godbert, E. I. Szerb, A. M. Talarico, *J. Mater. Chem.* **2009**, *19*, 7643 – 7649.
[24] D. Pucci, G. Barberio, A. Bellusci, A. Crispini, B. Donnio, L. Giorgini, M. Ghedini, M. La Deda, E. I. Szerb, *Chem. Eur. J.* **2006**, *12*, 6738 – 6747.
[25] D. Pucci, G. Barberio, A. Bellusci, A. Crispini, M. La Deda, M. Ghedini, E. I. Szerb, *Eur. J. Inorg. Chem.* **2005**, 2457 – 2463.
[26] D. Pucci, A. Crispini, M. Ghedini, E. I. Szerb, M. La Deda, *Dalton Trans.* **2011**, *40*, 4614 – 4622.
[27] E. I. Szerb, A. M. Talarico, I. Aiello, A. Crispini, N. Godbert, D. Pucci, T. Pugliese, M. Ghedini, *Eur. J. Inorg. Chem.* **2010**, 3270 – 3277.
[28] D. Pucci, I. Aiello, A. Bellusci, A. Crispini, M. Ghedini, M. La Deda, *Eur. J. Inorg. Chem.* **2009**, 4274 – 4281.
[29] D. Pucci, A. Crispini, M. Ghedini, M. La Deda, P. F. Liguori, C. Pettinari, E. I. Szerb, *RSC Adv.* **2012**, *2*, 9071 – 9078.
[30] F. Camerel, R. Ziessel, B. Donnio, C. Bourgogne, D. Guillon, M. Schmutz, C. Iacovita, J.-P. Bucher, *Angew. Chem. Int. Ed.* **2007**, *46*, 2659 – 2662; *Angew. Chem.* **2007**, *119*, 2713 – 2716.
[31] A. Y.-Y. Tam, K. M.-C. Wong, G. Wang, V. W.-W. Yam, *Chem. Commun.* **2007**, 2028 – 2030.
[32] A. Y.-Y. Tam, V. W.-W. Yam, *Chem. Soc. Rev.* **2013**, *42*, 1540 – 1567.
[33] Y. Chen, C.-M. Che, W. Lu, *Chem. Commun.* **2015**, *51*, 5371 – 5374.
[34] K. Li, G. S. M. Tong, Q. Wan, G. Cheng, W.-Y. Tong, W.-H. Ang, W.-L. Kwong, C.-M. Che, *Chem. Sci.* **2016**, *7*, 1653 – 1673.
[35] Y. J. Yadav, B. Heinrich, G. De Luca, A. M. Talarico, T. F. Mastropietro, M. Ghedini, B. Donnio, E. I. Szerb, *Adv. Opt. Mater.* **2013**, *1*, 844 – 854.
[36] C. Oliviero Rossi, C. Cretu, L. Ricciardi, A. Candreva, M. La Deda, I. Aiello, M. Ghedini, E. I. Szerb, *Liq. Cryst.* **2017**, *44*, 880 – 888.
[37] C. Cretu, A. A. Andelescu, A. Candreva, A. Crispini, E. I. Szerb, M. La Deda, *J. Mater. Chem. C* **2018**, *6*, 10073 – 10082.
[38] U. S. Schubert, S. Schmatloch, A. Precup, *Des. Monomers Polym.* **2002**, *5*, 211 – 221.
[39] X. Yao, X. Zeng, M. Xue, L. Cseh, Y. Liu, G. Ungar, *Nanoscale Horiz.* **2017**, *2*, 43 – 49.
[40] G. Annibale, M. Brandolisio, B. Pitteri, *Polyhedron* **1995**, *14*, 451 – 453.
[41] E. I. Szerb, D. Pucci, A. Crispini, M. La Deda, *Mol. Cryst. Liq. Cryst.* **2013**, *573*, 34 – 45.
[42] C. J. Whiteoak, G. Salassa, A. W. Kleij, *Chem. Soc. Rev.* **2012**, *41*, 622 – 631.
[43] S. Chakraborty, P. Mondal, S. K. Prasad, D. S. S. Rao, C. R. Bhattacharjee, *J. Mol. Liq.* **2017**, *246*, 290 – 301.
[44] B. A. Gregg, M. A. Fox, A. J. Bard, *J. Chem. Soc. Chem. Commun.* **1987**, 1134 – 1135.
[45] W. J. Geary, *Coord. Chem. Rev.* **1971**, *7*, 81 – 122.
[46] G. B. Deacon, R. J. Phillips, *Coord. Chem. Rev.* **1980**, *33*, 227 – 250.
[47] D. Myśliwiec, B. Donnio, P. J. Chmielewski, B. Heinrich, M. Stępień, *J. Am. Chem. Soc.* **2012**, *134*, 4822 – 4833.
[48] D. E. C. Corbridge, E. G. Cox, *J. Chem. Soc.* **1956**, 594 – 603.
[49] The Cambridge Structural Database. V. Phillips, F. G. Baddour, T. Lasanta, J. M. Lopez-de-Luzuriaga, J. W. Bacon, J. A. Golen, A. L. Rheingold, L. H. Doerrer, *Inorg. Chim. Acta* **2010**, *364*, 195 – 204.
[50] The Cambridge Structural Database. J. Zhao, I. A. Khan, F. R. Fronczek, *Acta Crystallogr. Sect. E* **2011**, *67*, o316 – o317.
[51] J. A. Bailey, M. G. Hill, R. E. Marsh, V. M. Miskowski, W. P. Schaefer, H. B. Gray, *Inorg. Chem.* **1995**, *34*, 4591 – 4599.
[52] V. W.-W. Yam, K. M.-C. Wong, N. Zhu, *J. Am. Chem. Soc.* **2002**, *124*, 6506 – 6507.
[53] S. C. F. Kui, Y.-C. Law, G. S. M. Tong, W. Lu, M.-Y. Yuen, C.-M. Che, *Chem. Sci.* **2011**, *2*, 221 – 228.
[54] G. Arena, G. Calogero, S. Campagna, L. Monsú Scolaro, V. Ricevuto, R. Romeo, *Inorg. Chem.* **1998**, *37*, 2763 – 2769.
[55] X. Chen, Q. Zhou, Y. Cheng, Y. Geng, D. Ma, Z. Xie, L. Wang, *J. Lumin.* **2007**, *126*, 81 – 90.
[56] W. Goodall, J. A. G. Williams, *Chem. Commun.* **2001**, 2514 – 2515.

© 2020 Wiley-VCH Verlag GmbH & Co. KGaA, Weinheim

[57] K. F. Bowes, I. P. Clark, J. M. Cole, M. Gourlay, A. M. E. Griffin, M. F. Mahon, L. Ooi, A. W.Parker, P. R. Raithby, H. A. Sparkes, M. Towrie, CCDC 263509: Experimental Crystal Structure Determination **2005**, https://doi.org/10.5517/cc8v69l.

Manuscript received: January 10, 2020
Accepted manuscript online: February 17, 2020
Version of record online: March 20, 2020

© 2020 Wiley-VCH Verlag GmbH & Co. KGaA, Weinheim

15213765, 2020, 21, Downloaded from https://chemistry-europe.onlinelibrary.wiley.com/doi/10.1002/chem.202000124 by Universita Della Calabria Sist. Wiley Online Library on [26/04/2023]. See the Terms and Conditions (https://onlinelibrary.wiley.com/terms-and-conditions) on Wiley Online Library for rules of use; OA articles are governed by the applicable Creative Commons License

Soft Matter

COMMUNICATION

View Article Online
View Journal | View Issue

Published on 26 November 2020. Downloaded by University of California - Santa Barbara on 5/16/2021 8:47:19 AM.

Check for updates

Cite this: *Soft Matter*, 2020, **16**, 10865

Received 14th November 2020,
Accepted 25th November 2020

DOI: 10.1039/d0sm02024a

rsc.li/soft-matter-journal

A quick one-step synthesis of luminescent gold nanospheres†

Angela Candreva,[ab] Giuseppe Di Maio[a] and Massimo La Deda *[ab]

Gold nanospheres, coated with luminescent molecules (1-pyrenemethylamine hydrochloride, fluorescein isothiocyanate or cresyl violet perchlorate), have been synthesized and purified by a fast one-step procedure. Luminescent nanoparticles have been obtained, in which the match of the plasmonic and emissive properties gives nanosized fluorophores useful in different application fields.

Gold nanoparticles (AuNPs) are routinely used or being evaluated in biomedical,[1] energy and electronic applications[2] due to their exceptional and useful optical properties deriving from localized-surface plasmon resonance,[3] which is related to their shape, size and metal–dielectric interface. Generally, the dielectric medium around metal NP coincides with the solvent in which it is dispersed; in fact, although the NPs are necessarily functionalized with a coating agent which avoids their coalescence, this agent forms a layer so thin that the refractive index of the dielectric surrounding the metallic NP practically coincides with that of the solvent in which it is dispersed. However, the coating agent has a capital importance in favouring or not the solubility of the AuNP in a given medium, thereby contributing to determining the plasmon properties. Moreover, the medium in which AuNPs are dispersed can induce self-assembly,[4] which in turn modifies their optical response.[5] In particular, an organized medium (*e.g.* liquid-crystals or mesoporous materials) can affect their assembling route.[6,7]

Nanoparticles can be obtained from larger pieces of matter following a "top–down" method[8] or by a "bottom–up" strategy through nucleating and growing particles from molecular or atomic sized precursors in a liquid or vapour phase. The most common procedure of AuNP synthesis is based on the chemical reduction of Au^{3+} ions in solution by an organic or inorganic reductant (such as sodium borohydride, sodium citrate, ascorbate, *N*,*N*-dimethylformamide) with a coating agent (generally a surfactant such as cetyl trimethylammonium bromide, CTAB).[9] As briefly mentioned above, the coating agent has a crucial role in the nanoparticle synthesis, because it stabilizes nanoparticles in the colloidal solution, guiding their shape and size in the growing step, and avoiding their merging and eventual precipitation. After synthesis, the coating agent can be replaced by other molecules so as to allow, for example, the transfer of nanoparticles from a polar to a non-polar phase (or *vice versa*) by exchanging a hydrophilic coater with a hydrophobic one (and *vice versa*).[10] Obviously, the coating agent exchange increases the time and cost of the synthetic procedure. Nevertheless, the coating agent can have a relevant role in AuNP applications:[11] it can transform a nanoparticle in an ideal multifunctional platform combining its optical and chemical properties with the intrinsic ones of the AuNPs. For example, biological molecules can be bonded to the nanoparticle surface replacing, flanking or conjugating to the original coating agent. The functionalization of the gold surface with luminescent molecules allows tracking of the nanoparticle kinetics in biological fluids: various luminescent molecules have been used to functionalize the gold surface, suggesting an important role in diagnosis and therapy.[12–14] In this perspective, it is advantageous to manage luminescent AuNPs in order to easily recognize them by means of fluorescence techniques in the medium in which they are dispersed.

Here we propose a fast way to obtain, by a versatile and cheap one-step synthesis, gold nanospheres (AuNSs) luminescent in a wide range of the visible spectrum. In particular, gold nanoparticles with different luminescent coating agents (1-pyrenemethylamine hydrochloride, PyAm, fluorescein isothiocyanate, FluoThio, and cresyl violet perchlorate, CryV; see Chart 1) have been prepared. All samples have been morphologically characterized by TEM and their photophysical properties have been recorded.

AuNSs synthesis was performed in an aqueous environment; three water solutions have been prepared, each containing one of the selected covering agents. The metallic precursor, $HAuCl_4$, and an inorganic reductant agent, $NaBH_4$, have been sequentially

[a] *Department of Chemistry and Chemical Technologies, University of Calabria, 87036 Rende (CS), Italy. E-mail: massimo.ladeda@unical.it*
[b] *CNR-NANOTEC, Istituto di Nanotecnologia U.O.S, Cosenza, 87036 Rende (CS), Italy*

† Electronic supplementary information (ESI) available. See DOI: 10.1039/d0sm02024a

Published on 26 November 2020. Downloaded by University of California - Santa Barbara on 5/16/2021 8:47:19 AM.

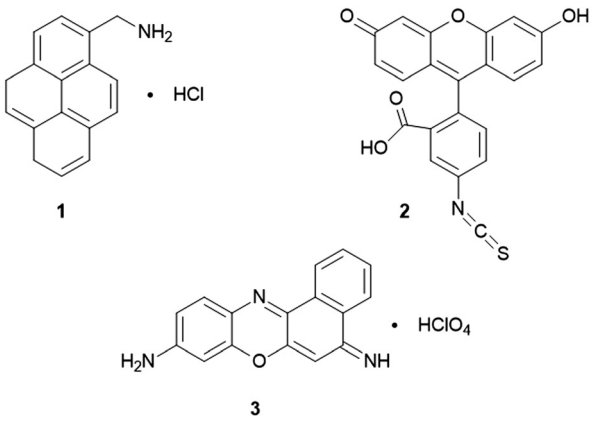

Chart 1 Molecular structures of the luminescent coating agents: (1) 1-pyrenemethylamine hydrochloride; (2) fluorescein isothiocyanate; (3) cresyl violet perchlorate.

added a few minutes from each other, under stirring, at room temperature. Instantaneously, the solutions change their colour following the Au^{3+} reduction and the consequent formation of the nanospheres, which is confirmed by TEM measurement. According to the covering agent, the synthetic procedures and purification are reported below.

AuNSs covered by 1-pyrenemethylamine hydrochloride, PyAm@AuNS

1.4 mg of 1-pyrenemethylamine hydrochloride 94% (Sigma Aldrich) was added to 20 mL of distilled water; after complete solubilisation, 20 μL of $HAuCl_4 \cdot 3H_2O$ 99.9% (Sigma Aldrich) water solution (50 mM) was added under mild stirring; 500 μL of $NaBH_4$ (Sigma Aldrich) water solution (100 mM) was added instantaneously and under vigorous stirring. Immediately, the solution became brown-violet, owing to the formation of nanoparticles, which precipitate in a few minutes on the vial bottom. To eliminate the excess of the reagents, in particular the unreacted PyAm, the pellet was washed with distilled water three times, dried and then dispersed in $CHCl_3$.

AuNSs covered by fluorescein isothiocyanate, FluoThio@AuNS

1.0 mg of fluorescein isothiocyanate (Sigma Aldrich) was added to 20 mL of distilled water. The procedure, reagents and their quantities are identical to those illustrated above. Even in this case, when the Au^{3+} reduction takes place, the solution changes its colour from green to brown, but, in a few minutes, it became again green, without the formation of any precipitate. Indeed, unlike 1-pyrenemethylamine hydrochloride, the fluorescein isothiocyanate stabilizes the formed nanospheres in water. Therefore, to completely remove the unreacted species, 50 μL of a 0.015 M water solution of *O*-(2-mercaptoethyl)-O′-methylpolyethylene glycol, PEG-SH (MA 2000, Sigma Aldrich), was added to the nanosphere sample. The presence of the thiol group allows PEG-SH to bind the AuNS surface, without removing the fluorescein molecules already present on it (see below): in this way the NSs with the two coating agents are soluble both in water and chloroform. Successively, the sample was dried and dispersed in chloroform, while free fluorescein isothiocyanate, poorly soluble in chloroform, was easily removed by centrifugation.

AuNSs covered by cresyl violet perchlorate, CryV@AuNS

1.2 mg of cresyl violet perchlorate (Sigma Aldrich) was added to 20 mL of distilled water. The procedure, reagents and their quantities are identical to those illustrated above. Just after the gold reduction, the solution changes its colour from violet to brown, but in a few minutes, it became violet again, and the nanospheres start to flocculate on the vial bottom. The pellet was washed with water three times before adding chloroform to the aqueous dispersion of nanoparticles. By vigorous stirring, the nanoparticles were transferred from water to chloroform: the water solution maintains the violet colour of the unreacted cresyl violet perchlorate, while the organic phase becomes yellow-orange, due to the nanosphere migration, and finally purified by free cresyl violet perchlorate, insoluble in chloroform.

TEM images (Fig. 1) show the obtained nanoparticles with an average size of 5 nm (see the ESI,† for the instrumental TEM description), while the size distribution was determined by DLS mesurements (Fig. S1 in the ESI†), confirming a good monodispersity of the three nanoparticle samples.

The three chloroform samples were analysed by optical spectroscopy, and their emission spectra and excited-state lifetimes compared with those of the free coating agent (see the ESI,† for the photophysical methods and apparatus description). The experimental results are compiled in Table 1. All nanoparticle samples are fluorescents and very stable in solution; TEM images and photophysical data were collected from the freshly prepared solutions and after one month, and the results obtained were identical. Furthermore, since as will be seen from the following discussion, it is important to ensure that the fluorophores grafted on the nanoparticle surface remain chemically unaltered, the reducing agent $NaBH_4$ was added to the free fluorophore solutions; it was thus possible to verify that no reaction occurs which could have modified the three chromophores.

Fig. 2 reports the emission spectrum of PyAm@AuNS in chloroform, while Fig. S2 in the ESI,† shows its absorption spectrum and the absorption and emission spectra of PyAm.

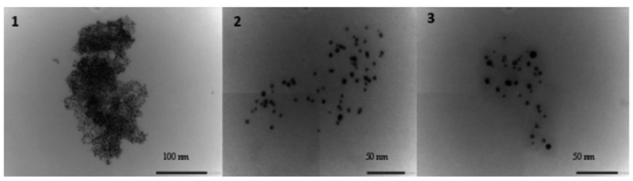

Fig. 1 TEM image of PyAm@AuNS (1), FluoThio@AuNS (2) and CryV@AuNS (3).

 This journal is © The Royal Society of Chemistry 2020

Published on 26 November 2020. Downloaded by University of California - Santa Barbara on 5/16/2021 8:47:19 AM.

Table 1 Photophysical properties of the coated AuNSs compared with those of the free fluorophores

Sample	Solvent	λ_{em} (nm)	Lifetime (ns)	PLQY
PyAm	$CHCl_3$	377,397,417	19.7	10%
PyAm@AuNS	$CHCl_3$	387,405,426	5.9	18%
FluoThio	H_2O	550	21.0	65%
FluoThio@AuNS	$CHCl_3$	550	1.5	15%
CryV	H_2O	629	3.0	31%
CryV@AuNS	$CHCl_3$	575	1.5	66%

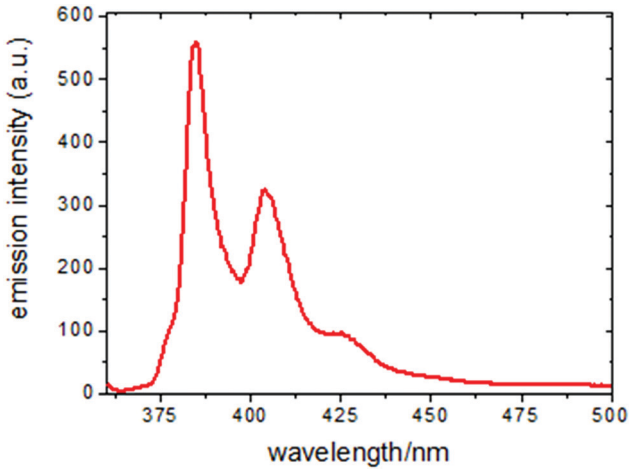

Fig. 2 Emission spectrum of PyAm@AuNS in chloroform solution (λ_{ex} = 330 nm).

The fluorescence spectrum shape of PyAm@AuNS is the same as that of the free PyAm, but the bands are red-shifted, showing two intense peaks at 387 and 405 nm, and a low-intensity one at 426 nm, as observed for other similar systems.[11] In addition, the lifetime of PyAm@AuNS is shorter with respect to that of the free pyrenemethylamine (5.9 ns and 19.7 ns, respectively). Photoluminescence quantum yield (PLQY) of the nanoparticles is increased with respect to the value of the free chromophore, going from 10% to 18% (Table 1).

Fluorescein and its derivatives are well known emitters;[15] the emission spectrum of FluoThio in chloroform (see Fig. S3 in the ESI†) shows an asymmetric band with a maximum at 550 nm; the emission spectrum of FluoThio@AuNS (Fig. 3) appears unvaried with respect to that of the chromophore. As mentioned above, fluorescein isothiocyanate is poorly soluble in chloroform, thus making it impossible to collect a reliable lifetime and PLQY value in this solvent. Therefore in Table 1 the values relating to the free chromophore are reported in water, while those of the nanoparticles are referred to a chloroform solution. The lifetime of the free fluorophore is 21.0 ns, which is reduced at 1.5 ns when the fluorophore is bonded to the gold nanoparticles. The PLQY which has the considerable value of 65% for FluoThio, is reduced to 15% for FluoThio@AuNS.

The comparison between the spectra of free CryV with CryV@AuNS is affected by the different solvents of the two samples. Fig. S4 in the ESI,† reports the absorption and

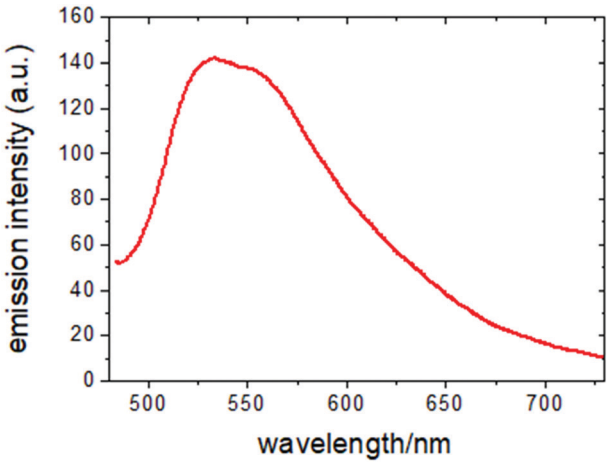

Fig. 3 Emission spectrum of FluoThio@AuNS in chloroform solution (λ_{ex} = 458 nm).

emission spectra of CryV in water solution and the absorption spectrum of CryV@AuNS in chloroform solution. The emission band of CryV@AuNS (in chloroform) is more blue-shifted than that of free CryV, with a maximum at 575 nm (Fig. 4). The lifetime of free CryV in water is 3.0 ns, while the lifetime of CryV@AuNS in chloroform is 1.5 ns. The PLQY of free CryV in water is 31%, while the PLQY of CryV@AuNS in chloroform is 66% (Table 1).

All solutions of chromophore-coated nanoparticles show different photophysical properties compared to the isolated chromophore, but these differences are attributable to at least two phenomena.[16] In fact, in the case of PyAm@AuNS and CryV@AuNS the effect of the binding of the chromophore to AuNS involves an increase in PLQY and a decrease in the lifetime (accompanied by a variation of the emission spectrum). On the other hand, in the case of FluoThio@AuNS, the binding effect of the chromophore to AuNS leads to a decrease in the PLQY and lifetime (while the emission spectrum remains unchanged). If we compare the emission spectra of the three chromophores, we note that only the FluoThio spectrum

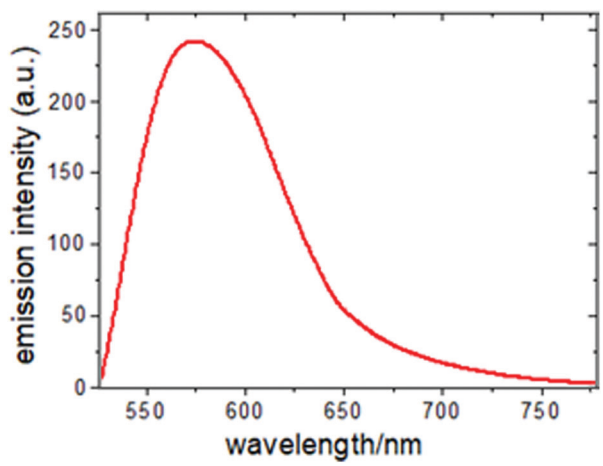

Fig. 4 Emission spectrum of CryV@AuNS in chloroform solution (λ_{ex} = 450).

Published on 26 November 2020. Downloaded by University of California - Santa Barbara on 5/16/2021 8:47:19 AM.

overlaps the spectral range of the AuNS plasmon;[17] this allows an energy transfer process[18] from the chromophore to the plasmon, and consequently a reduction in the PLQY and lifetime values, without changing the shape and position of the emission spectrum. Instead, in the case of PyAm and CryV, the emission spectra do not overlap with gold plasmons, and the effects observed following the binding on AuNSs (increase in PLQY, decrease in lifetime, variation of the emission spectrum) are attributable to metal-enahnced fluorescence.[11,19,20]

Conclusions

Nanoparticles are versatile materials and, slightly modifying the synthetic protocol, it is possible to set their properties. In particular, the interaction of gold nanoparticles with light has given rise to their wide use in various fields, from photogeneration devices to medicine, *i.e.* in photothermal and photodynamic therapy. Therefore, the possibility of making gold nanoparticles luminescent, so as to be able to topologically identify them using fluorescence microscopy, is of great interest.

A one-step synthetic protocol has been proposed to quickly obtain luminescent gold nanoparticles, avoiding the coating exchange reaction. We have presented three examples of gold nanoparticles emissive in a wide spectral range to demonstrate the simplicity and versatility of the synthesis, in order to expand the use of nanomaterials in current technological applications.

Unlike sodium citrate or CTAB, which coat the gold core by weak electrostatic interactions, the three molecules used are bonded to the gold surface by strong covalent bonds, formed through the amino group of 1-pyrenemethylamine hydrochloride and cresyl violet perchlorate, and the isothiocyanate group of fluorescein isothiocyanate. This implies the robustness of the nanoparticle system, which allows them to be purified completely. Furthermore, the one-step procedure makes it possible to avoid the presence of templating agents, such as CTAB, which make purification difficult.

Conflicts of interest

There are no conflicts to declare.

Acknowledgements

The authors are grateful to Dr Ida Perrotta of the Centre for Microscopy and Microanalysis (CM2) (Department of Biology, Ecology and Earth Sciences, University of Calabria, Italy) for TEM images. This research was supported by the project MERAVIGLIE (POR Calabria, FESR 2014–2020-Azione 1.2.2).

Notes and references

1 N. Elahia, M. Kamalia and M. Hadi Baghersad, *Talanta*, 2018, **184**, 537–556.
2 S. E. Lohse and C. J. Murphy, *J. Am. Chem. Soc.*, 2012, **134**, 15607–15620.
3 E. Hutter and J. H. Fendler, *Adv. Mater.*, 2004, **16**, 1685–1706.
4 M. Grzelczak, J. Vermant, E. M. Furst and L. M. Liz-Marzán, *ACS Nano*, 2010, **4**, 3591–3605.
5 P. K. Jain, S. Eustis and M. A. El-Sayed, *J. Phys. Chem. B*, 2006, **110**, 18243–18253.
6 C. Hanske, E. H. Hill, D. Vila-Liarte, G. González-Rubio, C. Matricardi, A. Mihi and L. M. Liz-Marzán, *ACS Appl. Mater. Interfaces*, 2019, **11**, 11763–11771.
7 M. Tebbe, M. Mayer, B. A. Glatz, C. Hanske, P. T. Probst, M. B. Müller, M. Karg, M. Chanana, T. A. F. König, C. Kuttner and A. Fery, *Faraday Discuss.*, 2015, **181**, 243–260.
8 V. Amendola, S. Polizzi and M. Meneghetti, *J. Phys. Chem. B*, 2006, **110**, 7232–7237.
9 N. R. Jana, L. Gearheart and C. J. Murphy, *Chem. Mater.*, 2001, **13**, 2313–2322.
10 R. A. Sperling and W. J. Parak, *Philos. Trans. R. Soc., A*, 2010, **368**, 1333–1383.
11 G. Battistini, P. G. Cozzi, J.-P. Jalkanen, M. Montalti, L. Prodi, N. Zaccheroni and F. Zerbetto, *ACS Nano*, 2008, **2**, 77–84.
12 J. Liu, M. Yu, C. Zhou, S. Yang, X. Ning and J. Zheng, *J. Am. Chem. Soc.*, 2013, **135**, 4978–4981.
13 R. K. DeLong, C. M. Reynolds, Y. Malcolm, A. Schaeffer, T. Severs and A. Wanekaya, *Nanotechnol., Sci. Appl.*, 2010, **3**, 53–63.
14 D. Chen, B. Li, S. Cai, P. Wang, S. Peng, Y. Sheng, Y. He, Y. Gu and H. Chen, *Biomaterials*, 2016, **100**, 1–16.
15 R. Sjöback, J. Nygren and M. Kubista, *Spectrochim. Acta, Part A*, 1995, **51**, L7–L21.
16 S. Franzen, J. C. W. Folmer, W. R. Glomm and R. O'Neal, *J. Phys. Chem. A*, 2002, **106**, 6533–6540.
17 N. G. Bastus, J. Comenge and V. Puntes, *Langmuir*, 2011, **27**, 11098.
18 U. S. Raikar, V. B. Tangod, B. M. Mastiholi and V. J. Fulari, *Opt. Commun.*, 2011, **284**, 4761–4765.
19 W. Deng and E. M. Goldys, *Langmuir*, 2012, **28**, 10152–10163.
20 K. Aslan, Z. Leonenko, J. R. Lakowicz and C. D. Geddes, *J. Fluoresc.*, 2005, **15**, 643–654.

 This journal is © The Royal Society of Chemistry 2020

Journal of Materials Chemistry C

ROYAL SOCIETY OF CHEMISTRY

PAPER

View Article Online
View Journal | View Issue

Check for updates

Cite this: J. Mater. Chem. C, 2022, 10, 115

Published on 11 November 2021. Downloaded on 11/19/2022 11:56:28 AM.

Very intense polarized emission in self-assembled room temperature metallomesogens based on Zn(II) coordination complexes: an experimental and computational study†

Massimo La Deda,[a] Giuseppe Di Maio,[a] Angela Candreva,[a] Benoît Heinrich,[b] Adelina-Antonia Andelescu,[c] Evelyn Popa,[c] Emilie Voirin,[b] Valentin Badea,[d] Mario Amati,[e] Otilia Costişor,[c] Bertrand Donnio *[b] and Elisabeta I. Szerb *[c]

Received 20th October 2021,
Accepted 10th November 2021

DOI: 10.1039/d1tc05059a

rsc.li/materials-c

Three room-temperature metallomesogens based on Zn(II) cations pentacoordinated by different chelating *N^N^N* terpyridines and two monodentate gallate co-ligands were designed and synthesized. Depending on the terpyridine ligand's tip functionality, the complexes self-assemble into either a 3D hexagonal mesophase or into a columnar hexagonal mesophase. A systematic study between the structure (molecular architecture, arrangement of the molecules and columns, and chains in both types of mesophases) and photophysical properties (emission maxima and yields, lifetimes of the excited states in the mesophase), correlated with investigations of single molecules in solution, was conducted. Remarkably, one complex exhibited a record quantum yield of 95.0% in solution, while in the mesophase, despite quenching due to the radiative deactivation from the ILCT state, still retained a considerable emission yield of ϕ = 20.2%. The polarized emission of an oriented film, determined for the first time in columnar metallomesogens, shows a dichroic emission ratio ($I_{\parallel}/I_{\perp}$) of 1.30. DFT and TDDFT computational studies confirmed the origin of the observed fluorescence anisotropy from the transition dipole moment oriented along the C_2 symmetry axis of the molecule combined with a high level of order in the 3D mesophase.

Introduction

Liquid crystals with intrinsic light-emitting properties are of great interest because such light-emitting materials may find a large variety of technological applications in various fields, such as OLEDs,[1] chemosensors,[2] optical information storage,[3] and liquid-crystal displays.[4] Despite these thrilling prospects, developing high-performance light-emitting liquid crystals remains a challenging task. Aggregation or self-organization is a spontaneous process in the formation of a mesophase, and incorporating luminophores into mesogens with preservation of both mesomorphism and luminescence properties is highly challenging.

Up to now, several synthetic strategies have been pursued with success to combine liquid crystal properties (*e.g.* anisotropy of the physical properties, fluidity, self-organization, dynamics, self-healing, and stimuli responsiveness) with high emission quantum yield materials. Of special interest here, the use of the unique optical properties of metal ions integrated in metallomesogens (MMs)[5] and lanthanidomesogens,[6] *i.e.* liquid crystalline *d*- and *f*-block metal coordination complexes, respectively, is one of such promising emerging approaches. Initially luminescence in the mesophase for MMs was somehow disregarded, mostly due to their high transition temperatures and poor thermal stabilities. In the last decade, the fine tuning

[a] Department of Chemistry and Chemical Technologies, University of Calabria, Rende 87036, CS, Italy
[b] Institut de Physique et Chimie des Matériaux de Strasbourg (IPCMS), UMR7504, CNRS-Université de Strasbourg, Strasbourg 67034, France. E-mail: bertrand.donnio@ipcms.unistra.fr
[c] "Coriolan Drăgulescu" Institute of Chemistry, Romanian Academy, 24 Mihai Viteazu Bvd, Timisoara 300223, Romania. E-mail: eszerb@acad-icht.tm.edu.ro
[d] Department of Applied Chemistry and Organic and Natural Compounds Engineering, Politehnica University Timisoara, Carol Telbisz 6, Timisoara RO-300001, Romania
[e] Dipartimento di Scienze, Università degli Studi della Basilicata, Campus di Macchia Romana, Potenza 85100, Italy

† Electronic supplementary information (ESI) available: Experimental section, synthesis and characterization, FT-IR spectra of complexes **Zn_1-3**, ^{1}H and ^{13}C NMR spectra of complexes **Zn_1-3**, mass spectra of complexes **Zn_1-3**, TGA traces of precursor complexes **Zn_P1-3** and complexes **Zn_1-3**, DSC traces of complexes **Zn_1-3**, S/WAXS patterns of complexes **Zn_1-3**, photophysical data of complexes **Zn_1-3**, and computational studies. See DOI: 10.1039/d1tc05059a

Published on 11 November 2021. Downloaded on 11/19/2022 11:56:28 AM.

of the molecular structure (nature of the metallic center, nature and functionalities of ligands, the presence of non-innocent counterions for ionic derivatives, *etc.*) to offer the right intermolecular interactions permitted a substantial decrease of the transition temperatures, obtaining low-temperature or even room-temperature MMs based on linearly coordinated Cu(I)[7] or Au(I)[7b,8] and Ag(I),[9] planar Au(III),[10] Pt(II) and Pd(II)[11] or Ni(II), Zn(II), and Cu(II)[12] and even for bulkier coordination geometries like tetrahedral or trigonal bipyramidal Zn(II),[13] Ag(I),[14] Cu(I),[15] octahedral Ir(III),[16] Ru(II)[17] or Rh(II)[18] metal centres.

Mesophase emission is due to either the intrinsic luminescence of the coordination compound, or is induced or enhanced in condensed states as a consequence of aggregation-induced emission (AIE).[19] The latter depends on the supramolecular arrangement or to the restriction of intramolecular motion (RIM),[20] due to high mesophase viscosity. In some cases, the luminescence of the coordination compounds is specifically due to a large pattern of conjugated aromatic rings of the ligands; therefore, the role of the metal is purely structural, as it confers stability to the compound, without modifying the electronic structure of the emissive state. Closed-shell *d*-metal ions, such as Zn(II), are ideal candidates to preserve the intense luminescence of polypyridinate molecules acting as ligands; therefore the challenge is to obtain liquid crystals of such complexes without turning the luminescence off.

Terpyridine (tpy) ligands are suitable for the construction of 2D and 3D programmable ordered "soft" and condensed supramolecular structures when coordinated to transition metals, yielding functional materials that gain interest in several application fields: stimuli responsive and/or self-healing supramolecular gels,[21] photoactive supramolecular architectures for optical devices,[22] MOFs, and catalysts.[23]

Previously we showed that lipophilic gallate could be a versatile unit for inducing liquid crystallinity in *d*-block metal coordination complexes[13b] eliminating several time consuming and money spending complex organic synthesis steps needed to functionalize ligands. Moreover, the presence of the electron donor benzoate group coordinated to a Zn(II) ion was found to considerably increase the emission quantum yield of the complex (24.5%) with respect to its dichloride precursor (6.4%) in solution. However, in condensed states, despite the reduction of non-radiative de-excitation pathways that occurred in the solid phase, a substantial reduction of the quantum yield (7.1%) due to different kinetics of the excited-state was observed. This prompted us to consider differently functionalized tpy ligands to fine-tune both the hexagonal arrangement in the mesophase and the excited state type, correlating changes in photophysical properties as a function of the supramolecular architecture.

Herein we report the synthesis and characterization of three new Zn(II) coordination complexes, **Zn_1-3** represented in Scheme 1, whose liquid crystallinity was induced through the use of two gallate monocoordinating units. The three complexes were mesomorphous over broad temperature ranges, showing a two-dimensional hexagonal columnar mesophase (Col_{hex}) or three-dimensional mesophase made of segmented columns (M_{hex}). Initially, we investigated the influence of the substituents on the liquid crystalline arrangements and on the luminescence, and then the molecular structure – supramolecular structure – photophysical property relationship. Finally, we selected the complex showing the highest emission quantum yield in the mesophase to evaluate the polarized emission. Polarized photoluminescence from a micropatterned film of columnar liquid crystals is rather difficult to observe, as it requires a high degree of orientational control, and furthermore the emission transition dipole moments give rise to a vector composition whose directions are much more difficult to correlate to the director than in classical nematic liquid crystals.[24] The obtained results show that the particular three-dimensional structure of **Zn_2** made it possible to obtain a remarkable emission anisotropy value.

Results and discussion

Synthesis and structural characterization

Complexes **Zn_1-3** were synthesised following a route reported previously[13b] that required prior synthesis of Zn(II) dichloride precursors (**Zn_P1-3** in Scheme 1). All Zn(II) complexes were obtained as white or yellow air stable solids in good yields (70–90%, see –the ESI†). The coordination of the carboxylate in an exclusive unidentate fashion was revealed by the separation of the stretching vibrations of the COO^- group (Δ) of

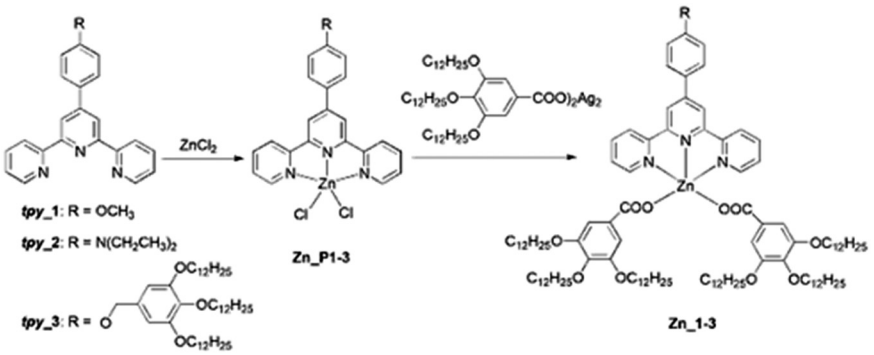

Scheme 1 Synthesis and chemical structure of Zn(II) precursor complexes **Zn_P1-3** and final complexes **Zn_1-3**.

 This journal is © The Royal Society of Chemistry 2022

Published on 11 November 2021. Downloaded on 11/19/2022 11:56:28 AM.

240–320 cm^{-1} (see Fig. S3–S5, ESI†).[13b] The structures and purity of the final Zn(II) complexes were confirmed by elemental analysis, ^{1}H and ^{13}C NMR and MS (see the ESI†).

Mesomorphic properties

The thermal behavior was investigated by polarized optical microscopy (POM), differential scanning calorimetry (DSC) and thermal gravimetric analysis (TGA). The thermal properties are presented in Table 1 and in the ESI† (Fig. S15–S20). Complexes **Zn_1-3** are room temperature liquid crystals with a wide range of mesophase existence.

By POM, complexes **Zn_1-3** show textures where hexagonal arrangement of columns can be envisaged from the occurrence of focal conic or mix mosaic textures (Fig. 1) and to the presence of homeotropic zones. The complete authentication of the mesophases' type was nevertheless unambiguously achieved by S/WAXS (Small- and Wide-Angle X-ray Scattering) and Grazing Incidence Wide-Angle X-Ray Scattering (GIWAXS).

In agreement with the POM observations and S/WAXS analysis (see below), **Zn_1** and **Zn_2** exhibit a three-dimensional mesophase (M_{hex}), and **Zn_3**, a two-dimensional hexagonal columnar mesophase (Col_{hex}). The M_{hex}/Col_{hex} transitions to isotropic liquid phase (Iso) are associated with significant enthalpy change and temperature delay, due to molecular self-assembly into cohesive mesomorphic structures. All complexes show transitions below room temperature to undefined mesomorphic and/or crystalline states (see Fig. S18–S20, ESI†).

S/WAXS patterns are typical of liquid-crystalline phases, with scattering signals arising from liquid-like lateral distances between molecular segments in the wide-angle region (undifferentiated h_{ch} and h_{ar} signals for aliphatic and aromatic parts, respectively, and stacking periodicity of the molecules along the columns, h_{π}) and sharp small-angle reflections from the nanosegregated structure formed by the antagonistic aromatic and aliphatic segments (Fig. 2 and Fig. S21–S23, ESI†).

Complex **Zn_3** self-assembles into columns surrounded by chains and forms a Col_{hex} structure, as evidenced by the semi-broad wide-angle signal h_{π} and the sharp small-angle reflections series (hk) of the hexagonal 2D-lattice. For the M_{hex} phase of **Zn_1** and **Zn_2**, (hk) series become ($hk0$) and coexist with crossed reflections ($hk1$) of a hexagonal 3D-structure resulting from the periodic segmentation of the columns. The geometrical parameters of the mesophases (lattice parameters a and c, cross-sectional areas, ...) are gathered in Table 2, and do not vary much with temperature (see Table 2).

Table 1 Thermal data for Zn(II) complexes **Zn_1-3**

Compound	$T_{dec5\%}$[a] [°C]	Mesophases,[b] transition temperatures (°C) and enthalpies (ΔH [kJ mol^{-1}])[c]
Zn_1	297	M_{hex} 229 [24.5] Iso/Iso 228 [28.0] M_{hex}
Zn_2	301	M_{hex} 188 [19.7] Iso/Iso 187 [25.1] M_{hex}
Zn_3	314	Col_{hex} 164 [19.7] Iso/Iso 167 [19.7] Col_{hex}

[a] Decomposition temperature at 5% weight-loss (from TGA). [b] M_{hex}: three-dimensional mesophase with a two-dimensional hexagonal lattice symmetry (see text), Col_{hex}: two-dimensional columnar hexagonal mesophase. [c] DSC data on the second heating and cooling cycles.

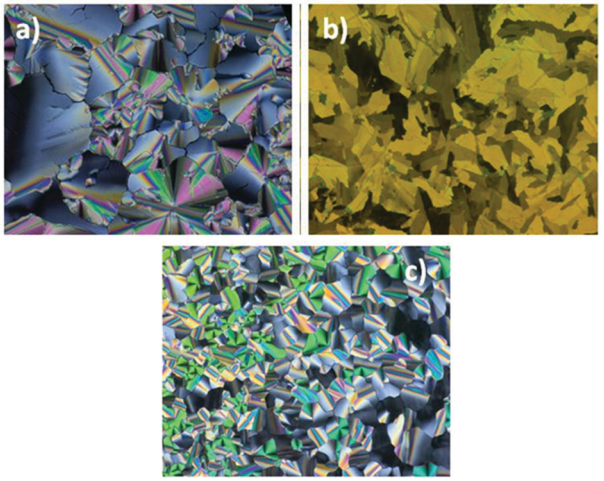

Fig. 1 POM micrographs of the textures developed by complex (a) **Zn_1** on first cooling, 120 °C, magnification 20x; (b) **Zn_2** on first cooling, 50 °C, magnification 10x; (c) **Zn_3** on second cooling, 45 °C, magnification 20x.

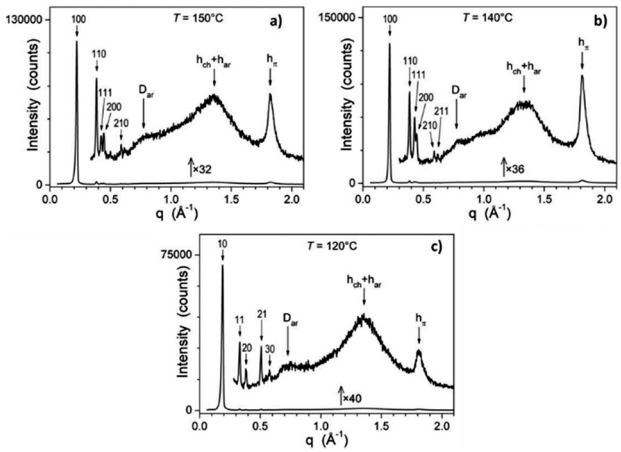

Fig. 2 Indexed S/WAXS patterns of the Zn(II) complexes in the mesophases (T, temperature of the measurement): (a) **Zn_1** (M_{hex}); (b) **Zn_2** (M_{hex}); (c) **Zn_3** (Col_{hex}). Miller indices (hk) and (hkl) of the reflections, h_{ch}, h_{ar} and h_{π} signals arising from aliphatic, aromatic parts, and stacking periodicity, respectively (see the text).

The GIWAXS pattern of **Zn_2** thin film recorded at 20 °C (Fig. 3) complies with a three-dimensional mesophase made of segmented columns of π-stacked complexes, $\boldsymbol{a} \times \boldsymbol{b}$ being the columnar plane and $\boldsymbol{c}$ the direction of stacking. Domains are oriented with the direction of columns parallel to the substrate and random in-plane orientation. Reflections were indexed in a three-dimensional hexagonal lattice. The space group of highest symmetry compatible with the presence of ($hk1$)/($hh1$) reflections and absence of ($h01$)/($0k1$) is $P6_3/mcm$. The space groups of lower symmetry with the same reflection conditions are $P63cm$ and $P6c2$.

The geometry of the complexes can be deduced from single-crystal structures of molecules including the same complex moiety. Thus, structures of several Zn(II) bis-(benzoato)-phenylterpyridine derivatives are available[25] and show irregular

Published on 11 November 2021. Downloaded on 11/19/2022 11:56:28 AM.

Table 2 Geometrical mesophase parameters[a]

Compounds phase	T	V_{mol} ρ	a $A[Z]$	h_{mol} h_π	χ_{ch} A_{core}	M_{hex} c V / Col_{hex} $D_{core,cyl}$ $S_{ZnAr,cyl}$	Z_{mol} $s_{ch,cyl}$ $q_{ch,cyl}$
Zn_1	20	2758	31.44	3.22	0.714	36.40	11.3
M_{hex}		1.06	856[1]	3.36	245	31160	
	50	2817	31.66	3.24	0.715	36.50	11.2
		1.03	868[1]	3.37	248	31640	
	150	3012	32.42	3.31	0.717	35.49	10.7
		0.97	910[1]	3.45	257	32340	
Zn_2	20	2838	31.72	3.26	0.722	33.70	10.4
M_{hex}		1.05	871[1]	3.39	242	29360	
	60	2918	31.95	3.30	0.723	34.35	10.4
		1.02	884[1]	3.41	244	30290	
	140	3080	32.56	3.35	0.725	34.08	10.2
		0.97	918[1]	3.46	252	31290	
Zn_3	20	3862	37.23	3.22	0.754	19.4	21.8
Col_{hex}		1.02	1200[1]	3.38	295	196	1.02
	60	3973	37.58	3.25	0.755	19.5	22.1
		1.00	1223[1]	3.42	297	199	1.01
	120	4141	37.75	3.36	0.756	19.6	22.9
		0.96	1234[1]	3.47	301	206	1.00

[a] T, temperature of the measurement (°C); V_{mol}, molecular volume (Å^3); ρ, density (g cm^{-3}); a, lattice parameter; $A = a^2\sqrt{3}/2$, lattice area (Å^2); Z, number of columns per lattice; $h_{mol} = V_{mol}/A/Z$, molecular slice thickness (Å); h_π, π-stacking distance from the peak position (Å); χ_{ch}, calculated aliphatic volume fraction; $A_{core} = (1 - \chi_{ch}) \times (A/Z)$, cross-sectional area of columnar cores (Å^2). For **Zn_1** and **Zn_2**: c, cell parameter (Å); $V = A \times c$, cell volume (Å^3); $Z_{mol} = V/V_{mol}$, number of molecules per cell. For **Zn_3**: $D_{core,cyl} = \sqrt{(4 \times A_{core}/\pi)}$, core diameter (Å) of equivalent cylinder of cross-sectional area A_{core}; $S_{ZnAr,cyl} = \pi D_{core,cyl} \times h_{mol}$, cylinder surface area per Zn(II) complex (Å^2); $s_{ch,cyl} = S_{ZnAr,cyl}/n_{ch}$, cross-section area per chain (Å^2), n_{ch} being the number of peripheral substituents per molecule ($n_{ch} = 9$ for **Zn_3**); $q_{ch,cyl} = s_{ch,cyl}/\sigma_{ch}$, chain packing ratio for the average cylindrical interface.

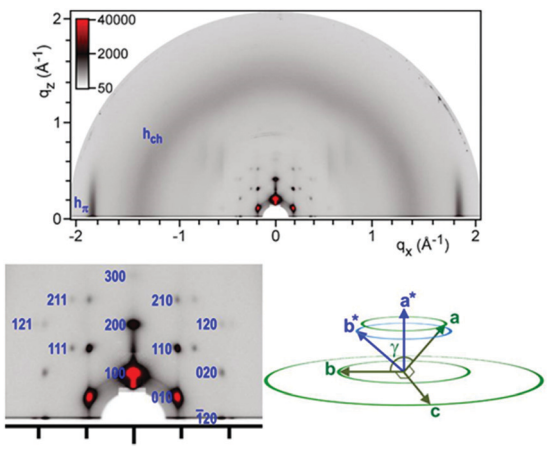

Fig. 3 Top GIWAXS pattern of the **Zn_2** thin film at 20 °C that displays the scattering ring of the molten chain h_{ch}, a π-stacking spot h_π centered on the equator and reflection spots of a large-lattice structure; bottom left: expanded small-range region with indexation of reflections (blue labels on the right of the spots) and bottom right: orientations of cell axes in reciprocal space (blue) and direct space (green).

trigonal bipyramidal geometries, in which both benzoate ligands lie nearly orthogonal to the tpy ring plane.

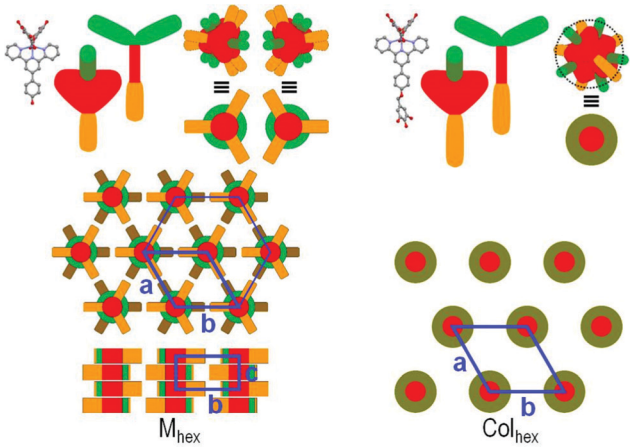

Fig. 4 Left, top: view of the aromatic moiety of **Zn_1**, representations of the molecular architecture and of groups of π-stacked molecules; left, center: supramolecular self-assembly of **Zn_1** and **Zn_2** in the M_{hex} phase: hexagonal arrangement of groups of π-stacked molecules (chains not represented, dark green: groups from the layer below the top layer); left, bottom: superposition of groups of π-stacked molecules into a row of segmented columns. Right, top: view of the aromatic moiety of **Zn_3**, representations of the molecular architecture and of columns of π-stacked complexes surrounded by a shell mixing gallate and benzyloxyphenyl segments; right, bottom: arrangement of columns and chains (not represented) in the Col_{hex} phase.

In **Zn_1** and **Zn_2**, the pattern composition and geometrical parameters indicate that both compounds self-organize through π-stacking of tpy rings into columnar structures (Fig. 4, left). The crowding of the long chains connected only on one side of the cores forces the complexes to stack on top of each other with rotation angles in the order of 120° that equally distribute chains and *R*-benzyloxyphenyl groups around the columnar cores. Consequently, the protruding benzyloxyphenyl moieties confer the shape of a cross with three branches to the cross-section of columns. The columns, disposed at the nodes of the hexagonal lattice, adopt the most compact in-plane arrangement for this shape that consists in directing "crossed branches" toward "cross centers" of neighboring columns. This arrangement by nature follows the hexagonal symmetry but combines the segmentation of columns into smaller subunits. Only three over six neighboring columns are indeed pointed by crossed branches (due to the chains' deficit on one side of the complex) and optimal space-filling presumably requires that pointed and non-pointed columns regularly swap along columnar axes, resulting in segmentation in groups of stacked molecules with inverted orientations. This segmentation defines the $P6_3/mcm$ symmetry of the structure and the periodicity of two groups along the *c*-axis. It is found that the elementary group involves 5.6 **Zn_1** molecules and 5.2 **Zn_2** molecules.

In **Zn_3**, beside the aliphatic chains introduced by the gallate units, three additional peripheral alkyl chains are introduced through the benzyloxyphenyl of the tpy ligand. This implies an expansion of the interface between antagonistic aromatic and alkyl chains segments and the aggregation of aromatic segments into columns surrounded by an aliphatic shell. The characteristic π-stacking signature h_π and the

 This journal is © The Royal Society of Chemistry 2022

Published on 11 November 2021. Downloaded on 11/19/2022 11:56:28 AM.

matching of the stacking distance with the molecular slice thickness h_{mol} further reveal that columnar cores consist of a single molecular strand of randomly orientated π-stacked tpy rings, each strand being located at the nodes of the hexagonal lattice. This strand is decorated with the gallate segments and *R*-benzyloxyphenyl groups of the individual complexes, whose average distances explain the additional broad scattering signals D_{ar} and h_{ar}. This decoration preserves the hexagonal lattice symmetry and the average interface with the aliphatic periphery is therefore a cylinder. Chain packing ratio $q_{ch,cyl}$[26] is close to unity, *i.e.* nearly ideal for an efficient nanosegregation, which improves the cohesion of the structure and obviously contributes to the extended Col_{hex} range.

Photophysics

The photophysical properties of **Zn_1-3** were collected from solutions and mesophase samples. The electronic states pattern is inferred from the spectra collected in diluted dichloromethane solutions (Fig. 5 and Table 3). The absorption band below 280 nm is present in all the complexes and it is due to ligand-centred (LC) transitions on the gallate ligands[13b] (see for example in Fig. S24 (ESI†) a comparison between the **Zn_2** and its dichloride precursor **Zn_P2** absorption spectra). The group of bands between 280 and 325 nm are attributed to charge-transfer (CT) transitions from the gallate to the tpy ligands (see the Computational results section).[13b,27] The band centered at 406 nm, present only in the **Zn_2** spectrum and responsible for the pale-green color of this sample, is due to a strong intraligand charge-transfer (ILCT) from the diethylaniline fragment to the aromatic rings of the tpy (see the Computational results section).[28]

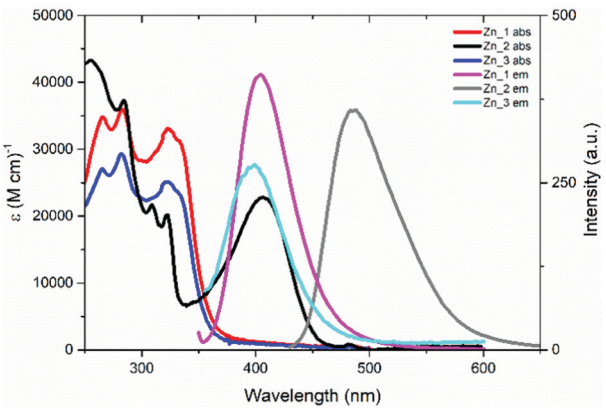

Fig. 5 Absorption and emission spectra of **Zn_1-3** in diluted dichloromethane solution at room temperature ([**Zn_1**] = 4.3 × 10^{-6} M; [**Zn_2**] = [**Zn_3**] = 3.6 × 10^{-6} M). Excitation wavelength: 333 nm for **Zn_1** and **Zn_3**; 410 nm for **Zn_2**.

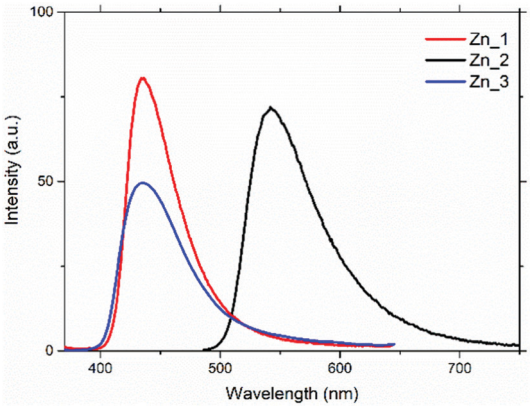

Fig. 6 Emission spectra of the samples in the mesophase at room temperature. Excitation wavelength: 340 nm for **Zn_1** and **Zn_3**; 450 nm for **Zn_2**.

Fluorescence emission was registered for all samples. The emission from the CT excited state, observed for **Zn_1** and **Zn_3** at 405 and 400 nm, respectively, is weak, providing an emission quantum yield (ϕ) value of 6.5 and 0.5%, respectively. Interestingly, the fluorescence originated from the ILCT excited state in **Zn_2** (centered at 488 nm) reaches the outstanding ϕ-value of 95%. The decay from the excited state follows a first order kinetic for all samples, with lifetime values between 2.0 and 4.2 ns (see Table 3).

The effect of temperature variation on the photophysical properties of **Zn_1-3** in the mesophase is reported in Tables S1–S3 (ESI†). The reported data clearly show that after the first heating cycle, the values of the emission maximum and of the quantum yield have a little dependence on the temperature. In particular, the emission maximum wavelength remains fixed, throughout a wide temperature range (30–180 °C), while the emission quantum yield value, as expected, decreases with increasing temperature, due to the rise of non-radiative deactivation. This behaviour suggests that the temperature does not have a direct effect on the emission, but it depends on the supramolecular organization. For this reason, it is worth comparing the photophysical data of the mesophase and solutions at room temperature. Emission spectra recorded from mesophase samples at room temperature (Fig. 6 and Table 4) have the same structure as those collected in solution. All suffer a red-shift with respect to the solutions, showing peaks at 435 nm for **Zn_1** (+30 nm) and **Zn_3** (+35 nm), and at 542 nm for **Zn_2** (+54 nm).

Compared to that measured in solution, the ϕ-value of **Zn_3** increases in the room-temperature mesophase (from 0.5 to 1.5%), while for **Zn_1** it decreases from 6.5 to 4.0%; for **Zn_2**

Table 3 Photophysical properties in CH_2Cl_2 solution

Sample	Abs, λ_{max}/nm (ε/M^{-1} cm^{-1})	Em, λ_{max}/nm	ϕ/%	τ/ns
Zn_1	266 (34820), 284 (35910), 323 (33160), 333 (31300)	405	6.5	2.0
Zn_2	255 (43320), 284 (37310), 309 (21770), 322 (20180), 406 (22830)	488	95.0	4.2
Zn_3	265 (27100), 282 (29320), 322 (25250), 333 (23410)	400	0.5	3.0

Published on 11 November 2021. Downloaded on 11/19/2022 11:56:28 AM.

Table 4 Photophysical properties in the mesophase at room temperature

Sample	Em, λ_{max}/nm	ϕ/%
Zn_1	435	4.0
Zn_2	542	20.2
Zn_3	435	1.5

it undergoes a drastic reduction from 95.0 to 20.2%. Generally, on going from solution to a condensed phase, the molecular packing reduces the vibrational motions and the consequent decrease of the non-radiative rate constant (k_{nr}) causes an increase in the luminescence intensity. While this statement is true for **Zn_3**, it is not for **Zn_1** and **Zn_2**.

Mesophase type of **Zn_3** (Col_{hex}) and of **Zn_1** and **Zn_2** (M_{hex}) exerts an effect on the quantum yield which adds to the reduction of vibrational motions. In fact, the columnar core of **Zn_1** and **Zn_2** consist of a three-molecule strand of π-stacked tpy rings, and this aggregation partially quenches luminescence; this is not effectively compensated by the reduction of k_{nr} and ultimately causes a reduction in the emission quantum yield for these compounds in the mesophase compared to the solution. In the columnar core of **Zn_3**, the poor π–π stacking does not effectively counterbalance the decrease in k_{nr}, and the quantum yield increases in the mesophase with respect to the solution. The behaviour of **Zn_2** (which, as already highlighted, undergoes a drastic reduction of the ϕ-value) deserves a particular explanation, also considering that the mesophase is the same as **Zn_1**. This depends on the nature of the emissive state of this complex, which (unlike **Zn_1** and **Zn_3**) is an ILCT from the diethylaniline fragment to the aromatic rings of the tpy. This transition became partially symmetry-forbidden in the mesophase, where the packing distorts the orientation between the diethylaniline fragment and the tpy core, causing a noticeable reduction of the emission quantum yield.

Nevertheless, the luminescence quantum yield value of **Zn_2** remains considerable even in the mesophase, and for this reason the polarized emission of an oriented film of this complex was measured. To correlate the orientational order of the liquid crystal with its optical anisotropy properties, it is necessary to consider the orientation of the molecular emission transition dipole moment (TM) with respect to the columnar director. Theoretical calculations (see below) demonstrate that in the **Zn_2** molecule the TM vector lies on the plane of the aromatic rings of the tpy, oriented by the amino group towards the centre of gravity of the molecule.[29] Molecules form π-stacked units according to a symmetry that identifies a ternary axis parallel to the director, as shown in Fig. 4, and the TMs point towards three directions placed at 120° from each other and perpendicular to the director. Considering that the π-stacked groups are offset by 60°, six TM vectors for each column (Fig. 7a) can be identified. The M_{hex} phase hexagonal arrangement allows an ordered organization of the TMs, and therefore an emission anisotropy can be detected.

Fig. 8 reports the absorption and polarized emission spectra of the thin film of **Zn_2**, prepared as described in the ESI.†

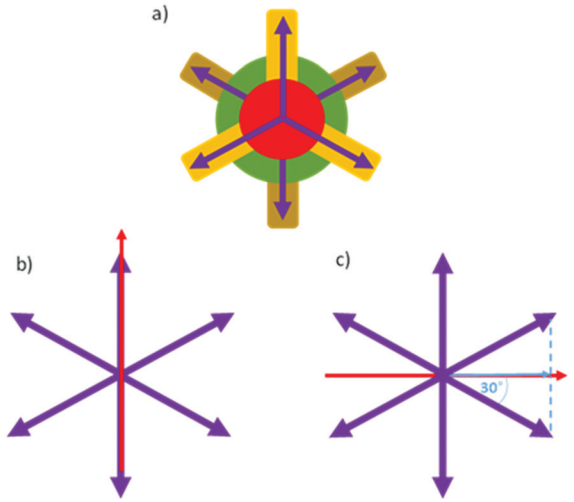

Fig. 7 (a) Assumed orientation of the TMs (purple arrows) of **Zn_2** seen along the column axis (see Fig. 4); (b) red arrow represents the direction of polarized emission light parallel to the TM; (c) red arrow represents the direction of polarized emission light perpendicular to the TM, while the blue arrow represents the projection of the vector TM along this direction.

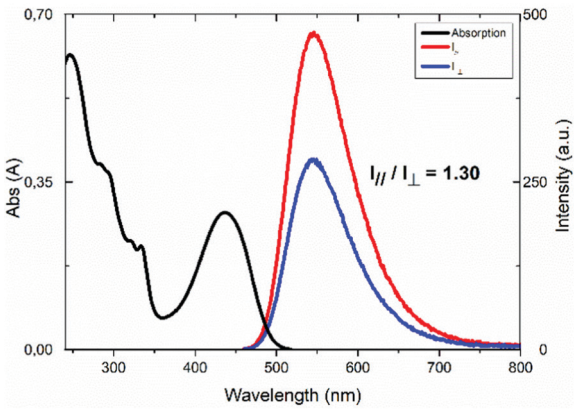

Fig. 8 Absorption and polarized emission spectra of **Zn_2** on an aligned thin film at room temperature (||: parallel emission light; ⊥: perpendicular emission light; λ_{ex} = 440 nm).

The absorption spectrum of the film shows the same electronic transitions as those reported in Fig. 5. Under un-polarised 440 nm excitation, the film shows a well-defined polarized emission band peaked at 546 nm, superimposable with that reported in Fig. 6. When the emission polarizer (Fig. 7b) is parallel (||) to the direction of one of the TM vectors (see the ESI†), the emission intensity is higher than when the polarizer (Fig. 7c) is perpendicular (⊥), since in this last direction the TM vector projection is lower.

The value of the $I_{||}/I_{\perp}$ ratio is 1.30, indicative of the average orientation of the luminescent liquid crystals, considering that the vector composition of the TMs always provide non-zero values of the emission intensity at each angular value; although this ratio is not high, this value is the first obtained for a columnar metallomesogen.

 This journal is © The Royal Society of Chemistry 2022

Published on 11 November 2021. Downloaded on 11/19/2022 11:56:28 AM.

Computational results

Zn_1 and **Zn_2** were the object of computational investigations based on the DFT and TD-DFT methods (see "Computational methods" in the ESI†). In particular, the high fluorescence quantum yield of **Zn_2** and the fluorescence anisotropy in its mesophase were investigated.

In this respect, the main reference point for our theoretical study was the photophysical characterization performed in CH_2Cl_2 solutions. As evident in the following, inclusion of solvent effects is essential for the correct prediction of **Zn_2** spectroscopy. However, the particular nature of the studied complexes induces uncertainness about the way to model the environment. In fact, the presence of six long hydrocarbon chains surrounding the core of the complex can modify the solvation environment of the core itself. Our choice was to perform the computational studies on model systems in which all the hydrocarbon chains were replaced with methyl groups and to carry out separate evaluations of the solvation effects by selecting *n*-hexane and CH_2Cl_2 as surrounding solvents. *n*-Hexane was used to simulate the hydrocarbon chains and the two solvents were chosen as extreme solvation environments, being the real environment in-between in terms of solute perturbation.

Fig. 9 provides a visual description of the computed **Zn_2** structure. Its general features can be directly extended to **Zn_1** due to the great structural similarity between the two complexes. Table 5 lists some relevant structural parameters computed for **Zn_1** and **Zn_2** both in the gas phase and in CH_2Cl_2 solution. **Zn_2** belongs to the C_2 point symmetry. Accordingly, the three nitrogen aromatic donor atoms are labelled as C_2-axial (N_{ax}) and non-C_2-axial (N_{nax}). The coordination geometry can be considered trigonal bipyramidal (TBPY-5), with N_{ax} and both the O atoms of the gallate ligands in the equatorial plane of the bipyramid. An evident deviation from the ideal TBPY-5 coordination geometry is the N_{nax}–Zn–N_{nax} angle, which is significantly smaller than 180°. The computed structure is in line with the experimental structural analysis performed on similar complexes.[25] Analogue considerations can be applied to **Zn_1** (Table 5) which show a high level of local C_2 symmetry in most of its structure, in particular in the metal–ligands core of the complex. In both complexes, the phenyl group linked to the tpy core is rotated with respect to that of the tpy core itself. The dihedral angle between the average planes of the two aromatic systems (Ph and tpy in Table 5) are 36.2 and 38.6 degrees (**Zn_2** and **Zn_1** in vacuum, respectively) and it is reduced by 6–8 degrees in CH_2Cl_2.

No relevant changes are attributed to solvation effects in comparison to computations in vacuum: the Zn–O bond distance increases by about 0.02 Å in CH_2Cl_2 by virtue of the increased solvation-induced stabilization of the "negatively charged" gallate ligands. As a consequence, the Zn–N bonds

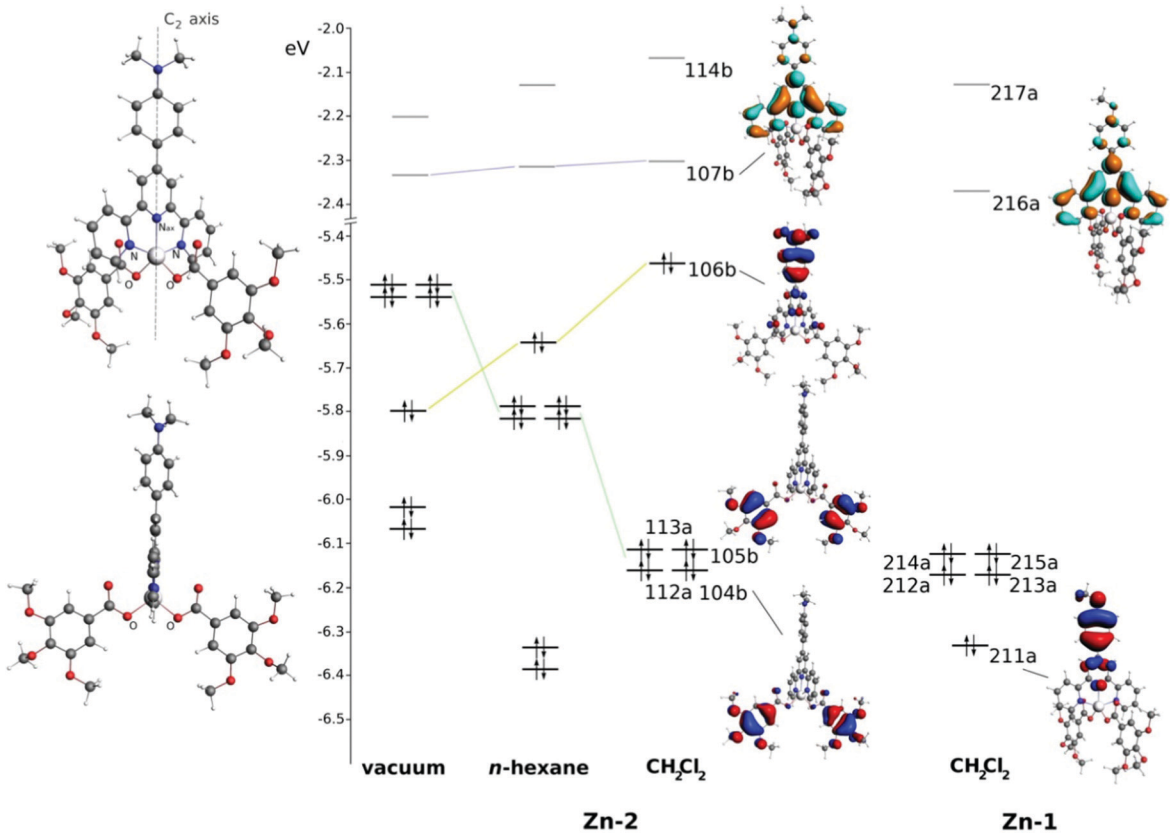

Fig. 9 The computed structure of **Zn_2** (on the left) from two different viewpoints; energy levels (eV) of the **Zn_2** MOs computed in vacuum, *n*-hexane and CH_2Cl_2. The environmental-induced energy shift of the shown **Zn_2** MOs is evidenced by connecting lines. Some relevant orbitals are shown in correspondence of their energy level in CH_2Cl_2.

Published on 11 November 2021. Downloaded on 11/19/2022 11:56:28 AM.

Table 5 Computed structural parameters (Å and degrees) of **Zn_1** and **Zn_2** in vacuum and in CH_2Cl_2 solution

	Zn_1		**Zn_2**	
	Vacuum	CH_2Cl_2	Vacuum	CH_2Cl_2
Zn–N_{ax}	2.133	2.104	2.127	2.097
Zn–N	2.238	2.224	2.240	2.226
	2.239	2.225		
Zn–O	1.969	1.992	1.971	1.991
	1.970	1.992		
N–Zn–N	148.3	149.8	148.4	150.0
O–Zn–O	105.6	98.8	105.4	98.1
O–Zn–N_{ax}	126.4	131.1	127.3	130.9
	128.0	130.2		
Ph-tpy dihedral angle	38.6	32.6	36.2	28.1

shorten by a similar amount. As expected, computed structural features in *n*-hexane are in-between the gas-phase and CH_2Cl_2 ones (Table S4 (ESI†) collects all the computed Cartesian coordinates).

Fig. 9 sketches the molecular orbitals (MOs) energies of **Zn_2** and **Zn_1** computed in different environments which are important for the description of the low energy part of the absorption spectrum and also for the emission properties. In CH_2Cl_2, the **Zn_2** HOMO (Highest Occupied Molecular Orbital, 106b in Fig. 9) is computed at −5.46 eV and is mainly localized on the diethylaniline group (86.5%). Lower in energy, in the range from −6.11 to −6.16 eV, gallate-localized MOs are present in the form of almost-degenerate symmetric (*A* symmetry) and corresponding asymmetric (*B* symmetry) combinations of the highest π bonding orbitals of gallate (for instance, 113a and 105b at −6.11 and −6.12 eV, respectively, only the asymmetric combination is shown in Fig. 9). The **Zn_2** LUMO (Lowest Unoccupied Molecular Orbital, 107b in Fig. 9) shows a larger localization on the tpy core (85.9%) with only small contributions from the diethylaniline group (8.0%). The contribution of the central metal atomic orbitals on all these MOs is negligible, being always lower than 1.2%. Passing from CH_2Cl_2 to *n*-hexane, the shape of the shown MOs does not significantly change but their energies shift in different ways. The gallate-localized MOs are destabilised as a consequence of the negative charge on them and the lower ability of *n*-hexane to polarize itself in the proximity. On the contrary, the HOMO (106b) is stabilized, being the polarization of the solvent less destabilizing on this part of the molecule in *n*-hexane (see Fig. S25, ESI,† for details about the COSMO surface around the complex). Computations in vacuum show that the lack of solvation effects further destabilizes the gallate-localized MOs, which become the highest in energy occupied orbitals.

Differently from the occupied MOs, the LUMO is less affected by environmental effects, being mainly localized on the inner part of the tpy ligand and less exposed to the solvent in comparison to the diethylaniline and gallate ligands.

In **Zn_1**, MOs close to the HOMO and LUMO are very similar to the **Zn_2** ones. MO 211a corresponds to MO 106b in **Zn_2** (Fig. 9). However, in **Zn_1**, the 211a MO is not the HOMO, neither in CH_2Cl_2, being lower in energy in comparison to the gallate-localized MOs (already described in **Zn_2** and found very similar also in **Zn_1**). This fact can be referred back to the lower π-conjugation of the OMe group (in comparison to the NEt_2) with the phenyl ring and also to the high electronegativity of the oxygen atom and consequently to its electron withdrawing ability. The **Zn_1** LUMO strongly resembles the **Zn_2** one, both in shape and in energy, because it is barely affected by the phenyl group and localized ''internally'' to the complex.

TD-DFT computations confirm the nature of the first singlet excited state (S_1) of **Zn_2** and **Zn_1** as already reported in the discussion of photophysical data in CH_2Cl_2 solution. **Zn_2** S_1 corresponds to an ILCT transition from the diethylaniline fragment to the tpy aromatic rings. In **Zn_1**, S_1 is predicted as a CT transition from the gallate to the tpy ligands. Table 6 lists some relevant features of S_1 of **Zn_2** and **Zn_1**. In **Zn_2**, S_1 can be assigned to a substantially pure HOMO–LUMO monoelectronic excitation (99.3% of contribution in CH_2Cl_2, 99.1% in *n*-hexane). The intensity of the related vertical electronic transition from the ground state (oscillator strength in Table 6) is computed to be rather large and it decreases passing from CH_2Cl_2 to the less polarizable *n*-hexane (in vacuum it is further lowered to 0.26, not reported in Table 6). Finally, being S_1 an *A*-symmetry state like the ground state, the transition dipole moment is fully directed along the C_2 axis of the molecule. All the higher singlet states (from S_2 to S_6) are characterised by a very low oscillator strength, hence no significant absorptions are predicted till 3.50 eV (354 nm, in CH_2Cl_2) or 3.13 eV (396 nm, in *n*-hexane). Thus, the low energy part of the **Zn_2** absorption spectrum is dominated by a single intense absorption toward S_1. In the experimental absorption spectrum (Fig. 5 and Table 3), **Zn_2** differs from **Zn_1** and **Zn_3** for the presence of a well-defined band at 406 nm, which now can be safely assigned to the HOMO–LUMO transition. Interestingly, this absorption is computed at 452 nm in CH_2Cl_2, in good agreement with the

Table 6 Computed lowest-energy singlet excited states properties

State	Energy	Oscillator strength	Composition
Zn_2 (CH_2Cl_2 solution)			
S_1 (2A)	2.74 eV; 452 nm	0.59	106b → 107b 99.3%
S_2 (1B)	2.90 eV; 428 nm	2.6×10^{-4}	106b → 114a 99.1%
S_3 (2B)	3.44 eV; 360 nm	4.5×10^{-5}	113a → 107b 99.8%
S_4 (3A)	3.44 eV; 360 nm	9.6×10^{5}	105b → 107b 99.8%
S_5 (3B)	3.50 eV; 354 nm	3.7×10^{-5}	112a → 107b 99.8%
S_6 (4A)	3.50 eV; 350 nm	3.6×10^{-4}	104b → 107b 99.8%
Zn_2 (*n*-hexane solution)			
S_1 (2A)	2.96 eV; 419 nm	0.47	106b → 107b 99.1%
S_2 (1B)	3.02 eV; 411 nm	4.1×10^{-5}	106b → 114a 98.9%
S_3 (2B)	3.09 eV; 401 nm	1.7×10^{-5}	113a → 107b 99.7%
S_4 (3A)	3.09 eV; 401 nm	6.5×10^{-5}	105b → 107b 99.6%
S_5 (3B)	3.13 eV; 396 nm	3.7×10^{-5}	112a → 107b 99.7%
S_6 (4A)	3.13 eV; 396 nm	4.8×10^{-9}	104b → 107b 99.7%
Zn_1 (CH_2Cl_2 solution)			
S_1	3.38 eV; 367 nm	3.1×10^{-5}	215a → 216a 68.8%
			214a → 216a 31.1%
S_2	3.38 eV; 367 nm	1.2×10^{-4}	215a → 216a 31.1%
			214a → 216a 68.8%
S_3	3.44 eV; 360 nm	1.3×10^{-4}	213a → 216a 94.3%
S_4	3.44 eV; 360 nm	9.1×10^{-6}	212a → 216a 94.3%
S_5	3.47 eV; 357 nm	0.56	211a → 216a 98.7%
S_6	3.63 eV; 342 nm	8.6×10^{-5}	215a → 217a 66.5%
			214a → 217a 31.4%

This journal is © The Royal Society of Chemistry 2022

Published on 11 November 2021. Downloaded on 11/19/2022 11:56:28 AM.

experiment. However, the agreement improves when *n*-hexane is used as the solvent (418 nm). This could be an indication of the importance of the long hydrocarbon chains in determining the S_1 energy with respect to the ground state. As reported in Table 6, S_2 consists of an almost pure monoelectronic excitation from 106b (HOMO) to 114a, whereas the four following transitions consist of charge transfers from the gallate-localized MOs (112a, 113a, 104b and 105b) to the tpy-localized LUMO. The involved excited states consist of almost-degenerate couples of *A* and *B* symmetry states (for instance S_3 and S_4). For symmetry reasons, the transition dipole moment of the B states is perpendicular to the C_2 rotation axis.

Passing to **Zn_1**, low-intensity gallate-to-tpy CTs become the lowest electronic transitions (Table 6). The intense tpy-centred absorption is now associated to S_5 rather than S_1, and it is predicted at 357 nm, in good agreement with the first intense features measured at 333 nm (Table 3). Interestingly, the weak absorption around 400 nm (appearing like a tail at lower energies respect to the first absorption band in Fig. 5) confirms the presence of lower in energy singlet states (from S_1 to S_4) with low absorption intensities. This tail is not visible in the **Zn_2** spectrum, a fact that further confirms the accuracy of the performed computations.

At this point we are able to explain the differences in fluorescence properties between **Zn_2** and **Zn_1**. The first difference is the fluorescence quantum yield. **Zn_2** is strongly emissive due to the large oscillator strength (transition dipole moment) of S_1 in this complex, which leads to fast fluorescence kinetics. In **Zn_1**, on the contrary, the lowest singlet states are different and associated to very low oscillator strengths. Accordingly, they are barely emissive due to unfavourable electronic properties. Also, the longer emission wavelength in **Zn_2** can be easily explained as a consequence of the lower HOMO–LUMO gap in comparison to **Zn_1**. In this case, a key role is played by the NEt_2 substituent of the diethylaniline of **Zn_2**, which is able to destabilize the phenyl-localized π MOs much more than the OMe group in **Zn_1**.

Zn_3 is expected to be similar to **Zn_1** in terms of electronic structure and (consequently) spectroscopy. The coupling between the OR substituent and the phenyl group in the tpy-based fragment is likely to be comparable to the OMe coupling in **Zn_1**. This prediction is corroborated by the similarity in absorption and emission spectroscopy between **Zn_3** and **Zn_1** (see Fig. 5).

Now it is possible to explain the observed fluorescence anisotropy from the **Zn_2** mesophase. In the previous paragraph, this observation was supposed to be originated by a transition dipole moment oriented along the metal-tpy direction, obviously combined to a high level of order in the columnar arrangement of the liquid crystal. This is in perfect agreement with the computational results. As discussed previously, in **Zn_2** the emission transition dipole must be directed along the C_2 symmetry axis of the molecule (Fig. 9), like the absorption transition dipole associated to S_1. This is imposed by symmetry, since the first excited state is of *A* symmetry.

Conclusions

With the increased importance in obtaining functional optical materials for practical applications, luminescent metallomesogens are promising for the next generation of emitters. The research is highly challenging due to the necessity of matching the structural requirements for inducing mesomorphic properties, high luminescence properties and fine tuning of mesophase architecture for preserving or improving the molecular properties. Among liquid crystal architectures, a columnar one is pivotal for electrical conduction; however, it may be detrimental for the metallomesogen optical properties, favouring quenching of luminescence due to the formation of new excited states by the close packing of emitters. On the other hand, its high viscosity that increases its rheological stability, favour aggregation induced emission as a result of RIM.

Therefore we designed and synthesized new room temperature metallomesogens based on bio-available low-cost Zn(II) ions through the monodentate coordination of two lipophilic gallate units. The complexes show different 3D (**Zn_1** and **Zn_2**: M_{hex}) or 2D (**Zn_3**: Col_{hex}) liquid crystalline columnar organizations as a function of the functional group inserted on the chelating *N^N^N* terpyridine ligand.

Systematic structural, computational and photophysical studies allowed the correlation between liquid crystalline architecture and emitting properties in the mesophase. While complexes **Zn_1** and **Zn_3** emit modestly, the fluorescence originated from the ILCT excited state in **Zn_2** from the electron-donating $-NEt_2$ group to the electron-withdrawing aromatic rings of the tpy ligand reach a record luminescence quantum yield in solution (95%). Although the efficiency is reduced in the mesophase due to distortion of the diethylaniline with respect to the aromatic rings of tpy, it still remains as high as 20%.

Taking advantage of this high emission quantum yield of the mesophase, the polarized fluorescence of an oriented film of a columnar metallomesogen was measured for the first time, giving a $I_{||}/I_{\perp}$ ratio of 1.30, while theoretical calculations on the orientation of the transition dipole moment support the discussion.

Author contributions

Conceptualization, M. L. D., B. D., M. A. and E. I. S.; methodology, E. I. S.; investigation, G. D. M., A. C., B. H., A. A. A., E. P., E. V., V. B. and M. A.; resources, E. I. S.; data curation, M. L. D., B. H., M. A., B. D. and E. I. S.; writing – original draft M. L. D., M. A., O. C., B. D. and E. I. S.; writing – review and editing, M. L. D., M. A., B. D. and E. I. S.

Conflicts of interest

There are no conflicts to declare.

Acknowledgements

This work was supported by a grant of the Romanian Ministry of Education and Research, CNCS – UEFISCDI, project number

PN-III-P4-ID-PCE-2020-1958, within PNCDI III. Italian Ministry of University and Research supported this research through DEMETRA project (PON ARS01_00401). We thank Pohang Accelerator Laboratory (PAL) for giving us the opportunity to perform the GIWAXS experiment, MEST and POSTECH for supporting this experiment, Dr Hyungju Ahn for adjustment of beamline and for doing the measurement. A. A. A., E. P., E. I. Sz. and O. C. acknowledge the Romanian Academy, Program 4. A. A. A. is grateful for the ''Ion Heliade Radulescu'' mobility scholarship. We acknowledge the Laboratoire de Spectrométrie de Masse BioOrganique (LSMBO) IPHC UMR 7178 for mass spectrometry analysis. BD and BH thank CNRS and the University of Strasbourg for support.

Published on 11 November 2021. Downloaded on 11/19/2022 11:56:28 AM.

Notes and references

1 (*a*) C. Keum, D. Becker, E. Archer, H. Bock, H. Kitzerow, M. C. Gather and C. Murawski, *Adv. Opt. Mater.*, 2020, 2000414; (*b*) G. Qian, X. Yang, X. Wang, J. D. Herod, D. W. Bruce, S. Wang, W. Zhu, P. Duan and Y. Wang, *Adv. Opt. Mater.*, 2020, **8**(20), 2000775; (*c*) J. De, W.-Y. Yang, I. Bala, S. P. Gupta, R. A. K. Yadav, D. K. Dubey, A. Chowdhury, J.-H. Jou and S. K. Pal, *ACS Appl. Mater. Interfaces*, 2019, **11**, 8291; (*d*) J. Han, S. Guo, H. Lu, S. Liu, Q. Zhao and W. Huang, *Adv. Opt. Mater.*, 2018, 1800538; (*e*) Y. Wang, J. Shi, J. Chen, W. Zhu and E. Baranoff, *J. Mater. Chem. C*, 2015, **3**, 7993; (*f*) Y. Wang, J. Fan, J. Shi, H. Qi, E. Baranoff, G. Xie, Q. Li, H. Tan, Y. Liu and W. Zhu, *Dyes Pigm.*, 2016, **133**, 238.

2 (*a*) X. Hao, B. Xiong, M. Ni, B. Tang, Y. Ma, H. Peng, X. Zhou, I. I. Smalyukh and X. Xie, *ACS Appl. Mater. Interfaces*, 2020, **12**, 53058; (*b*) C. Cuerva, J. A. Campo, P. Ovejero, M. R. Torres, E. Oliveira, S. M. Santos, C. Lodeiro and M. Cano, *J. Mater. Chem. C*, 2014, **2**(43), 9167.

3 Y. L. Zhuang, X. L. Ren, X. T. Che, S. J. Liu, W. Huang and Q. Zhao, *Adv. Photonics*, 2021, **3**(1), 014001.

4 (*a*) H.-W. Chen, J.-H. Lee, B.-Y. Lin, S. Chen and S.-T. Wu, *Light: Sci. Appl.*, 2018, **7**, 17168; (*b*) D. Zhao, H. He, X. Gu, L. Guo, K. S. Wong, J. W. Y. Lam and B. Z. Tang, *Adv. Opt. Mater.*, 2016, **4**, 534.

5 (*a*) D. Pucci and B. Donnio, Non-Conventional, Supramolecular, Chromonic and Amphiphilic Liq. Cryst., in *Handbook of Liquid Crystals: Metal-containing liquid crystals*, ed. J. W. Goodby, P. J. Collings, T. Kato, C. Tschierske, H. Gleeson and P. Raynes, Wiley-VCH, Weinheim, 2014, vol. 5; (*b*) C. Cuerva, M. Cano and C. Lodeiro, *Chem. Rev.*, 2021, **121**(20), 12966.

6 K. Rajendiran, S. T. Yoganandham, S. Arumugam, D. Arumugam and K. Thananjeyan, *J. Mol. Liq.*, 2021, **321**, 114793.

7 (*a*) R. Giménez, O. Crespo, B. Diosdado and A. Elduque, *J. Mater. Chem. C*, 2020, **8**, 6552; (*b*) A. Kishimura, T. Yamashita, K. Yamaguchi and T. Aida, *Nat. Mater.*, 2005, **4**, 546; (*c*) R. Chico, C. Dominguez, B. Donnio, B. Heinrich, S. Coco and P. Espinet, *Cryst. Growth Des.*, 2016, **16**(12), 6984–6991.

8 E. Beltrán, J. Barberá, J. L. Serrano, A. Elduque and R. Giménez, Phase, *Eur. J. Inorg. Chem.*, 2014, 1165–1173.

9 (*a*) J. Jiménez, J. A. Sanz, J. L. Serrano, J. Barberá and L. Oriol, *Inorg. Chem.*, 2020, **59**(7), 4842; (*b*) P. Dechambenoit, S. Ferlay, B. Donnio, D. Guillon and M. W. Hosseini, *Chem. Commun.*, 2011, **47**, 734–736.

10 R. R. Parker, D. H. Liu, X. K. Yu, A. C. Whitwood, W. G. Zhu, J. A. G. Williams, Y. F. Wang, J. M. Lynam and D. W. Bruce, *J. Mater. Chem. C*, 2021, **9**(4), 1287.

11 (*a*) G. Qian, X. Yang, X. Wang, J. D. Herod, D. W. Bruce, S. Wang, W. Zhu, P. Duan and Y. Wang, *Adv. Opt. Mater.*, 2020, 2000775; (*b*) B. Yang, H. Ni, H. Wang, Y. Hu, K. Luo and W. Yu, *J. Phys. Chem. C*, 2020, **124**(43), 23879; (*c*) L. Zhao, B. Yang, L. Zeng, K. Luo, H. Wang, H. Ni, C. Yang and Q. Li, *Dyes Pigm.*, 2019, **164**, 398; (*d*) C. Cuerva, J. A. Campo, M. Cano and C. Lodeiro, *Chem. – Eur. J.*, 2019, **25**(52), 12046; (*e*) C. Cuerva, J. A. Campo, M. Cano, R. Schmidt and C. Lodeiro, *J. Mater. Chem. C*, 2018, **2**, 9723; (*f*) E. Tritto, R. Chico, J. Ortega, C. L. Folcia, J. Etxebarria, S. Coco and P. Espinet, *J. Mater. Chem. C*, 2015, **3**(36), 9385; (*g*) V. N. Kozhevnikov, B. Donnio and D. W. Bruce, *Angew. Chem., Int. Ed.*, 2008, **47**, 6286.

12 (*a*) E. de Domingo, C. L. Folcia, J. Ortega, J. Etxebarria, R. Termine, A. Golemme, S. Coco and P. Espinet, *Inorg. Chem.*, 2020, **59**(15), 10482; (*b*) M. Park, D.-G. Kang, H. Ko, M. Rim, D. T. Tran, S. Park, M. Kang, T.-W. Kim, N. Kim and K.-U. Jeong, *Mater. Horiz.*, 2020, **7**(10), 2635; (*c*) S. Chakraborty, S. K. Prasad, D. S. S. Rao and C. R. Bhattacharjee, *Liq. Cryst.*, 2019, **46**(6), 872; (*d*) R. Zhang, H. Gao, Y. Ren, Y. Xiao, J. Hu and X. Cheng, *Chem. – Asian J.*, 2018, **13**(5), 536; (*e*) S. Chakraborty, P. Mondal, S. K. Prasad, D. S. S. Rao and C. R. Bhattacharjee, *Eur. J. Inorg. Chem.*, 2016, 4604; (*f*) S. Debnath, H. F. Srour, B. Donnio, M. Fourmigué and F. Camerel, *RSC Adv.*, 2012, **2**, 4453; (*g*) C. Cretu, L. Cseh, B. J. Tang, V. Sasca, V. Badea, E. I. Szerb, G. Mehl, S. Shova and O. Costisor, *Liq. Cryst.*, 2015, **42**, 1139.

13 (*a*) N. S. S. Kumar, M. Z. Shafikov, A. C. Whitwood, B. Donnio, P. B. Karadakov, V. N. Kozhevnikov and D. W. Bruce, *Chem. – Eur. J.*, 2016, **22**, 8215; (*b*) A.-A. Andelescu, B. Heinrich, M. A. Spirache, E. Voirin, M. La Deda, G. Di Maio, E. I. Szerb, B. Donnio and O. Costisor, *Chem. – Eur. J.*, 2020, **26**, 4850; (*c*) D. Pucci, A. Crispini, M. Ghedini, M. La Deda, P. F. Liguori, C. Pettinari and E. I. Szerb, *RSC Adv.*, 2012, **2**, 9071.

14 (*a*) L. Soria, P. Ovejero, M. Cano, J. A. Campo, M. R. Torres, C. Núñez and C. Lodeiro, *Dyes Pigm.*, 2014, **110**, 159; (*b*) D. Pucci, A. Crispini, M. Ghedini, E. I. Szerb and M. La Deda, *Dalton Trans.*, 2011, **40**, 4614.

15 C. Cretu, A. A. Andelescu, A. Candreva, A. Crispini, E. I. Szerb and M. La Deda, *J. Mater. Chem. C*, 2018, **6**, 10073.

16 (*a*) G. Zou, L. Zhao, L. Zeng, K. Luo, H. Ni, H. Wang, Q. Li, W. Yu and X. Li, *Inorg. Chem.*, 2019, **58**(1), 861; (*b*) A. M. Prokhorov, A. Santoro, J. A. G. Williams and

 This journal is © The Royal Society of Chemistry 2022

Published on 11 November 2021. Downloaded on 11/19/2022 11:56:28 AM.

D. W. Bruce, *Angew. Chem., Int. Ed.*, 2012, **51**, 95; (*c*) E. I. Szerb, A. M. Talarico, I. Aiello, A. Crispini, N. Godbert, D. Pucci and T. Pugliese, *Eur. J. Inorg. Chem.*, 2010, 3270.

17 (*a*) H. Ishida, M. Handa, I. Hiromitsu, S. Ujiie, D. Yoshioka, R. Mitsuhashi and M. Mikuriya, *New J. Chem.*, 2019, **43**, 1134; (*b*) D. Pucci, A. Bellusci, A. Crispini, M. Ghedini, N. Godbert, E. I. Szerb and A. M. Talarico, *J. Mater. Chem.*, 2009, **19**, 7643.

18 L. Rossi, C. Huck-Iriart, M. A. Castro and F. D. Cukiernik, *J. Coord. Chem.*, 2017, **70**(21), 3633.

19 P. Alam, C. Climent, P. Alemany and I. R. Laskar, *J. Photochem. Photobiol., C*, 2019, **41**, 100317.

20 T. Shu, J. Wang, L. Su and X. Zhang, *Crit. Rev. Anal. Chem.*, 2018, **48**(4), 330.

21 P. Peng, Y. Li, W. Song and X. Yu, *Colloids Surf., A*, 2020, **589**, 124439.

22 A. Agosti, E. Kuna and G. Bergamini, *Eur. J. Inorg. Chem.*, 2019, 577.

23 (*a*) A. Winter and U. S. Schubert, *ChemCatChem*, 2020, **12**, 2890; (*b*) C. Wei, Y. He, X. Shi and Z. Song, *Coord. Chem. Rev.*, 2019, **385**, 1; (*c*) Y. H. Budnikova, D. A. Vicic and A. Klein, *Inorganics*, 2018, **6**(1), 18.

24 (*a*) S. Furumi, D. Janietz, M. Kidowaki, M. Nakagawa, S. Morino, J. Stumpe and K. Ichimura, *Chem. Mater.*, 2001, **13**, 1434; (*b*) S. Zimmermann, J. H. Wendorff and C. Weder, *Chem. Mater.*, 2002, **14**, 2218.

25 The Cambridge Structural Database. Z. Ma, W. Lu, B. Liang and A. J. L. Pombeiro, *New J. Chem.*, 2013, **37**, 1529.

26 D. Myśliwiec, B. Donnio, P. J. Chmielewski, B. Heinrich and M. Stępień, *J. Am. Chem. Soc.*, 2012, **134**, 4822.

27 (*a*) X. Chen, Q. Zhou, Y. Cheng, Y. Geng, D. Ma, Z. Xie and L. Wang, *J. Lumin.*, 2007, **126**, 81; (*b*) W. Goodall and J. A. G. Williams, *Chem. Commun.*, 2001, 2514.

28 X. Bi and Y. Pang, *J. Phys. Chem. B*, 2016, **120**(13), 3311.

29 (*a*) A. Winter, C. Friebe, M. Chiper, M. D. Hager and U. S. Schubert, *J. Polym. Sci., Part A: Polym. Chem.*, 2009, **47**, 4083; (*b*) I. Eryazici, C. N. Moorefield and G. R. Newkome, *Chem. Rev.*, 2008, **108**, 1834; (*c*) M. Humbert-Droz, C. Piguet and T. A. Wesolowski, *Phys. Chem. Chem. Phys.*, 2016, **18**, 29387.

chemosensors

MDPI

Article

Luminescent Self-Assembled Monolayer on Gold Nanoparticles: Tuning of Emission According to the Surface Curvature

Angela Candreva [1,2], Giuseppe Di Maio [1], Francesco Parisi [1], Francesca Scarpelli [1], Alessandra Crispini [1], Nicolas Godbert [1], Loredana Ricciardi [2], Antonello Nucera [3], Carmen Rizzuto [3], Riccardo C. Barberi [2,3], Marco Castriota [2,3] and Massimo La Deda [1,2,*]

[1] Department of Chemistry and Chemical Technologies, University of Calabria, 87036 Rende, Italy; angela.candreva@unical.it (A.C.); giuseppe.dimaio@unical.it (G.D.M.); francesco.parisi@unical.it (F.P.); francesca.scarpelli@unical.it (F.S.); a.crispini@unical.it (A.C.); nicolas.godbert@unical.it (N.G.)

[2] Institute of Nanotechnology (NANOTEC), National Research Council (CNR), UOS Cosenza, 87036 Rende, Italy; loredana.ricciardi@cnr.it (L.R.); riccardo.barberi@fis.unical.it (R.C.B.); marco.castriota@fis.unical.it (M.C.)

[3] Department of Physics, University of Calabria, 87036 Rende, Italy; antonello.nucera@unical.it (A.N.); carmen.rizzuto@unical.it (C.R.)

* Correspondence: massimo.ladeda@unical.it

Abstract: Until now, the ability to form a self-assembled monolayer (SAM) on a surface has been investigated according to deposition techniques, which in turn depend on surface-coater interactions. In this paper, we pursued two goals: to form a SAM on a gold nanosurface and to correlate its formation to the nanosurface curvature. To achieve these objectives, gold nanoparticles of different shapes (spheres, rods, and triangles) were functionalized with a luminescent thiolated bipyridine (Bpy-SH), and the SAM formation was studied by investigating the photo-physics of Bpy-SH. We have shown that emission wavelength and excited-state lifetime of Bpy-SH are strongly correlated to the formation of specific aggregates within SAMs, the nature of these aggregates being in close correlation to the shape of the nanoparticles. Micro-Raman spectroscopy investigation was used to test the SERS effect of gold nanoparticles on thiolated bipyridine forming SAMs.

Keywords: self-assembled monolayer; gold nanorods; gold nanotriangles; gold nanospheres; emission spectroscopy; the curvature of nanosurface; SERS

check for updates

Citation: Candreva, A.; Di Maio, G.; Parisi, F.; Scarpelli, F.; Crispini, A.; Godbert, N.; Ricciardi, L.; Nucera, A.; Rizzuto, C.; Barberi, R.C.; et al. Luminescent Self-Assembled Monolayer on Gold Nanoparticles: Tuning of Emission According to the Surface Curvature. *Chemosensors* **2022**, *10*, 176. https://doi.org/10.3390/chemosensors10050176

Academic Editors: Iole Venditti, Paolo Prosposito and Alessandra Paladini

Received: 4 April 2022
Accepted: 3 May 2022
Published: 6 May 2022

Publisher's Note: MDPI stays neutral with regard to jurisdictional claims in published maps and institutional affiliations.

Copyright: © 2022 by the authors. Licensee MDPI, Basel, Switzerland. This article is an open access article distributed under the terms and conditions of the Creative Commons Attribution (CC BY) license (https://creativecommons.org/licenses/by/4.0/).

1. Introduction

Self-assembled monolayers (SAMs) are highly ordered organic molecular aggregates with a thickness of a single molecule, i.e., in the range of a few nanometers, chemisorbed on a substrate. SAMs of organic molecules have been the object of a very large number of investigations [1,2] in relation to a wide panel of applications in fields such as corrosion protection [3], biosensors [4], drug-delivery systems [5] and molecular electronics [6]. Specifically regarding SAMs on metal surfaces, many studies have focused on molecules bearing a thiol termination because of the ease of S-metal binding. In particular, alkanethiols, dithiols, thiophenes, and thiophenols on various substrates, such as Au, Ag, Pt, and Cu have been investigated [7–9]. In this regard, dithiol molecules have attracted particular attention owing to the possibility of using the thiol terminations to bind two different metallic entities. A dithiol SAM with free pendent SH groups allows for the grafting of metallic atoms or nanoparticles [10–13] that can, in turn, become a useful platform for the further growth of metallic contacts and more complex heterostructures [14]. In addition, SAMs formed on metallic nanoparticles have attracted a plethora of research efforts due to the possibility of combining the unique properties of nanosized metal clusters with those of ordered organic molecules in a new class of materials, i.e., monolayer-protected metal nanoparticles (MPMNs) [15]. A particularly relevant aspect of nanoparticles is that the

percentage of the total number of interfacial atoms is much greater than in bulk materials. Because the electronic states of interfacial atoms of nanoparticles affect their chemical, optical, and electronic properties, there is a strong synergy between nanoparticles and SAMs [7]. However, the structures of SAMs differ greatly depending on the curvature of a given surface [15]. Unlike SAMs formed on planar macro surfaces, MPMNs offer the possibility of studying the effect of curvature on the formation of monolayers, as it is possible to prepare metal nanoparticles with quite varied shapes, such as spheres, rods, stars, triangles, and cubes—each with a specific surface curvature.

The nanoscale surface curvature exerts a profound effect on the adsorbed molecules–nanoparticles interactions. For this reason, and due to the outstanding relationship between the shape of nanoparticles and the energy of their localized surface plasmon resonance [16] (which in the case of gold is included in the visible spectrum), gold nanoparticles covered with monolayers of thiol-functionalized molecules have been intensively studied, both for their applications and the exploration of phenomena due to the anisotropic surface stress [17]. Indeed, understanding the interface at the nanometer scale is crucial for a wide range of applications of gold nanoparticles such as labeling, sensing, drug delivery, medical therapies, molecular electronics, and catalysis [18]. For this purpose, many different thin-film characterization techniques have been applied to SAMs [2,3,19–21], including microscopy (e.g., STM, AFM), diffraction (e.g., LEED, GIXD, LEAD), and spectroscopy (e.g., SHG, SFG, XPS, RAIRS). All of the aforementioned techniques require the use of sophisticated and expensive instrumentation. However, it is worth noting that many of these techniques can hardly be applied to nanoparticle samples.

On the other hand, molecular luminescence is a formidable tool in a myriad of application fields, including biology, medicine, electronics, analytics, and material sciences [22]. The photophysical properties of an emitter are strongly influenced not only by the environment surrounding the luminophore (i.e., the solvent), but also by intermolecular interactions which become important in a concentrated solution, or more decisively, in a solid or mesophase. In particular, the formation of dimers or multimers in the ground electronic state or excited dimers/multimers (i.e., excimers), can result in different photophysical behavior with respect to the isolated molecule, leading to an increase or conversely, to quenching of the luminescence with the formation of a new emission band, in some cases [23]. Ordered structures of luminophores, such as crystals or liquid crystals or gel, can show emission properties affected by aggregation [24]. Self-assembled structures [25], derived from dissolving emitters in an organized medium (such as liquid crystals [26,27]) or depositing them onto orienting surfaces to form organized films (such as SAMs [28–30]), can show this luminescence tuning. For this reason, photophysical studies of luminescent SAMs can be highly useful to probe the type of aggregates formed within the layer.

Herein, we present the synthesis and photophysical characterization of differently shaped gold nanoparticles (rod, sphere, and triangle) functionalized with 5,5′-bis(mercapto methyl)-2,2′-bipyridine (briefly, Bpy-SH). The photophysical properties of the obtained MPMNs Bpy-SH@AuNR (rod), Bpy-SH@AuNS (sphere), and Bpy-SH@AuNT (triangle) were studied and compared with those of a Bpy-SH monolayer on gold plates (Bpy-SH@Au-plate).

The formation of a self-assembled monolayer on a gold nanosurface has been demonstrated through a deep analysis of luminescence data, revealing a dramatic change of the thiolated bipyridine emission, due to a face-to-face organization of the bipyridine similar to that observed in solid or concentrated solution [31]. Furthermore, the comparison between the luminescence properties of the newly synthesized SAM@AuNP and the shape (spherical, rod-shaped, or triangular) of the gold nanoparticles allowed for correlation between the SAM formation and the nanosurface curvature, providing the first example of a photophysical study of luminescent SAMs on nanoparticles with different shapes.

2. Materials and Methods

All chemicals were purchased from Sigma-Aldrich (Schnelldorf, Germany; highest purity grade available) and used as received.

2.1. Synthesis of Gold Nanorods

The synthesis of gold nanorods capped with cetyltrimethylammonium bromide (CTAB ($AuNR_{CTAB}$)), was conducted in an aqueous solution using the reported seed-mediated method [32,33]. The synthetic steps proceed through physical separation of the nucleation process (seed solution) from the growth process (growth solution), which allows an effective control of the final shape.

Preparation of the seed solution. A total of 25 µL of 5.0×10^{-2} M $HAuCl_4$ water solution was added to 4.7 mL of 0.1 M CTAB water solution and 300 µL of a freshly prepared 1.0×10^{-2} M $NaBH_4$ water solution was then rapidly injected under vigorous stirring. Excess borohydride was consumed by keeping the seed solution for 30 min at room temperature before use.

Preparation of the growth solution. A total of 45 mg of 5-bromosalicylic acid was added to 50 mL of 0.05×10^{-2} M CTAB water solution. After complete dissolution, 480 µL of 1.0×10^{-2} M $AgNO_3$ water solution was added. The solution was mildly stirred for 15 min at room temperature, and then 500 µL of 5.0×10^{-2} M $HAuCl_4$ water solution was added to the mixture. Finally, 130 µL of 0.1 M L-ascorbic acid water solution was added under vigorous stirring, followed by 80 µL of seed solution. After 30 s, the stirring was stopped and the mixture was left undisturbed at room temperature for at least 4 h. The sample was centrifuged to eliminate the unreacted reagents (9000 rpm, 20 min, 30 °C).

Coating agent exchange. CTAB capping agent was replaced with O-(2-mercaptoethyl)-O′-methylpolyethylene glycol (2000 Mn), PEG-SH, by dissolving 30 mg of polymer in 1 mL of deionized water, then adding this solution to 50 mL of 5×10^{-4} M water-dispersed $AuNR_{CTAB}$ [34]. The solution was left stirring overnight. The sample was then centrifuged at 9000 rpm for 30 min and the solid residue dissolved in dichloromethane. Because $AuNR_{CTAB}$ is not soluble in dichloromethane, this induced solubilization is evidence of the successful functionalization of the gold nanorods with PEG-SH, allowed by the formation of a strong sulphur–gold bond. Figure S1 in the Supplementary Materials shows the extinction spectra of the gold nanorods dispersed in solution before and after coating exchange.

Gold nanorods functionalization. A 5,5′-Bis (mercaptomethyl)-2,2′-bipyridine (Bpy-SH) dichloromethane solution (5.5 mL, 1.0×10^{-2} M) was mixed with a dichloromethane solution of $AuNR_{PEG\text{-}SH}$ (50 mL, 5×10^{-4}) and left under stirring for 12 h. As shown below, the formation of an S–Au bond between Bpy-SH and $AuNR_{PEG\text{-}SH}$ guarantees functionalization of the nanoparticles with mercaptomethyl-bipyridine (Bpy-SH@AuNR). Successively, by adding water, two phases were formed. After vigorous stirring, the pink organic phase discolors, while the aqueous phase turns pink due to the migration of the nanorods. PEGylated termination ensures the water solubility of nanorods while free Byp-SH, insoluble in water, remains in the organic phase. The two phases have been separated with a separating funnel and subsequent extractions to ensure the complete removal of the free Bpy-SH from the nanorod solution (thin-layer chromatography of the nanorods solution showed no trace of either labile or free Bpy-SH). Figure 1a shows a TEM image of the obtained Bpy-SH@AuNR nanorods, with an average size of 50×15 nm.

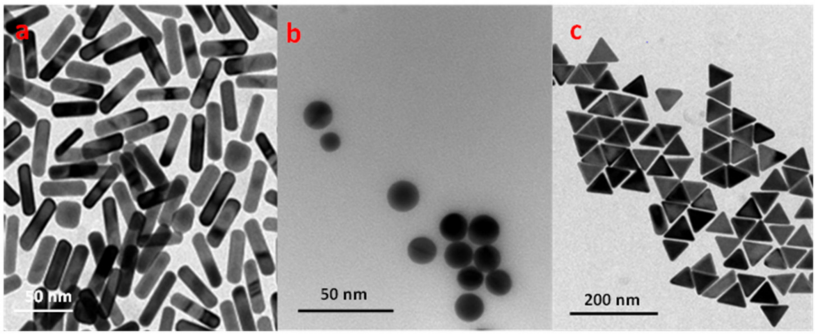

Figure 1. TEM images of Bpy-SH@AuNR (**a**), Bpy-SH@AuNS (**b**) and Bpy-SH@AuNT (**c**).

2.2. Synthesis of Gold Nanospheres

Gold nanospheres, with an average diameter of 18 nm (calculated using the TEM images), covered with sodium citrate ($AuNS_{SC}$) and dispersed in water have been synthesized through a one-step procedure. Sodium citrate (3 mg) was added to 40 mL of cold distilled water with stirring, $HAuCl_4$ water solution (0.020 mL, 0.05 M) was added and after a few minutes, 1.6 mL of a freshly prepared 1.0×10^{-2} M $NaBH_4$ water solution was injected with vigorous stirring. A centrifuge purification to eliminate unreacted reagents was performed. Figure S2 in Supplementary Materials shows the extinction spectrum of the gold nanospheres dispersed in water, where the plasmonic band shows a peak at 522 nm. The coating agent exchange and the functionalization with Bpy-SH of the obtained nano-spheres were achieved exactly as described above for the gold nanorods. Figure 1b reports a TEM image of the obtained Bpy-SH@AuNS nanoparticles.

2.3. Synthesis of Gold Nanotriangles

The synthesis of gold nanotriangles capped with cetyltrimethylammonium chloride (CTAC ($AuNT_{CTAC}$)) was conducted in an aqueous solution using an adaptation of the seed-mediated method [35].

Preparation of the seed solution. A total of 25 µL of 5.0×10^{-2} M $HAuCl_4$ water solution was added to 4.7 mL of 0.1 M CTAC water solution and 300 µL of a freshly prepared 1.0×10^{-2} M $NaBH_4$ water solution was then injected with vigorous stirring. Excess borohydride was consumed by keeping the seed solution at room temperature for 30 min before use.

Preparation of the growth solution. Two growth solutions were prepared, one (A) was used to grow the CTAC-capped seeds into larger nanoparticles; the second (B) was used to direct the anisotropic triangular-shaped growth. Solution A was prepared as follows: 6.4 mL of 0.1 M CTAC water solution was added to 32 mL of water. Subsequently, 160 µL of 5.0×10^{-2} M $HAuCl_4$ water solution was added. Solution B was prepared as follows: 313 mL of 5.0×10^{-2} M CTAC water solution was added to 3.91 mL of 5.0×10^{-2} M $HAuCl_4$ water solution, followed by 2.35 mL of 1×10^{-3} NaI water solution. Then, 160 µL and 3.13 mL of 0.1 M ascorbic acid water solution was added to solutions A and B, respectively, and both solutions were stirred until complete transparency of the solutions was achieved. Finally, 400 µL of 10 times diluted seed solution was added to solution A. At this point, solution A was added to solution B. The obtained dispersion was left undisturbed at room temperature for 2 h. The color, initially intense pink, soon turned into a purple solution containing nanoparticles with different shapes (cubes, spheres, and triangles), as observed by TEM (Figure S3a in Supplementary Materials) and by UV-Vis spectroscopy (Figure S4 in Supplementary Materials). To trigger the selective precipitation of triangles, a water CTAC solution (93.3 mL of 25% w/vol) was added, causing flocculation. After two hours, the supernatant was removed, while the precipitate was redispersed in 5.0×10^{-2} M CTAC water solution, obtaining the desired $AuNT_{CTAC}$ characterized by a blue water solution whose shape was confirmed with TEM (Figure S3c in Supplementary Materials) and UV-Vis spectroscopy (Figure S4, black line, in Supplementary Materials). TEM images and spectroscopic analysis confirm that differently shaped nanoparticles, together with a few triangles, remained in the supernatant (Figures S3b and S4 in Supplementary Materials). The coating agent exchange and the functionalization with Bpy-SH of the obtained nanotriangles were achieved exactly as described above for gold nanorods. Figure 1c reports a TEM image of the obtained Bpy-SH@AuNT nanoparticles, having an average length (along the side) of 50 nm.

2.4. Bpy-SH Covered Gold Plates

A Bpy-SH dichloromethane solution with a concentration of 3.5×10^{-2} M was prepared and degassed with argon. The gold substrate was obtained by thermal evaporation of 200 nm of gold (99.99% purity) onto either polished single crystal silicon (100) wafers primed on freshly cleaved mica at 340 °C. A film of Bpy-SH on the gold plate was deposited

by immersing the gold substrate into the Bpy-SH solution for 6 h at room temperature in the absence of ambient light in a sealed vessel, adapting a reported protocol [36]. Finally, the functionalized gold plate, Bpy-SH@Au-plate, was washed with dichloromethane.

3. Results and Discussion

3.1. Uv-Vis Spectroscopy

The photophysical properties of the investigated samples are reported in Table 1. Since their emission features are attributable to Byp-SH, the electronic transitions of this chromophore in solution will be described first.

Table 1. Photophysical properties of investigated samples.

Sample	Abs, λ/nm (ε/M^{-1} cm^{-1})	Emission Max, λ/nm	Excitation Bands, λ/nm	Lifetime, τ/ns (α/%)	
				at 352 nm	at 418 nm
Bpy-SH@AuNR [a]	273, 300(sh),368, 390(sh), 530, 840 [c]	435	320, 374, 395(sh)	1.6 (94.3), 11.1 (5.7)	0.7 (75.4), 5.2 (24.6)
Bpy-SH@AuNS [a]	291, 520 [c]	350	265	1.5 (79.3), 7.6 (20.7)	
Bpy-SH@AuNT [a]	294, 350(sh), 653 [c]	410	265, 382		0.7 (82.5), 2.4 (17.5)
"diluted" Bpy-SH solution (1.3×10^{-5} M) [b]	254 (15145), 295 (29355), 310 (20300, sh), 330 (1470, sh)	356	270	2.2 (40.2), 7.9 (59.8)	
"concentrated" Bpy-SH solution (3.5×10^{-2} M) [b]	Too intense	418	362		0.9 (81.5), 3.0 (18.5)
Solid Bpy-SH	Not available	435	397		0.7 (86.0), 2.7 (14.0)
Bpy-SH@Au-plate	Not available	435	280, 361		0.6 (5.5), 0.9 (94.5)

[a] Water solution. [b] Dichloromethane solution. [c] The molar extinction coefficient is not defined for the extinction spectrum where electronic transitions are present along with plasmonic resonances. sh = shoulder.

The absorption spectrum of the diluted Bpy-SH dichloromethane solution (1.3×10^{-5} M) is reported in Figure S5 of the Supplementary Materials. It shows two principal peaks at 254 and 295 nm (with a series of shoulders) due to aromatic ππ* transitions, and a weak band at approximately 330 nm, attributed to a symmetry forbidden nπ* transition involving the sulfur atom. In the absorption spectrum of an analogous solution of 2,2′-bipyridine, this band is absent (See Figure S6 in Supplementary Materials), which confirms this attribution. The deactivation originates from a mixed nπ*-ππ* singlet state giving an asymmetric and unstructured emission band at 352 nm (Figure 2); its intensity decay kinetics were deconvoluted with a biexponential function, providing lifetime values of 7.9 and 2.2 ns (with pre-exponential factors of 0.60 and 0.40, respectively). By increasing the concentration, the emission spectrum showed new features (Figure S7 in Supplementary Materials): the 352 nm emission band underwent a bathochromic shift up to 370 nm, and new emission structured peaks were detected at 396, 422, and 485 nm, becoming gradually more evident as the concentration increased. These new peaks can be attributed to the continuous formation of ππ-aggregates, which takes place in the ground electronic state, as can be inferred by comparison of the ground-state spectral patterns (i.e., the absorption spectrum of dilute Bpy-SH in Figure S5, and the excitation spectrum of concentrated Bpy-SH in Figure 2) of diluted and concentrated Bpy-SH to the emission spectral patterns: differences were observed in both cases, confirming aggregation in the ground state [22]. Very interestingly, by diluting the concentrated solutions, the shape of the emission spectrum was restored; thus, it confirms that these spectral variations are not due to the creation of new covalent species but to the formation of ππ-aggregates. The emission spectrum of a highly concentrated solution (3.5×10^{-2} M), reported in Figure 2, clearly shows the disappearance of the 356 nm band, attributed to the isolated Bpy-SH, and well-defined bands at 396 and 418 nm (with weak shoulders at around 445 and 485 nm) attributed to the π-aggregates.

Comparing the excitation spectrum of the diluted solution with that of the concentrated solution, it is evident that Bpy-SH molecules in the concentrated solution were aggregated (the weak band at 273 nm in the excitation spectrum of the concentrated solution is due to a small fraction of non-aggregated bipyridine). The absorption spectrum of the concentrated solution was not collected due to the high concentration. Emission spectrum of the concentrated solution as recorded by excitation at 273 nm gave a negligible emission. The intensity decay kinetics were deconvoluted with a biexponential function, giving lifetime values of 3.0 and 0.9 ns (with pre-exponential factors of 0.18 and 0.82, respectively), considerably shorter than those measured in a diluted solution.

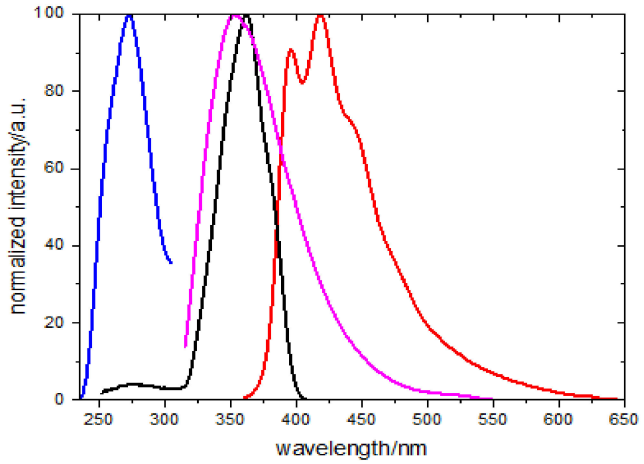

Figure 2. Excitation (λ_{em} = 356 nm, blue line) and emission (λ_{ex} = 270 nm, magenta line) spectra of Bpy-SH in diluted dichloromethane solution (1.3×10^{-5} M). Excitation (λ_{em} = 418 nm, black line) and emission (λ_{ex} = 362 nm, red line) spectra of Bpy-SH in concentrated dichloromethane solution (3.5×10^{-2} M).

The aggregate formation was confirmed by comparing the emission and excitation spectra of the concentrated solution with those of a powder sample (Figure 3). The maxima of the luminescence spectra (λ_{em}^{max} = 435 nm; λ_{ex}^{max} = 397 nm) and their shape gave evidence of the presence of aggregates both in the solid sample and in the concentrated solution.

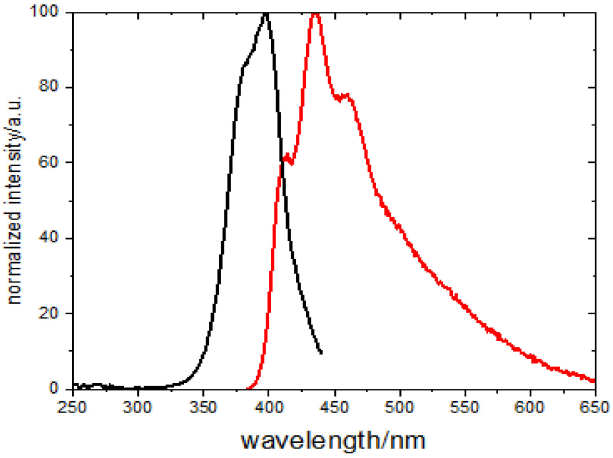

Figure 3. Excitation (λ_{em} = 435 nm, black line) and emission (λ_{ex} = 370 nm, red line) spectra of Bpy-SH in powder sample.

Lifetime values measured in solid (2.7 and 0.7 ns) are almost identical to those measured in the concentrated solution (Table 1) and considerably lower than those measured in the diluted solution, confirming that the formation of π–π stacking interactions between bipyridine molecules results in a faster radiative deactivation, stabilizing the energy levels

of the excited states and reducing the radiative rate constant. After carefully examining the photophysics of Bpy-SH, we will now illustrate and discuss the properties of gold nanoparticles functionalized with this chromophore. Starting from the nanorods Bpy-SH@AuNR, the absorption spectrum they display once dispersed in water is reported in Figure 4, while Figure 5 shows the relative excitation and emission spectra.

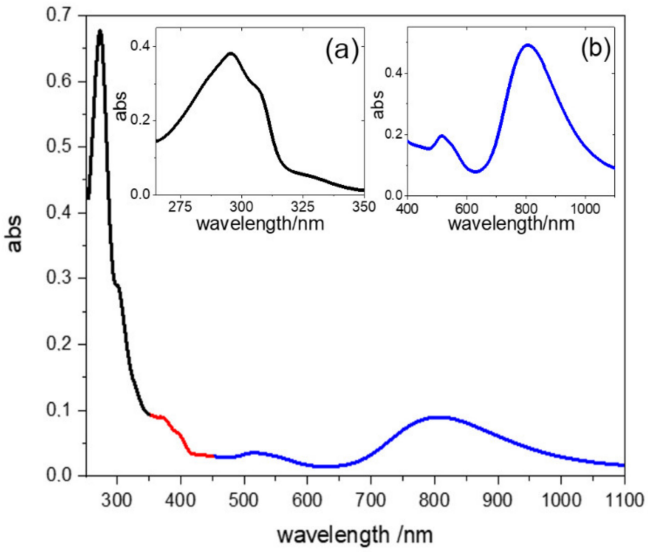

Figure 4. The absorption spectrum of Bpy-SH@AuNR in water solution. The three spectral zones are drawn in different colors: bands attributed to the isolated Bpy-SH transitions (black line), bands attributed to the aggregated Bpy-SH transitions (red line), bands due to the plasmonic resonances (blue line). Subfigure (**a**): absorption spectrum of diluted Bpy, see Figure S5 in Supplementary Materials; Subfigure (**b**): extinction spectrum of Bpy-SH@AuNR. The absorption spectrum of the concentrated solution was not collected due to the high concentration.

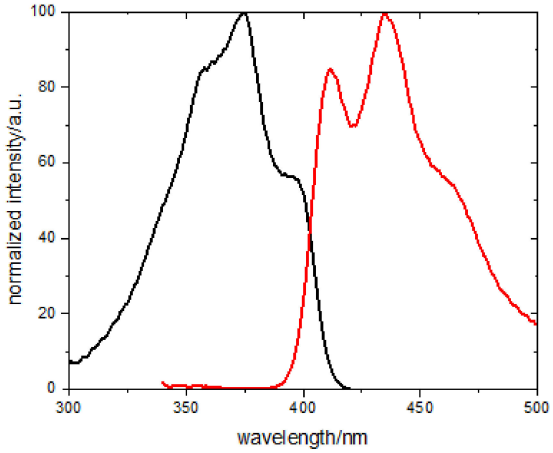

Figure 5. Excitation (λ_{em} = 435 nm, black line) and emission (λ_{ex} = 325 nm, red line) spectra of Bpy-SH@AuNR in water solution.

In the absorption spectrum, several bands are present due to the plasmon resonance of the nanorods and relative to the Bpy-SH molecules linked to the nanoparticles. Bands at 840 and 530 nm are due to the longitudinal and transversal plasmonic modes, respectively, while the spectroscopic features below 450 nm suggest the presence of both isolated and aggregated thiolated bipyridines.

In fact, within the range between 450 and 350 nm, a series of maxima (368 nm) and shoulders (at approximately 390 nm) attributable to Bpy-SH aggregates are present (see the excitation spectrum in Figure 2), while between 260 and 350 nm there are bands (at 273 nm

and the shoulder at approximately 300 nm) that can be attributed to the presence of isolated Bpy-SH molecules (see the absorption spectrum in Figure S5 in Supplementary Materials).

The presence of this different organization of Bpy-SH on the gold nanorods surface was corroborated by the examination of the Bpy-SH@AuNR emissive properties. Figure 5 reports the emission spectrum obtained by exciting at 325 nm. We chose to excite at this wavelength to highlight both the weak emission at about 350 nm, typical of isolated Bpy-SH molecules, and the well-structured emission band with a maximum at 435 nm, attributed to Bpy-SH molecules anchored on the metal through a strong S–Au bond [7,11] and stacked together to form a monolayer on the nanoparticle's surface.

The excitation spectrum in Figure 5 (recorded at 435 nm) confirms the identity of the emissive species; in fact, a comparison to the analogous spectra shown in Figures 2 and 3 suggests the presence of stacked chromophores. Figure S8 in Supplementary Materials reports the excitation spectrum of Bpy-SH@AuNR recorded at λ_{em} = 350 nm (i.e., on the emission maximum of the isolated chromophore), confirming the simultaneous presence of this species.

Our hypothesis is illustrated in Scheme 1: the photophysical data highlight both the presence of aggregated and isolated Bpy-SH molecules. This is plausible if we assume that a stacked Bpy-SH monolayer is formed on the gold nanorods' sides, while on the tips these molecules, anchored Bpy-SH molecules, are unable to form any efficient stacking due to the large curvature of the nanosurface, thus behaving as isolated molecules. The lifetime values (Table 1) collected on the emission maximum of the isolated molecule (i.e., at 352 nm) are longer than that of the monolayered stacked molecules (i.e., at 418 nm), upholding this picture. The model proposed herein is also in agreement with the self-assembly properties of Bpy-SH molecules deposited onto the gold surface, as proposed by Hamoudi and Esaulov [10]. Indeed, Bpy-SH molecules mainly constituted of a rigid core made of two consecutive aromatic rings are more likely to stand straight on the gold surface, leaving a free pendant SH group, rather than being anchored from both sides onto the gold surface. This staple-like geometry is indeed highly disfavored for steric hindrance, as the arms-bearing SH functional groups made of only one carbon atom are too short. Moreover, the existence of free SH moieties, which has been previously revealed by XPS measurements [11] is further corroborated by the high solubility of the functionalized nanoparticles in water.

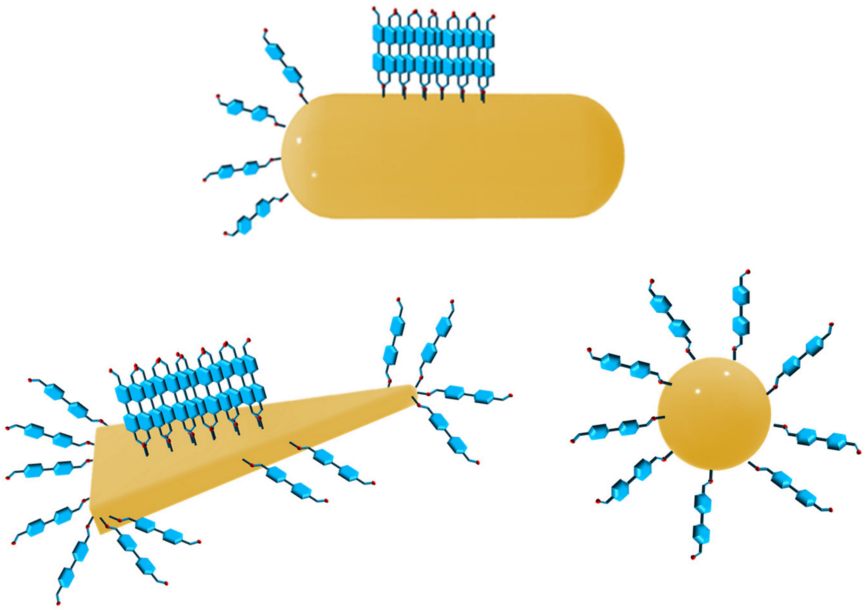

Scheme 1. Schematic representation of Bpy-SH@AuNR, Bpy-SH@AuNT, and Bpy-SH@AuNS (molecules are not in scale). The curvature of the nanosphere is identical to that of the nanorod's tips.

In any case, to further validate our hypothesis, we prepared (see Experimental section) and characterized a Bpy-SH monolayer deposited onto gold substrates (Bipy-SH@Au-plate). Furthermore, to confirm the role of the increased curvature of the tips of the nanorods, we prepared Bpy-SH-functionalized gold nanospheres (Bpy-SH@AuNS) of comparable diameter to the end parts of the nanorods and, finally, to obtain a planar nanosurface with zero curvature, we prepared thiolated bipyridine-functionalized gold nanotriangles (Bpy-SH@AuNT).

Figure 6 reports the emission and excitation spectra of Bipy-SH@Au-plate. The position and shape of the bands and the lifetime value (Table 1) of the monolayered chromophore on the gold surface completely overlap with the data collected from Bpy-SH@AuNR, confirming the formation of SAM onto the sides of the nanorod. Note that the slight differences in the lifetime values are most likely because the nanorods are dispersed in water, while the gold plates are not.

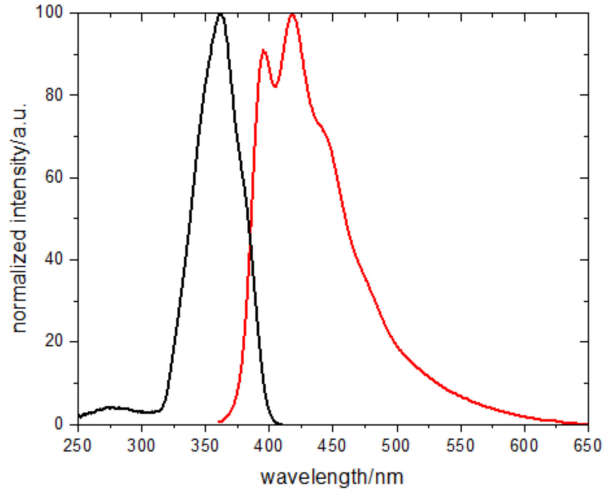

Figure 6. Excitation (λ_{em} = 435 nm, black line) and emission (λ_{ex} = 325 nm, red line) spectra of Bpy-SH@Au-plate.

Photophysical data recorded from the Bpy-SH@AuNS and Bpy-SH@AuNT solutions (Table 1) are of particular interest. The absorption spectrum of Bpy-SH@AuNS (Figure 7) shows a prominent band at 292 nm, due to the $\pi\pi^*$ transition on Bpy-SH, while in the inset, a plasmon resonance band is visible at 520 nm, exactly in the position expected for nanospheres of 18 nm in diameter (see Figure S2 in Supplementary Materials) [37]. Figure 8 reports the absorption spectrum of the gold nanotriangles functionalized with Bpy-SH, namely Bpy-SH@AuNT.

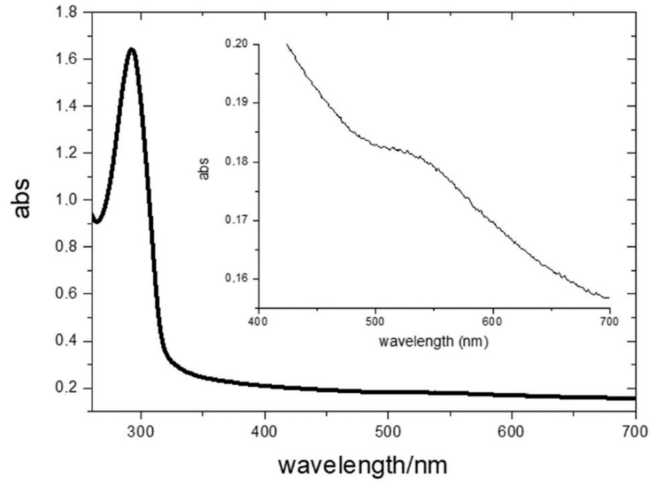

Figure 7. Absorption spectrum of Bpy-SH@AuNS in water solution.

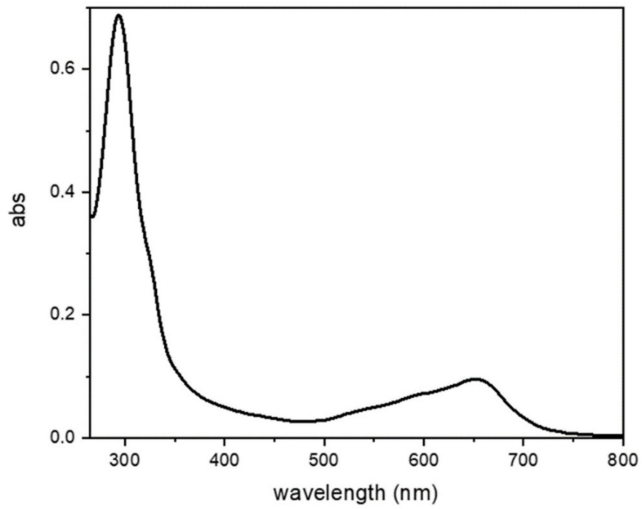

Figure 8. Absorption spectrum of Bpy-SH@AuNT in water solution.

In this spectrum, transitions attributed both to the isolated Bpy-SH molecules (the intense band at 294 nm) and to the aggregated Bpy-SH (the shoulder at about 350 nm) are observed, while the peaks between 550 and 660 are due to the plasmon resonance of the nanoparticles (see Figure S4 in Supplementary Materials). Emission and excitation spectra (Figure 9) of Bpy-SH@AuNS show maxima at 350 and 265 nm, respectively. The measured lifetime values are τ_1 = 1.5 ns and τ_2 = 7.6 ns (Table 1). These data, consistent with the absorption spectrum reported in Figure 7, account for the presence of non-aggregated Bpy-SH molecules on the nanosurface, as expected according to the nanospheres curvature being almost identical to that of the tips of the nanorods (see Scheme 1)

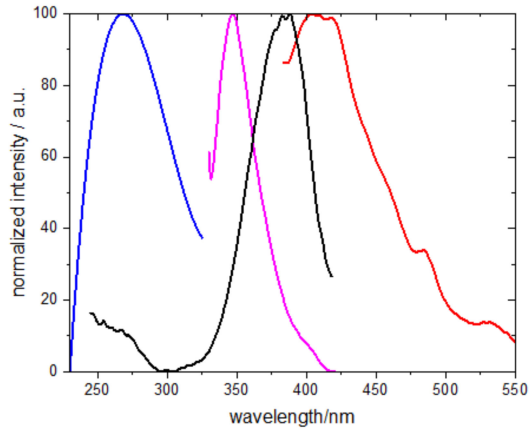

Figure 9. Excitation (λ_{em} = 350 nm, blue line) and emission (λ_{ex} = 265 nm, magenta line) spectra of Bpy-SH@AuNS in water solution. Excitation (λ_{em} = 410 nm, black line) and emission (λ_{ex} = 380 nm, red line) spectra of Bpy-SH@AuNT water solution.

Emission and excitation spectra of Bpy-SH@AuNT, reported in Figure 9, instead show maxima at 418 and 382 nm, respectively, and the measured lifetime values are τ_1 = 0.7 ns and τ_2 = 2.4 ns (Table 1). These values indicate the presence of mostly aggregated Bpy-SH, in line with what was expected, since the nanotriangles' surface has zero curvature, allowing SAM formation (Scheme 1). However, the absorption spectrum (Figure 8) shows not only features attributable to stacked aggregates, but also the presence of isolated Bpy-SH. Indeed, the excitation spectrum of Bpy-SH@AuNT (black line in Figure 9) shows a weak maximum at 265 nm, typical of isolated Byp-SH. The excitation spectrum of Bpy-SH@AuNT was collected at 410 nm, where even the isolated Bpy-SH has a weak emission. Since the Bpy-SH in aqueous solution is not soluble, this band is due to the presence of the chromophore bound on the nanotriangles that is unable to form aggregates.

Nanotriangles are characterized by large flat surfaces (with zero curvature) but have sharp angles at the vertexes (where the radius of curvature becomes very high). These vertexes are highly reactive sites where a high plasmonic field is generated [38]. Therefore, it is plausible to suppose that on the triangle's vertexes Bpy-SH molecules (Scheme 1), due to the largest curvature, are less prompted to form aggregates, and therefore must be responsible for the observed spectral bands.

It is important to note that none of the observed features can be imputed to coupling effects between the chromophore and the gold plasmonic resonance. The emission spectrum of Bpy-SH did not overlap with the plasmonic bands of the nanoparticles in any of the SAM@AuNP samples, excluding energy or electron transfer involved in coupling processes [16,39–42]. The photophysical properties are governed by stacking interactions between the aromatic rings of adjacent molecules; hence, only the shape of the nanoparticles is responsible of the observed differences and must be related exclusively to the type of organization within the SAMs deposited onto the surface of the nanoparticles.

3.2. Raman Spectroscopy

The formation of the SAM by the Bpy-SH on two sample preparations (i.e., Bpy-SH@Au-plate and Bpy-SH@AuNR) was investigated by Raman spectroscopy [43–49]. As a starting reference, the representative Raman spectrum of the thiolated bipyridine (Bpy-SH) powder collected with the laser source at 532 nm is shown in Figure 10. The Raman band attributions are reported in Table S1 in the Supplementary Materials. In the Raman spectra, collected by a laser source at 633 nm, no Raman features were detected and for this reason, relative spectra were not shown.

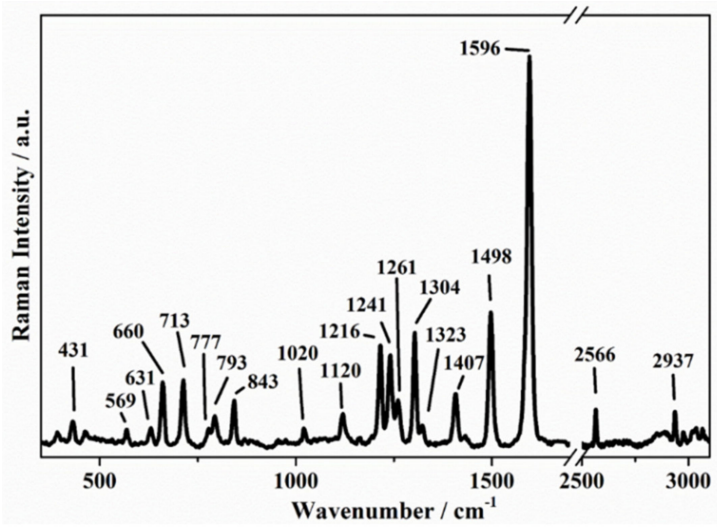

Figure 10. Raman spectrum of Bpy-SH in powder sample collected in the ranges between 350 and 1700 cm^{-1} and between 2500 and 3100 cm^{-1} (laser source at 532 nm).

When Bpy-SH is deposited onto a gold plate [50], a surface-enhanced Raman scattering (SERS) effect is observed. In Figure 11, the two representative SERS spectra collected on the sample Bpy-SH@Au-plate are shown. The first representative SERS spectra is shown in the range between 400 and 1650 cm^{-1} (Figure 11a), while the second representative SERS spectrum is shown in the ranges between 500 and 1100 cm^{-1}, 1170 and 1800 cm^{-1}, and 2450 and 3000 cm^{-1} (Figure 11b,c) [51–54]. The ranges not shown for both the spectra did not present any detectable features. The sharp peaks of Figure 11a that fall at 433, 465, 569, 630, 661, 713, 794, 843, 1022, 1119, 1215, 1240, 1260, 1301, 1321, 1406, 1496, and 1593 cm^{-1} can be assigned by using the modes described in Table S1 in the Supplementary Materials. Such Raman peaks are due to the presence of Bpy-SH. The SERS spectra shown in Figure 11b,c are quite interesting. In this case, the Raman band at 2561 cm^{-1} is assigned

to the S–H bond stretching and the bands at 747 and 1541 cm^{-1} are associated to the ν_5 (CH o.p. bend + ring o.p. def) and ν_2 (ring stret.) mode of Bpy-SH, respectively [55].

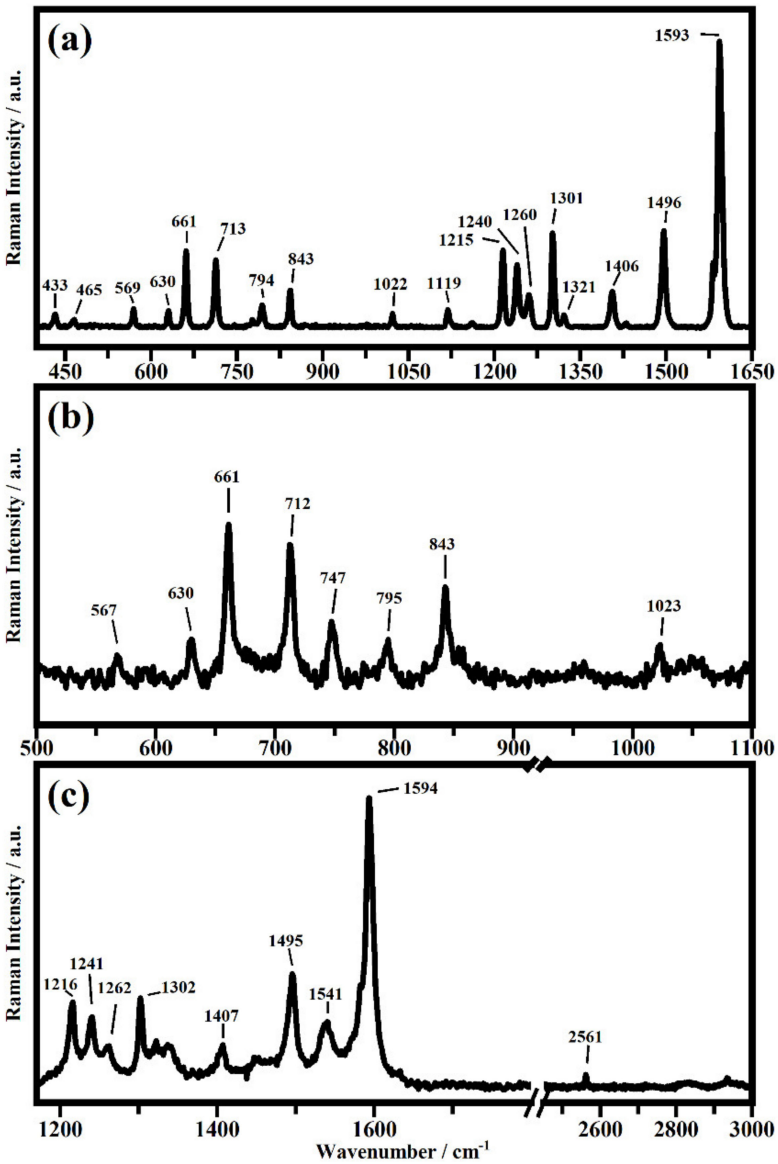

Figure 11. The first representative SERS spectrum of Bpy-SH@Au-plate in the range between 400 and 1650 cm^{-1} (laser source at 633 nm) (**a**) and the second representative SERS spectra of Bpy-SH@Au-plate in the ranges between 500 and 1100 cm^{-1} (**b**), 1170 and 1800 cm^{-1}, 2450 and 3000 cm^{-1} (**c**) (laser source at 633 nm).

The presence of the band associated with S-H stretching means that the SERS effect allows for the observation that the Bpy-SH layer on the gold plate in the Bpy-SH@Au-plate samples is not homogenous; in some areas, there are not thiol groups free and in others, there is the presence of free S-H groups. The explanation for such experimental evidence could be attributed to the orientation of the Bpy-SH molecules on the plate. When the S-H groups are detectable, the molecules of Bpy-SH are perpendicularly bonded to the gold surface and one of two thiols group remains free. On the areas where the S-H stretching is not visible (Figure 11), the Byp-SH molecules are bonded in parallel to the gold surface.

Figure 12 reports the representative Raman spectrum of Bpy-SH@AuNR in water solution, collected in the 400–1800 cm^{-1} range (in the other ranges there are no detectable Raman features).

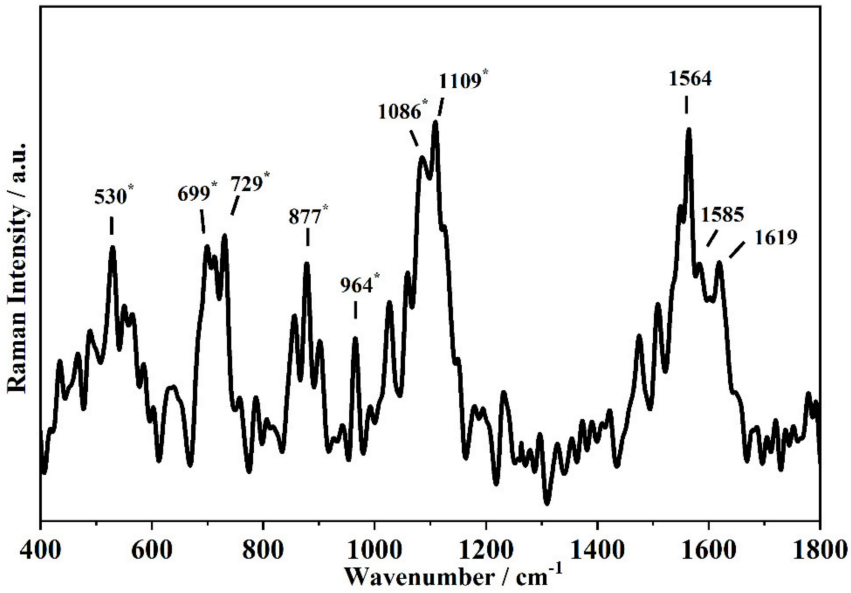

Figure 12. Raman spectrum of Bpy-SH@AuNR in water solution, collected in the 400–1800 cm^{-1} range (laser source at 532 nm). The peak indicated with the symbol "*" as an apex is assigned to PEG-SH while the others to Bpy-SH.

It is interesting to see the presence of many Raman bands that are very close to those observed in the spectra collected from the $AuNR_{PEG-SH}$ water sample (Figures S9 and S10 and Table S2 in Supplementary Materials): 530, 699, 729, 877, 964, 1086, and 1109 cm^{-1}. In addition to those Raman bands, the spectrum shows other bands at 1564, 1585, and 1619 cm^{-1} that are ascribed to the ring and C–N bond stretching of Bpy-SH deposited on the nanorods and become detectable for the SERS effect induced by the gold nanorods. Of course, it is well known that the solvent used in the last sample (water) has a very low Raman cross section. For this reason, the Raman signals coming from the nanoparticles are not covered by the Raman of the solvent [56–61].

4. Conclusions

Self-assembled monolayers are a key technology, not only because of their wide fields of application, but also because they constitute a fundamental research topic for the understanding of interfacial systems: shedding light on the wettability, electrostatic nature, and interaction properties of surfaces. SAMs are a prototypical form of nanotechnology; since they determine the interfacial properties of surfaces and nanostructures are predominantly "all surface", they are broadly useful when combined with metal nanoparticles. On the other hand, the great versatility with which it is possible to obtain different shapes of metal nanoparticles allows for the control of the formation of SAMs through careful tuning of the nanosurfaces' curvature.

In this work, for the first time, we used fluorescence to study SAM formation on gold nanoparticles in correlation with the nanosurface curvature by preparing spherical, rod-shaped, and triangular nanoparticles. Fluorescence spectroscopy, as an investigation technique, was successful as we have used a thiolated bipyridine as SAM brick molecule, whose emission wavelength and excited-state lifetime depend on the formation of close-contact ππ-stacked aggregates. When such aggregates are formed, the emission wavelength undergoes a considerable redshift accompanied by a decrease in the lifetime of the excited states.

Bpy-SH was carefully selected to have a methylene group between the terminal sulfured and the aromatic ring, considering that an SH group directly linked to the pyridine ring could have favored an electron transfer from the gold core to the chromophore, interfering with its photophysics. On the other hand, a longer aliphatic chain could have

favored Bpy-SH to deposit on the nanosurface (using both thiol terminals to bind to gold) preventing efficient $\pi\pi$ stacking in this case.

We have shown that on the faces of nanotriangles Bpy-SH molecules form highly compact SAMs, since the flat nanosurface allows the bipyridines to form $\pi\pi$-stacking interactions; on curved nanosurfaces, such as 18 nm diameter nanospheres, this is not possible. For nanorods, the observed spectral features can be ascribed to both stacked and isolated Bpy-SH, due to the functionalization of both the tips (which have a curvature similar to that of the spheres) and the sides (which are comparable to the faces of the nanotriangles). Since the use of fluorescence spectroscopy is an innovative technique for the detection of SAMs formed on gold nanoparticles, we performed a Raman spectroscopy investigation on the Bpy-SH functionalized nanosurfaces, since this is a technique already used to study SAMs on macro surfaces.

In this work, the attribution of the Raman spectra observed on the Bpy-SH powder has been propoosed. A SERS effect induced by gold nanorods and a gold plate has been shown on the Bpy-SH, with the characteristic ring stretching mode at about 1595 cm^{-1} seen in both the systems. Moreover, it has been shown that the Bpy-SH molecules are most likely bonded in two different ways: parallel to the gold surface (Figure 11) and perpendicularly to the surface (Figure 12). By exploiting the SERS effect due to the plasmonic field of the nanoparticles, the obtained outcome confirms what has been observed through the luminescence techniques.

The results obtained from these SAM@AuNPs are very encouraging, as they show a possibility of studying SAM formation using fluorescence spectroscopy and confirming the correlation between the curvature of a nanosurface and the growth of SAMs. This understanding can help to improve the properties of nanoparticles, such as stability and dispersibility, consolidating their use as platforms for the delivery of biomolecules and other therapeutic agents.

Supplementary Materials: The following supporting information can be downloaded at: https://www.mdpi.com/article/10.3390/chemosensors10050176/s1, Figure S1: Extinction spectrum of $AuNR_{CTAB}$ in water (black line) and of $AuNR_{PEG\text{-}SH}$ in dichloromethane (red line). Figure S2: Extinction spectrum of $AuNS_{SC}$ in water. Figure S3: TEM images of the obtained nanoparticles (see Section 2.3 in the main text) before the selective precipitation (a); after precipitation: supernatant (b) and precipitate (c). Figure S4: Extinction spectra of nanoparticles solutions before the selective precipitation (red line); after precipitation: supernatant (blue line) and precipitate (black line) containing $AuNT_{CTAC}$ purified nanoparticles (see Figure S3 for the correspondent TEM image). Figure S5: Absorption spectrum of Bpy-SH in diluted dichloromethane solution (1.3×10^{-5} M). Figure S6: Absorption spectrum of 2,2′-bipyridine in diluted dichloromethane solution (1.3×10^{-5} M). Figure S7: Emission spectra of Bpy-SH dichloromethane solutions at various concentrations (λ_{ex} = 306 nm). Figure S8: Excitation spectrum of **Bpy-SH@AuNR** in water solution (λ_{em} = 350 nm). Figure S9: Raman spectrum of PEG-SH in powder sample collected in the ranges between 150 and 1600 cm^{-1} and between 2400 and 3100 cm^{-1} (laser source at 532 nm). Figure S10: Raman spectrum of PEG-SH in powder sample collected in the ranges between 150 and 1600 cm^{-1} and between 2400 and 3100 cm^{-1} (laser source at 532 nm). Table S1: Raman modes attribution of Bpy-SH in powder sample. Table S2: PEG-SH Raman modes and their attribution.

Author Contributions: Synthesis and functionalization of nanoparticles, photophysical characterization, A.C. (Angela Candreva); Figures editing, F.P.; Bibliography, G.D.M. and F.S.; RAMAN investigation, A.N., C.R., R.C.B. and M.C.; Visualization and Validation, A.C. (Alessandra Crispini), N.G. and L.R.; Project administration, supervision and writing of the original draft, M.L.D. All authors have read and agreed to the published version of the manuscript.

Funding: This research was funded by the DEMETRA Project (PON ARS01_00401).

Institutional Review Board Statement: Not applicable.

Informed Consent Statement: Not applicable.

Data Availability Statement: Data are contained within the article.

Acknowledgments: The authors thank R. Termine (CNR Nanotec) for the preparation of gold substrates on silicon wafers. Angela Candreva is grateful to Luis Liz-Marzan (Ikerbasque Research Professor, Scientific Director at CIC biomaGUNE- San Sebastián, Spain) for welcoming her into his laboratory and for mentoring her in nanoparticle synthesis techniques.

Conflicts of Interest: The authors declare no conflict of interest.

References

1. Ulman, A. Formation and Structure of Self-Assembled Monolayers. *Chem. Rev.* **1996**, *96*, 1533–1554. [CrossRef] [PubMed]
2. Schreiber, F. Structure and Growth of Self-Assembling Monolayers. *Prog. Surf. Sci.* **2000**, *65*, 151–257. [CrossRef]
3. Kühnle, A. Self-Assembly of Organic Molecules at Metal Surfaces. *Curr. Opin. Colloid Interface Sci.* **2009**, *14*, 157–168. [CrossRef]
4. Chaki, N.K.; Vijayamohanan, K. Self-Assembled Monolayers as a Tunable Platform for Biosensor Applications. *Biosens. Bioelectron.* **2002**, *17*, 1–12. [CrossRef]
5. Motealleh, A.; Dorri, P.; Kehr, N.S. Self-Assembled Monolayers of Chiral Periodic Mesoporous Organosilica as a Stimuli Responsive Local Drug Delivery System. *J. Mater. Chem. B* **2019**, *7*, 2362–2371. [CrossRef]
6. Gankin, A.; Mervinetsky, E.; Alshanski, I.; Buchwald, J.; Dianat, A.; Gutierrez, R.; Cuniberti, G.; Sfez, R.; Yitzchaik, S. ITO Work Function Tunability by Polarizable Chromophore Monolayers. *Langmuir* **2019**, *35*, 2997–3004. [CrossRef]
7. Love, J.C.; Estroff, L.A.; Kriebel, J.K.; Nuzzo, R.G.; Whitesides, G.M. Self-Assembled Monolayers of Thiolates on Metals as a Form of Nanotechnology. *Chem. Rev.* **2005**, *105*, 1103–1170. [CrossRef]
8. Laibinis, P.E.; Whitesides, G.M.; Allara, D.L.; Tao, Y.T.; Parikh, A.N.; Nuzzo, R.G. Comparison of the Structures and Wetting Properties of Self-Assembled Monolayers of n-Alkanethiols on the Coinage Metal Surfaces, Copper, Silver, and Gold. *J. Am. Chem. Soc.* **1991**, *113*, 7152–7167. [CrossRef]
9. Heister, K.; Allara, D.L.; Bahnck, K.; Frey, S.; Zharnikov, M.; Grunze, M. Deviations from 1:1 Compositions in Self-Assembled Monolayers Formed from Adsorption of Asymmetric Dialkyl Disulfides on Gold. *Langmuir* **1999**, *15*, 5440–5443. [CrossRef]
10. Hamoudi, H.; Esaulov, V.A. Selfassembly of α,ω-Dithiols on Surfaces and Metal Dithiol Heterostructures. *Ann. Phys.* **2016**, *528*, 242–263. [CrossRef]
11. Hamoudi, H. Bottom-up Nanoarchitectonics of Two-Dimensional Freestanding Metal Doped Carbon Nanosheet. *RSC Adv.* **2014**, *4*, 22035–22041. [CrossRef]
12. Hamoudi, H.; Prato, M.; Dablemont, C.; Cavalleri, O.; Canepa, M.; Esaulov, V.A. Self-Assembly of 1,4-Benzenedimethanethiol Self-Assembled Monolayers on Gold. *Langmuir* **2010**, *26*, 7242–7247. [CrossRef] [PubMed]
13. Pethkar, S.; Aslam, M.; Mulla, I.S.; Ganeshan, P.; Vijayamohanan, K. Preparation and Characterisation of Silver Quantum Dot Superlattice Using Self-Assembled Monolayers of Pentanedithiol. *J. Mater. Chem.* **2001**, *11*, 1710–1714. [CrossRef]
14. Sarathy, K.V.; Thomas, P.J.; Kulkarni, G.U.; Rao, C.N.R. Superlattices of Metal and Metal-Semiconductor Quantum Dots Obtained by Layer-by-Layer Deposition of Nanoparticle Arrays. *J. Phys. Chem. B* **1999**, *103*, 399–401. [CrossRef]
15. Jackson, A.M.; Myerson, J.W.; Stellacci, F. Spontaneous Assembly of Subnanometre-Ordered Domains in the Ligand Shell of Monolayer-Protected Nanoparticles. *Nat. Mater.* **2004**, *3*, 330–336. [CrossRef] [PubMed]
16. Eustis, S.; El-Sayed, M.A. Why Gold Nanoparticles Are More Precious than Pretty Gold: Noble Metal Surface Plasmon Resonance and Its Enhancement of the Radiative and Nonradiative Properties of Nanocrystals of Different Shapes. *Chem. Soc. Rev.* **2006**, *35*, 209–217. [CrossRef]
17. Lu, W.; Suo, Z. Symmetry Breaking in Self-Assembled Monolayers on Solid Surfaces: Anisotropic Surface Stress. *Phys. Rev. B* **2002**, *65*, 085401. [CrossRef]
18. Häkkinen, H. The gold–sulfur interface at the nanoscale. *Nat. Chem.* **2012**, *4*, 443–455. [CrossRef]
19. Liang, J.; Rosa, L.G.; Scoles, G. Nanostructuring, Imaging and Molecular Manipulation of Dithiol Monolayers on Au(111) Surfaces by Atomic Force Microscopy. *J. Phys. Chem. C* **2007**, *111*, 17275–17284. [CrossRef]
20. Rieley, H.; Kendall, G.K.; Zemicael, F.W.; Smith, T.L.; Yang, S. X-ray Studies of Self-Assembled Monolayers on Coinage Metals. 1. Alignment and Photooxidation in 1,8-Octanedithiol and 1-Octanethiol on Au. *Langmuir* **1998**, *14*, 5147–5153. [CrossRef]
21. De Luca, O.; Caruso, T.; Turano, M.; Ionescu, A.; Godbert, N.; Aiello, I.; Ghedini, M.; Formoso, V.; Agostino, R.G. Adsorption of Nile Red Self-Assembled Monolayers on Au (111). *Langmuir* **2019**, *35*, 14761–14768. [CrossRef] [PubMed]
22. Lakowicz, J.R. *Principles of Fluorescence Spectroscopy*, 3rd ed.; Springer: New York, NY, USA, 2006.
23. Mei, J.; Leung, N.L.C.; Kwok, R.T.K.; Lam, J.W.Y.; Tang, B.Z. Aggregation-Induced Emission: Together We Shine, United We Soar! *Chem. Rev.* **2015**, *115*, 11718–11940. [CrossRef] [PubMed]
24. Scarpelli, F.; Ionescu, A.; Aiello, I.; La Deda, M.; Crispini, A.; Ghedini, M.; Brunelli, E.; Sesti, S.; Godbert, N. High Order in a Self-Assembled Iridium(III) Complex Gelator Towards Nanostructured IrO_2 Thin Films. *Chem.-Asian J.* **2018**, *12*, 2703–2710. [CrossRef] [PubMed]
25. Yin, K.; Lu, D.; Tian, W.; Zhang, R.; Yu, H.; Gorecka, E.; Pociecha, D.; Godbert, N.; Hao, J.; Li, H. Ordered structures of alkylated carbon dots and their applications in nonlinear optics. *J. Mater. Chem. C* **2020**, *8*, 8980–8991. [CrossRef]
26. Li, X.; Li, Q.; Wang, Y.; Quan, Y.; Chen, D.; Cheng, Y. Strong Aggregation-Induced CPL Response Promoted by Chiral Emissive Nematic Liquid Crystals (N*-LCs). *Chem. Eur. J.* **2018**, *24*, 12607–12612. [CrossRef]

27. Galyametdinov, Y.G.; Knyazev, A.A.; Dzhabarov, V.I.; Cardinaels, T.; Driesen, K.; Görller-Walrand, C.; Binnemans, K. Polarized Luminescence from Aligned Samples of Nematogenic Lanthanide Complexes. *Adv. Mater.* **2008**, *20*, 252–257. [CrossRef]
28. Agina, E.V.; Mannanov, A.A.; Sizov, A.S.; Vechter, O.; Borshchev, O.V.; Bakirov, A.V.; Shcherbina, M.A.; Chvalun, S.N.; Konstantinov, V.G.; Bruevich, V.V.; et al. Luminescent Organic Semiconducting Langmuir Monolayers. *ACS Appl. Mater. Interfaces* **2017**, *9*, 18078–18086. [CrossRef]
29. Yokota, H.; Okazaki, K.; Shimura, K.; Nakayama, M.; Kim, D. Photoluminescence Properties of Self-Assembled Monolayers of CdSe and CdSe/ZnS Quantum Dots. *J. Phys. Chem. C* **2012**, *116*, 5456–5459. [CrossRef]
30. Séro, L.; Sanguinet, L.; Derbré, S.; Boury, F.; Brotons, G.; Dabos-Seignon, S.; Richomme, P.; Séraphin, D. Fluorescent Self-Assembled Monolayers of Umbelliferone: A Relationship between Contact Angle and Fluorescence. *Langmuir* **2013**, *29*, 10423–10431. [CrossRef]
31. Sun, S.-S.; Lees, A.J. Photophysics and Evidence of Excimer Formation, Linear Bipyridines in Solution and Solid Films. *J. Photochem. Photobiol. A* **2001**, *140*, 157–161. [CrossRef]
32. Scarabelli, L.; Grzelczak, M.; Liz-Marzán, L.M. Tuning Gold Nanorod Synthesis through Prereduction with Salicylic Acid. *Chem. Mater.* **2013**, *25*, 4232–4238. [CrossRef]
33. Candreva, A.; Lewandowski, W.; La Deda, M. Thickness control of the silica shell: A way to tune the plasmonic properties of isolated and assembled gold nanorods. *J. Nanopart. Res.* **2021**, *24*, 19. [CrossRef]
34. Liu, Q.; Yuan, Y.; Smalyukh, I.I. Electrically and Optically Tunable Plasmonic Guest–Host Liquid Crystals with Long-Range Ordered Nanoparticles. *Nano Lett.* **2014**, *14*, 4071–4077. [CrossRef] [PubMed]
35. Scarabelli, L.; Coronado-Puchau, M.; Giner-Casares, J.J.; Langer, J.; Liz-Marzán, L.M. Monodisperse Gold Nanotriangles: Size Control, Large-Scale Self-Assembly, and Performance in Surface-Enhanced Raman Scattering. *ACS Nano* **2014**, *8*, 5833–5842. [CrossRef] [PubMed]
36. Sakotsubo, Y.; Ohgi, T.; Fujita, D.; Ootuka, Y. Tunneling Spectroscopy of Isolated Gold Clusters Grown on Thiol/Dithiol Mixed Self-Assembled Monolayers. *Phys. E Low-Dimens. Syst. Nanostruct.* **2005**, *29*, 601–605. [CrossRef]
37. Bastús, N.G.; Comenge, J.; Puntes, V. Kinetically Controlled Seeded Growth Synthesis of Citrate-Stabilized Gold Nanoparticles of up to 200 Nm: Size Focusing versus Ostwald Ripening. *Langmuir* **2011**, *27*, 11098–11105. [CrossRef]
38. Gao, M.; Zheng, X.; Khan, I.; Cai, H.; Lan, J.; Liu, J.; Wang, J.; Wu, J.; Huang, S.; Li, S.; et al. Resonant Light Absorption and Plasmon Tunability of Lateral Triangular Au Nanoprisms Array. *Phys. Lett. A* **2019**, *383*, 125881. [CrossRef]
39. Battistini, G.; Cozzi, P.G.; Jalkanen, J.-P.; Montalti, M.; Prodi, L.; Zaccheroni, N.; Zerbetto, F. The Erratic Emission of Pyrene on Gold Nanoparticles. *ACS Nano* **2008**, *2*, 77–84. [CrossRef]
40. Dulkeith, E.; Morteani, A.C.; Niedereichholz, T.; Klar, T.A.; Feldmann, J.; Levi, S.A.; van Veggel, F.C.J.M.; Reinhoudt, D.N.; Möller, M.; Gittins, D.I. Fluorescence Quenching of Dye Molecules near Gold Nanoparticles: Radiative and Nonradiative Effects. *Phys. Rev. Lett.* **2002**, *89*, 203002. [CrossRef]
41. Candreva, A.; Di Maio, G.; La Deda, M. A Quick One-Step Synthesis of Luminescent Gold Nanospheres. *Soft Matt.* **2020**, *16*, 10865–10868. [CrossRef]
42. De Luca, A.; Ferrie, M.; Ravaine, S.; La Deda, M.; Infusino, M.; Rashed, A.R.; Veltri, A.; Aradian, A.; Scaramuzza, N.; Strangi, G. Gain Functionalized Core-Shell Nanoparticles: The Way to Selectively Compensate Absorptive Losses. *J. Mater. Chem.* **2012**, *22*, 8846–8852. [CrossRef]
43. Scarpelli, F.; Ionescu, A.; Ricciardi, L.; Plastina, P.; Aiello, I.; la Deda, M.; Crispini, A.; Ghedini, M.; Godbert, N. A novel route towards water-soluble luminescent iridium(III) complexes via a hydroxy-bridged dinuclear precursor. *Dalton Trans.* **2016**, *45*, 17264–17273. [CrossRef] [PubMed]
44. Liguori, P.F.; Ghedini, M.; la Deda, M.; Godbert, N.; Parisi, F.; Guzzi, R.; Ionescu, A.; Aiello, I. Electrochromic behaviour of Ir(III) bis-cyclometalated 1,2-dioxolene tetra-halo complexes: Fully reversible catecholate/semiquinone redox switches. *Dalton Trans.* **2020**, *49*, 2628–2635. [CrossRef] [PubMed]
45. Ionescu, A.; Caligiuri, R.; Godbert, N.; Candreva, A.; la Deda, M.; Furia, E.; Ghedini, M.; Aiello, I. New electropolymerizable Ir(III) complexes with β-ketoiminate ancillary ligands. *Chem. Asian J.* **2019**, *14*, 3025–3034. [CrossRef]
46. Mutai, T.; Cheon, J.D.; Tsuchiya, G.; Araki, K. Tuning of fluorescence properties of aminopyridine*** fluorophores by N-substitution. *J. Chem. Soc. Perkin Trans. 2* **2002**, *2*, 862–865. [CrossRef]
47. Poizat, O.; Buntinx, G.; Valat, P.; Wintgens, V.; Bridoux, M. Photochemistry of 4,4′-Bipyridine. Nanosecond Absorption and Raman Study of the Hydrogen Atom Abstraction from Methanol and 2-Propanol. *J. Phys. Chem.* **1993**, *97*, 5905–5910. [CrossRef]
48. Gao, X. Reproducibility in Surface-Enhanced Raman Spectroscopy. *J. Phys. Chem.* **1990**, *94*, 6858–6864. [CrossRef]
49. Ducasse, L.; Dussauze, M.; Grondin, J.; Lassègues, J.C.; Naudin, C.; Servant, L. Spectroscopic study of poly(ethylene oxide)$_6$: LiX complexes (X = PF_6, AsF_6, SbF_6, ClO_4). *Phys. Chem. Chem. Phys.* **2003**, *5*, 567–574. [CrossRef]
50. Gupta, R.; Dyer, M.J.; Weimer, W.A. Preparation and characterization of surface plasmon resonance tunable gold and silver films. *J. Appl. Phys.* **2002**, *92*, 5264–5271. [CrossRef]
51. Yang, T.; Long, H.; Malkoch, M.; Gamstedt, E.K.; Berglund, L.; Hult, A. Characterization of Well-Defined Poly(ethylene glycol) Hydrogels Prepared by Thiol-ene Chemistry. *J. Polym. Sci. Part A Polym. Chem.* **2011**, *49*, 4044–4054. [CrossRef]
52. Ould-Moussa, L.; Castella-Ventura, M.; Kassab, E.; Poizat, O.; Strommen, D.P.; Kincaid, J.R. Ab initio and density functional study of the geometrical, electronic and vibrational properties of 2,2′-bipyridine. *J. Raman Spectrosc.* **2000**, *31*, 377–390. [CrossRef]

53. Kumar, J.; Thomas, R.; Swathi, R.S.; Thomas, K.G. Au nanorod quartets and Raman signal enhancement: Towards the design of plasmonic platforms. *Nanoscale* **2014**, *6*, 10454–10459. [CrossRef] [PubMed]
54. Joo, S.W.; Han, S.W.; Kim, K. Adsorption Characteristics of p-Xylene-r,r′-dithiol on Gold and Silver Surfaces: Surface-Enhanced Raman Scattering and Ellipsometry Study. *J. Phys. Chem. B* **1999**, *103*, 10831–10837. [CrossRef]
55. Kumar, J.; Thomas, K.G. Surface-Enhanced Raman Spectroscopy: Investigations at the Nanorod Edges and Dimer Junctions. *J. Phys. Chem. Lett.* **2011**, *2*, 610–615. [CrossRef]
56. Kertesz, M.; Choi, C.H.; Hong, S.Y. Conformational Information from Vibrational Spectra of Polyaniline. *Synth. Met.* **1997**, *85*, 1073–1076. [CrossRef]
57. Zhang, Z.; Lin, M. Fast loading of PEG–SH on CTAB-protected gold nanorods. *RSC Adv.* **2014**, *4*, 17760–17767. [CrossRef]
58. Serrano-Montes, A.B.; Jimenez de Aberasturi, D.; Langer, J.; Giner-Casares, J.J.; Scarabelli, L.; Herrero, A.; Liz-Marzán, L.M. A General Method for Solvent Exchange of Plasmonic Nanoparticles and Self-Assembly into SERS-Active Monolayers. *Langmuir* **2015**, *31*, 9205–9213. [CrossRef]
59. Yüce, M.; Kurt, H. How to make nanobiosensors: Surface modification and characterisation of nanomaterials for biosensing applications. *RSC Adv.* **2017**, *7*, 49386–49403. [CrossRef]
60. Conde, J.; Dias, J.T.; Grazú, V.; Moros, M.; Baptista, P.V.; de la Fuente, J.M. Revisiting 30 years of biofunctionalization and surface chemistry of inorganic nanoparticles for nanomedicine. *Front. Chem.* **2014**, *2*, 48. [CrossRef]
61. Whitney, A.V.; van Duyne, R.P.; Casadio, F. An innovative surface-enhanced Raman spectroscopy (SERS) method for the identification of six historical red lakes and dyestuffs. *J. Raman Spectrosc.* **2006**, *37*, 993–1002. [CrossRef]

Gold Bulletin (2022) 55:195–205
https://doi.org/10.1007/s13404-022-00320-0

RESEARCH

Post-synthesis heating, a key step to tune the LPR band of gold nanorods covered with CTAB or embedded in a silica shell

Angela Candreva[1,2] · Francesco Parisi[1] · Giuseppe Di Maio[1] · Francesca Scarpelli[1] · Iolinda Aiello[1,2] · Nicolas Godbert[1] · Massimo La Deda[1,2]

Received: 27 April 2022 / Accepted: 29 July 2022 / Published online: 8 August 2022
© The Author(s) 2022

Abstract
The transitioning of nanotechnology from laboratory to industrial-scale manufacturing poses various challenges in nanoparticle realization. From this perspective, beside the conventional synthetic procedure, based on the seed-mediated growth approach, a reshaping thermal strategy has been investigated to improve the control on gold nanorods aspect ratio, with the aim to point out a potential and encouraging way to better manage the scalability and reproducibility of nanoparticles. For this purpose, nanorods covered with CTAB and nanorods enclosed within a silica shell of tuned thickness have been synthesized and submitted to a post-thermal treatment at various temperatures, up to 300 °C for CTAB recovered gold nanorods (AuNR@CTAB), and up to 500 °C for silica-shell embedded gold nanorods (AuNR@SiO_2). For AuNR@CTAB, through accurate temperature control, the longitudinal plasmonic band can be moved very close to the transversal one upon slight reduction of their length. Instead, for AuNR@SiO_2, owing to the fully inorganic shell, a higher temperature of treatment can be reached leading to the possibility of reshaping the nanorods into spheres without the observation of any by-products.

Keywords Gold nanorods · Plasmon resonance · Thermal reshaping · FWHM

Introduction

The realization of nano-scale systems has been produced numerous benefits in everyday life in materials, electronics, medicine, energy conservation, and sustainability. At the bottom of this technological revolution, there are the nanoparticles and the processes that lead to their production [1–3]. As well known, metallic nanoparticles (MNPs), with a size smaller than the wavelength of the incident radiation, show resonance phenomena with the electro-magnetic field collectively called localized surface plasmon resonance (LSPR) [3–6]. LSPR properties are extremely interesting because they depend on, and consequently can be controlled by, the nature of the metal, the size and shape of the nanoparticles as well as the environment in which they are collocated [7–16]. In this way, an accurate synthetic method capable of controlling both the size and shape of the MNPs can allow tuning nanoparticle plasmonic properties [17, 18]. During the last decades, a variety of nanoparticles with specific shapes have been synthesized [19–21]. In particular, gold nanorods (AuNRs) have received vast attention due to their applications in biomedical technologies, plasmon-enhanced spectroscopies, optical and optoelectronic devices [22–25]. Indeed, the rod-like shape for its peculiar geometry with respect to other nanocrystals shows two plasmonic modes: a transversal and a longitudinal one. Actually, by tuning the length of the AuNRs during synthesis, the plasmon wavelength of the longitudinal mode can rather easily be adjusted in a wide spectral range, from the visible to the near-infrared region of the electromagnetic spectrum [26, 27]. Since their first discovery in 1991, for their wide perspective of applications, many synthetic protocols have been developed with the aim of improving the control over the yield of the synthesis, the uniformity in shape and dimension, but in particular on the most tricky part: the precise control of aspect ratio (the ratio between the length and the diameter), which mostly determines the features (shift and width) of the longitudinal band [28, 29]. To date, the most

✉ Angela Candreva
angela.candreva@unical.it

✉ Massimo La Deda
massimo.ladeda@unical.it

[1] Department of Chemistry and Chemical Technologies, University of Calabria, 87036 Rende, CS, Italy

[2] CNR-NANOTEC, Istituto Di Nanotecnologia U.O.S, 87036 Cosenza, Rende, Italy

effective way to control the shape of AuNRs has been achieved using the seeded growth method [30–32]. The basic principle of this shape-controlled method involves two steps: first, the preparation of small-size spherical AuNPs, and second, the growth of the prepared spherical particle in a rod-like micelle environment. To finely tune the morphology of the resulting nanorods, inorganic or organic additives can be added to the reaction media such as $AgNO_3$ [33–38] or 5-bromosalicylic acid [39–41].

In addition to chemical strategies, physical approaches based on thermal [42–44] and ultrafast laser-induced heating [45, 46] have also been proposed to modify the AuNR morphology. Indeed, since nanoparticles do melt at a lower temperature than the bulk of the relative element [46–50], heating can be employed to switch from the NRs to a thermodynamically more stable spherical shape. Furthermore, it has been found that the nanoparticle melting temperature is also greatly influenced by the nature of their capping agent or the medium in which they are dispersed [42, 48, 49]. Indeed, for this reason, and to efficiently employ AuNRs in specific applications, such as photothermal therapy, it is crucial to protect them from heat-induced shape deformation. In this regard, several methods were adopted to increase the stability of the core particles when applying heating, and in particular, enclosing AuNRs in a thick silica shell has been revealed to be a valid approach [35, 51–53].

In the present study, we first carefully investigated the role of the molecule/nanoparticle interaction in the seed-mediated growth approach by synthesizing gold nanorods covered with CTAB (AuNR@CTAB, sample A), and others covered with a silica shell of different thickness (AuNR@SiO_2, samples B_1, B_2, B_3). In a second phase, all prepared AuNRs have been exposed to an unconventional reshaping thermal treatment. The aspect ratio of the treated AuNRs has drastically changed thus allowing fine-tuning of the plasmonic response. While AuNR@CTAB were treated up to a temperature of 300 °C to avoid thermal degradation of CTAB organic the surfactant, AuNR@SiO_2 were exposed to temperature up to 500 °C. Upon temperature increase, an aspect ratio reduction was observed for all NRs, ultimately leading to the change of morphology from rod to sphere. In the case of AuNR@SiO_2, according to the thickness of the protective silica shell, this reduction of aspect ratio can however be attenuated. The homogeneity in shape and size of the nanoparticles has been ascertained, in each step, by TEM and photophysical analysis.

Results and discussion

AuNR@CTAB

Gold nanorods covered with CTAB, AuNR@CTAB, have been synthesized and dispersed in water according to the seed-mediated growth approach proposed by Scarabelli et al. [39, 54].

To prepare nanoparticles with anisotropic shape, it is necessary to use additional specific reagents acting as "template-mediated shape" such as CTAB itself or "shape directors" such as $Ag^{(I)}$ ions. Specifically, the synthetic mechanism proceeds through a physical separation of the nucleation process (seed formation solution) from the growth process (growth solution), allowing a more effective control of the final shape. Both solutions include a reductant, $HAuCl_4$ as gold source, and CTAB. In presence of CTAB, $AuCl_4^-$ anions undergo metathesis reactions ultimately leading to the formation of $AuBr_4^-$, which can be observed by the passing from a yellow solution to an orange one [31]. In the first step (seed solution), the strong reducing agent, $NaBH_4$ reduces $Au^{(III)}$ to $Au^{(0)}$ in presence of CTAB that covers the spherical seeds to prevent them from coalescence high-quality seed solution is necessary to obtain high-quality nanorods. Ideally, the seeds should be monodisperse and should also display the same crystallographic habit, which in practice, is achieved by adding the strong reducing agent in excess as fast as possible and under vigorous stirring. When the seeds are not monodispersed, the transversal band is broadened (Fig. 1) for the presence of by-products (such as spheres or cubes) into the sample.

In some cases, the longitudinal band can also appear broadened (Fig. 2) as this is due to the co-presence of different sizes of nanorods in solution. By centrifugation, it is sometimes possible to separate the nanorods by size: the heavier will fall at the bottom of the tube while the smaller will remain in the supernatant. This separation is generally achieved by centrifuging at least at 4500 rpm for 10 min.

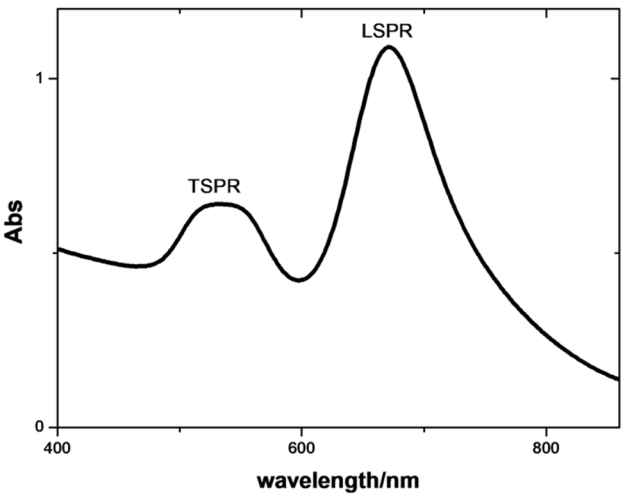

Fig. 1 Extinction spectrum of an AuNR@CTAB sample with the presence of by-products derived from an inhomogeneity of the seed size

Many actors are in play in the second step (growth solution) with regard to the growth processes of anisotropic gold nanoparticles and we tried to understand in depth their role, in particular, define which molecule/nanoparticle interactions are primarily responsible for shape control. In the preparation of the growth solution, we use CTAB and 5-BrSA in adequate proportion for which rod-like micelles are formed [40], these latter act as compartments of nanometric size, able to confine the nanocrystals growth, control and physically restrain their enlargement. We rationalized the mechanism underlying the process, taking into account that 5-BrSA acts as a weak reducing agent, reducing $Au^{(III)}$ to $Au^{(I)}$ (as showed by the bleaching of the starting $AuBr_4^-$ orange solution), and probably leading to the formation of a gold(I) complex [55–57]. This complex intercalates into the CTAB bilayer, stabilizing the structure and localizing Au(I) into the rod-like nanoreactor. To obtain rod-shaped, however, addition of an $AgNO_3$ water solution is necessary. Also, in this case, 5-BrSA is susceptible to complex $Ag^{(I)}$ [58] and, likewise to Au(I) ion, contribute to accumulate silver ion into the CTAB micelles. At this stage, seed solution is added to the growth solution just after ascorbic acid addition; the little spherical seeds, coated by CTAB, diffuse into the rod-like micelles. Silver ions form a monolayer on the seed surface, preferentially on the anisotropic faces that are eventually present. Au(I) ions, also deposited onto seed surface, suffer the following disproportion reaction:

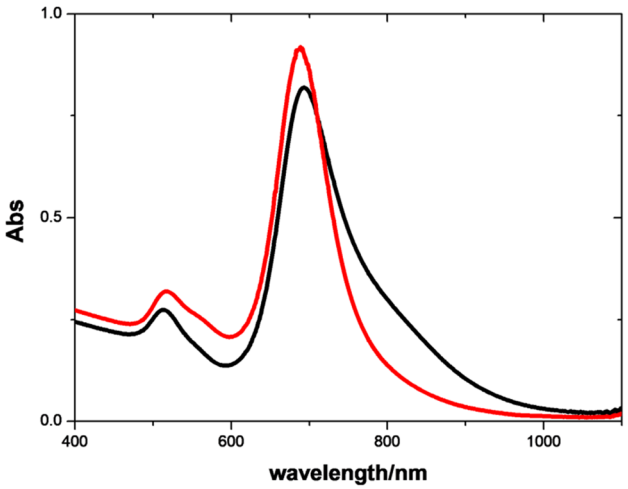

Fig. 2 Extinction spectra of NR@CTAB before (black line) and after (red line) centrifugation

$$3Au^{+} \rightarrow 2Au^{(0)} + Au^{3+} \quad (1)$$

The thus formed $Au^{(III)}$ is reduced back to $Au^{(I)}$ by ascorbic acid to $Au^{(I)}$, and the process goes on; the presence of silver ions driving the formation of the elongated shape. Indeed, the growth will occur on the faces where $Ag^{(I)}$ is absent. Ultimately $Ag^{(I)}$ ions are dislodged (we suggest for the lower Z-potential of $Ag^{(I)}$ with respect to $Au^{(I)}$) and the gold growth proceeds anisotropically (EDX analysis Fig. 1 SI). Scheme 1 recapitulates the steps of the synthesis.

Role of CTAB and $AgNO_3$ concentration in AuNR@CTAB synthesis

We reproduced the previous protocol by modifying CTAB and $AgNO_3$ concentrations, in order to investigate their contribution to the formation of the shape-like rod. In particular, by reducing the CTAB concentration of the growth solution from 0.05 to 0.025 M, nanorods with high polydispersity are formed, as shown in the TEM image below (Fig. 3).

Regarding the role of $AgNO_3$, we evidenced that its concentration plays a crucial role in the obtaining the nanorod shape. In fact, by reducing its amount, in our case

Scheme 1 Mechanism of $AuNR^{(0)}$@CTAB synthesis performed in water solution

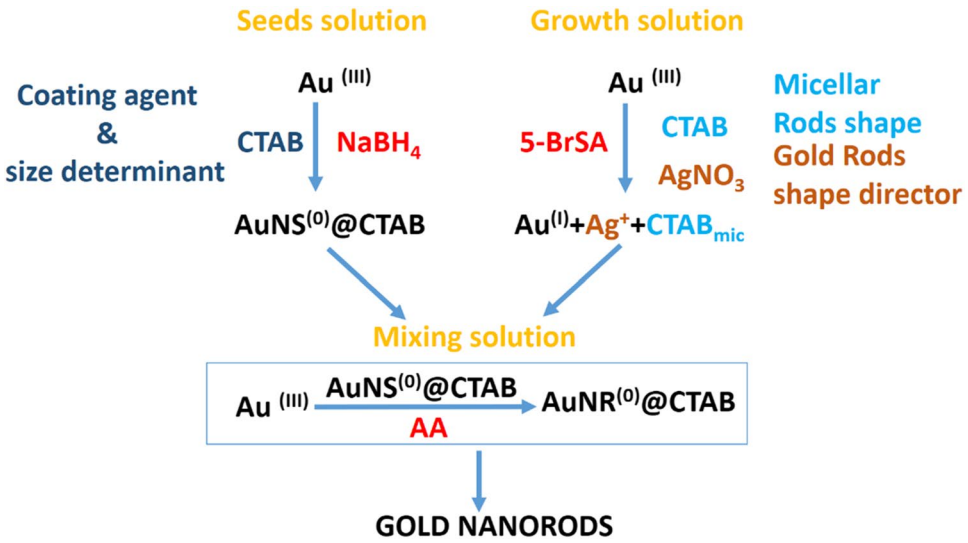

of 10 times respect the reported protocol in experimental section ("AuNR@CTAB" section), nanoparticles of elongated shape, similar to bipyramids, are formed (Fig. 4), while, in absence of $AgNO_3$, various shapes are then observed (Fig. 5), and preferential growth has been lost. These experimental results confirm the $AgNO_3$ directing power discussed above.

Furthermore, as explained by Scarabelli, there is also a correlation between the aspect ratio of AuNR@CTAB and the pre-reduction time (Au^{III} to Au^{I}); practically the aspect ratio is correlated to the $Au^{(I)}$ amount in the growth solution when ascorbic acid is added. We monitored the pre-reduction of $Au^{(III)}$ to $Au^{(I)}$ following the drop in absorbance of the $Au^{(III)}$ band at 396 nm recording for a shorter pre-reduction time (more $Au^{(III)}$ than $Au^{(I)}$ in solution) an increase in aspect ratio value, and for longer pre-reduction time (more $Au^{(I)}$ than $Au^{(III)}$ in solution) a decrease in aspect ratio value. As known, the longitudinal band shifts from red to blue with decreasing in the aspect ratio value. Figure 6 reports the results obtained by fixing the pre-reduction time when the absorbance at 396 nm was measured around 0.85, and then AA was added, obtaining AuNR@CTAB with longitudinal plasmonic peak at 794 nm, transversal plasmonic peak at 513 nm, and aspect ratio 4 (calculated from TEM images, Fig. 7a). TEM images show nanoparticles homogeneous in shape and size. The extinction spectrum in solution confirms this: the more the longitudinal band is symmetric (with a limited broadening), the more the sample results homogeneous [54]. Increasing the pre-reduction time, by adding ascorbic acid when the absorbance at 397 nm is around 0.75, the aspect ratio of AuNR@CTAB decreases from 4 to 3.3 (Fig. 7b) and, consequently, the longitudinal band blue shifts from 794 to 766 nm. Spectra in Fig. 8 have been obtained by varying, in a narrower range, the pre-reduction time.

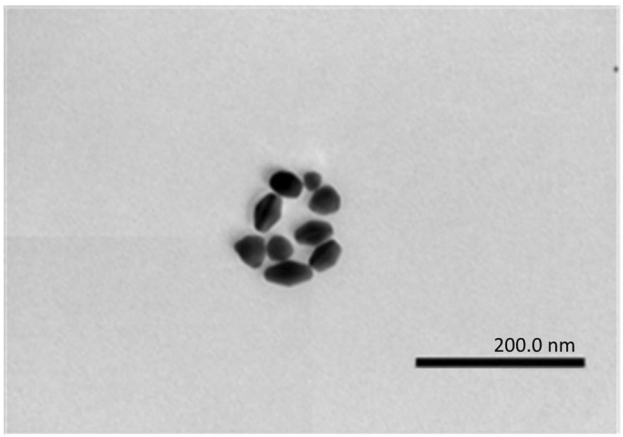

Fig. 4 TEM image of gold bipyramids

AuNR@SiO_2

According to our previous protocol [53], we covered presynthesized AuNR@CTAB, AR = 3, with a mesoporous silica shell of different thickness, that were obtained by varying the AuNR@CTAB concentration, as reported in Table 1. By increasing the AuNR@CTAB concentration, the silica thickness, around gold nanorods, is drastically reduced (Fig. 9 TEM images of samples B_1, B_2, B_3). In detail, sample B_1, which was derived from the lowest concentration of AuNR@CTAB used, showed the thickest silica shell (50 nm × 30 nm). Increasing the AuNR@CTAB concentration, the silica thickness is reduced to achieve the dimension of 10 nm × 5 nm in sample B_3. In all samples, the silica around the gold nanorods is rather homogeneous. The silica coating strategy is based on a pH-controlled condensation of tetraethyl orthosilicate (TEOS) precursor

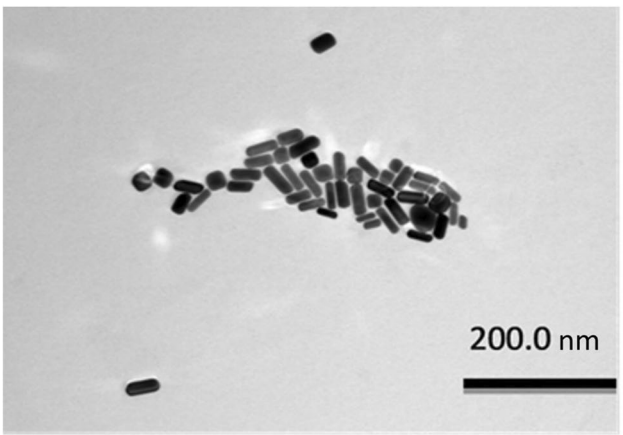

Fig. 3 TEM image of AuNR@CTAB with high polydispersity

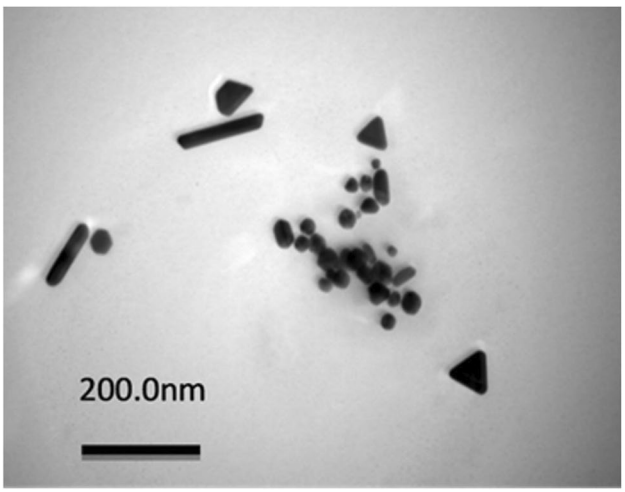

Fig. 5 TEM image of gold nanoparticles with various shapes

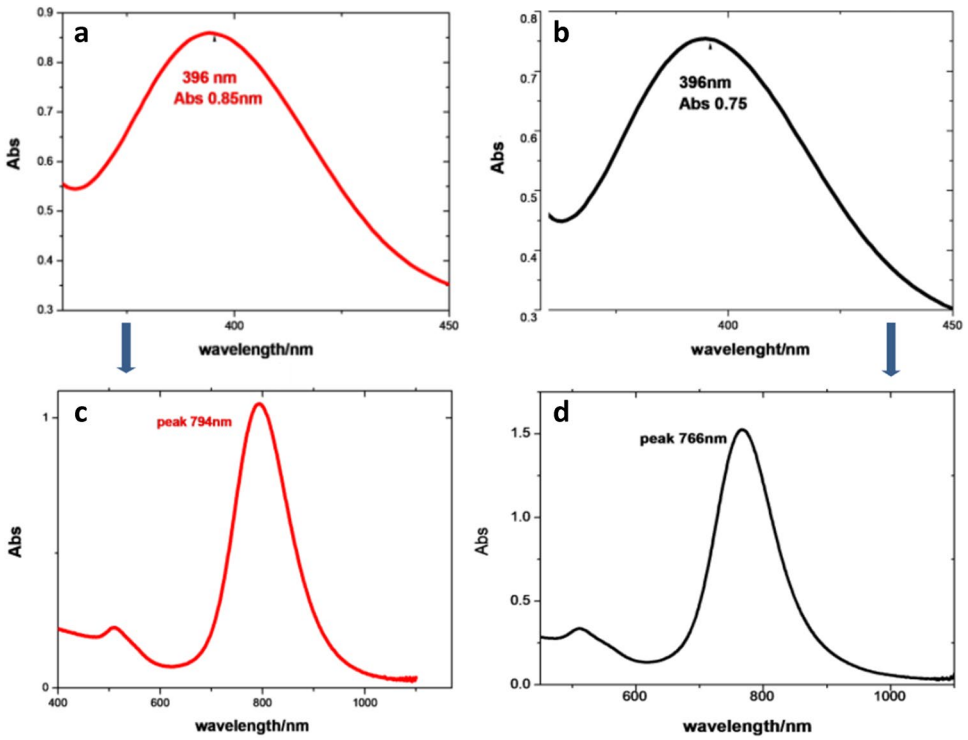

Fig. 6 Extinction spectra of gold nanorods with aspect ratio 4 (**c**) and 3.3 (**d**) respectively correlated with the amount of $Au^{(III)}$ present in the growth solution, Abs 0.85 (**a**) and 0.65 (**b**) respectively

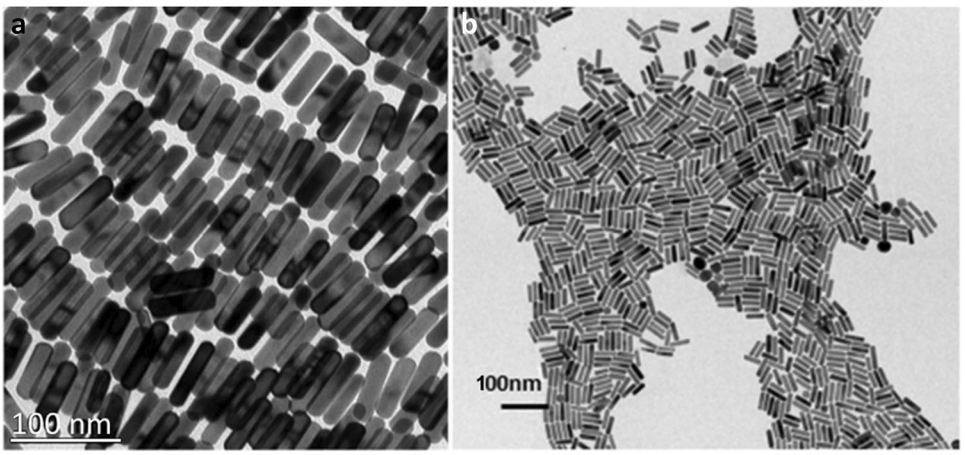

Fig. 7 TEM image of AuNR@CTAB aspect ratio 4 (on the right, **a**); TEM image of AuNR@CTAB aspect ratio 3.3 (on the left, **b**)

onto CTAB-capped AuNRs. Hydrolysis and condensation of TEOS require in this case basic conditions, reached by adding to the sample NaOH. CTAB surfactant deposited onto AuNRs is a structure-directing agent that facilitates the formation of mesostructured silica shell around the NRs.

Thermal treatment of gold nanorods

The four samples A (AuNR@CTAB), B_1, B_2, and B_3 (AuNR@SiO_2), dispersed in 2 mL of distilled water, were transferred into aluminum vials and placed in the center of a muffle furnace. The samples have been heated at different temperatures as indicated in the respectively caption and were maintained at this temperature for 30 min before letting the furnace to cool down at room temperature; samples were characterized by UV–Vis and TEM. After heating the sample, the NRs were all adhered onto the aluminum walls and were retrieved by addition of distilled water to the vial under sonication.

Sample A Analyzing the spectra showed in Fig. 10, a significant blue shift of the longitudinal plasmonic band is observed passing from 50 to 150 °C. For samples heated from 220 to 300 °C, no significant variation is observed. However, at 300 °C, a drastic absorbance decrease of the longitudinal band is registered, which becomes only barely

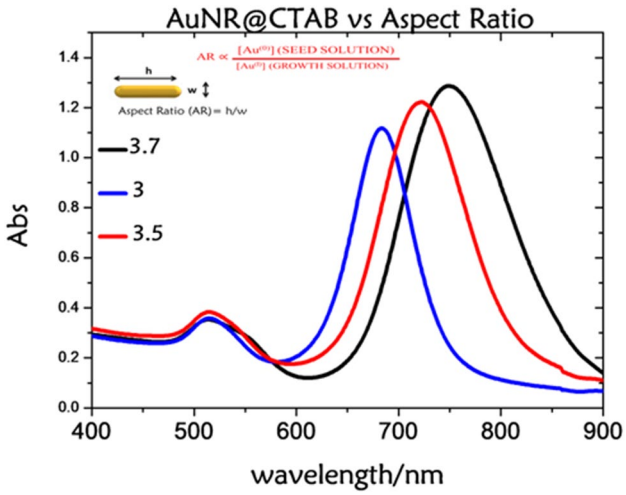

Fig. 8 Extinction spectra obtained by varying the pre-reduction time in a narrower range

Table 1 Correlation between [AuNR@CTAB]/M and silica thickness

Sample	[AuNR@CTAB]/M	Silica thickness
B_1 (36 µL TEOS)	5.0E − 5	60 nm × 40 nm
B_2 (12 µL TEOS)	1.0E − 4	30 nm × 15 nm
B_3 (12 µL TEOS)	3.0E − 3	10 nm × 5 nm

visible at 320 °C. By increasing temperature, the aspect ratio of AuNRs decreases, as confirmed by the morphological and optical characterization. TEM images (Fig. 11) show, as the treatment temperature was increased, a higher tendency of the nanoparticles to get shorter and bigger, which is in agreement with the progressive blue-shift of the longitudinal band, that approaches the transversal one with increase of temperature. However, it is worthy of note, as indicated by the narrowing of the longitudinal band (Fig. 10), that the NRs have gained in homogeneity of shape and size if the temperature of the treatment is kept under 300 °C. Figure 12 shows a graphic of FWHM (size dispersion measurement) vs. temperature. Unfortunately, owe to the organic nature of CTAB, further increase in temperature treatment was not possible for its thermal decomposition, hence irremediable agglomeration of the nanoparticles [59]. To palliate to such a drawback, we studied the effect of this post-synthesis heating treatment onto the AuNR@SiO_2.

Sample B_1 As observed for sample A, a blue shift of the longitudinal band with increasing of the temperature is still observed (Fig. 13), but the thick protective shell avoids a severe perturbation of the elongated rod shape (Fig. 14); in fact, the nanorods aspect ratio reduces only from 3 to 2.5, in agreement with the soft blue shift of the band. The difference in electron density of silica shell at 350 °C and 500 °C (more appreciable in SI Fig. 2) suggests a silica porosity increasing due the CTAB calcination.

Samples B_2 and B_3 As the thickness of the silica shell is reduced, the effect of the post-synthesis heating treatment is incremented. Again, homogeneity in size and shape is observed after all the heating treatments.

Only when the temperature is probably reaching the melting point of the gold nanoparticles (ca. 500 °C) the homogeneity might be reduced. This is particularly true for sample B_2 (Fig. 15) characterized by an intermediate thickness of shell, while instead for sample B_3 (Fig. 16) homogeneity in size and dimension is repristinate since all the NRs have switched shape to adopt a full spherical conformation. As for samples A and B_1, all these geometry changes of the NRs owe to the heat treatment can be followed by UV spectroscopy, where both blue-shifting and reducing of the half-height width of the longitudinal plasmonic band can be observed (Fig. 15). Noteworthy, the UV response of sample B_3 heated at 500 °C shows a unique band without any shoulder owe to the reaching of the full spherical shape (Fig. 16).

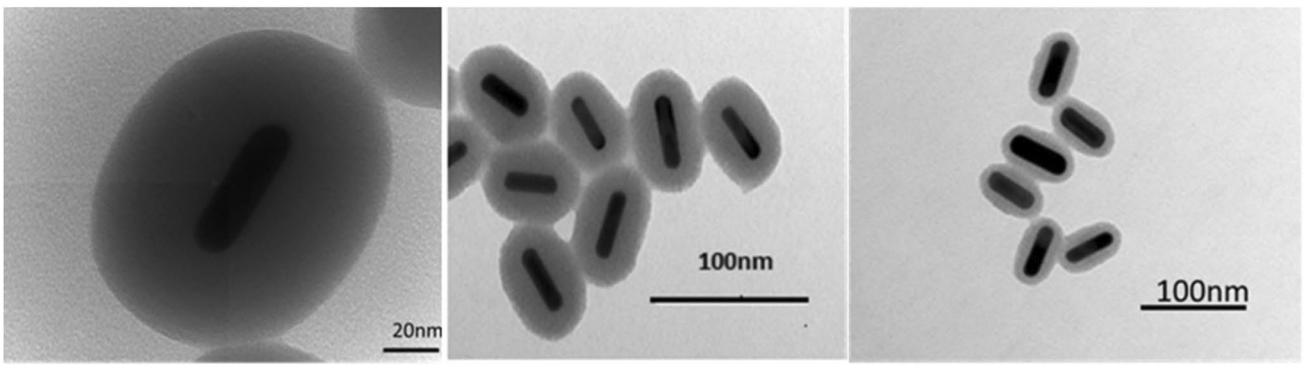

Fig. 9 TEM images of AuNR@SiO2 covered with a silica thickness of 50 nm × 30 nm (B1); 30 nm × 15 nm (B2); 10 nm × 5 nm (B3) long axis × short axis respectively (from left to right)

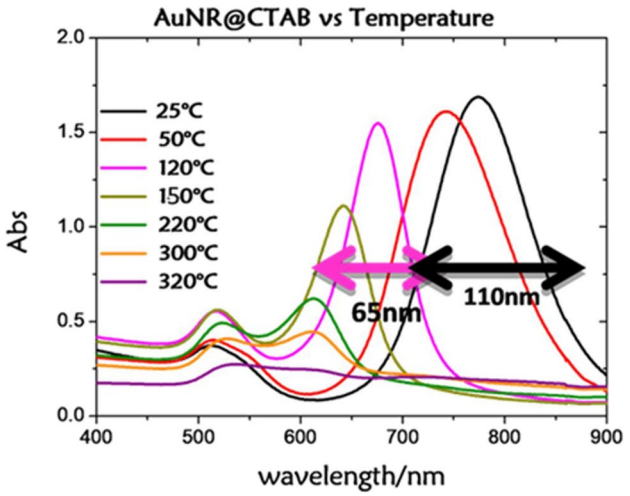

Fig. 10 Extinction spectra of sample A: AuNR@CTAB at different temperatures; the FWHM (full width at half maximum) decreases increasing the temperature (110 nm = 25 °C; 65 nm = 120 °C)

Conclusions

In gold nanorods, the longitudinal plasmonic resonance band can be tuned by adjusting their aspect ratio and, for this purpose, many synthetic protocols have been developed to control this morphological parameter. Here we discussed the synthetic mechanism seed-mediated growth to obtain gold nanorods, clarifying, for the best of our knowledge, the role of each reagent in the nanoparticle formation. Accurate photophysical studies of the plasmonic properties of these metal nanoparticles have been performed, correlating them to the size and shape. This synthetic strategy has some limitations in terms of aspect ratio reproducibility: we cannot assume that the longitudinal band always falls at the same wavelength keeping the same experimental conditions and, generally, data reported in literature do not show longitudinal band under 600 nm (near the transversal one) and a narrow half-height width corresponding to a high degree of homogeneity of the nanorod sample in size and shape. Furthermore, the synthesis provides various steps and a long and delicate purification by centrifuge if often necessary. Here we propose an unconventional reshaping thermal strategy to reach a fine control of aspect ratio of gold nanorods. Compared to the traditional procedure, which makes a correlation between the longitudinal band position of gold nanorods and the pre-reduction time (Au^{III} to Au^{I}), we tuned the longitudinal band by doing a correlation with the administered heating. In doing so, by preparing only one nanoparticle synthesis, we obtained various nanorod samples with different aspect ratio. The longitudinal band has been tuned very close to the transversal one, maintaining a homogeneity degree and better control of the aspect ratio reproducibility. We have shown that both CTAB-covered AuNRs and NRs embedded in a silica shell can be reshaped in this

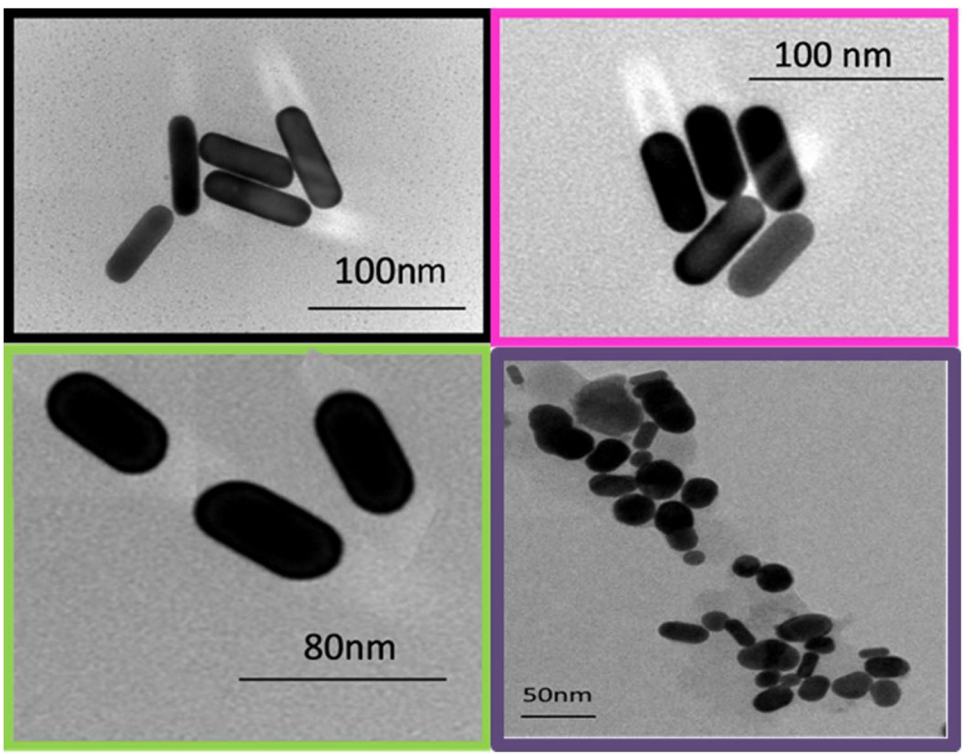

Fig. 11 TEM images of sample A: AuNR@CTAB at increasing temperature: from black (25 °C), magenta (120 °C), green (150 °C) to violet (320 °C) picture frame, according to the spectra in Fig. 10

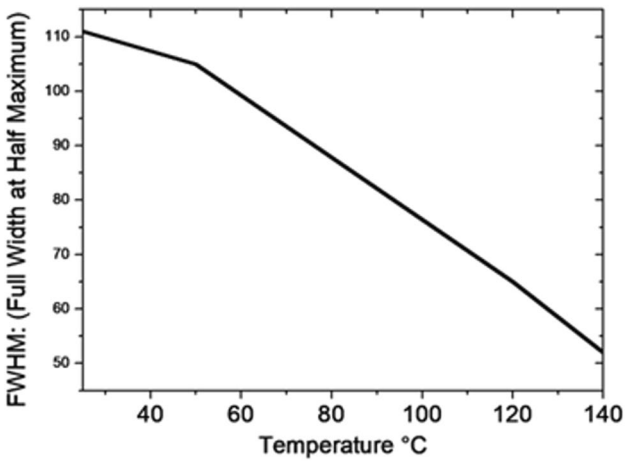

Fig. 12 Graphic of FWHM (size dispersion measurement) vs. temperature

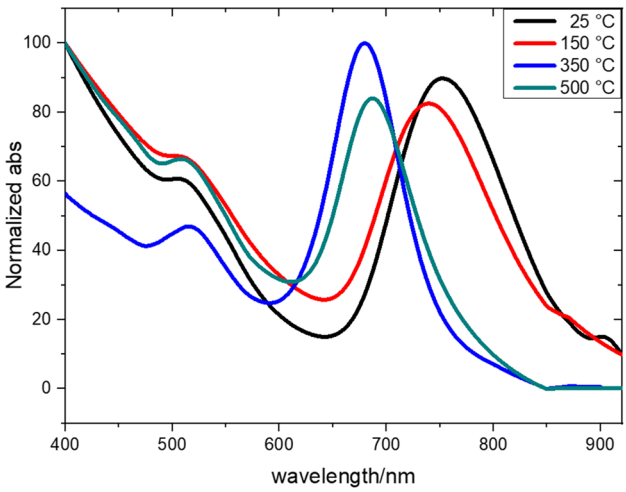

Fig. 13 Extinction spectra of sample B_1 AuNR@Si at different temperatures

manner, but with particular care and limits. For CTAB, only temperature below 300 °C can be used, while for SiO_2-covered AuNRs, the results in terms of controlling the aspect ratio of the NRs are highly depending on the thickness of the shell.

However, since 500 °C can be reached without any degradation in this case, AuNRs can be fully switched into perfect spheres without any by-products.

Respect to the conventional synthetic strategies, thermal treatment is a faster way to tune the aspect ratio of gold nanorods, correlating the position of the longitudinal plasmonic band to the temperature. The opportunity to adjust the longitudinal mode of gold nanorods, in a wide spectral range, opens up wide fields of applications. Thus, the thermal reshaping method can be applied as a general strategy to personalize plasmon response expanding the nanoparticle applications in photothermal therapeutics and different application fields of nanophotonics. The method described here is reproducible, scalable, and the optical response of the resulting gold nanoparticles nears the theoretical limit, giving a highly appealing approach toward the increasing applications of plasmonic nanoparticles.

Furthermore, the same thermal treatment can be proposed for other metal nanorods for which synthetical pathways failed in furnishing high homogeneity in size and shape. This rising unconventional strategy could become a developing technique to produce nano-systems on a larger scale and at higher rates.

Experimental section

Materials

Hexadecyltrimethylammonium bromide (CTAB, ≥ 96%), 5-bromosalicylic acid (technical grade, 90%), hydrogen tetrachloroaurate trihydrate ($HAuCl_4 \cdot H_2O$, ≥ 99.9%), silver nitrate ($AgNO_3$, ≥ 99.0%), L-ascorbic acid (A.A. ≥ 99%), sodium iodide (99.99%), trisodium citrate (99%),

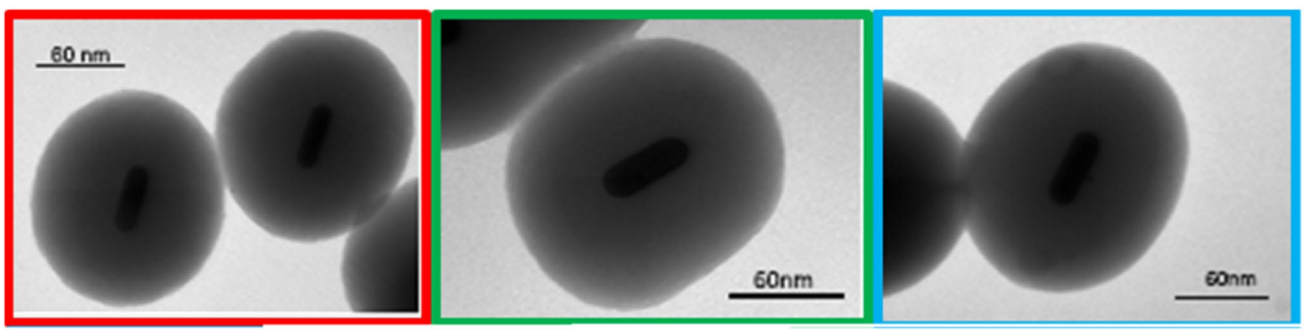

Fig. 14 TEM images of sample B_1 AuNR@Si at increasing temperature: from red (150 °C), gray (350 °C), to blue (500 °C) picture frame, according to the spectra in Fig. 13

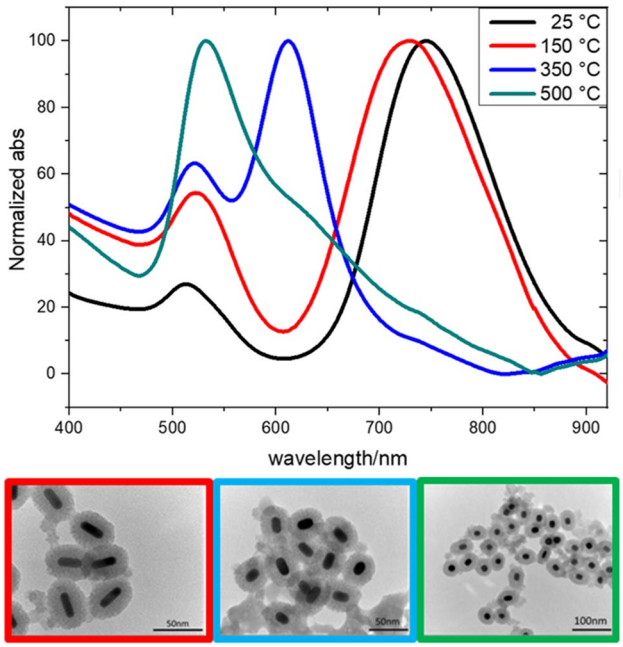

Fig. 15 Extinction spectra (on the left) of sample B_2: AuNR@Si at different temperatures; TEM images (on the right) of sample B_2: AuNR@SiO_2 at increasing temperature: from red (150 °C), blue (350 °C), to green (500 °C) picture frame, according to the spectra

polyvinylpolypyrrolidone (PVP K15, Mn 10000), and sodium borohydride ($NaBH_4$, 99%) were purchased from Aldrich and used for the preparation of gold nanorods covered with CTAB (AuNR@CTAB) as previously reported [39]. All the chemicals were used as received. Milli-Q water (resistivity 18.2 MΩ·cm at 25 °C) was used in all experiments. All glassware was cleaned with aqua regia, rinsed with water, sonicated threefold for 3 min with Milli-Q water, and dried before use. TEOS (Alfa Aesar, 99.9%), NaOH (Sigma Aldrich, 98%), and MeOH (Sigma Aldrich) were used for the SiO_2 over coating as reported in a previous work [53].

Methods

A Perkin Elmer Lambda 900 spectrophotometer was employed to obtain the extinction spectra. The size and the morphology of the gold nanoparticles were measured using a transmission electron microscope (Jeol JEM-1400 Plus 120 kV). The samples for transmission electron microscopy (TEM) were prepared by depositing a drop of a diluted solution on 300 mesh copper grids. After evaporation of the solvent in air at room temperature, the particles were observed at an operating voltage of 80 kV. For the heat treatment was used a muffle furnace Z 1200, GEFRAN 1001 temperature control.

AuNR@CTAB

Preparation of the seed solution Twenty-five microliters of 5.0E − 2 M $HAuCl_4$ water solution was added to 4.7 mL of 0.1 M CTAB water solution; 300 µL of a freshly prepared 1.0E − 2 M $NaBH_4$ water solution was then injected under vigorous stirring. Excess of sodium borohydride was consumed by keeping the seed solution for 30 min at room temperature prior to use.

Preparation of the growth solution Forty-five milligrams of 5-BrSA was added to 50 mL of 0.05E − 2 M CTAB water solution. After complete dissolution, 480 µL of 1.0E − 2 M $AgNO_3$ water solution was added. The solution was mildly stirred for 15 min at room temperature, and then 500 µL of 5.0E − 2 M $HAuCl_4$ water solution was added to the mixture, starting the pre-reduction step. At the selected pre-reduction time, 130 µL of 0.1 M ascorbic acid (AA) water solution was added under vigorous stirring, followed by 80 µL of seed solution. After 30 s, the stirring was stopped and the mixture was left undisturbed at room temperature for at least 4 h. The sample was finally centrifuged (9000 rpm, 20 min, 30 °C).

Fig. 16 Extinction spectra (on the left) of sample B_3: AuNR@Si at different temperatures; TEM images (on the right) of sample B_3: AuNR@SiO_2 at 500 °C

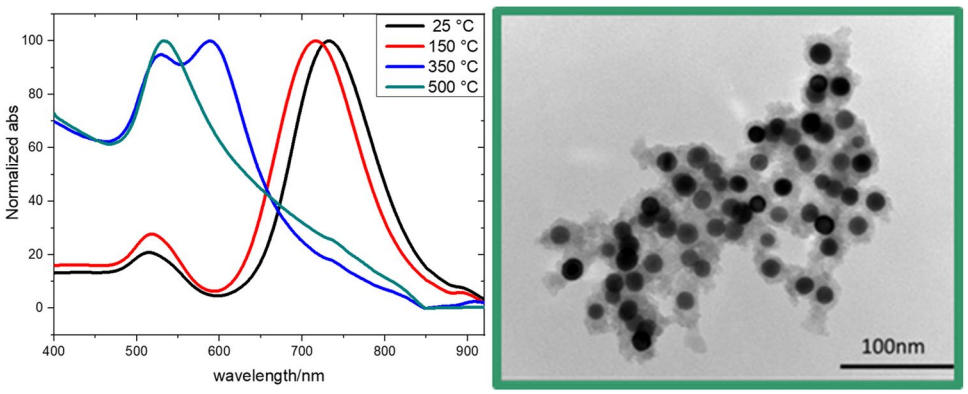

AuNR@SiO_2

An aqueous solution of CTAB (10 µL, 0.2 M) has been added to 2 mL of an aqueous dispersion of AuNR@CTAB at different concentration according to our previous work [40] (Table 1). After few seconds, 20 µL of a 0.1 M NaOH aqueous solution was added under vigorous stirring, reaching a pH value of 8.5, followed by three additions, each of 12 µL, of TEOS 20% v/v in methanol under gentle stirring, at room temperature. After 14 h, the mixture was centrifuged in Milli-Q water twice at 6000 rpm for 10 min and the sample was dispersed in 2 mL of Milli-Q water.

Thermal treatment

Two milliliters of each sample (A, B_1, B_2, B_3) was transferred into aluminum vials, placed in the center of a muffle furnace, and maintained at the chosen temperature (as indicated in the respectively figure caption) for 30 min. After this time, the same for all samples and for all temperatures tested, the temperature of the muffle was brought to room temperature and opened. Two milliliters of distilled water, under sonication, has been added to the aluminum vials thus bringing back into solution the dry nanoparticles.

Supplementary Information The online version contains supplementary material available at https://doi.org/10.1007/s13404-022-00320-0.

Author contribution A.C. synthesized and characterized the samples, wrote the main manuscript text; F.P. prepared the figures; G.D.M., F.S., I.A., N.G. reviewed the manuscript; M.L.D. supervised all steps, reviewed and validated the manuscript.

Funding Open access funding provided by Università della Calabria within the CRUI-CARE Agreement. DEMETRA Project (PON ARS01_00401) supports the research funds.

Data availability Not applicable.

Code availability Not applicable.

Declarations

Competing interests The authors declare no competing interests.

Open Access This article is licensed under a Creative Commons Attribution 4.0 International License, which permits use, sharing, adaptation, distribution and reproduction in any medium or format, as long as you give appropriate credit to the original author(s) and the source, provide a link to the Creative Commons licence, and indicate if changes were made. The images or other third party material in this article are included in the article's Creative Commons licence, unless indicated otherwise in a credit line to the material. If material is not included in the article's Creative Commons licence and your intended use is not permitted by statutory regulation or exceeds the permitted use, you will need to obtain permission directly from the copyright holder. To view a copy of this licence, visit http://creativecommons.org/licenses/by/4.0/.

References

1. Hutter E, Fendler JH (2004) Adv Mater 16:1685–1706
2. Mayer KM, Hafner JH (2011) Chem Rev 111:3828–3857
3. Myroshnychenko V, Rodríguez-Fernández J, Pastoriza-Santos I, Funston AM, Novo C, Mulvaney P, Liz-Marzán LM, García de Abajo FJ (2008) Chem Soc Rev 37:1792–1805
4. Candreva A, Di Maio G, La Deda M (2020) Soft Matter 16:10865–10868
5. Venkatesh N (2018) Biomed J Sci Tech Res 4:3765–3775
6. Chen H, Shao L, Li Q, Wang J (2013) Chem Soc Rev 42:2679–2724
7. Richard-Daniel J, Boudreau D (2020) ChemNanoMat 6:907–915
8. Kanoun MB, Cavallo L (2014) J Phys Chem C 118:13707–13714
9. H. gold nanorods, plasmon resonance, thermal reshaping, Abou-Hamad E, Jedidi A, Widdifield CM, Viger-Gravel J, Sangaru SS, Gajan D, Anjum DH, Ould-Chikh S, Hedhili MN, Gurinov A, Kelly MJ, El Eter M, Cavallo L, Emsley L, Basset JM (2017) Nat Chem 9:890–895
10. Wang J, Lu AH, Li M, Zhang W, Chen YS, Tian DX, Li WC (2013) ACS Nano 7:4902–4910
11. Lu AH, Salabas EL, Schüth F (2007) Angew Chem Int Ed 46:1222–1244
12. van der Meer SB, Seiler T, Buchmann C, Partalidou G, Boden S, Loza K, Heggen M, Linders J, Prymak O, Oliveira CLP, Hartmann L, Epple M (2021) Chem Eur J 27:1451–1464
13. Colangelo E, Comenge J, Paramelle D, Volk M, Chen Q, Lévy R (2017) Bioconjug Chem 28:11–22
14. Chen D, Luo Z, Li N, Lee JY, Xie J, Lu J (2013) Adv Funct Mater 23:4324–4331
15. Upadhyay Y, Bothra S, Kumar R, Sahoo SK (2018) ChemistrySelect 3:6892–6896
16. Hao E, Schatz GC, Hupp JT (2004) J Fluoresc 14:331–341
17 Vijaya Kumar S, Ganesan S (2011) Int J Green Nanotechnol Biomed 3:47–55
18. Pérez-Juste J, Pastoriza-Santos I, Liz-Marzán LM, Mulvaney P (2005) Coord Chem Rev 249:1870–1901
19. Saleh N, Yousaf Z (2017) Tools and techniques for the optimized synthesis, reproducibility and scale up of desired nanoparticles from plant derived material and their role in pharmaceutical properties. Elsevier Inc
20. Elahi N, Kamali M, Baghersad MH (2018) Talanta 184:537–556
21. Li JF, Li CY, Aroca RF (2017) Chem Soc Rev 46:3962–3979
22 De Sio L, Placido T, Comparelli R, Lucia Curri M, Striccoli M, Tabiryan N, Bunning TJ (2015) Prog Quantum Electron 41:23–70
23. Yang DP, Cui DX (2008) Chem Asian J 3:2010–2022
24. Yamada S, Niidome Y (2006) Handai Nanophotonics 2:255–274
25. Link S, El-Sayed MA (2005) J Phys Chem B 109:10531–10532
26. Jana NR, Gearheart L, Murphy CJ (2001) J Phys Chem B 105:4065–4067
27. Chhatre A, Thaokar R, Mehra A (2018) Cryst Growth Des 18:3269–3282
28. Nikoobakht B, El-Sayed MA (2003) Chem Mater 15:1957–1962
29. Kawamura G, Yang Y, Nogami M (2007) Appl Phys Lett 90:1–3
30. Murphy CJ, Sau TK, Gole A, Orendorff CJ (2005) MRS Bull 30:349–355
31. Razali NL, NisaMd Shah NZA, Morsin M, Mohd Noh FH, Salleh MM (2017) J Telecommun Electron Comput Eng 9:123–127
32. Wu WC, Tracy JB (2015) Chem Mater 27:2888–2894
33. Zhu J, Lennox RB (2021) ACS Appl Nano Mater 4:3790–3798
34. Kim BM, Seo SH, Joe A, Shim KD, Jang ES (2016) Bull Korean Chem Soc 37:931–937
35. Ghosh S, Manna L (2018) Chem Rev 118:7804–7864
36. Scarabelli L, Grzelczak M, Liz-Marzán LM (2013) Chem Mater 25:4232–4238

37. Ye X, Jin L, Caglayan H, Chen J, Xing G, Zheng C, Doan-Nguyen V, Kang Y, Engheta N, Kagan CR, Murray CB (2012) ACS Nano 6:2804–2817
38. Zou W, Xie H, Ye Y, Ni W (2019) RSC Adv 9:16028–16034
39. Horiguchi Y, Honda K, Kato Y, Nakashima N, Niidome Y (2008) Langmuir 24:12026–12031
40. Mohamed MB, Ismail KZ, Link S, El-Sayed MA (1998) J Phys Chem B 102:9370–9374
41. Ng KC, Cheng W (2012) Nanotechnology 23. https://doi.org/10.1088/0957-4484/23/10/105602
42. González-Rubio G, Díaz-Núñez P, Rivera A, Prada A, Tardajos G, González-Izquierdo J, Bañares L, Llombart P, Macdowell LG, Palafox MA, Liz-Marzán LM, Peña-Rodríguez O, Guerrero-Martínez A (2017) Science 358:640–644
43. Link S, Burda C, Nikoobakht B, El-Sayed MA (2000) J Phys Chem B 104:6152–6163
44. Zhao SJ, Wang SQ, Cheng DY, Ye HQ (2001) J Phys Chem B 105:12857–12860
45. Nanda KK (2009) Pramana J Phys 72:617–628
46. Dick K, Dhanasekaran T, Zhang Z, Meisel D (2002) J Am Chem Soc 124:2312–2317
47. Qi WH, Wang MP (2004) Mater Chem Phys 88:280–284
48. Gorelikov I, Matsuura N (2008) Nano Lett 8:369–373
49. Kosari M, Borgna A, Zeng HC (2020) ChemNanoMat 6:889–906
50. Candreva A, Lewandowski W, La Deda M (2021) J Nanopart Res 24:1–11
51. Scarabelli L, Sánchez-Iglesias A, Pérez-Juste J, Liz-Marzán LM (2015) J Phys Chem Lett 6:4270–4279
52. Gründlinger P, Mardare CC, Wagner T, Monkowius U (2021) Monatsh Chem 152:1201–1207
53. Petrenko A, Belyakov S, Arsenyan P (2020) Mendeleev Commun 30:572–573
54. He X, Yam VWW (2010) Inorg Chem 49:2273–2279
55. Cheng K, Zhu HL, Li YG (2006) Z Anorg Allg Chem 632:2326–2330
56. Goworek J, Kierys A, Gac W, Borówka A, Kusak R (2009) J Therm Anal Calorim 96:375–382
57. Cretu C, Andelescu AA, Candreva A, Crispini A, Szerb EI, La Deda M (2018) J Mater Chem C 6:10073–10082
58. Liguori PF, Ghedini M, La Deda M, Godbert N, Parisi F, Guzzi R, Ionescu A, Aiello I (2020) Dalton Trans 49:2628–2635
59. Ionescu A, Caligiuri R, Godbert N, Candreva A, La Deda M, Furia E, Ghedini M, Aiello I (2019) Chem Asian J 14:3025–3034

Publisher's note Springer Nature remains neutral with regard to jurisdictional claims in published maps and institutional affiliations.

ChemistrySelect

Research Article
doi.org/10.1002/slct.202201375

Chemistry Europe
European Chemical Societies Publishing

www.chemistryselect.org

Check for updates

Inorganic Chemistry

Synthesis and Characterization of Hyper-Branched Nanoparticles with Magnetic and Plasmonic Properties

Angela Candreva[+],[a, b] Francesco Parisi[+],[a] Rosa Bartucci,[a, c] Rita Guzzi,[b, c] Giuseppe Di Maio,[a] Francesca Scarpelli,[a] Iolinda Aiello,[a, b] Nicolas Godbert,[a] and Massimo La Deda*[a, b]

Hybrid nanoparticles, composed of an iron oxide magnetic core embedded with gold fractal-grown hyper branches, have been synthesized by a seed-mediated growth approach. Magnetic and plasmonic properties have been described respectively through ferromagnetic resonance (FMR) and extinction spectra. According to the hydroxylamine amount, used as a surface catalysed reducing agent, the number of branches and the intensity of the fractal growth have been finely tuned and were observed through TEM microscopy. The magnetic core allowed their motion control via an external magnetic field. The plasmonic properties of these hyper-branched hybrid nanoparticles were recorded similar to those shown by the branched gold nanoparticles, but it is interesting to note that they showed an encouraging photothermal response.

Introduction

Nanomaterials are increasingly used in various fields of research and applications, due to their intrinsic properties;[1–8] in fact, they have different characteristics compared to those of the same materials on a macroscopic scale, often due to the large surface to volume ratio. If adequately coated, their sub-colloidal dimension allows a stable dispersibility of these nanomaterials in various solvents. The coating of the nanoparticles is essential to avoid aggregation phenomena, which would lead to the loss of their peculiar properties due to their small size.

In nanotechnologies, much attention is paid to metal nanosheets[9,10] and nanoparticles of various composition, shape and size for their use in catalysis,[11–17] biomedicine,[7,18–24] electronics[4,25,26] and optics.[27,28]

In this regard, gold nanoparticles emerge as a paramount emblem. In fact, although gold is famous for being a noble metal, it exhibits a remarkable affinity for amino and thiol terminated molecules, which can act as coating agents for stabilising gold nanoparticles. Indeed, various substances, such as aminoacids, nucleic acids, oligonucleotides,[29] peptides,[30–32] enzymes,[33] drugs,[34,35] luminescent molecules[36–39] or organometallic complexes[40] have been used to coat nanoparticles.

However, the pivotal property of gold nanoparticles that make them rather appealing is the collective response of surface electrons triggered by means of light; this phenomenon is known as Localized Surface Plasmon Resonance (LSPR) and the stimulating wavelength varies according to the morphology of the nanoparticles.[41]

To date, gold nanoparticles have been synthesized in a variety of different shapes: nanospheres,[42,43] nanorods,[44,45] nanocubes,[46] nanotriangles,[47] nanostars[48] and other eccentric shapes.[49–54]

Noteworthy, the plasmonic field localized on the spikes of branched particles is particularly strong[55,56] and this local amplification effect is often used for detection at very low analyte concentration,[27,57] or for increasing the photothermal activity[58] displayed by such nanoparticles.

The change in chemical and physical behaviour due to the nanometric size is not an exclusive feature of precious metals; for example, iron oxide nanoparticles significantly modify their properties with respect to the bulk. Although iron oxide nanoparticles absorb radiation in the NIR,[59] they do not exhibit LSPR;[60] nevertheless, their peculiar magnetic response makes them particularly interesting.

It is ancestrally known that iron is magnetized by placing it in a magnetic field; this behaviour is called ferromagnetism and occurs because the magnetic polarization, induced by the applied field, is long-lasting. Down to the nanoscale, iron oxide particles show peculiar magnetic properties that make them particularly interesting for application in high-frequency operation,[61–64] as contrast agents in Magnetic Resonance Imaging (MRI),[65] or magnetic hyperthermia (MHT).[60,65]

However, to prevent the nanoparticles from aggregating, resulting in a reduction in magnetic properties, they must be adequately coated with an organic or inorganic layer, depending on the intended use.[66–68]

[a] *Dr. A. Candreva,[+] Dr. F. Parisi,[+] Prof. R. Bartucci, Dr. G. Di Maio, Dr. F. Scarpelli, Prof. I. Aiello, Dr. N. Godbert, Prof. M. La Deda*
Department of Chemistry and Chemical Technologies, University of Calabria, 87036 Rende (CS), Italy
E-mail: massimo.ladeda@unical.it

[b] *Dr. A. Candreva,[+] Prof. R. Guzzi, Prof. I. Aiello, Prof. M. La Deda*
CNR-NANOTEC, Istituto di Nanotecnologia U.O.S, Cosenza, 87036 Rende (CS),Italy

[c] *Prof. R. Bartucci, Prof. R. Guzzi*
Department of Physics, Molecular Biophysics Laboratory, University of Calabria, 87036 Rende (CS), Italy

[+] *The authors equally contributed to the manuscript*

Supporting information for this article is available on the WWW under https://doi.org/10.1002/slct.202201375

© 2022 The Authors. ChemistrySelect published by Wiley-VCH GmbH. This is an open access article under the terms of the Creative Commons Attribution License, which permits use, distribution and reproduction in any medium, provided the original work is properly cited.

© 2022 The Authors. ChemistrySelect published by Wiley-VCH GmbH

23656549, 2022, 26, Downloaded from https://chemistry-europe.onlinelibrary.wiley.com/doi/10.1002/slct.202201375 by CochraneItalia, Wiley Online Library on [19/11/2022]. See the Terms and Conditions (https://onlinelibrary.wiley.com/terms-and-conditions) on Wiley Online Library for rules of use; OA articles are governed by the applicable Creative Commons License

More recently, the idea of combining the properties exhibited at the nanoscale by different metals has come forward. In this perspective, several reports have already proposed hybrid iron/gold nanoparticles to couple both magnetic and optical responses.[63,69–75]

To synthesize hybrid nanoparticles with a high yield, the so-called "seed-mediated growth approach"[55,56] has been generally used. This method is based on the synthesis of small spherical shaped metal seeds which are then added to a growth solution containing additional metal ions together with one or more shape-directing agents, that are promoters of the anisotropic growth. Nucleation and growth of the anisotropic nanoparticles are temporally and physically separated, with precise control over the final nanoparticle shape and dimension. In fact, the morphology of the nanoparticle is governed by different factors such as size, shape and seed amount, the concentration of the capping agents, and the ratio of the metal salt to reductant in the growth solution.

Herein, we propose a new synthetic strategy, based on a seed-mediated growth approach, to obtain hybrid nanoparticles with iron oxide magnetic core and gold fractal growth hyper branches. Multibranched nanoparticles are attractive because they can be used for sensing applications due to their huge SERS effect[56,76] and as catalysts.[57,77] Moreover, applications of multibranched nanoparticles for biofilms, nanosensing, thermal treatments, and delivery systems are well known.[78]

Compared to what is reported in the literature,[79,80] we present a simpler method to make asymmetric multi-spiked nanoparticles. In particular, for our two-steps synthesis, only a few reagents are necessary; moreover, the final result can be controlled by adjusting the concentration of a single reagent (i.e. hydroxylamine, see below). The gold germination and growth are studied and correlated to the role of hydroxylamine, used as a surface-catalysed reducing agent on two different seeds, specifically iron oxide and gold. The iron/gold hybrid nanoparticles, sensitive to a magnetic field, and tested by ferromagnetic resonance (FMR) measurements, show plasmonic properties in Vis and NIR spectroscopic regions. Furthermore, an encouraging photothermal effect is recorded in the hyper-branched hybrid nanoparticles compared with homometallic branched gold counterparts.

Results and Discussion

Synthesis of hybrid nanoparticles and role of the hydroxylamine

Hybrid hyper-branched iron/gold nanoparticles have been obtained through a seed growth approach, proceeding via a two-step synthesis (see Experimental Section): the nucleation process (seeds solution) and the growth process (growth solution), allowing more effective control of the final shape.[81,82] Sodium citrate-coated iron oxide seeds (*Fe_3O_4@NaCit*), have been synthesized by co-precipitation of Fe(II) and Fe(III) chlorides,[64,83,84] in alkaline water solution at high temperatures. The reaction mechanism (eq.1) can be simplified as:

Eq.1

$$Fe^{2+} + 2Fe^{3+} + 8OH^- \leftrightarrows$$
$$Fe(OH)_2 + 2Fe(OH)_3 \rightarrow Fe_3O_4 \downarrow + 4H_2O$$

Sodium citrate (10 mg in 2 mL) has been added as a coating agent to prevent nanoparticle aggregation in 50 mL of seed solution. The magnetic properties of the *Fe_3O_4@NaCit* sample were ascertained by FMR measurements (see below) and macroscopically observed by the use of a permanent magnet placed close to a colloidal solution of the seeds (Figure 1). TEM image (Figure S1) revealed that the Fe_3O_4 seeds are rough of spherical shape with a diameter of ca. 30 to 60 nm.

Subsequently, the seed solution (15 μL) has been added to an aqueous solution of sodium citrate (98 mg in 73.75 mL), followed by the addition of tetrachloroauric acid. The Au^{3+} ions were promptly reduced to Au^0 by the addition of various amounts of hydroxylamine that induces the reduction of gold ions on the surface of the iron seeds. The hydroxylamine concentration is crucial for the shape of the final nanoparticle as already reported in the literature.[85–89] Three samples (A, B, and C) have been prepared with a growing amount of hydroxylamine. As expected, different nanoparticles have been obtained, and, as the hydroxylamine amount increases, the quantity of gold deposited onto the iron seeds increases as well. However, to better clarify the hydroxylamine role as a surface-catalysed reducing agent, three additional samples (A*, B*, C*) have been prepared for which the iron oxide seeds have been substituted by gold ones (*Au@NaCit* in Figure S2; see Experimental Section), following identical procedure and keeping the amount of all other reagents unaltered.

Synthesis of branched gold nanoparticles

To test the importance of the hyper-branched shape of the nanoparticles in photothermal activity, we have compared them with homometallic branched gold nanoparticles (*AuNB@TX100*)[90–92] specially synthesized.

In the first step, Au seeds covered with Triton X-100 as a capping agent (*Au@TX100*), were obtained by reduction of Au^{3+} to Au^0 in 21.2 mL aqueous solutions with a high surfactant concentration. In detail, tetrachloroauric acid was mixed with Triton X-100. Immediately, sodium borohydride, a strong

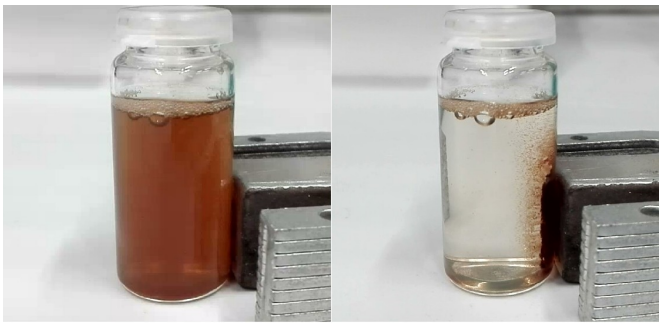

Figure 1. *Aqueous dispersion of iron oxide seeds (Fe_3O_4@NaCit) at the beginning (left) and after 10 minutes (right) of magnetic field application.*

© 2022 The Authors. ChemistrySelect published by Wiley-VCH GmbH

23656549, 2022, 26, Downloaded from https://chemistry-europe.onlinelibrary.wiley.com/doi/10.1002/slct.202201375 by CochraneItalia, Wiley Online Library on [19/11/2022]. See the Terms and Conditions (https://onlinelibrary.wiley.com/terms-and-conditions) on Wiley Online Library for rules of use; OA articles are governed by the applicable Creative Commons License

reducing agent, was added under vigorous stirring and the colour of the solution became red. According to the recorded TEM image (Figure S3), Au seeds of 5 nm in diameter were thus formed.

In the second step, the seeds solution (24 μL) was added to a water growth solution (21.3 mL) in which tetrachloroauric

acid and Triton X-100 are mixed with a weak reducing agent (ascorbic acid) and silver nitrate. These mild reducing agents have been reported[93,94] to induce a disproportion reaction(eq.2):

Eq.2

$$3\ Au^{+} \rightarrow 2\ Au^{0} + Au^{3}$$

Only in presence of Au seeds as catalysts, Au^0 assemble on the surface of the seeds, and no new particle nucleation takes place. Silver nitrate is added to direct the anisotropic growth, controlling the morphology of the final nanoparticles and increasing dramatically the yield of branched particles. By comparing the results obtained by different synthetic protocols,[90–92,95] our method allowed to obtain the best homogeneity and number of branches (see below).

Characterizations of samples

The TEM images of the synthetic results of all prepared samples are summarised in Figure 2, while the extinction spectra are grouped in Figure 3. The UV-Vis spectra and TEM images of both seed solutions (*Fe_3O_4@NaCit* and *Au@NaCit*) are reported in Figure S1 and Figure S2. Their TEM images showed a more homogeneous distribution in shape and dimension of gold seeds compared to the iron ones, with a diameter of ca. 5 nm. As expected, the gold seeds solution displays a broad absorbance band with a maximum centred at 520 nm owing to the plasmonic effect of the gold nanoseeds.

For sample A (0.188 mL hydroxylamine), the extinction spectrum (Figure 3) shows a plasmonic band centred at about 700 nm. In the NIR region, the electronic transition bands of Fe_3O_4 are detected,[59] while in the range between 350 and 500 nm is observed a relevant resonance Rayleigh scattering. These features are due to the big size of nanoparticles,[96] as displayed in the corresponding TEM images (Figure 2), that show nanoparticles having short and large branches with smooth fractal extremities and size around 100 nm.

For sample B (0.375 mL hydroxylamine), a more defined extinction spectrum has been recorded (Figure 3), again with a broadened band at 700 nm, given by gold hyper branches grown on the Fe_3O_4 surface (as showed in the TEM images in Figure 4a), but now with a shoulder at 540 nm.[77] This is due to an enhancement of the local plasmonic electromagnetic field that, as discussed below, originated by the multi-spikes of a fractal nature (Figure 4b) clearly visible on each branch (of ca. 180 nm from core to spike). The enhancement of the plasmonic band makes Fe_3O_4 electronic transitions less visible compared to sample A.

For sample C (0.750 mL hydroxylamine), the broadened extinction spectrum shows two shoulders at 556 nm and

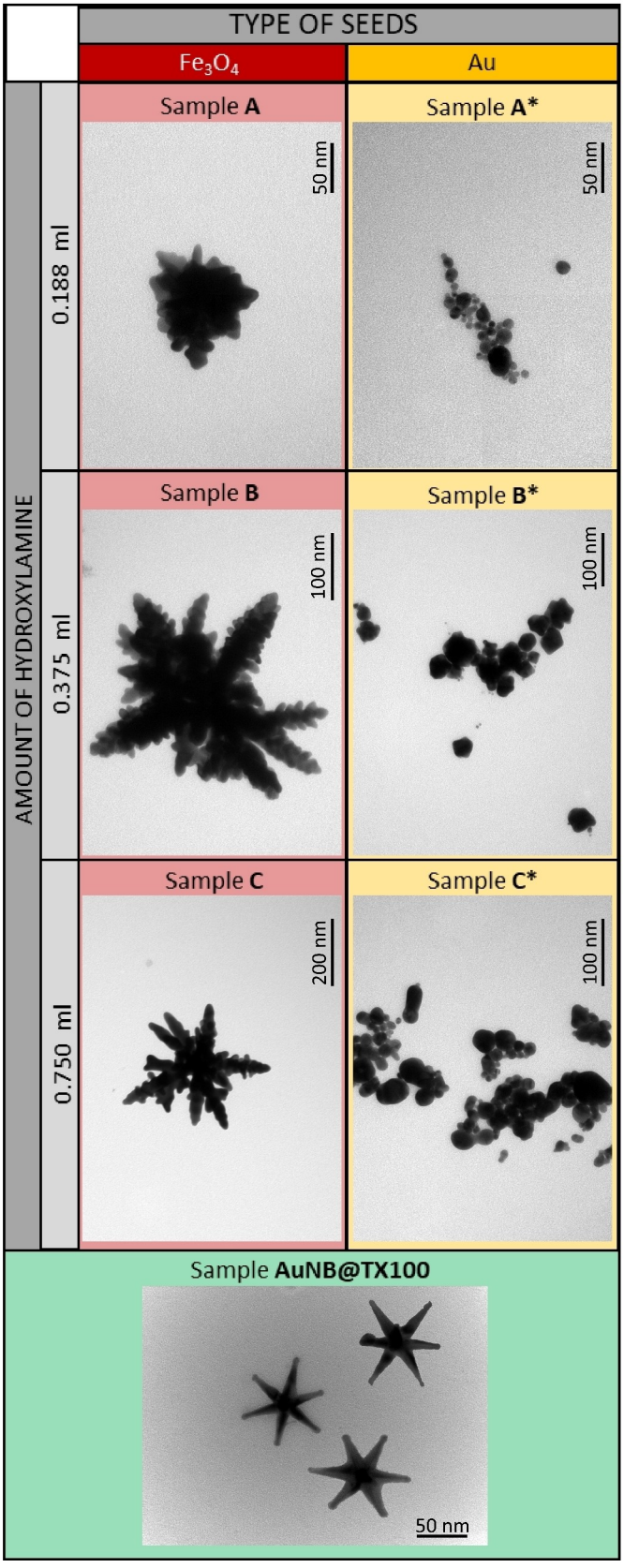

Figure 2. *TEM images of samples related to the amount of hydroxylamine and the type of seeds.*

© 2022 The Authors. ChemistrySelect published by Wiley-VCH GmbH

23656549, 2022, 26, Downloaded from https://chemistry-europe.onlinelibrary.wiley.com/doi/10.1002/slct.202201375 by CochraneItalia, Wiley Online Library on [19/11/2022]. See the Terms and Conditions (https://onlinelibrary.wiley.com/terms-and-conditions) on Wiley Online Library for rules of use; OA articles are governed by the applicable Creative Commons License

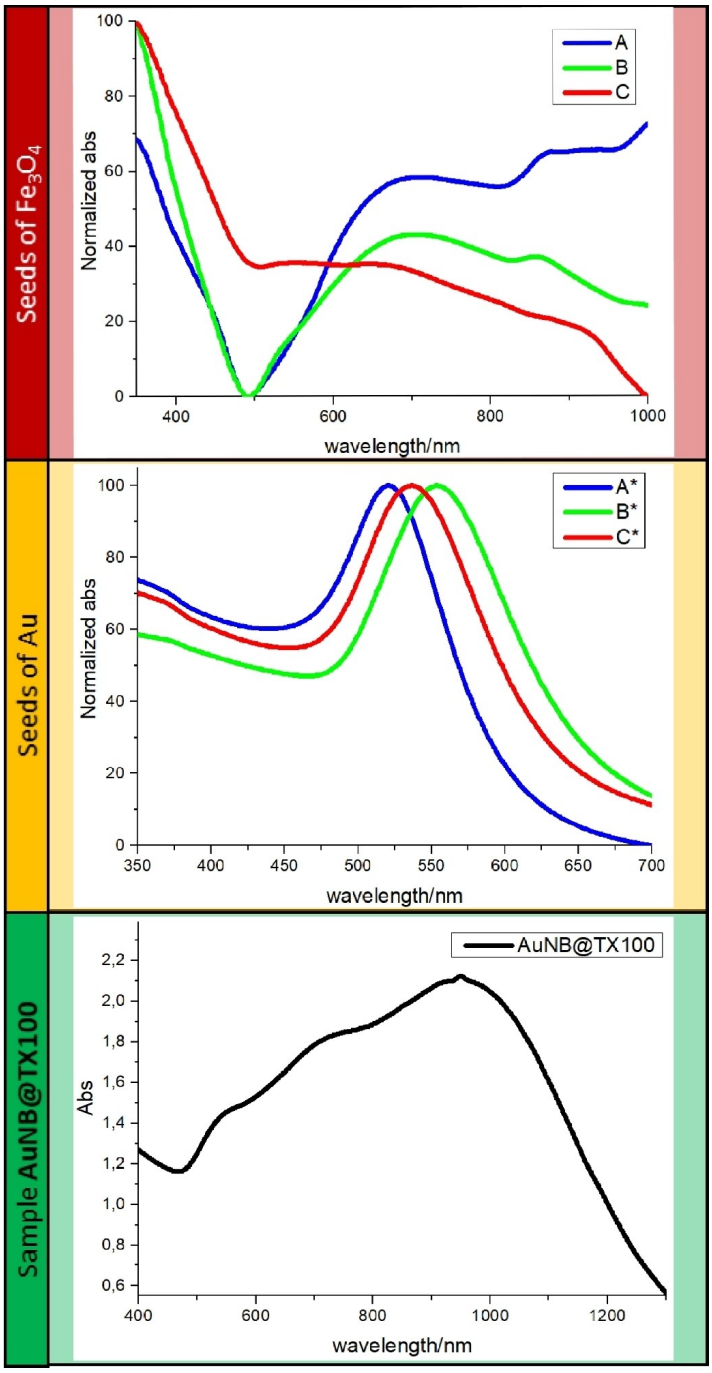

Figure 3. *Extinction spectra of all prepared samples, grouped by type.*

668 nm. Due to the massive presence of gold on the nanoparticles, the plasmonic band is completely superimposed on the Fe_3O_4 electronic transitions bands. It is important to underline that the nanoparticles of bigger size show sedimentation and do not allow to obtain a stable colloidal solution; only after the addition of Triton X-100 to the solution, we were able to obtain a stable dispersion and record the spectrum. The TEM image (Figure 2), indeed, shows that the hybrid nanoparticles have long branches of *ca.* 230 nm in length, whose surface is embedded by smooth and sparse fractal protuberances.

EDX analyses (Figure S4), performed on several randomly chosen nanoparticles for each sample, confirmed for A, B and C their bimetallic composition (i.e. Fe/Au).

Both colloidal solutions of samples A and B were reversibly attracted to a permanent magnet placed near the vial by the induced magnetic field (Figure 5). Redispersion of the nanoparticles into the solution occurs quickly as the magnet was

© 2022 The Authors. ChemistrySelect published by Wiley-VCH GmbH

23656549, 2022, 26, Downloaded from https://chemistry-europe.onlinelibrary.wiley.com/doi/10.1002/slct.202201375 by CochraneItalia, Wiley Online Library on [19/11/2022]. See the Terms and Conditions (https://onlinelibrary.wiley.com/terms-and-conditions) on Wiley Online Library for rules of use; OA articles are governed by the applicable Creative Commons License

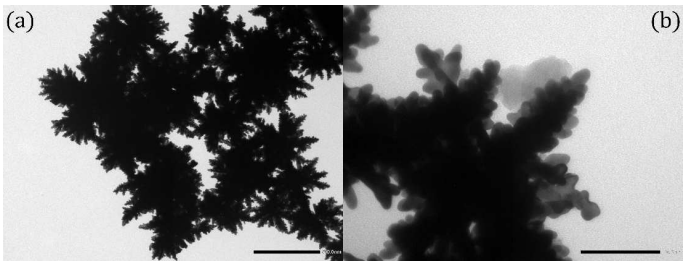

Figure 4. *TEM images of sample B at different magnifications: (a) scale bar 500 nm; (b) scale bar: 100 nm.*

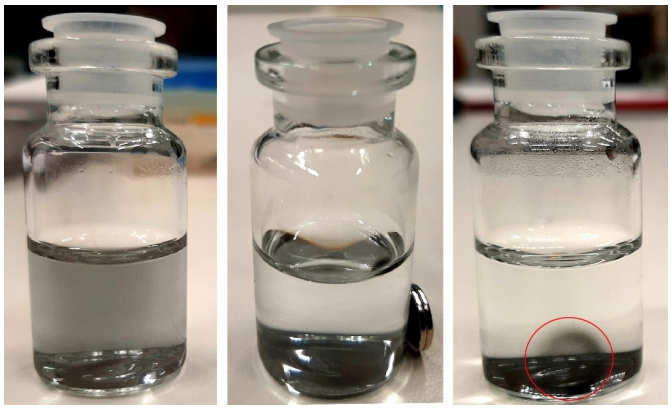

Figure 5. *Aqueous dispersion of hybrid nanoparticles (sample B): before, during and after removal of a magnet (from left to right).*

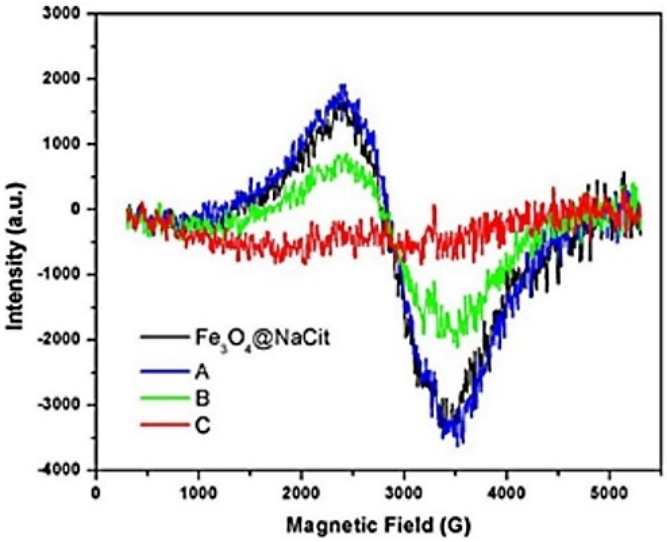

Figure 6. *FMR spectra ($\nu = 9.261$ GHz) at 77 K of iron oxide nanoparticles (Fe_3O_4@NaCit) and of A, B and C iron oxide nanoparticles covered with increasing amount of gold.*

moved away. Differently, sample C does not show magnet attraction.

FMR spectra recorded at 77 K on iron oxide seeds and on hybrid nanoparticles A, B and C are reported in Figure 6. The uncoated *Fe_3O_4@NaCit* seeds show an asymmetric broad-line due to the ferromagnetic core with a peak-to-peak width $\Delta Hp\text{-}p \approx 1050$ Gauss and a g-value ≈ 2.3. Similar spectral features have been recorded for ferric ions in various host matrices.[97–99] Relative to the not naked magnetic nanoparticles, the Au-coated nanoparticles display FMR spectra whose positions and widths remain almost unaltered whereas their intensities are influenced by the thickness of the gold shell. Indeed, the spectral intensity is unaffected in sample A, reduced in sample B and it is almost null in sample C. The line intensity is proportional to the number of the EPR paramagnetic species generating the absorption signal. As the samples for FMR measurements are prepared at the same iron oxide concentration (and thus at the same number of nanoparticles) and the spectra are recorded under the same FMR experimental conditions (i.e., microwave power and modulation amplitude, see Materials and Methods), the reduction of the signal, and ultimately its disappearance, is likely due to the increasing shielding of the microwaves by the thicker layers/longer branches of gold. Reduced magnetic responses in iron oxide nanoparticles by massive gold coverage have been previously reported by other groups.[72,73,100,101]

Regarding the samples with a gold core, in A* (0.1875 mL hydroxylamine), TEM images revealed spherical nanoparticles from 20 to 30 nm in diameter, characterised by a plasmonic band at 521 nm. In sample B*, increasing the hydroxylamine amount (0.375 mL hydroxylamine), the nanoparticles are displaying a faceted surface of an irregular spherical shape of ca. 50 nm of diameter, which induces a plasmonic band at 555 nm. In sample C* (0.750 mL hydroxylamine), with the highest amount of hydroxylamine, according to the TEM image, the degree of inhomogeneity increases, both in shape and dimension with nanoparticles spherical and ellipsoids with diameters ranging from 20 up to 60 nm. The plasmonic band is centred at 534 nm. As already reported, a too high amount of hydroxylamine boosts the reduction process leading to a loss in the directionality of the growth and resulting in a poor homogeneity of the final product.

According to the obtained results, the Au^{3+} reduction and gold growth, mediated by hydroxylamine, is also highly influenced by the chemical nature of the catalytic surface. This is clearly demonstrated here: indeed, the evident difference in overall shape between hybrid iron/gold (hyper-branched) and pure gold (spheroidal) nanoparticles can be explained if we consider that germination of Au, upon Au^{3+} reduction, takes place preferentially on the gold surface rather than iron oxide ones.

At the initial stage, the gold germination occurs slowly on the surface of iron oxide seeds; the subsequent further reduction of Au^{3+} is faster onto the just reduced gold, conferring ultimately a hyper-branched structure with a fractal growth mechanism. On the other hand, on the surface of gold seeds, both Au germination and Au^{3+} reduction happen indiscriminately without a preferential direction, producing nanoparticles with a final spheroidal shape (Scheme 1).

© 2022 The Authors. ChemistrySelect published by Wiley-VCH GmbH

23656549, 2022, 26, Downloaded from https://chemistry-europe.onlinelibrary.wiley.com/doi/10.1002/slct.202201375 by CochraneItalia, Wiley Online Library on [19/11/2022]. See the Terms and Conditions (https://onlinelibrary.wiley.com/terms-and-conditions) on Wiley Online Library for rules of use; OA articles are governed by the applicable Creative Commons License

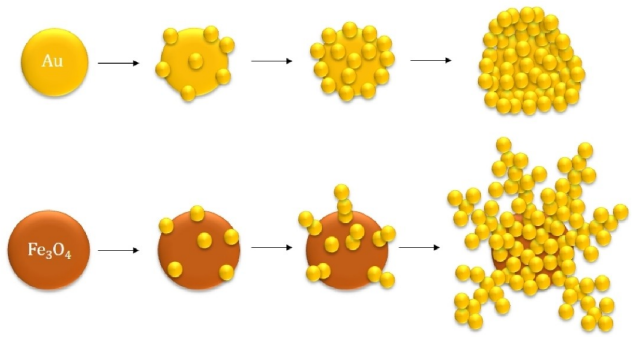

Scheme 1. *Sketch of different gold nucleation and grown on Au (top) or Fe_3O_4 (down) seed surfaces.*

Regarding branched nanoparticles (*AuNB@TX100)*, TEM images (Figure 2) show a length of 24 nm from core to tip. The extinction spectrum (Figure 3) is composed of three plasmonic bands at 546 nm, 716 nm and 941 nm of which the first is attributable to the LSPR of the core and the other to the tips and core-tip interactions.[77]

Photothermal activity is known to be enhanced by the presence of pointed tips on the nanoparticles.[102] Based on this premise, we compared the heat photogeneration triggered by the less- and high-branched Fe/Au nanoparticle samples with the monometallic *AuNB@TX100* sample. Although no relevant differences emerged in the plasmonic spectra of samples A, B and *AuNB@TX100*, their photothermal activity is different. Taking into account that the nanoparticle concentration could influence the temperature reached by the aqueous nanoparticles solution,[103] we conducted photothermal activity measurements using samples with the same concentration of nanoparticles. The three samples were irradiated for 15 minutes by a laser source ($\lambda = 532$ nm, 60 mW). In each sample temperature increase was observed; in particular, 2 °C for Sample A, 6 °C for Sample B and 3 °C for *AuNB@TX100* (Figure 7). We repeated the measures three times obtaining the same results. The best response is attributable to Sample B, probably for the local amplification of the plasmonic electromagnetic field located on the greater number of sharps.

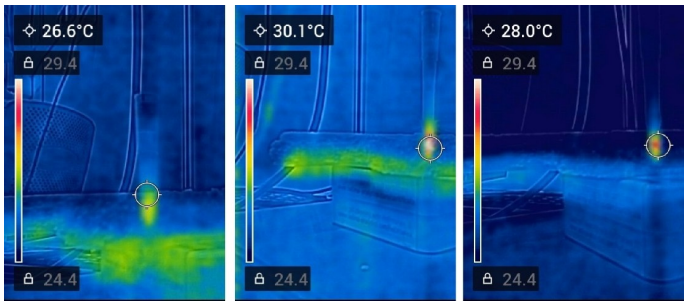

Figure 7. *Thermal photos of sample A, sample B and AuNB@TX100 (from left to right) after 15 minutes of LASER irradiation.*

Conclusion

Our work presents a new synthetic strategy, to the best of our knowledge, to obtain hybrid nanoparticles. Using hydroxylamine as a surface-catalysed reducing agent, the synthesis has been finely tuned to obtain iron/gold hybrid hyper-branched nanoparticles with magnetic and plasmonic behaviours. We synthesized iron seeds with a higher diameter (30–60 nm) than those commonly used. In doing so, several gold germinations occur and fractal growth, leading to hyper-branched nanoparticles, can be controlled according to the hydroxylamine amount used during reduction. The obtained nanoparticles, covered with sodium citrate, give colloidal aqueous solutions that are stable over a long period. They have a wide plasmonic band extending from visible to IR wavelengths and are easily displaced by a magnetic field. The iron oxide nanoparticles and those covered with a low and an intermediate gold shell are indeed responsive to a magnetic field.

By comparing the bimetallic nanoparticles with the gold branched nanoparticles, no relevant differences have been observed in the plasmonic properties, but a better photothermal response has been registered from the hyper-branched ones (i. e. Sample B).

The optical and magnetic behaviour with the possibility to further functionalize the surface of the nanoparticles, through the exchange of sodium citrate, makes it possible to forecast these nanoparticles as interesting tools in various application fields such as biotechnological and biomedical. Combining photothermal and hyperthermal activities they can be employed in heating treatment. Moreover, they can be used as magnetically piloted deliverers of photoactive molecules.

Moreover, the thermogenerative activity could be increased by soliciting the magnetic core through an alternating high-frequency magnetic field.

In conclusion, this study confirmed the synthetic, simple and inexpensive approach, with excellent results regarding the plasmonic activity coupled with the magnetic properties of these hybrid nanoparticles.

Supporting Information Summary

In Supporting Information are reported the Experimental Section, TEM images and Extinction spectra of Fe_3O_4@NaCit (Figure S1), Au@NaCit (Figure S2), Au@TX100 (Figure S3) and EDX analysis of sample A, sample B and sample C (Figure S4).

Acknowledgements

The authors are grateful to Dr Ida Perrotta of the Centre for Microscopy and Microanalysis (CM2) (Department of Biology, Ecology and Earth Sciences, University of Calabria, Italy) for TEM images. Open Access Funding provided by Universita della Calabria within the CRUI-CARE Agreement.

Conflict of Interest

The authors declare no conflict of interest.

© 2022 The Authors. ChemistrySelect published by Wiley-VCH GmbH

23656549, 2022, 26, Downloaded from https://chemistry-europe.onlinelibrary.wiley.com/doi/10.1002/slct.202201375 by CochraneItalia, Wiley Online Library on [19/11/2022]. See the Terms and Conditions (https://onlinelibrary.wiley.com/terms-and-conditions) on Wiley Online Library for rules of use; OA articles are governed by the applicable Creative Commons License

Data Availability Statement

Research data are not shared.

Keywords: hybrid nanoparticles · hyper branches · magnetism · plasmonics · nanomaterials

[1] M. C. Roco, R. S. Williams, P. Alivasatos, *Nanotechnology Research Directions: IWGN Workshop Report* **1999**.
[2] A. Thess, R. Lee, P. Nikolaev, H. Dai, P. Petit, J. Robert, C. Xu, Y. H. Lee, S. G. Kim, A. G. Rinzler, D. T. Colbert, G. E. Scuseria, D. Tománek, J. E. Fischer, R. E. Smalley, *Science* **1996**, *273*, 483–487.
[3] A. L. Linsebigler, G. Lu, J. T. Yates, *Chem. Rev.* **1995**, *95*, 735–758.
[4] W. C. W. Chan, D. J. Maxwell, X. Gao, R. E. Bailey, M. Han, S. Nie, *Curr. Opin. Biotechnol.* **2002**, *13*, 40–46.
[5] H. Zhang, R. L. Penn, R. J. Hamers, J. F. Banfield, *J. Phys. Chem. B* **1999**, *103*, 4656–4662.
[6] B. Z. Zhan, M. A. White, T. K. Sham, J. A. Pincock, R. J. Doucet, K. V. R. Rao, K. N. Robertson, T. S. Cameron, *J. Am. Chem. Soc.* **2003**, *125*, 2195–2199.
[7] H. Liang, H. Tian, M. Deng, X. Chen, *Chin. J. Chem.* **2015**, *33*, 1001–1010.
[8] J. Hori, K. Murata, T. Sugai, H. Shinohara, R. Noyori, N. Arai, N. Kurono, T. Ohkuma, *Adv. Synth. Catal.* **2009**, *351*, 3143–3149.
[9] B. Jiang, Y. Guo, J. Kim, A. E. Whitten, K. Wood, K. Kani, A. E. Rowan, J. Henzie, Y. Yamauchi, *J. Am. Chem. Soc.* **2018**, *140*, 12434–12441.
[10] C. Li, M. Iqbal, J. Lin, X. Luo, B. Jiang, V. Malgras, K. C. W. Wu, J. Kim, Y. Yamauchi, *Acc. Chem. Res.* **2018**, *51*, 1764–1773.
[11] M. Baghayeri, H. Veisi, H. Veisi, B. Maleki, H. Karimi-Maleh, H. Beitollahi, *RSC Adv.* **2014**, *4*, 49595–49604.
[12] H. Karimi-Maleh, M. Moazampour, V. K. Gupta, A. L. Sanati, *Sens. Actuators B* **2014**, *199*, 47–53.
[13] B. J. Sanghavi, W. Varhue, J. L. Chávez, C. F. Chou, N. S. Swami, *Anal. Chem.* **2014**, *86*, 4120–4125.
[14] B. J. Sanghavi, G. Hirsch, S. P. Karna, A. K. Srivastava, *Anal. Chim. Acta* **2012**, *735*, 37–45.
[15] B. J. Sanghavi, A. K. Srivastava, *Analyst* **2013**, *138*, 1395–1404.
[16] C. Li, M. Iqbal, B. Jiang, Z. Wang, J. Kim, A. K. Nanjundan, A. E. Whitten, K. Wood, Y. Yamauchi, *Chem. Sci.* **2019**, *10*, 4054–4061.
[17] C. Li, H. Tan, J. Lin, X. Luo, S. Wang, J. You, Y. M. Kang, Y. Bando, Y. Yamauchi, J. Kim, *Nano Today* **2018**, *21*, 91–105.
[18] R. Shukla, V. Bansal, M. Chaudhary, A. Basu, R. R. Bhonde, M. Sastry, *Langmuir* **2005**, *21*, 10644–10654.
[19] K. M. L. Taylor-Pashow, J. Della Rocca, R. C. Huxford, W. Lin, *Chem. Commun.* **2010**, *46*, 5832–5849.
[20] W. Qi, A. Wang, Y. Yang, M. Du, M. N. Bouchu, P. Boullanger, J. Li, *J. Mater. Chem.* **2010**, *20*, 2121–2127.
[21] J. H. Soh, Z. Gao, *Complex-Shaped Met. Nanoparticles Bottom-Up Synth. Appl.* **2012**, *15*, 477–519.
[22] E. Petryayeva, U. J. Krull, *Anal. Chim. Acta* **2011**, *706*, 8–24.
[23] S. Thota, D. C. Crans, *Metal Nanoparticles* **2018**.
[24] R. Niu, C. Song, F. Gao, W. Fang, X. Jiang, S. Ren, D. Zhu, S. Su, J. Chao, S. Chen, C. Fan, L. Wang, *Angew. Chem. Int. Ed.* **2021**, *60*, 11695–11701.
[25] J. L. Wilson, P. Poddar, N. A. Frey, H. Srikanth, K. Mohomed, J. P. Harmon, S. Kotha, J. Wachsmuth, *J. Appl. Phys.* **2004**, *95*, 1439–1443.
[26] C. Choi, M. K. Choi, T. Hyeon, D. H. Kim, *ChemNanoMat* **2016**, *2*, 1006–1017.
[27] L. Rodríguez-Lorenzo, R. A. Álvarez-Puebla, I. Pastoriza-Santos, S. Mazzucco, O. Stéphan, M. Kociak, L. M. Liz-Marzán, F. J. G. De Abajo, *J. Am. Chem. Soc.* **2009**, *131*, 4616–4618.
[28] K. Yamamoto, Z. An, N. Saito, M. Yamaguchi, *Chem. A Eur. J.* **2013**, *19*, 10580–10588.
[29] N. L. Rosi, D. A. Giljohann, C. S. Thaxton, A. K. R. Lytton-Jean, M. S. Han, C. A. Mirkin, *Science* **2006**, *312*, 1027–1030.
[30] S. Farfán-Castro, M. J. García-Soto, M. Comas-García, J. I. Arévalo-Villalobos, G. Palestino, O. González-Ortega, S. Rosales-Mendoza, *Nanomedicine (N. Y., NY, U. S.)* **2021**, *34*, 102372.
[31] S. Abe, B. Maity, T. Ueno, *Curr. Opin. Chem. Biol.* **2018**, *43*, 68–76.
[32] L. Wang, X. Jiang, M. Zhang, M. Yang, Y. N. Liu, *Chem. Asian J.* **2017**, *12*, 2374–2378.
[33] M. C. Daniel, D. Astruc, *Chem. Rev.* **2004**, *104*, 293–346.
[34] H. J. Kim, S. M. Lee, K. H. Park, C. H. Mun, Y. B. Park, K. H. Yoo, *Biomaterials* **2015**, *61*, 95–102.
[35] L. Huang, L. Ao, D. Hu, W. Wang, Z. Sheng, W. Su, *Chem. Mater.* **2016**, *28*, 5896–5904.
[36] A. Candreva, G. Di Maio, M. La Deda, *Soft Matter* **2020**, *16*, 10865–10868.
[37] J. Peng, N. Zhou, Y. Zhong, Y. Su, L. Zhao, Y. T. Chang, *Microchim. Acta* **2019**, *186*, 618.
[38] F. Wang, X. Liu, *Acc. Chem. Res.* **2014**, *47*, 1378–1385.
[39] X. Xie, W. Xu, X. Liu, *Acc. Chem. Res.* **2012**, *45*, 1511–1520.
[40] L. Ricciardi, M. La Deda, *SN Appl. Sci. 2021 33* **2021**, *3*, 1–14.
[41] N. Sarfraz, I. Khan, *Chem. Asian J.* **2021**, *16*, 720–742.
[42] X. Lu, A. Dandapat, Y. Huang, L. Zhang, Y. Rong, L. Dai, Y. Sasson, J. Zhang, T. Chen, *RSC Adv.* **2016**, *6*, 60916–60921.
[43] A. Candreva, W. Lewandowski, M. La Deda, *J. Nanopart. Res.* **2022**, 24–19 .
[44] X. Huang, I. H. El-Sayed, W. Qian, M. A. El-Sayed, *J. Am. Chem. Soc.* **2006**, *128*, 2115–2120.
[45] L. Scarabelli, M. Grzelczak, L. M. Liz-Marzán, *Chem. Mater.* **2013**, *25*, 4232–4238.
[46] R. Omar, A. E. Naciri, S. Jradi, Y. Battie, J. Toufaily, H. Mortada, S. Akil, *J. Mater. Chem. C* **2017**, *5*, 10813–10821.
[47] L. Scarabelli, M. Coronado-Puchau, J. J. Giner-Casares, J. Langer, L. M. Liz-Marzán, *ACS Nano* **2014**, *8*, 5833–5842.
[48] P. S. Kumar, I. Pastoriza-Santos, B. Rodríguez-González, F. J. G. de Abajo, L. M. Liz-Marzán, *Nanotechnology* **2007**, *19*, 015606.
[49] J. Yang, D. Shen, L. Zhou, W. Li, X. Li, C. Yao, R. Wang, A. M. El-Toni, F. Zhang, D. Zhao, *Chem. Mater.* **2013**, *25*, 3030–3037.
[50] X. Ji, R. Shao, A. M. Elliott, R. Jason Stafford, E. Esparza-Coss, J. A. Bankson, G. Liang, Z. P. Luo, K. Park, J. T. Markert, C. Li, *J. Phys. Chem. C* **2007**, *111*, 6245–6251.
[51] L. Gao, J. Fei, J. Zhao, H. Li, Y. Cui, J. Li, *ACS Nano* **2012**, *6*, 8030–8040.
[52] Y. Ma, X. Liang, S. Tong, G. Bao, Q. Ren, Z. Dai, *Adv. Funct. Mater.* **2013**, *23*, 815–822.
[53] M. Iqbal, Y. Bando, Z. Sun, K. C. W. Wu, A. E. Rowan, J. Na, B. Y. Guan, Y. Yamauchi, *Adv. Mater.* **2021**, *33*, 2004554.
[54] A. Candreva, G. Di Maio, F. Parisi, F. Scarpelli, A. Crispini, N. Godbert, L. Ricciardi, A. Nucera, C. Rizzuto, R. C. Barberi, M. Castriota, M. La Deda, *Chemosensors* **2022**, *10*, 1–17.
[55] C. Burda, X. Chen, R. Narayanan, M. A. El-Sayed, *Chem. Rev.* **2005**, *105*, 1025–1102.
[56] A. Guerrero-Martínez, S. Barbosa, I. Pastoriza-Santos, L. M. Liz-Marzán, *Curr. Opin. Colloid Interface Sci.* **2011**, *16*, 118–127.
[57] L. Rodríguez-Lorenzo, R. A. Álvarez-Puebla, F. J. G. De Abajo, L. M. Liz-Marzán, *J. Phys. Chem. C* **2010**, *114*, 7336–7340.
[58] T. Vo-Dinh, A. M. Fales, G. D. Griffin, C. G. Khoury, Y. Liu, H. Ngo, S. J. Norton, J. K. Register, H. N. Wang, H. Yuan, *Nanoscale* **2013**, *5*, 10127–10140.
[59] A. Espinosa, R. Di Corato, J. Kolosnjaj-Tabi, P. Flaud, T. Pellegrino, C. Wilhelm, *ACS Nano* **2016**, *10*, 2436–2446.
[60] R. E. Rosensweig, *J. Magn. Magn. Mater.* **2002**, *252*, 370–374.
[61] T. Ishizaki, K. Yatsugi, K. Akedo, *J. Nanopart. Res.* **2018**, *20*, 116.
[62] K. Yatsugi, T. Ishizaki, K. Akedo, M. Yamauchi, *J. Nanopart. Res.* **2019**, *21*, 60.
[63] Y. Hu, R. Wang, S. Wang, L. Ding, J. Li, Y. Luo, X. Wang, M. Shen, X. Shi, *Sci. Rep.* **2016**, *6*, 1–12.
[64] S. Sun, H. Zeng, D. B. Robinson, S. Raoux, P. M. Rice, S. X. Wang, G. Li, *J. Am. Chem. Soc.* **2004**, *126*, 273–279.
[65] A. K. Gupta, M. Gupta, *Biomaterials* **2005**, *26*, 3995–4021.
[66] X. Q. Li, D. W. Elliott, W. X. Zhang, *Crit. Rev. Solid State Mater. Sci.* **2006**, *31*, 111–122.
[67] J.-H. Yu, C.-W. Lee, S.-S. Im, J.-S. Lee, *Rev.Adv.Mater.Sci* **2003**, *4*, 55–59.
[68] L. M. Liz-Marzán, P. V. Kamat, *Nanoscale Materials*, Kluwer Academic Publishers, Boston, **2004**.
[69] J. Li, Y. Hu, J. Yang, P. Wei, W. Sun, M. Shen, G. Zhang, X. Shi, *Biomaterials* **2015**, *38*, 10–21.
[70] N. Atar, T. Eren, M. L. Yola, H. Karimi-Maleh, B. Demirdögen, *RSC Adv.* **2015**, *5*, 26402–26409.
[71] A. Espinosa, J. Reguera, A. Curcio, Á. Muñoz-Noval, C. Kuttner, A. Van de Walle, L. M. Liz-Marzán, C. Wilhelm, *Small* **2020**, *16*, 1–14.

© 2022 The Authors. ChemistrySelect published by Wiley-VCH GmbH

23656549, 2022, 26, Downloaded from https://chemistry-europe.onlinelibrary.wiley.com/doi/10.1002/slct.202201375 by CochraneItalia, Wiley Online Library on [19/11/2022]. See the Terms and Conditions (https://onlinelibrary.wiley.com/terms-and-conditions) on Wiley Online Library for rules of use; OA articles are governed by the applicable Creative Commons License

[72] G. Brennan, S. Bergamino, M. Pescio, S. A. M. Tofail, C. Silien, *Nanomaterials* **2020**, *10*, 1–16.
[73] P. Quaresma, I. Osório, G. Dória, P. A. Carvalho, A. Pereira, J. Langer, J. P. Araújo, I. Pastoriza-Santos, L. M. Liz-Marzán, R. Franco, P. V. Baptista, E. Pereira, *RSC Adv.* **2014**, *4*, 3659–3667.
[74] G. C. Lavorato, R. Das, J. Alonso Masa, M. H. Phan, H. Srikanth, *Nanoscale Adv.* **2021**, *3*, 867–888.
[75] M. A. M. Tarkistani, V. Komalla, V. Kayser, *Nanomater.* **2021**, *Vol. 11*, *Page 1227* **2021**, *11*, 1227.
[76] C. L. Nehl, J. H. Hafner, *J. Mater. Chem.* **2008**, *18*, 2415–2419.
[77] G. Chirico, M. Borzenkov, P. Pallavicini, *Gold Nanostars: Synthesis, P roperties and Biomedical Application* **2015**.
[78] T. Vo-Dinh, Y. Liu, A. M. Fales, H. Ngo, H.-N. Wang, J. K. Register, H. Yuan, S. J. Norton, G. D. Griffin, *Wiley Interdiscip. Rev. Nanomed. Nanobiotechnol.* **2015**, *7*, 17–33.
[79] A. Tomitaka, H. Arami, A. Ahmadivand, N. Pala, A. J. McGoron, Y. Takemura, M. Febo, M. Nair, *Sci. Rep.* **2020**, *10*, 1–10.
[80] J. Reguera, D. J. de Aberasturi, N. Winckelmans, J. Langer, S. Bals, L. M. Liz-Marzán, *Faraday Discuss.* **2016**, *191*, 47–59.
[81] K. R. Brown, D. G. Walter, M. J. Natan, *Chem. Mater.* **2000**, *12*, 306–313.
[82] C. Gao, J. Goebl, Y. Yin, *J. Mater. Chem. C* **2013**, *1*, 3898–3909.
[83] T. Hyeon, *Chem. Commun.* **2003**, *3*, 927–934.
[84] S. Nigam, K. C. Barick, D. Bahadur, *Surface engineered magnetic nanoparticles for removal of toxic metal ions and bacterial pathogens* **2011**, *323*, 237–243.
[85] C. Wang, Y. Chen, Z. Ma, T. Wang, Z. Su, *J. Nanosci. Nanotechnol.* **2008**, *8*, 5887–5895.
[86] H. You, X. Liu, H. Liu, J. Fang, *CrystEngComm* **2016**, *18*, 3934–3941.
[87] S. K. Kang, Y. Kim, M. S. Hahn, I. Choi, J. Lee, J. Yi, *Curr. Appl. Phys.* **2006**, *6*, 114–120.
[88] K. R. Brown, M. J. Natan, *Hydroxylamine Seeding of Colloidal Au Nanoparticles in Solution and on Surfaces* **1998**, *4*, 726–728.
[89] J. L. Lyon, D. A. Fleming, M. B. Stone, P. Schiffer, M. E. Williams, *Nano Lett.* **2004**, *4*, 719–723.
[90] P. Pallavicini, A. Donà, A. Casu, G. Chirico, M. Collini, G. Dacarro, A. Falqui, C. Milanese, L. Sironi, A. Taglietti, *Chem. Commun.* **2013**, *49*, 6265–6267.
[91] B. Bassi, G. Dacarro, P. Galinetto, E. Giulotto, N. Marchesi, P. Pallavicini, A. Pascale, S. Perversi, A. Taglietti, in *Nanotechnology*, IOP Publishing, **2018**.
[92] N. Cennamo, G. D'Agostino, A. Donà, G. Dacarro, P. Pallavicini, M. Pesavento, L. Zeni, *Sensors* **2013**, *13*, 14676–14686.
[93] P. Pallavicini, E. Cabrini, M. Borzenkov, L. Sironi, G. Chirico, **n.d.**, 43–59.
[94] J. Polte, M. Herder, R. Erler, S. Rolf, A. Fischer, C. Würth, A. F. Thünemann, R. Kraehnert, F. Emmerling, *Nanoscale* **2010**, *2*, 2463–2469.
[95] D. W. Mulder, M. M. Phiri, A. Jordaan, B. C. Vorster, *R. Soc. Open Sci.* **2019**, *6*, 190160.
[96] Y. Q. He, S. P. Liu, L. Kong, Z. F. Liu, *Spectrochim. Acta Part A* **2005**, *61*, 2861–2866.
[97] J. Salado, M. Insausti, L. Lezama, I. G. de Muro, M. Moros, B. Pelaz, V. Grazu, J. M. de la Fuente, T. Rojo, *Nanotechnology* **2012**, *23*, 315102.
[98] G. S. Shahane, K. V. Zipare, R. P. Pant, *Magn. Gidrodin.* **2013**, *49*, 317–321.
[99] L. F. Gamarra, W. M. Pontuschka, J. B. Mamani, D. R. Cornejo, T. R. Oliveira, E. D. Vieira, A. J. Costa-Filho, E. Amaro, *J. Phys. Condens. Matter* **2009**, *21*, 115104.
[100] Y. Li, J. Liu, Y. Zhong, J. Zhang, Z. Wang, L. Wang, Y. An, M. Lin, Z. Gao, D. Zhang, *Int. J. Nanomed.* **2011**, *6*, 2805.
[101] W. E. Hong, I. L. Hsu, S. Y. Huang, C. W. Lee, H. Ko, P. J. Tsai, D. Bin Shieh, C. C. Huang, *J. Mater. Chem. B* **2018**, *6*, 5689–5697.
[102] H. Chatterjee, D. S. Rahman, M. Sengupta, S. K. Ghosh, *J. Phys. Chem. C* **2018**, *122*, 13082–13094.
[103] A. M. M. Gherman, S. Boca, A. Vulpoi, M. V. Cristea, C. Farcau, V. Tosa, *Nanotechnology* **2020**, *31*, 125701.
[104] C. Cretu, A. A. Andelescu, A. Candreva, A. Crispini, E. I. Szerb, M. La Deda, *J. Mater. Chem. C* **2018**, *6*, 10073–10082.
[105] P. F. Liguori, M. Ghedini, M. La Deda, N. Godbert, F. Parisi, R. Guzzi, A. Ionescu, I. Aiello, *Dalton Trans.* **2020**, *49*, 2628–2635.

Submitted: April 6, 2022
Accepted: June 24, 2022

© 2022 The Authors. ChemistrySelect published by Wiley-VCH GmbH

23656549, 2022, 26, Downloaded from https://chemistry-europe.onlinelibrary.wiley.com/doi/10.1002/slct.202201375 by CochraneItalia, Wiley Online Library on [19/11/2022]. See the Terms and Conditions (https://onlinelibrary.wiley.com/terms-and-conditions) on Wiley Online Library for rules of use; OA articles are governed by the applicable Creative Commons License

JOURNAL OF COORDINATION CHEMISTRY
https://doi.org/10.1080/00958972.2022.2132483

Taylor & Francis
Taylor & Francis Group

Check for updates

Structural investigation of anionic cyclometalated Pt(II)-tetrabromocatecholate complexes: *quasi*-halogen bonding and elusive polymorphism at play

Francesca Scarpelli[a], Andreea Ionescu[a], Alessandra Crispini[a], Nadia Marino[a], Giuseppe Di Maio[a], Massimo La Deda[a,b], Nicolas Godbert[a] and Iolinda Aiello[a,b]

[a]MAT-INLAB (Laboratorio di Materiali Molecolari Inorganici), Dipartimento di Chimica e Tecnologie Chimiche, Universitá della Calabria, Arcavacata di Rende, Cosenza, Italy; [b]CNR NANOTEC-Istituto di Nanotecnologia U.O.S. Cosenza, Arcavacata di Rende, Cosenza, Italy

ABSTRACT

Four unusual anionic heteroleptic cyclometalated monomeric Pt(II) complexes bearing the aromatic tetrabromocatecholate dianion (Br_4cat) and either benzo[h]quinoline H(bzq) (**1**), (2,4-difluorophenyl)-pyridine H(F_2ppy) (**2**), 2-phenylpyridine H(ppy) (**3**) or 2,2′-thienylpyridine H(thpy) (**4**) as the cyclometalating ligand were synthesized, precipitated as NBu_4^+ salts and recrystallized from acetone solutions. Single-crystal XRD investigation indicated that in the crystal structures of **1–4** the monoanionic $[(C^\wedge N)Pt(Br_4cat)]^-$ [(C^N) = bzq (**1**), F_2ppy (**2**), ppy) (**3**), thpy (**4α**, **4β**)] moieties engage in various intermolecular interactions, including π-π stacking and Br···Br contacts (mostly of *quasi*-type II), which ultimately determine their aggregation into 2D (**1**) or 3D (**2–4**) supramolecular networks, albeit without short Pt···Pt contacts. A combined PXRD and DSC analysis of both microcrystalline powders and single-crystals of **1–4** unequivocally revealed the occurrence of solid-state polymorphism for **1**, **3** and **4**. Efforts to grow single-crystals of more than just one form of **1** and **3** were unsuccessful. Conversely, two polymorphs of **4** (**4α** and **4β**) could be isolated and studied. The deep structural investigation of **1–4** put forward herein contributes validating the hypothesized reasons behind the significant enhancement of luminescence in the solid-state previously reported for this series of heteroleptic cyclometalated Pt(II) monomers.

ARTICLE HISTORY
Received 3 August 2022
Accepted 8 September 2022

KEYWORDS
Cyclometalated anionic Pt(II) complexes; luminescence; tetrabromocatecholate anion; quasi-halogen bonding; solid-state polymorphism

CONTACT Nadia Marino nadia.marino@unical.it MAT-INLAB (Laboratorio di Materiali Molecolari Inorganici), Dipartimento di Chimica e Tecnologie Chimiche, Universitá della Calabria, 87036 Arcavacata di Rende, Cosenza, Italy.
This work is dedicated to Professor Giovanni De Munno, a mentor, a colleague, a friend, a terrific teacher, on the occasion of his retirement.

© 2022 Informa UK Limited, trading as Taylor & Francis Group

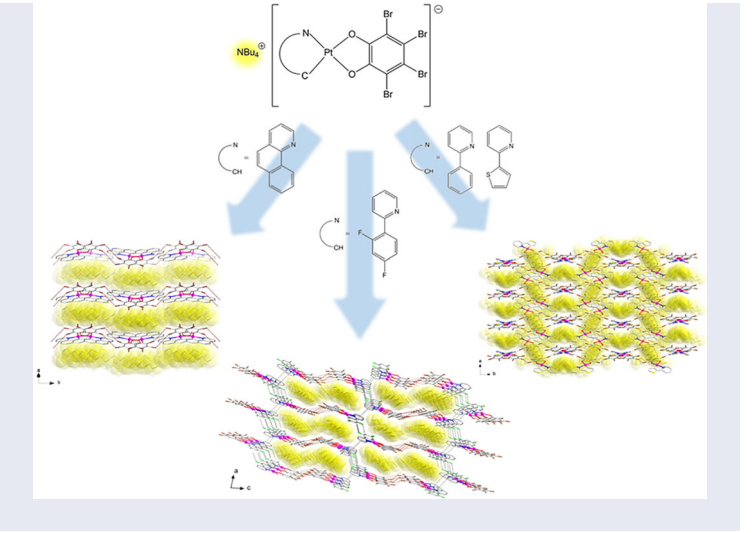

1. Introduction

Of continuous interest is the chemistry of cyclometalated Pt(II) complexes, mainly due to the variety of applications in optoelectronics (optical devices, chemosensing, photocatalysis) [1–6] and biomedicine (anticancer drugs and bioimaging) [7–10]. The cycloplatinated(II) emission properties, in particular phosphorescence properties both in solution and in the solid-state, and their modulation, are the basis of almost all of the above mentioned applications [11, 12].

Over time, many types of cyclometalating ligands have been developed to pursue molecular design strategies for control of the environment surrounding the square-planar platinum center [13]. This geometry, typical of d^8 ions, allows, in principle, strong intermolecular π-π stacking and/or Pt···Pt interactions in the condensed phase, thus nurturing the aggregation of the chromophores and tuning their optical behavior [12, 14].

Focusing our attention on bis-chelated heteroleptic cyclometalated monomeric Pt(II) complexes of general formula [(C^N)Pt(II)(X^Y)], where H(C^N) is the cyclometalating ligand, not only its features would be crucial in order to promote supramolecular organizations, but also the choice of the (X^Y) ancillary ligand would be key to the exact same purpose [15]. Ancillary ligands can influence the electron density at the metal center, also contributing to determining the overall charge of the cyclometalated Pt(II) complexes [(C^N)Pt(II)(X^Y)], thus yielding neutral or ionic species. The use of neutral or monoanionic (X^Y) ligands has returned so far a plethora of cationic and neutral luminescent Pt(II) complexes [16–21]. Anionic bis-chelated heteroleptic cyclometalated Pt(II) species have been much less explored instead [22, 23], even if the modulation of luminescence in these systems could make use of the appropriate counter cation.

Very recently Ionescu and co-workers reported two series of anionic cyclometalated Pt(II) monomers of general formula $[Pt(C^N)(X^Y)]^-$ bearing, as ancillary (X^Y) ligands, the tetrabromo-substituted aromatic dianionic bidentate catecholate (O^O) and the unsubstituted orotate (O^N) ligands [24]. These systems represent a rare example of

anionic Pt(II) complexes, with great potential toward the design of novel and potentially luminescent soft salt materials. Notably, both series were luminescent in solution and in the solid-state at 298 K, and both showed a significant (sometimes outstanding, for the orotate series) enhancement of the luminescence quantum yield in the solid phase. After ruling out other hypotheses, ascribing the observed improvement of the luminescence efficiency to chromophore aggregation *via* specific interaction patterns, such as Pt···Pt contacts and/or π-π stacking, seemed reasonable to the authors [24]. Literature examples of Pt(II) monomers including the dianionic orotate fragment (but either neutral or cationic) are scarce but available [25–27] and the plausible monomer aggregation *via* the abovementioned π-π pathways has been proved to occur easily between symmetry-related orotate fragments [26]. Conversely, structural studies on square-planar Pt(II) complexes (whether cyclometalated or not) containing the Br_4cat ligand have yet to be reported.

Considering the four bulky Br substituents at the catecholate moiety, along with additional interaction pathways accessible with such a ligand (e.g. among others, halogen or *pseudo*-halogen bonding [28–30]), it could be predicted that if any, π-π contacts in monomeric cyclometalated Pt(II) complexes bearing Br_4cat as the ancillary ligand should be ascribed more plausibly to the aromatic cyclometalating ligands rather than to Br_4cat.

In this context, it appears useful to shed some light into the solid-state structures of NBu_4[(C^N)Pt(Br_4cat)] (**1**–**4**) [24] containing, as the cyclometalating ligand, benzo[h]-quinoline H(bzq) (**1**), (2,4-difluorophenyl)-pyridine H(F_2ppy) (**2**), 2-phenylpyridine H(ppy) (**3**) or 2,2′-thienylpyridine H(thpy) (**4**) (Chart 1). Herein, a deep structural analysis, together with a preliminary thermal investigation of all possibly (albeit not exhaustive) isolated solid-state forms of **1**–**4** is presented and discussed.

2. Experimental

2.1. Materials and methods

All commercially available chemicals were purchased from Aldrich Chemical Co. and Alfa Aesar and were used without purification. FT-IR spectra (4000–400 cm^{-1}) were recorded on a Perkin-Elmer Spectrum One FT-IR spectrometer as KBr pellets. ^{1}H NMR spectra were recorded on a Bruker WH-300 spectrometer in deuterated solvents with TMS as an internal standard. ^{13}C NMR spectra were acquired on a Bruker Avance 500 MHz spectrometer in $CDCl_3$ with TMS as an internal standard. Melting points, retrieved from calorimetric analyses, were also corroborated by observations made with a Leica DMLP polarizing microscope equipped with a Leica DFC280 camera and a CalCTec (Italy) heating stage. DSC analysis was performed using a TA DSC Q2000 instrument with a refrigerated cooling unit (RCS 90). Indium metal standard was used for temperature calibrations. The samples were accurately weighted (1.0 mg *ca.*) and crimped in non-hermetic low-mass aluminum pans. They were heated/cooled at a heating/cooling rate of 5 °C/min under a dry nitrogen atmosphere (flow rate 50 ml/min) using an empty non-hermetic low-mass aluminum pan as reference. Powder X-ray diffraction patterns were acquired with a Bruker D2-Phaser equipped with Cu Kα

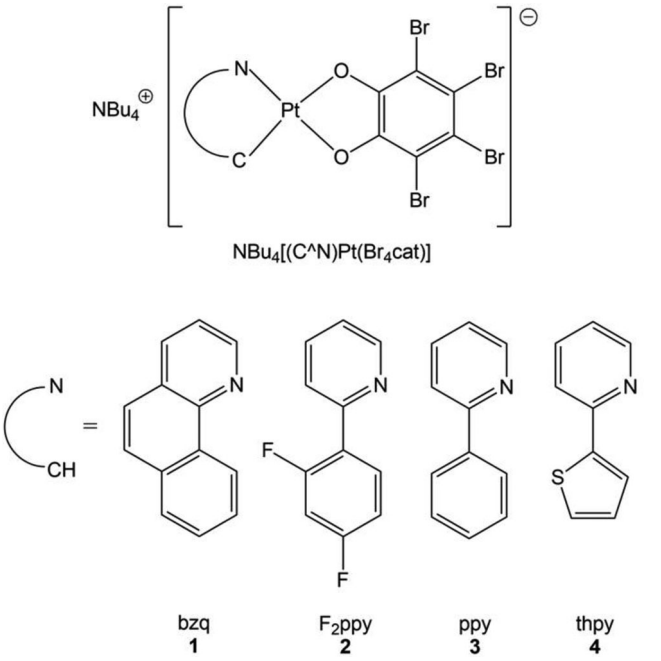

Chart 1. Molecular structures of the anionic Pt(II) square-planar $NBu_4[(C^N)Pt(Br_4cat)]$ (**1**–**4**) complexes [24] investigated in the present study.

radiation ($\lambda = 1.5418$ Å) and a Lynxeye detector at 30 kV and 10 mA with a step size of 0.01°(2θ) between 5 and 50°(2θ).

2.2. Preparation of $NBu_4[(bzq)Pt(Br_4cat)]$ (1), $NBu_4[(F_2ppy)Pt(Br_4cat)]$ (2), $NBu_4[(ppy)Pt(Br_4cat)]$ (3) and $NBu_4[(thpy)Pt(Br_4cat)]$ (4)

Compounds **1–4** were prepared according to the literature procedure [24]. Yields, colors, NMR, FT-IR spectra and melting points were consistent with those previously reported [24]. After confirming their nature and purity, microcrystalline powders of **1**–**4** were dissolved in acetone and placed into 2 ml glass capped vials, providing light orange needles for **1** and **3**, yellow plates for **2** and orange plates for **4** (hereafter noted **4α**), all suitable for single crystal X-ray diffraction analysis after standing at room temperature for 8 to 12 days. Slow evaporation was achieved by inserting a thin needle into each vial septum-equipped screw cap. Diluted acetone solutions of microcrystalline **1**–**4** were also placed into crystallization glass tubes, capped afterwards, to allow for a much slower evaporation. This second method only yielded, after about 3 months, a few light orange parallelepiped-shaped crystals of **4** (hereafter noted **4β**), which proved to be a solid-state polymorph of **4α**. All solids were similarly dissolved in methanol, and both the two above-described crystallization procedures were followed. Only slow evaporation of the methanolic solution of **1** placed in the 2 ml vials provided X-ray quality crystals, specifically the same polymorph of **1** obtained by using acetone as the solvent.

Table 1. Summary of crystal data and structure refinement for **1**–**3**, **4α** and **4β**.

	1	**2**	**3**	**4α**	**4β**
Formula	$C_{35}H_{44}Br_4N_2O_2Pt$	$C_{33}H_{42}Br_4F_2N_2O_2Pt$	$C_{33}H_{44}Br_4N_2O_2Pt$	$C_{31}H_{42}Br_4N_2O_2PtS$	$C_{31}H_{42}Br_4N_2O_2PtS$
F_w/g mol^{-1}	1039.45	1051.41	1015.43	1021.45	1021.45
T/K	296(2)	296(2)	296(2)	296(2)	296(2)
Crystal system	Monoclinic	Triclinic	Monoclinic	Triclinic	Monoclinic
Space group	$P2_1/n$	$P-1$	$P2_1/c$	$P-1$	$P2_1/c$
a/Å	12.884(2)	8.5724(5)	8.6816(7)	8.2553(16)	8.678(3)
b/Å	20.715(4)	9.3748(6)	32.218(3)	19.913(4)	32.088(12)
c/Å	13.821(3)	23.8565(13)	26.040(3)	22.501(4)	26.115(9)
α/°	90	79.840(3)	90	79.867(9)	90
β/°	101.343(8)	80.563(3)	96.863(4)	82.096(9)	98.060(14)
γ/°	90	86.241(3)	90	83.084(9)	90
V/Å^3	3616.4(12)	1860.29(19)	7231.3(11)	3589.0(12)	7200(4)
Z	4	2	8	4	8
D_c/g cm^{-3}	1.909	1.877	1.865	1.890	1.885
F(000)	2008	1012	3920	1968	3936
μ(Mo-Kα)/mm^{-1}	8.332	8.108	8.332	8.450	8.424
Refl. collected	62452	10123	74584	154763	89836
Refl. indep. [*R*int]	7931 [0.0359]	6108 [0.0313]	13108 [0.0548]	13081 [0.0404]	10012 [0.0746]
Refl. obs. [$I > 2\sigma(I)$]	6917	4057	10010	10988	7614
Data/restraints/parameters	7931/150/408	6108/290/383	13108/306/759	13081/1974/892	10017/250/727
GOOF [c]	1.137	1.074	1.030	1.140	1.074
R_1 [a] [$I > 2\sigma(I)$] (all)	0.0267 (0.0339)	0.0708 (0.1088)	0.0302 (0.0494)	0.0695 (0.0814)	0.0357 (0.0572)
wR_2 [b] [$I > 2\sigma(I)$] (all)	0.0547 (0.0567)	0.1741 (0.1902)	0.0654 (0.0717)	0.1683 (0.1732)	0.0714 (0.0783)
Largest diff. peak/hole/eÅ^{-3}	0.820, −0.720	2.267, −1.602	0.709, −0.650	2.371, −1.783	0.946, −0.909

$R_1 = \sum||F_o| - |F_c||/\sum|F_o|$. [b] $wR_2 = \{\sum w(F_o^2 - F_c^2)^2/\sum[w(F_o^2)^2]\}^{1/2}$ and $w = 1/[\sigma^2(F_o)^2 + (mP)^2 + nP]$ with $P = (F_o^2 + 2F_c^2)/3$, m = 0.0133 (1), 0.0735 (2), 0.0255 (3), 0.0170 (4α) and 0.0269 (4β), and n = 5.2227 (1), 13.6459 (2), 6.5396 (3), 59.5602 (4α) and 14.2825 (4β), [c] $S = [\sum w(|F_o| - |F_c|)^2/(N_o - N_p)]^{1/2}$.

2.3. Crystal structure determination and refinement

Diffraction data for **1**–**3**, **4α** and **4β** were collected at room temperature with a Bruker-Nonius X8-APEXII CCD area detector system by using graphite monochromated Mo-Kα radiation (λ = 0.71073 Å). Crystals of **2** and **4β** diffracted poorly (for **4β**, $\vartheta_{max} = 23°$), whereas crystals of **1**, **3** and **4α** were of better quality and more stable under the operating conditions. The data were processed through SAINT [31] reduction and SADABS [32] absorption software. The structures were solved by direct methods and subsequently completed by Fourier recycling using the SHELXTL-2018 software package [33, 34], then refined by full-matrix least-squares refinements based on F^2 with all observed reflections. All non-hydrogen atoms were refined anisotropically. The hydrogen atoms of the bzq (**1**), F_2ppy (**2**), ppy (**3**) and thpy (**4α**, **4β**) ligands, as well as those of the tetrabutylammonium cations in **1**–**3**, **4α** and **4β**, were included at geometrically calculated positions and refined using a riding model. The Pt-bound N and C sites at the *quasi* symmetrical cyclometalating ligands bzq (**1**) and ppy (**3**) were refined freely with a mixed occupancy, with the aid of positional and anisotropic displacement constraints [35, 36]; at convergence, the major and minor components of the disorder had occupancy factors of *ca*. 0.60:0.40 (**1**), 0.90:0.10 (**3**, Pt1 unit) and 0.70:0.30 (**3**, Pt2 unit). In both **1** and **2**, the terminal methyl group of one arm of the tetrabutylammonium cation was found disordered over two sites. The relative occupancies of the two disordered components were refined freely while constraining their sum to unity, using similarity restraints on 1,2- and 1,3-distances. Rigid-bond restraints were applied to the tetrabutylammonium cations in each structure [35, 36]. In **2**, the F_2ppy ligand was particularly

Table 2. Selected bond distances (Å) and angles (°) for **1–3** and **4β**.

	1	2	*Pt1 unit*	3	4β	*Pt2 unit*	3	4β
Pt1-O1	2.039(2)	2.057(10)	Pt1-O1	2.076(3)	2.064(4)	Pt2-O1′	2.066(3)	2.075(5)
Pt1-O2	2.050(2)	2.035(9)	Pt1-O2	2.013(3)	2.011(4)	Pt2-O2′	2.045(3)	2.033(4)
Pt1-N1	1.994(3)	2.023(11)	Pt1-N1	1.990(4)	2.011(5)	Pt2-N1′	1.985(4)	1.991(3)
Pt1-C17	1.989(3)	1.915(4)	Pt1-C13	1.970(5)	1.973(7)	Pt2-C13′	1.983(5)	1.987(8)
O1-Pt1-O2	82.37(9)	81.9(4)	O1-Pt1-O2	82.05(13)	81.73(13)	O1′-Pt2-O2′	82.67(18)	82.38(18)
N1-Pt1-C17	81.83(13)	79.7(5)	N1-Pt1-C13	80.91(18)	81.0(2)	N1′-Pt2-C13′	80.3(3)	79.2(3)
O1-Pt1-N1	98.73(11)	97.2(5)	O1-Pt1-N1	99.20(15)	98.06(16)	O1′-Pt2-N1′	97.8(2)	99.1(2)
O2-Pt1-C17	97.25(12)	101.1(3)	O2-Pt1-C13	97.80(17)	99.63(17)	O2′-Pt2-C13′	99.2(2)	99.6(3)
O1-Pt1-C17	176.75(11)	176.8(3)	O1-Pt1-C13	176.71(16)	177.17(15)	O1′-Pt2-C13′	176.3(2)	177.3(2)
O2-Pt1-N1	176.64(11)	178.6(5)	O2-Pt1-N1	178.60(15)	171.29(14)	O2′-Pt1-N1′	179.5(2)	171.80(18)

For the Pt coordination sphere in 1 and 3, labels are consistent with those given in Figure 1.

disordered; to help stabilize the refinement, both the phenyl and the pyridyl rings of the ligand were constrained as hexagonal rigid groups, while using rigid-bond and flat restraints as well. Similarity restraints on 1,2- and 1,3-distances were needed to refine the positions of the F substituents on the phenyl ring of the ligand. Lastly, similarity restraints on 1,2- and 1,3-distances were applied also to a somewhat disordered arm of one of the two independent tetrabutylammonium cations in **4β**. Of the two crystallographic independent Pt(II) complexes found in the asymmetric unit of polymorph **4α**, only one was found fully disordered. The disorder was treated as usual by following established procedures [35, 36]. The relative occupancies of the two disordered components, related by a twofold rotation about the shortest molecular axis, were refined freely and reached values of *ca*. 0.60:0.40 at convergence. To help stabilize the refinement, the phenyl moieties of each fully or partially occupied Br_4cat or thpy ligands in the structure were constrained as hexagonal rigid groups. Similarity restraints on 1,2- and 1,3-distances, as well as rigid-bond restraints, were applied diffusely. The final full-matrix least-squares refinements on F^2, minimizing the function $\Sigma w(|F_o|-|F_c|)^2$, reached convergence with the values of the discrepancy indices given in Table 1. The residual maximum and minimum in the final Fourier-difference maps of 2.267 and −1.602 e·Å^3 in **2** are near the Pt atom; the residual highest peak of 2.371 e·Å^3 in **4α** is located in the middle of the C1-C6 bond at the Br_4cat ligand of the undisordered Pt(II) unit; every attempt to find a second orientation also for this unit starting from such moderately high residual peak failed miserably with the data in hand. The final geometrical calculations and graphical manipulations were performed using the XP utility within SHELX [33, 34] and the Diamond software [37], respectively. A summary of the crystallographic data and structure refinements for **1**–**3**, **4α** and **4β** is given in Table 1. Main bond lengths and angles for **1**–**3** and **4β** are collected in Table 2; selected torsion angles are given in Table 3. Crystallographic data have been deposited at the Cambridge Crystallographic Data Centre and have been assigned CCDC reference numbers 2193444 (**1**), 2193445 (**2**), 2193446 (**3**), 2193448 (**4α**) and 2193447 (**4β**). These data can be obtained free of charge from the Cambridge Crystallographic Data Centre via www.ccdc.cam.ac.uk/data_request/cif.

3. Results and discussion

3.1. Description of the structures of 1–4

Single crystal X-ray diffraction investigation indicated that the crystal structures of **1**–**4** consist of NBu_4^+ cations and $[(bzq)Pt(Br_4cat)]^-$ (**1**), $[(F_2ppy)Pt(Br_4cat)]^-$ (**2**), $[(ppy)Pt(Br_4cat)]^-$ (**3**)

Table 3. Selected dihedral angles (°) for **1–3** and **4β**, with L = bzq (1), F_2ppy (2), ppy (3), thpy (4β).

			Pt1 unit		*Pt2 unit*	
Mean planes	**1**	**2**	**3**	**4β**	**3**	**4β**
phenyl/pyridine rings (L)	–	4.7(9)	5.8(2)	–	6.2(2)	–
phenyl/thienyl rings (L)	–	–	–	6.7(2)	–	6.9(3)
Pt-plane/Br_4Cat	7.0(1)	7.1(2)	7.5(1)	8.6(1)	18.4(1)	18.4(1)
Pt-plane/L	3.6(1)	6.0(3)	7.2(1)	5.9(1)	9.9(1)	10.1(2)
Br_4Cat/L	10.5(1)	13.1(2)	14.7(1)	14.5(1)	27.8(1)	28.0(1)

or $[(thpy)Pt(Br_4cat)]^-$ (**4α**, **4β**) anions, respectively, held together by electrostatic forces and a variety of intermolecular interactions.

$NBu_4[(bzq)Pt(Br_4cat)]$ (**1**) and $NBu_4[(F_2ppy)Pt(Br_4cat)]$ (**2**) crystallize in the monoclinic space group $P2_1/n$ and triclinic space group $P-1$, respectively, both with one molecular anion and one tetrabutylammonium countercation in the asymmetric unit.

Compound **3** and one of the two polymorphic phases of **4**, namely **4β**, conversely, are isomorphous and crystallize in the monoclinic space group $P2_1/c$ with two crystallographically independent $[(ppy)Pt(Br_4cat)]^-$ (**3**) or $[(thpy)Pt(Br_4cat)]^-$ (**4β**) complex anions and two tetrabutylammonium countercations in the asymmetric unit.

A view of the molecular structures of the $[(bzq)Pt(Br_4cat)]^-$ (**1**), $[(F_2ppy)Pt(Br_4cat)]^-$ (**2**), $[(ppy)Pt(Br_4cat)]^-$ (**3**) and $[(thpy)Pt(Br_4cat)]^-$ (**4β**) anions in **1**–**3** and **4β** is depicted in Figure 1.

In all cases, there is no sign of monomer aggregation through Pt···Pt contacts, the Pt···Pt closest distances ranging from *ca*. 8.0 (in **3**) to *ca*. 8.8 Å (in **1**), although the cyclometalating ligands do engage diffusely in *off-set* or *edge-to-edge* π-π stacking interactions, or even Br···π contacts, making thus use of their conjugated systems.

The crystal structure of the other polymorph of **4**, namely **4α**, is rather complex. According to the preliminary data in hand, the triclinic unit cell of **4α**, space group $P-1$, is very similar to that of **2**, albeit with a doubled *b* axis (Table 1). Indeed, the asymmetric unit of polymorph **4α** comprises two $[(thpy)Pt(Br_4cat)]^-$ complex anions and two tetrabutylammonium countercations, like **4β** (*vs*. one complex anion in the asymmetric unit of **2**). One of the crystallographically independent Pt(II) units in **4α** (namely Pt2) appears to exhibit whole molecule disorder, the two disorder components being flipped with respect to each other (Figure 2) and having a *ca*. 50:50 occupancy ratio. This would inevitably determine the co-existence, in **4α**, of two crystalline domains (hereafter noted **4α-A** and **4α-B**), making us speculate that **4α** could be regarded as a structure *pseudo-twinned by whole molecule disorder*.

Below, the crystal structures of **1–3** and polymorph **4β** are discussed in detail, together with a brief overview and a plausible interpretation of the crystal structure of polymorph **4α**.

3.1.1. Nbu4[(bzq)Pt(Br_4cat)] (1) and $NBu_4[(F_2ppy)Pt(Br_4cat)]$ (2)

The Pt(II) in **1** and **2** sits in a slightly distorted square planar coordination geometry. The small bite angle of each chelating ligand [with values of 82.4(1) (**1**) and 81.9(4)° (**2**) for O1-Pt1-O2, and of 81.3(1) (**1**) and 79.7(5)° (**2**) for N1-Pt1-C17] mostly accounts for such distortion. In both cases, the molecular anion as a whole is almost flat, as

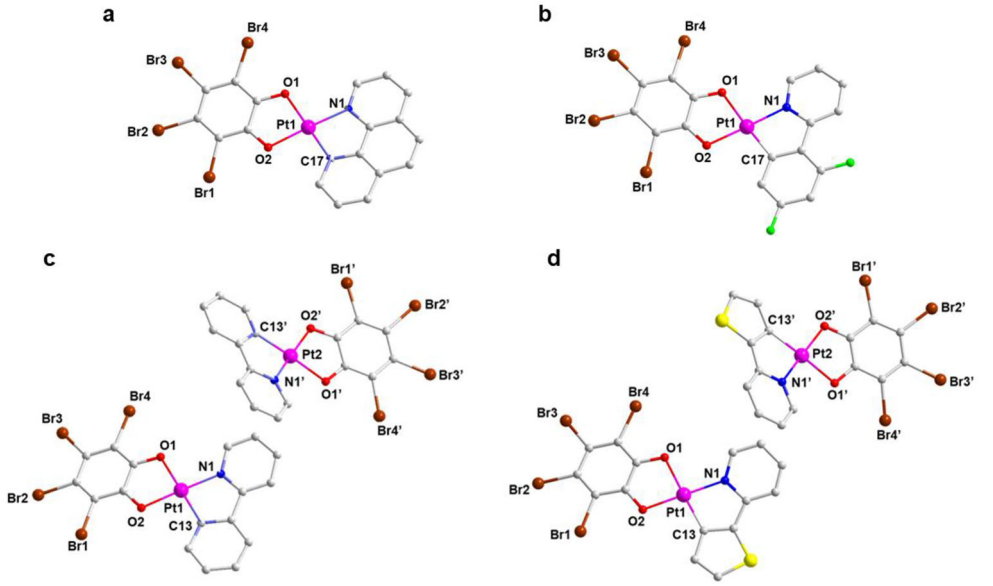

Figure 1. Molecular structures of the heteroleptic complex anions $[(bzq)Pt(Br_4cat)]^-$ (a), $[(F_2ppy)Pt(Br_4cat)]^-$ (b), $[(ppy)Pt(Br_4cat)]^-$ (c) and $[(thpy)Pt(Br_4cat)]^-$ (d) in the crystal structures of **1**, **2**, **3** and **4β**, respectively, with selected atomic labels (both crystallographically independent Pt1 and Pt2 units are shown in the case of **3** and **4β**). Color codes: Pt, purple; N, blue; C, grey; O, red; Br, brown; F, light green; S, yellow. For **1** and **3**, the N/C coordination sites at the chelating bzq (**1**) and ppy (**3**) ligands are blue/grey mixed-colored to indicate the presence of positional disorder; only one of the two components of the disorder has been labelled for clarity. Hydrogen atoms are not shown.

corroborated by the modest value of the dihedral angle between the catecholate and the cyclometalating ligand mean planes (10.5(1)° in **1** and 13.1(2)° in **2**, see Table 3).

Focusing on the Pt(II) coordination sphere, the molecular anions in **1** and **2** feature similar structural parameters. The Pt-O bond distances are 2.03(1)–2.05(1) Å, in agreement with the dianionic nature of the catecholate ligand [38–40]. Also, in **2**, the Pt-N and Pt-C bond lengths are consistent with literature data [23, 41–45], with the Pt-C bond distance being somewhat shorter than the Pt-N one (Table 2). In **1**, however, the Pt-N and Pt-C bond lengths are pretty much statistically identical. This supports the idea that the N1 and C17 sites at the bzq ligand in **1** are involved in positional disorder (meaning the ligand could be flipped one way or the other with basically no consequences on the crystal packing). Looking carefully at the interactions involving the cyclometalating bzq ligand in **1**, there are no classical bzq···bzq pathways, but rather a bzq···Br_4cat *off-set* stacking interaction which brings one Br substituent of the Br_4cat ligand (Br3) basically on-top of a Pt-bound ring of the bzq counterpart (with a Br-to-ring centroid distance of *ca.* 3.6 Å and a C-Br-to-ring centroid angle of *ca.* 85°). A literature survey, however, has revealed that Br substituted aryl rings could easily get involved in either parallel or orthogonal (aryl)Br···π contacts with both phenyl [46, 47] and pyridine [48, 49] ring types, making useless any attempt to discriminate between the two possible orientations of the bzq molecules through the crystal packing only based upon this interaction (with the crystallographic data in hand, our best model

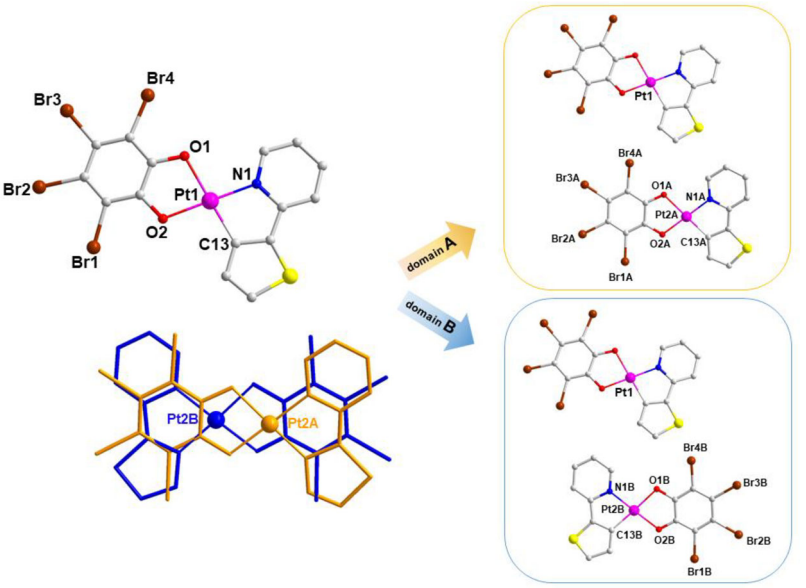

Figure 2. *Left:* A view of the asymmetric unit content in the case of polymorph **4α**. The whole molecule disorder of the Pt2 unit is highlighted by depicting the two possible molecular orientations with different colors (total orange and total blue for the Pt2A and Pt2B disorder components, respectively). *Right:* A view of the resulting Pt1/Pt2A and Pt1/Pt2B couples, giving two different domains, **4α-A** and **4α-B**, when considering the two disorder components separately with respect to the undisordered Pt1 unit. Color codes: Pt, purple; N, blue; C, grey; O, red; Br, brown; S, yellow. Hydrogen atoms are not shown.

converged to a 60 *vs.* 40% occupancy for the two possible orientations; however, a 50:50 occupancy is chemically reasonable and even more plausible). The Br_4cat ligand is further involved in the supramolecular organization of the square planar Pt(II) complexes in **1** *via* two other bromide substituents (Br1, Br2), which engage in a pair of symmetry equivalent Br···Br contacts (Br1···Br2a and Br1a···Br2, 3.787(1) Å, (a) 2−*x*, 1−*y*, 1−*z*), with a *cis* arrangement of the C-Br fragments and values of the θ_1 and θ_2 angles, as typically defined [28–30], of 144.8(1) and 117.5(1)°, respectively. With the $|\theta_1 - \theta_2|$ value only slightly less than 30°, the contact can be classified as *quasi* type II according to Ref. [28]. This latter interaction accounts for the formation of supramolecular dimers in **1** (Pt1···Pt1a, 13.692(2) Å), while interconnections between adjacent dimers happen *via* the bzq···Br_4cat pathway (Figure 3). The combination of these two interaction routes gives extended, slightly corrugated layers of $[(bzq)Pt(Br_4cat)]^-$ anions growing parallel to the crystallographic (11-1) plane, intercalated by layers of NBu_4^+ cations in a ABAB sequence along the [101] direction (Figure 4a). The way the *quasi* halogen-bonded supramolecular dimers of Pt(II) complex anions are arranged with respect to each other in forming the anionic layers, defines a distorted hexagonal network of Pt(II) ions, and the shortest Pt-Pt separations within each layer coincide with the hexagon sides (Pt1b···Pt1d 9.128(2) Å, Pt1···Pt1b and Pt1b···Pt1e, 10.634(2) Å, (e) 1−*x*, *y*, 1+*z*) (Figure 4b). Interestingly, the closest Pt-Pt distances observed in the crystal packing of **1** are inter-layers (Pt1···Pt1f, 8.835(1) Å, (f) −0.5+*x*, 0.5−*y*, −0.5+*z*) and not intra-layer.

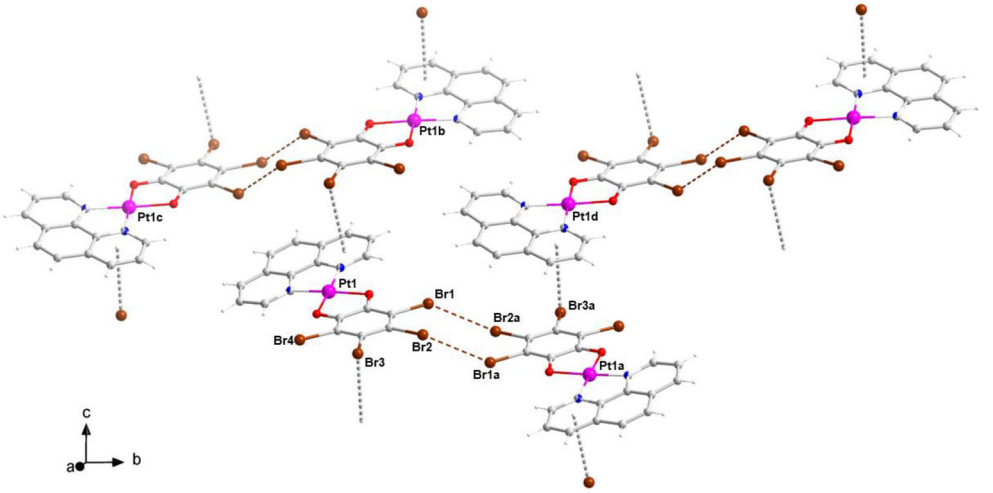

Figure 3. A view of a portion of the crystal packing of **1** showing the *quasi* halogen-bonded supramolecular dimers of Pt(II) complex anions and their mutual arrangement directed by bzq···Br_4cat *off-set* stacking interaction merging into a (cat)Br···π(Bzq) pathway. Symmetry codes: (a) 2−*x*, 1−*y*, 1−*z*; (b) −0.5+*x*, 0.5−*y*, 0.5+*z*; (c) 1.5−*x*, −0.5+*y*, 1.5−*z*; (d) 1.5−*x*, 0.5+*y*, 1.5−*z*.

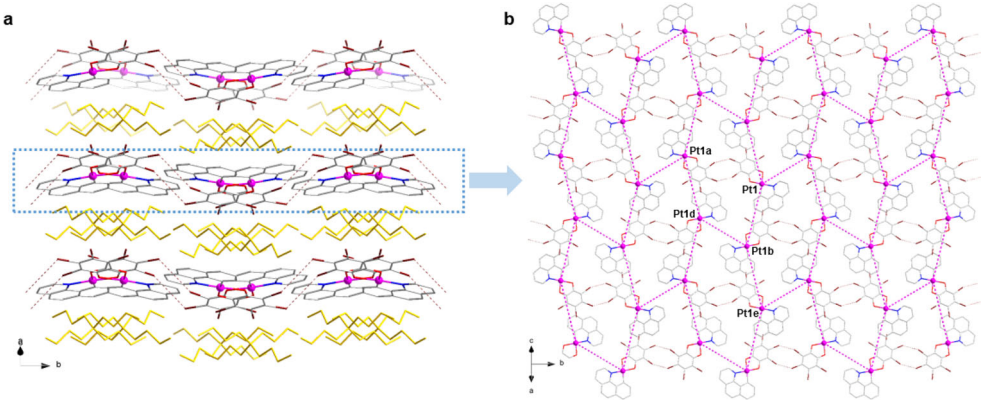

Figure 4. (a) A portion of the crystal packing of **1** viewed along the crystallographic [1 0 − 1] direction, showing the alternation of anionic and cationic layers of $[(bzq)Pt(Br_4cat)]^-$ complexes and NBu_4^+ cations (colored in total yellow for clarity) along the crystallographic [101] direction and (b) orthogonal view of a portion of a corrugated anionic layer in **1** highlighting the distorted hexagonal network of Pt(II) ions within it. Purple dotted lines are only a guide for the eyes. Hydrogen atoms are not shown. Symmetry codes: (a) 2−*x*, 1−*y*, 1−*z*; (b) −0.5+*x*, 0.5−*y*, 0.5+*z*; (d) 1.5−*x*, 0.5+*y*, 1.5−*z*; (e) 1−*x*, *y*, 1+*z*.

The crystal packing of **2** builds on interaction pathways only partially overlapping those noted for **1**. Interestingly, the consistent synthon is the *quasi* type II Br···Br contact [28], which, in perfect analogy with the previously described case, shows a (geometrically imposed) *cis* arrangement of the C-Br fragments coupled to a $|\theta_1 - \theta_2|$ value slightly less than 30° [with $\theta_1 = 130.3(4)$ and $\theta_2 = 158.4(4)°$]. The pair of involved Br substituents at the Br_4cat ligand are again Br1 and Br2, the Br1···Br2a (and Br1a···Br2, (a) 1−*x*, 1−*y*, −*z*) distance being 3.705(2) Å, thus shorter than that observed

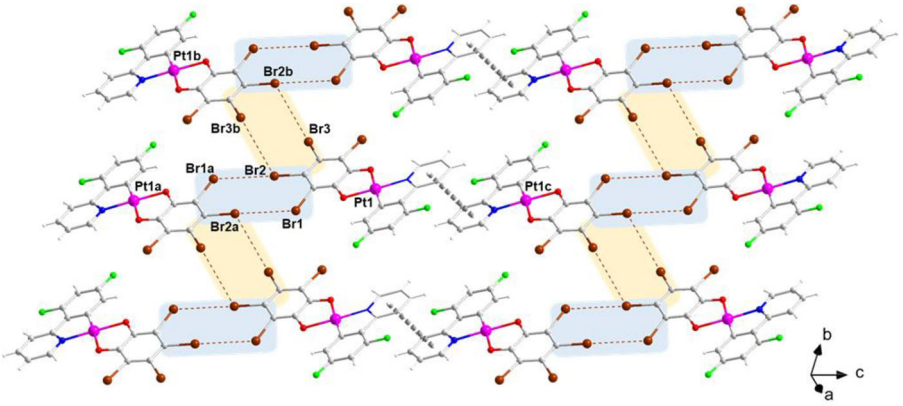

Figure 5. View of a portion of the corrugated anionic layers growing parallel to the crystallographic *bc* plane in **2**. The alternating *quasi* type II and type I Br···Br contacts, giving supramolecular ribbons of $[(F_2ppy)Pt(Br_4cat)]^-$ units, are highlighted in light blue and light orange, respectively. *Off-set* π-π stacking interactions between adjacent ribbons are depicted as grey dotted lines. Symmetry codes: (a) 1−*x*, 1−*y*, −*z*; (b) 1−*x*, 2−*y*, −*z*; (c) 1−*x*, 1−*y*, 1−*z*.

in **1** (3.787(1) Å), while the Pt1···Pt1a separation is much longer, 15.021(1) Å in **2** *vs.* 13.692(2) Å in **1**. This time, the so-formed supramolecular dimers further develop into ribbons *via* a second pair of symmetry equivalent, *cis* Br···Br contacts involving Br2 (again) and Br3, clearly two type I Br···Br interactions with the following structural parameters: Br2···Br3b and Br3···Br2b, 4.051(3) Å; $\theta_1 = 116.2(4)$, $\theta_2 = 132.8(4)°$; Pt1···Pt1b, 16.350(1) Å ((b) 1−*x*, 2−*y*, −*z*). Neighboring ribbons interact one another by *off-set* π-π stacking interactions involving, selectively, only the pyridine ring of the F_2ppy ligands (interplanar distance 3.6 Å, ring centroid-to-ring centroid distance 3.9 Å; Pt1···Pt1c, 9.062(1) Å; (c) 1−*x*, 1−*y*, 1−*z*), hence forming corrugated anionic layers of $[(F_2ppy)Pt(Br_4cat)]^-$ units, which extend parallel to the crystallographic *bc* plane in **2** (Figure 5).

In contrast to **1**, the corrugated anionic layers of Pt(II) complexes in **2** are not intercalated by layers of tetrabutylammonium cations in the orthogonal direction. Rather, adjacent layers, stacked along the crystallographic *a* axis, interact through a pair of weak, symmetry related hydrogen bonding interactions involving C14 and F1 of the F_2ppy ligand (C14-H14···F1d and C14d-H14d···F1, 2.829(7) Å; Pt1···Pt1d, 13.013(2) Å; (d) −*x*, −*y*, 1−*z*). These contacts lead to an overall 3D *pseudo* hexagonal anionic net whose channels, running in the direction of the crystallographic *b* axis, are filled by NBu_4^+ cations (Figure 6). Within the three-dimensional net of Pt(II) ions, the shortest Pt···Pt separation corresponds to the high of the *pseudo* hexagonal channels, Pt1···Pt1e, 8.572(1) Å, (e) −1+*x*, *y*, *z*.

3.1.2. Nbu4[(ppy)Pt(Br$_4$cat)] (3) and NBu$_4$[(thpy)Pt(Br$_4$cat)] (polymorph 4β)

The crystal packing of **3** and of the solid-state polymorph **4β** in this work are isomorphous and thus will be discussed together. Of the two crystallographically independent molecular anions in the asymmetric unit, one (Pt1) is only slightly more bent than the parent complex anions with bzq (**1**) and F_2ppy (**2**), while bending is much more consistent for the second unit (Pt2); see Table 3 for details on the dihedral

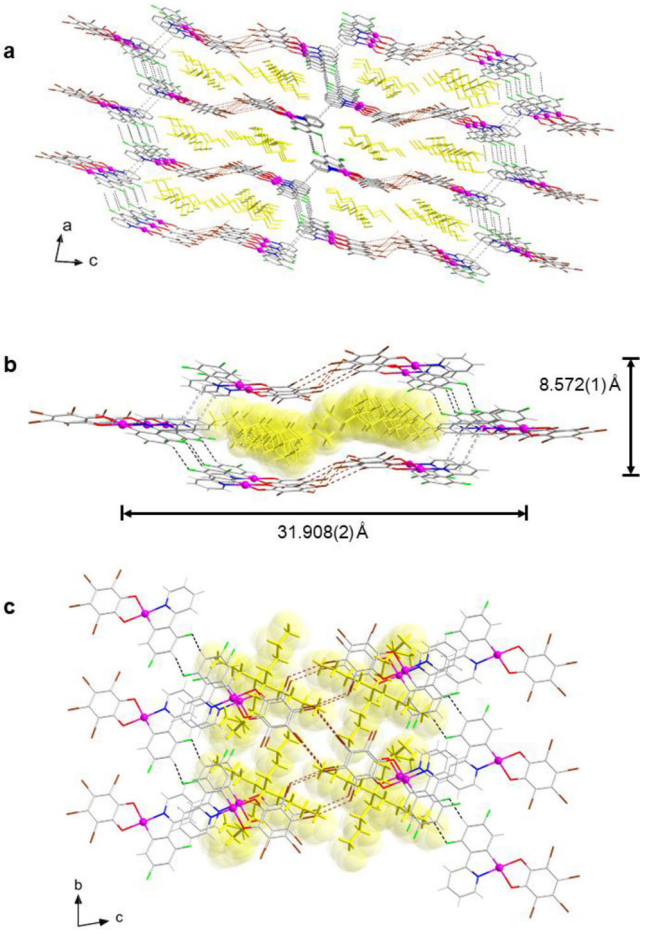

Figure 6. (a) Perspective view of a portion of the crystal packing of **2** along the crystallographic *b* axis, showing anionic layers of $[(F_2ppy)Pt(Br_4cat)]^-$ units growing parallel to the *bc* plane and interconnecting to each other *via* weak CH···F hydrogen bonds in the direction of the crystallographic *a* axis, and the resulting porous 3D *pseudo* hexagonal net, with the NBu_4^+ cations (colored in total yellow for clarity) filling the *pseudo* hexagonal channels. (b) Close view on one *pseudo* hexagonal channel. NBu_4^+ cations inside are in yellow and in van der Waals model. (c) Top view (along the *a* axis) of a portion of one *pseudo* hexagonal channel highlighting the mutual disposition of the NBu_4^+ cations inside.

angles. The Pt(II) coordination geometry is distorted square planar. For the Pt1 units, the small bite angle of the chelating ligands (with values of *ca.* 82.1(1) (**3**) and 82.7(2)° (**4β**) for O1-Pt1-O2, and of 80.9(2) (**3**) and 80.3(3)° (**4β**) for N1-Pt1-C13) mostly accounts for the distortion as the dihedral angle between the two chelating ligand mean planes is still rather small (<15°). For the Pt2 units, instead, both the small bite of the two chelating ligands (81.7(1) (**3**) and 82.4(2)° (**4β**) for O1′-Pt2-O2′; 81.0(2) (**3**) and 79.2(3)° (**4β**) for N1′-Pt2-C13′) and the significant dihedral angle between them (*ca.* 30°) contribute to such distortion.

Focusing on the Pt(II) coordination sphere, all bonds and angles are in agreement with **1** and **2** (Table 2) and with literature data [38–40, 50–54]. In the case of both

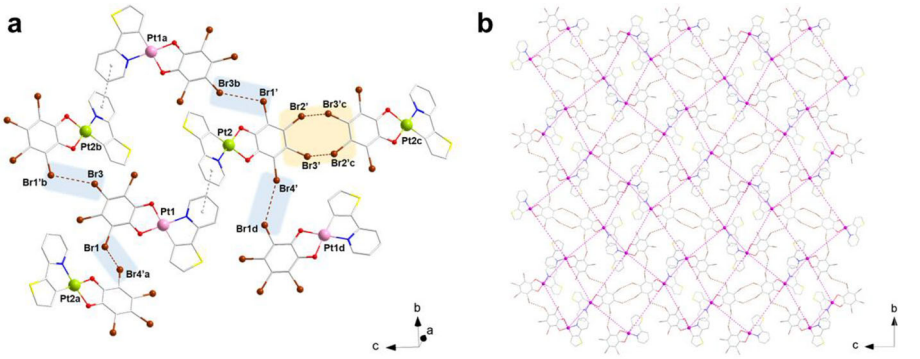

Figure 7. (a) View of a portion of the crystal packing of **3** and **4β** (shown here only for **4β**) displaying the immediate surrounding of the crystallographically independent Pt1 and Pt2 (depicted as big pink and light green spheres, respectively) units. Note that only two of the four Br substituents at the Br_4Cat ligand of the Pt1 unit are involved in Br···Br contacts, while the Pt2 unit uses all four Br. The *quasi* type II and type I Br···Br contacts are highlighted in light blue and light orange, respectively. thpy···thpy interactions between couples of independent Pt1 and Pt2 units are also depicted as grey dotted lines. (b) Top view of a portion of the supramolecular anionic layer in **3**/**4β** (shown again only for **4β**) highlighting the patchwork-like motif of Pt(II) ions within it. Purple dotted lines are only a guide for the eyes. Hydrogen atoms are not shown. Symmetry codes: (a) x, $0.5-y$, $0.5+z$; (b) $1-x$, $1-y$, $1-z$; (c) $1-x$, $1-y$, $-z$.

crystallographically independent $[(ppy)Pt(Br_4cat)]^-$ units in **3**, and in analogy with what has been noted for **1** already, the Pt-N and Pt-C bond lengths are more similar than the expected and this, again, seems to indicate the occurrence of positional disorder at the level of the ppy coordination C and N sites, although to a much less extent than for **1**, at least according to the crystallographic data in hand. In our best model, the C/N relative occupancy at each coordination site of the ppy ligand in **3** are far from a random 50:50 (refined occupancies of the two disorder components are ≈ 90:10 at Pt1 and 70:30 at Pt2); interestingly, the major component of such disorder aligns the pyridine rings of the two independent ppy ligands in **3** with the pyridine rings of the two independent thpy ligands in **4**.

Besides being one more bent than the other, the two crystallographically independent complex anions in the asymmetric unit of **3**/**4β** also have different surroundings. In particular, the Pt1 unit interacts with two Pt2 units *via* two independent *trans quasi* type II Br···Br contacts, using only two of the four Br substituents at the Br_4Cat ligand, Br1 and Br3 (Br1···Br4'a, 4.030(1) Å (**3**)/3.910(2) Å (**4β**); $\theta_1 = 124.5(2)^\circ$ (**3**)/$124.0(2)^\circ$ (**4β**), $\theta_2 = 151.6(2)^\circ$ (**3**)/$153.1(2)^\circ$ (**4β**), $|\theta_1 - \theta_2| \approx 27^\circ$ (**3**)/29° (**4β**); Pt1···Pt2a, 10.777(1) Å (**3**)/10.767(3) Å (**4β**); (a) x, $0.5-y$, $0.5+z$ and Br3···Br1'b, 3.627(1) Å (**3**)/3.770(2) Å (**4β**); $\theta_1 = 147.8(2)^\circ$ (**3**)/$144.0(2)^\circ$ (**4β**), $\theta_2 = 119.5(2)^\circ$ (**3**)/$115.1(2)^\circ$ (**4β**), $|\theta_1 - \theta_2| \approx 28^\circ$ (**3**)/29° (**4β**); Pt1···Pt2b, 11.755(1) Å (**3**)/11.452(3) Å (**4β**); (b) $1-x$, $1-y$, $1-z$); see Figure 6(a). The Pt2 unit, conversely, makes use of all four (cat)Br atoms, binding either Pt1 units (two of them, *via* Br1' and Br4' as just seen) or Pt2 units (one of them, *via* Br2' and Br3' simultaneously). The latter interaction is clearly of type I, with $\theta_1 \approx \theta_2$ and, given the *cis* orientation of the interacting C-Br fragments, the symmetry of the interaction as well as the specific Br substituents involved, it recalls the symmetric pair of type I Br···Br contacts found in the crystal packing of **2** (Br2'···Br3'c and Br3'···Br2'c,

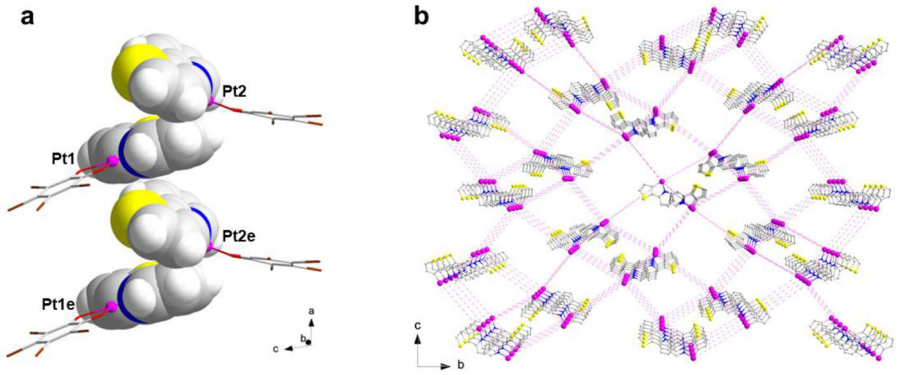

Figure 8. (a) Perspective view of the piling of couples of crystallographically independent Pt1 and Pt2 complex anions along the crystallographic *a* axis in **4β** (as representative for both **3** and **4β**) highlighting the close contact between the pyridine rings of the thpy cyclometalating ligand (depicted in van der Waals model) at each Pt atom. (b) Perspective view of the Pt(II) network in **3**/**4β** (shown for **4β**), showing only the coordinated thpy ligand at each Pt center, to highlight the column of intra and inter-layer *edge-to-edge* stacked ligands. Purple dotted lines are only a guide for the eyes.

3.765(2) Å (**3**)/3.732(2) Å (**4β**); $\theta_1 = 130.8(2)^\circ$ (**3**)/133.9(2)° (**4β**), $\theta_2 = 146.6(2)^\circ$ (**3**)/134.5(2)° (**4β**); Pt2···Pt2c, 16.981(2) Å (**3**)/16.828(5) Å (**4β**); (c) $1-x, 1-y, -z$); see Figure 7(a). Considered together, the Br···Br contacts in **3**/**4β** led to the formation of patchwork-like supramolecular anionic layers of Pt(II) complexes, growing parallel to the crystallographic *bc* plane (Figure 7b).

Intra-layer *edge-to-edge* stacking interaction between the ppy (**3**) or thpy (**4β**) ligands at each pair of independent Pt units (i.e. Pt1/Pt2, Pt1a/Pt2a, Pt1b/Pt2b, etc.) could be noted in **3**/**4β** (dihedral angle between the pyridine rings at each ligand: 50.8(1)° (**3**)/49.5(2)° (**4β**); ring centroid-to-ring centroid distance ≈ 4.6 Å (**3**)/4.9 Å (**4β**); closest contact: C7-H7···H9′-C9′, 2.67(1) Å (**3**)/2.88(1) Å (**4β**), Pt1···Pt2, 8.034(1) Å (**3**)/8.478(2) Å (**4β**)). The occurrence of such interaction through a net seemingly imposed by the Br···Br contacts is plausibly related (as cause or effect) to the significant overall bending of the Pt2 unit (Figure 8a). The stacking interaction not only contributes to the stability of the layer but also, perpetuating itself along the crystallographic *a* axis, brings adjacent anionic layers together, thus giving an intricate 3D anionic network of Pt(II) complex anions (Figures 8 and 9). For the inter-layer interaction: the ring centroid-to-ring centroid distance is about 4.4 Å (**3**)/4.6 Å (**4β**) (the dihedral angle between the involved rings is kept constant along the *a* axis), the closest contact is that between C9′-H9′ and N1 [2.96(1) Å (**3**)/2.83(1) Å (**4β**), note that in **3** the N1 site is partially occupied by C13 (90 *vs.* 10%)], and the inter-layer Pt-Pt distance along the columns of stacked ligands is Pt1···Pt2e, 8.061(1) Å (**3**)/8.406(2) Å (**4β**). These quasi-identical, intra and inter-layer Pt···Pt separations in the direction of the crystallographic *a* axis represent the closest metal-metal distances in **3**/**4β**. The NBu_4^+ cations occupy the interstitial cavities of this intricate, punched 3D net of Pt(II) complexes, as shown in Figure 9.

Given the importance of the Br···Br contacts in driving the crystal packing of **1**–**3** and **4β**, a summary of the relative main structural parameters is collected in Table 4.

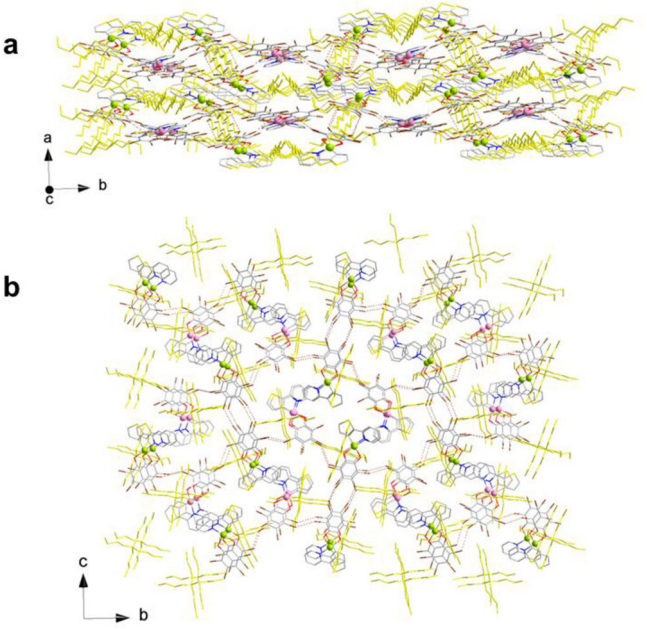

Figure 9. Perspective side (a) and top (b) views of a portion of the crystal packing of **3**/**4β** (shown here only for **4β**) showing the NBu_4^+ cations (colored in total yellow for clarity) occupying the interstitial cavities of the 3D anionic net and wrapping the Pt(II) anions around.

3.1.3. Nbu4[(thpy)Pt(Br$_4$cat)] (polymorph 4α)

The solid-state polymorph of **4**named **4α** in this work could be defined biphasic. Two crystalline networks could, in fact, originate by the peculiar combination of $Z' = 2$ and the whole molecule disorder by a two-fold rotation involving only one of the two crystallographically independent Pt(II) units in the asymmetric unit. We decided to refer to the two co-existing domains as **4α-A** (this phase includes Pt1 interacting with Pt2A units) and **4α-B** (this phase includes Pt1 interacting with Pt2B units). Focusing on the Pt(II) coordination sphere within all units (and domains), bond distances and angles are in agreement with those found in **1–3** and **4β** and within the literature. Looking at the supramolecular anion···anion connections within **4α-A** and **4α-B**, striking differences could be noted, as expected, although the final 3D network is similar and very much resembling that observed for **2**. At the first level of organization, the Pt(II) complexes look organized into 2D layers growing parallel to the crystallographic *bc* plane and stacking along the *a* axis, thanks to Br···Br contacts coupled to weak π-π stacking interactions involving either two thpy ligands (exclusively *via* the pyridine rings, domain **4α-A**, Figure 10b) or one thpy and one Br_4cat ligand (in this case a concomitant Br···π contact is also observed, domain **4α-B**, Figure 10c). Noteworthy, all Br···Br contacts seem of type I regardless of the specific domain (the average $|\theta_1 - \theta_2|$ value is about 20°). In domain **4α-B**, Br···S contact can also be found. At the final level of organization, as anticipated, both domains can be defined as 3D *pseudo* hexagonal anionic nets. Focusing on domain **4α-A**, the connection between neighboring layers is assured by the perpetuation of the thpy···thpy π-π stacking along the *a* axis, with a perfect alternation of intra- and inter-layer contacts (Figure 10b). For domain **4α-B**, the

Table 4. Structural details on the Br···Br contacts found in **1–3** and **4β**.

Polymorph	Geometry	Br-Br distance/Å	θ_1/°	θ_2/°	$\lvert\theta_1 - \theta_2\rvert$/°	Classification
1	*cis* (double)	3.787(1)	144.8(1)	117.5(1)	27.3	*quasi* type II
2	*cis* (double)	3.705(2)	130.3(4)	158.3(4)	28.0	*quasi* type II
	cis (double)	4.051(3)	116.2(4)	132.8(4)	16.6	type I
3	*trans* (single)	4.030(1)	124.5(2)°	151.6(2)°	27.1	*quasi* type II
	trans (single)	3.627(1)	147.8(2)	119.5(2)	28.3	*quasi* type II
	cis (double)	3.765(2)	130.8(2)°	146.6(2)°	15.8	type I
4β	*trans* (single)	3.910(2)	124.0(2)°	153.1(2)°	29.1	*quasi* type II
	trans (single)	3.770(2)	144.0(2)	115.1(2)	28.9	*quasi* type II
	cis (double)	3.732(2)	133.9(2)°	134.5(2)°	0.6	type I

perfect alternation of intra- and inter-layer contacts along the *a* axis should be referred to the previously cited thpy···Br_4cat π-π (or Br···π) pathway (Figure 10c).

As found in the crystal structure of the triclinic phase of **2**, the *pseudo* hexagonal channels of a 3D network of Pt(II) complex anions would be filled by well-organized, segregated NBu_4^+ cations (Figure 10d).

From the quality of the diffraction profile of the single crystals of polymorph **4α** and from failed attempts to solve the structure invoking non-merohedral twinning, we exclude the possibility those crystals could be formed by two macroscopic different crystallites corresponding to the defined **4α-A** and **4α-B** domains. As one possible interpretation of the puzzling structure of **4α** we could hypothesize that the two different **4α-A** and **4α-B** domains only exist at the 2D level and, given the nearly 50:50 occupancy ratio of the two disordered orientations of the Pt2 unit, we could even further speculate that the two domains alternate perfectly along the *a* axis, according to an ABAB sequence (Figure 10d). A deeper investigation of such a crystallographic interesting case is, however, desirable, and will be strongly pursued.

3.2. PXRD characterization of 1–4

The microcrystalline powders of **1**–**4** were subjected to routine powder X-ray diffraction (PXRD) analyses to evaluate solid-state phase homogeneity (as chemical purity was determined *via* NMR). Ever since the pioneering work by Morgan and Burstall in 1934 [55] followed, over the years, by a multitude of further exciting examples, that nearly flat square-planar Pt(II) complexes could engage in different supramolecular organization in the condensed phase is far from being considered unlikely. Indeed, solid-state polymorphism is relatively common among monomeric Pt(II) complexes [12, 56] and a few examples of dimeric Pt(II) complexes existing in different crystalline phases are also known [57].

The room-temperature PXRD profiles of the microcrystalline powders of **1**–**4** are shown in Figure 11 (black traces), along with the calculated patterns based on single-crystal data for **1**–**3** (Figure 11a–c, red traces), and for **4α**/**4β** (Figure 11d, blue and red traces, respectively).

In the case of NBu_4[(bzq)Pt(Br_4cat)] (**1**, Figure 11a), the microcrystalline precipitate looked monophasic but inconsistent with the single-crystal data. Both bulk homogeneity and phase consistency (powder vs. single-crystals) could be confirmed, instead, for NBu_4[(F_2ppy)Pt(Br_4cat)] (**2**, Figure 11b). These findings suggest the existence of one unambiguous solid-state phase for **2**, while indicating the existence of either

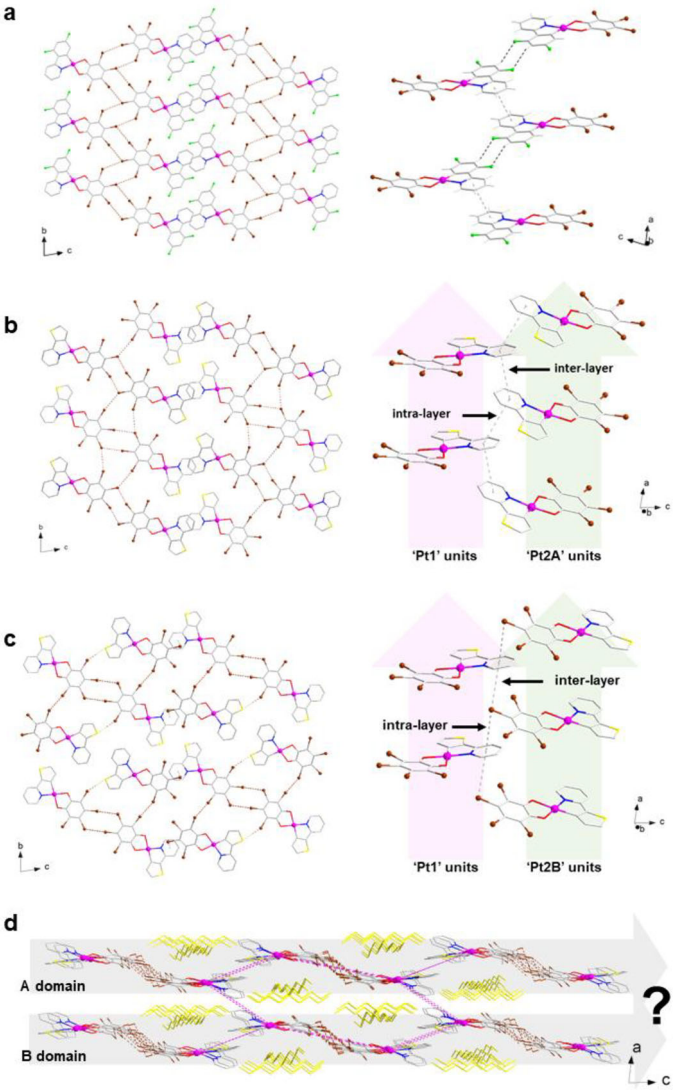

Figure 10. (a)–(c) *Left*. Comparative views of the supramolecular 2D motif of Pt(II) anions growing parallel to the *bc* plane in the crystal structures of **2** (a), domain **4α-A** (b) and domain **4α-B** (c). *Right*. Comparative views of the intra- and inter-layer connections along the crystallographic *a* axis in **2** (a), domain **4α-A** (b) and domain **4α-B** (c). (d) View of a portion of the 3D *pseudo* hexagonal anionic net in **4α**, together with the hypothesized alternation of the A and B domains within the structure, implying a consequent alternation of thpy···thpy and thpy···Br_4cat (Br···π) interaction pathways along the crystallographic *a* axis.

polymorphism or *pseudo*-polymorphism for **1**. Regardless of the efforts put into the task, however, the solid-state form of **1** corresponding to the microcrystalline precipitate could not be isolated as X-ray quality single-crystals so far, not even by using methanol (the reaction media) as the crystallization solvent.

The PXRD profile of the roughly microcrystalline precipitate of **4** is the least resolved of the four; still the matching with the theoretical pattern calculated for

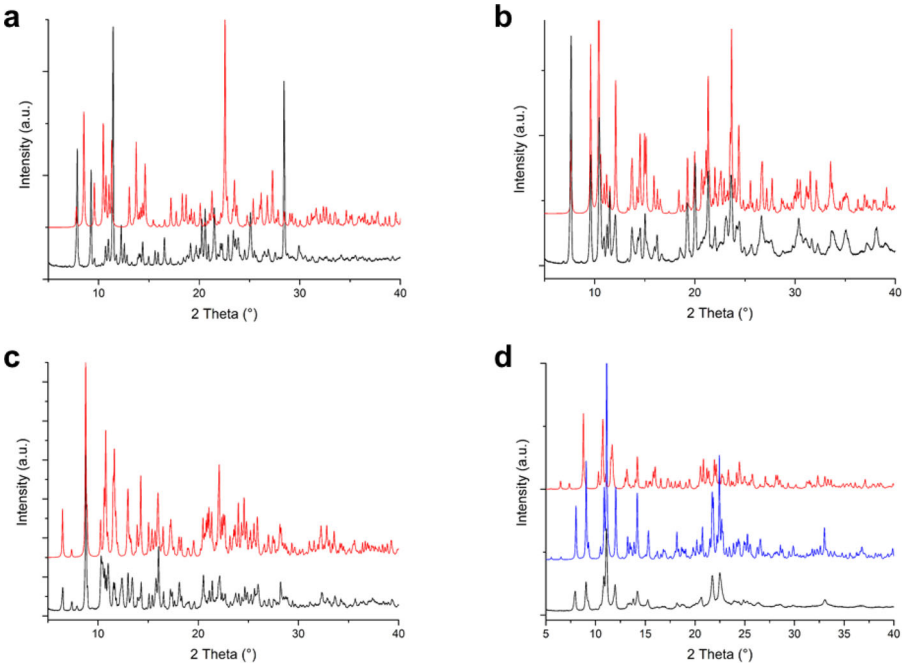

Figure 11. (a)–(c) PXRD profiles of the microcrystalline powders of **1** (a), **2** (b) and **3** (c) (black traces), compared to the theoretical PXRD pattern calculated from single-crystal data for **1**–**3**, respectively [red traces]. (d) PXRD profile of the roughly microcrystalline powder of **4** (black traces), compared to the theoretical PXRD pattern calculated from single-crystal data for polymorph **4α** (blue trace) and polymorph **4β** (red trace).

polymorph **4α** is striking, with no traces of **4β** or other solid-state phases (thus confirming bulk homogeneity). We might infer that **4α** represents the kinetic solid-state polymorph of **4**.

Particular attention should be given to NBu_4[(ppy)Pt(Br_4cat)] (**3**). A careful comparison between the experimental PXRD pattern recorded for its microcrystalline powder and the theoretical profile based on single-crystal data for **3** (Figure 11c) revealed that in this isolated case the synthetic precipitate is biphasic. Notably, of the two different phases found out *via* PXRD, at present one has remained elusive (similarly to what has happened for **1**), while the other is consistent with that obtained by recrystallization.

3.3. Thermal analysis of 1–4

Insights into the monophasic or multiphasic nature of the microcrystalline powders of **1**–**4**, as well as into their consistency with the crystallized phases, were sought through differential scanning calorimetry (DSC). Indeed, DSC is a widely used technique to detect and characterize polymorphs or *pseudo*-polymorphs (solvates/hydrates) of a given compound, since they typically display different physical properties, including unique thermal transitions [58–60].

Therefore, DSC heating/cooling curves of the microcrystalline powders of **1**–**4**, recorded between 30 °C and 250 °C, were compared to those of the corresponding single crystals (Figure 12). Furthermore, all samples (as both powders and single-

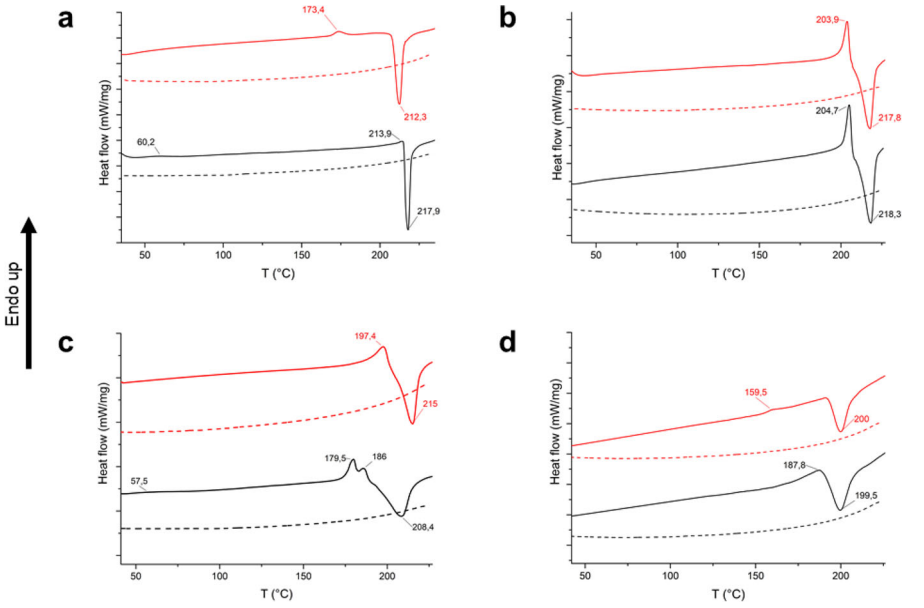

Figure 12. (a)–(c) DSC profiles (solid line: heating mode; dotted lines: cooling mode) of the microcrystalline powders of **1** (a), **2** (b) and **3** (c) (black traces), along with the DSC profiles recorded for the corresponding single crystals (red trace). (d) DSC profile of the microcrystalline powder of **4** (black trace), along with the DSC profile of crystalline polymorph **4β** (red trace). Curves were recorded with a heating/cooling rate of 5 °C/min.

crystals) were inspected under an optical polarized microscope (POM) during a heating cycle ranging from room temperature up to 250 °C (see Figure 13 for selected snapshots) to support the identification of the thermal events observed in the DSC profiles.

The DSC curve of solid microcrystalline **1** (Figure 12a, black trace) exhibits a barely visible, broad thermal event extending from *ca*. 45 °C to *ca*. 74 °C, easily attributable to the evaporation of methanol (the solvent used for the synthesis of **1** [24]). The compound melting, as corroborated by sample observation under polarized microscope, occurs at *ca*. 214 °C and appears as a very small endothermic peak rising just before a sharp and intense exothermic peak centered at *ca*. 218 °C. The DSC profile of crystalline **1** (Figure 12a, red trace) is significantly different from that of the precipitated sample, showing no sign of solvation (in agreement with the single-crystals XRD evaluation) and an endothermic event, confirmed under POM as the compound melting, taking place at a much lower temperature (173.4 °C) when compared to the melting of the raw precipitate. This contributes validating the hypothesis based on the PXRD investigation, that the microcrystalline and crystalline samples of **1** identify two different solid-state phases of this compound. The exothermic event appears, in this case, as a sharp peak centered at 212.3 °C.

The DSC profile of solid microcrystalline **2** (Figure 12b, black trace) shows an endothermic peak at 204.7 °C, corresponding to the compound melting, followed by an intense exothermic signal at 218.3 °C. The DSC profile of crystalline **2** (Figure 12b, red trace) is basically identical to that of the precipitated sample, the endothermic and exothermic peaks being centered this time at 203.9 °C and 217.8 °C.

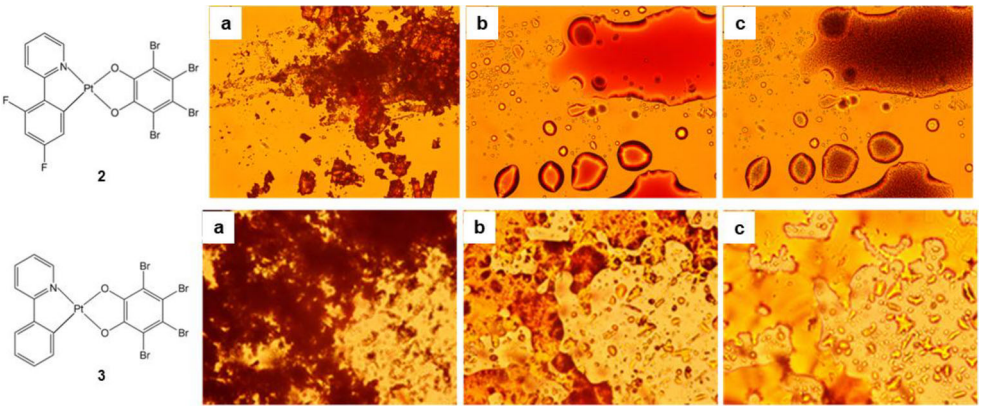

Figure 13. *Top*: Selected POM snapshots of microcrystalline $NBu_4[(F_2ppy)Pt(Br_4cat)]$ (**2**) at (a) room temperature, (b) 205 °C and (c) 218 °C. *Bottom*: Selected POM snapshots of microcrystalline $NBu_4[(ppy)Pt(Br_4cat)]$ (**3**) at (a) room temperature, (b) 179 °C and (c) 186 °C.

Concerning the thermal analysis of $NBu_4[(thpy)Pt(Br_4cat)]$ (**4**, Figure 12d), unfortunately we could only measure the microcrystalline powder (identified as virtually pure polymorph **4α** by PXRD) along with crystals of polymorph **4β**. The DSC curve of the powders of **4** (Figure 12d, black trace) exhibits a broad endothermic peak (due to compound melting) whose maximum appears at *ca*. 188 °C, just before the exothermic event happening around 199.5 °C. For the crystalline polymorph **4β** (Figure 12d, red trace) the exothermic transition occurs at about the same temperature; however, the melting signal is broad and centered at 159.5 °C. On the basis of the highly different melting temperatures, the raw microcrystalline product and the extremely slowly crystallized sample represent two different solid-state phases of **4**; furthermore, the DSC results confirmed phase homogeneity for the raw precipitate, in agreement with the PXRD analysis.

Lastly, in the DSC profile of solid microcrystalline **3** (Figure 12c, black trace) a scarcely visible, broad band centered at 57.7 °C could be noted and again, it could be reasonably ascribed to evaporation of methanol (the reaction solvent [24]). Here, the exothermic transition is intense and broader than elsewhere, but centered at 208.4 °C, basically in line with all the other examined DSC profiles. The most interesting aspect of this curve is, then, the occurrence of two close endothermic transitions appearing at 179.5 °C and 186 °C. By inspecting microcrystalline powder of **3** under the optical polarized microscope while heating to 250 °C, the two close and consecutive meltings could be very nicely detected. In fact, as shown in Figure 13, *bottom*, while part of the sample looked completely dissolved around 179 °C, some solid was still surviving at this temperature and did melt down only successively, around 186 °C. The DSC curve of the solid single phase of **3** obtained through crystallization (Figure 12c, red trace) exhibits, without surprise, only two peaks: one endothermic at 197.4 °C, corresponding to melting, and one exothermic at 215 °C. In the light of the PXRD analysis, we suggest that the thermal transition happening at 186 °C in the DSC curve of the biphasic precipitate of **3** should be ascribed to melting of the single-crystal polymorph (noted however at about 197 °C in its own pattern), the lower temperature being attributable to the presence of the other solid phase acting as an impurity.

Concerning the intense exothermic peak observed at 200 °C for each measured sample (as either microcrystalline powder or single-crystals), we feel confident in attributing it to the oxidation of the Br_4cat fragment. Given that a sudden darkening of the liquified (melted) samples was noted under POM in all cases at the corresponding temperature (see, as an example, Figure 13, *top*), the concomitant phenomenon might be Pt(II) reduction to Pt nanoparticles. While this remains speculation, compounds **1–4** surely fall apart irreversibly after the redox processes, as no more thermal transitions could be observed in cooling mode (Figure 12).

4. Conclusion

Four parent heteroleptic cyclometalated Pt(II) monoanionic monomers of general formula $[(C^N)Pt(Br_4cat)]^-$, bearing fully brominated catecholate dianion as the ancillary ligand and either bzq (**1**), F_2ppy (**2**), ppy (**3**) or thpy (**4**) as the (C^N) cyclometalating chelating moieties, were synthesized and isolated as NBu_4^+ salts according to a literature procedure [24]. Crystallization attempts were made in order to shed light on the still unknown solid-state crystal structures of these rare examples of emitting Pt(II) anionic complexes, all demonstrating enhanced luminescence in the solid-state *vs*. in solution. Slow recrystallization from acetone solutions of the synthetic microcrystalline powders was a successful method and good or somewhat low X-ray quality crystals could be obtained in each case, typically within 2 weeks. A combined PXRD and DSC analysis of both the microcrystalline bulks and the single-crystals of **1**–**4** revealed the occurrence of solid-state polymorphism for **1**, **3** and **4**, but not for **2**. Efforts to grow single crystals of more than just one form of **1**–**3** were unsuccessful, while a second solid-state polymorph of **4** could be attained by slowing the crystallization rate to about 3 months. Of these two polymorphs of **4**, i.e. **4α** and **4β**, one (**4α**) represents one of a kind crystallographic puzzle and only a preliminary interpretation of its complex structure has been given herein.

The deep structural investigation through single-crystal XRD of **1**–**3** and **4β** (isomorphous with **3**) has revealed the occurrence of a variety of supramolecular interaction pathways occurring between the Pt(II) anions in the analyzed structures, with both specific or aspecific contributions arising from the gradually different cyclometalating ligands. Thus, a supramolecular layered structure was obtained by using bzq, a porous 3D *pseudo* hexagonal network, achieved with F_2ppy while a non-porous 3D structure was accomplished with either ppy or thpy (**3**, **4β**). The latter case is especially interesting from a structural point of view, as the thienyl ring of the thpy ligand in **4β** does not appear to contribute explicitly to the building up of the non-covalent network, leaving all the work to the phenyl moiety. Even more interesting is that, according to the preliminary outcome shown here, nearly the same happens within polymorph **4α** where, by making use of the phenyl ring only, thpy proves itself useful for the construction of the same supramolecular network achievable with F_2ppy. Focusing on Br···Br contacts between Br_4cat fragments, they are predominant in all the structures. The pair of symmetry related *cis quasi* type II Br···Br contacts involving Br1 and Br2 (i.e. the Br substituents in ortho and meta with respect to O1), seen in the crystal structure of both **1** and **2**, does no longer appear in the crystal structure of **3**

(and **4β**), replaced by mono- *trans quasi* type II Br···Br interactions; however, a pair of *cis* type I Br···Br contacts involving the two *meta* Br atoms, noted for **2** but not for **1**, is also detectable in the crystal structure of **3** (and **4β**). Apart from the fascinating recurring aspect of such supramolecular synthons, most remarkable is the recurring "*quasi*" type II character of most of the described Br···Br contacts, despite the electrophilic nature of Br and its propensity for the formation of "true" Br···Br halogen bonds (aka type II contacts) have long been demonstrated thanks to milestone literature work [39]. It could be inferred that the concomitant effect of the other various π-π, Br···π, CH···F *etc.* interaction pathways in the crystal structures of **1**–**3** and **4β** contributes to the weakening of the halogen bonding strength due to some imposed geometrical constrain. In fact, while no sign of chromophores aggregation through Pt···Pt contacts could be found in **1**–**3** and **4β** (Pt···Pt closest contacts are in the range 8.0–8.8 Å *ca.*), interaction patterns involving the conjugated systems of all used cyclometalated ligands were diffusely present in every structure, although plausibly not to the possible larger extend. In fact, the NBu_4^+ cations are unlikely innocent in the formation of the observed 2D/3D anionic networks, and the use of smaller counterions should be explored to evaluate the consistency of the observed synthons and of crystal packings overall.

The present work contributes to clarify the supramolecular basis for the previously reported emitting properties of this series of heteroleptic cyclometalated Pt(II) monomers [24]. The knowledge of the exact interaction pathways arising within **1**–**4** from each diverse cyclometalating moiety in the presence of the fully halogenated Br_4cat dianion as a common ancillary ligand for the square-planar Pt(II) center, as well as the large NBu_4^+ counter cation, appears crucial for the rational design of novel solid-state highly luminescent parent systems as well as potentially luminescent multi-functional soft salts comprising both emitting Pt(II) cations and anions, passing also through ligand(s) best choice and/or specific ligand design.

Acknowledgements

A.C. and I. A. acknowledge the European Community's Seventh Framework Program (FP7 2007e2013) through the MATERIA Project (PONa3_00370).

Disclosure statement

No potential conflict of interest was reported by the authors.

References

[1] T. Fleetham, G. Li, J. Li. *Adv. Mater*, **29**, 1601861 (2017).
[2] Y. Chi, P.T. Chou. *Chem. Soc. Rev.*, **39**, 638 (2010).
[3] L.F. Gildea, J.A.G. Williams. *Iridium and Platinum Complexes for OLEDs*, Woodhead Publishing Series in Electronic and Optical Materials, Elsevier (2013).
[4] J. Kalinowski, V. Fattori, M. Cocchi, J.A.G. Williams. *Coord. Chem. Rev.*, **255**, 2401 (2011).
[5] K.M.-C. Wong, V.W.W. Yam. *Coord. Chem. Rev.*, **251**, 2477 (2007).
[6] J.J. Zhong, Q.Y. Meng, G.X. Wang, Q. Liu, B. Chen, K. Feng, C.H. Tung, L.Z. Wu. *Chemistry*, **19**, 6443 (2013).

[7] T.C. Johnstone, K. Suntharalingam, S.J. Lippard. *Chem. Rev.*, **116**, 3436 (2016).
[8] N. Cutillas, G.S. Yellol, C. De Haro, C. Vicente, V. Rodríguez, J. Ruiz. *Coord. Chem. Rev.*, **257**, 2784 (2013).
[9] S. Garbe, M. Krause, A. Klimpel, I. Neundorf, P. Lippmann, I. Ott, D. Brünink, C.A. Strassert, N.L. Doltsinis, A. Klein. *Organometallics*, **39**, 746 (2020).
[10] S. Lin, H. Pan, L. Li, R. Liao, S. Yu, Q. Zhao, H. Sun, W. Huang. *J. Mater. Chem. C*, **7**, 7893 (2019).
[11] M. Mauro, A. Aliprandi, D. Septiadi, N.S. Kehr, L.D. Cola. *Chem. Soc. Rev.*, **43**, 4144 (2014).
[12] A. Aliprandi, D. Genovese, M. Mauro, L.D. Cola. *Chem. Lett.*, **44**, 1152 (2015).
[13] C.L. Ko, W.Y. Hung, P.T. Chen, T.H. Wang, H.F. Hsu, J.L. Liao, K.T. Ly, S.F. Wang, C.H. Yu, S.H. Liu, G.H. Lee, W.S. Tai, P.T. Chou, Y. Chi. *ACS Appl. Mater. Interfaces*, **12**, 16679 (2020).
[14] M. Yoshida, M. Kato. *Coord. Chem. Rev.*, **355**, 101 (2018).
[15] H.R. Shahsavari, S. Paziresh, S. Aghakhanpour, R.B. Aghakhanpour, S. Chamyan. *Inorg. Chem. Res.*, **4**, 225 (2020).
[16] P.H. Lanoë, A. Moreno-Betancourt, L. Wilson, C. Philouze, C. Monnereau, H. Jamet, D. Jouvenot, F. Loiseau. *Dyes Pigm.*, **162**, 967 (2019).
[17] J. Kang, R. Zaen, K.-M. Park, K.H. Lee, J.Y. Lee, Y. Kang. *Cryst. Growth Des.*, **20**, 6129 (2020).
[18] Y. Yan, Z. Yu, C. Liu, X. Jin. *Dyes Pigm.*, **173**, 107949 (2020).
[19] J. Alemán, S. Cabrera, P. Domingo-Legarda, A. Casado-Sánchez, L. Marzo. *Inorg. Chem.*, **59**, 13845 (2020).
[20] A. Ionescu, L. Ricciardi. *Inorg. Chim. Acta*, **460**, 165 (2017).
[21] A. Ionescu, N. Godbert, L. Ricciardi, M.L. Deda, I. Aiello, M. Ghedini, I. Rimoldi, E. Cesarotti, G. Facchetti, G. Mazzeo, G. Longhi, S. Abbate, M. Fusè. *Inorg. Chim. Acta*, **461**, 267 (2017).
[22] M. Yoshida, M. Kato. *Coord. Chem. Rev.*, **408**, 213194 (2020).
[23] (a) A. Ionescu, N. Godbert, I. Aiello, L. Ricciardi, M. La Deda, A. Crispini, E. Sicilia, M. Ghedini. *Dalton Trans.*, 47, 11645 (2018). (b) A. Ionescu, A.R. Caligiuri, N. Godbert, L. Ricciardi, M. La Deda, M. Ghedini, N. Ferri, M.G. Lupo, G. Facchetti, I. Rimoldi, I. Aiello. *Appl. Organomet. Chem.*, **34**, e5455 (2020).
[24] L. Ricciardi, M.L. Deda, A. Ionescu, N. Godbert, I. Aiello, M. Ghedini. *Dalton Trans.*, **46**, 12625 (2017).
[25] A.D. Burrows, D.M.P. Mingos, A.J.P. White, D.J. Williams. *J. Chem. Soc., Dalton Trans.*, 149 (1996).
[26] T. Solin, K. Matsumoto, K. Fuwa. *BCSJ*, **54**, 3731 (1981).
[27] A.D. Burrows, D.M.P. Mingos, A.J.P. White, D.J. Williams. *J. Chem. Soc., Dalton Trans.*, 3805 (1996).
[28] A. Mukherjee, S. Tothadi, G.R. Desiraju. *Acc. Chem. Res.*, **47**, 2514 (2014).
[29] G. Cavallo, P. Metrangolo, R. Milani, T. Pilati, A. Priimagi, G. Resnati, G. Terraneo. *Chem. Rev.*, **116**, 2478 (2016).
[30] (a) A. Mukherjee, G.R. Desiraju. *IUCrJ*, **1**, 49 (2014). (b) P. Matrangolo, G. Resnati. *IUCrJ*, **1**, 5 (2014).
[31] Bruker SAINT (Version 7.68A. Bruker AXS Inc., Madison, WI (2009).
[32] Bruker SADABS (Version 2008/1). Bruker AXS Inc., Madison, WI (2008).
[33] G.M. Sheldrick. *Acta Crystallogr. A*, **64**, 112 (2008).
[34] G.M. Sheldrick. *Acta Crystallogr. C Struct. Chem.*, **71**, 3 (2015).
[35] P. Müller. *Crystallogr. Rev.*, **15**, 57 (2009).
[36] P. Müller, R. Herbst-Irmer, A.L. Spek, T. Schneider, M. Sawaya. *Crystal Structure Refinement: A Crystallographer's Guide to SHELXL, IUCr Texts on Crystallography*, Oxford University Press, Oxford, UK (2006).
[37] H. Putz, K. Brandenburg, *Diamond - Crystal and Molecular Structure Visualization (version 4.6.8)*, Crystal Impact, Bonn, Germany (2022).
[38] M.M. Dell'Anna, V. Censi, B. Carrozzini, R. Caliandro, N. Denora, M. Franco, D. Veclani, A. Melchior, M. Tolazzi, P. Mastrorilli. *J. Inorg. Biochem.*, **163**, 346 (2016).
[39] J.M. Clemente, C.Y. Wong, P. Bhattacharyya, A.M.Z. Slawin, D.J. Williams, J.D. Woollins. *Polyhedron*, **13**, 261 (1994).

[40] J. Best, I.V. Sazanovich, H. Adams, R.D. Bennett, E.S. Davies, A. Meijer, M. Towrie, S.A. Tikhomirov, O.V. Bouganov, M.D. Ward, J.A. Weinstein. *Inorg. Chem.*, **49**, 10041 (2010).
[41] N. Godbert, T. Pugliese, I. Aiello, A. Bellusci, A. Crispini, M. Ghedini. *Eur. J. Inorg. Chem.*, **2007**, 5105 (2007).
[42] A. Bossi, A.F. Rausch, M.J. Leitl, R. Czerwieniec, M.T. Whited, P.I. Djurovich, H. Yersin, M.E. Thompson. *Inorg. Chem.*, **52**, 12403 (2013).
[43] D. Poveda, Á. Vivancos, D. Bautista, P. González-Herrero. *Chem. Sci.*, **11**, 12095 (2020).
[44] H.R. Shahsavari, J. Hu, S. Chamyani, Y. Sakamaki, R.B. Aghakhanpour, C. Salmon, M. Fereidoonnezhad, A. Mojaddami, P. Peyvasteh, H. Beyzavi. *Organometallics*, **40**, 72 (2021).
[45] Q.Z. Yuan, F.S. Wan, T.T. Shen, D.K. Cao. *RSC Adv.*, **12**, 148 (2021).
[46] K.H. Asressu, C.-K. Chan, C.-C. Wang. *RSC Adv.*, **11**, 28061 (2021).
[47] L. Zong, C. Wang, A.M.P. Moeljadi, X. Ye, R. Ganguly, Y. Li, H. Hirao, C.-H. Tan. *Nat. Commun.*, **7**, 13455 (2016).
[48] A.W.-Y. Cheung, L.T.-L. Lo, C.-C. Ko, S.-M. Yiu. *Inorg. Chem.*, **50**, 4798 (2011).
[49] X. Ren, Q. Meng, Y. Song, C. Lu, C. Hu, X. Chen. *Inorg. Chem.*, **41**, 5686 (2002).
[50] S.-W. Lai, M.C.-W. Chan, S.-M. Peng, C.-M. Che. *Angew. Chem. Int. Ed.*, **38**, 669 (1999).
[51] M. Ghedini, A. Golemme, I. Aiello, N. Godbert, R. Termine, A. Crispini, M.L. Deda, F. Lelj, M. Amati, S. Belviso. *J. Mater. Chem.*, **21**, 13434 (2011).
[52] N.M. Shavaleev, H. Adams, J. Best, R. Edge, S. Navaratnam, J.A. Weinstein. *Inorg. Chem.*, **45**, 9410 (2006).
[53] W.C. Poh, H.L. Au-Yeung, A.K.W. Chan, E.Y.H. Hong, Y.H. Cheng, M.Y. Leung, S.L. Lai, K.H. Low, V.W.W. Yam. *Chem. Asian J.*, **16**, 3669 (2021).
[54] Á. Vivancos, D. Poveda, A. Muñoz, J. Moreno, D. Bautista, P. González-Herrero. *Dalton Trans.*, **48**, 14367 (2019).
[55] G.T. Morgan, F.H. Burstall. *J. Chem. Soc.*, 965 (1934).
[56] Y. Nishiuchi, A. Takayama, T. Suzuki, K. Shinozaki. *Eur. J. Inorg. Chem.*, **2011**, 1815 (2011).
[57] N. Marino, C.H. Fazen, J.D. Blakemore, C.D. Incarvito, N. Hazari, R.P. Doyle. *Inorg. Chem.*, **50**, 2507 (2011).
[58] D.Q.M. Craig. *Polymorphism: In the Pharmaceutical Industry*, Wiley-VCH Verlag GmbH & Co., KGaA, pp. 43–79 (2006).
[59] B. Perrenot, G. Widmann. *Thermochim. Acta*, **234**, 31 (1994).
[60] M.M.H. Smets, S.J.T. Brugman, E.R.H. Van Eck, J.A. Van Den Ende, H. Meekes, H.M. Cuppen. *Cryst. Growth Des.*, **15**, 5157 (2015).

Dalton Transactions

ROYAL SOCIETY OF CHEMISTRY

PAPER

Check for updates

Cite this: *Dalton Trans.*, 2022, **51**, 16545

Curcumin-based ionic Pt(II) complexes: antioxidant and antimicrobial activity†

Rossella Caligiuri,[a] Giuseppe Di Maio,[a] Nicolas Godbert,[a] Francesca Scarpelli,[a] Angela Candreva,[a,b] Isabella Rimoldi,[c] Giorgio Facchetti,[c] Maria Giovanna Lupo,[d] Emilia Sicilia,[e] Gloria Mazzone,[e] Fortuna Ponte,[e] Isabella Romeo,[f,g] Massimo La Deda,[a,b] Alessandra Crispini,[a] Renata De Rose[h] and Iolinda Aiello *[a,b]

Received 26th May 2022,
Accepted 16th September 2022

DOI: 10.1039/d2dt01653b

rsc.li/dalton

A series of novel cationic curcumin-based Pt(II) complexes with neutral (N^N) ligands and triflate anions as counterions, $[(N^N)Pt(curc)]CF_3SO_3$, **1–4**, were synthesised and fully characterised. The antioxidant radical scavenging activity of complexes **1–4** was measured spectrophotometrically using DPPH as the internal probe. Computational strategies have been exploited to ascertain the mechanism of antioxidant action of curcumin (H(curc)) and its Pt(II) complexes. Finally, compounds **1–4** were tested *in vitro* for their growth inhibitory activity against two bacteria (*Staphylococcus aureus* and *Escherichia coli*) by the disk diffusion technique at different Pt(II) complex solution concentrations. The effect of the complexation of H(curc) was investigated.

1. Introduction

Metal complexes based on naturally occurring bioactive molecules are recently spreading as pharmaceuticals and many research works are dedicated to the investigation of their biological activities. The interaction of metal ions with coordinating ligands is found to be responsible for the relevant changes in their chemical behaviour and biological properties, resulting in improved chemical stability, increased pharmacological activity, and reduction of side effects.[1–5] Moreover, the presence of a metal centre that is able to react with different nucleophiles at the cellular level makes these compounds active as therapeutic tools. Indeed, they are able to modulate different biological processes at once, an aspect otherwise unrealizable by carbon-based molecules or simple encapsulation processes.[6]

Within bioactive metal chelating ligands of natural extraction, particular interest has been devoted to curcumin, [1,7-bis (4-hydroxy-3-methoxyphenyl)-1,6-heptane-3,5-dione] (H(curc)), a lipophilic polyphenol extracted from the powdered rhizome of *Curcuma longa* L. as the principal colouring agent. Curcumin has been widely used as a spice and cosmetic component in traditional Ayurvedic and Chinese herbal medicine for a very long time.[7,8] Consumption of H(curc) has been associated with a plethora of beneficial effects on human health, spanning from anti-inflammatory, antithrombotic, and anti-arthritic to immunomodulatory and neuroprotective abilities.[9,10] H(curc) has also been extensively investigated for its antiproliferative, antimetastatic, and antiangiogenic properties.[11,12] Furthermore, H(curc) acts as a free radical scavenger and antioxidant.[13,14] Its potent activity is correlated to its peculiar structural characteristics, in particular, the position of the hydroxyl groups, the enol form of the diketone moiety, and the extended conjugated structure.[15–17] In addition, H(curc) is well known as an antimicrobial agent with a broad spectrum of activity, including against Gram-positive and Gram-negative bacteria, as well as several viruses.[18]

Thus in the last few decades, the study of the properties and mechanism of action of H(curc) has attracted ever-increas-

[a]*MAT-INLAB, LASCAMM CR-INSTM, Unità INSTM della Calabria, Dipartimento di Chimica e Tecnologie Chimiche, Università della Calabria, 87036 Arcavacata di Rende, CS, Italy. E-mail: iolinda.aiello@unical.it*
[b]*CNR NANOTEC-Istituto di Nanotecnologia UOS Cosenza, 87036 Arcavacata di Rende, CS, Italy*
[c]*Dipartimento di Scienze Farmaceutiche, Università degli Studi di Milano, 20133 Milan, Italy*
[d]*Dipartimento di Medicina, Università degli Studi di Padova, 35128 Padova, Italy*
[e]*Dipartimento di Chimica e Tecnologie Chimiche, 87036 Arcavacata di Rende, CS, Italy*
[f]*Dipartimento di Scienze della Salute, Università degli Studi "Magna Græcia" di Catanzaro, Campus "S. Venuta", Viale Europa, 88100 Catanzaro, Italy*
[g]*Net4Science Academic Spin-Off, Università degli Studi "Magna Græcia" di Catanzaro, Campus "S. Venuta", Viale Europa, 88100 Catanzaro, Italy*
[h]*LAB CF-INABEC, Dipartimento di Chimica e Tecnologie Chimiche, 87036 Arcavacata di Rende, CS, Italy*

† Electronic supplementary information (ESI) available: FT-IR, ^{1}H- and ^{13}C-NMR, ESI-MS spectra, absorption and emission spectra in MeOH, DMSO and 10% DMSO/PBS varying time, theoretical UV-Vis spectra and data, thermodynamic data, theoretical calculated lipophilicity, antimicrobial data. See DOI: https://doi.org/10.1039/d2dt01653b

ing attention. However, poor solubility, hydrolytic instability, very low bioavailability, and photodegradation are responsible for its still limited use in the pharmaceutical field, despite its promising biological preclinical and clinical effects.[19,20] Different strategies have been attempted to overcome these limitations, for example, its encapsulation in nanoparticles or its linkage to liposomes or micelles.[21–26] However, H(curc) complexation with a proper metal ion still provides the most fruitful approach to circumvent the challenges related to its low pharmacokinetic profile.[27,28] Taking advantage of the presence of the central β-diketo unit, H(curc) can form a large variety of metal chelates of 1 : 1 and 1 : 2 metal-to-ligand ratio with various divalent and trivalent metal ions, stabilizing its more resistant monoanionic enolic form and reducing its photodegradation.[27,28] Curc-based metal complexes have been widely probed for their anticancer properties, showing improved stability, better bioavailability and greater cytotoxicity in their effectiveness as anticancer agents with respect to pure H(curc).[29–42] Despite the well-known antioxidant and antibacterial activity shown by the H(curc) free ligand, the derived curc-based metal complexes have been much less investigated with regard to these potential applications. While only a few curc-based metal complexes have shown better antioxidant properties than pure H(curc), in most cases, the measured antioxidant activity has been found to be comparable to that of the free ligand.[29–32] Moreover, to the best of our knowledge, all the investigated metal derivatives are homoleptic complexes with the only exception of one of Cu(II).[31] Despite the fact that metal complexes containing antimicrobial agents could display synergistic activity as reported by Song *et al*. in the case of curc-based rare earth metal complexes, in most cases reported so far, curc-based metal complexes display comparable antibacterial activity with respect to pure H(curc).[29,33,34]

Herein, based on our experience in the study of ionic bioactive Pt(II) complexes,[35–38] we designed and studied novel heteroleptic cationic Pt(II) complexes of the general formula [(N^N)Pt(curc)]CF_3SO_3 with the intention to extend the studies on the potential application of transition metal complexes as antioxidant and antimicrobial curc carrier agents. To achieve ionic derivates that are able to introduce favourable electrostatic interactions and thus improve the bioactive properties of the resulting complexes, (N^N) ligands with different electronic and steric effects [(N^N) = 1,3-diaminopropane (pn), 2-picolylamine (pic), 2,2′-bipyridine (bipy) and 4,4′-dinonyl-2,2′-bipyridine (bipy-C_9)] have been selected. In particular, the structural differences of the (N^N) ligands in terms of the flexibility of the six and five-membered chelated rings formed upon the coordination to the Pt(II) metal ion as well as the extension of the aromatic character can be a suitable tool to appropriately tune the lipophilicity of the resulting synthesized complexes. Moreover, the choice to introduce triflate as the counterion, instead of the nitrate anion, which is usually used for the preparation of analogous cationic Pt(II) complexes, relies on the recognition of nitrate as a toxic agent, whereas for the triflate anion, non-clinical toxicological data are still available.[39–42] In addition, according to a recent study, the triflate anion could improve the solubility of the cationic species with respect to the nitrate counterpart.[43]

2. Experimental

2.1. Materials and methods

Curcumin was purchased from Carbosynth and used without further purification as we already reported the highest grade of purity of this supplier with respect to other commercially available sources.[44] All other reagents and solvents were purchased from Aldrich Chemical Co. or Alfa Aesar and were used without further purification. Cycloplatinated precursors [(pn)$PtCl_2$], **I**,[45] [(pic)$PtCl_2$], **II**,[46] [(bipy)$PtCl_2$], **III**,[46] and [(bipy-C_9)$PtCl_2$], **IV**[47] were synthesised following methods already reported. The Pt(II) complexes **1–4** were synthesised through microwave assisted syntheses that were carried out using a CEM Discover Synthesis Unit (CEM Corp., Matthews, NC) following our previously reported procedure for the preparation of ionic Pt(II) or Pt(IV) complexes.[36,48] Melting points were determined using a Leica DMLP polarising microscope equipped with a Leica DFC280 camera and a CalCTec (Italy) heating stage. Elemental analyses were performed using a PerkinElmer 2400 analyser CHNS/O. Conductivity measurements were performed in DMF or MeOH solutions using an InoLab Cond Level 1-720 conductometer equipped with an LR 325/001 immersion cell at *ca.* 1 mM. The IR spectra (KBr pellets) were recorded using a Spectrum One PerkinElmer FT-IR spectrometer. The ^{1}H NMR spectra were recorded using a Bruker Avance 300 MHz spectrometer in DMSO-d_6 with TMS as the internal standard. The ^{13}C NMR spectra were recorded in DMSO-d_6 using a Bruker DRX Avance 400 MHz equipped with a non-reverse probe. MS analyses were performed by using a Thermo Finnigan (MA, USA) LCQ Advantage system MS spectrometer with an electrospray ionization source and an 'Ion Trap' mass analyser. The MS spectra were obtained by direct infusion of a sample solution in MeOH. Eagle's minimum essential medium (MEM) was purchased from Sigma Aldrich, while trypsin–EDTA, penicillin, streptomycin, sodium pyruvate, non-essential amino acid solution, fetal calf serum (FCS), plates and Petri dishes were purchased from EuroClone. The Pt(II) complexes were dissolved in dimethyl sulfoxide (DMSO) at the maximal concentration of 200 μM. The amount of DMSO did not exceed 0.25% of the culture media volume. The UV/vis absorption spectra were recorded using a PerkinElmer Lambda 900 spectrophotometer using 1 cm path length quartz cuvettes. Stability measurements were carried out in MeOH, DMSO and 10% DMSO/PBS at a concentration of 10 μM registering the absorption spectra of the samples in a 48 h time interval. The samples in 10% DMSO/PBS (phosphate buffered saline in H_2O, pH = 7.4) were prepared starting from a DMSO mother solution and then directly diluting in a quartz cuvette to reach the desired concentration. Between measurements, the samples were stored at 25 °C in the dark.

 This journal is © The Royal Society of Chemistry 2022

2.2. Syntheses

[(pn)Pt(curc)]CF_3SO_3 (1). Complex **I** (150 mg, 0.44 mmol) and $AgCF_3SO_3$ (227 mg, 0.88 mmol) were suspended in 5 mL of degassed DMF and stirred at r.t., in the dark, overnight. Then, the precipitated AgCl was filtered off and the obtained solution was added dropwise to 4 mL of DMF containing H(curc) (162 mg, 0.44 mmol) and NEt_3 (45 mg, 0.44 mmol). The reaction mixture was heated, under microwave irradiation, for 10 min at 60 °C and 150 W. The brownish solution was cooled at r.t., filtered off and then evaporated under vacuum. The resulting reddish oily residue was precipitated with MeOH/Et_2O. The obtained solid was filtered off and washed with H_2O, Et_2O, and $CHCl_3$ and finally dried under high vacuum. Red solid (140 mg, 40%). Mp. 155 °C. $C_{25}H_{29}F_3N_2O_9PtS$ (MW = 785.65): Anal. calcd: C, 38.22; H, 3.72; N, 3.56%. Found: C, 38.25; H, 3.73; N, 3.55%. Λ_M in MeOH: 30.48 S cm^2 mol^{-1}. IR (KBr pellet) ν_{max}/cm^{-1} 3419w (NH), 3243br (OH), 2962w (CH aliphatic), 1619s (CC), 1596s (CO), 1513vs, [1278vs, 1030s, 639s] ($CF_3SO_3^-$). ^{1}H-NMR (300 MHz; DMSO-d_6; TMS) δH/ppm 9.63 (2H, s, –O*H*), 7.66 (2H, d, J_{H-H} = 15.6 Hz, H^c), 7.22 (2H, s, H^d), 7.06 (2H, d, J_{H-H} = 8.3 Hz, H^e), 6.81 (2H, d, J_{H-H} = 8.2 Hz, H^f), 6.67 (2H, d, J = 15.5 Hz, H^b), 5.88 (1H, s, H^a), 5.47 (4H, s_{br}, –NH_2) 3.82 (6H, s, –OCH_3), 2.72–2.60 (2H, m, $H^{a'}$), 2.47 (2H, s_{br}, $H^{a'}$), 1.52 (2H, s_{br}, $H^{b'}$). ^{13}C-NMR (75 MHz; DMSO-d_6; TMS) δH/ppm 174.84, 172.77, 149.49, 148.62, 140.78, 127.46, 123.00, 116.34, 110.95, 105.39, 55.87, 43.71, 34.25. MS (ESI): *m*/*z* 637.33 $[M + H]^+$.

[(pic)Pt(curc)]CF_3SO_3 (2). The reaction was conducted, as for **1**, using **II** (115 mg, 0.31 mmol), $AgCF_3SO_3$ (159 mg, 0.62 mmol), H(curc) (114 mg, 0.31 mmol) and NEt_3 (32 mg, 0.31 mmol). Light brown solid (114 mg, 45%). Mp. 230 °C. $C_{28}H_{27}F_3N_2O_9PtS$ (MW = 819.67): Anal. calcd: C, 41.03; H, 3.32; N, 3.42%. Found: C, 41.15; H, 3.32; N, 3.43%. Λ_M in DMF: 41.83 S cm^2 mol^{-1}. IR (KBr pellet) ν_{max}/cm^{-1} 3246br (OH), 2985w (CH aliphatic), 1623s (CC), 1595s (CO), 1515vs, [1278vs, 1030s, 639s] ($CF_3SO_3^-$). ^{1}H-NMR (300 MHz; DMSO-d_6; TMS) δH/ppm 9.71 (1H, d, J_{H-H} = 7.9 Hz, $H^{a'}$), 8.76 (1H, d, J_{H-H} = 5.5 Hz, $H^{d'}$), 8.23 (1H, t, J_{H-H} = 8.5 Hz, $H^{c'}$), 7.80–7.56 (3H, m, $H^{e,b'}$), 7.38 (1H, s, H^d), 7.26 (1H, s, H^d), 7.01 (2H, d, H^c), 6.90–6.74 (4H, m, H^f + H^b), 6.10 (1H, s, H^a), 4.31 (2H, s, –CH_2), 3.84 (6H, s, –OCH_3). ^{13}C-NMR (75 MHz; DMSO-d_6; TMS) δH/ppm 175.78, 172.02, 157.87, 153.33, 149.85, 148.47, 146.41, 139.98, 130.88, 128.75, 123.65, 120.77, 117.51, 111.82, 104.81, 56.81, 43.71, 42.79. MS (ESI): *m*/*z* 671.63 $[M + H]^+$.

[(bipy)Pt(curc)]CF_3SO_3 (3). The reaction was conducted, as for **1**, using **III** (120 mg, 0.28 mmol), $AgCF_3SO_3$ (146 mg, 0.56 mmol), H(curc) (105 mg, 0.28 mmol) and NEt_3 (29 mg, 0.28 mmol). Brown solid (139 mg, 57%). Mp. 178 °C. $C_{32}H_{27}F_3N_2O_9PtS$ (MW = 867.71): Anal. calcd: C, 44.30; H, 3.14; N, 3.23%. Found: C, 44.36; H, 3.13; 3.22%. Λ_M in DMF: 42.42 S cm^2 mol^{-1}. IR (KBr pellet) ν_{max}/cm^{-1} 3243br (OH), 2989w (CH aliphatic), 1619s (CC), 1594s (CO), 1513vs, [1279vs, 1030s, 639s] ($CF_3SO_3^-$). ^{1}H-NMR (300 MHz; DMSO-d_6; TMS) δH/ppm 9.75 (2H, s_{br}, –O*H*), 8.94 (2H, d, J_{H-H} = 4.9 Hz, $H^{a'}$), 8.61 (2H, d, J_{H-H} = 7.9 Hz, $H^{c'}$), 8.45 (2H, t, $H^{b'}$), 7.92 (2H, t, J_{H-H} = 6.6 Hz, $H^{d'}$), 7.71 (2H, d, J_{H-H} = 15.7 H, H^c), 7.35 (2H, s, H^d), 7.25 (2H, d, J_{H-H} = 7.9 Hz, H^e), 6.84 (2H, d, J_{H-H} = 8.1 Hz, H^f), 6.76 (2H, d, J_{H-H} = 15.9 Hz, H^b), 6.11 (1H, s, H^a), 3.85 (6H, s, –OCH_3). ^{13}C-NMR (75 MHz; DMSO-d_6; TMS) δH/ppm 177.61, 173.88, 166.37, 149.88, 148.76, 147.31, 144.72, 141.44, 140.66, 138.95, 129.91, 128.74, 126.17, 124.75, 123.71, 115.09, 111.89, 111.02, 107.11, 61.33, 41.15. MS (ESI): *m*/*z* 718.47 $[M + H]^+$.

[(bipy-C_9)Pt(curc)]CF_3SO_3 (4). The reaction was conducted, as for **1**, using **IV** (150 mg, 0.22 mmol), $AgCF_3SO_3$ (114 mg, 0.44 mmol), H(curc) (82 mg, 0.22 mmol) and NEt_3 (22.5 mg, 0.22 mmol). The oily residue obtained after the evaporation of the solvent under reduced pressure was extracted three times with $CHCl_3/H_2O$ (v/v: 1/3). The organic phase was dried over Na_2SO_4 anhydrous and the solvent was evaporated. The obtained solid was reprecipitated twice by Et_2O/*n*-hexane. Successively, the product was filtered off and washed with H_2O and *n*-hexane. Orange solid (111 mg, 45%). Mp. 100 °C. $C_{50}H_{63}F_3N_2O_9PtS$ (MW = 1120.19): Anal. calcd: C, 53.61; H, 5.67; N, 2.50%. Found: C, 53.68; H, 5.68; N, 2.49%. Λ_M in MeOH: 47.28 S cm^2 mol^{-1}. IR (KBr pellet) ν_{max}/cm^{-1} 3290br (OH), 2925s (CH aliphatic), 2854w (CH aliphatic), 1623s (CC), 1594s (CO), 1514vs, [1268vs, 1030s, 638s] ($CF_3SO_3^-$). ^{1}H-NMR (300 MHz; DMSO-d_6; TMS) δH/ppm 9.76 (2H, s_{br}, –O*H*), 8.55 (2H, d, J_{H-H} = 6.0 Hz, $H^{a'}$), 8.35 (2H, s, $H^{c'}$), 7.59 (2H, d, J_{H-H} = 5.9 Hz, $H^{b'}$), 7.47 (2H, d, J_{H-H} = 15.7 Hz, H^c), 7.27 (2H, s, H^d), 7.19 (2H, d, J_{H-H} = 8.1 Hz, H^e), 6.84 (2H, d, J_{H-H} = 8.1 Hz, H^f), 6.55 (2H, d, J_{H-H} = 15.7 Hz, H^b), 5.86 (1H, s, H^a), 3.83 (6H, s, –OCH_3), 2.64 (4H, m, –CH_2), 1.58 (4H, m, –CH_2–), 1.23 (24H, m, –(CH_2)$_6$–), 0.85 (6H, m, –CH_3). ^{13}C-NMR (75 MHz; DMSO-d_6; TMS) δH/ppm 176.11, 173.65, 159.79, 158.77, 150.19, 149.88, 147.43, 144.89, 143.77, 129.65, 128.67, 127.08, 126.32, 124.05, 122.29, 119.83, 115.56, 113.46, 57.76, 40.59, 37.67, 35.26, 33.46, 31.73, 23.77, 22.54, 14.74. MS (ESI): *m*/*z* 971.03 $[M + H]^+$.

2.3. Cell viability assay

A sulphorhodamine B (SRB) assay was performed to assess cell viability after treatments. 5×10^3 cells per well were seeded in a 96-well tray in triplicate. After 24 h of incubation, the cells were treated with different concentrations of compounds. An SRB assay was performed after 48 h as previously described.[49]

2.4. DPPH radical scavenging activity

The antioxidant activity was measured using 2,2-diphenyl-1-picrylhydrazyl (DPPH) as a scavenger adapting a spectrophotometric method already reported.[50,51] DPPH is a stable radical chemical species that presents an intense band in the visible region (515 nm) of the absorption spectrum (Fig. S1, ESI†), due to the presence of an unpaired electron, that produces an intense violet colour. Antioxidant molecules are able to acquire the unpaired electron, resulting in a reduction of the 515 nm band absorbance of the probe and a consequent decolouration of the initial solution.[50,51] Thus, the antioxidant activity can be spectrophotometrically quantified by measuring the decrease in this band intensity by mixing a known amount of the analyte with the DPPH solution. Various concentrations

of each sample solution were investigated (*i.e.* 10, 20, 30, 40, 50 μM) by mixing them with a fixed concentration of the probe (100 μM) in 3 mL of spectroscopic grade MeOH. Absorbance was measured 3 h after sample preparation to ensure that stationary conditions were reached: during this time, the samples were incubated in the dark at room temperature. Each measure was conducted in triplicate, on three independent preparations. The antioxidant activity for each sample was calculated by determining the decrease in the absorbance (A) of DPPH at 515 nm according to the following equation:

$$\%\text{Antioxidant activity} = \left[\frac{A^{t=x}_{\text{sample}} - (A^{t=0}_{\text{sample}} + \alpha)}{A^{t=0}_{\text{sample}}}\right] \times 100$$

where $A^{t=0}_{\text{sample}}$ is the absorbance at 515 nm of the sample at time t = 0 (obtained by the mathematical sum of the absorption spectra of DPPH and the absorption spectra of the analyte); $A^{t=x}_{\text{sample}}$ is the absorbance at 515 nm of the sample at the investigated time (3 h). Finally, α is a correction factor, which takes into account a slight decrease in the optical density of the DPPH solution in MeOH (Fig. S1, ESI†), that overestimates the antioxidant activity of each sample:

$$\alpha = A^{t=0}_{\text{DPPH}} - A^{t=x}_{\text{DPPH}}$$

where $A^{t=0}_{\text{DPPH}}$ is the absorbance at 515 nm of DPPH in MeOH at time t = 0 and $A^{t=x}_{\text{DPPH}}$ is the absorbance at the same wavelength of DPPH at the investigated time. The % of the antioxidant activity was reported as mean ± SEM (standard error of the mean, depicted as error bars in Fig. 2) of each triplicate group of measures. The data obtained from each sample with varying concentrations were fitted with a four-parameter sigmoidal function using the GraphPad Prism 9 software to extrapolate the IC_{50} values (*i.e.* the concentration of the sample necessary to obtain a 50% reduction in DPPH at 515 nm absorption band).[52]

2.5. Computational details

All the calculations were performed using the Gaussian16 software package.[53] Geometry optimizations and frequency calculations were carried out by employing the hybrid B3LYP as the exchange and correlation functional[54,55] and the standard triple-ζ basis set 6-311++G(d,p) for all the atoms except for platinum, for which the SDD effective core potential and the corresponding split valence basis set were used. The continuum solvation model based on density (SMD)[56] was included in all the calculations to simulate the MeOH environment experimentally used, with a dielectric constant of 32.6. The local minima and transition states (TSs) were identified by the number of imaginary frequencies (0 and 1, respectively). The intrinsic reaction coordinate (IRC) calculations were used to verify whether the located transition states are properly connected with the relative minima.[57,58] Unrestricted calculations were used for open shell systems, where radicals are involved. No spin contamination was found, the $\langle S^2 \rangle$ value being about 0.750 in all cases. Thermodynamic corrections at 298.15 K were included in the calculation of the relative energies.

The absorption spectra were simulated in the MeOH environment within the time-dependent framework of density functional theory. For this purpose, fifty excitation states were computed by using the MN15 exchange and correlation functional[59] coupled with the basis sets employed in the optimization calculations.

The O–H bond dissociation enthalpy (BDE), the ionization potential (IP), the O–H proton dissociation enthalpy (PDE), the anion proton affinity (PA) and the electron transfer enthalpy (ETE), accounting for the different oxidation mechanisms described below, were calculated under a MeOH implicit environment at 298.15 K, according to the following expressions:

$$\text{BDE} = \text{H}(\text{H}_{n-1}\text{Antiox}^{\bullet}) + \text{H}(\text{H}^{\bullet}) - \text{H}(\text{H}_n\text{Antiox})$$

$$\text{IP} = \text{H}(\text{H}_n\text{Antiox}^{\bullet+}) + \text{H}(\text{e}^-) - \text{H}(\text{H}_n\text{Antiox})$$

$$\text{PDE} = \text{H}(\text{H}_{n-1}\text{Antiox}^{\bullet}) + \text{H}(\text{H}^+) - \text{H}(\text{H}_n\text{Antiox}^{\bullet+})$$

$$\text{PA} = \text{H}(\text{H}_{n-1}\text{Antiox}^-) + \text{H}(\text{H}^+) - \text{H}(\text{H}_n\text{Antiox})$$

$$\text{ETE} = \text{H}(\text{H}_{n-1}\text{Antiox}^{\bullet}) + \text{H}(\text{e}^-) - \text{H}(\text{H}_{n-1}\text{Antiox}^-)$$

Proton and electron solvation enthalpies computed at the same level of theory were used.[60]

To predict the pharmacokinetic properties of all the complexes, the SwissADME (**https://www.swissadme.ch/**) web tool was used. It calculates the adsorption, distribution, metabolism, and excretion (ADME) parameters, pharmacokinetics, bioavailability, and drug-like behaviour. The Brain Or IntestinaL EstimateD permeation method (BOILED-Egg) was used to estimate the solubility, polarity, and lipophilicity of the investigated complexes.[61]

2.6. Experimental measurement of log P_{ow}

RP-HPLC analysis was performed to correlate the hydrophobicity of the complexes with their retention time. The chromatograms were analyzed using a reversed-phase HPLC column (Partisil C18-ODS), at 25 °C, using KI as the internal standard and water/methanol in the ratio of 80/20 as mobile phase in the presence of HCOOH 15 mM (flow rate: 1 mL min^{-1}, λ = 210 nm). The calibration curve was realized in comparison with the reference compounds (cisplatin, carboplatin and oxaliplatin).[35,79]

2.7. Antibacterial activity

The *in vitro* antibacterial activity of H(curc) and complexes **1–4** against Gram-positive (*Staphylococcus aureus*) and Gram-negative (*Escherichia coli*) bacteria were tested and evaluated using the modified Kirby–Bauer disk diffusion method.[62,63] *S. aureus* (DSM 346) and *E. coli* (DSM 1576) were provided by DSMZ (German Collection of Microorganisms and Cell Cultures, Braunschweig) and grown respectively in 50 mL of DSM medium 92 and DSM medium 1 for 24 h at 37 °C. When the bacterial cultures of each microorganism were in their exponential phase of growth, dilution with sterile 0.8% saline solution was performed to reach a suspension of 10^8 cells per mL,

 This journal is © The Royal Society of Chemistry 2022

and then the concentrations were spectrophotometrically determined. Then, 100 μL of bacterial culture suspensions were spread onto the surface of Nutrient Agar (NA) (Beef extract, peptone, sodium chloride and agar) plates. H(curc) and complexes **1–4** were dissolved in DMSO at concentrations of 0.5 μg μL^{-1} (w/v). The other diluted concentrations used (0.4–0.05 μg μL^{-1}) were prepared by separately diluting them in the culture medium, so that the effective DMSO concentration did not exceed 0.1%. At this concentration, DMSO had no visually observable growth inhibiting effect. Filter paper disks of 6 mm diameter, previously sterilized in an autoclave, were placed on the surface of NA inoculated plates, pressed gently, and directly wet with 10 μL of each concentration of H(curc) and the tested complexes. Wet disks with fresh DMSO were used as the negative control. The inhibition zones were measured after overnight incubation in the dark at 37 °C. Each inhibition zone was measured three times with a calibre to obtain an average value. The antibacterial activity was calculated as a mean of three replicated experiments and all data are presented as mean ±standard deviation (SD). The absence of bacterial growth in the area around the disks was regarded as positive antibacterial activity. The minimal inhibitory concentration (MIC) was approximately deduced considering the lowest concentration at which the compound was still able to produce a transparent halo of inhibition larger than 6 mm (diameter of the disk paper).

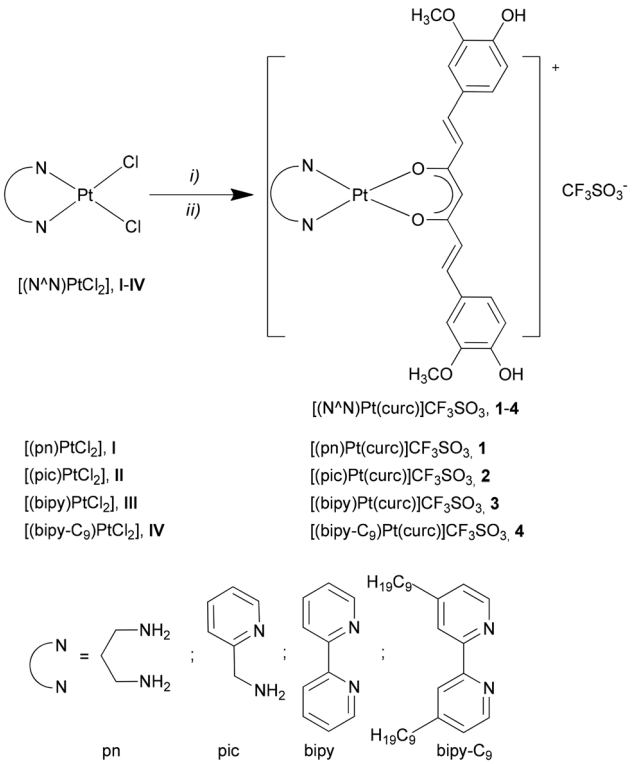

Scheme 1 Synthetic pathway of the $[(N^N)Pt(curc)]CF_3SO_3$ complexes, **1–4**. Reagents and conditions: (*i*) $AgCF_3SO_3$, DMF, N_2, r.t., dark, overnight; (*ii*) DMF, H(curc), NEt_3, 60 °C, 150 W, 10 min.

3. Results and discussion

3.1. Synthesis

The novel series of cationic Pt(II) complexes were synthesized starting from their corresponding precursors $[(N^N)PtCl_2]$, **I–IV**,[45–47] through reaction with an equimolar amount of $AgCF_3SO_3$ in DMF solution. To the resulting solution containing the *in situ* formed solvate intermediate, $[(N^N)Pt(solv)_2][CF_3SO_3]_2$, was directly added a solution of the triethylammonium curc salt. The resulting mixture was placed in a microwave oven following the procedure already used in previous works for the synthesis of metal complexes[48,64,65] to afford the derivatives $[(N^N)Pt(curc)][CF_3SO_3]$ **1–4** in a very short reaction time (Scheme 1).

Complexes **1–4** were obtained as reddish-brown or orange-yellow powders in moderate yields, similar to already known curc–Pt(II) complexes.[39–41] They are stable in the air and soluble in MeOH, DMF and DMSO. All complexes were characterized by the determination of their melting point, elemental analyses, mass spectrometry, molar conductivity, and FT-IR, ^1H and ^{13}C NMR and UV/vis spectroscopy. The molar conductivity values in either MeOH (30–50 S cm^3 mol^{-1}) or DMF (40–45 S cm^3 mol^{-1}), according to complexes **1–4** solubility, confirm the 1 : 1 electrolytic nature of the synthesized compounds.[66] Considering the IR spectra (Fig. S2, S6, S10, and S14, ESI†), the curc coordination is confirmed by the shift in bands predominantly related to the overlapping stretching vibrations of C=C and C=O. Indeed, in the free ligand, these bands are found at 1628 cm^{-1} and 1603 cm^{-1} while in complexes **1–4** they are shifted to lower wavenumbers, in particular within the frequency ranges of 1619–1623 cm^{-1} and 1594–1596 cm^{-1}, respectively.[67] The shift of these absorption bands always occurs upon the coordination of curc to a metal centre, due to the redistribution of the electron density in the curc complexes.[34,68] Moreover, the characteristic stretching bands associated with the presence of the counterion are an additional confirmation of the complex's formation and its ionic nature. In particular, the intense absorption stretching band at *ca.* 1270 cm^{-1} is related to the asymmetric stretching vibration of the SO_3^- ionic group.[69] In the ^1H NMR spectra of the Pt(II) complexes (Fig. S3, S7, S11, and S15, ESI†), the characteristic signals of the γ-proton of the methylene group and the methoxy groups of the coordinated curc are shifted to high fields in comparison with those of H(curc), confirming the metal–ligand coordination.[67] In particular, a singlet of γ-proton is present in the ppm range of 5.86–6.13 and those of methoxy groups at the ppm value of *ca.* 3.90. Furthermore, the effective coordination of curc to the Pt(II) fragment is also supported by the shift to the lower field of signals related to the (N^N) ligands. In addition, regarding ^{13}C-NMR, data are in agreement with the Pt(II) complexes analogues already reported.[39–41]

3.2. UV/vis spectroscopy

The absorption spectra of H(curc) and **1–4** were recorded for all samples in MeOH diluted solutions (Fig. 1). The H(curc)

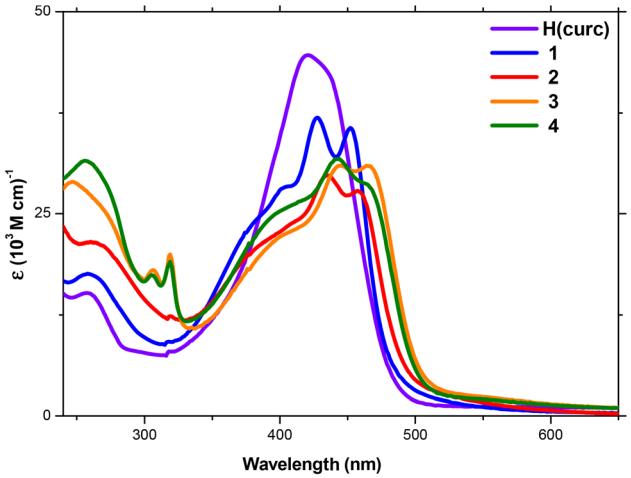

Fig. 1 Absorption spectra of H(curc) (violet) and complexes **1** (blue), **2** (red), **3** (orange) and **4** (red) in MeOH dilute solution [10 μM].

absorption spectrum shows a low intensity band in the UV region with the maximum peak at 258 nm and a broad and intense absorption band in the visible portion of the electromagnetic spectrum with the maximum peak centred at 420 nm and a shoulder peak at 432 nm, both attributed to the ππ* transitions of its enolic form.[70,71]

For a better description of the spectral features of **1–4**, two distinct regions of the absorption spectra, *i.e.*, the visible and the UV regions have been separately considered. In the visible region, the shape of the spectra is rather similar for all complexes. This is due to the presence of the curc–Pt electronic transitions that generate a large double-peaked band with a shoulder centred around 400 nm. The red shifted peak and the shoulder peak around 400 nm are attributed to the ligand-to-metal charge transfer (LMCT) transition from curc to the metallic centre, while the blue shifted peak is due to a ππ* ligand centred (LC) transition on curc. The latter is red shifted with respect to the analogous transition in H(curc) due to the coordination to Pt(II) ion. The only difference observed in the visible region is regarding the exact position of this band. For complexes **3** and **4**, a red shift of the band, with respect to the analogous transitions of **1** and **2**, is observed, which is attributed to the rigidity imparted by the presence of the bipy and bipy-C_9 ligands, respectively. The simulated spectra (Fig. S18 and Table S1, ESI†) and the corresponding natural transition orbitals (NTOs, Fig. S19, ESI†) confirm the assignment of the lowest energy band for free ligand H(curc) and Pt(II) cationic complexes **1–4**. The broad and intense bands observed for all the complexes around 450 nm are LMCT in character and involve the HOMO and LUMO; they are red-shifted because of the evident participation of the metal in the NTOs (Fig. S11, ESI†). Whilst the transition around 400 nm (computed to be around 360 nm) starts from the HOMO−1 orbitals thus becoming of the LC type, though a little participation of MLCT can be observed for all the complexes.

In the UV region, the spectra show differences due to the LC electronic transitions localized on the different N^N ligands. For complexes **1** and **2** only the ππ* LC transition of curc, centred respectively at 260 nm and 265 nm, is observed. The slight red-shift of this transition in **2** is caused by the greater rigidity imparted by the pic ligand with respect to the pn one. As expected, the non-aromatic N^N ligand in **1** does not take part in the electronic transitions and the band corresponds to the excitation from the primarily metal d-orbital (HOMO−1) with the population of the ligand-localized orbital (LUMO+1) generating an absorption band of MLCT character, though a considerable part of the CT is centred on the curc ligand in this case as in the other. On the other hand, the LUTO associated with such a transition in **2** shows the evident participation of the aromatic portion of the pic ligand into the orbital (Fig. S19, ESI†). Finally, for complexes **3** and **4**, the broad and destructured band observed at low wavelengths is attributed to a combination of LC transition on curc and bipy aromatic rings. The typical ππ* electronic transitions on bipy aromatic rings are also observed at 305 and 320 nm.[31] Indeed, the computed band originate from the electronic transitions centred on the bipy ligand as well as from the CT from orbitals primary localized on curc with the population of orbitals centred on the bipy ligand.

3.3. Stability

Complexes **1–4** and H(curc) show a pale-yellow colour both in MeOH and DMSO dilute solutions. In MeOH, they are stable in the time laps of 48 h. The absorption spectra retained the same shape with no significant variations in the intensity band ratio (Fig. S20–S24, ESI†). The slight variations in absorption intensity observed for complexes **1**, **2**, and **3** are probably due to their negligible crystallization taking place over time rather than effective degradation. These variations are minimal at the wavelength of 515 nm eventually proving that the acquired data for antioxidant activity (see section 3.4) are only dependent on the scavenging activity of the analytes. To study the behaviour of complexes **1–4** with respect to H(curc) under biological pH conditions, their stability in DMSO and an aqueous solution of 10% DMSO/PBS was also evaluated. The absorption spectra of all samples over time show only slight variations in intensity, with no significant variations in the interband ratio, again attributed to negligible crystallization event (Fig. S25–S29, ESI†).[72] When diluted with PBS aqueous solution, a colour variation from yellow to pink was observed for all the samples. This variation is more visible for complexes **1–4** than H(curc). Comparing the spectra registered in DMSO and in PBS solution (Fig. S30–S34, ESI†) at t = 0 h two aspects can be highlighted. The lower intensity of the spectra and the greater destructuration with respect to their analogues in DMSO solution are due to the worst solubility of the samples in an aqueous environment. The presence of a new absorption band (centred above 540 nm for complexes **1–4** and 530 nm for H(curc) and responsible for the pink coloration of the buffer) is attributed to the weak deprotonation of the H(curc) hydroxyl groups, due to the slight alkalinity of the buffer solution.[73] Considering the absorption spectra over time in DMSO/PBS

 This journal is © The Royal Society of Chemistry 2022

solution, different behaviour for complexes **1–3** than **4** and H(curc) were observed. H(curc), as known, experienced strong degradation under biological pH conditions. This is proved by the strong intensity reduction of the spectra with increasing time and by the dramatic variation of the ratio between the absorption bands centred at 365 and 430 nm, already observed after 1 h in the DMSO/PBS mixture. This ultimately results in the complete discoloration of its solution after 48 h (Fig. S30, ESI†). It is believed that the degradation of H(curc) goes through an autoxidation mechanism. Reacting with O_2 the main degradation product is a bicyclopentadione formed by the double cyclization of the heptadienedione chain between the two methoxyphenol rings.[74] This cyclization causes the cleavage of the strongly conjugated heptadienedione chain, responsible for the strong reduction of the absorption maximum intensity (80%). Interestingly, this strong reduction of the absorption band and the consequent variation of the interband ratio already after 1 h were only partially observed in complex **4**; They were not observed at all for complexes **1–3**. For complex **4** after t = 3 h a strong reduction in absorption intensity was observed (of about 50% on the absorption maximum), accompanied by a variation in the ratio between the three absorption peaks. From this point on, only a weak reduction in the intensity of the entire spectrum was observed, suggesting the stabilization of the sample with the only crystallization event (confirmed by the observation of the observed presence of a powder at the bottom of the cuvette). Conversely, complexes **1–3** did not undergo any degradation. Only a reduction in intensity over time was observed with no variations in the interband ratio, attributable to the worst solubility in the aqueous solution that induces partial crystallization of the powders over time. Thus, we can conclude that the complexation of curc with Pt(II) and the various (N^N) ligands improves its stability in biological pH conditions. This is true in particular for complexes **1–3** that did not show any degradation, and from this point of view are more suitable for their application in biological fields.

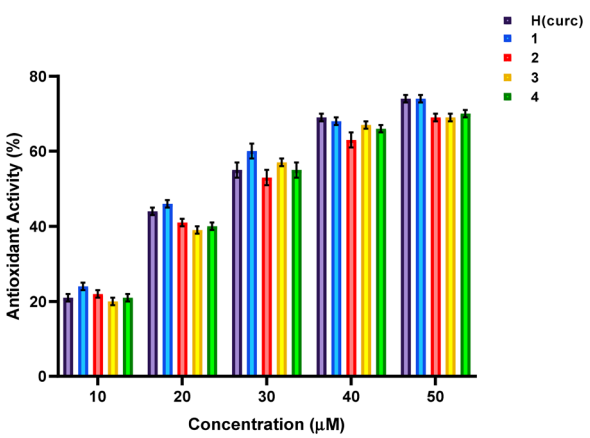

Fig. 2 Antioxidant activity of H(curc) and complexes **1–4** as a function of concentration.

3.4. Antioxidant activity

It is well known that Pt(II) metal complexes are toxic for humans and, thanks to their capability in particular to reduce the vitality of the cancer cell lines, are often used as antitumor agents.[75] Considering the possibility to utilize Pt(II) complexes for treating alternative diseases than cancer, their potential antiproliferative effects must be evaluated. Complexes **1–4** are not cytotoxic with IC_{50} values up to 200 μM against one breast cancer cell line (MDA-MB-231),[49,76] thus opening the possibility of using them as antioxidant and antibacterial agents.

The antioxidant activity of complexes **1–4** was evaluated spectrophotometrically (see the Experimental section), and compared with that of H(curc). The % antioxidant activity plotted against the concentration is reported in the histogram presented in Fig. 2. The data follow a sigmoidal curve, *i.e.*, the antioxidant activity increases monotonically with concentration, with slow growth when the data approach 0 and 100%. The corresponding IC_{50} value and the correlation coefficient (*i.e.*, R^2) extrapolated from the plot are reported in Table 1. The R^2 coefficient of determination approaches unity for all the curves, confirming the goodness of the model adopted. The value of IC_{50} for H(curc) of 24 ± 2 μM is found similar to that reported by Sökmen *et al.* (8.4 μg mL^{-1} that corresponds to 22.8 μM), while Halevas *et al.* obtained an IC_{50} of 16.6 ± 2 μM.[31,77] This discrepancy could be due to the choice of fitting the data with a linear function rather than a non-linear equation. The IC_{50} values for complexes **1–4** are all within the limit of the experimental errors and comparable with that of H(curc) (Table 1). A similar behaviour was already observed for a Cu(II) complex with the same ligands as complex **3**.[31] Thus, both the complexation with Pt(II) and the presence of different (N^N) ligands left the antioxidant properties of H(curc) unchanged. However, the best bioavailability of **1–3** evidenced by stability measurement in 10% DMSO/PBS (see section 3.3) makes these new curc-based metal complexes more suitable as antioxidant agents.

To get a deep insight into the mechanism of action of **1–4** as antioxidants, computational tools were exploited. A primary antioxidant like H(curc), generally indicated as H_nAntiox, can prevent oxidation by acting as a free radical scavenger. The

Table 1 IC_{50} values of H(curc) and complexes **1–4**

Compound	H(curc)	**1**	**2**	**3**	**4**
IC_{50} (μM) [correlation coefficient, R^2]	24 ± 2 [0.9941]	23 ± 1 [0.9992]	27 ± 1 [0.9995]	26 ± 3 [0.9891]	26 ± 1 [0.9987]

main mechanisms by which the antioxidant activity can be exerted are essentially three:

(i) hydrogen atom transfer (HAT)

$$H_nAntiox + {}^{\bullet}R \rightarrow H_{n-1}Antiox^{\bullet} + RH$$

(ii) single-electron transfer followed by proton transfer (SET-PT)

$$H_nAntiox + {}^{\bullet}R \rightarrow H_nAntiox^{+\bullet} + R^{-}$$

$$H_nAntiox^{+\bullet} \rightarrow H_{n-1}Antiox^{\bullet} + H^{+}$$

(iii) sequential proton loss electron transfer (SPLET)

$$H_nAntiox \rightarrow H_{n-1}Antiox^{-} + H^{+}$$

$$H_{n-1}Antiox^{-} + {}^{\bullet}R \rightarrow H_{n-1}Antiox^{\bullet} + R^{-}$$

Hydrogen abstraction (HAT) by the free radical $^{\bullet}R$ to form the $H_nAntiox^{\bullet}$ radical occurs in one single step. Instead in the SET-PT mechanism, first the radical cation $H_nAntiox^{+\bullet}$ is formed *via* electron transfer from the antioxidant to the free radical, which in turn deprotonates yielding the $H_nAntiox^{\bullet}$ radical. In addition, in the SPLET mechanism, two consecutive steps have to take place: the deprotonation of the phenolic compound and the subsequent electron transfer from the phenoxide anion to $^{\bullet}R$ to form the $H_nAntiox^{\bullet}$ radical. In both the stepwise mechanisms, SET-PT and SPLET, the RH is formed in the last step of the whole reaction mechanism ($R^{-} + H^{+} \rightarrow RH$).

The ability of a compound to act as an antioxidant can be predicted by computing some of its intrinsic properties, accounting for the different mechanistic hypotheses described above: (i) bond dissociation enthalpy (BDE), (ii) adiabatic ionization potential (IP) and O–H dissociation enthalpy (PDE), (iii) proton affinity (PA) and electron transfer enthalpy (ETE) for the three reaction mechanisms, respectively.

On the basis of calculations previously reported on H(curc), the main mechanism considered viable for H(curc) and its derivatives is the HAT one.[78,79] It involves the direct transfer of an H atom from the hydroxyl group of the antioxidant to the free radical. Accordingly, among the descriptors cited above, BDE represents the best reliable thermochemical parameter to describe such a mechanism. However, in order to ascertain the mechanism through which even the curc-based Pt(II) complexes **1–4** can exhibit the antioxidant activity, all the descriptors were estimated. For the sake of comparison, the same parameters were computed even for neutral H(curc), the most abundant species at physiological pH,[80] simulated in its enol form, as it is reported to be more stable than the keto one.[78] The outcomes of these calculations are shown in Fig. S27.† These data show that homolytic breaking of the H(curc) O–H bond requires the lowest amount of energy to take place, as both IP and ETE values, accounting for the rate determining steps of SET-PT and SPLET, respectively, entail a greater amount of energy for such reactions to occur. Accordingly, it can be concluded that the HAT mechanism remains the preferred pathway through which the curc bound to Pt(II) centre in **1–4** exerts its antioxidant activity. In particular, looking at the BDE values computed for the complexes (reported in Table 2), it appears evident that the radicalization of the hydroxyl group of the curc ligand requires essentially the same amount of energy expense in all cases, similar to that of the free ligand. Moreover, as the lowest BDE (weakest O–H bond) is expected to lead to the greatest antioxidant activity, comparing the computed BDE values with that of the other antioxidant molecules, the hydrogen transfer should occur rather fast. Even looking at the band gap (Fig. 3) no significant differences were found between H(curc) and its ionic Pt(II) complexes, though both the HOMO and LUMO are stabilized by the complexation. The HOMO plots of the complexes show the typical π-like molecular orbital characteristics of the curcumin ligand, whilst the LUMO plots show the implications of the metal centre in all the cases even if outspread on the whole curc π system.

Therefore, the computation of the thermochemical parameters allows to ascertain that the H(curc) HAT mechanism remains the preferred one even upon Pt(II) complexation. The free radical scavenging activity was further explored by analysing the HAT mechanism even from a kinetic point of view. This was performed by taking into consideration the hydroperoxyl radical ($HOO^{\bullet}$) as the reactive oxygen species to be quenched. Peroxyl radicals ($ROO^{\bullet}$) are, indeed, the major compounds causing oxidative stress in biological systems.[81] Moreover, since they display low to moderate reactivity, they represent a proper choice for exploring the antioxidant activity of the ionic Pt(II) complexes. The HAT mechanism was, thus, simulated by the quenching of the smallest member of the peroxyl family, $HOO^{\bullet}$, as it plays a key role in the toxic side effects accompanying aerobic respiration.[82] The relative activation and formation of free energies are included in Table 2.

Table 2 Bond dissociation enthalpy (BDE), free energy of formation (ΔG_f) and activation free energy ($\Delta G^{\ddagger}$) computed for the HAT mechanism of H(curc) and its Pt(II) complexes **1–4**. Energies are in kcal mol^{-1}

	H(curc)	1	2	3	4
BDE	76.3	76.6	76.7	76.7	76.7
ΔG_f	−9.8	−10.0	−9.7	−9.6	−9.7
$\Delta G^{\ddagger}$	13.5	12.8	13.6	12.9	13.4

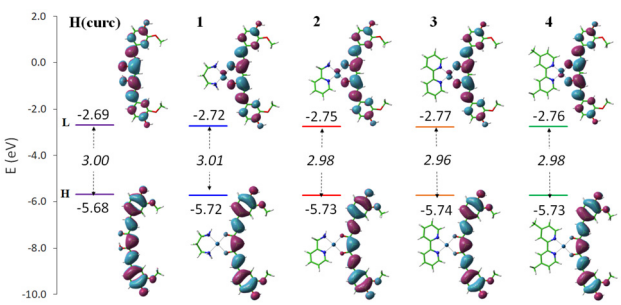

Fig. 3 Band gap (eV) in italic and the plots of frontier molecular orbitals, HOMO (H) and LUMO(L).

This journal is © The Royal Society of Chemistry 2022

From these data it emerges that the exergonicity of the HAT reaction obtained for the radical quenching by curcumin or its complexes remains in a range of less than 1 kcal mol^{-1}. Similarly, the energy barrier that has to be overcome for H abstraction from H(curc) is essentially the same whether or not curcumin is coordinated to the metal centre. The energy expense of no more than 10 kcal mol^{-1} makes the antioxidant particularly active in quenching the free radical. The obtained results for H(curc) are in agreement with a very recent study on H(curc) and its analogue behaviour in the gas phase and H_2O environment, for which the activation energy was computed to be in the range of 9.9–13.3 kcal mol^{-1}.[79]

Furthermore, in order to predict the pharmacokinetics of the curc–metal based compounds, their ADME physiochemical descriptors were estimated. As it is known, the path of each administered compound in the body relies on the physiological factors that regulate its absorption, distribution, metabolism and excretion (ADME). We considered lipophilicity, size, polarity, solubility, and the ability to satisfy the drug-likeness criteria of these Pt(II) complexes. The obtained results are collected in Table S2 in the ESI.† All the complexes have only one violation of Lipinski's rule of five associated with a high MW, the value ranging from 636.75 to 971.11, with the exception of complex **4** for which an additional violation related to $\log P_{ow}$ was found. The investigated complexes show the following properties: H-bond acceptors = 6, 2 < H-bond donors < 4, −0.32 < $\log P_{ow}$ < 8.01. The $\log P_{ow}$ value, used to denote the permeation, of the compounds to have a reasonable probability of being well absorbed, must not be greater than 5.0. Therefore, complexes **1–3** could be able to better cross the cell lipid bilayer membrane to reach the site of action, characterized by increased lipophilicity as a function of the (N^N) ligand size increase. This is indeed asserted by the experimental determination of the $\log P_{ow}$ which follows the same trend than the computed one (Table S3, ESI†). A BOILED-Egg diagram, that represents an intuitive model to predict the passive human gastrointestinal absorption (HIA) and the blood–brain barrier (BBB) permeation, is built-up using the additional data extracted from the ADME analysis. Such a diagram (Fig. S36 in ESI†) indicates that **1–3** (in the white region) can be passively absorbed by the gastrointestinal tract and are predicted to be a substrate for the efflux transporter P-glycoprotein from the central nervous system.

3.5. Antimicrobial activity

In the investigation of the antimicrobial activity of complexes **1–4**, the nature of the N-donor ligands and their chelation effects should be evaluated. Moreover, the molecular structure, the charge and the presence and nature of the counterions all have their influence on this activity.[83]

The antibacterial activity of **1–4** against *E. coli* and *S. aureus* are tested using H(curc) and DMSO as the positive and negative controls, respectively. The complexes are solubilised in DMSO at different concentrations in the range of 0.05–0.5 μg μL^{-1}. The antibacterial activities expressed as the diameter of growth inhibition area in mm with the subtraction of paper disk diameter (6 mm), are listed in Table S3, ESI.† The inhibition halos of complexes **1–4** and H(curc) at maximum concentration value for both microorganisms are reported in Fig. S37.†

The presented data clearly show that, in the concentration range considered, each Pt(II) complex and H(curc) exhibit varying degrees of inhibitory effect on the growth of the tested bacterial species. DMSO did not display any bacterial asset, confirming that the observed inhibitory effects are attributable only to the Pt(II) complexes or H(curc). Complexes **1–4** exhibit antibacterial activity against both Gram-positive and Gram-negative microorganisms with a trend depending on concentration, but with differences related to the diversity of the different (N^N) ligands coordinated to the metal centre ion. As regards *E. coli*, the bacterial growth inhibition of complexes **1–4** increases with the increase in the aromaticity of the (N^N) ligands and their overall rigidity as highlighted by the increase in the bacterial inhibition area diameter measured at various concentrations (Fig. 4). Noteworthy, in *E. coli* all the Pt(II) complexes perform better than H(curc). This increased activity with respect to H(curc) could be explained on the basis of Tweedy's chelation theory for which the polarity of the ligand and the central metal ion are reduced through charge equilibration over the whole chelated ring.[84] The sharing of the positive charge of the metal centre with the donor groups of coordinated ligands and the π-electron delocalization on the aromatic rings increases the lipophilic character of the metal complex and hence its liposolubility. These features favour the permeation of metal chelates through the lipidic layer of the bacterial membranes, causing the death of the organism.[85] It is worth noting that the lipid membrane surrounding the cells favours the passage of lipid-soluble agents, an important factor controlling the antimicrobial activity (Overton's concept). Moreover, the data obtained from the antimicrobial activity with respect to *E. coli* are in accordance with the theor-

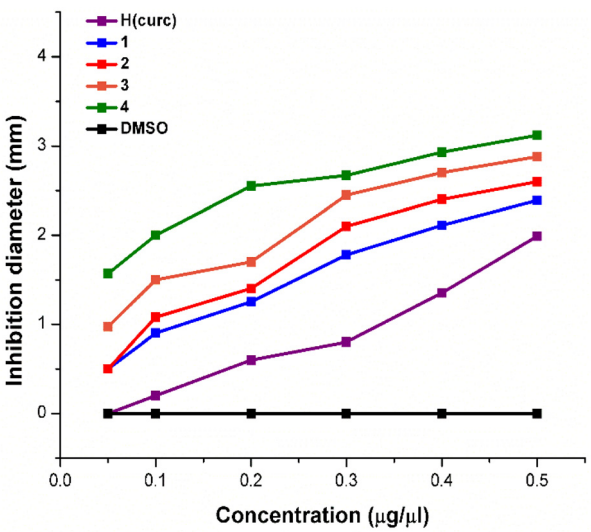

Fig. 4 The trend of bacterial inhibition area diameter against *E. coli* at various concentrations.

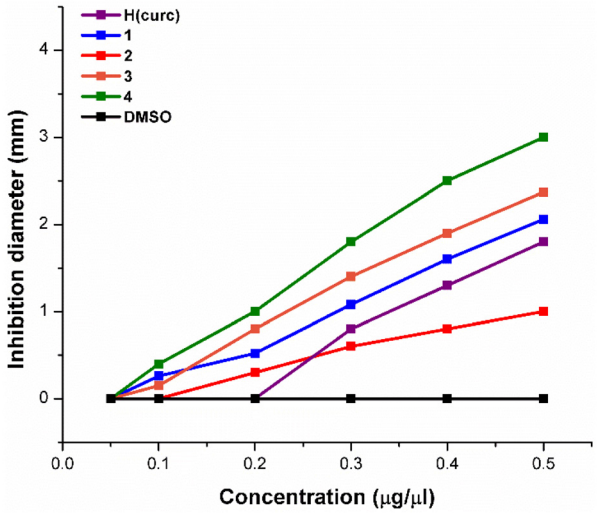

Fig. 5 The trend of bacterial inhibition area diameter against *S. aureus* at various concentrations.

etically calculated lipophilicity of complexes **1–4** (Table S2, ESI†). Indeed, the induced increase in lipophilicity should enhance the penetration of the complexes into the lipid membranes, and eventually blocks the metal binding sites in the enzymes of microorganisms. Remarkably, this trend is common for all diluted concentrations considered even for 0.05 μg μL^{-1} while at this concentration H(curc) does not show any activity (Fig. 4).

As regards *S. aureus*, data suggest that all complexes **1–4** and H(curc) are less active than in *E. coli* as is evident from Fig. 5, Table S4,† and Table 3. Accordingly, the estimation of MIC (minimum inhibitory concentration) shows that lower amounts of the complexes are needed to inhibit *E. coli* than *S. aureus*, demonstrating a greater sensitivity of *E. coli* to these complexes (Table 3).

Although the antibacterial activity of all complexes against this microorganism is lower than that measured against *E. coli*, the inhibitory effect is once again higher than the free ligand which reduces its activity until 0.3 μg μL^{-1}. In terms of halos of inhibition, the trend **4** > **3** > **2** > **1** observed for *E. coli* is almost confirmed also for *S. aureus*, except for complex **2** which shows a higher resistance with respect to **1**. Thus, probably, in the case of *S. aureus*, other mechanisms, that go beyond the lipophilic parameter, have to be taken into consideration. In any case, the non-compliant behaviour of complex **2** is still better than H(curc) at low concentrations (0.2 μg μL^{-1}) because of the loss of the activity of the free ligand at that value.

Table 3 Presumed MIC (μg μL^{-1}) for H(curc) and the complexes **1–4**

		MIC[a]			
Microrganism	H(curc)	**1**	**2**	**3**	**4**
S. aureus	0.2–0.3	0.05–0.1	0.1–0.2	0.05–0.1	0.05–0.1
E. coli	<0.05	<0.05	<0.05	<0.05	<0.05

[a] Range of inhibition (μg μL^{-1}).

4. Conclusions

With the aim to develop new curc–metal based compounds with multi-functional biological properties, nominally antioxidant and antimicrobial, new cationic curcumin–Pt(II) complexes, of the general formula $[(N^N)Pt(curc)]CF_3SO_3$, **1–4**, were synthesized and fully characterised. Different (N^N) bidentate ligands (pn, pic, bipy and phen) were used to evaluate the influence on both the physical and biological properties of the derived Pt(II) complexes. From the photophysical characterization data, under physiological pH conditions, the coordination of H(curc) to the Pt(II) ion in complexes **1–4** appears evident, implying consistent structural modifications of free H(curc) and inducing its stability, albeit with some differences related to the (N^N) chelated unit. Indeed, complexes **1–3** did not show any degradation under these conditions, overcoming the major drawbacks of H(curc) related to poor bioavailability and easy oxidability and photodegradability. Otherwise, the presence of substituents on the 2,2′-bipyridine ligand results in the destabilization of the derived complex **4** which, in the biological environment, undergoes a certain level of degradation. Once the absence of cytotoxic activity against one breast cancer cell line (MDA-MB-231) is tested, the antioxidant properties of complexes **1–4** were evaluated spectrophotometrically and compared with that of H(curc). As a result, the antioxidant activity of H(curc) remains unchanged upon coordination to the Pt(II) ion, with no differences related to the different (N^N) chelating ligands. Moreover, the same mechanism of antioxidant action is confirmed by both experimental and theoretical studies. For better stability under biological conditions (at least in the case of complexes **1–3**) and their antioxidant activity, these new curc-based metal complexes are therefore more suitable antioxidant agents with respect to H(curc).

Finally, complexes **1–4**, showed enhanced antimicrobial activity with respect to pure H(curc), as revealed by the growth inhibition of *E. coli* and *S. aureus* microorganisms even at low concentrations. The antibacterial activity is found to be concentration dependent and related to the nature of the (N^N) chelating ligands. Indeed, the bacterial growth inhibition of complexes **1–4** increases with the increase in the aromaticity of the (N^N) ligands, which implies an increase of lipophilicity, as confirmed through theoretical calculations.

Concluding the complexation of H(curc) to Pt(II) metal ions for the formation of the new ionic $[(N^N)Pt(curc)]CF_3SO_3$ complexes appears to be a successful way to obtain photochemical metal-based curc carrier antioxidant agents and more efficient antimicrobial species. Moreover, the careful choice of the ancillary (N^N) ligands is able to modulate the lipophilicity properties of the derived Pt(II) complexes, necessary for the enhancement of the antibacterial activity.

This journal is © The Royal Society of Chemistry 2022

Author contributions

R. C. and G. D. M. contributed equally to this work as first authors.

Conflicts of interest

There are no conflicts to declare.

Acknowledgements

This research was supported by the project PON "Ricerca e Innovazione" 2014-2020–Progetto STAR 2–PIR01_00008 funded by MIUR (Ministero dell'Università e della Ricerca) and the project PON ARS01_00401, "Sviluppo di tecnologie di materiali e di tracciabilità per la sicurezza e la qualità dei cibi—Demetra". I. A. is grateful to Alessio Giovinazzo for his contribution to the preparation of the selected complexes and to Prof. Nicola Ferri for the cytotoxic activity measurements, respectively.

References

1 A. K. Renfrew, *Metallomics*, 2014, **6**, 1324–1335.
2 K. Karami, Z. Mehri Lighvan, H. Farrokhpour, M. Dehdashti Jahromi and A. A. Momtazi-borojeni, *J. Biomol. Struct. Dyn.*, 2018, **36**, 3324–3340.
3 P. Štarha and Z. Trávníček, *Coord. Chem. Rev.*, 2019, **395**, 130–145.
4 B. Sanz Mendiguchia, I. Aiello and A. Crispini, *Dalton Trans.*, 2015, **44**, 9321–9334.
5 M. G. A. El-Wahed, M. S. Refat and S. M. El-Megharbel, *J. Mol. Struct.*, 2008, **892**, 402–413.
6 K. L. Haas and K. J. Franz, *Chem. Rev.*, 2009, **109**, 4921–4960.
7 S. C. Gupta, B. Sung, J. H. Kim, S. Prasad, S. Li and B. B. Aggarwal, *Mol. Nutr. Food Res.*, 2013, **57**, 1510–1528.
8 Z. Stanić, *Plant Foods Hum. Nutr.*, 2017, **72**, 1–12.
9 S. Hewlings and D. Kalman, *Foods*, 2017, **6**, 92.
10 B. Salehi, Z. Stojanović-Radić, J. Matejić, M. Sharifi-Rad, N. V. Anil Kumar, N. Martins and J. Sharifi-Rad, *Eur. J. Med. Chem.*, 2019, **163**, 527–545.
11 M. Urošević, L. Nikolić, I. Gajić, V. Nikolić, A. Dinić and V. Miljković, *Antibiotics*, 2022, **11**, 135.
12 K. Bairwa, J. Grover, M. Kania and S. M. Jachak, *RSC Adv.*, 2014, **4**, 13946.
13 T. Ak and I. Gülçin, *Chem.-Biol. Interact.*, 2008, **174**, 27–37.
14 G. K. Jayaprakasha, L. Jaganmohan Rao and K. K. Sakariah, *Food Chem.*, 2006, **98**, 720–724.
15 K. I. Priyadarsini, D. K. Maity, G. H. Naik, M. S. Kumar, M. K. Unnikrishnan, J. G. Satav and H. Mohan, *Free Radicals Biol. Med.*, 2003, **35**, 475–484.
16 Y. M. Sun, H. Y. Zhang, D. Z. Chen and C. B. Liu, *Org. Lett.*, 2002, **4**, 2909–2911.
17 L. Shen and H. F. Ji, *Spectrochim. Acta, Part A*, 2007, **67**, 619–623.
18 S. Zorofchian Moghadamtousi, H. Abdul Kadir, P. Hassandarvish, H. Tajik, S. Abubakar and K. Zandi, *BioMed Res. Int.*, 2014, **2014**, 1–12.
19 C. D. Lao, M. T. Ruffin IV, D. Normolle, D. D. Heath, S. I. Murray, J. M. Bailey, M. E. Boggs, J. Crowell, C. L. Rock and D. E. Brenner, *BMC Complementary Altern. Med.*, 2006, **6**, 4–7.
20 P. Anand, A. B. Kunnumakkara, R. A. Newman and B. B. Aggarwal, *Mol. Pharm.*, 2007, **4**, 807–818.
21 Z. Hussain, H. E. Thu, S. F. Ng, S. Khan and H. Katas, *Colloids Surf., B*, 2017, **150**, 223–241.
22 A. C. da Silva, P. D. de F. Santos, J. T. do P. Silva, F. V. Leimann, L. Bracht and O. H. Gonçalves, *Trends Food Sci. Technol.*, 2018, **72**, 74–82.
23 M. F. S. Jadid, B. Shademan, R. Chavoshi, N. Seyyedsani, E. Aghaei, E. Taheri, P. Goleij, S. Hajazimian, V. Karamad, J. Behroozi, M. N. Sabet, A. Isazadeh and B. Baradaran, *Environ. Toxicol.*, 2021, **36**, 1043–1051.
24 A. Zarrabi, A. Zarepour, A. Khosravi, Z. Alimohammadi and V. K. Thakur, *Fibers*, 2021, **9**, 1–17.
25 S. Sun, X. Du, M. Fu, A. R. Khan, J. Ji, W. Liu and G. Zhai, *Int. J. Pharm.*, 2021, **595**, 120227.
26 M. Bagheri, M. H. Fens, T. G. Kleijn, R. B. Capomaccio, D. Mehn, P. M. Krawczyk, E. M. Scutigliani, A. Gurinov, M. Baldus, N. C. H. Van Kronenburg, R. J. Kok, M. Heger, C. F. Van Nostrum and W. E. Hennink, *Mol. Pharm.*, 2021, **18**, 1247–1263.
27 A. Shakeri, Y. Panahi, T. P. Johnston and A. Sahebkar, *BioFactors*, 2019, **45**, 304–317.
28 S. Wanninger, V. Lorenz, A. Subhan and F. T. Edelmann, *Chem. Soc. Rev.*, 2015, **44**, 4986–5002.
29 T. Q. Hieu and D. T. T. Thao, *J. Chem.*, 2019, **2019**, 1–8.
30 Q. H. Tran and T. T. Doan, *New J. Chem.*, 2020, **44**, 13036–13045.
31 E. Halevas, A. Pekou, R. Papi, B. Mavroidi, A. G. Hatzidimitriou, G. Zahariou, G. Litsardakis, M. Sagnou, M. Pelecanou and A. A. Pantazaki, *J. Inorg. Biochem.*, 2020, **208**, 111083.
32 L. Gorgannezhad, G. Dehghan, S. Y. Ebrahimipour, A. Naseri and J. E. Nazhad Dolatabadi, *J. Mol. Struct.*, 2016, **1109**, 139–145.
33 E. H. Ismail, D. Y. Sabry, H. Mahdy and M. M. H. Khalil, *J. Sci. Res.*, 2014, **6**, 509–519.
34 Y. M. Song, J. P. Xu, L. Ding, Q. Hou, J. W. Liu and Z. L. Zhu, *J. Inorg. Biochem.*, 2009, **103**, 396–400.
35 G. Mazzone, S. Scoditti, R. Caligiuri, L. Ricciardi, E. Sicilia, M. G. Lupo, I. Rimoldi, N. Godbert, M. La Deda, A. Ionescu, M. Ghedini, I. Aiello and G. Facchetti, *Inorg. Chem.*, 2022, **61**, 7188–7200.
36 L. Ricciardi, M. La Deda, A. Ionescu, N. Godbert, I. Aiello and M. Ghedini, *Dalton Trans.*, 2017, **46**, 12625–12635.
37 A. Ionescu, R. Caligiuri, N. Godbert, L. Ricciardi, M. La Deda, M. Ghedini, N. Ferri, M. G. Lupo, G. Facchetti, I. Rimoldi and I. Aiello, *Appl. Organomet. Chem.*, 2020, **34**(3), 1–11.
38 A. Ionescu, N. Godbert, L. Ricciardi, M. La Deda, I. Aiello, M. Ghedini, I. Rimoldi, E. Cesarotti, G. Facchetti, G. Mazzeo, G. Longhi, S. Abbate and M. Fusè, *Inorg. Chim. Acta*, 2017, **461**, 267–274.

39 K. Mitra, S. Gautam, P. Kondaiah and A. R. Chakravarty, *Angew. Chem., Int. Ed.*, 2015, **54**, 13989–13993.
40 K. Mitra, S. Gautam, P. Kondaiah and A. R. Chakravarty, *Eur. J. Inorg. Chem.*, 2017, **2017**, 1753–1763.
41 A. Upadhyay, S. Gautam, V. Ramu, P. Kondaiah and A. R. Chakravarty, *Dalton Trans.*, 2019, **48**, 17556–17565.
42 E. A. Thackaberry, *Expert Opin. Drug Metab. Toxicol.*, 2012, **8**, 1419–1433.
43 P. Sacchi, L. Loconte, G. Macetti, S. Rizzato and L. Lo Presti, *Cryst. Growth Des.*, 2019, **19**, 1399–1410.
44 A. A. Abe, C. Oliviero Rossi, P. Caputo, M. P. De Santo, N. Godbert and I. Aiello, *Materials*, 2021, **14**, 1622.
45 J. Josephsen, *Inorg. Chim. Acta*, 2018, **478**, 54–58.
46 K. A. Mitchell and C. M. Jensen, *Inorg. Chem.*, 1995, **34**, 4441–4446.
47 M. Kato and M. Ikemori, *Acta Crystallogr., Sect. C: Cryst. Struct. Commun.*, 2003, **59**, m25–m26.
48 A. Ionescu, N. Godbert, I. Aiello, L. Ricciardi, M. La Deda, A. Crispini, E. Sicilia and M. Ghedini, *Dalton Trans.*, 2018, **47**, 11645–11657.
49 I. Rimoldi, G. Facchetti, G. Lucchini, E. Castiglioni, S. Marchianò and N. Ferri, *Bioorg. Med. Chem.*, 2017, **25**, 1907–1913.
50 M. S. Blois, *Nature*, 1958, **181**, 1199–1200.
51 S. B. Kedare and R. P. Singh, *J. Food Sci. Technol.*, 2011, **48**, 412–422.
52 Z. Chen, R. Bertin and G. Froldi, *Food Chem.*, 2013, **138**, 414–420.
53 M. J. Frisch, G. W. Trucks, H. B. Schlegel, G. E. Scuseria, M. A. Robb, J. R. Cheeseman, G. Scalmani, V. Barone, G. A. Petersson, H. Nakatsuji, X. Li, M. Caricato, A. V. Marenich, J. Bloino, B. G. Janesko, R. Gomperts, B. Mennucci, H. P. Hratchian, J. V. Ortiz, A. F. Izmaylov, J. L. Sonnenberg, D. Williams-Young, F. Ding, F. Lipparini, F. Egidi, J. Goings, B. Peng, A. Petrone, T. Henderson, D. Ranasinghe, V. G. Zakrzewski, J. Gao, N. Rega, G. Zheng, W. Liang, M. Hada, M. Ehara, K. Toyota, R. Fukuda, J. Hasegawa, M. Ishida, T. Nakajima, Y. Honda, O. Kitao, H. Nakai, T. Vreven, K. Throssell, J. A. Montgomery Jr., J. E. Peralta, F. Ogliaro, M. J. Bearpark, J. J. Heyd, E. N. Brothers, K. N. Kudin, V. N. Staroverov, T. A. Keith, R. Kobayashi, J. Normand, K. Raghavachari, A. P. Rendell, J. C. Burant, S. S. Iyengar, J. Tomasi, M. Cossi, J. M. Millam, M. Klene, C. Adamo, R. Cammi, J. W. Ochterski, R. L. Martin, K. Morokuma, O. Farkas, J. B. Foresman and D. J. Fox, *Gaussian 16, Revision C.01*, Gaussian, Inc., Wallin, 2019.
54 A. D. Becke, *Phys. Rev. A*, 1988, **38**, 3098–3100.
55 P. J. Stephen, F. J. Devlin, C. F. Chabalowski and M. J. Frisch, *J. Phys. Chem.*, 1994, **98**, 11623–11627.
56 A. V. Marenich, C. J. Cramer and D. G. Truhlar, *J. Phys. Chem. B*, 2009, **113**, 6378–6396.
57 K. Fukui, *Acc. Chem. Res.*, 1981, **14**, 363–368.
58 H. P. Hratchian and H. B. Schlegel, in *Theory and Applications of Computational Chemistry: The First 40 Years*, 2005, pp. 195–249.
59 H. S. Yu, X. He, S. L. Li and D. G. Truhlar, *Chem. Sci.*, 2016, **7**, 5032–5051.
60 Z. Marković, J. Tošović, D. Milenković and S. Marković, *Comput. Theor. Chem.*, 2016, **1077**, 11–17.
61 A. Daina, O. Michielin and V. Zoete, *Sci. Rep.*, 2017, **7**, 1–13.
62 J. H. Ortez, in *Manual of Antimicrobial Susceptibility Testing*, ed. M. B. Coyle, 2005, pp. 39–52.
63 A. W. Bauer, M. M. Kirby, J. C. Sherris and M. Turck, *Am. J. Clin. Pathol.*, 1966, **45**, 493–496.
64 N. Godbert, T. Pugliese, I. Aiello, A. Bellusci, A. Crispini and M. Ghedini, *Dalton Trans.*, 2007, **32**, 5105–5111.
65 F. Scarpelli, A. Ionescu, L. Ricciardi, P. Plastina, I. Aiello, M. La Deda, A. Crispini, M. Ghedini and N. Godbert, *Dalton Trans.*, 2016, **45**, 17264–17273.
66 W. J. Geary, *Coord. Chem. Rev.*, 1971, **7**, 81–122.
67 R. Benassi, E. Ferrari, S. Lazzari, F. Spagnolo and M. Saladini, *J. Mol. Struct.*, 2008, **892**, 168–176.
68 M. A. Subhan, K. Alam, M. S. Rahaman, M. A. Rahman and R. Awal, *J. Sci. Res.*, 2013, **6**, 97–109.
69 D. H. Johnston and D. F. Shriver, *Inorg. Chem.*, 1993, **32**, 1045–1047.
70 C. Párkányi, M. R. Stem-Beren, O. R. Martínez, J. J. Aaron, M. Bulaceanu-MacNair and A. F. Arrieta, *Spectrochim. Acta, Part A*, 2004, **60**, 1805–1810.
71 K. I. Priyadarsini, *J. Photochem. Photobiol., C*, 2009, **10**, 81–95.
72 All the differences observed between the absorption spectra in MeOH and DMSO are attributable to both the different polarity of the solvents and to the solubility of each species in these media.
73 Y. B. Tsaplev, V. A. Lapina and A. V. Trofimov, *Dyes Pigm.*, 2020, **177**, 108327.
74 M. Griesser, V. Pistis, T. Suzuki, N. Tejera, D. A. Pratt and C. Schneider, *J. Biol. Chem.*, 2011, **286**, 1114–1124.
75 G. Facchetti and I. Rimoldi, *Bioorg. Med. Chem. Lett.*, 2019, **29**, 1257–1263.
76 G. Facchetti, N. Ferri, M. G. Lupo, L. Giorgio and I. Rimoldi, *Eur. J. Inorg. Chem.*, 2019, **2019**, 3389–3395.
77 M. Sökmen and M. Akram Khan, *Inflammopharmacology*, 2016, **24**, 81–86.
78 A. Galano, R. Álvarez-Diduk, M. T. Ramírez-Silva, G. Alarcón-Ángeles and A. Rojas-Hernández, *Chem. Phys.*, 2009, **363**, 13–23.
79 A. Purushothaman, K. S. Teena Rose, J. M. Jacob, R. Varatharaj, K. Shashikala and D. Janardanan, *Food Chem.*, 2022, **373**, 131499.
80 M. Bernabé-Pineda, M. T. Ramírez-Silva, M. Romero-Romo, E. González-Vergara and A. Rojas-Hernández, *Spectrochim. Acta, Part A*, 2004, **60**, 1091–1097.
81 P. Terpinc and H. Abramovič, *Food Chem.*, 2010, **121**, 366–371.
82 A. D. N. J. De Grey, *DNA Cell Biol.*, 2002, **21**, 251–257.
83 A. Regiel-Futyra, J. M. Dąbrowski, O. Mazuryk, K. Śpiewak, A. Kyzioł, B. Pucelik, M. Brindell and G. Stochel, *Coord. Chem. Rev.*, 2017, **351**, 76–117.
84 G. B. Tweedy, *Phytopathology*, 1964, **55**, 910–914.
85 S. J. Sabounchei, P. Shahriary, S. Salehzadeh, Y. Gholiee and A. Chehregani, *C. R. Chim.*, 2015, **18**, 564–572.

This journal is © The Royal Society of Chemistry 2022

nanomaterials

MDPI

Article

The Rainbow Arching over the Fluorescent Thienoviologen Mesophases

Giuseppina Anna Corrente [1], Giuseppe Di Maio [2], Massimo La Deda [2,3,*], Odda Ruiz de Ballesteros [4], Bartolo Gabriele [5], Lucia Veltri [5], Finizia Auriemma [4] and Amerigo Beneduci [1,*]

1 Laboratory of Physical Chemistry, Materials and Processes for Industry, Environment and Cultural Heritage, Department of Chemistry and Chemical Technologies, University of Calabria, Via P. Bucci, Cubo 15D, 87036 Arcavacata di Rende, CS, Italy
2 Laboratory of Inorganic Molecular Materials, Department of Chemistry and Chemical Technologies, University of Calabria, Via P. Bucci, Cubo 14C, 87036 Arcavacata di Rende, CS, Italy
3 CNR Nanotec, Institute of Nanotechnology, U.O.S. Cosenza, 87036 Arcavacata di Rende, CS, Italy
4 Dipartimento di Scienze Chimiche, Università di Napoli Federico II, Complesso Monte Sant'Angelo, Via Cintia, 80126 Napoli, Italy
5 Laboratory of Industrial and Synthetic Organic Chemistry (LISOC), Department of Chemistry and Chemical Technologies, University of Calabria, Via Pietro Bucci 12/C, 87036 Arcavacata di Rende, CS, Italy
* Correspondence: massimo.ladeda@unical.it (M.L.D.); amerigo.beneduci@unical.it (A.B.)

Abstract: Thermofluorochromic materials exhibit tunable fluorescence emission on heating or cooling. They are highly desirable for applications ranging from temperature sensing to high-security anti-counterfeiting. Luminescent matrices based on liquid crystals are very promising, particularly those based on liquid crystals with intrinsic fluorescence. However, only a few examples have been reported, suggesting ample margins for development in the field, due to the wide range of fluorophores and supramolecular organizations to be explored. Moreover, thermofluorochromic liquid crystals can be tailored with further functionalities to afford multi-stimuli responsive materials. For the first time, herein we report the thermofluorochromism of thienoviologen liquid crystals, already known to show bulk electrochromism and electrofluorochromism. In particular, we studied their photophysics in the 25 °C–220 °C range and as a function of the length of the N-linear alkyl chains, *m* ($9 \leq m \leq 12$ C atoms), and the type of anion, *X* (*X* = OTs^-, OTf^-, BF_4^-, NTf_2^-). Interestingly, by changing the parameters *m*, *X* and T, their fluorescence can be finely tuned in the whole visible spectral range up to the NIR, by switching among different mesophases. Importantly, by fixing the structural parameters *m* and *X*, an interesting thermofluorochromism can be achieved for each thienoviologen in a homologous series, leading to a switch of the emitted light from red to green and from white to blue as a consequence of the temperature-induced variation in the supramolecular interactions in the self-assembled phases.

Keywords: thienoviologens liquid crystals; self-assembly; supramolecular interactions; bulk fluorescence; thermofluorochromism; anticounterfeiting; single layer thermofluorochromic devices

check for updates

Citation: Corrente, G.A.; Di Maio, G.; La Deda, M.; Ruiz de Ballesteros, O.; Gabriele, B.; Veltri, L.; Auriemma, F.; Beneduci, A. The Rainbow Arching over the Fluorescent Thienoviologen Mesophases. *Nanomaterials* **2022**, *12*, 4284. https://doi.org/10.3390/nano12234284

Academic Editors: Paola Astolfi, Shin-Tson Wu, Michela Pisani and Francesco Vita

Received: 12 November 2022
Accepted: 30 November 2022
Published: 1 December 2022

Publisher's Note: MDPI stays neutral with regard to jurisdictional claims in published maps and institutional affiliations.

Copyright: © 2022 by the authors. Licensee MDPI, Basel, Switzerland. This article is an open access article distributed under the terms and conditions of the Creative Commons Attribution (CC BY) license (https://creativecommons.org/licenses/by/4.0/).

1. Introduction

Smart luminescent materials able to exhibit different colors in response to external stimuli have aroused immense attention in the fields of lighting, sensing, displays, and optoelectronics [1–3]. These materials are known as fluorochromic, whose prefix depends on the external stimulus to which they are responsive, i.e., thermo-, electro-, vapo-, solvato-, and mechano- [4–6]. Thermofluorochromism (TFC) deals with the reversible modulation of the emission color by temperature [7–9]. These materials are gaining a lot of attention due to their potential applications in sensors, optoelectronic devices, and anticounterfeiting market, among others [10–14]. The two main strategies employed to afford TFC materials are the use of intrinsically switchable emitters [15], whose photoluminescence

modulation depends on their intrinsic sensitivity to temperature changes or the use of emitters in bulk arrangements or embedded into a matrix for which a thermal stimulus changes the environmental structural parameters, thereby inducing a modulation of the photoluminescence, e.g., liquid crystals, gels, and polymers [16]. The main challenges in this field are the development of multithermofluorochromic materials by which a gradual color modulation could be achieved and of TFC materials capable of working in wide temperature ranges [17]. Moreover, TFC materials that respond to further stimuli other than the thermal one are highly desirable for multi-level anticounterfeiting technology [8,13,14,17,18]. Luminescent matrices based on liquid crystals (LCs) have received a great deal of attention because they can be developed either by incorporating a fluorophore in the LC mesophase [16] or by designing LCs with intrinsic photoluminescence [17–22]. The last ones are particularly interesting due to their intrinsic light-emitting ability [18] and unique supramolecular organization [19,20]. Lu et al. reported a novel luminescent liquid crystal, (2Z,2′Z)-2,2′-(1,4-phenylene)bis(3-(4-(dodecyloxy)phenyl)acrylonitrile) (PDPA), which shows green, yellow, and orange colors depending on the self-assembled structure. Its luminescence can be tuned by mechanical shearing and thermal annealing, indicating good capability for piezochromic and thermochromic luminescence switching [21]. More recently, Liao and coworkers, showed the thermochromism of two pyrene liquid crystal derivatives, 1,6-Bis((3,4,5-tris(dodecyloxy)phenyl)-ethynyl)pyrene and 1,6-Bis((3,4,5-tributoxyphenyl)ethynyl)-pyrene, which underwent an apparent emission color change from yellow to green as a function of the liquid crystalline phase. The thermochromic behavior of these materials is mainly due to changes in intermolecular interactions [22]. In an effort to design multiresponsive fluorochromic materials, a promising class is that of ionic liquid crystals (ILCs), because they share properties typical of liquid crystals and some properties of ionic liquids (ILs) [23–28]. Indeed, in addition to their exceptional mesophase electrochemical properties (high ion conductivity, high electronic charge mobility, reversible redox chemistry), they can be designed to incorporate conjugated rigid cores with specific redox active and optical properties, among which are electrochromism [28–39] and electrofluorochromism [37,40,41].

Beneduci et al. [40,41] discovered electrofluorochromism in π-conjugated ILCs by demonstrating that the electrochemical reduction of thienoviologen bistriflimide ILCs, in both columnar and smectic phases, increases fluorescence intensity when the radical cation is formed, while quenching occurs upon further reduction to the neutral species [41]. Furthermore, when monoreduction occurs in the isotropic liquid state, the intensity of the fluorescence increases with a red shift (100 nm) of the light emission due to an electric-field-induced transition to the smectic mesophase. Starting from this knowledge and from the rich thermotropic behavior of the liquid crystalline thienoviologens of the type *m*VX with *m* ($9 \leq m \leq 12$ C atoms) defining the length of the promesogenic linear alkyl chains used for pyridine quaternization and X defining the counterion (X = OTs^-, OTf^-, NTf_2^-, BF_4^-) (Figure 1); herein, we studied their thermofluorochromic properties in a wide temperature range (25 °C–220 °C) and as a function of the above structural parameters. Interestingly, by changing the parameters *m*, *X*, and T, their fluorescence can be finely tuned in the whole visible spectral range up to the NIR, by switching among different mesophases. Importantly, by fixing the structural parameters *m* and *X*, an interesting thermofluorochromism can be achieved for each thienoviologen in a homologous series, leading to a switch of the emitted light from red to green and from almost white to blue, as a consequence of the temperature-induced variation of the supramolecular interactions in the self-assembled phases.

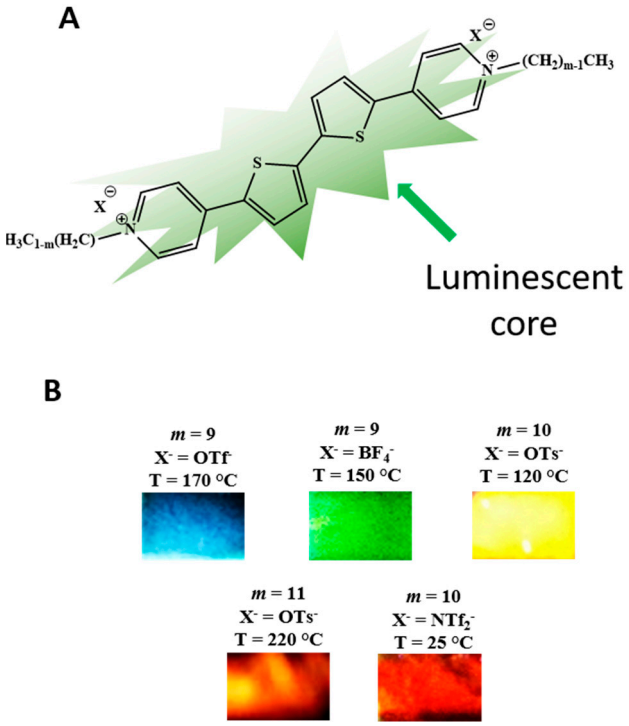

Figure 1. (**A**) Structures of the thienoviologens salts mVX forming ionic liquid crystals, with m indicating the promesogenic alkyl chains attached to the π-extended luminescent thienopyridinium core (V) and X^- the anion. (**B**) Photographs of the light emitted (excitation at 430 nm) by thin films formed between two glass substrates by some thienoviologen salts in the LC state, showing the full color palette obtainable as a function of X^-, m and the temperature (T).

2. Materials and Methods

2.1. Synthesis and Characterization

Thienoviologens 4,4′-(2,2′-bithiophene-5,5′-diyl)bis(1-alkylpyridinium) triflate, tosilate, and triflimide were prepared by metathesis from the corresponding iodide as previously reported [29]. The same procedure was employed for the preparation of 4,4′-(2,2′-bithiophene-5,5′-diyl)bis(1-nonylpyridinium) tetrafluoroborate 9V(BF_4) starting from 4,4′-(2,2′-bithiophene-5,5′-diyl)bis(1-nonylpyridinium) iodide (for more details see the Supporting information section). The newly synthesized 9V(BF_4) compound was added to this large series to further evaluate the influence of the anion on the mesomorphic and photophysical properties.

All other materials were commercially available and used without further purification. The compounds were characterized by IR, ^{1}H NMR, ^{19}F NMR spectroscopy, and HR mass spectrometry. ^{1}H NMR spectra were recorded at 25 °C in MeOH-d_4 on a Avance 300 Bruker NMR spectrometer (Bruker, Milano, Italy) at 300 MHz with Me_4Si as an internal standard. ^{19}F NMR spectra were recorded at 25 °C in MeOH-d_4 on an Avance 500 Bruker NMR spectrometer at 471 MHz with $CFCl_3$ as an internal standard. Chemical shifts (δ) and coupling constants (J) are given in ppm and in Hz, respectively. IR spectra were taken with a Shimadzu IR Affinity-1S spectrometer (Shimadzu, Milano, Italy). Mass spectra were obtained using a Q-TOF-MS, equipped with an electrospray ion source (ESI) operated in dual ion mode (Agilent, Milano, Italy). A total of 10 µL of the sample solutions (CH_3OH) was introduced by continuous infusion at a flow rate of 200 L min^{-1} with the aid of a syringe pump. Experimental conditions were as follows: capillary voltage, 4000 V; nebulizer pressure, 20 psi; flow rate of drying gas, 10 L/min; temperature of sheath gas, 325 °C; flow rate of sheath gas, 10 L/min; skimmer voltage, 60 V; OCT1 RF Vpp, 750 V; fragmentor voltage, 170 V. The spectra data were recorded in the m/z range of 100–1000 Da

in a centroid pattern in full-scan MS analysis mode. The MS/MS data of the selected compounds were obtained by regulating diverse collision energies (18–45 eV).

2.2. Polarizing Optical Microscopy (POM), Differential Scanning Calorimetry (DSC), and X-ray Powder Diffraction (XRD)

The thermotropic behavior of the sample $9VBF_4$ was studied by POM, DSC, and XRD. Sample textures were observed by a Leitz Laborlux 12 POL polarizing optical microscope (ZEISS, Milano, Italy). Samples were analyzed on thin films formed between cover slides on heating and cooling thermal cycles controlled by a Linkam LTS350 hot stage (Linkam, Salford, UK). DSC thermograms were recorded with a DSC apparatus Mettler DSC-822 (Mettler-Toledo, Milano, Italy), operating in a flowing N_2 atmosphere at a 10 °C min^{-1} scanning rate. DSC data were treated, if it was necessary, by a deconvolution algorithm to produce separated Gauss shape curves related to the different thermic events using the software of the DSC apparatus.

TGA measurements were performed using an analytical thermobalance PerkinElmer TGA 4000 (Mettler-Toledo, Milano, Italy), operating at a heating rate of 10 °C/min in air atmosphere.

X-ray powder diffraction data were collected with an automatic Philips diffractometer (Malvern Panalytical S.r.l., Lissone (MI), Italy), equipped with a variable temperature camera Anton Paar TTK450 (Rivoli (TO), Italy) and equipped with a standard sample holder for measurements in reflection geometry (depth 500 μm), using Ni-filtered Cu Kα radiation (λ = 1.5418 Å), at a continuous scanning rate of 0.1°(Δ2θ)/14.3s(Δt) with a 2θ diffraction angle. The samples were heated and cooled stepwise at a rate of 10 °C/min to the appropriate temperature, and diffraction data were recorded immediately after reaching the selected temperature.

2.3. Photophysical Measurements

Spectrofluorimetric grade solvents were used for photophysical investigations in solution at room temperature. A Perkin Elmer Lambda 900 spectrophotometer (PerkinElmer Inc., Waltham, MA, USA) was employed to obtain the absorption spectra. Steady-state emission spectra were recorded on a HORIBA Jobin-Yvon Fluorolog-3 FL3-211 spectrometer (Horiba Jobin Yvon, Orbassano, Italy) equipped with a 450-W xenon arc lamp, double-grating excitation and single-grating emission monochromators (2.1 nm mm-1 dispersion; 1200 grooves mm^{-1}), and a Hamamatsu R928 photomultiplier tube. The glass slab sandwich, containing the LC film sample, was placed into the fluorimeter sample holder on a customized temperature-controlled hot stage realized in Teflon by CaLCTec s.r.l. (Rende, Italy), with 1 °C uncertainty in the temperature. Measurements were performed in a front-face geometry.

Time-resolved measurements were performed using the time-correlated single-photon-counting option on the Fluorolog 3. Laser Nanoled at 379 nm, full-width-half-maximum 750 ps, with repetition rate at 1 MHz, was used to excite the sample. Excitation sources were mounted directly on the sample chamber at 90° to a single-grating emission monochromator (2.1 nm mm^{-1} dispersion; 1200 grooves mm^{-1}) and collected with a TBX-04-D single-photon-counting detector. The photons collected at the detector are correlated by a time-to-amplitude converter to the excitation pulse. Signals were collected using an IBH Data Station Hub photon-counting module, and data analysis was performed using the commercially available DAS6 software (HORIBA Jobin-Yvon IBH). Goodness of fit was assessed by minimizing the reduced χ2-function and visual inspection of the weighted residuals.

The emission quantum yields of the samples were obtained by means of a Labsphere optical Spectralon integrating sphere (diameter of 102 mm), which provides a reflectance >99% over 400 to 1500 nm range (>95% within 250–2500 nm). The sphere accessories were made from Teflon (rod and sample holders) or Spectralon (baffle). The sphere was mounted in the optical path of the spectrofluorometer using, as excitation source, a 450 W xenon lamp coupled with a double-grating monochromator for selecting wavelengths. Cylindrical tubes

containing the solution samples were placed into the sphere, while the glass slab sandwich containing the LC film sample was placed into the sphere on a customized temperature-controlled hot stage realized in Teflon by CaLCTec s.r.l. (Rende, Italy), with 1 °C uncertainty in the temperature. The procedure used to determine the emission quantum yield was based on the de Mello method [42], slightly modified [43,44]. The emission quantum yield determination is given by:

$$\Phi_L = \frac{(E_c \ - (1 - A)E_a)}{L_a \ A}$$

where A is the value of the absorbance of the sample at the excitation wavelength measured as:

$$A = \frac{(L_a \ - L_c)}{L_a}$$

where L_a is the integrated excitation profile when the reference sample is diffusely illuminated by the integrated sphere's surface; L_c is the integrated excitation profile when the sample is diffusely illuminated by the integrated sphere's surface; E_c and E_a are the integrated luminescence (corrected for the detector wavelength response) of the sample and the reference sample, respectively, caused by indirect illumination from the sphere. The reference sample is an empty glass slab sandwich. The experimental uncertainties were 1 nm for the band maxima of the luminescence spectra and 5% for the emission quantum yield values.

2.4. Molecular Mechanics Calculation

Low-energy model structures of the dimeric building units were obtained using the Biovia Materials Studio program (Milano, Italy) through the utility Forcite. The forcefield COMPASS was used for geometry optimization [45].

3. Results

3.1. Thermotropic Behavior

As summarized in Table 1, variation in either the anion or the length of the promesogenic chains allowed us to afford a wide mesophases range that spans smectic (SmC and SmA), columnar rectangular (Colr), lamello-columnar (Coll), and nematic discotic/columnar (N_D/N_C) ones [29,32,33].

Table 1. Transition temperature and transition enthalpy values (in brackets) for the thienoviologen salts mVX[1].

Compounds mVX	Transition	Temperature (°C)	[Enthalpy] (J/g)
9V(OTf) [2]	IL→SmC	≈180–170	[n.d.] [3]
	SmC→Col_L	157.5	[13.3]
	Col_L→K(Col_{ro})	131.9	[15.3]
10V(OTf) [2]	IL→Col_{ro1}	170.1	[13.1]
	Col_{ro1}→K(Col_{ro2})	147.0, 139.1 (double peak)	[12.9]
11V(OTf) [2]	IL→N_C	182.9	[9.3]
	N_C→K(Col_L)	147.5	[8.0]
9V(OTs) [2]	SmC→Col_L/Col_{rd}	222.1, 209.4	[15.9]
	Col_L/Col_{rd}→K(Col_{ro2})	194.1	[13.0]
10V(OTs) [2]	N_D/N_C→Col_{rd2}	229.7	[8.1]
	Col_{rd2}→Col_{rd1}	158.7	[3.8]
	Col_{rd1}→K(Col_{ro})	113.5	[5.8]
11V(OTs) [2]	IL→N_D/N_C	233.0	[5.9]
	N_D/N_C→K(N_D/N_C)	194.3	[15.2]

Table 1. *Cont.*

Compounds mVX	Transition	Temperature (°C)	[Enthalpy] (J/g)
9V(BF_4) [4]	IL→SmA	203.0	[12.0]
	SmA→Glassy SmA	144.9	[9.9]
9V(NTf_2) [5]	IL→Col_{ro1}	128.8	[13.2]
	Col_{ro1}→Col_{ro2}	109.2	[5.2]
10V(NTf_2) [5]	IL→SmA	134.2	[5.8]
	SmA→Col_L	115.1	[0.9]
11V(NTf_2) [5]	IL→SmA	146.0	[5.8]
	SmA→Glassy SmA	114.3	[8.8]
12V(NTf_2) [6]	IL→SmA	190	[n.d.]
	SmA→Glassy SmA	123.5	[6.7]
	Glassy SmA→K	108	[6.5]

[1] Determined by DSC analysis at a scan rate of 10 °C min^{-1} in the 2nd cooling scan; abbreviations: K = solid mesophase; Colro and Colrd = ordered and disordered columnar rectangular phases, respectively; Coll = lamello-columnar phase; SmA and SmC = smectic A and smectic C phase, respectively; ND, NC = discotic nematic and columnar nematic phases, respectively; IL = isotropic liquid state. The type of phases was deduced from X-ray diffraction analysis. [2] From Ref. [32]. [3] Transition not detectable in the DSC thermogram, n.d. = not determined and determined by POM. [4] See Figures S1–S4. [5] From Ref. [32] and [6] from Ref. [33].

3.2. Bulk Photophysics and Thermofluorochromism

All compounds have been characterized in bulk samples from room temperature to the higher transition temperature, and the emission spectra are reported in Figure 2. All of the compounds exhibit significant changes in the fluorescent emission in the LC state by varying the temperature. At room temperature, two emission maxima characterize the spectra of the compounds, one centered in the 620 to 690 nm range (red band) and another peaking in the 485 to 530 nm range (green band). The mutual intensity of the two peaks, as well as the position of the maximum, varies greatly from one sample to another; in some spectra, one of the two peaks appears as a shoulder, and the spectrum seems to consist of a single band (see, for example, the spectra of 9V(OTs), 11V(OTs), 9V(NTf_2), 10V(NTf_2), 12V(NTf_2)). The room temperature emission intensity decay (Table 2) was measured on the most intense peak and, where evident, also on the secondary peak. The best fit was obtained with a three-exponential function for all the triflate and tosylate series, except in the case of 11V(OTs), which is the only one, among the compounds, showing a single emission band (Figure 2), while a double exponential fitting is needed for the bistriflimide series and for 9V(BF_4). The three lifetime values, ranging between 0.3 and 7.0 ns, imply an overlapping of the red and green bands (Table 2).

The highest emission wavelength has the longest decay time, except for that of 9V(OTf), 10V(OTs), and 11V(OTf).

The emission quantum yields (Table 2) are rather low but substantially similar for all compounds, except for those with NTf_2^- as counterion, which show exceptionally high values, partially tuned by the aliphatic chain length. This behavior has a counterpart in solution, where a concentration-dependent photoluminescence behavior occurs. In dilute solution (CH_2Cl_2, 10^{-7} to 10^{-5} mol/L), the thienoviologens show a very intense green fluorescence band (λ_{em}~530 nm; λ_{ex} = 450 nm; $\Phi \geq 80\%$; τ = 1–2 ns) (Figure S5 and Table S1), while, for concentrations >10^{-5} mol/L, excitation at 540 nm results in a red emission in the range 640 to 710 nm with a lower quantum yield (up to 3.4%) and a shorter decay lifetime (Table S1), originated by the aggregate form. It is clear that we have more than one emissive species, whose contribution depends on the aggregation/self-assembling properties of the thienoviologen compounds. However, while fluorescence is almost independent on the chain length and of the anion nature in solution, these two structural parameters play a crucial role in the bulk. Indeed, the aggregate formation depends on the distance between two chromophoric units, which is tuned by (i) the volume of the counterion (by increasing

counterion volume, the distance increases; see the NTf_2 case), and (ii) the discoid volume, which, in turn, depends on the mesophase. Notably, these structural properties can be well tuned by the temperature.

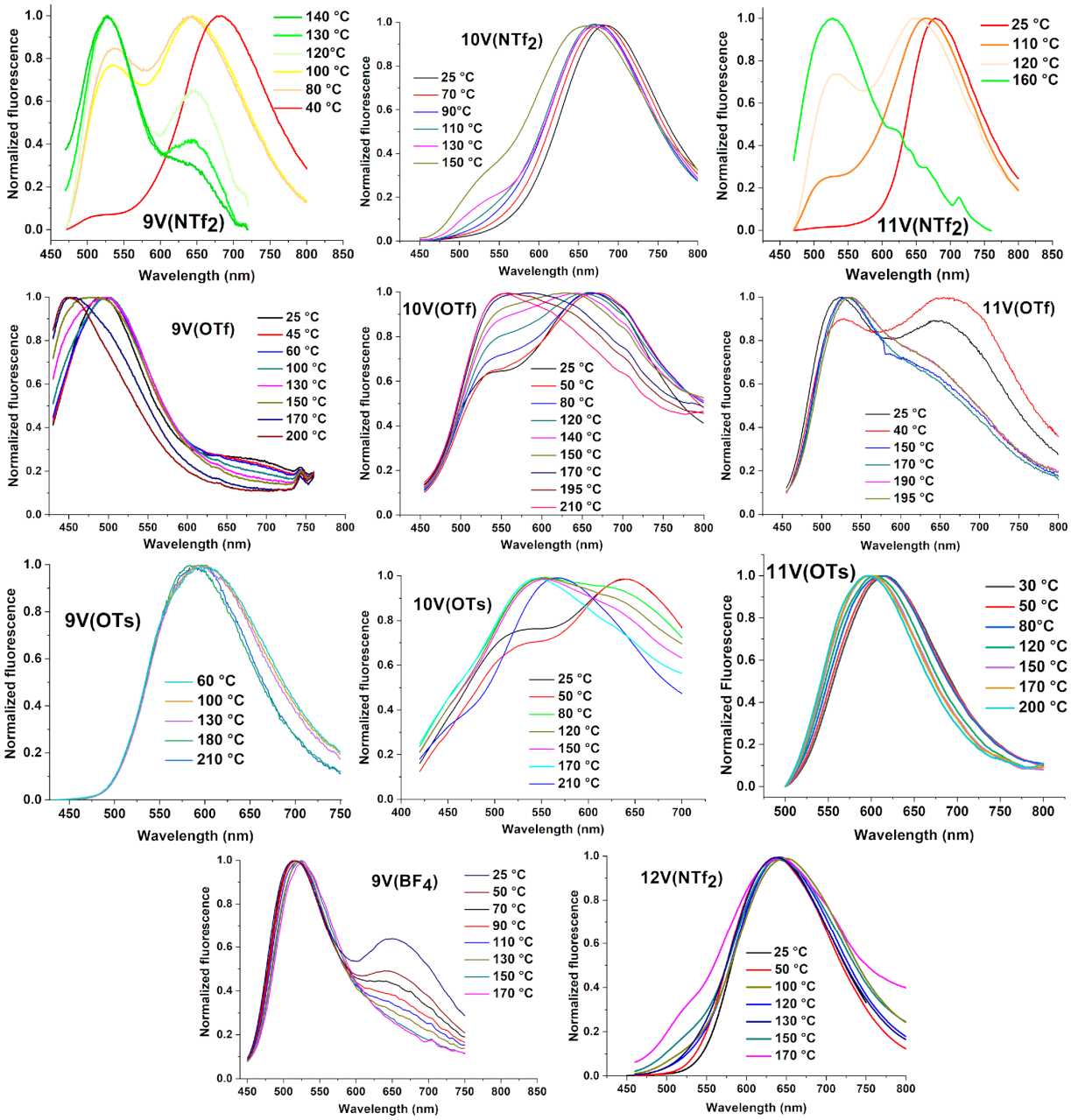

Figure 2. Normalized emission spectra of some thienoviologens recorded at different temperatures in the whole thermotropic range.

At higher temperatures, a relative increase of the green emission at the expense of the red emission and/or a blue shift of the emission band, is generally observed in the bulk fluorescence spectra (Figure 2).

Notably, in most instances, the phase transition can be clearly detected based on the significant spectral changes occurring at the transition point, leading to the formation of a quite definite isosbestic point in the normalized fluorescence spectra (Table 1 and Figure 2 and Figure S1). The emission quantum yield values decrease by increasing temperature, generally halving at the highest temperature value compared to the value measured at room temperature (see Supporting Information).

The thermofluorochromic behavior of the mVX is highlighted in the CIE 1931 color space (Figure 3 and Figure S6) and in Table 3. Notably, all of the luminescent ILCs studied show reversible trajectories within the CIE diagram as a function of the temperature, denoting a fine tuning of the emission color in a wide temperature range, made possible by the gradual spectral changes induced by the temperature (Figure 2). Table 3 reports the characteristic color of emission for each phase characterizing the thermotropic behavior of the mVX compounds, thus highlighting the temperature-induced color switching that occurs across each phase transition. Importantly, a temperature-induced switch of the color can be achieved in the mVOTf compounds from green to blue, from orange to yellow, and from yellow to green, as m increases from 9 to 11, from yellow to red in $11VNTf_2$, and, notably, from green to yellow and then to red in the $9VNTf_2$ (Figure 3).

Table 2. Photophysical properties of the thienoviologens in bulk state at room temperature.

Compound	λ_{em} [nm]	Φ [%]	τ_1 [ns]	τ_2 [ns]	τ_3 [ns]
9V(OTs)	610	0.50	0.70 (10%)	3.40 (76%)	6.90 (14%)
10V(OTs)	535 635	0.58	0.50 (40%) 0.30 (23%)	2.10 (44%) 1.60 (60%)	5.90 (16%) 4.34 (17%)
11V(OTs)	630	0.54		1.00 (20%)	3.90 (80%)
9V(OTf)	480 620	0.64	0.26 (87%) 0.45 (45%)	0.90 (10%) 1.49 (50%)	2.50 (3%) 5.33 (5%)
10V(OTf)	530 660	0.77	0.60 (27%) 0.40 (16%)	1.90 (61%) 1.70 (71%)	6.44 (12%) 5.10 (13%)
11V(OTf)	525 640	0.84	0.46 (20%) 0.45 (53%)	2.20 (56%) 1.70 (42%)	5.70 (24%) 7.00 (5%)
9V(BF_4)	520 648	0.46	0.60 (56%) 1.00 (43%)	2.8 (44%) 3.1 (57%)	
9V(NTf_2) [1]	630	51.0	0.54 (30%)	1.80 (70%)	
10V(NTf_2)	650	15.0	1.00 (47%)	3.00 (53%)	
11V(NTf_2) [1]	670	48.0	0.81 (37%)	2.67 (63%)	
12V(NTf_2)	647	28.0	1.00 (33%)	3.10 (67%)	

[1] From Ref. [41].

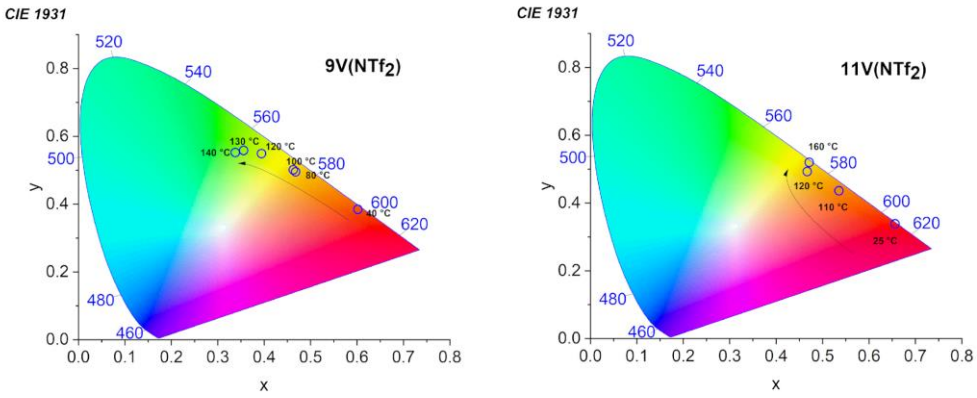

Figure 3. *Cont.*

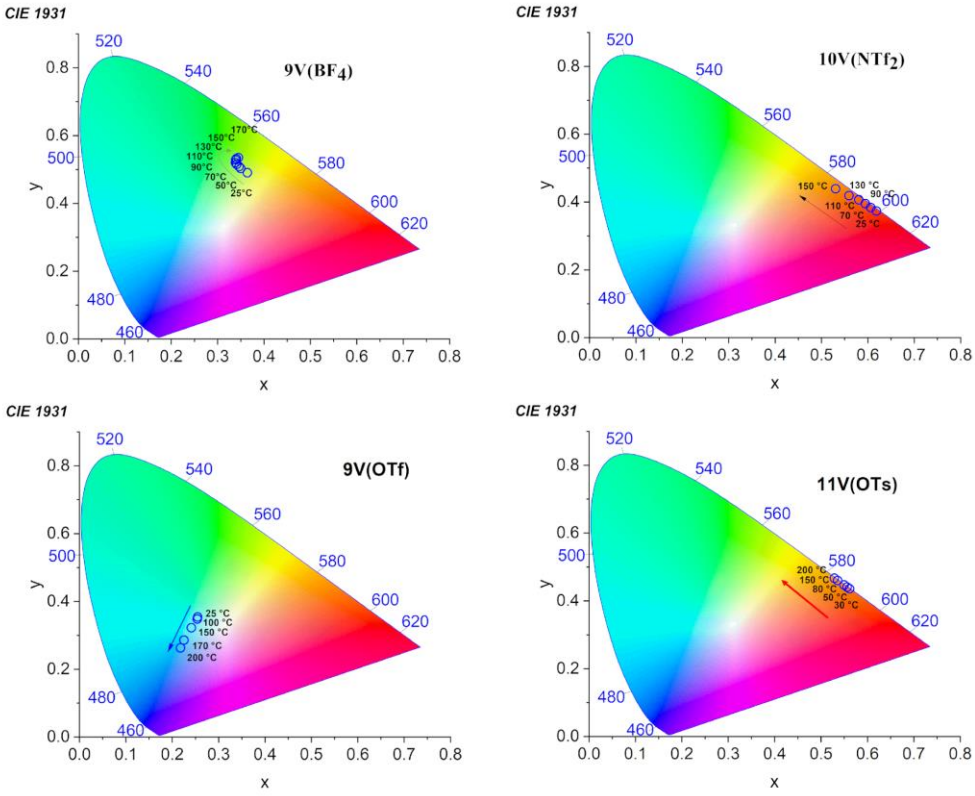

Figure 3. Temperature dependent 1931 CIE chromaticity coordinates of the fluorescent emission of 9V(NTf_2), 9V(BF_4), 9V(OTf), 10V(NTf_2), 11V(NTf_2), 11V(OTs).

Table 3. Thermofluorochromic behavior of mVX compounds: characteristic colors and CIE coordinates for each phase.

X^-	m	Phase	CIE Coordinates [T °C]	Coloration
OTf^-	9	IL	(0.218; 0.263) [200]	
		SmC	(0.241; 0.323) [160]	
		Col_L	(0.248; 0.339) [130]	
		$K(Col_{ro})$	(0.254; 0.348) [25]	
	10	IL	(0.44; 0.489) [195]	
		Col_{ro1}	(0.453; 0.481) [150]	
		$K(Col_{ro2})$	(0.46; 0.462) [25]	
	11	IL	(0.412; 0.506) [190]	
		N_C	(0.399; 0.509) [150]	
		$K(Col_L)$	(0.432; 0.481) [40]	
OTs^-	9	SmC	(0.509; 0.479) [210]	
		Col_L/Col_{rd}	(0.513; 0.475) [200]	
		$K(Col_{ro2})$	(0.512; 0.475) [100]	
	10	Col_{rd2}	(0.399; 0.434) [210]	
		Col_{rd1}	(0.385; 0.420) [120]	
		$K(Col_{ro})$	(0.413; 0.41) [50]	

Table 3. *Cont.*

X^-	m	Phase	CIE Coordinates [T °C]	Coloration
	11	N_D/N_C	(0.529; 0.467) [200]	
		$K(N_D/N_C)$	(0.561; 0.436) [30]	
BF_4^-	9	SmA	(0.345; 0.535) [170]	
		Glassy SmA	(0.364; 0.491) [25]	
NTf_2^-	9	IL	(0.338; 0.553) [140]	
		Col_{ro1}	(0.394; 0.549) [120]	
		Col_{ro2}	(0.602; 0.385) [40]	
	10	IL	(0.53; 0.439) [150]	
		SmA	(0.559; 0.419) [130]	
		Col_L	(0.618; 0.343) [25]	
	11	IL	(0.471; 0.52) [160]	
		SmA	(0.535; 0.437) [110]	
		Glassy SmA	(0.656; 0.339) [25]	
	12	SmA	(0.523; 0.442) [170]	
		Glassy SmA	(0.585; 0.407) [120]	
		K	(0.608; 0.389) [25]	

4. Discussion

This thermofluorochromic response accounts for the dependence of the emission color on the self-assembling in the LC phase and can be associated with changes in the structural parameters of the liquid crystalline state occurring across the phase transition temperature, even though the color change is almost gradual within the entire thermotropic range from the isotropic liquid state to the crystalline one. By considering the results in solutions, it is clear that the chromophoric unit (i.e., the thienoviologen) shows a green fluorescence (520 nm) with high EQY, which declines with increasing concentration, probably due to the formation of $\pi-\pi$ aggregates that quench the emission. On the other hand, in concentrated solution, the thienoviologens show a red emission, originating from the aggregate form. The same behavior is observed in bulk, but in this case the aggregate formation depends on the interaction between two chromophoric units, which is tuned by the volume of the counterion and partially by the chain length. Indeed, two thienoviologen dications have a strong tendency to form disk-like dimers where the counterions are the bridging units through ionic interactions [29]. These dimers are the discoid nanoparticles (approximate dimensions 300 Å2) which constitutes the building blocks for the columnar phases. Aggregate formation is therefore also dependent on the discoid volume, which is modulated by the temperature that determines the type of phase. The formation of higher-order aggregates among the dimers in the bulk LC phase can lead either to a red shift or a blue shift of the light emission, depending on the nature of the intermolecular interactions between the thienoviologens in the dimer, as well as among the dimers in the self-assembled aggregate (cluster) [46].

A classification of the thienoviologens mVX based on their photophysical properties, according to the aliphatic chain length and the nature of the counterion, is not straightforward, although the presence of NTf_2 implies emission quantum yield (EQY) values that are about two orders of magnitude higher than those of the other counterions (in bulk samples). Actually, the above parameters, in addition to the temperature, combine with differentiated and unpredictable weights to provide the observed photophysical data. However, some general quantitative considerations can be provided in order to try to better understand the

thermofluorochromic behavior of these compounds. In general, we observe that, for each compound, a red shift of the fluorescent emission occurs on cooling from the isotropic liquid state, with profound spectral changes and clear isosbestic points in correspondence with the phase transition temperatures, determined by the intensity decrease of the low-energy emission band (650 nm) and the intensity increase of the high-energy one (530 nm).

Moreover, in the triflate and tosylate series, on cooling, the disordered-to-ordered mesophase transition is most often characterized by a change in the 2D space group symmetry from p2mm to p2mg, corresponding to a significant increase in the lattice constant parameters and in the number of salt units from 2 to 4. This corresponds to a quite general increase of the area of the discoid nanoparticles (disk basal area) and a decrease in the ar/br ratio (Table 4). In contrast, in the cases in which the above symmetry transition does not occur (for 9VTf, 10VOTs), a significant decrease in the discoid area can be calculated, which is determined by the decrease of the unit cell parameters a_r, causing the thermofluorochromic behavior. In all cases, the intracolumnar distance (D) is almost unaffected by any phase transition or change in structural parameters/symmetry (within the second decimal unit) (Table 4). Interestingly, by comparing the columnar ILCs, it can be seen that, in the triflate and tosylate compounds, the intracolumnar distance is smaller than in the corresponding bistriflimide thienoviologens [33,41]. Another interesting difference is in the unit cell parameters, which are larger in the bistriflimide homologous compounds (Table 4).

Table 4. Effect of temperature on the structural parameters of the mesophases upon the first disordered/ordered phase transition (on cooling from the IL state).

		Space Group Symmetry Changes					
Phases	**Compound**	**Space Group Symmetry** [1]	**Number of Salt Units/Cross Section (Z)**	**Intracolumnar Correlation Distance** [2] **D (Å)**	**a_r (Å)**	**b_r (Å)**	**Disk Basal Area (Å)** [2]
Columnar	9V(OTf)	p2mg/p2mg	4/4	4.45/4.45	42.40/33.30	30.74/33.34	326/278
	10V(OTf)	p2mm/p2mg	2/4	4.47/4.47	24.07/40.00	26.37/33.34	317/333
	11V(OTf)	p2mm/p2mg	2/4	4.47/4.47	25.14/41.38	27.18/36.06	342/373
	9V(OTs)	p2mm/p2mg	2/4	4.39/4.36	25.79/39.36	25.61/32.13	330/316
	10V(OTs)	p2mg/p2mg	4/4	4.39/4.18	39.36/35.20	32.13/33.34	316/293
	11V(OTs)	p2mm/p2mg/P1	2/4	4.41/4.36	17.85/35.06	36.06/32.65	322/286
	9V(NTf_2)	p21/a	4/4	4.50	55.8/54.2	22.6/22.0	315/298
	10V(NTf_2)	SmA/Col_L	4 (Col_L)	4.50 (Col_L)	4.70 (Col_L)	20.3 (Col_L)	
Smectic		Interplanar distance (Å)					
	11V(NTf_2)						
	12V(NTf_2)	35/34					
	9V(BF_4)	20.3					

[1] From Ref [29]; [2] From Ref [29] for compounds with X = OTf, OTs and from Ref [32,33] for compound with X = NTf_2.

This may be due to the larger dimension of the NTf_2^- anion, which induces an increase in the intracolumnar distance and in the disk dimensions. This can occur only if the two thienoviologen dication units forming the disk are arranged into larger aggregates with larger intercationic distance and a staggered configuration. This configuration and the larger D values in the m$VNTf_2$ series may explain their higher fluorescence quantum yields than the homologous series with the other anions that show significantly lower quantum yields (Table 2).

Summarizing the most important experimental observations, we have: (i) a significant quenching effect of the fluorescence in the solid state (mesophases and crystalline phase) and in concentrated solution for all of the mVX except for the bistriflimide ones; (ii) the appearance of a further band at 540 nm in the absorption spectra, clearly due to aggregation in solution; (iii) a general increase in the contribution of the green emission (blue shift) to the fluorescence spectra at increasing temperature; (iv) a general change (most often a decrease) in the average disk basal area in the columnar compounds with increasing temperature; and (v) the temperature independence of the intracolumnar distance in columnar compounds. All of the above observations could find a qualitative explanation from the knowledge that, when two conjugated chains interact in cofacial configurations (simulating the aggregation in solid state or in concentrated solution), leading to the formation of dimers, fluorescence quenching occurs (aggregation caused quenching) [29,47–51], generally with a resulting blue shift of the lowest optically allowed transition in the dimer with respect to the isolated molecule. This is due to the energy splitting of the excited state energy of the dimer as a consequence of the interaction between the optically allowed energy states of each fluorophore. The lowest excited energy level of the dimer corresponds to a favorable dipole–dipole interaction with an antiparallel arrangement, while, in the highest energy state, corresponds to a parallel orientation of the dipoles. In a cofacial configuration, the transition to the lowest excited state is forbidden, resulting in quenching and a blue shift of the emission with respect to the individual fluorophore. Interestingly, the optical coupling between the ground and excited states in a dimer can be increased in a staggered geometry, wherein the fluorophores in the dimer are translated with respect to one another by a certain amount. In such a case, the lowest excited state corresponds to the allowed optical transition, producing a red shift of the fluorescence compared to the individual fluorophore. Based on this, the geometrical configuration of the fluorophores in the dimer can be assumed to strongly affect the photophysics in the aggregated state. This configuration is affected by the structural parameters *m* and X and mainly by the temperature, which can induce phase transitions leading to important changes in the cofacial configuration of the dimer. Indeed, any increases/decreases in the basal disk area, such as those reported in Table 4, can be accounted for by changes in the geometrical configuration of the dimers in the different mesophases and with a decrease of the disk area attributable to a translation of one thienoviologen with respect to the other from a staggered configuration to a cofacial one upon cooling. Interestingly, this would correspond to a red shift of the fluorescence [29], as we do indeed observe on cooling.

Finally, the strong aggregation-caused quenching effect observed in thienoviologens tosilates, triflates, and tetrafluoroborates does not occur in the blistriflimide homologous series. This can be attributed to the larger van der Waals volume of the latter anion, which acts as bulky units to separate the interacting thienoviologens in the dimer [29,47–51].

Molecular mechanics estimations indicate that the thienoviologens can assume different low-energy cofacial configurations in the dimer, such as those reported in Figure 4, pointing toward a qualitative rationalization of the observed photophysical properties. In model A (Figure 4), the planar cores have a parallel arrangement of the dipole moments associated with the thiophene rings, while model B is characterized by a translation of the planar cores parallel to the long axis and by an anti-parallel arrangement of the dipole moments associated with the thiophene rings. Translation in B allows for alleviating the electrostatic interactions between the positive charges located on the N atom of the pyridyl units, thus originating a blue-shifted emission with respect to A. Additional cofacial arrangements may be easily built with the assumption of an antiparallel arrangement of dipole moments of the thiophene rings for the model A and a parallel arrangement of dipole moments of the thiophene rings for the model B.

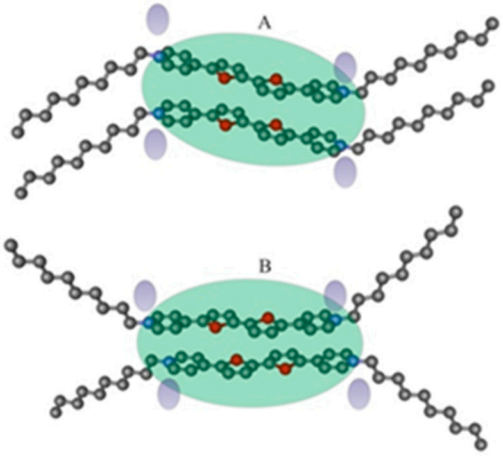

Figure 4. Low-energy models of dimer formed by thienoviologen salt units giving rise to a disc-like motif of elliptic shape (discoid). (**A**): face-to-face configuration where the planar cores have a parallel arrangement of the dipole moments associated with the thiophene rings. (**B**): translation of the planar cores parallel to the long axis and an anti-parallel arrangement of dipole moments associated with the thiophene rings. The counterions are indicated by the shadowed small ovals. The pendant decyl chains are drawn as pointing in the same direction in the zig-zag model A and in opposite directions in B, as an example. In general, they are in a disordered conformation. The intercore distance is 0.4 nm in A and 0.37 nm in B.

5. Conclusions

The thienoviologens mVX exhibit a very rich thermotropism, giving rise to a wide range of mesophases, characterized by a dimeric self-assembling unit consisting of two dications and the bridging interacting anions. They exhibit strong fluorescence in dilute solution (up to 90%) but are generally quenched in concentrated solution and in the solid/liquid crystalline state in all the compounds except the bistriflimide ones. In the latter cases, the quenching effect caused by the cofacial configuration of the thienoviologens in the dimer is mitigated by the large anion dimensions. The bulk fluorescence properties of the thienoviologen liquid crystals are determined by the nature of the anion (X), the length of the alkyl chain (m), and the temperature (T). The first two parameters mainly affect the fluorescence properties by determining the configuration in which the dications interact with each other in the aggregates and take into account the different mesomorphism of these compounds across the homologous series. By fixing these two parameters, the effect of temperature changes from room temperature to the isotropic liquid state is revealed by the significant changes of the emission spectra of these compounds, in terms of a modulation of the contribution of the two bands in the green and red regions, characterizing the spectra of all the compounds. Actually, the temperature systematically changes the structural parameters of the phases by changing the geometrical configuration of the fluorophores in the thienoviologen dimer, which is the self-assembling unit in the aggregated state. This leads to a fine tuning of the emission across wide chromaticity coordinates, which can involve the whole visible spectral range.

The results achieved with this work are of noteworthy importance from an application point of view. Indeed, the thermofluorochromic effect is added to the well-known properties of electrochromism and electrofluorochromism in thienoviologens, paving the way for these materials to be excellent candidates in the development of multilevel anti-counterfeiting devices.

In the near future, we will explore different π-conjugated cores and different chains with the main objectives of improving the quantum yield and exploring different termofluorochromic ranges by taking advantage of the high structural versatility of extended viologens.

Supplementary Materials: The following supporting information can be downloaded at: https://www.mdpi.com/article/10.3390/nano12234284/s1, Scheme S1. Synthesis scheme of the thienoviologens; Figure S1: Representative POM images of the textures of the compound $9VBF_4$ acquired on cooling from the isotropic liquid state at 5 °C/min; Figure S2: DSC thermograms of the sample $9VBF_4$. The phase transitions experienced by the sample in the first heating scan (not reported) are monotropic; Figure S3: TGA of the sample 9VBF4; Figure S4: WAXS profiles of the sample $9VBF_4$, recorded during the second and successive heatings and coolings steps. The phase transitions experienced by the sample in the first heating scan (not reported) are monotropic. The diffraction peak at $2\theta \approx 5°$ indicates that the smectic period corresponds to 20.3 Å.; Figure S5: Emission spectra in dichloromethane solution at different concentrations; Table S1: Photophysical properties of mVX2 thienoviologens in dichloromethane solution. Figure S6: Temperature-dependent 1931 CIE chromaticity coordinates of the fluorescent emission of 9V(OTs), 10V(OTs), 10V(OTf), 11V(OTf), $12V(NTf_2)$.

Author Contributions: Conceptualization, A.B. and M.L.D.; methodology, A.B.; M.L.D. and F.A.; validation, A.B., M.L.D., F.A. and B.G.; formal analysis, G.A.C., G.D.M., L.V. and O.R.d.B.; investigation, G.A.C., G.D.M., L.V. and O.R.d.B.; resources, data curation, writing—original draft preparation, A.B.; writing—review and editing, A.B., M.L.D., F.A. and B.G.; supervision, A.B.; funding acquisition, A.B. All authors have read and agreed to the published version of the manuscript.

Funding: The authors are grateful to the Ministero dell'Università e della Ricerca Italiano (MUR) and the University of Calabria for supporting this project in the framework of the ex 60% budget grant.

Data Availability Statement: Not applicable.

Acknowledgments: The authors are grateful to the Ministero dell'Università e della Ricerca Italiano (MUR) and the University of Calabria for supporting this project in the framework of the ex 60% budget grant.

Conflicts of Interest: The authors declare no conflict of interest.

References

1. Zhang, K.Y.; Liu, S.; Zhao, Q.; Huang, W. Stimuli–responsive metallopolymers. *Coord. Chem. Rev.* **2016**, *319*, 180–195. [CrossRef]
2. Conesa-Egea, J.; Zamora, F.; Amo-Ochoa, P. Perspectives of the smart Cu-Iodine coordination polymers: A portage to the world of new nanomaterials and composites. *Coord. Chem. Rev.* **2019**, *381*, 65–78. [CrossRef]
3. Dong, Y.; Xu, B.; Zhang, J.; Tan, X.; Wang, L.; Chen, J.; Lv, H.; Wen, S.; Li, B.; Ye, L.; et al. Piezochromic Luminescence Based on the Molecular Aggregation of 9,10-Bis((E)-2-(pyrid-2-yl)vinyl)anthracene. *Angew. Chem. Int. Ed.* **2012**, *51*, 10782–10785. [CrossRef] [PubMed]
4. Qin, Z.W.; Wang, Y.; Lu, X.F.; Chen, Y.J.; Peng, J.; Zhou, G. Multistimuli-Responsive Luminescence Switching of Pyrazine Derivative Based Donor–Acceptor–Donor Luminophores. *Chem. Asian J.* **2016**, *11*, 285–293. [CrossRef] [PubMed]
5. Feng, X.; Chen, Y.; Lei, Y.; Zhou, Y.; Gao, W.; Liu, M.; Huang, X.; Wu, H. Multifunctional properties of a star-shaped triphenylamine-benzene-1,3,5-tricarbohydrazide fluorescent molecule containing multiple flexible chains. *Chem. Commun.* **2020**, *56*, 13638–13641. [CrossRef]
6. Mitani, M.; Ogata, S.; Yamane, S.; Yoshio, M.; Hasegawab, M.; Kato, T. Mechanoresponsive liquid crystals exhibiting reversible luminescent color changes at ambient temperature. *J. Mater. Chem. C* **2016**, *4*, 2752–2760. [CrossRef]
7. Fedorenko, E.V.; Mirochnik, A.G.; Gerasimenko, A.V.; Beloliptsev, A.Y.; Merkulov, E.B. Mechanofluorochromism, thermofluorochromism, solvatochromism, and solid-state luminescence of difluoroboron o-hydroxy-, p-benzoyloxydibenzoylmetanates. *Dyes Pigm.* **2018**, *159*, 557–572. [CrossRef]
8. Bellacanzone, C.; Otaegui, J.R.; Hernando, J.; Ruiz-Molina, D.; Roscini, C. Tunable Thermofluorochromic Sensors Based on Conjugated Polymers. *Adv. Opt. Mater.* **2022**, *10*, 2102423. [CrossRef]
9. Ishchenko, A.A.; Kulinich, A.V.; Bondarev, S.L.; Knyukshto, V.N.; Turban, A.A. Thermochromism and thermofluorochromism of merocyanines with a positive solvatochromism. *Opt. Spectrosc.* **2006**, *101*, 90–97. [CrossRef]
10. Seeboth, A.; Lötzsch, D. *Thermochromic Phenomena in Polymers*; Smithers Rapra: Shawbury, UK, 2008.
11. Seeboth, A.; Lötzsch, D.; Ruhmann, R.; Muehling, O. Thermochromic Polymers—Function by Design. *Chem. Rev.* **2014**, *114*, 3037–3068. [CrossRef]
12. Wang, X.; Wolfbeis, O.S.; Meier, R.J. Luminescent probes and sensors for temperature. *Chem. Soc. Rev.* **2013**, *42*, 7834–7869. [CrossRef] [PubMed]
13. Ren, W.; Lin, G.; Clarke, C.; Zhou, J.; Jin, D. Optical Nanomaterials and Enabling Technologies for High-Security-Level Anticounterfeiting. *Adv. Mater.* **2020**, *32*, 1901430. [CrossRef] [PubMed]

14. Abdollahi, A.; Roghani-Mamaqani, H.; Razavi, B.; Kalajahi, M.S. Photoluminescent and Chromic Nanomaterials for Anticounterfeiting Technologies: Recent Advances and Future Challenges. *ACS Nano* **2020**, *14*, 14417–14492. [CrossRef] [PubMed]
15. Vázquez-Mera, N.A.; Otaegui, J.R.; Sánchez, R.S.; Prats, G.; Guirado, G.; Ruiz-Molina, D.; Roscini, C.; Hernando, J. Color-Tunable White-Light-Emitting Materials Based on Liquid-Filled Capsules and Thermally Responsive Dyes. *ACS Appl. Mater. Interfaces* **2019**, *11*, 17751–17758. [CrossRef] [PubMed]
16. Sol, J.A.H.P.; Dehm, V.; Hecht, R.; Wgrthner, F.; Schenning, A.P.H.J.; Debije, M.G. Temperature-Responsive Luminescent Solar Concentrators: Tuning Energy Transfer in a Liquid Crystalline Matrix. *Angew. Chem. Int. Ed.* **2018**, *57*, 1030–1033. [CrossRef]
17. Otaegui, J.R.; Ruiz-Molina, D.; Latterini, L.; Hernando, J.; Roscini, C. Thermoresponsive multicolor-emissive materials based on solid lipid nanoparticles. *Mater. Horiz.* **2021**, *8*, 3043–3054. [CrossRef]
18. Liao, R.; Gu, S.; Wang, X.; Zhang, X.; Xie, X.; Sun, H.; Huang, W. Approaching an adjustable organic thermochromic luminophore library via the synergistic effects between structure-related molecular dynamics and aggregation-related luminescence. *J. Mater. Chem. C* **2020**, *8*, 8430–8439. [CrossRef]
19. Yu, Z.Q.; Li, X.; Wan, W.; Li, X.S.; Fu, K.; Wu, Y.; Li, A.D.Q. Cooperatively assembled liquid crystals enable temperature-controlled Förster resonance energy transfer. *Chem. Sci.* **2021**, *12*, 3146–3151. [CrossRef]
20. Zhang, X.; Lin, G.; Guo, H.; Yang, F. Tetraphenylethylene-rufigallol-tetraphenylethylene trimers: Novel fluorescence liquid crystals in aggregated states. *J. Mol. Struct.* **2022**, *1249*, 131643. [CrossRef]
21. O'Neill, M.; Kelly, S.M. Liquid Crystals for Charge Transport, Luminescence, and Photonics. *Adv. Mater.* **2003**, *15*, 1135–1146. [CrossRef]
22. Vijayaraghavan, R.K.; Abraham, S.; Akiyama, H.; Furumi, S.; Tamaoki, N.; Das, S. Photoresponsive Glass-Forming Butadiene-Based Chiral Liquid Crystals with Circularly Polarized Photoluminescence. *Adv. Funct. Mater.* **2008**, *18*, 2510–2517. [CrossRef]
23. Lu, H.; Zhang, S.; Ding, A.; Yuan, M.; Zhang, G.; Xu, W.; Zhang, G.; Wang, X.; Qiu, L.; Yang, J. A luminescent liquid crystal with multistimuli tunable emission colors based on different molecular packing structures. *New J. Chem.* **2014**, *38*, 3429–3433. [CrossRef]
24. Liao, R.; Wang, X.; Peng, L.; Sun, H.; Huang, W. Achieving Organic Smart Fluorophores by Controlling the Balance between Intermolecular Interactions and External Stimuli. *ACS Appl. Mater. Interfaces* **2021**, *13*, 27491–27499. [CrossRef] [PubMed]
25. Goossen, K.; Lava, K.; Bielewski, C.W.; Binnemans, K. Ionic Liquid Crystals: Versatile Materials. *Chem. Rev.* **2016**, *116*, 4643–4807. [CrossRef] [PubMed]
26. Axenov, K.V.; Laschat, S. Thermotropic Ionic Liquid Crystals. *Materials* **2011**, *4*, 206–259. [CrossRef]
27. Mansueto, M.; Laschat, S. Ionic Liquid Crystals. In *Handbook of Liquid Crystals*, 2nd ed.; Nanostructured and Amphiphilic Liquid Crystals; Goodby, J.W., Collings, P.J., Kato, T., Tschierske, C., Gleeson, H., Raynes, P., Eds.; Wiley-VCH: Weinheim, Germany, 2014; Volume 6, p. 231.
28. Uchida, J.; Soberats, S.; Gupta, G.; Kato, T. Advanced Functional Liquid Crystals. *Adv. Mater.* **2022**, *34*, 2109063. [CrossRef] [PubMed]
29. Veltri, L.; Maltese, V.; Auriemma, F.; Santillo, C.; Cospito, S.; La Deda, M.; Chidichimo, G.; Gabriele, B.; De Rosa, C.; Beneduci, A. Mesophase Tuning in Discotic Dimers π-Conjugated Ionic Liquid Crystals through Supramolecular Interactions and the Thermal History. *Cryst. Growth Des.* **2016**, *16*, 5646–5656. [CrossRef]
30. Yazaki, S.; Funahashi, M.; Kato, T. An Electrochromic Nanostructured Liquid Crystal Consisting of π-Conjugated and Ionic Moieties. *J. Am. Chem. Soc.* **2008**, *130*, 13206–13207. [CrossRef]
31. Yazaki, S.; Funahashi, M.; Kagimoto, J.; Ohno, H.; Kato, T. Nanostructured Liquid Crystals Combining Ionic and Electronic Functions. *J. Am. Chem. Soc.* **2010**, *132*, 7702–7708. [CrossRef]
32. Beneduci, A.; Cospito, S.; Crispini, A.; Gabriele, B.; Nicoletta, F.P.; Veltri, L.; Chidichimo, G. Switching from columnar to calamitic mesophases in a new class of rod-like thienoviologens. *J. Mater. Chem. C* **2013**, *1*, 2233–2240. [CrossRef]
33. Cospito, S.; Beneduci, A.; Veltri, L.; Salamonczyk, M.; Chidichimo, G. Mesomorphism and electrochemistry of thienoviologen liquid crystals. *Phys. Chem. Chem. Phys.* **2015**, *17*, 17670–17678. [CrossRef] [PubMed]
34. Beneduci, A.; Cospito, S.; Imbardelli, D.; De Simone, B.C.; Chidichimo, G. n-Type Columnar Liquid Crystal Combining Ionic and Electronic Functions. *Mol. Cryst. Liq. Cryst.* **2015**, *610*, 108–115. [CrossRef]
35. Pibiri, I.; Beneduci, A.; Carraro, M.; Causin, V.; Casella, G.; Corrente, G.A.; Chidichimo, G.; Pace, A.; Riccobono, A.; Saielli, G. Mesomorphic and electrooptical properties of viologens based on non-symmetric alkyl/polyfluoroalkyl functionalization and on an oxadiazolyl-extended bent core. *J. Mater. Chem. C* **2019**, *7*, 7974–7983. [CrossRef]
36. Veltri, L.; Cavallo, G.; Beneduci, A.; Metrangolo, P.; Corrente, G.A.; Ursini, M.; Romeo, R.; Terraneo, G.; Gabriele, B. Synthesis and thermotropic properties of new green electrochromic ionic liquid crystals. *New J. Chem.* **2019**, *43*, 18285–18293. [CrossRef]
37. Beneduci, A.; Corrente, G.A.; Chidichimo, G. Electrochromic and Electrofluorescence Liquid Crystals. In *Electrochromic Smart Materials: Fabrication and Applications*; Xu, J.W., Chua, M.H., Shah, K.W., Eds.; The Royal Society of Chemistry: Cambridge, UK, 2019; pp. 261–292.
38. Chidichimo, G.; De Simone, B.C.; Imbardelli, D.; De Benedittis, M.; Barberio, M.; Ricciardi, L.; Beneduci, A. Influence of oxygen impurities on the electrochromic response of viologen-based plastic films. *J. Phys. Chem. C* **2014**, *118*, 13484–13492. [CrossRef]
39. Cospito, S.; De Simone, B.C.; Beneduci, A.; Imbardelli, D.; Chidichimo, G. Novel electrochromic gel with high optical contrast in the visible and near-infrared. *Mater. Chem. Phys.* **2013**, *140*, 431–434. [CrossRef]

40. Beneduci, A.; Cospito, S.; La Deda, M.; Chidichimo, G. Highly Fluorescent Thienoviologen-Based Polymer Gels for Single Layer Electrofluorochromic Devices. *Adv. Funct. Mater.* **2015**, *25*, 1240–1247. [CrossRef]
41. Beneduci, A.; Cospito, S.; La Deda, M.; Veltri, L.; Chidichimo, G. Electrofluorochromism in π-conjugated ionic liquid crystals. *Nat. Commun.* **2014**, *5*, 3105. [CrossRef]
42. de Mello, J.C.; Wittmann, H.F.; Friend, R.H. An improved experimental determination of external photoluminescence quantum efficiency. *Adv. Mater.* **1997**, *9*, 230–232. [CrossRef]
43. Palsson, L.O.; Monkman, A.P. Measurements of Solid-State Photoluminescence Quantum Yields of Films Using a Fluorimeter. *Adv. Mater.* **2002**, *14*, 757–758. [CrossRef]
44. Porres, L.; Holland, A.; Palsson, L.O.; Monkman, A.P.; Kemp, C.; Beeby, A. Absolute Measurements of Photoluminescence Quantum Yields of Solutions Using an Integrating Sphere. *J. Fluoresc.* **2006**, *16*, 267–272. [CrossRef] [PubMed]
45. Akkermans, R.L.C.; Spenley, N.A.; Robertson, S.H. COMPASS III: Automated fitting workflows and extension to ionic liquids. *Mol. Simul.* **2021**, *47*, 540–551. [CrossRef]
46. Cornil, J.; Beljonne, D.; Calbert, J.P.; Brédas, J.L. Interchain Interactions in Organic π-Conjugated Materials: Impact on Electronic Structure, Optical Response, and Charge Transport. *Adv. Mater.* **2001**, *13*, 1053–1067. [CrossRef]
47. Corrente, G.A.; Beneduci, A. Overview on the Recent Progress on Electrofluorochromic Materials and Devices: A Critical Synopsis. *Adv. Opt. Mater.* **2020**, *8*, 2000887. [CrossRef]
48. Reeves, B.D.; Unur, E.; Ananthakrishnan, N.; Reynolds, J.R. Defunctionalization of ester-substituted electrochromic dioxythiophene polymers. *Macromolecules* **2007**, *40*, 5344–5352. [CrossRef]
49. Chen, G.; Li, W.; Zhou, T.; Peng, Q.; Zhai, D.; Li, H.; Yuan, W.Z.; Zhang, Y.; Tang, B.Z. Conjugation-induced rigidity in twisting molecules: Filling the gap between aggregation-caused quenching and aggregation-induced emission. *Adv. Mater.* **2015**, *27*, 4496–4501. [CrossRef]
50. Liu, J.; Li, M.; Wu, J.; Shi, Y.; Zheng, J.; Xu, C. Electrochromic polymer achieving synchronous electrofluorochromic switching for optoelectronic application. *Org. Electron.* **2017**, *51*, 295–303. [CrossRef]
51. Yuan, W.Z.; Lu, P.; Chen, S.; Lam, J.W.Y.; Wang, Z.; Liu, Y.; Kwok, H.S.; Ma, Y.; Tang, B.Z. Changing the Behavior of Chromophores from Aggregation-Caused Quenching to Aggregation-Induced Emission: Development of Highly Efficient Light Emitters in the Solid State. *Adv. Mater.* **2010**, *22*, 2159–2163. [CrossRef]

applied sciences

MDPI

Article

Solvent-Dispersible Nanostructured MIMI: An Experimental and Computational Study

Angela Candreva [1,2,*], Giuseppe Di Maio [1], Giovanna Palermo [2,3], Alexa Guglielmelli [2,3], Giuseppe Strangi [2,3,4] and Massimo La Deda [1,2,*]

[1] Department of Chemistry and Chemical Technologies, University of Calabria, 87036 Rende, Italy
[2] CNR-NANOTEC, Istituto di Nanotecnologia, 87036 Rende, Italy
[3] Department of Physics, NLHT-Lab, University of Calabria, 87036 Rende, Italy
[4] Department of Physics, Case Western Reserve University, 2076 Adelbert Rd., Cleveland, OH 44106, USA
* Correspondence: angela.candreva@unical.it (A.C.); massimo.ladeda@unical.it (M.L.D.)

Abstract: A MIMI (metal–insulator-metal–insulator) nanoparticle was conceived and synthesized. It consists of a core of gold nanoparticles of different shapes, covered by a silica shell in turn covered by a layer of gold and finally by another silica shell. This hybrid nano-matryoshka, completely dispersed in water, was characterized by UV–Vis and TEM spectroscopy, comparing the architecture and photophysical properties of each synthetic step. Through a numerical simulation, it was possible to study in depth the absorption and extinction cross sections, determining the role of the various layers. This is an example of architecture used in the construction of metamaterials, the first in the form of a water-dispersed nanoparticles.

Keywords: dispersed nanostructure; metal–insulator–metal–insulator; hybrid nano-matryoshka; photophysical properties; construction of metamaterials; numerical simulation

check for updates

Citation: Candreva, A.; Di Maio, G.; Palermo, G.; Guglielmelli, A.; Strangi, G.; La Deda, M. Solvent-Dispersible Nanostructured MIMI: An Experimental and Computational Study. *Appl. Sci.* **2023**, *13*, 2982. https://doi.org/10.3390/app13052982

Academic Editors: Andrea Li Bassi and Aimin Yu

Received: 26 December 2022
Revised: 21 February 2023
Accepted: 23 February 2023
Published: 25 February 2023

Copyright: © 2023 by the authors. Licensee MDPI, Basel, Switzerland. This article is an open access article distributed under the terms and conditions of the Creative Commons Attribution (CC BY) license (https://creativecommons.org/licenses/by/4.0/).

1. Introduction

Nanofabrication technologies [1–3] have attracted researchers to explore the field of plasmonic modes [4–7], such as localized surface plasmons (LSPs) [8,9] and coupled plasmonic systems [10–12], which strongly increase an interacting electromagnetic field [13,14]. These features are generally shown by suitably coupling a metal with a dielectric, while, more recently, metal–insulator–metal–insulator structures (MIMI) have provided encouraging results. MIMI is a new architecture in which an insulator is enclosed by two metal claddings, highlighting potential attractive features [15–19] which depend on the thickness and composition of the surfaces that compose it [20–22]. On the MIMI structures are based metamaterials, that constitute the last frontier in the search for new materials, possessing properties not found in nature [23–25].

A further step forward is represented by three-dimensional MIMI systems composed of nanoparticle films that can achieve major advances compared to multilayered planar devices; their electronic and optical properties are encouraging for numerous applications such as third-generation solar cells, light-emitting diodes, field-effect transistors [26–29]. Ultimately, the performance of these devices is based on the modulation of the energy levels and optical properties of the nanoparticles by regulating their shape, size, surface and chemical composition [30–34].

With respect to the available MIMI devices, which consist of a solid array [18,35], the aim of this work was to obtain a MIMI nanoparticle in colloidal dispersion. Among the many advantages of having a potential metamaterial in colloidal dispersion, there is their in vivo use for the detection of particular analytes present in biological fluids, while the current detection systems based on metamaterials require the collection of these fluids [36]. Recent advances in nanofabrication have encouraged the development of new plasmonic biosensors that can go beyond the limits of conventional plasmonic sensors [37–39]. A. V.

Kabashin et al. demonstrated an improvement in biosensing technology using a plasmonic metamaterial based on a porous nanorods layer [40]. Furthermore, the possibility of having nanosized metamaterials allows the functionalization of these nanoplatforms, favoring extreme versatility.

To obtain solvent-dispersible nanoparticle MIMI, a synthetic protocol based on a seed-mediated growth approach [41–45] is presented, to obtain a nano-matryoshka array by the alternation of gold and silica layers.

A numerical simulation based on a Finite Element Method (FEM) analysis was conducted on each member of the rod–core MIMI family (samples a, b, c, d) to evaluate the absorption and extinction cross section of a single nano-object, displaying a good agreement with the experimental results.

2. Materials and Methods

All chemicals were purchased from Sigma Aldrich (highest purity grade available) and used as received.

2.1. Chemicals

CTAB (hexadecyltrimethylammonium bromide, ≥96%), 5-bromosalicylic acid (5-BrSA, technical grade, 90%), tetrachloroauric acid trihydrate ($HAuCl_4 \bullet H_2O$, ≥99.9%), $AgNO_3$, (≥99.0%), L-ascorbic acid (AA, ≥99%), sodium citrate (99%), sodium borohydride ($NaBH_4$, 99%) were used as received. Milli-Q water (resistivity 18.2 MΩ•cm at 25 °C) was used in all experiments. All glassware was washed with aqua regia, rinsed with water, sonicated three times for 3 min in Milli-Q water, and dried before use. TEOS (tetraethyl orthosilicate, 99.9%), NaOH (98%), APTES (3-Aminopropyl triethoxysilane), NH_4OH (34%) and MeOH were used for the SiO_2 overcoating.

2.2. Instruments

The extinction spectra were acquired with a Perkin Elmer Lambda 900 spectrophotometer. The size and morphology of the gold nanoparticles were investigated by a Jeol JEM-1400 Plus 120 kV transmission electron microscope (TEM). The samples for TEM were prepared by depositing a drop of a diluted colloidal dispersion on 300-mesh copper grids. After evaporation of the solvent in air at room temperature, the particles were observed at an operating voltage of 80 kV. The core dimension and the thickness of the shell were measured graphically on the TEM images, using the ImageJ program. For each sample, 100 nanoparticles were considered, and for this data population, the standard deviation was obtained.

2.3. Synthetic Procedure

The synthetic strategy involved the preparation of CTAB-coated gold nanorods [46,47] (AuNR), which were subsequently coated with a silica shell (AuNR@SiO_2). By suitably functionalizing the silica surface [48,49], the gold nanorods (AuNR@SiO_2) were decorated with gold seeds, indicated below as AuNS@NaCit, (AuNR@SiO_2@seed), which then gave rise to a homogeneous gold shell (AuNR@SiO_2@Au). Finally, these nanorods were covered with an additional silica shell (AuNR@SiO_2@Au@SiO_2), providing the MIMI structure.

To study both the versatility of the synthetic protocol and the effect on the plasmonic properties of the nano-matryoshka, the starting nanoparticles which formed the core of the nano-matryoshka, were produced in a mix of shapes, AuNP@CTAB, and constituted the starting nanoparticles for a similar family of MIMI systems which led to the final production of a nano-matryoshka with a mixed-shape core, AuNP@SiO_2@Au@SiO_2. Each member of this family was isolated, characterized and compared with the members of the analogous family having a rod-shaped core, as previously illustrated.

Chart 1 reports the synthetic steps followed in the preparation of the two MIMI systems, i.e., AuNR@SiO_2@Au@SiO_2 and AuNP@SiO_2@Au@SiO_2.

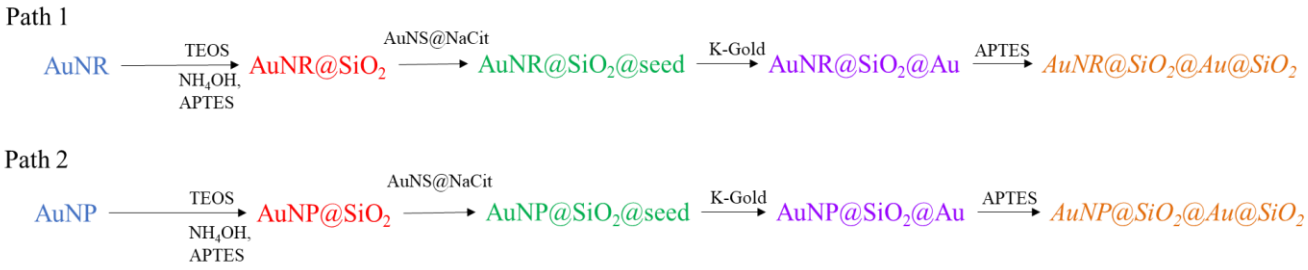

Chart 1. The growth of the gold nanoparticles capped with CTAB was conducted in an aqueous environment using a seed-mediated method. The first step was the preparation of the *seed solution*, and the second was the preparation of the *growth solution*.

2.4. AuNR

Preparation of the seed solution. We added 25 µL of a 5.0x-2 M metal salt tetrachloroauric acid, $HAuCl_4$, water solution to 4.7 mL of a 0.1 M CTAB water solution. At this point, 300 µL of a freshly prepared 1.0x-2 M sodium borohydride, $NaBH_4$, aqueous solution was injected under vigorous stirring. The metal reduction was complete (from Au(III) to Au(0)). The color of the solution became brown. The seed solution was left undisturbed for 30 min, before use, to ensure that the excess sodium borohydride was consumed [46,50,51].

Preparation of the growth solution. We injected 45 mg of 5-BrSA into 50 mL of a 0.05x-2 M CTAB aqueous solution. Only after complete solubilization was ascertained, 480 µL of a 1.0x-2 M $AgNO_3$ water solution was added. The sample remained under slow stirring for 15 min at a temperature of 25 °C, and then 500 µL of a 5.0x-2 M $HAuCl_4$ aqueous solution was added to the mixture, starting the pre-reduction step. At the selected pre-reduction time, 130 µL of a 0.1 M AA aqueous solution was added under vigorous stirring, followed by 80 µL of the seed colloidal dispersion. After a few seconds, the stirring was turned off, and after 4 h, the sample was centrifuged (9000 rpm, 20 min, 30 °C). A clear aqueous colloidal dispersion was obtained.

In this step (growth), elongated micelles of CTAB formed that acted as templating agents for the successive AuNR growth. Here, no nucleation process took place. The compound 5-BrSa, introduced as an aromatic additive to a CTAB water solution, intercalated within the CTAB bilayer, improving the stiffness and symmetry of the growing particles. Silver nitrate was added to promote the anisotropic rod-like shape [46,52].

2.5. AuNP@CTAB

The synthetic protocol was the same reported for AuNR@CTAB, with the exception of CTAB and $AgNO_3$ concentrations in the growth solution, which were reduced by 10 times [52].

2.6. AuNP@SiO$_2$, AuNR@SiO$_2$

According to the protocol reported in a previous paper [48], an aqueous solution of CTAB was added to 2 mL of an aqueous dispersion of gold nanoparticles (0.3x-3 M), reaching the final concentration of 1.0x-3 M. After a few seconds, a 0.1 M NaOH aqueous solution was added under vigorous stirring, reaching a pH value of 8.5, followed by three additions (under gentle stirring, at room temperature) of 12 µL each of TEOS 20% *v/v* in methanol, at 1 h intervals from each other. After 14 h, the mixture was centrifuged in MilliQ water twice at 6000 rpm for 10 min, and the sample was dispersed in 4 mL of EtOH. At this point, 0.5 mL of distilled water and 0.5 mL of NH_4OH were added to the nanoparticle dispersion, followed, 30 min later, by 3.75 µL of TEOS and 3.75 µL of APTES. After 12 h, 3 cycles of centrifuge were carried out, and a pellet was obtained. A part of this pellet was dissolved in water, obtaining a clear colloidal dispersion.

2.7. AuNS@NaCit

Sodium citrate (3 mg) was added to 40 mL of distilled water under stirring and at a controlled temperature (30 °C). Then, a $HAuCl_4$ water solution (0.020 mL, 0.05 M) was added and, after a few minutes, 1.6 mL of a freshly prepared 1.0 x-2 M $NaBH_4$ water solution was injected under vigorous stirring. Instantaneously, the solution became, red confirming the formation of small gold nanospheres, AuNS@NaCit [52] (Figure S1 in ESI, TEM images and UV–Vis spectra).

2.8. AuNP@SiO_2@seed, AuNR@SiO_2@seed

An aqueous dispersion of AuNS@NaCit (4 mL, 1.0x-4 M) was added to the pellet of silica shell/gold core nanoparticles (AuNP@SiO_2, AuNR@SiO_2) under sonication. After a few minutes, a cloud of nanoparticles precipitated at the bottom of the vial, leaving the solution colorless. The supernatant was removed, and the precipitate was dispersed in distilled water, obtaining a clear colloidal dispersion.

2.9. K-Gold Solution

A water solution of K_2CO_3 (14 mg in 50 mL) was prepared and added to 750 mL of $HAuCl_4$ (25 mM). The mixture was aged in the dark, overnight [53].

2.10. AuNP@SiO_2@Au, AuNR@SiO_2@Au

We added 200 µL of AuNP@SiO_2@seed or AuNR@SiO_2@seed nanoparticles samples to 3 mL of the K-Gold solution. Then, 40 µL of 37 wt% formaldehyde in water was added, and the mixture was rapidly shaken until the solution became grey-purple. After 30 min, the solution was purified by one cycle of centrifugation at 9000 rpm for 15 min, and a clear water solution was obtained.

2.11. AuNP@SiO_2@Au@SiO_2, AuNR@SiO_2@Au@SiO_2

We added 30 µL of APTES 20% ***v/v*** in methanol, drop by drop. to the AuNP@SiO_2@Au or AuNR@SiO_2@Au nanoparticles colloidal dispersions, in alkaline conditions, under mild stirring for 3 h. Then, a centrifugation at 9000 rpm for 15 min was performed, obtaining a clear water solution.

The concentrations of the nanoparticles were calculated according to Scarabelli et al. [47], considering that all Au^{3+} was reduced to Au^0.

2.12. Theoretical Calculations

Simulations regarding the optical characteristics of the nanorods-derived nanomatryoshka were conducted using the commercially available finite element analysis software COMSOL Multiphysics (COMSOL, Inc., Burlington, MA, USA) version 5.4, module 'Electromagnetic Waves, Frequency Domain' (EWFD) [54–58]. With this module, it is possible to study electromagnetic wave propagation, resonance effects at the nanoscale, electromagnetic field distributions through a scattered field formulation. The finite element method operates by discretizing the modeling domains into smaller, simpler domains, named elements. The solution is computed by assembling and solving a set of equations over all the elements of the model. The 3D simulation domain contained the nanoparticle immersed in the surrounding medium, which was in turn surrounded by a Perfectly Matched Layer (PML) to mimic an open and nonreflecting infinite domain. The amplitude of the plane wave $|\boldsymbol{E_0}|$ was calculated for the incoming illumination intensity $\boldsymbol{I_0}$ according to $\boldsymbol{I_0 = nc\varepsilon_0|E_0|^2/2}$, where $\boldsymbol{n}$ is the refractive index of the surrounding medium, $\boldsymbol{c}$ is the speed of light, and $\boldsymbol{\varepsilon_0}$ is the vacuum permittivity. Maxwell's equations, intended for the scattering of electromagnetic radiation with nanoparticles, were solved in the model [59]. In particular, the wavelength-dependent optical characteristics, including the absorption cross section and the scattering cross section, were calculated. Parametric Sweep was introduced from 400 nm to 1000 nm, with a step size of 5 nm. The simulation computed the local electromagnetic field on each mesh point, accompanied by an incident plane wave propagating

in the z-direction by the electric field polarized along the *x*-axis and *y*-axis to opportunely excite the transversal and longitudinal resonance of the gold nanorods. The nanoparticle was modeled in all its constituent parts, starting from (i) AuNR@CTAB, (ii) AuNR@SiO_2, (iii) AuNR@SiO_2@Au and (iv) AuNR@SiO_2@Au@SiO_2. An "extra-fine" mesh, consisting of a free triangular and tetrahedral geometry with about 25,000–80,000 elements (from the AuNR@CTAB to the AuNR@SiO_2@Au@SiO_2 structure) was considered. For the outer boundary of the spherical domain, the scattering boundary condition was used to make the boundary transparent for the scattered wave. All the parameters used in the numerical modelling are listed in Table S1. The absorption cross section and the scattering cross section were derived by the calculation of the rate of the electromagnetic energy that was absorbed (W_{abs}) and scattered (W_{sca}) by the nanoparticle with respect to the incident irradiance, defined as the energy flux of the incident wave (P_{inc}): $\sigma_{abs} = W_{abs}/P_{inc}$ and $\sigma_{sca} = W_{sca}/P_{inc}$, respectively. The total absorbed energy was derived by integrating the energy loss (Q_{loss}) over the volume of the particle ($W_{abs} = \iiint_{V_P} Q_{loss} dV$), while the scattered energy was derived by integrating the Poynting vector (P_{sca}) over an imaginary sphere around the particle ($W_{sca} = \oiint_S P_{sca} \cdot n \, dS$). The extinction cross section (σ_{ext}) represents the amount of energy removed from the incident field due to absorption and scattering ($\sigma_{ext} = \sigma_{abs} + \sigma_{sca}$).

3. Results and Discussion

All the samples were morphologically characterized by TEM and, from a spectroscopic point of view, by collecting the extinction spectra of the aqueous colloidal dispersion. For samples with a core consisting of gold nanorods, the theoretical spectra were calculated. Following Chart 1, we first discuss all nanoparticles having a gold rod-shaped core. Figure 1a reports the TEM images of AuNR@CTAB, showing the gold nanorods coated with CTAB (57 × 18 nm), while Figure 2 (blue line) displays the experimental extinction spectrum of its water dispersion.

A longitudinal band at 732 nm and a transversal one at 515 nm were observed. According to the FWHM of the longitudinal band and TEM image, the sample was homogeneous in shape and size. By modeling CTAB-covered gold nanorods of 57 × 18 nm (Figure 3a), the calculated spectrum fit satisfactorily with the experimental one. In Figure 1b, the TEM image of the AuNR@SiO_2 sample is reported: a thick silica shell of 60 nm formed around the gold core. When the gold nanorods were covered by the silica shell, their longitudinal band red-shifted to 770 nm (Figure 2, red line). The simulated absorption and extinction cross sections for AuNRs in the same conditions as the experimental measurements (Figure 3a,b) showed a good agreement with the experimental results. In particular, with the addition of the silica shell, the two plasmonic peaks red-shifted, appearing at 520 nm and 775 nm, respectively, due to a change in the refractive index of the surrounding medium (from water to silica) around the gold nanorods. The metal–dielectric interface in the case of nanoparticles covered with CTAB consisted of water ($n_d{}^{20}$ = 1.33, water refractive index) embedding CTAB. In the case of nanoparticles covered with the silica shell, the dielectric had a higher refractive index ($n_d{}^{20}$ = 1.45, silica refractive index) [60–62]. The TEM image of AuNR@SiO_2@seed (Figure 1c) shows the whole silica surface functionalized with the small gold seeds. After the seed solution addition, the transversal band increased, due to the contribution of the seeds (Figure 2, green line), while the position of the transversal and longitudinal bands remained unvaried with respect to that observed for the previous sample. In the AuNR@SiO_2@Au sample, the gold seeds gave way to a gold shell with a thickness of about 55 × 28 nm, giving rise to MIMI nanoparticles with overall dimensions of about 280 × 200 nm (Figure 1d). The spectral behavior (Figure 2, violet line), confirmed by calculations (Figure 3c) dramatically changed with respect to the previous samples: scattering appeared to be predominant over absorption, and a broadened band in the range from 730 nm to 1200 nm was recorded. The transversal band appeared barely visible.

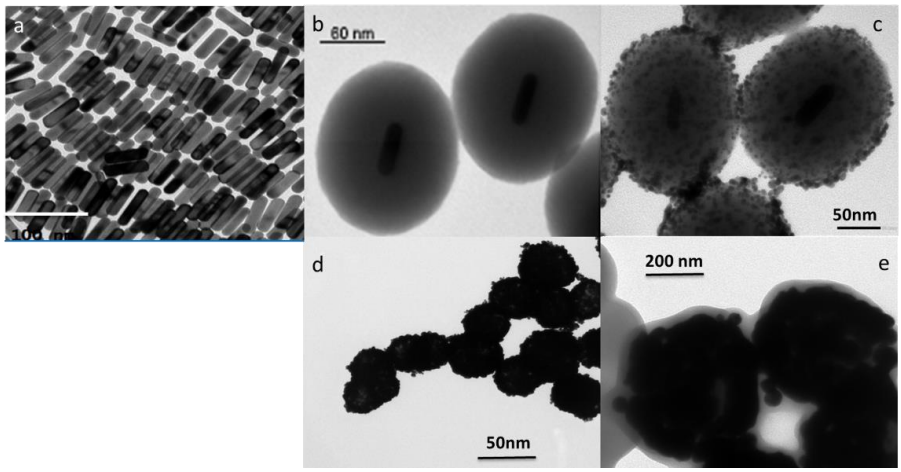

Figure 1. TEM images: AuNR@CTAB (**a**); AuNR@SiO_2 (**b**); AuNR@SiO_2@seed (**c**); AuNR@SiO_2@Au (**d**); AuNR@SiO_2@Au@SiO_2 (**e**).

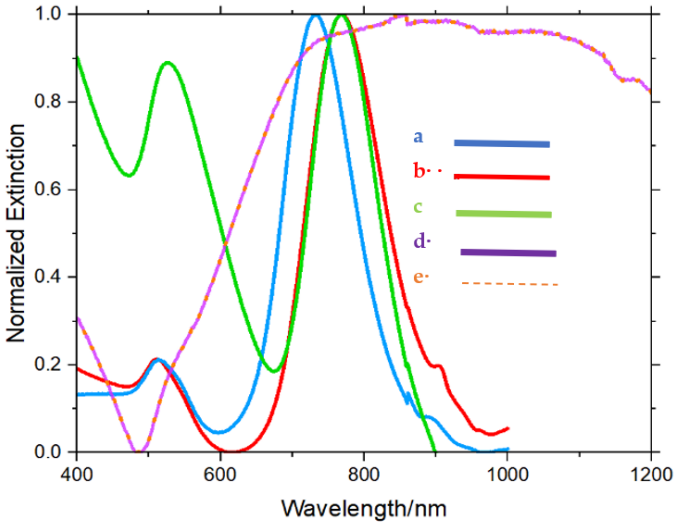

Figure 2. Experimental spectra: extinction spectra of the aqueous colloidal dispersions: AuNR (**a**, blue line); AuNR@SiO_2 (**b**, red line); AuNR@SiO_2@seed (**c**, green line); AuNR@SiO_2@Au (**d**, violet line) overlapping with AuNR@SiO_2@Au@SiO_2 (**e**, orange dotted line).

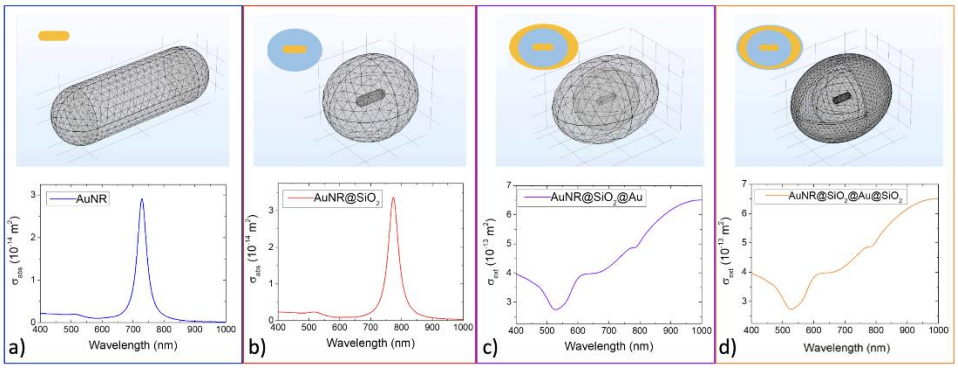

Figure 3. Shown is the 3D meshing of the model geometry of the constitutive elements of the nano-matryoshka and simulated absorbance cross sections of (**a**) AuNR, (**b**) AuNR@SiO_2 and scattering cross sections of (**c**) AuNR@SiO_2@Au and (**d**) AuNR@SiO_2@Au@SiO_2.

Finally, the previous MIMI nanoparticle was covered by a 3 nm thick silica shell, giving rise to the MIMI nano-matryoshka AuNR@SiO_2@Au@SiO_2, reported in the TEM image of Figure 1e. The outermost shell of silica of a few nm did not make any contribution to the optical response of the nanoparticle, as shown by the spectrum in Figure 2 (orange dotted line) and confirmed by calculation (Figure 3d). EDX measurements were conducted on AuNR@SiO_2@Au@SiO_2 (Figure S3 in ESI)

The comparison between the experimental and the calculated extinction spectra allowed evaluating the contribution of scattering and absorption (see Figure S2 in ESI). In the case of AuNR and AuNR@SiO_2, it was evident that the scattering contribution was negligible compared to the absorption one, while in the case of AuNR@SiO_2@Au and AuNR@SiO_2@Au@SiO_2, the scattering contribution was preponderant over that of absorption. This was attributable to the larger size of the last two samples compared to the first two.

As described in the previous paragraph, the same synthetic procedure applied to rod-shaped nanoparticles (i.e., AuNR@CTAB) was applied to a mix of gold nanoparticles with different shapes (i.e., AuNP@CTAB), in order to test its applicability and to study the influence of the starting material on the final product (i.e., AuNP@SiO_2@Au@SiO_2). Figure 4 shows the TEM image of the family system reported in Path 2 of Chart 1. Comparing these images with those shown in Figure 1, the most relevant difference obviously concerns the shape of the starting AuNPs, while the other samples evidence the same architecture of the family system of Path 1 (see Chart 1), confirming the versatility of the proposed synthetic protocol.

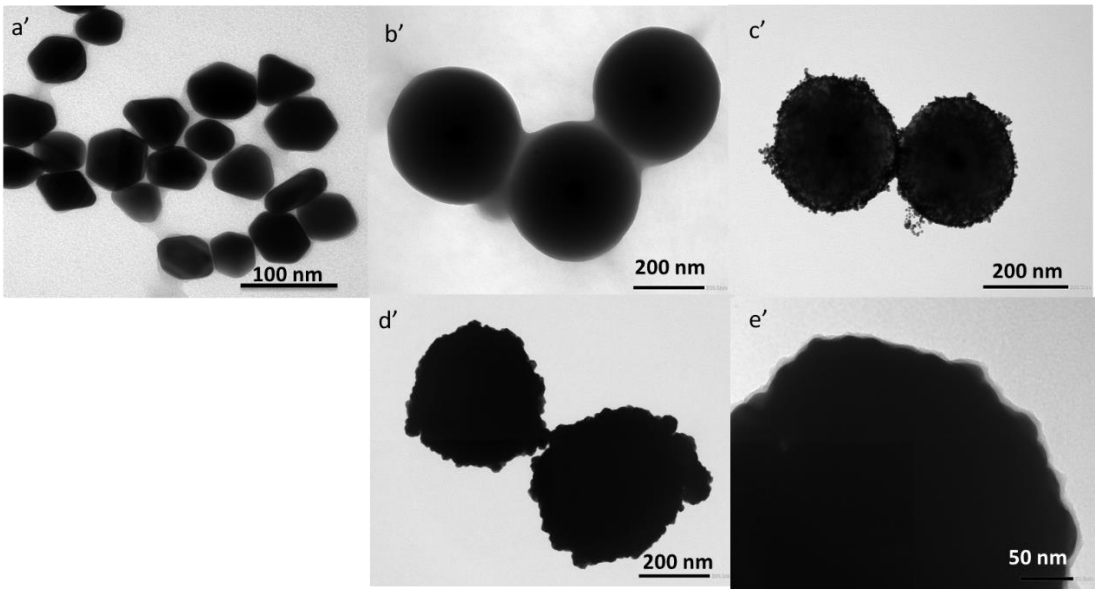

Figure 4. TEM images: AuNP@CTAB (50–70 nm) (**a'**); AuNP@SiO_2 (250 nm) (**b'**); AuNP@SiO_2@seed (**c'**); AuNP@SiO_2@Au (350 nm) (**d'**); AuNP@SiO_2@Au@SiO_2 (**e'**).

Making a comparison between AuNR and the AuNP family, it is clear that the plasmonic properties of the nano-matryoshka changed according to the metal core. The plasmonic peaks moved to different wavelengths as the shape of the nanoparticle changed. In fact, in both proposed cases, AuNR and AuNP (Figures 2 and 5, experimental spectra), the plasmonic bands changed as the matryoshka took shape. As shown in Figure 5, AuNP showed only one plasmonic band. The peaks of AuNP@SiO_2@Au and AuNP@SiO_2@Au@SiO_2, violet line and dotted orange line, respectively, were quite similar because the contribution of the thin silica shell in AuNP@SiO_2@Au@SiO_2 was negligible. On the other hand, the two peaks of AuNR, red shifted as the matryoshka took shape (Figure 2). The broadening of the longitudinal band was impressive in the last two steps, AuNR@SiO_2@Au and AuNR@SiO_2@Au@SiO_2 (violet

line and orange dotted line in Figure 2), due to the large dimensions of the nano-matryoshka. Also in this case, there was an overlap between the two bands, because the contribution of the thin silica shell was negligible.

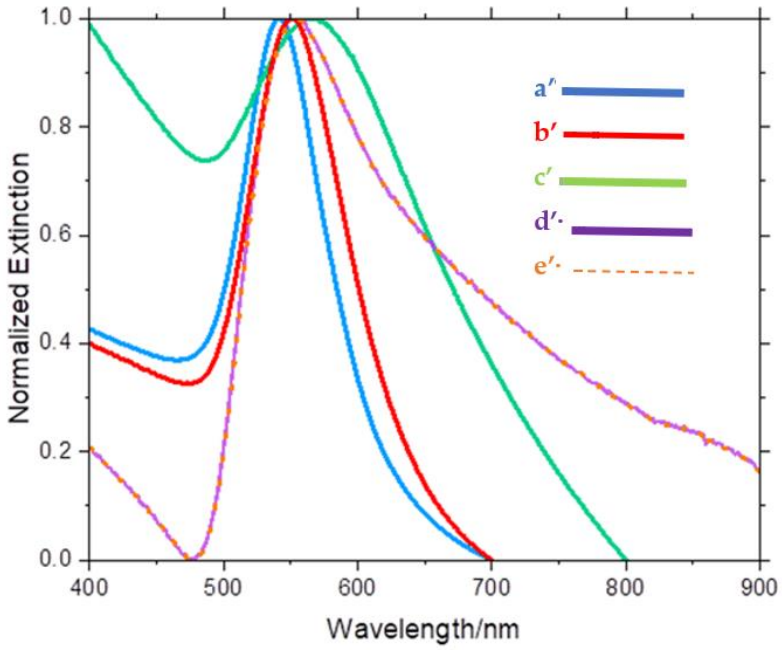

Figure 5. Experimental spectra: extinction spectra of the aqueous colloidal dispersions: AuNP@CTAB (**a′**, blue line); AuNP@SiO_2 (**b′**, red line); AuNP@SiO_2@seed (**c′**, green line); AuNP@SiO_2@Au (**d′**, violet line) overlapping with AuNP@SiO_2@Au@SiO_2 (**e′**, orange dotted line).

4. Conclusions

This paper presents the first example of a nanomaterial with MIMI architecture dispersed in an aqueous environment. The nanomaterial was designed and synthesized according to a seed-mediated growth approach which, starting from CTAB-coated gold nanorods, gave shape, step by step, to a hybrid hierarchical structure consisting of the alternation of gold and silica shells, recalling the structure of a matryoshka. The same protocol was applied to any shape of the nanoparticles, and the final plasmonic properties of the nano-matryoshka depended on the shape of the metal core.

All the intermediates were characterized, both from a morphological point of view, by TEM, and optically, by UV–Vis spectroscopy. When the matryoshka took shape, the spectrum of both samples changed drastically: the longitudinal band of the nanorods widened substantially until reaching wavelengths in the NIR range, the band of the AuNP@CTAB-derived nanosystems continued to fall into the visible range, but a shoulder around 700 nm was impressive. The computational results, based on an FEM analysis, confirmed the experimental ones, highlighting that the final plasmonic properties of the nano-matryoshka depended on the shape of the metal core and on the refractive index of the surrounding media and could be suitably tuned to the NIR spectrum region. Furthermore, the comparison between the experimental and the calculated spectra allowed estimating the mutual contribution of scattering and absorption to the optical properties of the nanosystems. The computational effort represents a practical tool for the development of matryoshka with specific plasmonic features.

These findings could have application in various fields; in particular, the construction of metamaterials in aqueous solution is an exceptional goal, considering the possibility to properly functionalize the nanoparticle surface, obtaining a biocompatible nano-matryoshka that, by exploiting the sensitivity of a metamaterial, could be used for in vivo biopsies.

Supplementary Materials: The following supporting information can be downloaded at: https://www.mdpi.com/article/10.3390/app13052982/s1, Figure S1: TEM images and Uv–Vis spectra of AuNS@NaCit; Cross section calculations; Figure S2: Calculated extinction, absorption and scattering cross sections of (a) AuNR, (b) AuNR@SiO_2, (c) AuNR@SiO_2@Au and (d) AuNR@SiO_2@Au@SiO_2; Figure S3: EDX measurement of AuNR@SiO_2@Au@SiO_2; Table S1: Parameters used in the numerical modelling of the nanostructures.

Author Contributions: A.C. synthesized and characterized the samples, wrote the draft of the manuscript, prepared the figures; G.D.M. reviewed the manuscript; G.P., A.G. and G.S., conducted the theoretical study; M.L.D. supervised all steps, wrote the main manuscript text, reviewed and validated the manuscript. All authors have read and agreed to the published version of the manuscript.

Funding: This research received no external funding.

Institutional Review Board Statement: Not applicable.

Informed Consent Statement: Not applicable.

Data Availability Statement: We encourage all authors of articles published in MDPI journals to share their research data. In this section, please provide details regarding where data supporting reported results can be found, including links to publicly archived datasets analyzed or generated during the study. Where no new data were created, or where data is unavailable due to privacy or ethical restrictions, a statement is still required. Suggested Data Availability Statements are available in section "MDPI Research Data Policies" at https://www.mdpi.com/ethics.

Acknowledgments: The authors are grateful to NLHT, Nanoscience Laboratory for Human Technologies, POR Calabria FESR-FSE 14/20, and to "Progetto STAR 2—PIR01_00008"—Ministero dell'Università e Ricerca/Italian Ministry of University and Research.

Conflicts of Interest: The authors declare no conflict of interest.

References

1. Roco, M.C. Nanotechnology: Convergence with modern biology and medicine. *Curr. Opin. Biotechnol.* **2003**, *14*, 337–346. [CrossRef] [PubMed]
2. Roco, M.C. Principles of convergence in nature and society and their application: From nanoscale, digits, and logic steps to global progress. *J. Nanoparticle Res.* **2020**, *22*, 321. [CrossRef] [PubMed]
3. Candreva, A.; De Rose, R.; Perrotta, I.D.; Guglielmelli, A.; La Deda, M. Light-Induced Clusterization of Gold Nanoparticles: A New Photo-Triggered Antibacterial against *E. coli* Proliferation. *Nanomaterials* **2023**, *13*, 746. [CrossRef]
4. Fu, Y.; Fang, F.; Xu, Z. Nanofabrication and Characterization of Plasmonic Structures. *Nanofabrication* **2011**, *4*, 243–266. [CrossRef]
5. Henzie, J.; Lee, J.; Lee, M.H.; Hasan, W.; Odom, T.W. Nanofabrication of plasmonic structures. *Annu. Rev. Phys. Chem.* **2009**, *60*, 147–165. [CrossRef]
6. Rane, A.V.; Kanny, K.; Abitha, V.K.; Thomas, S. *Methods for Synthesis of Nanoparticles and Fabrication of Nanocomposites*; Elsevier Ltd.: Amsterdam, The Netherlands, 2018.
7. Mohan Bhagyaraj, S.; Oluwafemi, O.S. *Nanotechnology: The Science of the Invisible*; Elsevier Ltd.: Amsterdam, The Netherlands, 2018.
8. Amendola, V.; Pilot, R.; Frasconi, M.; Maragò, O.M.; Iatì, M.A. Surface plasmon resonance in gold nanoparticles: A review. *J. Phys. Condens. Matter* **2017**, *29*, 1–48. [CrossRef] [PubMed]
9. Tang, Y.; Zeng, X.; Liang, J. Surface plasmon resonance: An introduction to a surface spectroscopy technique. *J. Chem. Educ.* **2010**, *87*, 742–746. [CrossRef] [PubMed]
10. Chen, J.; Gong, M.; Fan, Y.; Feng, J.; Han, L.; Xin, H.L.; Cao, M.; Zhang, Q.; Zhang, D.; Lei, D.; et al. Collective Plasmon Coupling in Gold Nanoparticle Clusters for Highly Efficient Photothermal Therapy. *ACS Nano* **2022**, *16*, 910–920. [CrossRef] [PubMed]
11. Scheeler, S.P.; Mühlig, S.; Rockstuhl, C.; Hasan, S.B.; Ullrich, S.; Neubrech, F.; Kudera, S.; Pacholski, C. Plasmon coupling in self-assembled gold nanoparticle-based honeycomb islands. *J. Phys. Chem. C* **2013**, *117*, 18634–18641. [CrossRef]
12. M.C. Daniel, D.A. Plasmon coupling in self-assembled gold nanoparticle-based honeycomb islands. *Chem. Rev.* **2004**, *104*, 293–346.
13. Hanske, C.; Tebbe, M.; Kuttner, C.; Bieber, V.; Tsukruk, V.V.; Chanana, M.; König, T.A.F.; Fery, A. Strongly coupled plasmonic modes on macroscopic areas via template-assisted colloidal self-assembly. *Nano Lett.* **2014**, *14*, 6863–6871. [CrossRef]
14. Ritchie, R.H. Surface plasmons in solids. *Surf. Sci.* **1973**, *34*, 1–19. [CrossRef]
15. Kazanskiy, N.L.; Khonina, S.N.; Butt, M.A. Plasmonic sensors based on Metal-insulator-metal waveguides for refractive index sensing applications: A brief review. *Phys. E Low-Dimensional Syst. Nanostructures* **2020**, *117*, 113798. [CrossRef]
16. Ghasemi, M.R.; Bayati, M.S. Proposal for metal–insulator–metal plasmonic power splitter and demultiplexer suitable for implementation in optical switches. *IET Optoelectron.* **2021**, *15*, 200–206. [CrossRef]

17. Liang, Z.; Wen, Y.; Zhang, Z.; Liang, Z.; Xu, Z.; Lin, Y.S. Plasmonic metamaterial using metal-insulator-metal nanogratings for high-sensitive refraction index sensor. *Results Phys.* **2019**, *15*, 102602. [CrossRef]
18. Tamura, M.; Kagata, H. Analysis of metal-insulator-metal structure and its application to sensor. *IEEE Trans. Microw. Theory Tech.* **2010**, *58*, 3954–3960. [CrossRef]
19. Shin, Y.J.; Son, J.H.; Lee, D.H.; Lee, M.H. Insulator-metal-insulator-metal-insulator and metal-insulator-metal vertical directional couplers with surface plasmon polariton waveguides. *J. Nanosci. Nanotechnol.* **2017**, *17*, 7093–7100. [CrossRef]
20. Yan, M. Metal-insulator-metal light absorber: A continuous structure. *J. Opt.* **2013**, *15*, 025006. [CrossRef]
21. Hung, C.C.; Oates, A.S.; Lin, H.C.; Chang, P.; Wang, J.L.; Huang, C.C.; Yau, Y.W. New understanding of Metal-Insulator-Metal (MIM) capacitor degradation behavior. *Annu. Proc.-Reliab. Phys.* **2007**, *5*, 630–631. [CrossRef]
22. Ekanayake, S.R.; Ford, M.; Cortie, M. Metal-insulator-metal (MIM) nanocapacitors and effects of material properties on their operation. *Mater. Forum* **2004**, *27*, 15–20.
23. Sreekanth, K.V.; De Luca, A.; Strangi, G. Negative refraction in graphene-based hyperbolic metamaterials. *Appl. Phys. Lett.* **2013**, *103*, 023107. [CrossRef]
24. Le, K.Q.; Ngo, Q.M.; Nguyen, T.K. Nanostructured Metal-Insulator-Metal Metamaterials for Refractive Index Biosensing Applications: Design, Fabrication, and Characterization. *IEEE J. Sel. Top. Quantum Electron.* **2017**, *23*, 388–393. [CrossRef]
25. Ogawa, S.; Kimata, M. Metal-insulator-metal-based plasmonic metamaterial absorbers at visible and infrared wavelengths: A review. *Materials* **2018**, *11*, 458. [CrossRef]
26. Yang, J.; Sauvan, C.; Jouanin, A.; Collin, S.; Pelouard, J.L.; Lalanne, P. Quality factor of 3D Metal-Insulator-Metal nanoresonators. In Proceedings of the 2013 7th International Congress on Advanced Electromagnetic Materials in Microwaves and Optics, Talence, France, 16–21 September 2013; pp. 397–399. [CrossRef]
27. Kharlamov, V.F.; Korostelev, D.A.; Bogoraz, I.G.; Milovidova, O.A. Electrical properties of the metal-insulator nanoparticles-metal structure. *Phys. Solid State* **2012**, *54*, 1281–1288. [CrossRef]
28. Thissen, P.; Schindler, B.; Diesing, D.; Hasselbrink, E. Optical response of metal-insulator-metal heterostructures and their application for the detection of chemicurrents. *New J. Phys.* **2010**, *12*, 113014. [CrossRef]
29. Periasamy, P.; O'Hayre, R.P.; Berry, J.J.; Parilla, P.A.; Ginley, D.S.; Packard, C.E. A novel way to characterize metal-insulator-metal devices via nanoindentation. In Proceedings of the 2011 37th IEEE Photovoltaic Specialists Conference, Seattle, WA, USA, 19–24 June 2011; pp. 001754–001757. [CrossRef]
30. Hamon, C.; Sanz-Ortiz, M.N.; Modin, E.; Hill, E.H.; Scarabelli, L.; Chuvilin, A.; Liz-Marzán, L.M. Hierarchical organization and molecular diffusion in gold nanorod/silica supercrystal nanocomposites. *Nanoscale* **2016**, *8*, 7914–7922. [CrossRef]
31. Hamon, C.; Novikov, S.; Scarabelli, L.; Basabe-Desmonts, L.; Liz-Marzán, L.M. Hierarchical self-assembly of gold nanoparticles into patterned plasmonic nanostructures. *ACS Nano* **2014**, *8*, 10694–10703. [CrossRef]
32. Turković, A.; Dubček, P.; Fox, N.D. Self-organization of nanoparticles in a TiO2 thin film on a glass substrate. *Vacuum* **2005**, *80*, 108–112. [CrossRef]
33. Caputo, G.; Pinna, N. Nanoparticle self-assembly using π-π Interactions. *J. Mater. Chem. A* **2013**, *1*, 2370–2378. [CrossRef]
34. Candreva, A.; Morrone, E.; La Deda, M. Gold Sea Urchin-Shaped Nanoparticles: Synthesis and Characterization of Energy Transducer Candidates. *Plasmonics* **2022**, *18*, 291–298. [CrossRef]
35. Song, W.; Yoshitake, M.; Yamauchi, Y.; Lykhach, Y. Fabrication of nano-scale metal-insulator-metal cathode: Control of film structure and thickness. In Proceedings of the IVESC 2004. The 5th International Vacuum Electron Sources Conference Proceedings (IEEE Cat. No. 04EX839), Beijing, China, 6–10 September 2004; pp. 131–133. [CrossRef]
36. Sreekanth, K.V.; Alapan, Y.; Elkabbash, M.; Ilker, E.; Hinczewski, M.; Gurkan, U.A.; De Luca, A.; Strangi, G. Extreme sensitivity biosensing platform based on hyperbolic metamaterials. *Nat. Mater.* **2016**, *15*, 621–627. [CrossRef]
37. Wu, C.; Khanikaev, A.B.; Adato, R.; Arju, N.; Yanik, A.A.; Altug, H.; Shvets, G. Fano-resonant asymmetric metamaterials for ultrasensitive spectroscopy and identification of molecular monolayers. *Nat. Mater.* **2012**, *11*, 69–75. [CrossRef]
38. Zeng, S.; Sreekanth, K.V.; Shang, J.; Yu, T.; Chen, C.K.; Yin, F.; Baillargeat, D.; Coquet, P.; Ho, H.P.; Kabashin, A.V.; et al. Graphene-Gold Metasurface Architectures for Ultrasensitive Plasmonic Biosensing. *Adv. Mater.* **2015**, *27*, 6163–6169. [CrossRef]
39. Liu, N.; Weiss, T.; Mesch, M.; Langguth, L.; Eigenthaler, U.; Hirscher, M.; Sönnichsen, C.; Giessen, H. Planar metamaterial analogue of electromagnetically induced transparency for plasmonic sensing. *Nano Lett.* **2010**, *10*, 1103–1107. [CrossRef]
40. Kabashin, A.V.; Evans, P.; Pastkovsky, S.; Hendren, W.; Wurtz, G.A.; Atkinson, R.; Pollard, R.; Podolskiy, V.A.; Zayats, A.V. Plasmonic nanorod metamaterials for biosensing. *Nat. Mater.* **2009**, *8*, 867–871. [CrossRef]
41. Gao, C.; Goebl, J.; Yin, Y. Seeded growth route to noble metal nanostructures. *J. Mater. Chem. C* **2013**, *1*, 3898–3909. [CrossRef]
42. Xia, Y.; Gilroy, K.D.; Peng, H.C.; Xia, X. Seed-Mediated Growth of Colloidal Metal Nanocrystals. *Angew. Chemie-Int. Ed.* **2017**, *56*, 60–95. [CrossRef] [PubMed]
43. Millstone, J.E.; Wei, W.; Jones, M.R.; Yoo, H.; Mirkin, C.A. Iodide ions control seed-mediated growth of anisotropic gold Nanoparticles. *Nano Lett.* **2008**, *8*, 2526–2529. [CrossRef]
44. Leng, W.; Pati, P.; Vikesland, P.J. Room temperature seed mediated growth of gold nanoparticles: Mechanistic investigations and life cycle assesment. *Environ. Sci. Nano* **2015**, *2*, 440–453. [CrossRef]
45. Candreva, A.; Parisi, F.; Bartucci, R.; Guzzi, R.; Maio, D. Synthesis and Characterization of Hyper-Branched Nanoparticles with Magnetic and Plasmonic Properties. *ChemistrySelect* **2022**, *7*, 202201375. [CrossRef]

46. Scarabelli, L.; Grzelczak, M.; Liz-Marzán, L.M. Tuning gold nanorod synthesis through prereduction with salicylic acid. *Chem. Mater.* **2013**, *25*, 4232–4238. [CrossRef]
47. Scarabelli, L.; Sánchez-Iglesias, A.; Pérez-Juste, J.; Liz-Marzán, L.M. A "Tips and Tricks" Practical Guide to the Synthesis of Gold Nanorods. *J. Phys. Chem. Lett.* **2015**, *6*, 4270–4279. [CrossRef] [PubMed]
48. Candreva, A.; Lewandowski, W.; La Deda, M. Thickness control of the Silica Shell: A way to tune the Plasmonic Properties of isolated and assembled Gold Nanorods. *J. Nanoparticle Res.* **2022**, *24*, 19. [CrossRef]
49. Murphy, C.J.; Thompson, L.B.; Chernak, D.J.; Yang, J.A.; Sivapalan, S.T.; Boulos, S.P.; Huang, J.; Alkilany, A.M.; Sisco, P.N. Gold nanorod crystal growth: From seed-mediated synthesis to nanoscale sculpting. *Curr. Opin. Colloid Interface Sci.* **2011**, *16*, 128–134. [CrossRef]
50. Candreva, A.; Di Maio, G.; Parisi, F.; Scarpelli, F.; Crispini, A.; Godbert, N.; Ricciardi, L.; Nucera, A.; Rizzuto, C.; Barberi, R.C.; et al. Luminescent Self-Assembled Monolayer on Gold Nanoparticles: Tuning of Emission According to the Surface Curvature. *Chemosensors* **2022**, *10*, 176. [CrossRef]
51. Candreva, A.; Parisi, F.; Di, G.; Francesca, M.; Iolinda, S.; Godbert, N.; La, M. Post—Synthesis heating, a key step to tune the LPR band of gold nanorods covered with CTAB or embedded in a silica shell. *Gold Bull.* **2022**, *55*, 195–205. [CrossRef]
52. Candreva, A.; Di Maio, G.; La Deda, M. A quick one-step synthesis of luminescent gold nanospheres. *Soft Matter* **2020**, *16*, 10865–10868. [CrossRef] [PubMed]
53. Hinman, J.G.; Stork, A.J.; Varnell, J.A.; Gewirth, A.A.; Murphy, C.J. Seed mediated growth of gold nanorods: Towards nanorod matryoshkas. *Faraday Discuss.* **2016**, *191*, 9–33. [CrossRef]
54. ZIMMERMAN, W.B.J. Introduction To Comsol Multiphysics. *Multiphys. Model. Finite Elem. Methods* **2006**, *6*, 1–26. [CrossRef]
55. Yushanov, S.P.; Crompton, J.S.; Koppenhoefer, K.C. Scattering of Electromagnetic Waves Overview. In Proceedings of the 2013 COMSOL Conference, Boston, MA, USA, 9-11 October 2013.
56. Palermo, G.; Cataldi, U.; Condello, A.; Caputo, R.; Bürgi, T.; Umeton, C.; De Luca, A. Flexible thermo-plasmonics: An opto-mechanical control of the heat generated at the nanoscale. *Nanoscale* **2018**, *10*, 16556–16561. [CrossRef]
57. Palermo, G.; Strangi, G. Thermoplasmonic-biosensing demonstration based on the photothermal response of metallic nanoparticles. *J. Appl. Phys.* **2020**, *128*, 164302. [CrossRef]
58. Nucera, A.; Grillo, R.; Rizzuto, C.; Barberi, R.C.; Castriota, M.; Bürgi, T.; Caputo, R.; Palermo, G. Effect of the Combination of Gold Nanoparticles and Polyelectrolyte Layers on SERS Measurements. *Biosensors* **2022**, *12*, 895. [CrossRef] [PubMed]
59. Ichimaru, S. Scattering of Electromagnetic Waves. *Stat. Phys. Dense Plasmas* **2019**, *6*, 39–52. [CrossRef]
60. Novo, C.; Mulvaney, P. Charge-Induced Rayleigh Instabilities In Small Gold Rods. *Nano Lett.* **2007**, *7*, 520–524. [CrossRef]
61. Chen, H.; Kou, X.; Yang, Z.; Ni, W.; Wang, J. Shape- and size-dependent refractive index sensitivity of gold nanoparticles. *Langmuir* **2008**, *24*, 5233–5237. [CrossRef]
62. Anker, J.N.; Hall, W.P.; Lyandres, O.; Shah, N.C.; Zhao, J.; Duyne, R.P. Van 2008 [review] Biosensing with plasmonic nanosensors. *Nat. Mater.* **2008**, *7*, 8–10.

Disclaimer/Publisher's Note: The statements, opinions and data contained in all publications are solely those of the individual author(s) and contributor(s) and not of MDPI and/or the editor(s). MDPI and/or the editor(s) disclaim responsibility for any injury to people or property resulting from any ideas, methods, instructions or products referred to in the content.

CRYSTAL GROWTH & DESIGN

pubs.acs.org/crystal

Article

Conjugation of a Silver-Based Coordination Polymer with Curcumin: A New Case of an Inorganic Polymeric Co-crystal

Alessandra Crispini, Massimo La Deda, Giuseppe Di Maio, Nicolas Godbert, Antonio Tagarelli, Rosangela Elliani, Angela Candreva, Renata De Rose, Iolinda Aiello, Mario Amati, and Francesca Scarpelli*

Cite This: https://doi.org/10.1021/acs.cgd.3c00042

Read Online

ACCESS | Metrics & More | Article Recommendations | Supporting Information

ABSTRACT: A new structural form of the already reported silver-based 1D coordination polymer (CP) $[(bpy)Ag(OTf)]_\infty$ (bpy = 2,2′-bipyridine; OTf = trifluoromethanesulfonate) has been synthesized and fully characterized through single-crystal and powder XRD, DSC, and FTIR analysis. The reaction of both structural forms of the Ag(I) CP with curcumin (curc) afforded the formation of a new solid form, specifically an inorganic polymeric co-crystal between curc and [(bpy)Ag (OTf)] in a 1: 4 molar ratio, respectively. The co-crystal has been characterized both in solution and in the solid state through ^{1}H NMR, PXRD, DSC, IR, and UV−vis spectroscopies. In addition, a thorough computational study has been carried out to reveal the possible interaction modes between the co-crystal components. The Ag(I) compounds here presented have been preliminarily tested for antimicrobial activity against *Staphylococcus aureus* and *Escherichia coli* strains, all showing promising results.

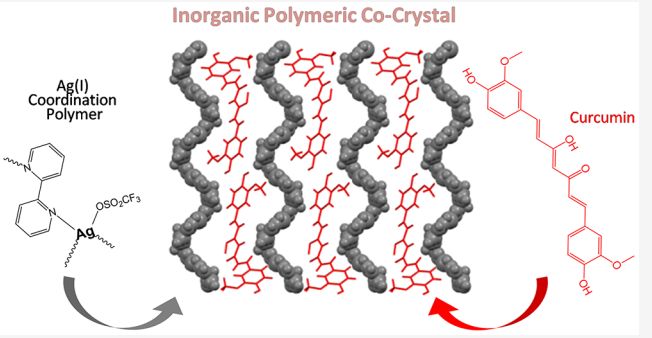

1. INTRODUCTION

Metallopolymers or metal-containing polymers (MPs) represent an innovative approach for the design of multifunctional macromolecular materials. Typically obtained by incorporating various metal centers (main-group metals, transition metals, and lanthanides) into an organic polymer backbone, MPs benefit from the properties of the polymeric frameworks and the functionalities of the metal centers, showing a notable range of applications in the field of material science, catalysis and bio-catalysis, environmental, and biomedicine.[1−6] Contextually, the field of MPs profited from the development of metal-mediated self-assembly as a tool to reach supramolecular metallopolymers.[7,8] The versatility of the strength and the number of metal−ligand interactions by varying the metal binding sites and the simple organic ligands has allowed the generation of one, two, or three-dimensional supramolecular metallopolymers, generally referred as coordination polymers (CPs), in particular, metal−organic frameworks (MOFs) or porous coordination polymers (PCPs) when porosity is present in the supramolecular network.[9,10] This new class of inorganic−organic hybrid materials has been recognized to possess a potential significant range of applications in antimicrobials, gas absorption and separation, luminescent materials, and drug delivery based on their different topologies and structures.[11−14] One-dimensional CPs, the simplest topological type of coordination arrangement, despite being considered the least structurally interesting, have received increasing attention due to the ease of synthesis and tunability of the resulting frameworks when compared to 3D CP structures.[15] Moreover, 1D CPs have shown a rich range of applications depending on the metal ions and the simple coordinating organic ligands, working as luminescent probes, dye adsorbers, and drug delivery systems.[16−18] In the case of silver-based CPs, the modulation of the dimensionality is well related to the variable coordination number and flexible geometries reached by this metal ion. Silver coordination compounds have received great attention owing to their appealing properties, in particular, their interesting biological activities.[19] Low toxicity, antimicrobial, anticancer, anti-inflammatory, antifungal, and antiplasmodial properties have been reported for many Ag(I) complexes.[20−24] In addition, the bacterial resistance to silver is rare and transitory;[24] thus, Ag(I) complexes could be considered as an alternative to common antibiotics against which resistant bacterial strains have developed. Moreover, the reaction between Ag(I) salts and

Received: January 11, 2023
Revised: March 31, 2023

Downloaded via UNIV DELLA CALABRIA on April 26, 2023 at 17:01:54 (UTC).
See https://pubs.acs.org/sharingguidelines for options on how to legitimately share published articles.

ACS Publications

© XXXX American Chemical Society

bridging bidentate ligands frequently affords the formation of 1D Ag(I) polymers, which can be considered excellent candidates as antibacterial agents.[25−30]

Recently, much attention has been focused on the preparation of co-crystals, which find application in the pharmaceutical and food sectors[31,32] as well as in the design of the next-generation electro-optical systems.[33−35] Generally, co-crystals are multicomponent crystalline materials composed of two or three small organic molecules. In addition, new categories of multicomponent crystals are currently under development. In particular, the rare polymeric co-crystals in which at least one component is a polymer are promising materials since the choice of a polymeric drug and/or co-former could represent an ingenious pharmaceutical strategy to modulate the stability, the solubility, and the release of poorly soluble drugs.[36−38] However, polymeric co-crystals as well as inorganic co-crystals have been infrequently obtained due to the fact that, in order to obtain a co-crystal, the starting materials should possess structural similarity, comparable potential energies, and almost identical crystallization kinetics.[39,40] Indeed, although a great number of organic co-crystals are known,[41] few examples of co-crystals including a metal complex have been reported so far.[42−48] Metal complexes with their precise geometries hardly exhibit lattice packing forces and crystallization kinetics similar to small organic compounds. Many examples of inorganic co-crystals are actually composed of two parent metal complexes[44,45] or geometrical isomers of the same coordination compound.[49]

In the past, we have been strongly involved in investigations concerning the formation of silver-based coordination compounds obtained through the interaction between the Ag(I) ion and 4,4′-disubstituted-2,2′-bipyridines where the careful choice of the substituents on the bipyridyl ligand and the nature of the counterions played a fundamental role in the modulation of the desired properties, such as liquid crystallinity.[25,50] Moreover, the use of 2,2′-bipyridine (bpy) in combination with silver salts in a 1:1 molar ratio has highlighted that the anion drove the coordination mode of the nitrogen ligand, giving rise to structures ranging from a discrete molecule to 1D CPs.[25,51] Continuing to explore the ability of bpy to generate 1D silver-based CPs as a ligand less investigated when compared with typical bipyridinium-bearing ligands used in the synthesis of CPs,[52] herein, we report the synthesis and the characterization of a new structural form ($\{[(bpy)Ag][OTf]\}_\infty$, hereafter referred to as the β-form) of the chiral silver-based coordination polymer of formula $[(bpy)Ag(OTf)]_\infty$ (hereafter referred to as the α-form) previously reported.[25] The two forms, namely, α and β, are characterized by the same building blocks but display a different arrangement of them, thus representing two structural isomers.

Both isomeric forms of the Ag(I) polymer have been used to explore their ability to accommodate organic molecules through non-covalent interactions, co-crystallizing, in particular, curcumin (curc), which is a fascinating molecule showing several beneficial properties to human health[53−55] and, most importantly, a very low tendency to coordinate the Ag(I) ion. This polyphenol for which in the solid state three different polymorphs (forms I, II, and III) are known[56] is characterized by poor bioavailability and low stability in solution, which are aspects that can both be overcome with the formation of co-crystals.[57−60] The best reaction conditions for the preparation of a binary $[(bpy)Ag(OTf)]_\infty$-curc co-crystal have been searched and found considering the difficulties related to both the formation of Ag(0) as a side event in the reaction between the Ag(I) polymer and curc polyphenol and the limited number of intermolecular sites on the Ag(I) polymer. The new $[(bpy)Ag(OTf)]_\infty$-curc species has been characterized through powder X-ray diffraction (PXRD), differential scanning calorimetry (DSC), FTIR, and UV−vis spectroscopies, while theoretical investigation has been performed to determine the possible interaction modes between the co-crystal components. Moreover, both Ag(I) polymeric forms and the $[(bpy)Ag(OTf)]_\infty$-curc co-crystal have been preliminarily tested for antimicrobial activity against *Staphylococcus aureus* (*S. aureus*) and *Escherichia coli* (*E. coli*) strains as models for Gram-positive and Gram-negative bacteria, respectively, with all showing promising results.

2. EXPERIMENTAL SECTION

2.1. Materials. All commercially available starting materials were used as received without further purification. Silver trifluoromethansulfonate (≥99%; AgOTf), 2,2′-bypiridine (≥99%; bpy), and ethylcellulose (EC; degree of substitution equal to 48.0−49.5% *w*/*w*) were purchased from Sigma-Aldrich. Curcumin (98%; curc, 1,7-bis(4-hydroxy-3-methoxyphenyl)-1,6-heptadiene-3,5-dion) was purchased from Carbosynth. ^{1}H NMR spectra were acquired on a Bruker Advance 300 MHz spectrometer in $CDCl_3$ solution (with TMS as the internal standard). FTIR spectra (KBr) in the range of 4000−400 cm^{-1} were recorded with a Spectrum One FT-IR PerkinElmer spectrometer. Elemental analyses were performed with a PerkinElmer 2400 microanalyzer. Powder X-ray diffraction patterns of the powder samples were acquired on a Bruker D2 Phaser equipped with Cu Kα radiation (λ = 1.5418 Å) and a Lynxeye detector at 30 kV and 10 mA with a step size of 0.01° (2θ). The obtained diffractograms were analyzed with DIFFRAC.EVA diffraction software. DSC analysis was performed on a DSC Q2000 TA instrument. The samples were accurately weighed (1.5−2 mg) and crimped in non-hermetic aluminum pans. The samples were heated at a heating rate of 5 °C min^{-1} under a dry nitrogen atmosphere (flow rate of 50 mL min^{-1}) using an empty non-hermetic aluminum pan as reference.

2.2. X-ray Crystallographic Analysis. Single crystal X-ray diffraction data of the β-form of $\{[(bpy)Ag][OTf]\}_\infty$ were collected at room temperature with a Bruker-Nonius X8APEXII CCD area detector system equipped with a graphite monochromator with radiation Mo Kα (λ = 0.71073 Å). Data were processed through SAINT reduction and SADABS absorption software.[61,62] The structure was solved by direct methods and refined by full-matrix least squares based on F^2 through the SHELX and SHELXTL software package.[63,64]

The carbon, sulfur, and oxygen atoms of the OTf anion are found to be disordered (named as C11A, S1A, F1A, F2A, F3A, and O3A). The relative occupancies of the two disordered components were refined freely while constraining their sum to unity,[65] and they reached values of approximately 0.77 and 0.23 at convergence. All non-hydrogen atoms were refined anisotropically and hydrogen atoms were included as idealized riding atoms. All graphical representations have been obtained using Olex2[66] and CCDC Mercury 4.3.0.[67] Details of data and structure refinements are reported in Table S1.

2.3. Synthesis of α-$[(bpy)Ag(OTf)]_\infty$. The α-form of the Ag(I) polymer was synthesized according to the procedure reported.[25] Specifically, bpy (150 mg, 0.96 mmol) was added to a degassed $CHCl_3$ solution of AgOTf (246.7 mg, 0.96 mmol). The resulting solution was stirred in the dark at room temperature and under an inert atmosphere (N_2). After 12 h, a white solid was recovered through filtration and recrystallized from CH_2Cl_2/diethyl ether. Yield: 68%, 270 mg; m.p. 168 °C. Anal. calcd for $[C_{11}H_8AgF_3N_2O_3S]$ (MW 413.12 g mol^{-1}): C 31.98, H 1.95, N 6.78%. Found: C 31.83, H 1.75, N 6.67%. ^{1}H NMR (300 MHz, $CDCl_3$ TMS), δ (ppm): 8.69 (d, J = 5.0 Hz, 2 H); 8.25 (d, J = 7.9 Hz, 2H); 8.06 (td, J = 7.6 Hz; 1.8 Hz, 2

https://doi.org/10.1021/acs.cgd.3c00042
Cryst. Growth Des. XXXX, XXX, XXX−XXX

H); 7.57 (m, 2 H). FTIR (KBr cm^{-1}): 3066, 1590, 1472, 1438, 1254, 1168, 1032.

2.4. Synthesis of β-{[(bpy)Ag][OTf]}$_\infty$. To ca. 30 mL of a degassed $CHCl_3$ solution of bpy (150 mg, 0.96 mmol) was added AgOTf (246.7 mg, 0.96 mmol). The reaction mixture was stirred at room temperature under an inert atmosphere (N_2) and protected from light. After 12 h, a white solid was recovered through filtration and recrystallized from CH_2Cl_2/diethyl ether. Yield: 80%, 316 mg; m.p. 155 °C. Anal. calcd for $[C_{11}H_8AgF_3N_2O_3S]$ (MW 413.12 g mol^{-1}): C 31.98, H 1.95, N 6.78%. Found: C 31.87, H 1.82, N 6.82%. ^{1}H NMR (300 MHz, $CDCl_3$, TMS), δ (ppm): 8.80 (d, J = 4.8, 2H), 8.18 (d, J = 8.0 Hz, 2H), 8.04 (td, J = 7.8; 1.6 Hz, 2H), 7.59 (td, J = 6.7; 1.7, 2H). FTIR (KBr cm^{-1}): 3067, 1589, 1469, 1259, 1244, 1155, 1028. Single crystals were obtained by dissolving a few milligrams of the powder in hot $CHCl_3$ and letting the solution rest at room temperature for several days.

2.5. Preparation of 1a. A degassed MeOH solution of curc (142 mg, 0.39 mmol), protected from light was added to a degassed (N_2) MeOH solution of the Ag(I) polymer (α- or β-form; 160 mg, 0.39 mmol) in MeOH, protected from light. The resulting mixture was stirred at room temperature in the dark and under an inert atmosphere for 2 h. After this time, the reaction mixture was filtered through celite and concentrated through a rotavapor. A dark yellow precipitate (40 mg) obtained upon the addition of diethyl ether was recovered through filtration.

2.6. Preparation of 1. To a solution of curc (136 mg, 0.37 mmol) in MeOH was rapidly added KOH (20.7 mg, 0.37 mmol) under an inert atmosphere (N_2), keeping the reaction vessel protected from light. After a few minutes, this solution was added to a degassed (N_2) solution of the Ag(I) polymer (α- or β-form; 152 mg, 0.37 mmol) in MeOH, protected from light. The resulting mixture was stirred at room temperature in the dark and under an inert atmosphere for 2 h. After this time, the reaction mixture was filtered through celite and concentrated through a rotavapor. A red precipitate obtained upon the addition of diethyl ether was recovered through filtration. Yield: 80%, 150 mg; m.p. 142 °C. ^{1}H NMR (300 MHz, $CDCl_3$, TMS), δ (ppm): 8.67 (d, J = 6.8, 8H), 8.34 (d, J = 8.0 Hz, 8H), 8.03 (td, J = 6; 1.7 Hz, 8H), 7.55 (m, 10H), 7.14 (dd, J = 6.4; 1.7 Hz, 2H), 7.05 (m, 2H), 6.94 (d, J = 8 Hz, 2H), 6.48 (d, J = 15 Hz, 2H), 5.89 (s, 2H), 5.80 (s, 1H), 3.95 (s, 6H). IR (KBr cm^{-1}): 3420, 2916, 1626, 1592, 1514, 1263, 1229, 1169, 1033.

2.7. UV−Vis Characterization. Spectrofluorimetric grade CH_2Cl_2 was used for the photophysical investigations in solution. As previously reported,[68] a PerkinElmer Lambda 900 spectrophotometer was employed to obtain the UV−vis absorption spectra, a PerkinElmer LS 50B spectrofluorometer was used to obtain the emission spectra in solution, and in both cases, quartz cuvettes of a 1 cm path length were used.

Solid-state emission spectra were recorded on a Horiba Jobin Yvon Fluorolog 3 spectrofluorometer equipped with a Hamamatsu R-928 photomultiplier tube, and samples were prepared by placing a given amount of powder between two quartz slides and standardizing the layer.

2.8. Antibacterial Activity. The antibacterial activity of the two structural forms of the Ag(I) polymer, the co-crystal [(bpy)Ag]OTf$_\infty$-curc, and curc was tested against two bacterial strains, namely, *S. aureus* (DSM 346) as a model for Gram-positive bacteria and *E. coli* (DSM 1576) as a model for Gram-negative bacteria from DSMZ (German Collection of Microorganisms and Cell Cultures, Braunschweig). The lyophilized microorganisms were pre-cultured aerobically in 50 mL of DSM Medium 1 for *E. coli* and DSM Medium 92 for *S. aureus* for 18/24 h at 37 °C. The bacteria were maintained on a slant of nutrient agar (0.5% beef extract, 1% peptone, 0.5% NaCl, and 1.5% agar) at 4 °C and subcultured at regular intervals of 30 days to maintain the cell viability. For the preparation of microorganism suspensions, each bacterium was transferred from a stored slant to 10 mL of nutrient broth (meat extract, peptone, and NaCl) and cultivated overnight at 37 °C. The bacterial cultures were then diluted in sterile saline solution (0.9% NaCl) and adjusted to a cell suspension of 10^8 cells mL^{-1} using a UV spectrophotometer. The concentrations of bacteria were determined by measuring the optical density (OD) at 600 nm. Typically, for *E. coli*, an $OD_{600\ nm}$ of 0.1 corresponds to a concentration of 10^8 cells mL^{-1}.

Two milligrams of each sample (curc, α-[(bpy)Ag(OTf)]$_\infty$, β-{[(bpy)Ag][OTf]}$_\infty$, and [(bpy)Ag]OTf$_\infty$-curc) were mixed and finely ground with 100 mg of EC used as a diluting agent then pressed into pellets. A pellet containing only EC (EC0) was also prepared and used as the negative control.

The antibacterial activity of each sample was evaluated using the growth inhibition assay. The inhibitory effect of each compound on the growth of *S. aureus* and *E. coli* over 24 h of contact was evaluated by determining the number of viable bacteria for each specimen (CFU mL^{-1}). The pellets were placed in Petri dishes and immersed in 10 mL of a nutrient broth diluted 1:500 with the addition of the microorganism suspension at 10^6 cells mL^{-1} and incubated for 24 h at 35 °C in a humid environment. After this time, the inoculum was recovered and the dishes were washed with 10 mL of SCDLP broth, a neutralizer. The solutions were collected, and the microbial concentrations were determined by plating 100 μL of the appropriate dilution over the surface of the nutritive agar using a sterile bent plastic rod. All agar plates were incubated at 35 °C for 24 h with 95% humidity, and then, for each test specimen, the number of viable bacteria recovered after 24 h was determined. Each experiment was performed in duplicate and repeated four times for each test strain. The inhibitory effect was calculated using the following formula:

$$\text{percent inhibition} = 1 - T/C \times 100$$

where T is the CFU per milliliter of the test sample after 24 h, and C is the CFU per milliliter of the control (EC0) after 24 h. Generally, the bactericidal effect is obtained with a lethality percentage of 90% for 6 h, which is equivalent to 99% of lethality for 24 h.

2.9. Release Test for the Specific Migration of Ag(I) from the EC Tablet. The release of silver from tablets was measured by inductively coupled plasma−mass spectrometry (ICP-MS) analysis. The determinations were carried out utilizing an Elan DRC-e ICP-MS instrument (PerkinElmer SCIEX, Canada), and the sample delivery system consisted of a PerkinElmer autosampler model AS-93 Plus with a peristaltic pump and a cross-flow nebulizer with a Scott-type spray chamber. The ICP torch was a standard torch (Fassel-type torch) with a platinum injector. A solution containing Rh, Mg, Pb, Ba, and Ce (10 μg L^{-1}, Merck) was used to optimize the instrument in terms of sensitivity, resolution, and mass calibration. A multi-element solution containing Ag (100 mg/L, Merck) was used for the preparation of aqueous calibration standard solutions after appropriate dilution.

To evaluate the release of silver in physiological conditions, a tablet of α-[(bpy)Ag(OTf)]$_\infty$, β-{[(bpy)Ag][OTf]}$_\infty$, and [(bpy)Ag(OTf)]$_\infty$-curc was immersed in 10 mL of 0.9% NaCl solution at 37 °C. The release from each tablet was tested two times on contact: 6 and 24 h. After the time has elapsed, the tablet was removed, 100 μL of HNO_3 65% was added to the solution, and ICP-MS analysis was carried out. Each experiment was performed in duplicate.

2.10. Computational Methods. Gaussian 09, version D01,[69] was used for the structure optimizations of adducts between curcumin and Ag(I)-containing coordination units. A preliminary screening of all the possible adducts were performed with the use of the B3LYP xc functional[70] and def2-SVP basis set on all the atoms plus the related ECP on Ag only.[71] Such a survey of possible adducts is reported in the Supporting Information; in it, model systems were used in place of the real [(bpy)Ag(OTf)]$_\infty$ polymer: [(py)$_2$Ag]$^+$ and [(py)$_2$Ag][OTf] were placed in proximity of possible coordinating atoms of curcumin and full optimizations were performed starting from these choices. Adducts sketched in Figure 10 were found to be the most stable in which curc is in its EK and KK forms; they were refined by the means of full-structure optimizations with the same B3LYP xc functional and the more extended def2-TZP basis set and related ECP on Ag.[71] Default thresholds were used for structure optimizations and SCF computations. Integration grids were enhanced with the "int = ultrafine" keyword. The reported energies in Figure 10 are relative energies of the sketched structures with respect to their relaxed

https://doi.org/10.1021/acs.cgd.3c00042
Cryst. Growth Des. XXXX, XXX, XXX−XXX

fragments, that is, relaxed curc and $[(py)_2Ag]^+$ for EK-2, EK-3, and KK-2 and relaxed curc and $[(py)_2Ag(OTf)]$ for EK-4 and KK-3. By "relaxed curc", we mean the fully optimized EK-1 tautomer. In all the cases of full-structure optimization, an analytical evaluation of the Hessian was performed to ensure that minima points of the PES were reached.

The Amsterdam density functional (ADF) program, version 2019,[72−74] was used for the decomposition of the binding energy in EK-2 and EK-4 (values in Table 4). In these computations, relativistic effects were included though the zero-order regular approximation (ZORA).[75,76] The B3LYP xc functional and the ZORA/TZP basis set included in the software were chosen for consistency with the methods used in the other computations. The decomposition scheme implemented in the program resulted from the modification of Ziegler and Rauk[77] of the original Morokuma and Kitaura scheme.[78] According to this approach, the bonding energy between two fragments is decomposed in terms of the Pauli repulsion energy between fragments, electrostatic interaction energy, and finally, orbital interaction. The last one takes into account all the stabilizing modifications of the electron density when passing from isolated fragments to their adduct. As a result, it includes both charge-transfer effects from one fragment to the second one and changes inside each fragment (polarization) due to the interaction between fragments. The preparation energy is the energy loss due to fragment deformation from their relaxed structures (isolated molecules) to the structures they assume in the adduct. This destabilizing energy term (positive energy) is summed to the favorable bonding energy between interacting fragments (negative energy) for obtaining the total interaction energy (negative in stable adducts). This analysis was performed on the structure computed with Gaussian 09 software as presented above without any modification.

Interactions between couples of curc molecules in their crystals (forms I, II, and III) were obtained after partial optimizations in which the C and O atoms were frozen in their experimental structure (polymorph I in ref 56) and only the H atoms were fully optimized in their positions. In this respect, the interaction energies in Figure 11 (ΔE_{inter}) are the energy difference between the whole adduct ("couple" in the figure) and the sum of the energies of the two isolated molecules, each frozen in the structure of the same adduct. An initial study aimed to the choice of the best xc functional was performed; results of this study are reported in the Supporting Information. The MP2 (second order Møller−Plesset correlation-corrected energy) and def2-TZP basis sets were used as reference for computing the interaction energies in couples 1, 2, and 4 (Figure 11). The B3LYP and M06[79] xc functionals demonstrated to be not sufficiently accurate. On the contrary, adding empirical dispersion in the D3 Grimme's approximation[80] (B3LYP-D3 and M06-D3; the standard "empiricaldispesion = gd3" keyword was used) strongly improved their performances. The B3LYP-D3 xc functional was chosen as the DFT method in these studies, and the def2-TZP basis set was combined to it. Anharmonic OH stretching wavenumbers in Figure 11 and Table 5 were obtained through numerical differentiation along selected harmonic normal modes: the keyword "freq = (anharmonic, select anharmonic modes)" was used, and the OH stretching mode of interest was selected. Inclusion of additional modes (stretching and bending modes) of all the OH and CO bonds involved in each couple of Figure 11 did not produce significant changes (a few units of cm^{-1}) with respect to selecting the single stretching mode reported in the figure.

3. RESULTS AND DISCUSSION

3.1. Preparation and Characterization of $\{[(bpy)Ag][OTf]\}_\infty$ (β-Form). Considering the coordination versatility of the N^N ligand bpy with respect to the Ag(I) ion in the presence of trifluoromethanesulfonate (OTf) as a counterion, the synthesis of Ag(I) CPs is a delicate procedure since, as already demonstrated by Klausmeyer et al., a modification of the stoichiometric ratio between the N^N ligand and the silver precursor could lead to the formation of a discrete compound rather than a polymer.[51] Moreover, polymorphism is frequently encountered in Ag(I) coordination polymers[81−84] as a result of the structural flexibility of the polymeric chains. It is known that, in a given reaction, the addition sequence of the reagents can influence the formation of different polymorphs[85−87] probably as a consequence of different solubilization rates of the reagents. On this basis, to test the formation of possible different structural forms of (bpy-Ag(I)-OTf) CPs, the synthetic procedure previously reported for the preparation of the α derivative[25] has been modified by reversing the order of the reagents' addition, keeping unchanged the stoichiometric ratio between the precursors. In particular, the α-form of the Ag(I) polymer was originally prepared through the addition of the bpy ligand to a AgOTf chloroform solution. This synthetic method afforded the formation of a Ag(I) coordination polymer with an empirical formula $[(bpy)Ag(OTf)]$ in the asymmetric unit crystallized in the $P3_121$ space group.[25] In this structural form, all metal centers are coordinated to the OTf anions. The α-form was thus re-prepared and obtained as white crystalline powder, whose identity has been confirmed by comparison between its PXRD pattern and that calculated from single-crystal data deposited at the Cambridge Crystallographic Data Centre (CCDC; Figure S1a). Moreover, all the characterizations are consistent with those previously reported.[25]

By inverting the addition sequence of the reagents with respect to the synthesis of the α-form, a white crystalline powder has been isolated, whose characterization in solution by ^1H NMR spectroscopy has highlighted the formation of a different structural form. Indeed, the different chemical shifts of the bpy proton signals of this new form of the Ag(I) polymer, that is, the β-form (see the Experimental Section), with respect to that reported in the literature for the α-form[25] is an indication of the different chemical environments experienced by Ag(I) ions.

The PXRD pattern of the new Ag(I) polymer has been found to be different than that recorded from the α-form (Figure 1).

Furthermore, the FTIR spectrum of the β-form (Figure 2, black line) exhibits significant differences with respect to that of the α-form (Figure 2, red line), particularly in the frequency region in which the OTf vibration bands occur. As already reported for Ag(I) coordination polymers bearing OTf as a

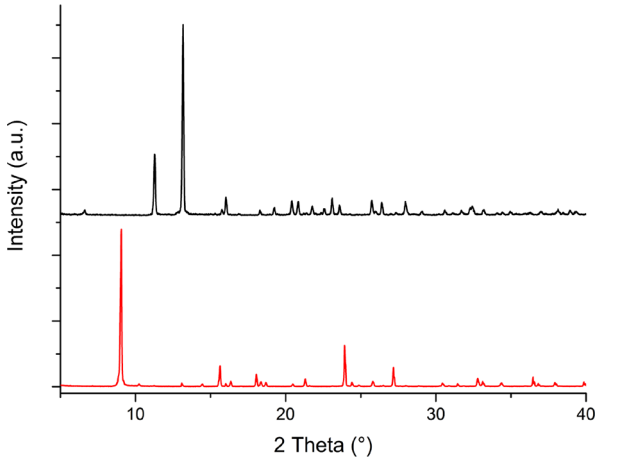

Figure 1. Comparison between the PXRD patterns of the α- (red) and β-form (black) of the Ag(I) polymer.

https://doi.org/10.1021/acs.cgd.3c00042
Cryst. Growth Des. XXXX, XXX, XXX−XXX

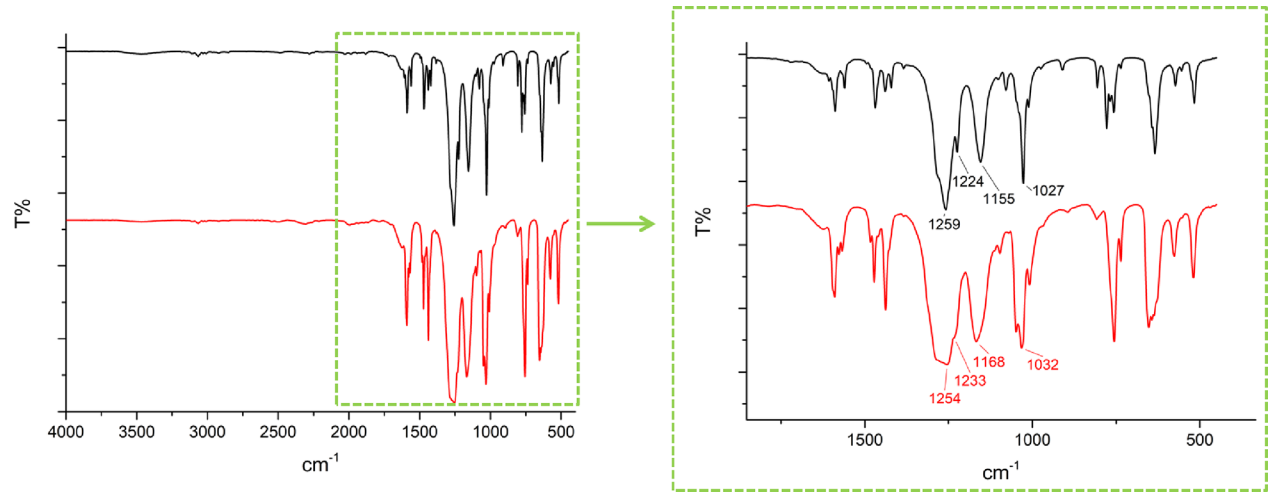

Figure 2. FTIR spectra of the α- (red) and β-form (black) of the Ag(I) polymer.

counterion,[88] the FTIR absorption bands of the OTf group could appear at different wavenumber values depending on whether or not the anion is coordinated to the metal ion. In the FTIR spectrum of the α-form, the bands attributed to the symmetric and asymmetric stretching of $-SO_3$ and $-CF_3$ groups, respectively, occur at 1032 and at 1168 cm^{-1}. These two vibration bands move to lower wavenumbers (1027 and 1155 cm^{-1}, respectively) in the FTIR spectrum of the β-form, suggesting the different interaction mode of OTf with the metal ion.

The thermal behavior of the β-form of the Ag(I) polymer was investigated through DSC and compared to that of the α-form. The DSC curve of the β-form (Figure 3, black line)

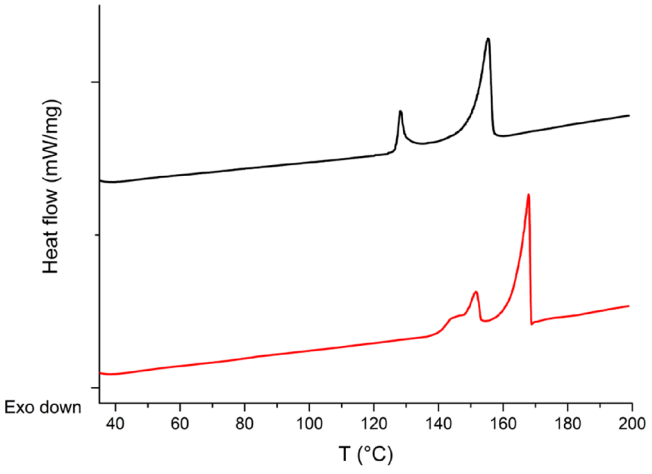

Figure 3. DSC curves of the α- (red) and β-form (black) of the Ag(I) polymer.

shows two thermal events: a solid−solid transition observed at 128 °C followed by the compound melting at 155 °C. The DSC trace of the α-form (Figure 3, red line) exhibits similar transitions to the β-form but at different temperature values; in particular, for the α-form, two very close solid−solid transitions occur at 144 °C ca. and 151 °C with the first appearing as a shoulder. The α-form melting is observed at 168 °C, revealing its higher thermal stability with respect to the β-form, probably deriving from greater lattice packing forces.

A molecular insight of the β-form was given by single crystal X-ray diffraction analysis performed on suitable single crystals grown from slow evaporation of a $CHCl_3$ solution of the powder sample. The β-form exhibits a polymeric structure but, differently from the α-form, presents an empirical formula [(bpy)Ag][OTf] in the asymmetric unit and crystallized in the $P2_1/c$ space group (Figure 4a). In the β-form, every Ag(I) ion is coordinated to the nitrogen atoms of two half bpy ligands, adopting a slightly distorted linear geometry (N(1)−Ag(1)−N(2) of 173.4(2)°). Bpy acts exclusively as a bridging ligand with a dihedral angle between the two aromatic rings of 52.2(2)°. As suggested by FTIR analysis, the OTf anions experience a different chemical environment with respect to the α-form; indeed, in the β-form, the OTf anions confined between the polymeric strands do not coordinate the silver centers (Figure 4a). The O(1) and O(2) atoms of each OTf anion weakly interact with two neighboring Ag(I) ions at distances of 2.951(6) and 2.798(5) Å, respectively, acting as a pincer-like anion and forcing the polymeric chains to adopt a zigzag conformation. As a consequence of this structural conformation, the O(3) atom of the OTf anion is found to be weakly interacting with the metal ion (distance of 3.12(1) Å). In the β-form, differently than what is observed in the α-form, no $\pi-\pi$ stacking between bpy ligands and no argentophilic interactions are present since the Ag···Ag distances are found to be of 5.320(1) Å. The additional intermolecular interactions found in the α-form whose structure is reported in Figure 4b could reflect the increased temperature values of the thermal events associated to the α-form.

The monophasic nature of the powder sample of β-$\{[(bpy)Ag][OTf]\}_\infty$ was confirmed by a comparison between the PXRD pattern measured on the powder sample and the simulated one derived from the single-crystal X-ray structure (Figure S1b).

3.2. Preparation and Characterization of the [(bpy)-Ag(OTf)]$_\infty$-curc Co-crystal. Recently, it has been reported that organic linear polymers can co-crystallize with small organic molecules by adjusting their conformation to accommodate a portion of the organic molecules.[36] Hence, both structural forms, α- and β-, of the Ag(I) polymer were used for the preparation of co-crystals with curc by virtue of their one-dimensional conformations, potentially capable of hosting the polyphenol. This approach is based on the idea to

https://doi.org/10.1021/acs.cgd.3c00042
Cryst. Growth Des. XXXX, XXX, XXX−XXX

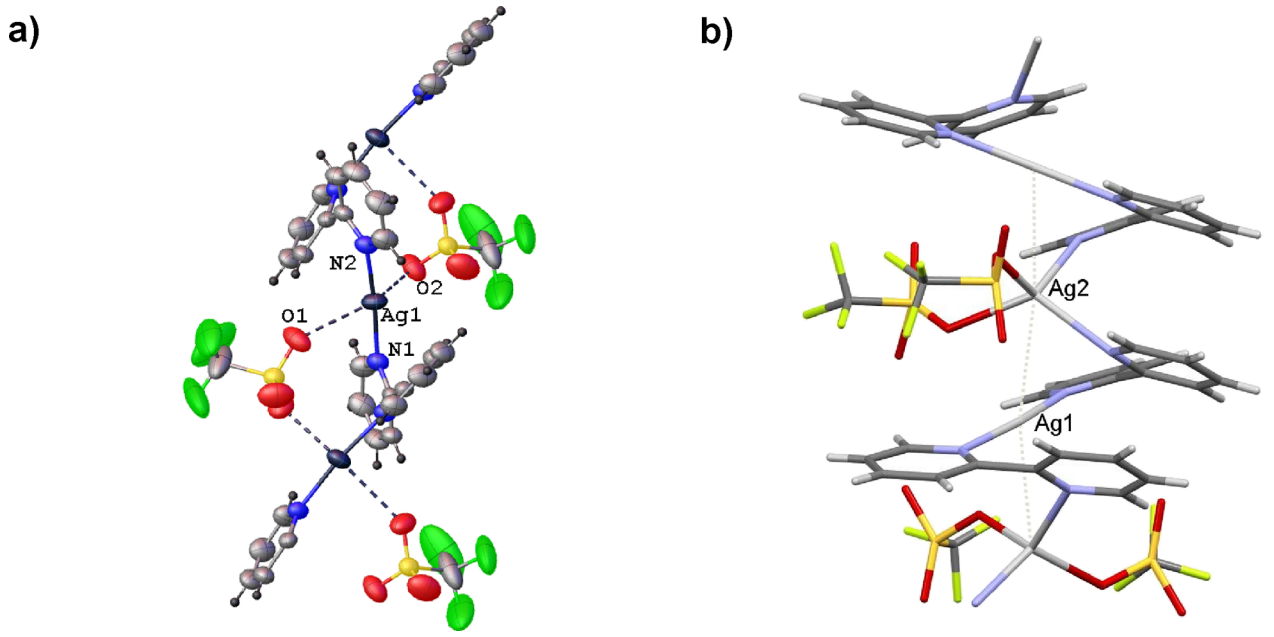

Figure 4. Perspective view of the β- (a) and α-form (b) of the Ag(I) polymer.

enhance the curc chemical stability and eventually bioavailability without its metalation to the Ag(I) centers, knowing that O,O-chelation to Ag(I) ions is highly improbable as testified by the presence of only one curc−Ag(I) complex in the literature.[89]

Considering that curc is generally prone to the formation of co-crystals through its keto-enolic and phenolic groups,[57,58,90,91] the formation of a Ag(I) polymer−curc co-crystal based on metal-to-oxygen intermolecular interactions could be expectable. However, since curc displays a certain tendency to reduce Ag(I) to Ag(0),[92−95] the formation of Ag(0) could happen as a side event in the reaction between the Ag(I) polymer and the polyphenol. Therefore, the preparation of $[(bpy)Ag(OTf)]_\infty$-curc co-crystals was attempted following two experimental conditions, namely, a neutral and an alkaline medium, in the search for the minimal reduction of Ag(I) to Ag(0). The basic conditions have been tried taking into account that (i) the reducing properties of curc are generally ascribed to its phenolic groups deprotonated in alkaline medium[96−98] and (ii) curc undergoes degradation much faster than under acidic/neutral conditions.[96,99]

The reactions between α-$[(bpy)Ag(OTf)]_\infty$ and β-$\{[(bpy)Ag][OTf]\}_\infty$ polymers and the form I of curc were first performed in the absence of a base. Both these reactions resulted in the formation of a significant amount of a dark-grey powder whose PXRD pattern is unequivocally attributable to the formation of zero-valence silver (Figure S2). Moreover, the same dark-yellow solid was recovered in a low yield from the filtrate of both reactions and analyzed through PXRD. The diffractogram of the yellow solid, referred as product **1a**, is characterized by a large and poorly resolved band in the 2θ range of 15−30° and a few diffraction peaks in the low-medium angle region, which are absent in the PXRD patterns of the precursors, which is thus diagnostic of the formation of a new product (Figure S3). However, this product has not been found to be a single species as evidenced by its DSC profile (Figure S4), which shows several thermal events. It is reasonable to assume that the poorly resolved PXRD pattern of product **1a** in addition to a new solid form also includes the diffraction peaks from other species.

The reactions between α-$[(bpy)Ag(OTf)]_\infty$ and β-$\{[(bpy)Ag][OTf]\}_\infty$ polymers and curc were subsequently performed in basic conditions. In this case, from both reactions, only a small amount of Ag(0) was formed and a pure red solid was recovered (see below DSC for purity). Both reactions yield the same solid, hereafter referred to as product **1**, as confirmed by PXRD analysis (Figure S5). This product was then characterized both in solution and in the solid-state. In particular, the ^{1}H NMR spectrum in solution (Figure S6) shows signals attributable to the free uncoordinated and fully protonated curc and the $[(bpy)Ag(OTf)]$ repetition unit of the Ag(I) polymer in a 1:4 ratio, respectively. This finding excludes the possibility of curc chelation to the metal center since the typical changes in the ^{1}H NMR chemical shifts of curc are not observed.[100,101] Moreover, in the ^{1}H NMR spectra of the new species, the bpy proton signals are observed at slightly different frequency values with respect to both the structural isomers of the Ag(I) polymer, indicating a possible structural change in the polymer. The full protonation of curc is also proved by SEM−EDX performed on product **1**, showing the complete absence of the potassium element. The PXRD analysis provided clear evidence of the formation of a new solid species. Indeed, the PXRD pattern of the new product is different from that of the pristine materials, curc, α-$[(bpy)Ag(OTf)]_\infty$, and β-$\{[(bpy)Ag][OTf]\}_\infty$ as evidenced in Figure 5. The diffractogram of product **1** (Figure 5, blue line) is characterized by the presence of new diffraction peaks, which are absent in the PXRD profiles of individual constituents (Figure 5, red, pink, and black lines) and, at the same time, by the absence of the distinctive reflections of the starting materials, pointing out the formation of a binary solid that is the $[(bpy)Ag(OTf)]_\infty$-curc co-crystal.

The formation of a new pure solid product was highlighted also by DSC analysis. Indeed, as shown in Figure 6, the thermal profile of product **1** ($[(bpy)Ag(OTf)]_\infty$-curc co-crystal, blue line) presents a single endothermic peak at 141.9 °C, thus at a temperature value different from the thermal

https://doi.org/10.1021/acs.cgd.3c00042
Cryst. Growth Des. XXXX, XXX, XXX−XXX

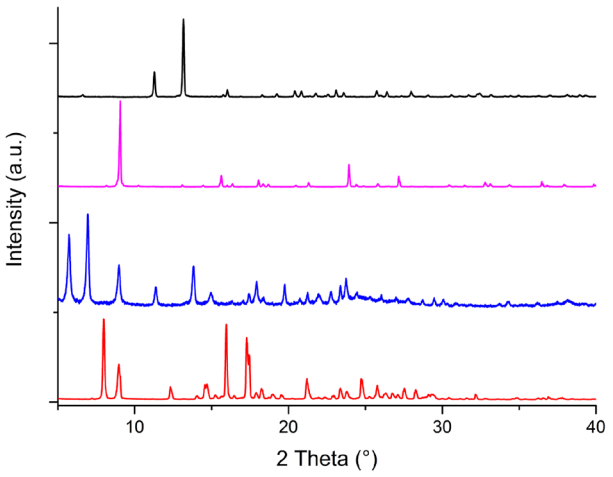

Figure 5. PXRD patterns of curc (red line), product **1** (blue line), α-[(bpy)Ag(OTf)]$_\infty$ (pink line), and β-{[(bpy)Ag][OTf]}$_\infty$ (black line).

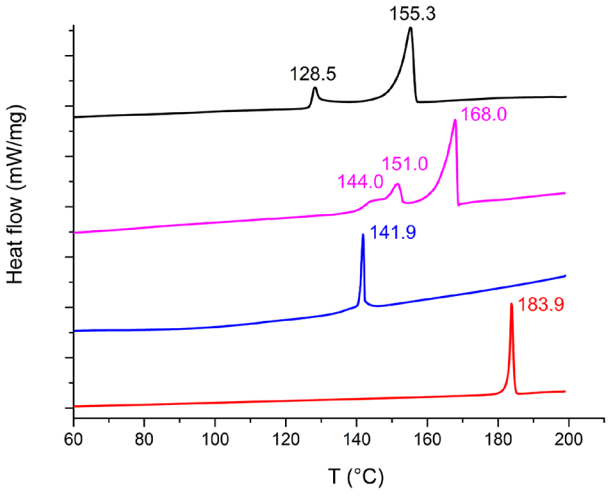

Figure 6. DSC curves of curc (red line), [(bpy)Ag(OTf)]$_\infty$-curc co-crystal (blue line), α-[(bpy)Ag(OTf)]$_\infty$ (pink line), and β-{[(bpy)-Ag][OTf]}$_\infty$ (black line).

transitions of curc (red line), α-[(bpy)Ag(OTf)]$_\infty$, and β-{[(bpy)Ag][OTf]}$_\infty$ precursors (pink and black line, respectively). Hence, the peak at 141.9 °C, corresponding to the compound melting, is indicative of a homogeneous crystalline phase.

A careful comparison between product **1** and product **1a** highlighted the formation of the [(bpy)Ag(OTf)]$_\infty$-curc co-crystal even if in a low yield and not pure, also from the reaction carried out in the absence of a base. Indeed, in the PXRD pattern of product **1a**, the most intense reflections of the co-crystal are recognizable (Figure S7). In addition, in the DSC curve of product **1a** (Figure S3), the endothermic peak at 142 °C ca., which is attributable to the melting of the co-crystal, can be detected. However, in the absence of a base, the reaction between curc and the Ag(I) polymer mainly proceeds toward the formation of Ag(0). It can be hypothesized that the alkaline medium increases the speed of the process of curc degradation[96,99,102] particularly in the absence of stabilization through metalation of any deprotonated curc form, decreasing then the amount of curc available for the reduction of the Ag(I) ion in the polymeric system [(bpy)Ag(OTf)]$_\infty$.

Moreover, it should be noted that, whether starting from the α- or the β-form of the Ag(I) polymer, the same product is attained. This finding indicates that, when the Ag(I) polymer is mixed in solution with curc, a structural rearrangement occurs, allowing the formation of the same product despite the starting structural form of the Ag(I) polymer. FTIR analysis was performed to investigate the possible structural rearrangement of the Ag(I) polymer within the co-crystal. The FTIR spectrum of the co-crystal was thereby compared to the FTIR spectra of α-[(bpy)Ag(OTf)]$_\infty$, β-{[(bpy)Ag][OTf]}$_\infty$, and curc precursors (Figure 7). In the co-crystal spectrum (Figure 7, blue line), some bands of the starting precursors appear shifted (Table 1). In particular, in the FTIR spectrum of [(bpy)Ag(OTf)]$_\infty$-curc, the absorption bands resulting from the OTf vibrations (ν_{as} SO_3, ν_s SO_3, ν_{as} CF_3, and ν_s CF_3) all appear at higher frequency values with respect to the spectrum of the β-{[(bpy)Ag][OTf]}$_\infty$ form, while only the ν_{as} SO_3 and ν_s CF_3 bands are displaced with respect to the bands in the α-[(bpy)Ag(OTf)]$_\infty$ form (Table 1). This observation points out that, after the interaction with curc in the formation of the co-crystal, the structure of the Ag(I) polymer is more like the α-form than the β-form. Furthermore, differences

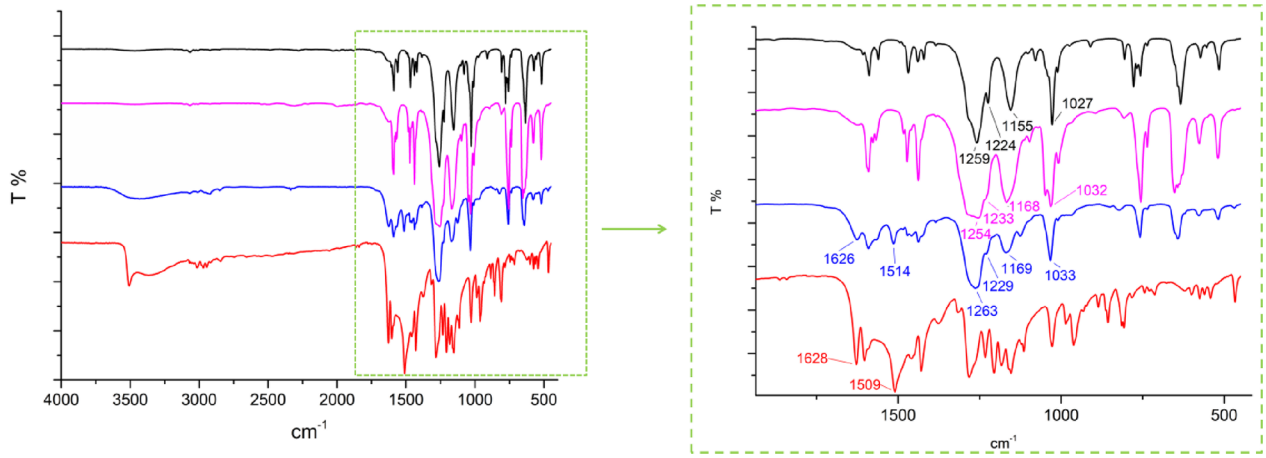

Figure 7. FTIR spectra of curc (red line), the [(bpy)Ag(OTf)]$_\infty$-curc co-crystal (blue line), α-[(bpy)Ag(OTf)]$_\infty$ (pink line), and β-{[(bpy)Ag][OTf]}$_\infty$ (black line).

https://doi.org/10.1021/acs.cgd.3c00042
Cryst. Growth Des. XXXX, XXX, XXX−XXX

Table 1. FTIR Spectrum Data of curc, $[(bpy)Ag(OTf)]_\infty$-curc, and the Ag(I) Polymer (α- and β-Forms)

vibration	curc	$[(bpy)Ag(OTf)]_\infty$-curc	α-$[(bpy)Ag(OTf)]_\infty$	β-$\{[(bpy)Ag][OTf]\}_\infty$
νOH	3507, 3360 ca.	3440 ca.		
mixed νC=C/νC=O	1628	1626		
mixed νC=O/δC−C	1509	1514		
ν_{as} SO_3		1263	1254	1259
ν_s CF_3		1229	1233 (shoulder)	1224
ν_{as} CF_3		1169	1168	1155
ν_s SO_3		1033	1032	1027

emerge from the comparison between the FTIR spectra of curc and the co-crystal. In particular, the curc spectrum is characterized by a sharp peak at 3507 cm^{-1} and a broad band centered at 3360 cm^{-1} ca. with both arising from the stretching vibration of the hydroxyl groups.[103] Conversely, in the co-crystal spectrum, the O−H vibration generates a single broad band centered at 3440 cm^{-1} ca. The very large band at 2500 cm^{-1} ca. that is barely visible in the curc spectrum, which is attributable to the strong intramolecular hydrogen bonds of the enolic O−H,[104−106] disappears in the co-crystal spectrum. Moreover, the band at 1628 cm^{-1}, which is attributable to mixed νC=C/ νC=O vibrations of curc,[103] slightly shifts to a lower wavenumber (1626 cm^{-1}) in the FTIR spectrum of the co-crystal, whereas the band at 1509 cm^{-1}, due to mixed ν C=O/δ C−C vibrations of curc,[107] moves to higher wavenumber (1514 cm^{-1}) in the co-crystal spectrum. These findings indicate that both the keto-enolic function and the phenolic groups of curc could be involved in weak interactions with the Ag(I) polymer.

3.3. Photophysical Analysis. The photophysical analysis of the $[(bpy)Ag(OTf)]_\infty$-curc co-crystal was carried out both in the solid state and in CH_2Cl_2 dilute solution. The emission and excitation spectra of $[(bpy)Ag(OTf)]_\infty$-curc powder are reported in Figure 8. In the solid state $[(bpy)Ag(OTf)]_\infty$-curc

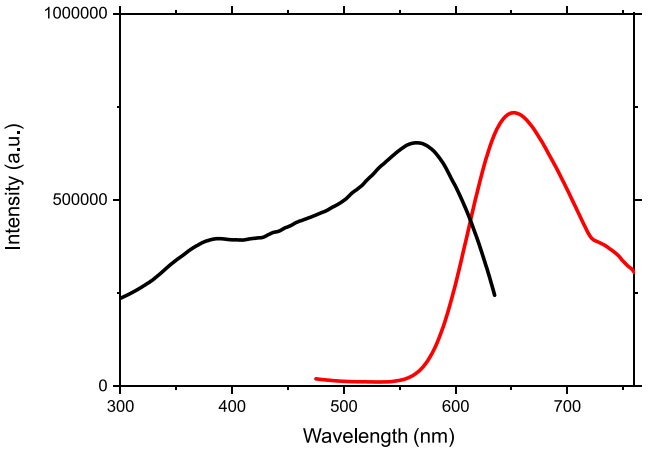

Figure 8. Emission (red line) and excitation (black line) spectra of the $[(bpy)Ag(OTf)]_\infty$-curc powder sample.

shows a single emission band centered at 655 nm with a shoulder at 730 nm. A comparison with emission and excitation spectra of the Ag(I) polymer (α- and β-form) and curc powders (Figures S8 and S9, respectively) confirms that a new chemical species that is different from its precursors is formed. Moreover, spectra reported in Figure S8 shows that α- and β-forms of the Ag(I) polymer have identical electronic transitions.

The absorption spectrum of $[(bpy)Ag(OTf)]_\infty$-curc in CH_2Cl_2 dilute solution (Figure 9, magenta line) shows a

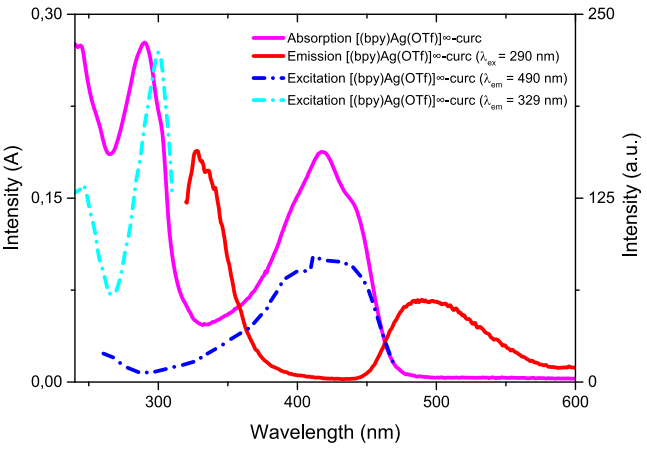

Figure 9. Absorption, emission, and excitation spectra of $[(bpy)Ag(OTf)]_\infty$-curc in CH_2Cl_2 dilute solution.

large band in the visible region of the electromagnetic spectrum with a maximum centered at 419 nm and two shoulders at 397 and 438 nm, respectively. Two further bands are visible in the UV region: a band centered at 290 nm with a shoulder at 302 nm and a band with a maximum at 247 nm and a shoulder at 256 nm. The comparison of this spectrum with the absorption spectra of curc (Figure S10, black line) and α/β-forms of the Ag(I) polymer (Figure S11, cyano and magenta lines, respectively) shows that the spectrum of the co-crystal in CH_2Cl_2 is exactly the sum of the absorption spectra of its constituents.

The emission and excitation spectra further confirm this statement. Exciting the co-crystal solution at 290 nm, two emission bands centered at 329 and 490 nm are obtained (Figure 9, red line). The blue-shifted emission and its corresponding excitation spectrum (Figure 9, cyano dot line) are like the absorption and emission features of the Ag(I) polymer (α- and β-form) (Figure S11), while the red-shifted one and its excitation spectrum (Figure 9, blue dot line) are similar to the absorption and emission spectra of curc (Figure S10).

Thus, while, in the solid state, the $[(bpy)Ag(OTf)]_\infty$-curc co-crystal maintains its integrity and only one emission signal is detected, in solution, a cleavage of the co-crystal superstructure takes place, resulting in the release of curc and $[(bpy)Ag(OTf)]_\infty$, and two different emission bands are detected.

3.4. Preliminary Antimicrobial Activity and Ag(I) Migration Test. Silver and its coordination compounds are known to show antimicrobial properties. In the case of Ag(I) complexes, different biological behaviors are related to

https://doi.org/10.1021/acs.cgd.3c00042
Cryst. Growth Des. XXXX, XXX, XXX−XXX

Table 2. Antibacterial Activity (CFU Values) of α- and β-Forms of the Ag(I) Polymer, $[(bpy)Ag(OTf)]_\infty$-curc, curc, and EC0 and Relative Percentage of Growth Inhibition (%) against *S. aureus* and *E. coli*

sample	*S. aureus* CFU mL^{-1} after 24 h	percentage of growth inhibition	*E. coli* CFU mL^{-1} after 24 h	percentage of growth inhibition
EC0	3.2×10^8	0%	3.2×10^8	0%
α-$[(bpy)Ag(OTf)]_\infty$	≤1	100%	≤1	100%
β-$\{[(bpy)Ag][OTf]\}_\infty$	≤1	100%	≤1	100%
$[(bpy)Ag(OTf)]_\infty$-curc	4×10^3	99.9%	≤1	100%
curc	6.8×10^7	78%	13×10^7	60%

Table 3. Ag(I) Migration Expressed in Terms of Ag in Micrograms in 10 mL of Release from Pellets

time	α-$[(bpy)Ag(OTf)]_\infty$	β-$\{[(bpy)Ag][OTf]\}_\infty$	$[(bpy)Ag(OTf)]_\infty$-curc
6 h	2.8 ± 0.2	2.9 ± 0.2	3.6 ± 0.6
24 h	5.2 ± 0.7	4.9 ± 0.9	5.1 ± 0.7

different Ag(I)−ligand combinations, pointing out that the mere presence of silver is not sufficient for inducing antimicrobial activity.[108] Several works have been dedicated to explain that the bactericidal action of silver-based materials arises from the release of biocidal Ag(I) ions into the surrounding environment.[29,109] In an attempt to combine in one system the antimicrobial properties mainly expected from the silver polymer and the several biological activities carried by curc, here, the antibacterial performances of pellets containing the two structural forms α-$[(bpy)Ag(OTf)]_\infty$ and β-$\{[(bpy)Ag][OTf]\}_\infty$, the co-crystal $[(bpy)Ag(OTf)]_\infty$-curc, and curc were evaluated against *S. aureus* and *E. coli* microorganisms. Pellets were prepared using ethylcellulose (EC) powder as an inert diluting agent. Moreover, a pellet containing only EC (EC0) was tested as the negative control. The antibacterial activity of each compound was measured using the growth inhibition assay to count the colony forming units (CFUs) after 24 h of contact of the two microorganisms with the studied compounds. The results obtained by the growth inhibition assay are reported in Table 2.

The two structural forms α-$[(bpy)Ag(OTf)]_\infty$ and β-$\{[(bpy)Ag][OTf]\}_\infty$ display excellent bactericidal activity since, after 24 h of incubation, a total inhibition effect (100%) against both *S. aureus* and *E. coli* was registered. The same inhibition effect was measured for the co-crystal $[(bpy)Ag(OTf)]_\infty$-curc. Clearly, the high amount of the Ag(I) polymer used in the preparation of the samples does not allow either to differentiate the bactericidal activity against the two different microbial agents or to give a precise percentage of growth inhibition due to experimental limitation. However, the curc-containing pellets, although prepared with the same experimental condition used for the silver pellets, show only moderate antibacterial performance with respect to both *S. aureus* and *E. coli* microorganisms. Therefore, the high bactericidal effect observed for the co-crystal containing pellets could be only attributable to the presence of the Ag(I) polymer.

Moreover, to test the amount of silver ions released by each metal-charged EC pellet, Ag(I) migration has been tested in physiological conditions. In particular, the Ag(I) release was measured after 6 and 24 h of contact with a 0.9% NaCl solution at 37 °C. The overall Ag(I) migration values expressed in terms of micrograms per 10 mL of solution are reported in Table 3. Although after 6 h of contact, the release of Ag(I) is slightly greater from the tablet containing the co-crystal with respect to the ones containing the two isomers, while no relevant differences are observed between the three Ag(I) compounds after 24 h of contact. In all the tested tablets, despite the high quantity of Ag(I) compounds present (2 mg for each tablet), the Ag(I) release is very low with values of approximately 0.25% (w/w) after 24 h of contacts for all the tablets. These preliminarily results are encouraging for the possible use of these Ag(I) compounds as additives in antimicrobial polymeric carrier materials with a low metal release.

4. COMPUTATIONAL STUDY

In the absence of structural information on the co-crystal $[(bpy)Ag(OTf)]_\infty$-curc, a computational study in which several adducts between curc and $[(bpy)Ag(OTf)]_\infty$ were modeled was performed, aiming to suggest how the two components interact in setting up the co-crystal. The computational study was restricted at the interaction energy between the Ag(I) ion and curc with the silver centers in their low coordination number being the best interaction sites for the oxygen atoms of curc molecules. As a model system, the simpler $[(py)_2Ag]^+$ unit was used in the calculations in which two pyridine ligands coordinated to Ag(I) model the coordination of the two bridging bipyridines of the real polymer. The formation energy between curc and the Ag(I)-containing unit was calculated, as detailed in the Computational Methods. Some adducts are shown in Figure 10 together with their energies and other computed properties. Indeed, many further structures were optimized in which different curc conformations were considered and the OTf position was varied along with the Ag(I) coordination site. Many of the found structures are reported in the Supporting Information, while, herein, the most stable adducts and the most relevant ones are discussed. curc was considered both in its keto-enolic form (EK was used to label the different adducts associated with this curc tautomer) and diketonic form (named as KK). The KK tautomer was taken into consideration due to both experimental and computational evidence according to which the weak interaction between curc and external molecules (such as water) can make the KK form competitive with the EK ones.[110] In this sense, a coordination interaction with Ag(I) could impart a similar effect, potentially allowing the KK form to be present in the solid phase.

The energy difference between EK-1 and KK-1 (reported in Figure 10) is a measure of the stability gap between the two tautomers, which intrinsically originates in the single curc molecule. The calculated gap of 26.2 kJ/mol, in line with that reported in similar computational studies (24.6 kJ/mol[110] and

https://doi.org/10.1021/acs.cgd.3c00042
Cryst. Growth Des. XXXX, XXX, XXX−XXX

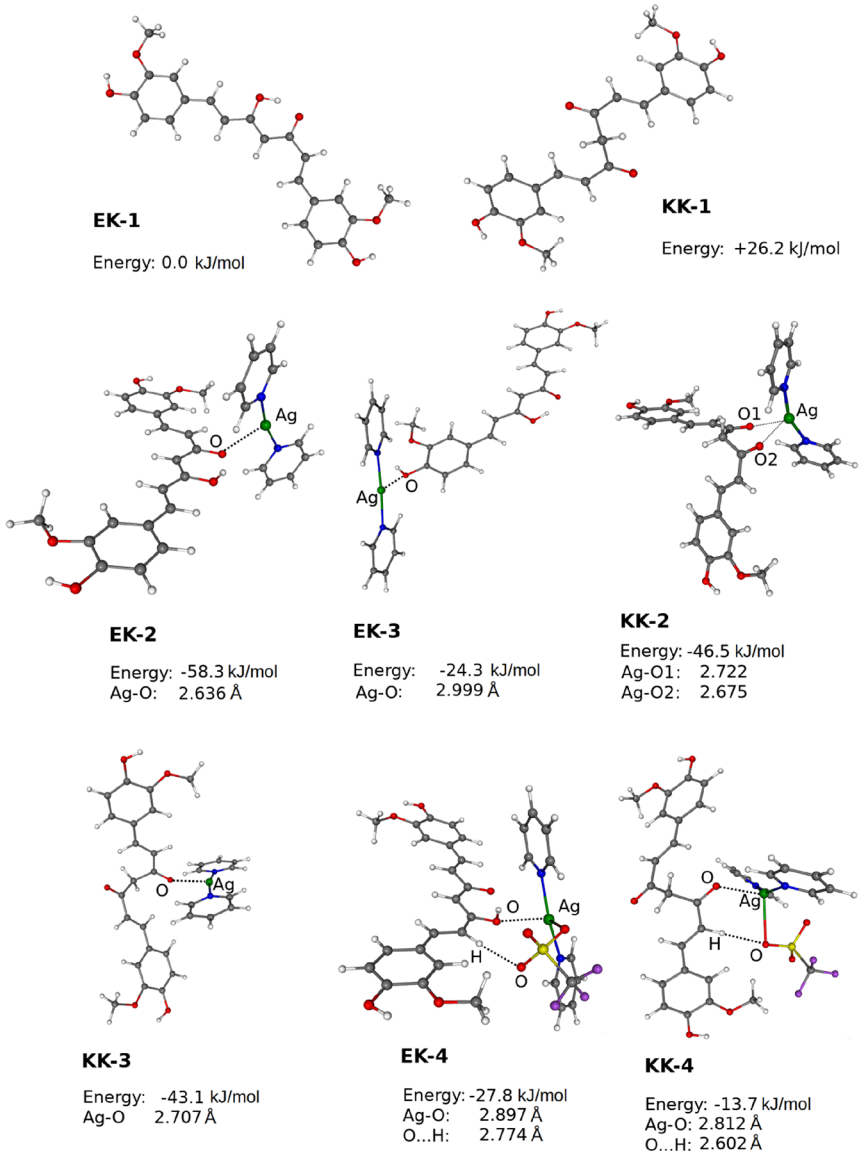

Figure 10. EK-1and KK-1 are the computed structures of curc in vacuum in its keto-enol and diketo forms, respectively. Their relative energies are reported (EK-1 is more stable); EK-2-3 and KK-2-3 are computed adducts between curc and $[(py)_2Ag]^+$. The reported energies are formation energies with respect to relaxed curc (EK-1 in all the four cases) and relaxed $[(py)_2Ag]^+$; EK-4 and KK-4 are the most stable adducts found between curc and $[(py)_2Ag][OTf]$. The reported energies are formation energies with respect to relaxed curc (EK-1) and relaxed $[(py)_2Ag][OTf]$.

~20 kJ/mol[111]), confirms the largely accepted higher stability of the EK form.

Considering all the computed adducts between $[(py)_2Ag]^+$and curc in its EK and KK forms (EK-2-3 and KK-2-3 in Figure 10), it is evident that the EK form still results as the most favored. EK-2 results indeed as the most stable adduct in which the Ag(I) ion interacts with the ketonic function of the EK curc moiety. Ag(I) interactions with the phenolic −OH and −OMe groups are much less effective as evidenced by the energy value of EK-3 in comparison with EK-2. The KK forms are not able to compete with the EK ones in terms of stability; KK-2 is the most stable structure found with curc in the KK form.

With the aim to include the possible effects due to the presence of the OTf counterion in the solid phase, adducts between curc and $[(py)_2Ag][OTf]$ were investigated. EK-4 and KK-4 were found to be the most stable structures (Figure 10) for the two curc tautomers. Evidently, the picture described above is not substantially changed. Likewise, the presence of a couple of $[(py)_2Ag]^+$ was additionally investigated and is described in the Supporting Information. In this case, in all the calculations, the EK form is found to be more stable with respect to the KK ones.

The Ag(I)−curc interaction was further investigated by means of the bonding energy decomposition scheme as implemented in the used ADF software, which is based on the Ziegler and Rauk modification of the Morokuma and Kitaura analysis of the bonding energy between interacting fragments (see the Computational Methods for details and references).

Table 4 collects the results of EK-2 and EK-4. In the first case, while curc and $[(py)_2Ag]^+$ are the two interacting fragments, in the EK-4 analysis, $[(py)_2Ag][OTf]$ is used as a metal-containing fragment. From the reported values, it appears evident that the orbital interaction term is important in establishing the bonding energy. However, it includes

https://doi.org/10.1021/acs.cgd.3c00042
Cryst. Growth Des. XXXX, XXX, XXX−XXX

Table 4. Decomposition of the Bonding Energy between curc and $[(Py)_2Ag]^+$ in EK-2 and between curc and $[(py)_2Ag][OTf]$ in EK-3[a]

energy term	EK-2	EK-4
preparation Energy	+14.1	+23.0
steric repulsion (ΔE_{Pauli})	+72.8	+50.2
electrostatic interaction (ΔE_{elec})	−96.3	−74.0
total steric repulsion ($\Delta E_{Pauli} + \Delta E_{elec}$)	−23.5	−23.8
orbital interaction	−47.8	−26.7
total	−57.1	−27.0
curc charge	Mulliken: +0.06	Mulliken: +0.03
	Hirshfeld: +0.08	Hirshfeld: +0.02

[a]The ZORA/B3LYP/TZP approach was used. Values are in kJ/mol.

polarization effects inside the linked fragments and not only the charge transfer between them. Judging from the computed curc charge in the adduct, only a small amount of charge transfer is described from curc to the Ag(I)-containing fragment (0.06 and 0.03 electrons in EK-2 and EK-4 as estimated through the Mulliken scheme and 0.08 and 0.02 electrons estimated through the Hirshfeld charges, respectively). The lowering of charge transfer passing from EK-2 to EK-4 can be associated to the elongation of the Ag···O distance reported in Figure 10 and also to a reduction of curc polarization passing from the charged $[(py)_2Ag]^+$ to neutral $[(py)_2Ag]OTf$. Moreover, such a lower polarization seems to be mainly responsible for the smaller orbital interaction energy in EK-4 with respect to EK-2. This further supports the hypothesis of a general weak energy gain associated to a charge donation from curc to Ag(I).

From above, curc interacts with the Ag(I) ion mostly through an electrostatic interaction enhanced by polarization effects.

It is possible to summarize the data in Figure 10 and the discussion above with the following statements:

(a) **curc** is expected to maintain the EK form also following the coordination interaction with one or two Ag(I) ions.
(b) The EK-2 adduct (and the related EK-4) spots the more favorable curc interaction site for Ag(I); hence, it is the more worthy to be further investigated. In other words, curc first employs its keto-enolic function when interacting with the $[(bpy)Ag(OTf)]_\infty$ polymer.

With the aim to find experimental evidence of the second statement, FTIR spectra underwent a deeper investigation. In Section 3.2, the changes in the OH stretching bands were discussed (see Figure 7, Table 1, and related discussion). The very broad keto-enol OH stretching band is visible in the curc FTIR spectrum around 2500 cm^{-1} and disappears in the co-crystal. This evidence is a clue in favor of changes in the environment surrounding the curc EK core. In this sense, it could be ascribed to the establishment of the interaction with the Ag(I) center in the co-crystal. However, more insights were gathered from changes in the phenolic OH stretching bands.

As already discussed in Section 3.2, in the curc experimental FTIR spectrum, two bands were detected for the phenolic OH stretching mode at 3507 and ∼3360 cm^{-1}. The band at 3360 cm^{-1} is more intense and broader. This finding allows assigning the solid phase of curc under investigation to the polymorph I, which is the most stable crystalline phase reported to date.[56] The reported and less stable polymorph II shows two phenolic −OH peaks stretching bands as well, whereas form III only presents a single broad OH band (Table 5).[56]

The presence of two bands in the experimental FTIR spectrum of curc was also reported in KBr pellets[111] and is common in FTIR spectra of solid curc due to the higher stability of form I. On the contrary, in solution, a single phenolic OH band is visible: in CCl_4 and $CDCl_3$, sharp bands were reported at 3545 and 3536 cm^{-1}, respectively, which is considered diagnostic of the phenolic groups undergoing weak intramolecular H-bonds. Differently, in acetonitrile, a broader and more intense band at 3374 cm^{-1} was recorded, which is explained as a consequence of a strong H-bond with the solvent.[111] On this basis, we can infer that the two phenol rings of curc are differently involved in H-bonds and/or other interactions with neighboring molecules at least in the two polymorphs I and II.

With the aim to achieve a deeper comprehension, the interactions between adjacent molecules of curc in its polymorph I have been considered. Figure 11 shows couples of curc molecules, which are in contact in the crystal, resulting from the crystallographic analysis.[56] The computed interaction energies of each couple are shown in Figure 11 along with selected structural and spectroscopic data (see the Computational Methods for details about the used methods in the applied structure optimization). Inside the crystal, each curc molecule assumes a non-planar structure in its EK tautomeric form, differently from what is computed in the gas phase in this work and also computed in solution in previous reports.[110,111]

One of the two phenolic groups is clearly rotated with respect to the remaining structure (the keto-enolic central part and the co-planar second phenol ring; see Table 5 for further

Table 5. Experimental and Computed Phenolic OH Stretching Modes and curc Structural Distortion in the Three Polymorphs of Solid curc

crystal	curc distortion (degrees)[a]	experimental phenol νOH (cm^{-1})	computed phenol νOH (cm^{-1}) and their assignment
form I	46.8[a]	two bands: 3507; 3360[c]	3392, phenol−EK core H-bond[e]
		two bands: 3511; 3399[d]	3527−3533, phenol−phenol H-bond[f]
form II	17.0; 12.1[b]	two bands: 3254; 3401[d]	3197, phenol−EK core H-bond[g]
			3406, phenol−phenol H-bond[g]
form III	12.6[b]	one band: 3441[d]	3383, phenol−EK core H-bond[g]
			3432, phenol−phenol H-bond[g]

[a]Dihedral angle between the average plane of the distorted phenol ring (only the ring) and the average plane of the remaining of curc structure; only C and O atoms are used, methyl is fully excluded; experimental values are taken from ref 56. [b]Dihedral angle between the average plane of the distorted phenol ring plus the CHCH group directly connected to it and the average plane of the remaining of curc structure; only C and O atoms are used, methyl is fully excluded. [c]This work. [d]Ref 56. [e]Couple 1 in Figure 11. [f]Couple 3 in Figure 11. [g]See the Supporting Information for details.

https://doi.org/10.1021/acs.cgd.3c00042
Cryst. Growth Des. XXXX, XXX, XXX−XXX

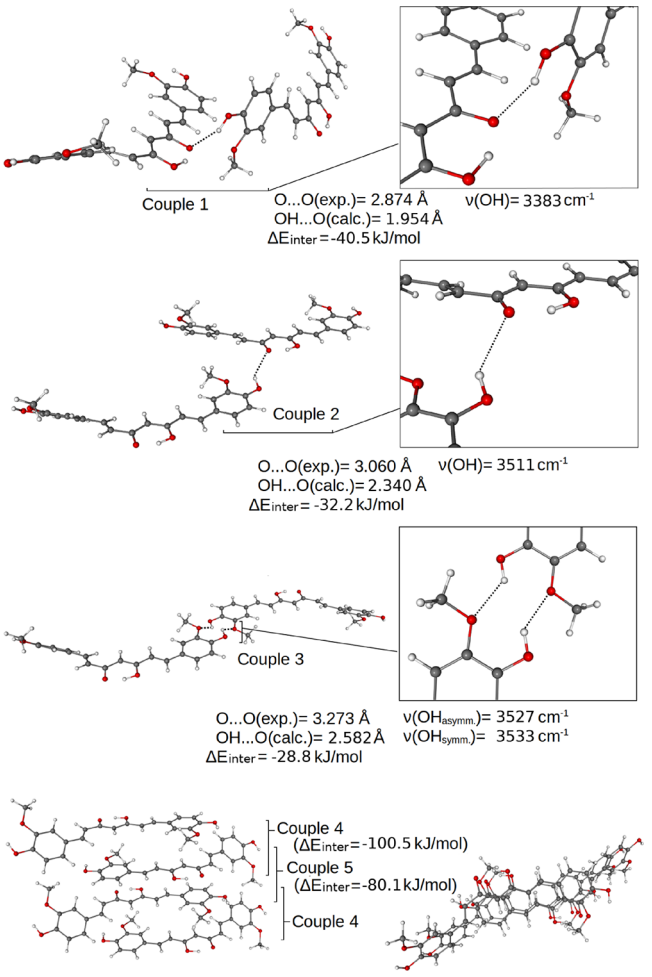

Figure 11. Couples of curc molecules found in contact in the form I crystal. Couples 1−3 model the H-bond contacts. Couples 4−5 alternate themselves to form an infinite monodimensional stack. Two views of a four-molecule part of the stack are sketched in bottom-right and left corners. See the Computational Methods for details on the listed interaction energies (ΔE_{inter}); ν(OH) is the stretching wavenumbers in the anharmonic approximations. In the case of couple 3, symmetric and asymmetric double-OH stretching modes are distinguished.

details). This distortion is to maximize the interaction between the phenolic OH group and the EK central moiety of the adjacent curc molecule. Such a contact is modeled by couple 1 in Figure 11, which shows the shorter of the experimental O···O distances, the shorter of the computed OH···O distances between all the H-bond-forming couples of adjacent molecules (couples 1−3 in Figure 11), and the stronger H-bond (ΔE_{inter} in Figure 11).

Couples 2 and 3 show longer O···O and OH···O distances in comparison to couple 1. They involve the phenolic group coplanar with the keto-enolic central part of the curc structure. Thus, the "distorted" phenol gives rise to the strongest H-bond (couple 1) and the consequently lower computed OH stretching wavelength with respect to couples 2 and 3 (Figure 11 and Table 5). The computed stretching frequency corrected for anharmonicity (ν_{anharm}) amounts to 3392 cm^{-1}. In couples 2 and 3, the same anharmonic wavelengths are calculated to be equal to 3511 and in the 3527−3533 cm^{-1} range, respectively, which is in line with calculations performed on a single curc molecule in vacuum (3538 and 3540 cm^{-1}; the two phenol rings are not symmetry-related) where only the intramolecular phenolic H-bond is present.

From above, our computations clearly assign the red-shifted IR band at ∼3360 cm^{-1} to the rotated phenol ring, which is the one undergoing the stronger H-bond with the EK core of the adjacent curcumin. The sharper and weaker band at 3507 cm^{-1} is assigned to the planar phenol ring, which is not interested in strong H-bond interactions (apart from the intramolecular H-bond). This is in perfect agreement with the previously discussed results on the IR spectra in solutions with different abilities to form H-bonds.

Interestingly, the stronger interactions between curc molecules in the crystal are not H-bonds; rather, they are associated to stacks of almost parallel curc molecules described by couples 3 and 4 in Figure 11. Their interaction energies are largely superior to the ones in couples 1−3, and, in this light, the fact that similar stacks are also present in curc forms II and III can be easily explained. In forms II and III, H-bonds are also present, and they were studied by applying similar computational methods to form I. These results are discussed in the Supporting Information, here, we summarize some findings in Table 5 and in the short discussion below. In both the forms, a lower (but still present) distortion from planarity is present in the curc structure (Table 5). In form II, distorted (17.0°) curc molecules form H-bonds with the EK core of adjacent molecules in a similar way to couple 1 in form I. The resulting phenol OH-stretching mode is computed at 3197 cm^{-1}, which is very close to the experimental peak at 3254 cm^{-1} (Table 5). The other computed OH-stretching modes are associated to weaker phenol H-bonds and to the experimental band at 3401 cm^{-1}. In form III, curc shows a lower distortion from planarity (12.6°) and a weaker H-bond with the EK core of a second molecule. As a result, the related OH stretching mode shifts at 3383 cm^{-1} and overlaps with the OH-stretching bands of the other phenol rings (computationally estimated at 3432 cm^{-1}) to produce a single experimental band at 3441 cm^{-1}.

To summarize the discussion above, a clear correspondence is highlighted between the involvement of the phenol ring in H-bonds with the EK core of a second molecule and the presence of red-shifted bands in the zone of the phenol OH stretching. The point is that, as shown in Figure 7, passing from polymorph I of curc to the co-crystal, a single absorption band at ∼3440 cm^{-1} (blue spectrum) replaces the two peaks (red spectrum) of form I. This finding further confirms the change in the environment surrounding the EK function of curc, which can be easily referred to the interaction of the EK site with the Ag(I) ion. Comparing the computed formation energies of EK-2 and EK-4 (Figure 10) with the interaction energies of couple 1 (Figure 11), it appears evident that the Ag(I) interaction can replace the H-bond between adjacent molecules. On the contrary, the stacks of curc (couples 4 and 5) are expected to be preserved in the formation of the co-crystal owing to their strong interaction.

From above, it is possible to propose tentatively some basic structural characteristics of the $[(bpy)Ag(OTf)]_{\infty}$-curc co-crystal: during co-crystallization, the curc crystal packing is likely preserved in terms of the stack of parallel molecules (couples 4 and 5 in Figure 11, evolving in a similar pattern). The strong H-bond described by couple 1 in Figure 11 is replaced by the Ag(I) coordination interaction. Hence, curc loses the energetic drive for distorting itself from planarity and the two phenolic rings become more symmetric, giving rise to

https://doi.org/10.1021/acs.cgd.3c00042
Cryst. Growth Des. XXXX, XXX, XXX−XXX

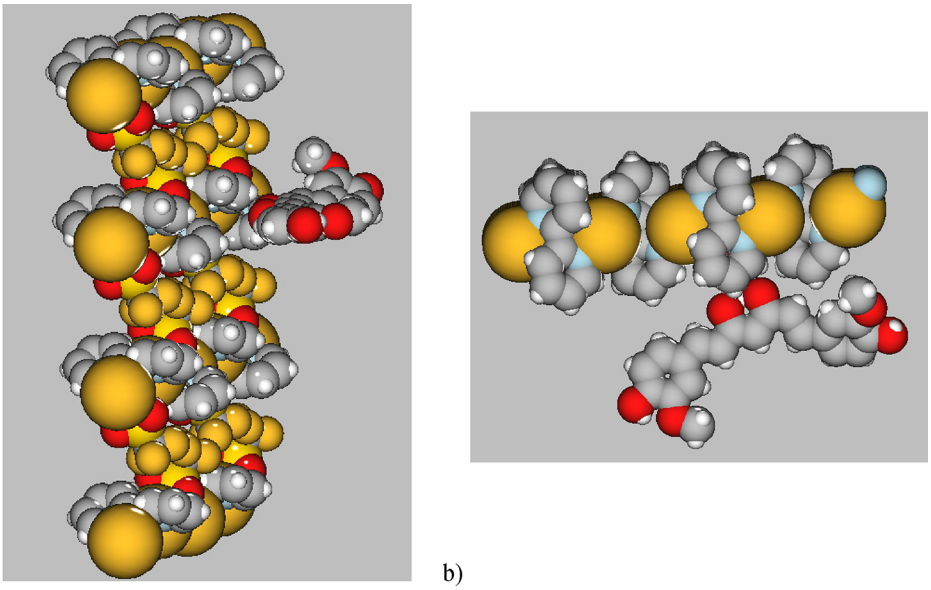

a) b)

Figure 12. Proposed model for the curc-$[(bpy)Ag(OTf)]_\infty$ co-crystal pictured from two different viewpoints, showing (a) the proximity between curc and the $[(bpy)Ag]^+$ cationic chain and (b) the dimensionality ratio between curc and four $[(bpy)Ag]^+$ repeating units.

a single FTIR OH-stretching band. The co-crystal would result in a repetition of two domains: the curc domains (stacks) and adjacent $[(bpy)Ag(OTf)]_\infty$ domains (chains), interacting via coordination interactions between the curc EK moiety and one Ag(I) ion for every four in the crystal. Figure 12, which is obtained by extracting a part of the curc stack in its form I crystal[56] and a small part of the $[Ag(bpy)]^+_\infty$ chain from α-$[(bpy)Ag(OTf)]_\infty$, shows the proposed model for the $[(bpy)Ag(OTf)]_\infty$-curc co-crystal addressed to give a possible description of its crystal structure. Considering that the length of a single curc molecule of approximately 17 Å from the crystal structure in its polymorph I is comparable with the length of four $[(bpy)Ag]^+$ repeating units, it is reasonable to propose that not all the Ag(I) ions are involved in the curc coordination interactions and each curc molecule is surrounded by four Ag(I) metal ions, which is in agreement with the 1:4 ratio between curc and $[(bpy)Ag(OTf)]$ unit as evidenced by NMR measures in this work.

5. CONCLUSIONS

A new structural isomer (β-form) of the already reported Ag(I)-CP $[(bpy)Ag(OTf)]_\infty$ (α-form) has been synthetized and fully characterized. In particular, the β-form was obtained by inverting the sequence of the reagent's addition with respect to the synthesis of the α-form. Hence, the Ag(I) coordination versatility of the bpy ligand is demonstrated when a slight modification of the known synthetic procedure is sufficient to significantly modify the resulting coordination polymer, removing the spontaneous chiral resolution process occurring during crystallization observed in the α-form.

Both isomers of the Ag(I)-CP, α- and β-forms, by virtue of their flexible conformations and silver ions in a low coordination number were used in the preparation of co-crystals with curc (polymorph I). However, curc displays a certain tendency to reduce Ag(I) to Ag(0), which is reasonably ascribed to the reducing properties of the phenolic groups of the polyphenol. Hence, in the attempt to find the best conditions minimizing the formation of Ag(0), the reaction between the α- and β-forms of the Ag(I)-CP and curc was performed in the absence and presence of KOH. In both experimental conditions, a new solid form as evidenced by PXRD analysis was formed; however, in the absence of the base, the new solid form was obtained in a low yield and was not pure since the reaction between curc and the Ag(I) polymer mainly proceeds toward the formation of Ag(0). Therefore, the deprotonation of the phenolic moieties in KOH decreases the reactivity of curc toward the reduction of Ag(I) in the polymeric system $[(bpy)Ag(OTf)]_\infty$. The presence of protonated curc within the binary co-crystal even if obtained in alkaline conditions as well as the decreased reduction of Ag(I) to Ag(0) point out that the lack of chelation or any type of metal coordination of the anionic forms of curc allows for their fast degradation process toward degradation products less powerful as reducing agents. Indeed, the characterization of this new product highlighted the formation of a co-crystal composed of $[(bpy)Ag(OTf)]_\infty$ and curc, meaning a homogeneous crystalline phase in which there is no evidence of a proper metal coordination of curc. Moreover, as proven by the photophysical studies, in the solid state, the $[(bpy)Ag(OTf)]_\infty$-curc co-crystal maintains its integrity, showing distinctive emission and excitation spectra, whereas, in solution, a cleavage of the co-crystal superstructure takes place, resulting in the release of curc and $[(bpy)Ag(OTf)]_\infty$. A comprehensive computational study was performed to unveil the possible interaction modes between the co-crystal components. The theoretical analysis suggested that, within the co-crystal, curc maintains the EK form and the strong H-bond between the ketonic function and a phenolic group of curc observed in the crystal structure of polymorph I is replaced by a coordination interaction between the keto-enol moiety and Ag(I) ions. Finally, preliminary antimicrobial and release tests performed on EC pellets containing the Ag(I)-CP (α- or β-form), the co-crystal, and curc indicate the high antibacterial activity of the Ag(I)-based compounds with a low Ag(I) release. Although curc exhibits much lower antibacterial activity with respect to the Ag(I)-CPs, the co-crystal retains the high antimicrobial performance of the Ag(I) species. On this basis, the co-crystal could be considered to be a multifunc-

https://doi.org/10.1021/acs.cgd.3c00042
Cryst. Growth Des. XXXX, XXX, XXX−XXX

tional system, potentially displaying the multiple properties of curc besides the antimicrobial activity typical of Ag compounds.

■ ASSOCIATED CONTENT

Supporting Information

The Supporting Information is available free of charge at https://pubs.acs.org/doi/10.1021/acs.cgd.3c00042.

Comparison between the PXRD patterns calculated from single-crystal data and those measured on powder samples for the α-form and β-form, crystallographic data for the β-form of $\{[(bpy)Ag][OTf]\}_\infty$, PXRD profile of the grey powder obtained as a byproduct in the preparation of **1a** compared with the Ag reference pattern, PXRD profile of product **1a** compared with curc, α-$[(bpy)Ag(OTf)]_\infty$, and β-$\{[(bpy)Ag][OTf]\}_\infty$ patterns, DSC curve of **1a**, PXRD profiles of product **1** (obtained from the reaction between the α-form and curc; obtained from the reaction between the β-form and curc), ^{1}H NMR spectrum in $CDCl_3$ of product **1**, comparison between PXRD patterns of compounds **1** and **1a**. Excitation and emission spectra of α- and β-form powders, excitation and emission spectra of curc powder, absorption and emission spectra of curc in CH_2Cl_2 solution, absorption and emission spectra of the Ag(I) polymer (α- and β-forms) in diluted CH_2Cl_2 solution, the chosen DFT method applied to the intermolecular interactions in solid curc, hydrogen bonds in curc forms II and III, and a survey on the studied curc−Ag(I) interaction (PDF)

Accession Codes

CCDC 2235451 contains the supplementary crystallographic data for this paper. These data can be obtained free of charge via www.ccdc.cam.ac.uk/data_request/cif, or by emailing data_request@ccdc.cam.ac.uk, or by contacting The Cambridge Crystallographic Data Centre, 12 Union Road, Cambridge CB2 1EZ, UK; fax: +44 1223 336033.

■ AUTHOR INFORMATION

Corresponding Author

Francesca Scarpelli − *MAT-InLAB, LASCAMM CR-INSTM, Unità INSTM della Calabria, Dipartimento di Chimica e Tecnologie Chimiche, Università della Calabria, 87036 Arcavacata di Rende, CS, Italy;* orcid.org/0000-0002-3461-0478; Email: francesca.scarpelli@unical.it

Authors

Alessandra Crispini − *MAT-InLAB, LASCAMM CR-INSTM, Unità INSTM della Calabria, Dipartimento di Chimica e Tecnologie Chimiche, Università della Calabria, 87036 Arcavacata di Rende, CS, Italy;* orcid.org/0000-0002-7522-9323

Massimo La Deda − *MAT-InLAB, LASCAMM CR-INSTM, Unità INSTM della Calabria, Dipartimento di Chimica e Tecnologie Chimiche and CNR-NANOTEC, Istituto di Nanotecnologia UOS Cosenza, Università della Calabria, 87036 Arcavacata di Rende, CS, Italy;* orcid.org/0000-0002-8611-5575

Giuseppe Di Maio − *MAT-InLAB, LASCAMM CR-INSTM, Unità INSTM della Calabria, Dipartimento di Chimica e Tecnologie Chimiche, Università della Calabria, 87036 Arcavacata di Rende, CS, Italy*

Nicolas Godbert − *MAT-InLAB, LASCAMM CR-INSTM, Unità INSTM della Calabria, Dipartimento di Chimica e Tecnologie Chimiche, Università della Calabria, 87036 Arcavacata di Rende, CS, Italy; Laboratorio Preparazione Materiali, Star-Lab, Università della Calabria, 87036 Arcavacata di Rende, CS, Italy;* orcid.org/0000-0002-5659-8844

Antonio Tagarelli − *Dipartimento di Chimica e Tecnologie Chimiche, Università della Calabria, 87036 Arcavacata di Rende, CS, Italy*

Rosangela Elliani − *Dipartimento di Chimica e Tecnologie Chimiche, Università della Calabria, 87036 Arcavacata di Rende, CS, Italy*

Angela Candreva − *MAT-InLAB, LASCAMM CR-INSTM, Unità INSTM della Calabria, Dipartimento di Chimica e Tecnologie Chimiche and CNR-NANOTEC, Istituto di Nanotecnologia UOS Cosenza, Università della Calabria, 87036 Arcavacata di Rende, CS, Italy*

Renata De Rose − *Dipartimento di Chimica e Tecnologie Chimiche, Università della Calabria, 87036 Arcavacata di Rende, CS, Italy*

Iolinda Aiello − *MAT-InLAB, LASCAMM CR-INSTM, Unità INSTM della Calabria, Dipartimento di Chimica e Tecnologie Chimiche and CNR-NANOTEC, Istituto di Nanotecnologia UOS Cosenza, Università della Calabria, 87036 Arcavacata di Rende, CS, Italy; Laboratorio Preparazione Materiali, Star-Lab, Università della Calabria, 87036 Arcavacata di Rende, CS, Italy;* orcid.org/0000-0003-4804-2667

Mario Amati − *Dipartimento di Scienze, Università degli Studi della Basilicata, 85100 Potenza, Italy*

Complete contact information is available at: https://pubs.acs.org/10.1021/acs.cgd.3c00042

Notes

The authors declare no competing financial interest.

■ ACKNOWLEDGMENTS

This work was supported by the Programma Operativo Regionale (POR) Calabria FESR-FSE 2014/2020 and the project PON "Ricerca e Innovazione" 2014-2020, Progetto STAR 2, PIR01_00008, funded by MIUR (Ministero dell'Università e della Ricerca). F.S. is grateful to the project PON "Ricerca e Innovazione" 2014−2020, Asse IV "Istruzione e ricerca per il recupero," and Azione IV.6 "Contratti di ricerca su tematiche Green" (CUP: H25F21001230004; identification code: 1062_R8_GREEN).

■ REFERENCES

(1) Musgrave, R. A.; Russell, A. D.; Hayward, D. W.; Whittell, G. R.; Lawrence, P. G.; Gates, P. J.; Green, J. C.; Manners, I. Main-Chain Metallopolymers at the Static-Dynamic Boundary Based on Nickelocene. *Nat. Chem.* **2017**, *9*, 743−750.

(2) Eloi, J. C.; Chabanne, L.; Whittell, G. R.; Manners, I. Metallopolymers with Emerging Applications. *Mater. Today* **2008**, *11*, 28−36.

(3) Mauro, M.; Bellemin-Laponnaz, S.; Cebrián, C. Metal-Containing Polymers as Light-Emitting and Light-Responsive Materials and Beyond. *Chem. - A Eur. J.* **2017**, *23*, 17626−17636.

(4) Wang, Y.; Astruc, D.; Abd-El-Aziz, A. S. Metallopolymers for Advanced Sustainable Applications. *Chem. Soc. Rev.* **2019**, *48*, 558−636.

(5) Dzhardimalieva, G. I.; Rabinskiy, L. N.; Kydralieva, K. A.; Uflyand, I. E. Recent Advances in Metallopolymer-Based Drug Delivery Systems. *RSC Adv.* **2019**, *9*, 37009−37051.
(6) Yan, Y.; Zhang, J.; Ren, L.; Tang, C. Metal-Containing and Related Polymers for Biomedical Applications. *Chem. Soc. Rev.* **2016**, *45*, 5232−5263.
(7) Bentz, K. C.; Cohen, S. M. Supramolecular Metallopolymers: From Linear Materials to Infinite Networks. *Angew. Chem., Int. Ed.* **2018**, *57*, 14992−15001.
(8) Li, N.; Feng, R.; Zhu, J.; Chang, Z.; Bu, X. H. Conformation Versatility of Ligands in Coordination Polymers: From Structural Diversity to Properties and Applications. *Coord. Chem. Rev.* **2018**, *375*, 558−586.
(9) Rubio-Martinez, M.; Avci-Camur, C.; Thornton, A. W.; Imaz, I.; Maspoch, D.; Hill, M. R. New Synthetic Routes towards MOF Production at Scale. *Chem. Soc. Rev.* **2017**, *46*, 3453−3480.
(10) Viciano-Chumillas, M.; Mon, M.; Ferrando-Soria, J.; Corma, A.; Leyva-Pérez, A.; Armentano, D.; Pardo, E. Metal-Organic Frameworks as Chemical Nanoreactors: Synthesis and Stabilization of Catalytically Active Metal Species in Confined Spaces. *Acc. Chem. Res.* **2020**, 520.
(11) Wyszogrodzka, G.; Marszałek, B.; Gil, B.; Dorozyński, P. Metal-Organic Frameworks: Mechanisms of Antibacterial Action and Potential Applications. *Drug Discovery Today* **2016**, *21*, 1009−1018.
(12) Liu, A.; Wang, C. C.; Wang, C. Z.; Fu, H. F.; Peng, W.; Cao, Y. L.; Chu, H. Y.; Du, A. F. Selective Adsorption Activities toward Organic Dyes and Antibacterial Performance of Silver-Based Coordination Polymers. *J. Colloid Interface Sci.* **2018**, *512*, 730−739.
(13) Liu, J. Q.; Luo, Z. D.; Pan, Y.; Kumar Singh, A.; Trivedi, M.; Kumar, A. Recent Developments in Luminescent Coordination Polymers: Designing Strategies, Sensing Application and Theoretical Evidences. *Coord. Chem. Rev.* **2020**, *406*, No. 213145.
(14) Lawson, H. D.; Walton, S. P.; Chan, C. Metal-Organic Frameworks for Drug Delivery: A Design Perspective. *ACS Appl. Mater. Interfaces* **2021**, *13*, 7004−7020.
(15) Leong, W. L.; Vittal, J. J. One-Dimensional Coordination Polymers: Complexity and Diversity in Structures, Properties, and Applications. *Chem. Rev.* **2011**, *111*, 688−764.
(16) Loukopoulos, E.; Kostakis, G. E. Review: Recent Advances of One-Dimensional Coordination Polymers as Catalysts. *J. Coord. Chem.* **2018**, *71*, 371−410.
(17) Zhu, H.; Liu, D.; Li, Y. H.; Cui, G. H. A 1D Silver(I) Coordination Polymer as Luminescent Probe for Cu2+ and Effective Photocatalyst for Degradation Organic Dyes. *Inorg. Chem. Commun.* **2019**, *108*, No. 107539.
(18) Mondal, S.; Dastidar, P. Zn(II)-Coordination Polymers with a Right- And Left-Handed Twist: Multifunctional Metal-Organic Hybrid for Dye Adsorption and Drug Delivery. *Cryst. Growth Des.* **2020**, *20*, 7411−7420.
(19) Medici, S.; Peana, M.; Crisponi, G.; Nurchi, V. M.; Lachowicz, J. I.; Remelli, M.; Zoroddu, M. A. Silver Coordination Compounds: A New Horizon in Medicine. *Coord. Chem. Rev.* **2016**, *327*−*328*, 349−359.
(20) Lin, I. W. S.; Lok, C. N.; Yan, K.; Che, C. M. A Silver Complex of N, N′-Disubstituted Cyclic Thiourea as an Anti-Inflammatory Inhibitor of IκB Kinase. *Chem. Commun.* **2013**, *49*, 3297−3299.
(21) Scarpelli, F.; Crispini, A.; Giorno, E.; Marchetti, F.; Pettinari, R.; Di Nicola, C.; De Santo, M. P.; Fuoco, E.; Berardi, R.; Alfano, P.; Caputo, P.; Policastro, D.; Oliviero Rossi, C.; Aiello, I. Preparation and Characterization of Silver(I) Ethylcellulose Thin Films as Potential Food Packaging Materials. *Chempluschem* **2020**, *85*, 426−440.
(22) Teyssot, M.-L.; Jarrousse, A.-S.; Manin, M.; Chevry, A.; Roche, S.; Norre, F.; Beaudoin, C.; Morel, L.; Boyer, D.; Mahiou, R.; Gautier, A. Metal-NHC Complexes: A Survey of Anti-Cancer Properties. *Dalton Trans.* **2009**, *35*, 6894.
(23) Hemmert, C.; Fabié, A.; Fabre, A.; Benoit-Vical, F.; Gornitzka, H. Synthesis, Structures, and Antimalarial Activities of Some Silver(I), Gold(I) and Gold(III) Complexes Involving N-Heterocyclic Carbene Ligands. *Eur. J. Med. Chem.* **2013**, *60*, 64−75.
(24) Kalinowska-Lis, U.; Szewczyk, E. M.; Chęcińska, L.; Wojciechowski, J. M.; Wolf, W. M.; Ochocki, J. Synthesis, Characterization, and Antimicrobial Activity of Silver(I) and Copper-(II) Complexes of Phosphate Derivatives of Pyridine and Benzimidazole. *ChemMedChem* **2014**, *9*, 169−176.
(25) Bellusci, A.; Ghedini, M.; Giorgini, L.; Gozzo, F.; Szerb, E. I.; Crispini, A.; Pucci, D. Anion Dependent Mesomorphism in Coordination Networks Based on 2,2′-Bipyridine Silver(i) Complexes. *Dalt. Trans.* **2009**, *36*, 7381−7389.
(26) Khlobystov, A. N.; Blake, A. J.; Champness, N. R.; Lemenovskii, D. A.; Majouga, A. G.; Zyk, N. V.; Schröder, M. Supramolecular Design of One-Dimensional Coordination Polymers Based on Silver(I) Complexes of Aromatic Nitrogen-Donor Ligands. *Coord. Chem. Rev.* **2001**, *222*, 155−192.
(27) Kordestani, N.; Rudbari, H. A.; Fateminia, Z.; Caljon, G.; Maes, L.; Mineo, P. G.; Cordaro, A.; Mazzaglia, A.; Scala, A.; Micale, N. Antimicrobial and Antiprotozoal Activities of Silver Coordination Polymers Derived from the Asymmetric Halogenated Schiff Base Ligands. *Appl. Organomet. Chem.* **2020**, *2020*, 1−14.
(28) Lu, X.; Ye, J.; Sun, Y.; Bogale, R. F.; Zhao, L.; Tian, P.; Ning, G. Ligand Effects on the Structural Dimensionality and Antibacterial Activities of Silver-Based Coordination Polymers. *Dalton Trans.* **2014**, *43*, 10104−10113.
(29) Fromm, K. M. Silver Coordination Compounds with Antimicrobial Properties. *Appl. Organomet. Chem.* **2013**, *27*, 683−687.
(30) Kordestani, N.; Rudbari, H. A.; Fateminia, Z.; Caljon, G.; Maes, L.; Mineo, P. G.; Cordaro, A.; Mazzaglia, A.; Scala, A.; Micale, N. Antimicrobial and Antiprotozoal Activities of Silver Coordination Polymers Derived from the Asymmetric Halogenated Schiff Base Ligands. *Appl. Organomet. Chem.* **2021**, *35*, 1−14.
(31) Steed, J. W. The Role of Co-Crystals in Pharmaceutical Design. *Trends Pharmacol. Sci.* **2013**, *34*, 185−193.
(32) Spizzirri, U. G.; Carullo, G.; De Cicco, L.; Crispini, A.; Scarpelli, F.; Restuccia, D.; Aiello, F. Synthesis and Characterization of a (+)-Catechin and L-(+)-Ascorbic Acid Cocrystal as a New Functional Ingredient for Tea Drinks. *Heliyon* **2019**, *5*, No. e02291.
(33) Lu, B.; Fang, X.; Yan, D. Luminescent Polymorphic Co-Crystals: A Promising Way to the Diversity of Molecular Assembly, Fluorescence Polarization, and Optical Waveguide. *ACS Appl. Mater. Interfaces* **2020**, *12*, 31940−31951.
(34) Christopherson, J. C.; Topić, F.; Barrett, C. J.; Friščić, T. Halogen-Bonded Cocrystals as Optical Materials: Next-Generation Control over Light-Matter Interactions. *Cryst. Growth Des.* **2018**, *18*, 1245−1259.
(35) Khan, A.; Wang, M.; Usman, R.; Sun, H.; Du, M.; Xu, C. Molecular Marriage via Charge Transfer Interaction in Organic Charge Transfer Co-Crystals toward Solid-State Fluorescence Modulation. *Cryst. Growth Des.* **2017**, *17*, 1251−1257.
(36) Chappa, P.; Maruthapillai, A.; Voguri, R.; Dey, A.; Ghosal, S.; Basha, M. A. Drug-Polymer Co-Crystals of Dapsone and Polyethylene Glycol: An Emerging Subset in Pharmaceutical Co-Crystals. *Cryst. Growth Des.* **2018**, *18*, 7590−7598.
(37) Zhong, Z.; Guo, C.; Chen, L.; Xu, J.; Huang, Y. Co-Crystal Formation between Poly(Ethylene Glycol) and a Small Molecular Drug Griseofulvin. *Chem. Commun.* **2014**, *50*, 6375−6378.
(38) Ganesh, M.; Ubaidulla, U.; Rathnam, G.; Jang, H. T. Chitosan-Telmisartan Polymeric Cocrystals for Improving Oral Absorption: In Vitro and in Vivo Evaluation. *Int. J. Biol. Macromol.* **2019**, *131*, 879−885.
(39) Mukherjee, P.; Drew, M. G. B.; Gómez-García, C. J.; Ghosh, A. (Ni2), (Ni3), and (Ni2 + Ni3): A Unique Example of Isolated and Cocrystallized Ni2 and Ni 3 Complexes. *Inorg. Chem.* **2009**, *48*, 4817−4827.
(40) Datta, J.; Nandi, A. K. Cocrystallization of Poly(Vinylidene Fluoride) and Vinylidene Fluoride-Tetrafluoroethylene Copolymers: 1. Effect of Chain Structure and Crystallization Conditions. *Polymer* **1994**, *35*, 4804−4812.

https://doi.org/10.1021/acs.cgd.3c00042
Cryst. Growth Des. XXXX, XXX, XXX−XXX

(41) Thakur, T. S.; Thakuria, R. Crystalline Multicomponent Solids: An Alternative for Addressing the Hygroscopicity Issue in Pharmaceutical Materials. *Cryst. Growth Des.* **2020**, *20*, 6245−6265.
(42) Shaffer, C. C.; Liu, W.; Oliver, A. G.; Smith, B. D. Supramolecular Paradigm for Capture and Co-Precipitation of Gold(III) Coordination Complexes. *Chem. - A Eur. J.* **2021**, *27*, 751−757.
(43) Gao, X. S.; Dai, H. J.; Tang, Y.; Ding, M. J.; Pei, W. B.; Ren, X. M. Crystal Structures, Photoluminescence, and Magnetism of Two Novel Transition-Metal Complex Cocrystals with Three-Dimensional H-Bonding Organic Framework or Alternating Noncovalent Anionic and Cationic Layers. *ACS Omega* **2019**, *4*, 12230−12237.
(44) Hadadzadeh, H.; Mansouri, G.; Rezvani, A. R.; Khavasi, H. R. A Novel 1:1 Co-Crystal of Bis(1,10-Phenanthroline) (1,10-Phenanthroline-5, 6-Dione)Nickel(II) Hexafluorophosphate and Tris(1,10-Phenanthroline)Nickel(II) Hexafluorophosphate Complexes, [Ni-(Phen) 2(Phen-Dione)] [Ni(Phen) 3] (PF 6) 4. *J. Chem. Crystallogr.* **2012**, *42*, 486−493.
(45) Golbedaghi, R.; Salehzadeh, S.; Khavasi, H. R.; Blackman, A. G. Mn(II) Complexes of Three [2 + 2] Macrocyclic Schiff Base Ligands. Synthesis and X-Ray Crystal Structure of the First Binuclear-Di(Binuclear) Cocrystal. *Polyhedron* **2014**, *68*, 151−156.
(46) Nayak, M.; Jana, A.; Fleck, M.; Hazra, S.; Mohanta, S. A Unique Example of a Three Component Cocrystal of Metal Complexes. *CrystEngComm* **2010**, *12*, 1416−1421.
(47) Das, L. K.; Biswas, A.; Gómez-García, C. J.; Drew, M. G. B.; Ghosh, A. Isolation of Two Different Ni2Zn Complexes with an Unprecedented Cocrystal Formed by One of Them and a "Coordination Positional Isomer" of the Other. *Inorg. Chem.* **2014**, *53*, 434−445.
(48) Scarpelli, F.; La Deda, M.; Godbert, N.; Marino, N.; Crispini, A.; Aiello, I. The Strange Case of Metal Coordination in Disubstituted-Biquinolines: Competition between Ligands and Formation of a Hybrid Organic/Inorganic Cu(II)/Cu(I) Ternary Cocrystal. *J. Coord. Chem.* **2022**, *75*, 2448−2470.
(49) Purcell, W.; Basson, S. S.; Leipoldt, J. G.; Roodt, A.; Preston, H. First Structural Confirmation of Different Geometrical Isomers in the Same Crystal Lattice: The Crystal Structure of Benzoylacetonato-carbonyltriphenylphosphinerhodium(I). *Inorganica Chim. Acta* **1995**, *234*, 153−156.
(50) Bellusci, A.; Crispini, A.; Pucci, D.; Szerb, E. I.; Ghedini, M. Structural Variations in Bipyridine Silver(i) Complexes: Role of the Substituents and Counterions. *Cryst. Growth Des.* **2008**, *8*, 3114−3122.
(51) Hung-Low, F.; Renz, A.; Klausmeyer, K. K. An X-Ray Diffraction Study of Anion and Ratio Dependence in the Formation of Discrete Molecules versus Polymeric Arrays Involving Silver Salts and Bipyridine Ligands. *Polyhedron* **2009**, *28*, 407−415.
(52) Sun, J. K.; Yang, X. D.; Yang, G. Y.; Zhang, J. Bipyridinium Derivative-Based Coordination Polymers: From Synthesis to Materials Applications. *Coord. Chem. Rev.* **2019**, *378*, 533−560.
(53) Gupta, N.; Verma, K.; Nalla, S.; Kulshreshtha, A.; Lall, R.; Prasad, S. Free Radicals as a Double-Edged Sword: The Cancer Preventive and Therapeutic Roles of Curcumin. *Molecules* **2020**, *25*, 1−20.
(54) Zheng, D.; Huang, C.; Huang, H.; Zhao, Y.; Khan, M. R. U.; Zhao, H.; Huang, L. Antibacterial Mechanism of Curcumin: A Review. *Chem. Biodiversity* **2020**, DOI: 10.1002/cbdv.202000171.
(55) Hewlings, S.; Kalman, D. Curcumin: A Review of Its Effects on Human Health. *Foods* **2017**, *6*, 92.
(56) Sanphui, P.; Goud, N. R.; Khandavilli, U. B. R.; Bhanoth, S.; Nangia, A. New Polymorphs of Curcumin. *Chem. Commun.* **2011**, *47*, 5013.
(57) Sanphui, P.; Goud, N. R.; Khandavilli, U. B. R.; Nangia, A. Fast Dissolving Curcumin Cocrystals. *Cryst. Growth Des.* **2011**, *11*, 4135−4145.
(58) Rathi, N.; Paradkar, A.; Gaikar, V. G. Polymorphs of Curcumin and Its Cocrystals With Cinnamic Acid. *J. Pharm. Sci.* **2019**, *108*, 2505−2516.
(59) Wong, S. N.; Hu, S.; Ng, W. W.; Xu, X.; Lai, K. L.; Lee, W. Y. T.; Chow, A. H. L.; Sun, C. C.; Chow, S. F. Cocrystallization of Curcumin with Benzenediols and Benzenetriols via Rapid Solvent Removal. *Cryst. Growth Des.* **2018**, *18*, 5534−5546.
(60) Dal Magro, C.; dos Santos, A. E.; Ribas, M. M.; Aguiar, G. P. S.; Volfe, C. R. B.; Lopes, M. L. L. C.; Siebel, A. M.; Müller, L. G.; Bortoluzzi, A. J.; Lanza, M.; Oliveira, J. V. Production of Curcumin-Resveratrol Cocrystal Using Cocrystallization with Supercritical Solvent. *J. Supercrit. Fluids* **2021**, *171*, No. 105190.
(61) Bruker. SAINT. Madison, WI: Bruker AXS Inc. 2003.
(62) Sheldrick, G. M. *SADABS Empirical Absorption Program*. 2003.
(63) Sheldrick, G. M. A Short History of SHELX. *Acta Crystallogr. Sect. A Found. Crystallogr.* **2008**, *64*, 112−122.
(64) Sheldrick, G. M. Crystal Structure Refinement with SHELXL. *Acta Crystallogr. Sect. C Struct. Chem.* **2015**, *71*, 3−8.
(65) Müller, P. Practical Suggestions for Better Crystal Structures. *Crystallogr. Rev.* **2009**, *15*, 57−83.
(66) Dolomanov, O. V.; Bourhis, L. J.; Gildea, R. J.; Howard, J. A. K.; Puschmann, H. OLEX2 : A Complete Structure Solution, Refinement and Analysis Program. *J. Appl. Crystallogr.* **2009**, *42*, 339−341.
(67) Macrae, C. F.; Sovago, I.; Cottrell, S. J.; Galek, P. T. A.; McCabe, P.; Pidcock, E.; Platings, M.; Shields, G. P.; Stevens, J. S.; Towler, M.; Wood, P. A. Mercury 4.0 : From Visualization to Analysis, Design and Prediction. *J. Appl. Crystallogr.* **2020**, *53*, 226−235.
(68) Ionescu, A.; Godbert, N.; Ricciardi, L.; La Deda, M.; Aiello, I.; Ghedini, M.; Rimoldi, I.; Cesarotti, E.; Facchetti, G.; Mazzeo, G.; Longhi, G.; Abbate, S.; Fusè, M. Luminescent Water-Soluble Cycloplatinated Complexes: Structural, Photophysical, Electrochemical and Chiroptical Properties. *Inorganica Chim. Acta* **2017**, *461*, 267−274.
(69) Frisch, M. J.; Trucks, G. W.; Schlegel, H. B.; Scuseria, G. E.; Robb, M. A.; Cheeseman, J. R.; Scalmani, G.; Barone, V.; Mennucci, B.; Petersson, G. A.; Nakatsuji, H.; Caricato, M.; Li, X.; Hratchian, H. P.; Izmaylov, A. F.; Bloino, J.; Zheng, G.; Sonnenb, D. J. *Gaussian 09*, Revision D.01. Gaussian, Inc.: Wallingford CT 2010.
(70) Becke, A. D. A New Mixing of Hartree−Fock and Local Density-functional Theories. *J. Chem. Phys.* **1993**, *98*, 1372−1377.
(71) Weigend, F.; Ahlrichs, R. Balanced Basis Sets of Split Valence, Triple Zeta Valence and Quadruple Zeta Valence Quality for H to Rn: Design and Assessment of Accuracy. *Phys. Chem. Chem. Phys.* **2005**, *7*, 3297.
(72) ADF2019, SCM, *Theoretical Chemistry*, Vrije Universiteit, Amsterdam, The Netherlands, Http://Www.Scm.Com.
(73) te Velde, G.; Bickelhaupt, F. M.; Baerends, E. J.; Fonseca Guerra, C.; van Gisbergen, S. J. A.; Snijders, J. G.; Ziegler, T. Chemistry with ADF. *J. Comput. Chem.* **2001**, *22*, 931−967.
(74) Fonseca Guerra, C.; Snijders, J. G.; te Velde, G.; Baerends, E. J. Towards an Order- N DFT Method. *Theor. Chem. Acc.* **1998**, *99*, 391−403.
(75) van Lenthe, E.; Baerends, E. J.; Snijders, J. G. Relativistic Regular Two-component Hamiltonians. *J. Chem. Phys.* **1993**, *99*, 4597−4610.
(76) van Lenthe, E.; Baerends, E. J.; Snijders, J. G. Relativistic Total Energy Using Regular Approximations. *J. Chem. Phys.* **1994**, *101*, 9783−9792.
(77) Ziegler, T.; Rauk, A. On the Calculation of Bonding Energies by the Hartree Fock Slater Method. *Theor. Chim. Acta* **1977**, *46*, 1−10.
(78) Kitaura, K.; Morokuma, K. A New Energy Decomposition Scheme for Molecular Interactions within the Hartree-Fock Approximation. *Int. J. Quantum Chem.* **1976**, *10*, 325−340.
(79) Zhao, Y.; Truhlar, D. G. The M06 Suite of Density Functionals for Main Group Thermochemistry, Thermochemical Kinetics, Noncovalent Interactions, Excited States, and Transition Elements: Two New Functionals and Systematic Testing of Four M06-Class Functionals and 12 Other Function. *Theor. Chem. Acc.* **2008**, *120*, 215−241.

https://doi.org/10.1021/acs.cgd.3c00042
Cryst. Growth Des. XXXX, XXX, XXX−XXX

(80) Grimme, S.; Antony, J.; Ehrlich, S.; Krieg, H. A Consistent and Accurate Ab Initio Parametrization of Density Functional Dispersion Correction (DFT-D) for the 94 Elements H-Pu. *J. Chem. Phys.* **2010**, *132*, 154104.
(81) Beheshti, A.; Zafarian, H. R.; Khorramdin, R.; Fattahi Monavvar, M.; Abrahams, C. T. Novel Silver(I) Pyrazole-Based Coordination Polymers: Synthetic and Structural Studies. *Polyhedron* **2012**, *48*, 245−252.
(82) Vitõrica-Yrezábal, I. J.; Libri, S.; Loader, J. R.; Mínguez Espallargas, G.; Hippler, M.; Fletcher, A. J.; Thompson, S. P.; Warren, J. E.; Musumeci, D.; Ward, M. D.; Brammer, L. Coordination Polymer Flexibility Leads to Polymorphism and Enables a Crystalline Solid-Vapour Reaction: A Multi-Technique Mechanistic Study. *Chem. - A Eur. J.* **2015**, *21*, 8799−8811.
(83) Kulovi, S.; Pradhan, A.; Maiti, S.; Puschmann, H.; Zangrando, E.; Dalai, S. Polymorphism in [Ag(Bpetan)]n Coordination Polymers with Nitrate and Isophthalate Anions: Photocatalytic and Antibacterial Activity, Hemolysis Assay and Study of Cytotoxicity. *ChemistrySelect* **2020**, *5*, 3337−3346.
(84) Robin, A. Y.; Sague Doimeadios, J. L.; Neels, A.; Vig Slenters, T.; Fromm, K. M. Structure-Property Relationships: Polymorphism, Solvates, and Clay Behavior in the One-Dimensional Coordination Polymer Chains [Ag(L)(NO3)](H2O)n, L = Ethanediyl Bis-(Isonicotinate), n = 0, and 2. *Inorganica Chim. Acta* **2007**, *360*, 212−220.
(85) Janasi, S. R.; Rodrigues, D.; Emura, M.; Landgraf, F. J. G. Barium Ferrite Powders Obtained by Co-Precipitation. *Phys. Status Solidi Appl. Res.* **2001**, *185*, 479−485.
(86) Newman, A. Specialized Solid Form Screening Techniques. *Org. Process Res. Dev.* **2013**, *17*, 457−471.
(87) Kuzmicheva, G. M.; Savinkina, E. V.; Obolenskaya, L. N.; Zubavichus, Y. V.; Murzin, V. Y.; Podbelskiy, V. V.; Sadovskaya, N. V. Synthesis of Mn-Sensitized TiO 2 Nanoparticles: Influence of Sequence of Reagents on Phase Composition and Photocatalytic Activity. *J. Nanopart. Res.* **2015**, *17*, 1−12.
(88) Argyle, V. J.; Woods, L. M.; Roxburgh, M.; Hanton, L. R. Triflate Anion and Ligand Influences in Silver(i) Coordination Polymers of Four Isomeric Dipyridyl Ketone Oximes. *CrystEngComm* **2013**, *15*, 120−134.
(89) Syed, H. K.; Iqbal, M. A.; Haque, R. A.; Peh, K. K. Synthesis, Characterization and Antibacterial Activity of a Curcumin-Silver(I) Complex. *J. Coord. Chem.* **2015**, *68*, 1088−1100.
(90) Sanphui, P.; Bolla, G. Curcumin, a Biological Wonder Molecule: A Crystal Engineering Point of View. *Cryst. Growth Des.* **2018**, *18*, 5690−5711.
(91) Sathisaran, I.; Dalvi, S. V. Crystal Engineering of Curcumin with Salicylic Acid and Hydroxyquinol as Coformers. *Cryst. Growth Des.* **2017**, *17*, 3974−3988.
(92) Verma, A. D.; Jain, N.; Singha, S. K.; Quraishi, M. A.; Sinha, I. Green Synthesis and Catalytic Application of Curcumin Stabilized Silver Nanoparticles. *J. Chem. Sci.* **2016**, *128*, 1871−1878.
(93) Gupta, A.; Briffa, S. M.; Swingler, S.; Gibson, H.; Kannappan, V.; Adamus, G.; Kowalczuk, M.; Martin, C.; Radecka, I. Synthesis of Silver Nanoparticles Using Curcumin-Cyclodextrins Loaded into Bacterial Cellulose-Based Hydrogels for Wound Dressing Applications. *Biomacromolecules* **2020**, *21*, 1802−1811.
(94) Khan, M. J.; Shameli, K.; Sazili, A. Q.; Selamat, J.; Kumari, S. Rapid Green Synthesis and Characterization of Silver Nanoparticles Arbitrated by Curcumin in an Alkaline Medium. *Molecules* **2019**, *24*, 719.
(95) Soto-Quintero, A.; Guarrotxena, N.; García, O.; Quijada-Garrido, I. Curcumin to Promote the Synthesis of Silver NPs and Their Self-Assembly with a Thermoresponsive Polymer in Core-Shell Nanohybrids. *Sci. Rep.* **2019**, *9*, 1−14.
(96) Kumavat, S. D.; Chaudhari, Y. S.; Borole, P.; Mishra, P.; Shenghani, K.; Duvvuri, P. Degradation Studies of Curcumin. *Int. J. Pharm. Rev. Res.* **2013**, *3*, 50−55.
(97) Schneider, C.; Gordon, O. N.; Edwards, R. L.; Luis, P. B. Degradation of Curcumin: From Mechanism to Biological Implications. *J. Agric. Food Chem.* **2015**, *63*, 7606−7614.
(98) Jankun, J.; Wyganowska-Swiatkowska, M.; Dettlaff, K.; JelinSka, A.; Surdacka, A.; Watróbska-Swietlikowska, D.; Skrzypczak-Jankun, E. Determining Whether Curcumin Degradation/Condensation Is Actually Bioactivation (Review). *Int. J. Mol. Med.* **2016**, *37*, 1151−1158.
(99) Kharat, M.; Du, Z.; Zhang, G.; McClements, D. J. Physical and Chemical Stability of Curcumin in Aqueous Solutions and Emulsions: Impact of PH, Temperature, and Molecular Environment. *J. Agric. Food Chem.* **2017**, *65*, 1525−1532.
(100) Zhao, X. Z.; Jiang, T.; Wang, L.; Yang, H.; Zhang, S.; Zhou, P. Interaction of Curcumin with Zn(II) and Cu(II) Ions Based on Experiment and Theoretical Calculation. *J. Mol. Struct.* **2010**, *984*, 316−325.
(101) Priyadarsini, K. I. The Chemistry of Curcumin: From Extraction to Therapeutic Agent. *Molecules* **2014**, *19*, 20091−20112.
(102) Zhu, J.; Sanidad, K. Z.; Sukamtoh, E.; Zhang, G. Potential Roles of Chemical Degradation in the Biological Activities of Curcumin. *Food Funct.* **2017**, *8*, 907−914.
(103) Mohan, P. R. K.; Sreelakshmi, G.; Muraleedharan, C. V.; Joseph, R. Water Soluble Complexes of Curcumin with Cyclodextrins: Characterization by FT-Raman Spectroscopy. *Vib. Spectrosc.* **2012**, *62*, 77−84.
(104) Tayyari, S. F.; Zeegers-Huyskens, T.; Wood, J. L. Spectroscopic Study of Hydrogen Bonding in the Enol Form of *β*-Diketones—I. Vibrational Assignment and Strength of the Bond. *Spectrochim. Acta, Part A* **1979**, *35*, 1265−1276.
(105) Chiavassa, T.; Verlaque, P.; Pizzala, L.; Roubin, P. Vibrational Studies of Methyl Derivatives of Malonaldehyde: Determination of a Reliable Force Field for *β*-Dicarbonyl Compounds. *Spectrochim. Acta, Part A* **1994**, *50*, 343−351.
(106) Hansen, P. E.; Spanget-Larsen, J. NMR and IR Investigations of Strong Intramolecular Hydrogen Bonds. *Molecules* **2017**, *22*, 552.
(107) Subhan, M. A.; Alam, K.; Rahaman, M. S.; Rahman, M. A.; Awal, R. Synthesis and Characterization of Metal Complexes Containing Curcumin ($C_{21}H_{20}O_6$) and Study of Their Anti-Microbial Activities and DNA-Binding Properties. *J. Sci. Res.* **2014**, *6*, 97−109.
(108) Frei, A.; Zuegg, J.; Elliott, A. G.; Baker, M.; Braese, S.; Brown, C.; Chen, F. G.; Dowson, C.; Dujardin, G.; Jung, N.; King, A. P.; Mansour, A. M.; Massi, M.; Moat, J.; Mohamed, H. A.; Renfrew, A. K.; Rutledge, P. J.; Sadler, P. J.; Todd, M. H.; Willans, C. E.; Wilson, J. J.; Cooper, M. A.; Blaskovich, M. A. T. Metal Complexes as a Promising Source for New Antibiotics. *Chem. Sci.* **2020**, *11*, 2627−2639.
(109) Lu, X.; Ye, J.; Zhang, D.; Xie, R.; Bogale, R. F.; Sun, Y.; Zhao, L.; Zhao, Q.; Ning, G. Silver Carboxylate Metal-Organic Frameworks with Highly Antibacterial Activity and Biocompatibility. *J. Inorg. Biochem.* **2014**, *138*, 114−121.
(110) Manolova, Y.; Deneva, V.; Antonov, L.; Drakalska, E.; Momekova, D.; Lambov, N. The Effect of the Water on the Curcumin Tautomerism: A Quantitative Approach. *Spectrochim. Acta Part A* **2014**, *132*, 815−820.
(111) Kolev, T. M.; Velcheva, E. A.; Stamboliyska, B. A.; Spiteller, M. DFT and Experimental Studies of the Structure and Vibrational Spectra of Curcumin. *Int. J. Quantum Chem.* **2005**, *102*, 1069−1079.

https://doi.org/10.1021/acs.cgd.3c00042
Cryst. Growth Des. XXXX, XXX, XXX−XXX